Tests on Concrete Beams with GFRP Flexural and Shear Reinforcements
&
Analysis Method for Indeterminate Strut-and-Tie Models with Brittle Reinforcements

by

Martin D. Krall

A thesis
presented to the University of Waterloo
in fulfilment of the
thesis requirement for the degree of
Master of Applied Science
in
Civil Engineering

Waterloo, Ontario, Canada, 2014

Author’s Declaration

I hereby declare that I am the sole author of this thesis. This is a true copy of the thesis, including any required final revisions, as accepted by my examiners.

I understand that my thesis may be made electronically available to the public.

Abstract

This thesis is a summary of research on the use of glass fibre reinforced polymer (GFRP) bars and stirrups as internal reinforcement for concrete beams. Fibre reinforced polymer bars are geometrically similar to conventional steel reinforcement. They are made of a bundle of long glass fibres bound together by a polymer matrix. The bars are strong when loaded in tension parallel to the fibres, and weak when loaded in any other direction. Fibre reinforced polymers are linear-elastic-to-brittle-rupture materials. Unlike steel reinforcement, bent FRP shapes must be made at the time of manufacture, before the polymer cures.

Fibre reinforced polymer stirrups, and other bent shapes, are known to prematurely rupture at the bends. Initially, this was a concern for the shear design of FRP reinforced concrete beams; however, the phenomenon is generally accepted by those who work with the material and aspects of the phenomenon are considered in the provisions of modern FRP reinforced concrete design codes and standards.

On occasion other researchers observed full utilization of the straight portion strength of FRP stirrups, and one study suggested that the longitudinal bar arrangement may impact stirrup utilization. Therefore, the experimental program described in this thesis was devised to investigate the influence of longitudinal bar arrangements on GFRP stirrup utilization for beams failing in diagonal shear-tension.

However, the experimental beams all failed in a form of shear-compression & strut-crushing and not by diagonal shear tension, so no stirrups ruptured and the original objective could not be tested. The failure modes were concrete controlled and the experimental results indicated deep beam behaviour.

The original analysis method was precluded by the unintended failure modes, so an element of novelty was incorporated into the research by applying an analysis method for strut-and-tie modelling of steel reinforced concrete that did not require the assumption of steel yielding to find a lower bound solution. That method was developed by Kim and Yun (2011a). A generalized form of the method was modified for this research to account for FRP, which necessitated modifications to other aspects such as the failure conditions and element geometry. The modified method is referred to as the Indeterminate Strut-and-Tie (IST) method throughout this thesis.

Current literature on the strut-and-tie modelling of FRP reinforced concrete focuses exclusively on deep beams without stirrups, which are modelled by determinate strut-and-tie trusses. Without the yielding assumption it is not possible to solve an indeterminate strut-and-tie truss without resorting to traditional structural analysis methods. The novelty of the IST method is not simply the application of Yun's work to FRP reinforced concrete, but that it is also the only method capable of finding a lower bound solution to FRP reinforced deep beams with indeterminate strut-and-tie trusses.

The IST method uses traditional structural analysis methods to solve for the forces in a strut-and-tie truss. The concrete struts are modelled using one-dimensional, non-linear material behaviour that is modified with softening coefficients as described in Yun's research. The method applies load in increasing increments and at each increment the stiffness matrix updates by accounting for changes in concrete strut elasticity. The IST method is also capable of modelling other beam behaviours such as strains and deflections.

The research found that the IST method was the best at predicting the strength of the experimental beams when compared to both the best available academic model and the most modern design standard.

Acknowledgements

I would like to thank:

- Dr. Maria-Anna Polak, my graduate supervisor, who allowed me great independence in my studies, and the freedom to make mistakes and learn from them.
- Joe Stoner, my officemate, for his assistance during the beam tests, for keeping my remote connection working while I was off campus, and for running copies of my thesis around campus in the final days before its acceptance. Thank you so much for all your help!
- Ben Scott for his help constructing the formwork.
- Alireza Masnavi & Dritan Topuzi who assisted with the concrete pour.
- Dan Pickle for his help patching the beams in a clutch moment just after the concrete pour.
- Serhan Kırlangıç for his help with the first test just before leaving for Turkey with his doctorate in hand.
- Other members of Dr. Polak's research team: Paulina Arczewska for our relaxed and technical conversations, Katerina Genikomsou for her grace and intellect, and George Balomenos, the unofficial member, for being the most approachable and friendliest PhD candidate in the department.
- Dr. Robert Gracie, for insisting I learn MATLAB, and for graciously allowing me to borrow and modify segments of his CivE 611 assignment code to develop the analysis method.
- Richard Morrison, Doug Hirst, Rob Sluban, and Mike Burgetz, the Structures Lab technicians, without whom the beam specimens would be mere calculations and drawings; but especially Richard, who always found the time and patience to mentor students through their problems.
- Dr. Mahesh Pandey, who made the study of engineering statistics approachable and enjoyable.
- Kristine Meier, for providing a welcome, comforting space, and refreshing conversation.
- Dr. Scott Walbridge, for teaching me Concrete 2 and later allowing me to be a teaching assistant for it, and who need no longer worry about assigning stiffness values to the elements of an indeterminate strut-and-tie model, as he strongly advised me against doing a full year and a half before I ever read the papers that formed a basis for the analysis method presented in this thesis.
- Dr. Young Mook Yun, whom I have never met, for his innovative PhD and post-doctoral work on the analysis of strut-and-tie models using non-linear, one-dimensional, concrete material models.
- The Ontario Centres of Excellence, for their financial contributions to Dr. Polak's research projects.
- Schöck, for donating glass fibre reinforced polymer bars and stirrups to this research programme.
- HOGG Ready Mix, for donating the concrete of the beam specimens.
- Daniel Wrobel, my partner, for providing his love and support through the entire process.
- Dan Krall and Diane Brouwer, my parents for their emotional and financial support.
- Elizabeth Jaeger, my grandmother, for her genuine interest in my research, and for our bi-weekly fish-and-chips dinners.

I would also like to acknowledge:

- Steven McPherson & Adam Garcia for helping to settle Catan a few hundred times, James Saliba for opening his home to me, Shirley Springall for always having a smile and a moment, Victoria Tolton for so much, Fred Bakker & Jorge Cruz of the Engineering Machine Shop, Doug Morton the civil engineering librarian, Lara Saliba, Colin Van Niejenhuis, & Jamie Yeung.
- The Engineering C'n'D, Pita Factory, & Kismet, for so many lunches and dinners.

Table of Contents

List of Figures ..... **ix**
List of Tables ..... **xi**
List of Symbols ..... **xii**

1 Introduction **1**
1.1 Fibre Reinforced Polymers as Internal Reinforcing in General 1
1.1.1 Fibre Reinforced Polymer Components 1
1.1.2 Material Behaviour 2
1.2 Use of FRP Reinforcing Bars 3
1.3 Manufacture of FRP Reinforcement 3
1.4 Bend Strength 4
1.4.1 Manufacturing Defects for Bent Bars 5
1.4.2 Transverse Loading Along the Bend 6
1.4.3 Transverse Loading Across Shear Cracks 6
1.5 Shear Transfer Mechanisms 7
1.6 Bend Strength Exceptions 9
1.7 Aspects of Strut-and-Tie Modelling 10
1.8 Objectives 10
1.8.1 Original Objective 10
1.8.2 Modified Objectives 11
1.9 Thesis Organization 11
2 Literature Review **13**
2.1 Experimental Tests 13
2.1.1 “Mechanical Performance of Curved FRP Rebars – Part I: Experimental Study” by Imjai et al., 2007 13
2.1.2 “Performance Evaluation of Glass Fiber-Reinforced Polymer Shear Reinforcement for Concrete Beams” & “Shear Performance of RC Bridge Girders Reinforced with Carbon FRP Stirrups” by Ahmed et al., 2010 15
2.1.3 “Shear Strength of Large Concrete Members with FRP Reinforcement” by Bentz et al., 2010 17
2.1.4 “Fibre Reinforced Polymer Shear Reinforcement for Concrete Members: Behaviour and Design Guidelines” by Shehata et al., 2000 19
2.2 Shear Strength Prediction Methods for FRP Reinforced Concrete Beams 21
2.2.1 CSA S806-12 Design and Construction of Building Structures with Fibre-Reinforced Polymers – Sectional Shear Method 21
2.2.2 “Revisiting the Shear Design Equations for Concrete Beams Reinforced with FRP Rebar and Stirrup” by Machial et al., 2012 24
2.2.3 “Proposed Shear Design Equations for FRP-Reinforced Concrete Beams Based on Genetic Algorithms Approach” Nehdi et al., 2007 25
2.3 Strut-and-Tie Modelling of FRP Reinforced Concrete Beams 27

2.3.1 CSA S806-12 Design and Construction of Building Structures with Fibre-Reinforced Polymers – Strut-and-Tie Method 28
2.3.2 ACI 318-08 Building Code Requirements for Structural Concrete 29
2.3.3 "Strength Modelling of Concrete Deep Beams Reinforced with Internal Fiber-Reinforced Polymer" by Andermatt et al., 2013 30
2.3.4 "Optimal efficiency factor in strut-and-tie model for FRP-reinforced concrete short beams with (1.5 < a/d <2.5)" by Nehdi et al., 2008 32
2.3.5 "Shear Behavior of FRP-Reinforced Concrete Deep Beams without Web Reinforcement" by Farghaly et al., 2013 35
2.4 Dr. Young Mook Yun's Analysis Method for Indeterminate Strut-and-Tie Models with Steel Reinforcement 37
2.5 Summary of Observations on Strut-and-Tie Modelling with FRP Reinforcements 43
2.6 Alternative Concrete Material Model 44
3 Experimental Design 46
3.1 Introduction 46
3.2 Experimental Design Parameters 46
3.3 Shear and Flexural Strength Predictions 50
3.4 The Selection of Concrete Strength and Stirrup Spacing by Monte-Carlo Analysis 52
3.5 Reinforcing Materials 53
3.5.1 Stirrups and Closed Loop Detailing 54
3.6 Specimen Fabrication 56
3.7 Instrumentation 60
3.8 Beam Set-up and Test Procedure 62
4 Experimental Observations 64
4.1 Concrete 64
4.2 General Observations 64
4.2.1 Stirrups 64
4.2.2 Failure Modes 65
4.2.3 Cracking 66
4.2.4 Longitudinal Strain 66
4.2.5 Stirrup Strain 68
4.2.6 Other Observations 70
4.3 Individual Beam Results 70
4.3.1 BM12-INF 71
4.3.2 BM16-INF 72
4.3.3 BM25-INF 73
4.3.4 BM12-220 74
4.3.5 BM16-220 76
4.3.6 BM25-220 78
4.3.7 BM12-150 80
4.3.8 BM16-150 82
4.3.9 BM25-150 84

4.3.10 BM12-s230 86
4.3.11 BM16-s230 88
4.3.12 BM25-s230 90
4.4 Summary of Results by Beam Series 92
5 Development of the Indeterminate Strut-and-Tie Analysis Method for FRP Reinforced Concrete 95
5.1 Motivation for the Development of the Indeterminate Strut-and-Tie Analysis Method for FRP Reinforced Concrete 95
5.1.1 The Indeterminate Strut-and-Tie Method in Brief 96
5.1.2 Chapter Organization 97
5.2 Strut-and-Tie Modelling Philosophy 97
5.2.1 Design and Analysis with Steel Ties 97
5.2.2 Exploiting Lower Bound Plasticity Theory when Modelling with FRP Ties 98
5.3 Failure Conditions for FRP Strut-and-Tie Models 100
5.3.1 System Failure 100
5.3.2 Strut Crushing 100
5.3.3 Tie Rupture 100
5.3.4 Node Crushing 101
5.3.5 Other Considerations 101
5.4 Idealizing Continuous Cracked Reinforced Concrete as Simple Truss Elements 101
5.4.1 Tie Elements 102
5.4.2 Struts Elements 103
5.4.3 Node Elements 104
5.5 Defining the Geometry of Strut-and-Tie Elements for use with the Indeterminate Strut-and-Tie Method 105
5.5.1 Defining the Geometry of Ties 105
5.5.2 Defining the Geometry of Nodes 106
5.5.3 Defining the Geometry of Struts and Internal Nodes for the Indeterminate Strut-and-Tie Method 107
5.6 Material Models 110
5.6.1 FRP Tension Ties 110
5.6.2 Concrete Struts 110
5.6.3 Softening Coefficient Modified Hognestad Parabola (Kim and Yun, 2011a) 111
5.6.4 Softening Coefficient Modified Model by Thorenfeldt et al. (1987) 112
5.6.5 Nodal Zones 114
5.7 Design and Analysis Process 114
5.8 Design Example Applied to BM25-220 115
5.8.1 Model Geometry 115
5.8.2 Commentary on Node Geometry 117
5.8.3 Clarification on Assigning Node and Strut Dimensions 117
5.8.4 Define Material Properties and Element Strengths 118
5.8.5 Results and Discussion on General Model Behaviour 118

5.8.6 Other Observations 121
5.9 On the Choice of Material Model and Initial Parameters 121
5.9.1 A Comment on the Choice of Softening Coefficients 123
5.9.2 Input Parameters Used in the Analysis Presented in Chapter 6 124
6 Analysis 125
6.1 Comparing Predictions to Experimental Results 125
6.1.1 Truss Models for the Indeterminate Strut-and-Tie Method 125
6.1.2 Tensile Failures 129
6.1.3 The Comparison 130
6.2 Analysis of Beam Behaviour 133
6.2.1 Determining the Concrete Contribution to Shear Strength 133
6.2.2 Experimental Beam Behaviour 137
6.3 Investigation into the Ability of the Indeterminate Strut-and-Tie Method to Model Beam Behaviour 141
6.3.1 Capturing Strain and Displacement Behaviour 141
6.3.2 Strains and Displacements at Peak Load 145
6.4 On Analytical and Design Models of the IST Method 148
6.4.1 On Designing with the IST Method 149
7 Conclusions and Recommendations 150
7.1 Review of Thesis 150
7.2 Conclusions 151
7.2.1 Experimental Observations and Beam Behaviour 151
7.2.2 The Indeterminate Strut-and-Tie Method 153
7.2.3 CSA-S806-12 154
7.3 Recommendations 154
References 156
Appendices 162
A: Monte Carlo Analysis of Probable Shear Failure 163
B: Procedure for Affixing Strain Gauges to GFRP Surface 174
C: Experimental Procedure for GFRP Shear Critical Beam Tests 178
D: Compressive Strength and Tensile Strength Testing 183
E: Individual Beam Descriptions 186
F: MATLAB Code for the Indeterminate Strut-and-Tie Method 334

List of Figures

Figure 1.1: Comparison of Reinforcement Stress-Strain Behaviours 2
Figure 2.1: Strut-and-Tie Model Adapted from Kim and Yun (2011a) 41
Figure 3.1: Elevation for Beam BM25-220 and Schematic Cross-Sections for All Beams 49
Figure 3.2: Scatter Plot of Predicted Failure Load against Concrete Strength 53
Figure 3.3: Collection of Closed Loop GFRP Stirrup Photos 54
Figure 3.4: Collection Rebar Cage Photos for Beam BM16-150 57
Figure 3.5: Collection of Formwork Module Photos for the Group 16 Beams 58
Figure 3.6: Collection of Rebar Blocking Photos 58
Figure 3.7: Typical Extent of Honeycombing 60
Figure 3.8: LVDT Gauge Set-up and Positioning 61
Figure 3.9: Schematic of Beam Ready for Testing 62
Figure 4.1: BM12-220 Bend of Stirrup 7 65
Figure 4.2: Post-Peak Photos 65
Figure 4.3: BM25-150 Plot of Load vs Mid-Span Strain 66
Figure 4.4: BM16-220 Arch Action Plot 67
Figure 4.5: BM25-150 Plot of Load vs Stirrup Strain 68
Figure 4.6: BM16-150 Straight Portion Stirrup Action Plot 69
Figure 4.7: BM12-INF Peak Load Crack Diagram 71
Figure 4.8: BM12-INF Plot of Load vs Displacement 71
Figure 4.9: BM16-INF Peak Load Crack Diagram 72
Figure 4.10: BM16-INF Plot of Load vs Displacement 72
Figure 4.11: BM25-INF Peak Load Crack Diagram 73
Figure 4.12: BM25-INF Plot of Load vs Displacement 73
Figure 4.13: BM12-220 Peak Load Crack Diagram 74
Figure 4.14: BM12-220 Plot of Load vs Displacement 74
Figure 4.15: BM12-220 Plot of Load vs Strain on Stirrups 75
Figure 4.16: BM16-220 Peak Load Crack Diagram 76
Figure 4.17: BM16-220 Plot of Load vs Displacement 76
Figure 4.18: BM16-220 Plot of Load vs Strain on Stirrups 77
Figure 4.19: BM25-220 Peak Load Crack Diagram 78
Figure 4.20: BM25-220 Plot of Load vs Displacement 78
Figure 4.21: BM25-220 Plot of Load vs Strain on Stirrups 79
Figure 4.22: BM12-150 Peak Load Crack Diagram 80
Figure 4.23: BM12-150 Plot of Load vs Displacement 80
Figure 4.24: BM12-150 Plot of Load vs Strain on Stirrups 81
Figure 4.25: BM16-150 Peak Load Crack Diagram 82
Figure 4.26: BM16-150 Plot of Load vs Displacement 82
Figure 4.27: BM16-150 Plot of Load vs Strain on Stirrups 83
Figure 4.28: BM25-150 Peak Load Crack Diagram 84

Figure 4.29: BM25-150 Plot of Load vs Displacement 84
Figure 4.30: BM25-150 Plot of Load vs Strain on Stirrups 85
Figure 4.31: BM12-s230 Peak Load Crack Diagram 86
Figure 4.32: BM12-s230 Plot of Load vs Displacement 86
Figure 4.33: BM12-s230 Plot of Load vs Strain on Stirrups 87
Figure 4.34: BM16-s230 Peak Load Crack Diagram 88
Figure 4.35: BM16-s230 Plot of Load vs Displacement 88
Figure 4.36: BM16-s230 Plot of Load vs Strain on Stirrups 89
Figure 4.37: BM25-s230 Peak Load Crack Diagram 90
Figure 4.38: BM25-s230 Plot of Load vs Displacement 90
Figure 4.39: BM25-s230 Plot of Load vs Strain on Stirrups 91
Figure 4.40: All Beam Comparison of Load vs Displacement 93
Figure 5.1: Considering the Location of a Critical Shear Crack with Respect to Stirrup Bends 106
Figure 5.2: GFRP Stress-Strain Curve for the 25 mm Bars 110
Figure 5.3: Material Model Comparison with Softening Coefficient Influence 113
Figure 5.4: Centre-Line Geometry of the Strut-and-Tie Truss for beam BM25-220 115
Figure 5.5: Centre-Line Geometry of the Strut-and-Tie Truss for beam BM25-220 116
Figure 5.6: Evolution of Strut Elasticity 119
Figure 5.7: Applied Load Carried by Each Load Transfer Mechanism 120
Figure 5.8: Diagram for the Clarification of the Process by which Nodal Stresses are Determined 121
Figure 5.9: Plot of the Results of the Investigation into Modelling Parameters 123
Figure 6.1: Strut-and-Tie Model Truss Types for Analysis 126
Figure 6.2: Determining V_c from load vs stirrup strain plots for BM16-s230 134
Figure 6.3: V_A, V_s, &V_c curves for BM25-150 135
Figure 6.4: Concrete Contribution Comparison Chart 137
Figure 6.5: Variation in V_c with Flexural Reinforcement Ratio 138
Figure 6.6: Variation in V_c with Shear Reinforcement Ratio 138
Figure 6.7: Variation in V_s with Shear Reinforcement Ratio 139
Figure 6.8: Variation in V_s with Shear Reinforcement Ratio 139
Figure 6.9: Variation the Product of Peak Load and Flexural Reinforcement Ratio against Shear Reinforcement Ratio 140
Figure 6.10: Longitudinal Strain at Mid-Span for BM25-150 with the IST Method Prediction 141
Figure 6.11: Longitudinal Strain at Mid-Span for BM16-INF with the IST Method Prediction 142
Figure 6.12: Stirrup Strain for BM25-150 with the IST Method Prediction 143
Figure 6.13: Stirrup Strain for BM12-s230 with the IST Method Prediction 143
Figure 6.14: Mid-Span Displacement for BM25-150 with the IST Method Prediction 144
Figure 6.15: Mid-Span Displacement for BM12-s230 with the IST Method Prediction 145

List of Tables

Table 2.1: ACI 318-08 Factors Accounting for Cracking and Confining Effects 30
Table 3.1: Test Specimen Names 46
Table 3.2: Test Specimen Parameters *As-Designed* 48
Table 3.3: Predicted Applied Failure Loads and Mid-Span Displacements 51
Table 3.4: Percent Probability of Shear Failure & (Flexural Failure) 53
Table 4.1: Results 92
Table 5.1: Evolution of Strut Elasticity with Load Increments 119
Table 5.2: Results of the Investigation into Modelling Parameters 122
Table 6.1: Association of Model Types with Experimental Beam Specimens 126
Table 6.2: Summary of Results for Models of Type I, III, and IV 127
Table 6.3: Summary of Results for Models of Type II 129
Table 6.4: Experimental Results and Predicted Strengths 131
Table 6.5: Estimates on the Concrete Contribution, V_c 136
Table 6.6: Summary of the Ability of the IST Method to Predict Longitudinal Strains at Mid-Span 146
Table 6.7: Summary of the Ability of the IST Method to Predict Average Stirrup Strains 147
Table 6.8: Summary of the Ability of the IST Method to Mid-Span Displacements 148

List of Symbols

The following list of symbols is provided to clarify their meaning; however, all variables are defined within the text of the subsections where they appear. Commonly, the symbols for variables of equations found in the Literature Review Chapter were presented as they would appear in the source materials. As such, there are several variables which may represent the same parameter.

Symbol	Unit	Definition
A_{cs}	mm^2	Cross-sectional area of a strut-and-tie model concrete strut as found in both ACI 318-08 and CSA S806-12
A_F, A_f	mm^2	Total area of longitudinal/flexural reinforcement
A_{FT}	mm^2	Total area of bars in the tension tie of a strut-and-tie model, CSA S806-12
A_v	mm^2	Generically, the area of shear reinforcement taken as either the total area of one stirrup or as the area of one stirrup leg depending on context. This also specifically defines the total area of one steel stirrup in CSA A23.3-04.
$A_{Fv,}$ A_{fv}	mm^2	As above, but specifically applying to FRP reinforcement
A_{nz}	mm^2	Area of a strut-and-tie model nodal zone face, ACI 318-08
A_p	mm^2	Area of prestressing tendons, CSA S806-12
a	mm	Length of shear span from centre of the bearing point to the centre of the loading point
a/d	-	Shear-span-to-effective-depth ratio
b, b_w	mm	Beam width, or the width of the beam web
d	mm	Effective depth to longitudinal/flexural reinforcement
$d_{node,x}$, $d_{node,y}$	mm	Length of the x/y-dimension of a strut-and-tie nodal zone, Equations 5.7 & 5.8
d_v	mm	Effective shear depth taken as the greater of $0.9 \cdot d$ or $0.72 \cdot h$, CSA S806-12
E	MPa	Generic symbol for elastic modulus
E_c	MPa	Commonly known as the concrete elastic modulus, but which is actually the secant modulus of elasticity taken using some stress between 0.4 and 0.5 of f'_c
E_f, E_{fl}	MPa	Elastic modulus of longitudinal/flexural reinforcement
E_{fv}, E_{vFRP}	MPa	Elastic modulus of the FRP stirrup straight portion
E_p	MPa	Elastic modulus of prestressing tendons
E_s	MPa	Elastic modulus of steel
E^t_c	MPa	Initial tangent modulus of elasticity for a one-dimension concrete element, taken at an axial strain equal to zero.
E'_c	MPa	An elastic modulus parameter used by the concrete material model of Thorenfeldt et al. (1987) and equal to f'_c/ε_0
F_{nn}	N	Strength of a strut-and-tie model nodal zone, ACI 318-08
F_{ns}	N	Nominal compressive strength of a strut-and-tie model concrete strut without longitudinal reinforcement, ACI 318-08
f	MPa	Generic symbol for stress/strength

Symbol	Unit	Definition
f_c	MPa	Concrete stress, the dependant variable in one-dimensional concrete material models
f_{ce}, f_{cu}	MPa	Strength of a strut-and-tie model concrete strut, ACI 318-08 & CSA S806-12
f_{Fu}, $f_{Fu,straight}$, f_{fuv}, f_{uv}	MPa	Generically, the ultimate strength of FRP reinforcement. Where bent shapes are considered it is the strength of the straight portions of the bent shapes.
$f_{Fu,bent}$	MPa	Bend portion strength of bent FRP. Specifically, it is the stress in the straight portion of a bent shape when the rupture occurs at the bent portion.
f_{fv}	MPa	Stress in the legs of FRP stirrups
f_{po}	MPa	Stress in the prestressing tendons, CSA S806-12
f_y	MPa	Yield strength of steel
f'_c	MPa	Concrete strength, typically taken as the 28 day cylinder strength. Also, the peak stress on a concrete stress-strain curve
h	mm	Beam height
k	-	Factor to modify the strut strength reduction factor in Nehdi et al. (2008). Or, tail shape factor for the concrete material model of Thorenfeldt et al. (1987).
k_a	-	Factor accounting for the effect of arch action on shear strength, CSA S806-12
k_m	-	Factor accounting for the effect of moment on shear strength, CSA S806-12
k_r	-	Factor accounting for the effect of reinforcement rigidity on shear strength, CSA S806-12
k_s	-	Factor accounting for the effect of member size on shear strength, CSA S806-12
l	mm	Total length of beam from end-to-end, or from centre of support to centre of support, depending on context
M_f	N·mm	Factored moment acting on a section, CSA S806-12
M_r	N·mm	Factored bending strength/resistance/capacity at a section, CSA S806-12
N_f	N	Factored normal force acting on a section, CSA S806-12
n	-	Curve fitting factor for the concrete material model of Thorenfeldt et al. (1987)
n_{Bar}	amnt	Number of longitudinal bars per beam cross-section
P	N	Applied load
P_E	N	Specimen experimental strength, the maximum load recorded during the experimental test
P_p	N	Predicted applied load causing failure, or equivalent applied load at failure calculated from shear or moment strength using statics or beam diagrams depending on context.
r_{Bend}	mm	Corner bend radius for the bent portions of bent FRP reinforcement
s	mm	Centre-to-centre spacing of stirrups
s_{xe}	mm	Effective crack spacing
V_A	N	Applied shear load at any given data point recorded during the test taken as $0.5 \cdot P$
V_c, V_{cf}	N	Concrete contribution to shear strength/resistance/capacity

Symbol	Unit	Definition
V_{cr}	N	Shear load when the first shear crack forms on an experimental specimen taken as $0.5 \cdot P$
$V_{c,max}$	N	Maximum shear strength/resistance/capacity, CSA S806-12
V_E, V_{test}	N	Specimen experimental shear strength, the maximum shear load recorded during the experimental test taken as $0.5 \cdot P_E$
V_f	N	Factored shear acting on a section, CSA S806-12
V_p	N	Component of the effective prestressing force actin in the direction of the shear, CSA S806-12
V_r, V_{rf}	N	Shear strength/resistance/capacity, factored shear strength/resistance/capacity at a section, CSA S806-12
V_s, V_{sf}	N	Stirrup contribution to shear strength/resistance/capacity
V_{sF}	N	FRP stirrup contribution to shear strength/resistance/capacity, CSA S806-12
V_{ss}	N	Steel stirrup contribution to shear strength/resistance/capacity, CSA S806-12
v	-	Strut strength efficiency factor taken as $0.85 \cdot \beta_s$
w	mm	Strut width perpendicular to the orientation of the strut
β_n	-	Factor accounting for the effect of tie anchorage on the effective compressive strength of a nodal zone, ACI 318-08
β_s	-	Factor accounting for cracking or confining effects acting on a strut, ACI 318-08
γ_c	kg/m^3	Cured concrete density
ε	-	Generic symbol for strain, occasionally expressed as a percent
ε_0	-	Strain at peak stress on a concrete stress-strain curve
ε_1	-	Tensile strain transverse to the orientation of a concrete strut in a strut-and-tie model, CSA S806-12
ε_c	-	Uniaxial strain in a one-dimensional concrete element, the independent variable in one-dimensional concrete material models
ε_F	-	Tensile strain in the bar of a strut-and-tie model tie located closest to the tension face and which is inclined θ_s to the strut, CSA S806-12
ε_{Fu}	-	Rupture strain of a FRP bar, occasionally expressed as a percent
ε_l	-	Strain in the longitudinal/flexural reinforcement, CSA S806-12
ε_{max}	-	Maximum strain recorded during the experimental test for any given gauge
ε_x	-	Calculated mid-span strain at beam mid-depth, CSA S806-12
ζ	-	Softening coefficient for a one-dimensional material model as defined by Pang et al. (1995) and used by Kim and Yun (2011a).
θ	degree	Angle of the principle compressive stress, CSA S806-12
θ_s	degree	The smallest angle between the strut and adjoining ties in a strut-and-tie model, CSA S806-12
θ_{strut}	degree	Strut angle, Equations 5.7 & 5.8
λ	-	Factor to account for concrete density
ρ_f, ρ_{fl}, ρ_{Fw}	-	Longitudinal/flexural reinforcement ratio, occasionally expressed as percent
ρ_{fv}, ρ_v	-	Shear reinforcement ratio = $A_v/(s \cdot b_w)$, occasionally expressed as a percent

Symbol	Unit	Definition
φ_c	-	Material factor of safety for concrete, CSA S806-12
φ_f	-	Material factor of safety for FRP, CSA S806-12
φ_s	-	Material factor of safety for steel, CSA S806-12

1 Introduction

This chapter is a synopsis of background material which explains the phenomenon that the research programme investigated. The end of this chapter contains the objectives and outlines the organization of this thesis.

1.1 Fibre Reinforced Polymers as Internal Reinforcing in General

Fibre reinforced polymer (FRP) reinforcing bars are geometrically similar to conventional steel bars and are available in similar lengths and diameters. Fibre reinforced polymers are composite materials consisting of a bundle of long fibres which span the length of the bar, and which are held together by a stiff polymer matrix. The surface of FRP reinforcement is designed to promote good bond with concrete, similar to steel bars by using shear ribs or sand coatings.

1.1.1 Fibre Reinforced Polymer Components

There are two fibre types commonly used to manufacture FRP reinforcement: glass fibres and carbon fibres. Glass fibres are most commonly E-glass, a material originally designed for electronics. Carbon fibres are commonly produced from poly-acrylonitrile, but may also be made from rayon petroleum pitch. Glass and carbon fibre properties may differ between manufacturers and manufacturing methods.

Initial research into the field of FRP as internal reinforcements for concrete structures also investigated aramid fibre composites, though research is limited. Aramid fibres are more expensive than glass and carbon fibres, but they do not perform significantly better than the glass or carbon composites to warrant the expense. They tend to be omitted from modern day papers published in the field.

A number of different polymers may be used to form the matrix. Modern glass fibre reinforced polymer (GFRP) bars use either a polyester or vinylester polymer; though the particular resin formulation is typically a trade secret. Polyesters have a higher potential for durability related concerns because of moisture uptake and alkali infiltration. Moisture uptake results in swelling, stress corrosion, and may hydrolyze the many ester bonds, whereas the alkali may attack the fibres. Vinylester polymers have less moisture uptake, lower permeability, significantly fewer ester bonds, and have been shown to generally outperform polyesters. Carbon fibre reinforced polymer (CFRP) bars typically use an epoxy polymer, though it is possible to use other plastics as well. Epoxy resins are more expensive than vinylesters, which are more expensive than polyesters.

Fibre reinforced polymer bars also have an often forgotten third component referred to as the fibre sizing. The sizing is a very thin film that coats individual fibres, and it is applied by the fibre manufacturer. Fibre manufacturers tailor the sizing compound to the specific end use of the fibres, and without the sizing compound the fibres would not bond well to the resins of the polymer matrix. The sizing also has other purposes, such as protecting the fibres from microscopic damage during manufacture and processing. Sizing compounds are trade secrets, and serve to differentiate manufactures of fibre products that would otherwise be nearly identical.

However, the sizing compound is not generally discussed in civil engineering literature. The component is microscopically thin and reacts with the polymer resins during the manufacture of FRP bars. Observing this film on an unloaded bare bar is very difficult and requires sophisticated imaging

technologies; observing this film while the bar is loaded is impossible and thus civil engineers cannot readily assess its influence. The sizing compound will not be discussed further in this thesis.

1.1.2 Material Behaviour

Fibre reinforced polymer reinforcing bars are anisotropic composites. The bars have different properties, such as elasticity, plasticity, and strength, depending how they are loaded and in which direction they are loaded. The composite bars will respond differently when loaded parallel to the fibres, transverse to the fibres, transversely in shear, etc, and the response for each type of loading will also differ depending on if the force acts in tension or compression. However, FRP reinforcing bars are significantly stronger when loaded in tension parallel to the fibres, compared to any other direction, and are thus considered unidirectional composites. As a result, FRP bars are characterized by their behaviour in tension parallel to the fibres.

In general, FRP bars are linear-elastic-to-brittle-rupture materials; they show no capacity for plastic deformation when loaded in tension. The rupture of GFRP bars loaded in tension is preceded only by the occasional sound of snapping glass fibres before the bar explodes leaving the two halves looking like the frayed end of a witch's broom. To account for this behaviour, design provisions for FRP reinforced concrete require the concrete to fail before the reinforcement since concrete failures are the more ductile failure mode.

Fibre reinforced polymers bars are considered high strength reinforcement, with modern manufacturers producing both GFRP and CFRP bars with strengths exceeding 1000 MPa. However, FRP bars are less stiff than common steel reinforcements; GFRP and CFRP bars may have elastic moduli which are in the range of 50 and 120 GPa, respectively, depending on manufacturer. Figure 1.1 shows the assumed stress-strain behaviour of several commercially available GFRP and CFRP reinforcements, alongside a typical bi-linear mild steel stress-strain curve for comparison.

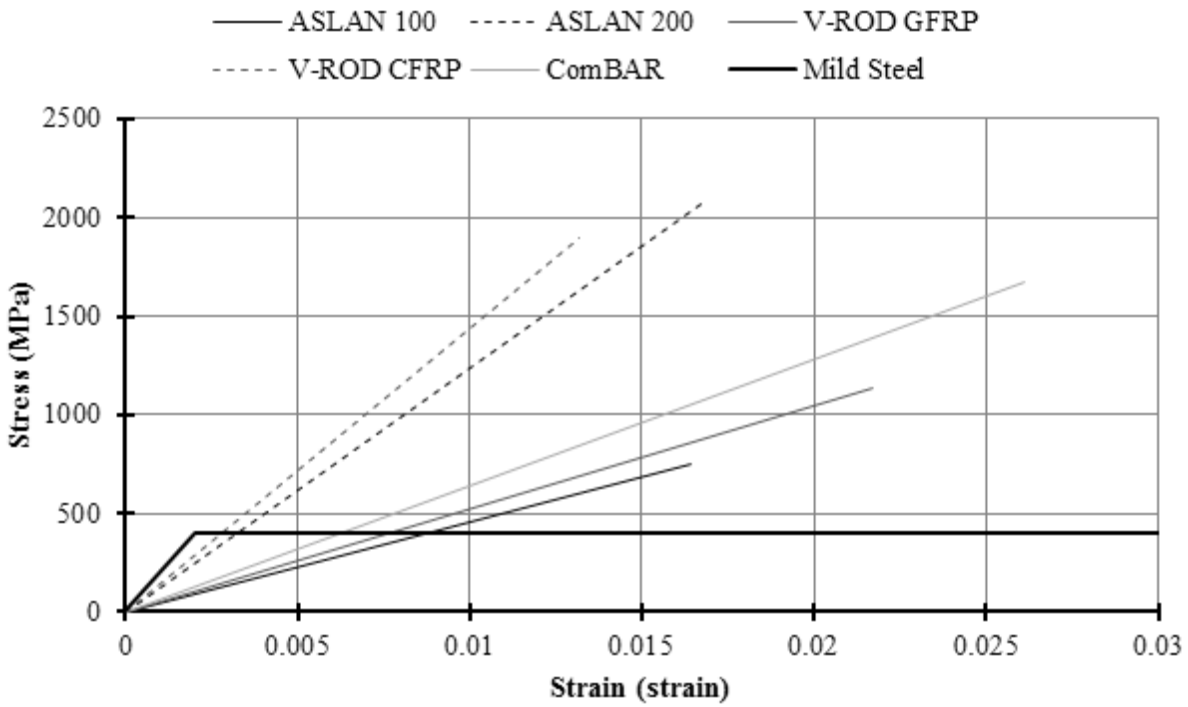

Figure 1.1: Comparison of Reinforcement Stress-Strain Behaviours

The ASLAN brand of bars are manufactured by Hughes Brothers Ltd. ASLAN 100 are their GFRP line and ASLAN 200 are their CFRP line, they have moduli of elasticity of 46 and 124 GPa and

rupture strains of 1.64 and 1.67 percent, respectively, for their 126.7 mm^2 bars. The V-ROD brand is manufactured by Pultrall. The GFRP and CFRP V-ROD bars have moduli of elasticity of 53.5 and 144 GPa and rupture strains of 2.17 and 1.32 percent, respectively, for their 126.7 mm^2 bars. ComBAR is manufactured by Schoeck and is a GFRP bar with a modulus of elasticity of 64 GPa and a rupture strain of 2.61 percent for their 201 mm^2 bars. All bar data was retrieved from technical information available on the manufactures' websites at the time this thesis was published.

Attempts were made to compare bars of similar sizes since FRP bars show a tensile size-effect behaviour: as bar diameters, and thus fibre bundles, become larger the rupture stress, and strain, of the bars become smaller for the same length of bar, though overall they carry larger loads (Batdorf et al., 1984).

Often manufactures will report a guaranteed tensile strength, for use with design, which is lower than the equivalent strength for the reported rupture strain. Some manufacturers will also report on bond strength and thermal expansion coefficients; however, they will not often provide any elasticity or strength values for loading in any other direction, except perhaps transvers shear strength depending on the manufacturer.

1.2 Use of FRP Reinforcing Bars

Fibre reinforced polymer bars may be preferred over conventional steel bars for use in environments where corrosion, conductance, or electromagnetic interference is a concern, because the materials used to make FRP composites do not participate in electrochemical reactions, are non-conductive, and are non-magnetic. Fibre reinforced polymers are also attractive because they are light weight and have a high tensile strength when compared to steel. However, FRP bars are more expensive than conventional steel bars; they have lower moduli of elasticity, and higher failure strains. Other advantages and disadvantages are discussed by Erki et al. (1993).

Specifically, FRP reinforcement may be considered for use in corrosive environments such as marine structures, bridge and roadway infrastructure exposed to de-icing salts, or effluent and wastewater treatment facilities. They may also be considered for use in electromagnetically sensitive environments such as medical facilities with magnetic resonance imaging devices, or laboratories like those in the Quantum-Nano Centre at the University of Waterloo, which used FRP reinforcements in the floor slab to avoid interference with highly sensitive equipment. The non-conductive nature of the reinforcement also makes it attractive in electrical transmission towers or electrical rooms where stray currents could result in a hazardous environment.

It is worth noting that conventional steel bars will remain the reinforcement of choice for the vast majority of concrete construction owing to their low cost and familiarity within the industry from design through construction. FRP reinforcements are a type of speciality reinforcement used to address specific durability or functional structural requirements.

1.3 Manufacture of FRP Reinforcement

The process for manufacturing straight FRP bars is referred to as pultrusion, and the remainder of this paragraph describes the process in brief. The composite starts at the fibre spools, known as bobbins, which are stored on shelves at the beginning of the process. The spools store fibre rovings, which are a small bundle of fibres. The rovings are threaded through a pre-former, which is a type of die, to align the strands before they are grouped together into a larger bundle. After moving through the pre-former the rovings are coated in liquid resin by bath immersion. The coated fibres are then pulled through a series of dies which continue to align the individual fibre rovings. As the fibres pass through these dies they are bundled closer together while excess resin is forced out. A final, and very long, heated die cures the polymer resins as the fibre bundle is pulled through. The curing process causes the individual resin molecules to cross-link with one another which forms a stiff matrix. The material leaving the heated die is

the newly formed composite. The fibres are pulled through the process at a constant rate by a caterpillar system or hydraulic clamps which grip and pull on the final product. The process is best understood when seen, and pultursion videos are readily available on the internet.

The pultrusion process results in bars with a smooth finish. Manufactures of reinforcing bars will apply some form of surface treatment to promote a good concrete bond. A common surface treatment is to coat the bar in sand particles. The bonding agent may or may not be the same polymer resin at the FRP bar matrix, and the sand particles may or may not be added to the surface of the bar before the entire bar is cured. Another surface treatment, by at least one manufacturer, involves cutting shear ribs into the bar. As well, some manufacturers braid or twist smaller fibre bundles and claim that the natural undulations of the surface promote good bond (Baena et al., 2009).

Early FRP reinforcement products bonded large protrusions to the surface in the form of a helical or spiral ribbon. However, these treatments often failed prematurely at the interface between the bar and ribbon in pullout tests and are not commonly found on modern FRP reinforcements. Still others added protruding globs of resin to the outside of the bars, but those too would shear-off in pullout tests (Cosenza et al., 1997).

In contrast, bent bars, such as stirrups, are manufactured using hand lay-up methods as the industry has yet to develop a robust process for forming bent bars. Because FRP bars are not ductile, they cannot be bent after the polymer has cured, so the bent bars must be formed while the resin is still liquid. The processes used by the major manufacturers are patented and not openly discussed in literature.

In general, to form bent bars, such as hooks, stirrups, or more complicated shapes, the fibres have to be immersed in polymer resin, formed to shape, and cured in an oven. In each of these stages there are opportunities for defects or inconsistency to develop: fibres must be closely spaced, resin must be evenly applied, bar cross-sections must be maintained, the overall shape must be geometrically consistent, all bends have to be well-formed, multiple copies of the same shape must be made consistently to within a certain tolerance, and surface treatments for bonding must be consistent, etc.

Researchers have also explored the use of polymer bars made with thermoplastic resins. The bars are manufactured straight or are cut from a mat, and are bent after being heated. The thermoplastic resins become pliable with heat allowing the bar to be shaped. However, these bars have not gained much popularity. This will be discussed further in the Literature Review Chapter in the summary of the paper by Imjai et al. (2007).

1.4 Bend Strength

Bent FRP is wont to rupture at the bend (Maruyama et al, 1993)(Nagasaka et al., 1993)(Currier et al., 1994)(Ueda et al., 1995)(Ehsani et al., 1995)(Nakamura et al, 1995)(Imjai et al., 2007a)(Shehata et al., 2000)(Ahmed et al., 2010a)(Ahmed et al., 2010b)(Bentz et al., 2010). For example, in a pullout test the stress in the straight portion of the bar will be a fraction of the full straight portion strength when the bend portion ruptures, and that lower strength is referred to as the bend strength. There are a number of specific parameters which influence the bend strength, and they are presented the Literature Review Chapter.

This phenomenon was considered problematic; earlier research found that bend strength varied between 30 to 80 percent of the straight portion strength (Nagasaka et al., 1993). At the time there was little research available to civil engineers to explain the wide range, and so it was too risky to use bent FRP as a structural material. However, a decade of research and development improved the situation; manufacturers improved their bent FRP products and engineers developed specific detailing recommendations for bent FRPs (Shehata et al., 2000). Today large technical organizations, such as the Canadian Standards Association and the American Concrete Institute, have published a number of design guidelines and standards for the use of FRP as internal reinforcement for concrete structures.

Engineers familiar with the material now accept the bend strength phenomenon. Conventional engineering practice seeks to fully utilize the strength of materials in order to make the most efficient use of them; so the fact that the straight portion of a stirrup must be designed for the bend strength is considered uneconomical.

Though bend strength is accepted, research into the phenomenon continues because the bend problem is a concern for the shear design of concrete beams. Stirrups, are a form of bent bar, and they commonly fail prematurely at the bend in tests on shear-critical slender beams. More specifically, the problem is that the FRP stirrups are brittle. A beam reinforced with steel stirrups may not fail when a stirrup yields as yielded steel continues to carry load. However, a beam reinforced with FRP stirrups is likely to fail when a stirrup ruptures because the concrete will not likely be able to carry the load once carried by the stirrup.

Three factors conspire to cause the bend strength phenomenon for bent FRP reinforcements, and they are presented and described in the following subsections.

1.4.1 Manufacturing Defects for Bent Bars

The first factor concerns manufacturing defects. Manufacturing defects likely contribute the most to weakening bent bars, though most defects are not discussed in scientific literature. What follows is a discussion of defects observed by the author, but which are not limited to, nor exclusive to, nor present in their entirety with the reinforcement used in this research programme; nor is the discussion meant to be exhaustive; nor is it meant to rank defects in terms of impact.

Further, it is important to note that these defects may not be present on every bent bar or stirrup. Different manufactures, as they strive to compete, have addressed specific issues in the manufacture of their product. Overtime the industry as a whole will develop robust manufacturing methods to reduce the severity of defects, if not eliminate them entirely. A summary of common production related defects is provided in ASTM D4385 the Standard Practice for Classifying Visual Defects in Thermosetting Reinforced Plastic Pultruded Products.

Some defects appear in the polymer matrix. Inconsistently applied polymer may leave some parts of a bar with too little resin, or produce bubbly void spaces. As a result some fibres will not be fully bonded within the vicinity of the defect and may be subject to stress concentrations. It is also possible to have too much resin which forms blobs or protrusions in the bar profile that distorts its shape. Unusual protrusions will impact how bond forces are transferred from the concrete to the fibres and may also give rise to stress concentrations. Defects may also include inconsistently cured polymer, where curing represents the amount of polymer cross-linking. Poorly cured polymer may decrease the rigidity of the matrix and the means by which bond stress are transferred through the resin and transformed into tensile stresses in the fibres.

Defects may also occur in the fibre phase. Fibre kinging across the bend is one well observed defect (Ahmed, 2010c). Kinking is the result of bending a bundle, which buckles fibres on the inside of the bend. Another defect includes bunched fibres, which may occur when there is slack in a roving of the bundle. The slack may create a fibre blister or may expose easily malleable and friable group of fibres. Fibre waving is also possible, where fibres in an otherwise straight section of bar show a waveform with a peak, or multiple peaks, even if the overall geometry of the bar is consistent. Waving may occur if the bundle is exposed to twisting actions acting about the central axis of the bundle. In general any misalignment of the fibres destroys the unidirectional nature of the composite within the vicinity of the defect.

There may also be problems with the overall geometry. One well observed issue is the variation in cross-sectional shape over the bent portions; the variations are common as fibres are pulled tight over a jig, or form, thus squishing the cross-section (Imjai, 2007b)(Ahmed, 2010c). Distortions in the cross-section along the straight portion are also possible. Further, there may be unnecessary and unexplained

distortions in shape, which occur sometimes to accommodate overlapping portions of complex shapes, such as the standard hooks on stirrups, or which occurs as copies of the same shape are stacked in preparation for curing, or which may occur for other unknown reasons. Changes in cross-section are a defect which may give rise to stress concentrations, whereas defects in overall shape may introduce unnecessary bending.

Surface treatment defects also occur and may include uneven, poorly bonded, or insufficient sand coatings; and squished or deformed shear ribs. These defects may lead to poor bond, which interferes with the transfer of forces from the concrete to the reinforcement, and may lead to lower strength or unexpected pullout behaviour.

Again, the impact that these defects have on strength is not known as there is no *perfect* bent bar or stirrup to which they may be compared. Also, many of these defects also have implications for durability of FRP reinforcements, but that is a subject which will not be discussed in this thesis.

1.4.2 Transverse Loading Along the Bend

The second phenomenon concerns the unidirectional nature of FRP bars. They perform well when subject to a tensile stress acting parallel to the direction of the fibres, but not when subject to a multiaxial state of stress.

Consider a pullout test performed on a standard 90 degree hook. The straight portion of the bar will be subject only to bond stresses developed between the bar and concrete, and which act parallel to the direction of the reinforcement and fibres. However, the bend of the hook will be subject to bond and transverse bearing stresses simultaneously; bearing stresses will act perpendicular to the axis of the bend. The magnitude of each stress will vary over the arc of the bend, and around the circumference of the cross-section.

The transverse bearing stresses develop to change the direction of the force internal to the reinforcement from vertical at one end of the hook to horizontal at the other, or to otherwise satisfy the statics of the system.

The combination of transverse and parallel external stresses will create a multiaxial state of stress internal to the reinforcement, in which stresses do not act in the direction of the fibres. Different components of the internal stress will load the composite along weaker axes. If the stress along one of the weaker axes exceeds the strength in that direction under that loading type then the composite reinforcing bar will fail. The same principle applies to the bend of a stirrup after shear cracks form (Ueda et al., 1995)(Nakamura et al, 1995)(Shehata et al., 2000)(Imjai et al., 2007a)(Imjai et al., 2007b)(Ahmed et al., 2010a)(Ahmed et al., 2010b)(Ahmed et al., 2010c)(Bentz et al., 2010). This is an inherent weakness of bent FRP and will not vanish with improvements in manufacturing, but its impact is exacerbated by manufacturing defects.

1.4.3 Transverse Loading Across Shear Cracks

The third phenomenon involves the normal and transverse displacement of crack faces. The normal displacement of crack faces, such as in flexural cracks, are not a concern since they will typically load reinforcements in tension. However, the transverse displacement causes internal shear and moment forces to develop locally in the reinforcement. This is a concern for stirrups because shear cracks are known to produce large transverse and normal displacements within the web of a beam, and because shear cracks cross stirrups by design.

The displacement of crack faces creates a multiaxial state of stress in the composite spanning the crack faces in which internal stresses act along weaker axes, similar to the weakening mechanism of the second phenomenon. Though similar, this is considered a separate phenomenon because the mechanism by which the mutliaxial state of stress is developed is different, and because it may influence both bent and straight portions of a bar depending on the relative location of the crack. The displacement of crack faces has been observed to reduce the expected strength along stirrup legs (Maruyama et al,

1989)(Nagasaka et al., 1993)(Kanematsu et al., 1993)(Ueda et al., 1995)(Shehata et al., 2000). This is of specific concern for FRP stirrups because flexural cracks tend to form at the location of stirrups, which may turn into critical flexural-shear cracks.

In reality the fact that bent FRP reinforcements have two strengths, a straight portion strength and a bent portion strength, is not really a problem; it is simply the nature of the material.

1.5 Shear Transfer Mechanisms

To understand the bend problem better, in terms of the shear strength of beams, it is important to consider the role of FRP stirrups in the transfer of forces in a concrete beam. Machial et al. (2012) provide a good summary of these mechanisms as they apply to FRP reinforced beams, in addition to how specific parameters have been observed to influence strength.

Machial et al. (2012) indicate that shear force is transferred through beams, regardless of reinforcing material, by six mechanisms: dowel action, aggregate interlock, shear resistance in uncracked concrete in the compression zone, shear resistance through tensile forces across crack tips, arch action, and by transverse reinforcement.

Dowel action is the component of shear resistance attributed to the longitudinal reinforcement acting as a dowel, and it is generally thought to be negligible in FRP reinforced beams since the transverse stiffness of FRP reinforcement is quite low.

Aggregate interlock is the component of shear transferred across shear crack faces, and is attributed to friction. As shear cracks open, the two rough crack faces slide past one another. Shear is transferred across the crack faces by friction as the protrusions, such as aggregates, scrape along the opposite crack face. This is generally thought to be one of the most significant shear resisting mechanisms. However, this mechanism disappears when cracks become wide.

Shear resistance in uncracked concrete in the compression zone is very simply the amount of force that can be carried in uncracked concrete. Uncracked concrete will behave like a linear elastic, isotropic material and so it will transfer shear forces as such.

Shear resistance through tensile forces across crack tips is very difficult to quantify. Concrete cracks grow in a complex manner which involves a zone of concrete ahead of a crack tip that is in a state of tension and in which a number of micro-cracks form. As load increases the micro-cracks grow larger and coalesce, some of them will connect with the main crack and the main crack will grow larger. The tensile forces transferred across this crack tip will also contribute to the overall shear resistance of the beam.

Arch action is a separate shear transfer phenomenon. It is insignificant in slender beams, but becomes very significant in deep beams as the shear-span-to-effective-depth ratio becomes small. Essentially, if a load acts close to a support then a portion of the load will transfer to the support in a line directly through the concrete. The direct line through which the compressive forces transfer is commonly called a compressive strut.

Transverse reinforcement is the most versatile shear resisting mechanism as it is the one with which designers have the most control. Transverse reinforcement is intended to cross shear cracks and transfer shear forces across them as tension in the stirrup legs. Changing the type, size, and spacing of transverse reinforcement changes the amount of shear force that may be resisted, so designers are able to fit the shear strength to the design requirements.

However, the addition of transvers reinforcement influences the other shear transfer mechanisms as well. Stirrup legs are stiff and will restrain the relative displacement of the shear crack faces which will improve the aggregate interlock mechanism. In deep beams the shear stirrups will also confine the concrete in the compressive struts which increases the strut strength. The stirrups also act to prevent the formation of tensile splitting cracks which run parallel to the longitudinal reinforcement, and thus improve dowel action as well.

It is not possible to account for the specific amounts by which each mechanism resists shear or how those mechanisms are improved by transverse reinforcement, as their contribution to shear resistance changes with loading and with a number of design parameters. Design provisions tend to separate shear resistance, V_r, into the sum of two contributing factors: V_c, which is the shear resisted by the concrete, and V_s, which is shear resisted by the stirrups.

The concrete contribution to shear strength accounts for the dowel action, aggregate interlock, and uncracked concrete mechanisms; often the concrete contribution term is formulated to predict the strength of beams without stirrups. The stirrup contribution accounts for the shear resisted by the transverse reinforcement, or more precisely the increase in shear strength by including stirrups when compared to those without, as it also accounts for any improvements to the other mechanisms by the presence of shear stirrups.

Machial et al. (2012) also discuss specific parameters which influence shear strength, such as the longitudinal reinforcement ratio. In general, as the longitudinal reinforcement ratio increases so does the concrete contribution to shear strength. In their summary Machial et al. reference authors who indicate that increases in the longitudinal reinforcement ratio caused the neutral axis of the beam to move lower, which improved the uncracked concrete shear resisting mechanism. Increases in the longitudinal reinforcement ratio will also improve the dowel action as there will be more reinforcement area, and aggregate interlock through increases in beam stiffness which vicariously restrains the opening of cracks by causing the beam to deflect less.

The authors also observed that increases in the shear reinforcement ratio increased the strength of beams, quite obviously by increasing the stirrup contribution. However, there was some disagreement over the nature of the relationship, and the investigation was marred by a lack of data from beams with varied shear reinforcement ratios to clearly define the trend.

Reinforcement stiffness, for both longitudinal and transverse reinforcements, was also a factor. Different types of FRP have significantly different moduli of elasticity, and stiffness is often estimated as the product of the elastic modulus and reinforcement area. Researchers are interested in this property because it may explain behavioural differences and similarities between beams with different FRP types. Machial et al. (2012) reference other works and note that increases in the longitudinal reinforcement stiffness have been attributed to increasing the stirrup performance, and the overall shear strength. The mechanisms for increasing shear strength were as described earlier for the longitudinal reinforcement ratio alone. Nothing was written about stirrup stiffness.

The shear-span-to-effective-depth ratio has also been observed to influence shear strength. Experimental observations, summarized by Machial et al. (2012), indicate that increases in the shear-span-to-effective-depth ratio show a decrease in shear strength. The decrease in strength is attributed to a decrease in the arch action, as the proportion of load carried by the direct strut diminishes as beams become more slender. One set of authors observed that as the shear-span-to-effective-depth ratio becomes smaller, as beams become deeper, the strain in the stirrups decreases; though other authors made conflicting observations.

The concrete strength also influences the shear strength. Generally as concrete strength increases so does the shear strength. However, Machial et al. (2012) noted that shear strength decreased when high strength concrete was used. High strength concretes tend to have cements which are stronger than the aggregates, so cracks tend to grow through the aggregates instead of around them. As a result crack faces are smoother and the aggregate interlock shear resisting mechanism becomes less effective.

Stirrup spacing was also a major factor. As the spacing of stirrups becomes smaller the shear strength increases. This occurs because more stirrups are likely crossed by a shear crack when they are closely spaced, and thus they may carry a larger portion of the load. However, closely spaced stirrups also better confine the concrete which tends to improve concrete strength.

1.6 Bend Strength Exceptions

Though FRP reinforced beams failing in shear are known to fail by rupture of the stirrup bends, there are always a few exceptions. Occasionally, shear failures are not precipitated by ruptures of the stirrup bend, or any stirrup rupture, yet measures of the force in the stirrups would suggest that the bend strength was exceeded. Two papers, one by Ahmed et al. (2010a) and another by Bentz et al. (2010), both of which are summarized in the Literature Review Chapter, reported on such observations.

In the paper by Ahmed et al. the authors tested three FRP reinforced slender beams in 4-point loading, each with a different spacing of GFRP stirrups. Their analysis showed that all three beams had a ratio of applied stirrup stress over stirrup straight portion strength very close to unity when the beams failed by rupture of the stirrup bends. Ahmed et al. attributed the results to the fact that the bend strength was 58 percent of the straight portion strength, a high proportion, which negated the impact of weak bends. Stirrup strains tend to be higher at the mid-height of beams and lower the top and bottom near the bends.

The study by Bentz et al. examined a number of FRP reinforced beams with different geometry and reinforcement arrangements. The beams in their study failed in an array of different modes, though mostly by shear. They observed that a beam with four layers of flexural reinforcement failed by rupture of the stirrup straight portion above the longitudinal bars. In contrast, an otherwise identical beam but with only one layer of flexural reinforcement failed by rupture of the stirrup bend. To investigate the observation the authors modelled the shear stress on the cross-section with Response2000. In the beam with four layers of flexural reinforcement the maximum shear stress was located at the top of the cross-section and the shear stress diminished rapidly over the depth of flexural reinforcement layers. In contrast the maximum shear stress for the other beam was located at the stirrup bend. Bentz et al. attributed the results to the fact that the many layers of flexural reinforcement protected the bend from shear stresses since part of the shear force was carried by the longitudinal bars.

Ahmed et al. also tested CFRP reinforced beams (2010b). The analysis by the authors indicated that the stirrups were stressed to between 72 and 60 percent of the stirrup straight portion strength when the stirrup bends ruptured and the beams failed in shear. In the case of the CFRP beams the stirrup bend strength was 46 percent of the straight portion strength, which explains why Ahmed et al. would suggest that having a higher bend strength compared to the straight portion strength could increase stirrup strength utilization before rupture.

Ahmed's observations contrast with those of Bentz et al. In the experiments by Ahmed et al. the GFRP and CFRP beams were identical in every way, including stirrup geometry, diameter, etc., except for the stirrup material. And every beam used the same arrangement of flexural reinforcement: three layers each with three steel 7-wire strands. So, both types of stirrups in the papers by Ahmed et al. should have been fully utilized at the point of shear failure according to the hypothesis by Bentz et al.; the layers of longitudinal bars that protected the bends of the GFRP stirrups in Ahmed's study should have protected the bends of the CFRP stirrups as well.

There are further complications in the comparison of the experiments and the observations by the authors. The strength of the straight portion of GFRP stirrups in the study by Ahmet et al. was 664 MPa, whereas the strength of CFRP stirrups was 1538 MPa, and the beams with GFRP stirrups failed at applied loads lower than those with CFRP stirrups. So, when the CFRP stirrups failed they were carrying much more load than the GFRP stirrups were when they failed, though strains were similar. The protection offered by the longitudinal reinforcement might have been enough for the GFRP stirrups, which carried lower loads, but not enough for the CFRP stirrups, which carried higher loads. But the different bend strengths are still a complicating factor.

From the perspective of a practical academic investigation the hypothesis by Ahmed et al., that full FRP stirrup straight portion strength utilization at the point of stirrup bend rupture could be realized if the bend strength is at least 60 percent of the straight portion strength, is an entirely un-testable

hypothesis. If manufacturers had direct control over the strength of the stirrup bends then the phenomenon of FRP stirrup bend ruptures may very well have vanished long ago.

The hypothesis by Bentz et al., that multiple layers of longitudinal bars protect flexural tension zone stirrup bends from shear stresses and premature rupture, is much more attractive. In fact, if there is a relationship between specific longitudinal bar arrangements and improved stirrup strength utilization then the results could lead to practical conclusions, and eventually to specific engineering design provisions.

Though not discussed in detail here, other evidence in papers by Fam et al. (1997) and Hegger et al. (2011) support this observation, and will be discussed later in Section 3.5.1.

1.7 Aspects of Strut-and-Tie Modelling

The analysis of the results required a the use of strut-and-tie modelling, for reasons which were outlined in the Abstract and against in the Objectives below. Strut-and-tie modelling is an analysis method for reinforced concrete beams. The method simplifies complex stress fields by replacing them with discrete truss elements. Compressive strut elements represent regions of large principle compressive stresses, tensile tie elements represent regions of large principle tensile stresses, and node regions represent the joints where these elements intersect. In general, the truss elements are oriented to align with the angle of the principle stress they represent, but elements typically deviate from that precise orientation since all of the elements must connect at nodes. As with any truss system, forces may only enter or leave the system at the nodes.

The method is mainly concerned with identifying a valid strut-and-tie truss model, computing the forces in each of the truss elements, using those forces and element strengths to compute the necessary area of elements, and then confirming that those elements can fit within the problem domain. Some iteration, where the truss geometry is modified, is required to find a final solution. The purpose of the method is to determine the largest load that may be applied to the system before failure, and this is possible since the method is rooted in the lower bound theory of plasticity.

Strut-and-tie modelling is used to design and analyze reinforced concrete regions with discontinuities. For example, strut-and-tie modelling is not commonly used to design slender beams, as simpler slender beam design methods assume that plane sections remain plane, which implies that the strain profile along the cross-section varies linearly. However, within the region of an applied load or support on a slender beam the strain profile varies non-linearly, and strut-and-tie modelling could be used to design these isolated regions, though strut-and-tie modelling could be used to design the entire beam as well. Strut-and-tie models are mostly used to design beams with openings, the tension flanges of T-beams, shear walls with openings, footings, etc, and of course deep beams, as is the case with this research programme.

1.8 Objectives

The research programme had only one objective originally, but unexpected experimental results required modification to that objective.

1.8.1 Original Objective

To investigate the influence of longitudinal bar arrangements on the effective strength of GFRP stirrups.

The bend strength of GFRP bars limits use of the material and this research programme intended to investigate this issue. Unfortunately, the experimental results did not produce any ruptured stirrups, and without stirrup failures the strength of the stirrups cannot be known; the investigation of the original objective could not be effectively completed. In short, the stirrups did not rupture because the shear-span-to-effective-depth ratio for the experimental beams was set at 2.5 and they behaved more like deep beams

than like slender beams; the beams tested by Ahmed et al. (2010a)(2010b) and Bentz et al. (2010) had ratios of 3.0 or greater and behaved like slender beams. The choice of shear-span-to-effective-depth ratio is explained in the Experimental Design Chapter of this thesis.

A modified set of objectives were devised after testing to better suit the results, and to recognize the significance of the analysis method used on the results.

1.8.2 Modified Objectives

1) To investigate the influence of flexural and transverse reinforcement arrangements on the shear strength of GFRP reinforced, deep beams.

2) To investigate if the strut-and-tie modelling method of Kim and Yun (2011a) may be modified and successfully applied to FRP reinforced concrete deep beams.

In general, the results of the experiments were rather plain; the beams behaved exactly as FRP reinforced deep beams should, and the variations in their behaviour were readily explained by the differences in the experimental parameters. However, the specimens behaved like deep beams and it was thought that they could be analyzed by strut-and-tie models. As will be explained at several points in this thesis, there is no robust strut-and-tie analysis method for FRP reinforced concrete currently available. So, a strut-and-tie analysis method for steel reinforced beams developed by Kim and Yun, which did not require the designer to rely on the yielding of steel to find a lower bound solution, was adapted.

1.9 Thesis Organization

The second chapter is a review of literature relevant to the bend strength phenomenon, the original objective, FRP reinforced beam sectional shear strength analysis methods, current FRP reinforced beam strut-and-tie analysis methods, and the strut-and-tie analysis method of Kim and Yun (2011a).

The third chapter is an explanation of how the experimental specimens were designed and fabricated. The choices behind the experimental design parameters are reviewed. Then aspects of predicting the shear strength, which were used to finalize the values of design parameters, are discussed. Information on the stirrups is introduced, and potential problems that arise from having multiple methods of forming closed loop style stirrups are explored. Finally, details on the specimen fabrication and instrumentation, and the overall test method are provided.

The fourth chapter is a summary of the results of the experimental investigation. It starts by commenting on general observations of beam behaviour in terms of failure modes, cracking, longitudinal strains, and stirrup strains. Then selected results for each beam are presented, followed by results which are grouped for different sets of beams.

The fifth chapter is a presentation of the Indeterminate Strut-and-Tie analysis method. First, the use of of Dr. Young Mook Yun's analysis method is justified. Then the overall philosophy of strut-and-tie modelling as it applies to steel and FRP reinforced beams is compared and contrasted. The necessary modifications to the failure modes of strut-and-tie models are discussed. Each element of a strut-and-tie model is examined in more detail while simultaneously considering their use in a strut-and-tie model for FRP reinforced beams, and considering modifications to Yun's method. Then considerations for element geometry in the analysis method are presented, followed by a discussion of the material models. A procedure for the analysis method is provided along with a design example. The chapter ends by discussing the choice of modelling parameters which are used in the following chapter.

The sixth chapter is an analysis of the results and of the analysis method itself. First, the ability of the analysis method to predict the strength of the experimental beams is investigated. Then the behavioural influence of reinforcement arrangements on beam behaviour is further explored. Lastly, the chapter ends by investigating how well the analysis method could predict other beam behaviours beyond just the failure load.

The seventh chapter is the conclusion to the thesis with recommendations for future work.

The Appendices are as follows:

- Appendix A is a presentation of the information and MATLAB computer code used to perform the Monte Carlo analysis of Chapter 3. The analysis was used to finalize the concrete design strength and stirrup spacing parameters of the experimental specimens.
- Appendix B is a presentation of the procedure used to affix strain gauges to the FRP reinforcement.
- Appendix C is a presentation the procedure used for beam testing.
- Appendix D is a summary of the compressive strength testing and tensile split testing of concrete cylinders.
- Appendix E is a beam by beam presentation all of the relevant design parameters, beam drawings, photographs, and experimental results which are occasionally overlain with the predictions of Indeterminate Strut-and-Tie method where applicable.
- Appendix F is a copy of the MATLAB computer code used to perform the Indeterminate Strut-and-Tie analysis on BM25-220 of the experimental beams.

2 Literature Review

This chapter is a review of literature that provides a background for understanding the research programme and a basis for the analysis method.

2.1 Experimental Tests

This section of the Literature Review is a summary of selected papers on the topics of bent FRP bars and FRP reinforced beams failing in shear. The first paper is a summary of the factors which influence the strength of bent FRP based on observations from a large number of pullout tests. The remaining papers are observations from tests on large scale FRP reinforced beams failing in shear. The observations from the second, third, and fourth paper were made on tests of large beam specimens where an analysis showed full stirrup strength utilization. Those papers formed the basis of the original objective. The last paper in the section is a summary of tests specifically directed at FRP stirrups, in addition to beam tests.

2.1.1 "Mechanical Performance of Curved FRP Rebars – Part I: Experimental Study" by Imjai et al., 2007

Imjai et al. (2007) present results from a large number of pullout tests on bent FRP bars embedded in concrete blocks. The paper highlights all of the known factors which affect the strength of bent FRP bars, and thus FRP stirrups.

The authors open the paper by noting that a multiaxial state of stress reduces the strength of bent FRP, and references a number of the papers previously cited in the Introduction Chapter of this thesis. Imjai et al. note that premature failure at the bend may occur when the bars are required to carry high tensile stresses. The authors identify other literature, such as Shehata et al. (2000), summarized in another subsection, which indicates that the bend strength may be as low as 40 percent of the straight portion strength.

The experimental program used rectangular FRP strips cut from a sheet, which had a cross-section of 10 mm by 3 mm. The fibres were imbedded in a thermoplastic resin, so the researchers used heat and a specially designed jig to form the strips into bent L-shapes with varied corner radii. The tensile strength parallel to the fibres, straight portion strength, was 720 MPa, with an elastic modulus of 28 GPa. The experimental specimens were created by encasing the bent bars in concrete blocks; the test program included 47 specimens in 19 unique configurations.

The intentionally varied experimental parameters were the bend-radius-to-bar-thickness ratio, concrete strength, tail length, surface treatment, and length of bond ahead of the bend. Two concrete strengths were used: 45 MPa for normal strength and 95 MPa for high strength based on cube tests. The tail length is the length of bar past the bend on the unloaded portion of the bar. The bars were manufactured smooth, so some bars were coated in sand to roughen the surface texture. The variation in bond took two forms: one in which the bars were de-bonded from the top of the concrete to the top of the bend, and another in which 140 mm of bond was allowed above the start of the bend. The different types of specimens were meant to simulate a shear crack crossing just above the bend, and also further from the bend.

The results were measured in terms of failure strength, failure mode, and bar strain. Strains were measured at five locations: on the bar outside the concrete, just before the bend, on the inside and outside of the mid-point of the bend, and just after the bend.

The authors observed that 85 percent of the specimens failed by rupture of the bend; the other specimens failed by crushing of the bar in the grips. Imjai et al. compared bar strains from two specimens which only differed by length of bond ahead of the bend. In both specimens the strains measured on the inside and outside of the bend increased in a non-linear fashion, and towards the end of the test showed higher increases in strain with increases in load when compared to the other gauges on non-bent portions. The bend strains in the fully de-bonded specimen increased just after load was applied, and at failure the bend strains were larger than the strains from any other gauge. In the specimen with 140 mm of bond the bend strain only increased after some amount of load was initially applied, and the bend strains did not exceed the strains from any other gauge. It is clear that the amount of bond ahead of the bend plays an important role in determining the magnitude of bend strain.

The paper includes several plots to highlight changes in behaviour with changes in the experimental parameters. In general, failure loads increase as the bend-radius-to-bar-thickness ratio increases. Failure loads were greater for specimens with 140 mm of bond when compared to the fully de-bonded specimens. Specimens with high strength concrete showed slightly higher bend strengths than those with normal strength concrete. Further, specimens with a tail length that was 10 times the bar thickness showed a slight strength increase when compared to specimens with smaller tail lengths. Specimens with sand coated bars showed a 15 percent increase in strength when compared to those without. Further, the increases in strength with concrete strength, tail length, and surface roughness suggest that bend strength is related to bond. However, the authors observed considerable variability in failure load between identical specimens.

The authors conclude the paper by repeating many of the observations summarized above. They also note that the bend-radius-to-bar-thickness ratio appears to be the most significant factor affecting bend strength. Their experiments found that bend strength could range between 25 to 85 percent of the straight portion strength, but note that if the bend radius is 4 times the bar thickness then a bend strength of 40 percent of the straight portion may be achieved.

This paper is reviewed in this thesis because the observations by its authors clearly identify the factors affecting the performance of bent FRP reinforcement. However, the experimental specimens are not representative of actual FRP reinforcing bars.

First, FRPs as internal reinforcements are all but exclusively made with a polyester or vinylester polymer matrix, which are thermoset plastics. The experiments presented in this paper used a composite with a ploypropylene matrix, which is thermoplastic. The authors suggest that such a composite could be used on a construction site to form special one off shapes; however, from a practical standpoint this is undesirable. Large quantities of heat must be applied to form the shape, and if improperly applied it may burn or melt the polymer thus weakening or destroying the bar.

Second, on a construction site the forming of the shape is likely to occur in an uncontrolled process, as the site would be unlikely to have special forming mandrels on which to bend the bar. There is little guarantee that the bend will conform to a prescribed level of quality, or otherwise be geometrically proper with a constant curvature, etc. Improper bending may also kink or damage the fibres. Poor bend geometry and damaged fibres will further weaken the bar.

Lastly, even steel shapes are routinely sent to construction sites pre-bent, and there is a general expectation that FRP reinforcement suppliers are to provide the same service.

2.1.2 "Performance Evaluation of Glass Fiber-Reinforced Polymer Shear Reinforcement for Concrete Beams" & "Shear Performance of RC Bridge Girders Reinforced with Carbon FRP Stirrups" by Ahmed et al., 2010

These two papers by Ahmed et al. (2010a)(2010b) are an unofficial companion pair. One paper is a presentation of test results on beams with carbon fibre stirrups and the other with glass fibre stirrups; but both contain references to the same steel reinforced control specimen. The specimens also have identical experimental parameters such as cross-sections, longitudinal reinforcement, stirrup spacing, etc.

The intent of the study in the two papers was to evaluate the shear performance of large beams with FRP stirrups and to compare the results to recently published shear design provisions.

The authors begin each paper by noting that there is no rational model which satisfactorily predicts the shear strength of beams with FRP stirrups. They acknowledge that bent FRP is weak at the bend and attribute the weakness to: stress concentrations in the curve of the bend, perpendicular loading of bent fibres, and the kinking of fibres in the bend as part of the manufacturing processes. They comment that even though these factors are known, the behaviour of FRP stirrups has not been investigated thoroughly in large scale beam specimens, which is a comment repeated in the paper by Bentz et al. (2010) summarized in another subsection.

The results of seven T-beam specimens are presented between the two papers. The beams had a height of 700 mm, and effective depth of d = 600 mm, a web width of 180 mm, a flange width of 750 mm, and a flange thickness of 85 mm. All beams had the same longitudinal reinforcement, which was comprised of three layers each with three steel 7-wire strands; the flexural capacity was specifically designed to be greater than the shear strength. There were three beams with GFRP stirrups, three with CFRP stirrups, and one control with steel stirrups. The FRP stirrup spacing was $d/2$, $d/3$, and $d/4$, and the control had stirrups spaced at $d/2$. The beams were 7000 mm long with two 2000 mm shear spans, and one 2000 mm constant moment span; they were tested in 4-point loading.

The target concrete strength was 35 MPa, but the concrete strength in individual beams varied from 33.5 to 42.2 MPa. All stirrups were a nominal 9.5 mm in diameter, and the bend radius was 4 times the bar diameter. The GFRP stirrups had a straight portion strength of 664 MPa, a bend strength of 387 MPa, and an elasticity of 45 GPa; the CFRP stirrups had a straight portion strength of 1538 MPa, a bend strength of 712 MPa, and an elasticity of 130 GPa; bend strength was tested by the ACI 440.3R-04 B.5 test method. The steel stirrups had strength of 450 MPa. Other details are available in the paper.

Strain gauges were affixed to the longitudinal reinforcement at several locations, and to each stirrup in the shear spans on the straight and bent portions. Other measurements were also taken.

The authors observed that in all but one beam the strength was governed by the strength of the stirrups, and failure initiated by rupture of a stirrup bend in beams with FRP stirrups. However, the specimen with CFRP stirrups spaced very closely failed by yielding of the longitudinal reinforcement. Both beam strength and the amount of inclined cracks increased as the spacing of the stirrup decreased. The beams with CFRP stirrups had higher strengths than their GFRP counter parts when the results presented in the two papers are compared.

Load-deflection plots showed linear behaviour to shear failure, and a bilinear response for the flexural failure. The control specimen showed a small amount of non-linear behaviour as the stirrups yielded.

The stirrup strains were of more interest to the authors at the time since the revised CSA S6-09 standard was recently published; that standard uses a calculated estimate of the stirrup strains in its shear design provisions. Ahmed et al. observed that at any given load level the average stirrup strain was higher for beams with larger stirrup spacings. They also observed that beams with FRP stirrups with a shear reinforcement index ($\rho_v \cdot E_{vFRP}/E_s$) similar to the shear reinforcement ratio of the control beam showed similar behaviour on a plot of load against average stirrup strain. Maximum stirrup bend strains were always much lower than straight portion strains.

The authors then write at length on the possibility of increasing the stirrup strain limit in the CSA S6-09 standard but that discussion is not repeated here.

More importantly, the authors also investigated stirrup strength utilization at failure. To do this they assumed a 45° truss model, and that the concrete contribution to shear strength was equal to the load at which the first shear crack formed. The equation was as follows:

$$f_{fv} = \frac{(V_{test} - V_{cr})s}{A_{fv}d} \tag{2.1}$$

where f_{fv} is the stress in the stirrups in MPa, V_{test} is the shear strength at failure in N, V_{cr} is the shear load at which the shear crack formed in N, s is the stirrup spacing in mm, A_{fv} is the area of a single FRP stirrup in mm^2, and d is the effective depth of the beam in mm.

Stirrup stress utilization was computed by dividing the stirrup stress by the stirrup straight portion strength. Ahmed et al. found that beams with GFRP stirrups showed a utilization ratio very close to unity. The utilization ratio was slightly less than unity for the smaller stirrup spacing and slightly more for the larger spacing. However, the utilization ratio for the CFRP stirrups was lower than unity, at 72 and 60 percent for the two specimens that failed in shear; 72 percent was for the beam with the larger stirrup spacing. The authors compared their results to those from a study by Shehata et al. (2000), which is summarized in another subsection, and the authors found that the results for CFRP stirrups were similar to the results of Shehata et al. who also used CFRP stirrups.

The authors then confidently conjecture, in the GFRP paper, that beams may fully utilize FRP stirrup straight portion capacity when the stirrup bend strength is at least 60 percent of the straight portion strength. This observation formed part of the basis of the original objective of the research programme presented in this thesis.

In their papers Ahmed et al. had GFRP stirrups with a bend strength to straight portion strength ratio of 0.58, while the CFRP stirrups had a ratio of 0.46 which matched the same ratio from the study by Shehata et al. (2000). The authors do not justify their conjecture. Implicit justification comes from their observation that stirrup bend strains were significantly lower than stirrup straight portion strains, noted earlier.

The authors go on to explain that the trend of decreasing utilization with decreasing stirrup spacing occurs because there is a higher probability that a crack will pass through a stirrup bend in the beams with smaller stirrup spacings; an explanation which is also found in the study by Shehata et al. (2000).

In the study on CFRP bars, the authors break the concrete strength down into its concrete and stirrup contributions at each data point in the experiment. The stirrup contribution is calculated using the average stirrup strains, and the concrete contribution is computed by subtracting the stirrup contribution from the applied shear. They observed that the concrete contribution component was always larger than the load at which the first shear crack formed, and conclude that CFRP stirrups increase the concrete contribution by improving confinement.

The remainder of the paper examined shear crack widths and examined the performance of shear prediction provisions, which are omitted from this summary. However, the authors observed that shear crack widths between beams with FRP stirrups and steel stirrups did not correlate with the shear reinforcement index, and presumably other experimental parameters; instead they suggest that the this behaviour might be more readily attributed to bond parameters in addition to stirrup elasticity. The authors do not provide any insight into how shear crack widths are related to bond.

2.1.3 "Shear Strength of Large Concrete Members with FRP Reinforcement" by Bentz et al., 2010

The results of an investigation by Bentz et al. (2010) into the influence of size-effect on the shear strength of FRP reinforced beams of a number of sizes are presented in this paper.

The authors begin by referencing another paper which concluded that small depth flexural members without shear reinforcement show no difference in shear behaviour when they are reinforced with FRP or steel as long as the reinforcement stiffness is considered. The intent of the paper was to present results on a similar investigation done on beams with large depths, a study that necessitates investigating size-effect.

Bentz et al. reference CSA A23.3-04 which attributes the shear strength of beams to the combined actions of a strain-effect and size-effect. Size-effect predicts lower shear strengths for larger beams, and strain-effect predicts lower shear strengths for beams with large longitudinal strains.

There was a relatively large database of small and medium sized FRP reinforced beams failing in shear; however, to develop a more robust database of large beams, and to test specific variables, they cast a series of 11 beam specimens. Ahmed et al. (2010a)(2010b), summarized in another subsection, made a similar observation. The beams were reinforced with GFRP bars with three effective depths of 1000, 500, and 250 mm, and a shear-span-to-effective-depth ratio of 3.0. The reinforcement ratios were either 0.5 or 2.0 percent. The authors varied the quantity of stirrups from zero to 1.4 according to a shear reinforcement ratio equal to $A_v \cdot f_{uv} / b_w \cdot s$, where A_v is the area of one stirrup in mm^2, f_{uv} is the straight portions strength of the stirrup in MPa, b_w is beam width in mm, and s is the stirrup spacing in mm; traditionally, the shear reinforcement ratio is defined as $A_v/(s \cdot b_w)$.

The deepest beams were designed with different shear reinforcement in each shear span. Steel plates and high strength bolts were used to force a state of compression in the side not being tested to strengthen it. The large beams were tested in 4-point bending, and when the first span was tested the point loads were equal; asymmetric 3-point bending was used to test the remaining side. Smaller beams were tested in 3-point bending and had the same amount of shear reinforcement in both spans.

The authors tested the properties of the GFRP bars and were surprised to find that the two bar sizes they used had strengths that were 73 and 69 percent of the manufacturer's stated strength for the #8 and #4 bars, respectively. They also found that the elastic modulus was 90 percent of the stated value. Stirrup bar properties were not tested. The authors formed closed loop stirrups by overlapping two U-shaped stirrups from the top and bottom. At a few points the authors subtly suggest that this arrangement may have influenced the tested strength. More commentary on this strategy for creating closed loop stirrups are presented in Chapter 3.

For beams without stirrups the authors observed that the largest and most lightly reinforced beam failed at a shear stress that was 51 percent of the smallest beam with the same reinforcement ratio. For a heavily reinforced pair the larger failed at shear stress that was 69 percent of the smaller. Ergo, the results suggest that size-effect is a significant factor, and confirm that strain-effect is a factor as well.

The authors summarize the results for beams with stirrups individually as the failure of each was unique. A large specimen with few stirrups and a small flexural reinforcement ratio failed by stirrup rupture at the stirrup bends; a similar beam with more stirrups failed by rupture of the flexural reinforcement which was attributed to their unexpectedly low strength. A large specimen with few stirrups and large flexural reinforcement ratio failed by sliding along a large crack which ruptured stirrup legs. A medium sized beam with a large flexural reinforcement ratio and few stirrups failed along a plane which ran between two stirrups; the results showed an anti-size-effect and the authors suggest that its results should not be included in research databases. Finally, a large specimen with a large number of stirrups and a large reinforcement ratio failed by flexural crushing.

The most important observation that the authors made was that stirrup bends ruptured in the large beam with few stirrups and a small reinforcement ratio, but the bends did not rupture in a similar beam with a larger reinforcement ratio. In the later beam the stirrups ruptured near the lap splice location of the overlapping U-shaped stirrups even though the beam eventually failed by flexural crushing. The authors attributed the difference to reinforcement detailing: the beam with the smaller reinforcement ratio had only one layer of longitudinal bars, but the other had four layers.

Bentz et al. used Response-2000 to plot the predicted shear stress demand on the section for the two beams at a load level which was 80 percent of the predicted ultimate by Response-2000. The plot indicated that the shear stress demand in the beam with one layer of reinforcement was highest at the depth of that layer, which coincides with the stirrup bend location. In the beam with four layers, the shear stress demand was highest near the top of the beam; the shear stress demand decreased as the plot moved lower in the section and was diminished at the depth of the stirrup bend. The authors suggest that the multiple layers of reinforcement protected the stirrup bends, and suggest that it may be prudent to design GFRP beams with multiple layers.

However, the authors also observed that shear failures tended to provide more warning in advance of failure than beams that did not fail in shear. They suggest that the beams made more noises, ejected more concrete particles ahead of time, and had much wider cracks. Bentz et al. suggest that it may be more desirable to design beams with brittle reinforcement to failure in shear as a result, if only good shear prediction methods existed.

The authors model the results in the next section of the paper; Response-2000 was capable of predicting the flexural tensile load at which that one beam failed. However, the program over predicted the strength of the beam which failed by flexural compression, though the program did closely predict the load at which crushing first initiated.

However, the authors were more interested in shear strength predictions. Bentz et al. used a modified form of the concrete contribution equation as presented in a paper by Hoult et al. (2008) to check if it could correctly model both size- and strain-effects in FRP and steel reinforced beams of varying sizes. That equation follows:

$$V_c = \frac{0.30}{0.5 + (1000\,\varepsilon_x + 0.15)^{0.7}} \times \frac{1300}{(1000 + s_{xe})} \sqrt{f'_c}\, b_w d_v \tag{2.2}$$

where V_c is the concrete contribution to shear strength in N, ε_x is the average calculated mid-span strain at beam mid-depth, s_{xe} is the effective crack spacing in mm, f'_c is the concrete strength in MPa, b_w is the beam width in mm, and d_v is the effective shear depth in mm. The equations for estimating ε_x and s_{xe} are found in the paper. The first term in Equation 2.2 is the strain-effect term and the second is the size-effect term.

When only the specimens without stirrups are considered Equation 2.2 performed well. The authors added their beams to the database in the paper by Hoult et al. and included a number of steel reinforced beams with varied design parameters. Then the authors normalized the experimental strengths in the database by dividing out the concrete strength and size-effect term. The resulting plot showed that a normalized form of Equation 2.2 fit the data rather well visually; however, parameters to measure the adequacy of fit were not included. The same was done for the strain effect term with similar results.

The impact of strain- and size-effect on beams with stirrups is more complicated. Equations for the stirrup contribution, as presented in the paper, follow:

$$V_s = \frac{A_v f_y}{s} d_v \cot\theta \tag{2.3}$$

$$\theta = \left(29^o + 7000\varepsilon_x\right)\left(0.88 + \frac{s_{xe}}{2500}\right) \leq 75^o \tag{2.4}$$

where f_y is the yield strain of steel in MPa, A_v is the area of one stirrup in mm^2, and θ is the angle of the principle compressive stress in degrees. In beams with sufficient stirrups the crack spacing effect may be taken as 300 mm, and thus the second term in Equation 2.4 goes to unity. The authors question using these formulae on beams with FRP reinforcements and ask: "… is it appropriate to use the angle θ from [Equation 2.4] which is implicitly based on a derivation assuming plastic behaviour of 400-MPa steel stirrups? Second, with what should the term f_y in [Equation 2.3] be replaced?" Bentz et al. (2010).

To investigate this Bentz et al. assembled a database of FRP and steel reinforced beams. They only included beams from literature with published crack diagrams which could be interpreted correctly with respect to parallax. The crack diagrams were used to assess the value of the principle compressive stress angle. The database was used to create a plot of a size normalized measured crack angle against the calculated mid-depth strain; a line representing Equation 2.4 was also included.

The authors made three conclusions from the effort. First that Equation 2.4 was a good model for the crack angles. Second, the trend was easier to see with the larger strain of the FRP reinforced beams as much of the data was scattered about the lower range of strains typically seen in steel reinforced beams. And lastly, that the value of the crack angle is essentially the same for both FRP and steel reinforced beams.

The authors then use the results to comment on maximum allowable FRP stirrup spacing. They observe that a stirrups spacing limit of $0.5 \cdot d$ may not be sufficient to ensure cracks are crossed by at least one stirrup given the large strains, and thus steep crack angles, are produced in some FRP reinforced beams. They reference two of their own shear failures in which cracks ran between the stirrup legs. This is made clear in a plot included in their paper. The plots also suggests that the stirrup spacing for beams with very high longitudinal strains may be impractically small, and that in such cases it would be appropriate to consider pre-tensioning.

However, the authors conclude their paper by noting that the question regarding the replacement of the f_y term in Equation 2.3 is unanswered.

2.1.4 "Fibre Reinforced Polymer Shear Reinforcement for Concrete Members: Behaviour and Design Guidelines" by Shehata et al., 2000

Shehata et al. (2000) summarize the results of two experimental investigations and present a shear strength prediction algorithm for FRP reinforced beams in addition to several design provisions. The algorithm was later adopted by the CSA S806-02 standard.

The authors investigated the strength of stirrups and beams in separate experimental programmes. The first program tested the bend and kinking strength of GFRP, CFRP, and steel stirrups. The bend strength tests were done according to a procedure similar to what is now referred to as the, "Test method for FRP bent bars and stirrups" from Annex D of the CSA S806-12 standard. In this procedure the two ends of a stirrup are encased in separate blocks of concrete. An actuator with a load cell is placed between the two blocks and pushes them apart; ideally failure takes place in the stirrup instead of the concrete block. The test method is very similar to one presented in a paper by Currier et al. (1994)

Shehata et al. tested 42 such specimens, 26 of which were unique test configurations with two sets, one of 10 and another of 6, which examined repeatability. The experimental parameters were FRP type, stirrup bend radius, bar diameter, tail length, and anchorage type. A stirrup tail is the portion of the stirrup hook between the bend and the free end of the bar.

The anchorage types require more explanation. In the tests the stirrup legs were de-bonded from the concrete in only one of the two blocks. So type A specimens were concerned with the stirrup end where the stirrup is anchored by hooks, which is typically found in the flexural compression zone of a

concrete beam since the compressive forces are thought to anchor the free ends of the stirrup bar. Type B specimens were concerned with the other end where the stirrup bar is continuous between the two bends, which is typically placed in the flexural tension zone of a concrete beam.

The results indicated that the bend strength of stirrups could be as low as 35 percent of the straight portion strength. The authors observed that bend strength decreased with decreases in the stirrup bend radius; however, the repeatability set indicated that the strength for a given bend radius could vary greatly. Observations on specimens with Type A anchorage found that the bend strength of stirrups was significantly reduced for stirrups with short tail lengths. The authors attributed this observation to the possibility of slip, though that parameter was not measured. Authors provide specific dimensions to provide specific stirrup strength and performance in the paper. These observations match similar observation made by Imjai et al. (2007) on bent bars, which was summarized in another subsection.

A set of ten FRP, and two steel, X-shaped specimens were used to investigate the impact of opening shear crack faces that subject stirrup legs to kinking action. The specimens encased two stirrups in concrete. The top and bottom of the X were separated by a small gap that was formed when the specimens were cast; the gap is intended to represent a shear crack. The stirrups were placed at an angle to the plane of the gap to simulate inclined cracking, and at an angle to one another such that the specimen was symmetrical about both a vertical and horizontal axis. An actuator was positioned between what would be the equivalent of outmost serifs of the letter X on both sides of the X. The actuators were connected such that they applied equal load to both sides.

The authors observed a reduction in stirrup strength for specimens with stirrups that had an angle less than 90 degrees to the plane of the crack; however, they found no clear trend between strength decreases and the stirrup angle. The strength of stirrups inclined to the plane of the crack was as low as 65 percent of the straight portion strength. So the authors concluded that the impact of the stirrup bend was more significant than the angle of the shear crack when it intersects the stirrups.

The second experimental programme conducted 10 tests on T-beams. Eight of the beams were reinforced in flexure with steel strands and two were reinforced with CFRP strands; the steel reinforced specimens were designed so that the strands operated within the linear elastic range. Four of the beams had GFRP stirrups, four had CFRP stirrups, one had steel stirrups, and another had no stirrups. The beams were tested in 4-point loading with a simply supported span of 5.0 m and shear spans of 1.5 m. The experimental parameters were the stirrup material, the flexural reinforcing material, and the stirrup spacing.

Eight of the specimens failed in shear-tension, and failure was initiated by stirrup rupture at a bend in the flexural tension zone; two specimens failed by shear-compression. To assess the performance of the stirrups the authors computed the effective stirrup strength using Equation 2.1 as presented in the summary of the papers by Ahmed et al. (2010a)(2010b). Stirrup performance was computed using a metric equal to effective stirrup stress divided by the strength of the straight portion.

The authors observed that the strength of the stirrups, according to the performance metric, could be as low as 50 percent of the straight portion strength when they were tested in actual beams. No specimen showed full utilization of the stirrup straight portion strength. They also observed that stirrup performance decreased with decreases in the ratio of stirrup spacing over effective depth. The authors attributed this behaviour to the fact that closely spaced stirrups increase the chance that a shear crack will cross a stirrup bend, thus weakening the stirrup.

The authors also observed that the strength of beams reinforced with CFRP strands was less than that of beams with steel strands. To assess the influence of flexural reinforcement type the authors separated the shear strength into the concrete and stirrup contributions again, but this time they calculated the stirrup contribution using stirrup strains. The concrete contribution was simply the difference between the applied load and the stirrup contribution, and could be calculated at every data point. The authors observed that the concrete contribution for beams reinforced with steel strands was higher than that for beams with CFRP strands regardless of stirrup type. They attributed the use of FRP flexural

reinforcement to a decrease in the size of the flexural compression stress block, wider cracks, and less dowel contribution which decreased the concrete contribution. The authors also included observations on stirrup strains and cracking, but they are omitted from this summary.

The paper then presents a modified form of the CSA A23.3-94 shear design equations appropriate for use on FRP reinforced concrete beams. The equations were tested against a database of 118 beams with varying reinforcement types and arrangements. The database was then used to calibrate a set of material factors of safety for FRP reinforcements. Those equations follow:

$$V_{rf} = V_{cf} + V_{sf} \tag{2.5}$$

$$V_{cf} = 0.2\lambda\phi_c\sqrt{f'_c}\,b_w d\sqrt{\frac{E_{fl}}{E_s}} \tag{2.6}$$

$$V_{sf} = 0.4\phi_f f_{uv}\frac{A_{fv}d}{s} \le 0.8\lambda\phi_c\sqrt{f'_c}\,b_w d\sqrt{\frac{E_{fv}}{E_s}} \tag{2.7}$$

where V_{rf} is the shear strength in N, V_{cf} is the concrete contribution in N, V_{sf} is the stirrup contribution in N, λ is a factor accounting for the density of concrete, φ_c is the material factor of safety for concrete, f'_c is the concrete strength in MPa, b_w is the beam width in mm, d is the effective depth in mm, E_{fl} is the elastic modulus of the flexural reinforcement in MPa, E_s is the elastic modulus of steel in MPa, f_{fuv} is the strength of the straight portion strength of stirrups in MPa, A_{fv} is the area of one stirrup in mm^2, s is the stirrup spacing in mm, and E_{fv} is the elastic modulus of the stirrups in MPa.

Equation 2.6 is a slightly modified form of the concrete contribution found in the simplified method of the CSA A23.3-94 standard. This form includes a square-root term which accounts for the reduced stiffness of FRP reinforcements when compared to steel.

Equation 2.7 is a slightly modified form of the stirrup contribution found in the in the simplified method of the CSA A23.3-94 standard. The equation includes a factor of 0.4 which comes from a statistical analysis and was chosen to ensure that 95 percent of beams would show an effective stirrup stress greater than 40 percent of the straight portion strength at ultimate (Shehata, 1999). The term on the right of the inequality limits the contribution to account for the possibility of concrete crushing instead of stirrup rupture. In his thesis, Shehata includes provisions for shear design by way of a modified form of the general method of the CSA A23.3-94 standard (Shehata, 1999).

The paper then goes on to provide provisions for minimum shear reinforcement, and to limit the stirrup strains at service load levels, but those provisions are not repeated here.

2.2 Shear Strength Prediction Methods for FRP Reinforced Concrete Beams

In this section of the Literature Review are summaries of the sectional shear design method of the CSA S806-12 standard and the shear strength model by Nehdi et al. (2007). There are also summaries of the findings of a study that assessed the performance of several shear strength predictors using a large database of specimens. The provisions of the CSA S806-12 standard were used to design the experimental specimens of this research programme as discussed in Chapter 3.

2.2.1 CSA S806-12 Design and Construction of Building Structures with Fibre-Reinforced Polymers – Sectional Shear Method

The sectional shear design provisions of the CSA S806-12 standard conform to the traditional approach of computing the concrete and stirrup shear strength contributions separately, and then summing

them to find the sectional shear strength. The sectional shear strength provisions are found within clause 8.4.4 of the standard.

Clause 8.4.4.2 indicates that sections located within the effective shear depth, d_v, of the face of a support, where compression is induced in the support, may be designed for the same shear force as a section located d_v from the support for non-prestressed beams. Where d_v is the effective shear depth in mm, and which is taken as either $0.9 \cdot d$ or $0.72 \cdot h$, where d is the effective depth and h is the total height of the section.

Clause 8.4.4.4 provides two equations to compute the strength of the section; the choice of equation depends on the stirrup material, either FRP or steel. The clause also provides an equation which defines the maximum allowable strength. Those equations follow:

$$V_r = V_c + V_{sF} \quad \text{CSA S806-12 Equation 8-14} \tag{2.8}$$

$$V_r = V_c + V_{ss} \quad \text{CSA S806-12 Equation 8-15} \tag{2.9}$$

$$V_{r,\max} = 0.22\phi_c f'_c b_w d_v + 0.5V_p + \left[\left(M_{dc}V_f\right)/M_f\right] \quad \text{CSA S806-12 Equation 8-16} \tag{2.10}$$

where V_r is the sectional shear strength in N, V_c is the concrete contribution to shear strength in N, V_{sF} is the FRP stirrup contribution to shear strength in N, V_{ss} is the steel stirrup contribution to shear strength in N, φ_c is the material factor of safety for concrete, f'_c is the concrete strength in MPa, b_w is the beam width in mm, V_p is the component of the effective prestressing force acting in the direction of the shear in N, M_{dc} is not defined anywhere in the standard, V_f is the factored shear force acting on the section in N, and M_f is the factored moment acting on the section in N·mm.

Clause 8.4.4.5 provides the base algorithm for computing the concrete contribution to shear strength. The concrete contribution may be modified by clauses 8.4.4.6 through 8.4.4.8. The equations for the concrete contribution follow:

$$V_c = 0.05\lambda\phi_c k_m k_r \left(f'_c\right)^{1/3} b_w d_v \quad \text{CSA S806-12 Equation 8-17} \tag{2.11}$$

$$0.11\phi_c\sqrt{f'_c}\,b_w d_v \le V_c \le 0.22\phi_c\sqrt{f'_c}\,b_w d_v \tag{2.12}$$

$$k_m = \sqrt{\frac{V_f d}{M_f}} \le 1.0 \quad \text{CSA S806-12 Equation 8-18} \tag{2.13}$$

$$k_r = 1 + \left(E_f \rho_{Fw}\right)^{1/3} \quad \text{CSA S806-12 Equation 8-19} \tag{2.14}$$

where λ is a factor accounting for concrete density which is normally taken as 1.0, k_m is a factor accounting for the effect of moment on shear strength, k_r is a factor accounting for the effect of reinforcement rigidity on shear strength, E_f is the elastic modulus of the reinforcement, and ρ_{Fw} is the longitudinal reinforcement ratio.

Clause 8.4.4.6 presents a factor to account for the increase in strength experienced by concrete adjacent to a support where compression is induced, which the standard refers to as the arch effect factor. The factor multiplies with the concrete contribution, V_c, as computed in clause 8.4.4.5 for sections located within a distance of $2.5 \cdot d$ of a support where compression is induced parallel to the direction of the shear force. The equations follow:

$$V_c = k_a V_c \tag{2.15}$$

$$k_a = \frac{2.5 V_f d}{M_f} \quad \text{CSA S806-12 Equation 8-20} \tag{2.16}$$

$$1.0 \le k_a \le 2.5 \tag{2.17}$$

where k_a is a factor accounting for the effect of arch action on shear strength.

Clause 8.4.4.7 presents a factor to account for size-effect. The factor multiplies with the concrete contribution, V_c, as computed in clause 8.4.4.5. The factor is only applied to members with an effective depth, d, greater than 300 mm and which have less than the minimum amount of reinforcement specified by clause 8.4.5.2 which is reviewed later. The equations follow:

$$V_c = k_s V_c \tag{2.18}$$

$$k_s = \frac{750}{450 + d} \le 1.0 \quad \text{CSA S806-12 Equation 8-21} \tag{2.19}$$

where k_s is a factor accounting for the effect of member size on shear strength.

Clause 8.4.4.8 is a supplement to clause 8.4.4.7, which indicates that if members have an effective depth greater than 300 mm and which have stirrup reinforcement equal to or greater than the amount specified by clause 8.4.5.2 then the concrete contribution to shear strength, V_c, is equal to the value determined in clause 8.4.4.5. Or put simply, the factor k_s of clause 8.4.4.7 does not apply to such beams.

Clause 8.4.4.9 provides the algorithm for calculating the stirrup contribution to shear strength, and the equations follow:

$$V_{sF} = \frac{0.4 \phi_f A_{Fv} f_{Fu} d_v}{s} \cot\theta \quad \text{CSA S806-12 Equation 8-22} \tag{2.20}$$

$$V_{ss} = \frac{\phi_s A_v f_y d_v}{s} \cot\theta \quad \text{CSA S806-12 Equation 8-22} \tag{2.21}$$

$$\theta = 30^o + 7000\varepsilon_l \quad \text{CSA S806-12 Equation 8-23} \tag{2.22}$$

$$30^o \le \theta \le 60^o \tag{2.23}$$

$$\varepsilon_l = \frac{\frac{M_f}{d_v} + \left(V_f - V_p\right) + 0.5 N_f - A_p f_{po}}{2\left(E_F A_F + E_P A_P\right)} \quad \text{CSA S806-12 Equation 8-24} \tag{2.24}$$

where φ_f is the material factor of safety for FRP, A_{Fv} is the area of one FRP stirrup in mm^2, f_{Fu} is the strength of FRP stirrup reinforcement in MPa, s is the spacing of the stirrups in mm, φ_s is the material factor of safety for steel, θ is the angle of the principle compressive stress in degrees, A_v is the area of one steel stirrup in mm^2, f_y is the yield strength of steel in MPa, ε_l is strain in the longitudinal reinforcement, N_f is the factored normal force acting on the section in N, A_p is the area of prestressing tendons in mm^2, f_{po} is the stress in the prestressing tendon when the concrete strain is zero in MPa, A_F is the area of flexural reinforcement in mm^2, and E_p is the modulus of elasticity of the prestressing tendons in MPa.

The value of f_{Fu} is equal to the strength of the stirrup reinforcement, but shall not be greater than $0.005 \cdot E_f$. The standard provides no guidance on whether to take the strength of stirrup reinforcement as the manufacture's reported straight portion strength or bend strength. However, the works of Shehata (1999) and Shehata et al. (2000) suggest that the straight portion strength should be used. Further, V_f and M_f are taken as positive, and M_f should not be smaller than $(V_f - V_p) \cdot d_v$. Lastly, the strain in the longitudinal reinforcement, ε_l shall not be taken as less than zero.

The remaining parts of clause 8.4.4 include design provisions not directly related to determining the shear strength of an FRP reinforced section, and the clauses are briefly presented.

Clauses 8.4.4.10 and 8.4.4.11 provide equations for the concrete contrition for members subjected to significant axial forces.

Clause 8.4.5.1 indicates that shear reinforcement is required where the factored shear force, V_f, is greater than $0.5 \cdot V_c + \varphi_f \cdot V_p$. The clause also indicates four specific situations in which that requirement may be waived. Clause 8.4.5.2 then provides an equation, which follows, for the minimum amount of shear reinforcement:

$$A_{vF} = 0.07\sqrt{f'_c}\,\frac{b_w s}{0.4 f_{Fu}} \quad \text{CSA S806-12 Equation 8-28} \tag{2.25}$$

where are all variables are as previously defined in this subsection.

Clause 8.4.6 details provisions for the maximum spacing of stirrup reinforcement. The clause decreases the allowable spacing for large factored shear loads, or significant torsion.

Clause 8.4.7 provides several provisions for proportioning the flexural reinforcement, which were considered when designing the experimental specimens later.

Clause 8.4.8 provides an algorithm to determine the amount of reinforcement needed to resist torsion for sections subject to significant shear and torsion.

2.2.2 "Revisiting the Shear Design Equations for Concrete Beams Reinforced with FRP Rebar and Stirrup" by Machial et al., 2012

Machial et al. (2012) present a thorough review of current methods for predicting the shear strength of concrete beams internally reinforced with FRP. The CSA S806-02 standard was one of the methods investigated, but not the 2012 version used to design the specimens of this research programme.

This paper is included to justify the use of the Nehdi et al. model for shear strength, which is reviewed in the following summary. A detailed discussion of the performance of all the methods in the paper is not reproduced here.

The first part of the paper is a good review of shear transfer mechanisms and the parameters which affect the shear strength of beam with FRP reinforcements. These sections were referenced in the Introduction Chapter and are not repeated here. The paper compares the performance of 11 methods for predicting the shear strength of beams without stirrups using a database of 114 beams, and eight methods for beams with stirrups using a database of 46 beams.

The authors conclude that the design equations from a paper by Nehdi et al. were overall the best performing method for beams with and without stirrups. However, Nehdi et al. (2007) present two forms of the equations in that paper: an optimized form and a design form. The design equations are the same as the optimized equations, except the coefficients of the design equations were rounded to make them slightly more conservative. The coefficients on the stirrup contribution were reduced the most.

The authors used several metrics to measure the performance of each method. The first was an overall-performance metric equal to the inverse of the slope of a linear least squared regression line from

a plot of predicted strength against experimental strength. The second was a performance metric equal to the average, for all beams, of a ratio of the predicted strength over the experimental strength. The last was an average absolute error statistic which was an average, for all beams, of a ratio of the absolute difference between the experimental strength and predicted strength divided by the experimental strength for all beams.

The Nehdi et al. models out performed many common methods for predicting shear strength such as the ACI 440.1R-06 guidelines, the CSA S806-02 standard, the CSA S6-06 & -09 standards, the JSCE guidelines, and the ISIS-M03-01 standard, among others.

Where beams without stirrups were concerned:

- The Nehdi et al. design equations had the best overall-performance metric, the third best performance metric with the second best standard deviation, and the best average absolute error.
- The Nehdi et al. optimized equations had the second best overall-performance metric, the best performance metric with the best standard deviation, and third best average absolute error.

Where beams with stirrups were concerned:

- The Nehdi et al. design equations had the fourth best overall-performance metric, the third best performance metric which had the third best standard deviation, and the second best average absolute error.
- The optimized equations were never compared for beams with stirrups and the authors provided no explanation for this omission.

Otherwise, Machial et al. concludes that most design standards and guidelines are conservative predictors, specifically ACI 440.1R-06, CSA S806-02, CSA S6-06, CSA S6-09, JSCE, and ISIS-M03-01. Where beams with stirrups were concerned, the CSA S806-02 standard had the fourth best overall performance metric and the fourth best performance metric. Another metric in the paper which measured conservativeness found that the CSA S806-02 model was just under twice as conservative as the Nehdi et al. optimized equations. However, these conclusions cannot be extended to the CSA S806-12 standard, since there were significant revisions made to its shear provisions, which will discussed further in Section 6.1.2.

The optimized equations are used at various points throughout this thesis and are used instead of the design equations because academic investigations, such as this research programme, are concerned with accurately predicting the strength of the specimens; adjusting predictive models to make design predictions occurs after the investigation. Further, the optimized form of the Nehdi et al. equations should perform better for beams with stirrups since the coefficients of the stirrup contribution in the design equations were reduced the most to make them artificially conservative, and may explain why the design equations performed worse for beams with stirrups than for beams without.

2.2.3 "Proposed Shear Design Equations for FRP-Reinforced Concrete Beams Based on Genetic Algorithms Approach" Nehdi et al., 2007

Nehdi et al. (2007) present a model for the shear strength of FRP reinforced beams. The model is among the simplest and most accurate available to academics. The entire model is expressed by only two functions, one for the concrete contribution and another for the stirrup contribution. The model was derived using a mathematical technique known as genetic algorithm programming, which is a very sophisticated form of "curve fitting". The genetic algorithm method is explained in the paper, though a better explanation of the method is given by Kara (2011), who used it to develop an equation for the shear strength of FRP beams without stirrups; the model by Nehdi et al. is applicable to beams both with and

without FRP stirrups. The form of the concrete contribution equation between the papers by Kara and Nehdi et al. are nearly identical.

Briefly, the method treats equations, called individuals, like chromosomes. Equations are made up of a number of symbols and mathematical expressions that the method treats as the genes of the chromosome. Each equation is a potential solution to a problem, and in this case they predict shear strength. The method starts with a set of individuals known as the population, and the population is tested against a database of experimental results. In this case the fittest individuals are the ones which most closely predict beam strength, and they are used to produce a new generation of individuals.

Individuals in a new generation are created by one of three methods. The new generation may include new individuals that result from a cross-over method, where new chromosomes are created by sharing genes between the fittest individuals; more plainly, new equations are created by swapping operators, symbols, or entire terms between successful equations. The new generation may also include some successful equations from the parent generation, by a method called reproduction. Or the new generation may include mutated individuals, where a mutation occurs in a parent equation by way of changing/including/removing one of the symbols or operators.

In general, each generation should become more and more successful at solving the problem since only the best solutions from each generation are used to create the next generation.

Nehdi et al. used a database of 68 FRP reinforced beams without shear stirrups, and a database of 100 beams with stirrups to develop the shear model. The authors used a modified form of the Zutty equations as a starting point for the analysis. One modification was to include the ratio of the elasticity of FRP over steel to account for the lower elasticity of FRP reinforcements. Another was to multiply the equations by the beam width and effective depth to output shear strength in terms of force instead of stress. Lastly, the authors added an expression to account of the stirrup contribution. The starting equation had four coefficient parameters and the genetic algorithm method was used to modify only those four coefficients.

After an unsuccessful initial trial, the authors ran the analysis on the concrete contribution equation first to develop a function which was a good predictor for beams without stirrups. Then they added the concrete contribution to the stirrup contribution and ran the analysis again, modifying only the coefficients of the stirrup contribution. The result was a pair of equations that predict the strength of FRP reinforced beams both with, and without, stirrups as follows:

$$V_r = V_{cf} + V_{fv} \tag{2.26}$$

$$V_{cf} = 2.1\left(\frac{f'_c\,\rho_{fl} d}{a}\cdot\frac{E_{fl}}{E_s}\right)^{0.23} b_w d \quad \text{for } a/d > 2.5, \text{ multiply } V_{cf} \text{ by } (2.5\cdot a/d) \text{ otherwise} \tag{2.27}$$

$$V_{fv} = 0.74\left(\rho_{fv} f_{fv}\right)^{0.51} b_w d \tag{2.28}$$

where V_{cf} is the concrete contribution in N, f'_c is the concrete strength in MPa, ρ_{fl} is the flexural reinforcement ratio, d is the effective depth of the beam in mm, a is the shear span length in mm, E_{fl} is the elastic modulus of the longitudinal reinforcement in MPa, E_s is the elastic modulus of steel in MPa, b_w is the beam width in mm, V_{fv} is the stirrup contribution in N, ρ_{fv} is the shear reinforcement ratio, and f_{fv} is the stirrup strength in MPa.

Equations 2.27 & 2.28 are the optimized equations. Nehdi et al. also proposed a set of design equations, the coefficients of which were rounded to provide predictions that were slightly more conservative. In the design equations the exponent on the concrete contribution was rounded up to 0.3, and both constants on the stirrup contribution were rounded down to 0.5. The reduction of the coefficient on the stirrup contribution likely has the largest influence. These design equations are among the best

predictors of beam strength when compared to some of the most common design models (Machial et al. 2012).

It is interesting to note that these equations are not a sectional method since they do not consider the actual loading on any given section, nor would any of the parameters typically vary along the length of the span.

The authors used two metrics to measure the performance of their method against the performance of the ACI 440.1R-03 & -06 guidelines, the CSA S806-02 standard, the JSCE-97 guidelines, and the ISIS Canada-01 guidelines. The first was an average absolute error metric which averaged, for all beams, a ratio of the absolute difference between the experimental strength and predicted strength divided the experimental strength. The second was a performance metric equal to the average of the ratio of the predicted strength over the experimental strength for all beams.

Where beams without shear reinforcement were concerned, Nehdi et al. found that the proposed design equations had the lowest average absolute error, a performance metric closest to unity, and the lowest standard deviation on the performance metric. Where beams with shear reinforcement were concerned, the authors found the proposed design equations also had the lowest average absolute error, had the fourth lowest performance metric, and the lowest standard deviation on the performance metric which was tied with the ISIS-Canada-01 method. A similar analysis was not done for the optimized equations presented earlier.

Though these equations are a good predictor of beam strength they are not referred to by any guideline, standard, or code. The reason is likely because the equations are a result of a very sophisticated curve fitting algorithm and not from mechanics. For example, a unit analysis will show that the units on the left side of the equation do not match those on the right side. They do not match because the objective of the genetic algorithm method was to find values for the coefficients which would minimize the error between the predicted and experimental shear strengths, the method was not concerned, or capable, of finding a solution that conformed to the physical mechanics of the system. So theoretically there may exist a set of beams with a combination of design parameters which were not included in the database used to develop the equations and which the Nehdi et al. equations will make bad, possibly un-conservative, predictions.

2.3 Strut-and-Tie Modelling of FRP Reinforced Concrete Beams

There does not currently exist, outside of this thesis, a robust strut-and-tie method for FRP reinforced deep beams with indeterminate truss models. However, there are separate discussions on the topics of strut-and-tie methods for FRP reinforced deep beams with determinate trusses and of methods for the solution of indeterminate strut-and-tie trusses for steel reinforced members which do not require the yield assumption.

The overall strut-and-tie formulation for FRP reinforced structures, regardless of any particular study, rely on one of two general strut-and-tie modelling approaches that come from either the CSA or the ACI; however, the overall the strut-and-tie method is so similar between the two that the only major difference concerns the strength of strut elements (Andermatt et al., 2013). In fact, the three papers on FRP reinforced deep beams summarized in this section only write about the treatment of strut strength when they discuss the differences between the two approaches, or when they discuss the difference between steel and FRP reinforcement. And in general, the assumption that concrete must fail before FRP ruptures is taken for granted by the authors of each paper.

In this section of the Literature Review are summaries of papers on the strut-and-tie strength provisions of the CSA S806-12 standard and the ACI 318-08 code. Authors use the ACI code as a guide

to develop methods applicable to their research even though it is only intended for use with steel reinforced structures.

Later in this section are summaries of three papers in which the authors applied both strut-and-tie approaches to the behaviour of deep beams without transverse reinforcement. An effort was made to find varied papers on the topic of strut-and-tie modelling for concrete structures reinforced internally with FRP, but the search found only studies which investigated deep beams with determinate trusses, and without transverse reinforcement. The three papers summarized here may not exhaust the supply of papers on the topic, but other papers will likely not present trusses which are any more complicated. After a while the search effort moved to a more productive area.

In the last part of this section is a summary of a suite of papers that present a strut-and-tie method applicable to structural elements with indeterminate strut-and-tie model trusses that do not require the steel to yield to find a lower bound solution. This suite of papers forms the basis for the Indeterminate Strut-and-Tie (IST) analysis method, which is presented in in Chapter 5. The search for papers with similar topics was extensive; it would appear that only two researchers, separately, worked on such a topic.

2.3.1 CSA S806-12 Design and Construction of Building Structures with Fibre-Reinforced Polymers – Strut-and-Tie Method

The CSA S806-12 standard is the only design guide for FRP reinforced structures with thorough provisions for strut-and-tie modelling. However, the standard has received little attention since its publication and only one of the three papers summarized later makes reference to it. In that paper Farghaly et al. (2013) notes that the same strut-and-tie modelling method is used by all of the following design documents: CSA A23.3-04, CSA S6-06, AASHTO-07, and CSA S806-12. However, the CSA S806-12 standard has removed all references to steel and yielding, and it does not contain a commentary with design advice or interpretation.

The content of the standard does not indicate when designers should use a strut-and-tie model; so designers are free to use either the sectional method or strut-and-tie modelling as they see fit. The sectional method was presented earlier in this chapter. The strut-and-tie provisions are found within clause 8.5 of the CSA S806-12 standard.

Clause 8.5.2.1 indicates that strut stress shall not exceed $\varphi_c \cdot f_{cu} \cdot A_{cs}$, where φ_c is the concrete material factor of safety, f_{cu} is the strength of the strut in MPa, and A_{cs} is the cross-sectional area of the strut in mm. Clause 8.5.2.2 directs designers to a figure to assist in determining A_{cs}.

Clause 8.5.2.4 provides the formulae used to determine strut strength, which follow:

$$f_{cu} = \frac{f'_c}{0.8 + 170\varepsilon_1} \leq 0.85 f'_c \quad \text{CSA S806-12 Equation 8-37} \tag{2.29}$$

$$\varepsilon_1 = \varepsilon_F + (\varepsilon_F + 0.002)\cot^2 \theta_s \quad \text{CSA S806-12 Equation 8-38} \tag{2.30}$$

where f'_c is the concrete strength in MPa, ε_1 is the tensile strain transverse to the orientation of the strut, ε_F is the tensile strain in the tie bar located closest to the tension face and which is inclined θ_s to the strut, and θ_s is the smallest angle between the strut and adjoining ties. If the strain in the tie changes over the strut width, it may be taken as the strain at the centreline of the strut.

The formulation of the strut strength is such that any increase in the transverse tensile strain will cause a decrease in the strut strength. The transverse tensile strain is function of the angle between the strut and adjoining tie and the strain in that tie bar; as the angle between the strut and adjoining tie becomes small so too does the strut strength, and as the strain in the tie increases the strut strength decreases. Finally, the strut strength is directly proportional to concrete strength.

Clause 8.5.3.1 indicates that the total area of the bars in the tension tie, A_{FT} in mm^2, shall be large enough to ensure the force does not exceed $0.65 \cdot \varphi_F \cdot A_{TF} \cdot f_{Fu}$, where φ_F is the material factor of safety for the reinforcement, and f_{Fu} is the ultimate strength of the FRP reinforcement in MPa. The next clause indicates provisions for the anchorage of ties, but otherwise this is the extent to which the standard addresses FRP reinforcement.

Clause 8.5.4.1 provides the limiting compressive stress in node regions: $0.85 \cdot \varphi_c \cdot f'_c$ for nodes bounded by only struts, $0.75 \cdot \varphi_c \cdot f'_c$ for nodes anchoring one tie, $0.65 \cdot \varphi_c \cdot f'_c$ for nodes anchoring ties in more than one direction.

Clause 8.5.4.2 indicates that the stress limits of clause 8.5.4.1 are satisfied if bearing stresses produced by concentrated loads or reactions do not exceed the limit, or if the tie reinforcement is evenly distributed over an effective area of concrete equal to the tie force divided by the limit. With this particular verbiage the CSA standard implicitly indicates to designers that node faces which do not anchor ties, or which are not subject to a concentrated load or reaction, do not need to be checked.

Clause 8.5.5 provides provisions for crack control reinforcement. However crack control reinforcement is often omitted from experimental designs in academic investigations. The crack control reinforcement, by way of restraining cracks, will increase the strength of the struts through increased confinement. In many actual designs the crack control reinforcement will take on the form of shear stirrups, and the standard allows designers to count shear stirrups as crack control reinforcement if spacing requirements are satisfied.

Clause 8.6 provides special provisions for the design of brackets and corbels, and the requirements are identical to those of the CSA A23.3-04 standard. However, there exist no academic papers, or any other investigation, into the strength of FRP reinforced brackets, corbels, or dapped-end beams; so it is unusual that the standard condones such designs. It is even more unusual since common design methods for brackets, corbels, and dapped-end beams require tie bars to be anchored by standard hooks, which would be bent FRP bars in this case. In fact, the standard even recognizes this in clause 9.2.2, which forbids designers from using hooks or mechanical devices to anchor bars in tension unless proper testing has demonstrated that the method can develop at least 1.67 times the required tension in the bar.

The provisions of this standard are appropriate for determinate strut-and-tie models; however, they are inadequate for any complicated strut-and-tie truss with the slightest degree of indeterminacy. These inadequacies are more thoroughly explained at several points throughout this thesis, but particularly in the introductory section of Chapter 5.

2.3.2 ACI 318-08 Building Code Requirements for Structural Concrete

A 2011 version of the ACI code exists, but the ACI 318-08 code is reviewed here since it is the version referenced later by two of the three papers in this section on FRP reinforced deep beams; the third references the 2006 version. However, a quick review of the two versions of the code found that there are no significant differences where strut-and-tie modelling is concerned.

Clause A.3.1 defines the strength of a strut as $F_{ns} = f_{ce} \cdot A_{cs}$, where F_{ns} is the nominal compressive strength of a strut without longitudinal reinforcement in N, f_{ce} is the compressive strength of the strut in MPa, and A_{cs} is the cross-sectional area of the strut. The commentary of the code directs its readers to a few figures to provide guidance on computing A_{cs}.

Clause A.3.2 defines the strength of a strut as $f_{ce} = 0.85 \cdot \beta_s \cdot f'c$, where β_s is a factor accounting for cracking or confining effects acting on the strut, and f'_c is the concrete strength in MPa. The product of

$0.85 \cdot \beta_s$ is commonly referred to as the strut efficiency factor, and is commonly represented by v; however, in this thesis that product is referred to as the strut strength reduction factor. The factor β_s is defined qualitatively by the code in clauses A.3.2.1 to A3.2.4 and is summarized in Table 2.1.

Table 2.1: ACI 318-08 Factors Accounting for Cracking and Confining Effects

$\beta_s = 1.0$, for a strut with uniform cross-sectional area over its length, a.k.a a prismatic strut.
$\beta_s = 0.75$, for a strut where the width of the mid-section is larger than the width at the nodes and which is reinforced in accordance with A.3.3, a.k.a. a reinforced bottle-shaped strut.
$\beta_s = 0.60 \cdot \lambda$, for a strut where the width of the mid-section is larger than the width at the nodes and which is not reinforced, a.k.a. an unreinforced bottle-shaped strut. The factor λ accounts for light weight concrete.
$\beta_s = 0.4$, for struts in tension members such as tension flanges of beams, box girders, or walls.
$\beta_s = 0.6 \cdot \lambda$, any other case not covered above, and λ is defined as above.

The provisions for ties are omitted since the ACI 318-08 code only applies to steel reinforced members, and as such are not applicable to FRP reinforced deep beams.

Clause A.5.1 defines the strength of nodes as $F_{nn} = f_{ce} \cdot A_{nz}$, where F_{nn} is the strength of the nodal zone in N, f_{ce} is the effective compressive strength in the nodal zone in MPa, and A_{nz} is the area of the face of the nodal zone under consideration taken perpendicular to the force being considered in mm^2.

Clause A.5.2 provides the equation for the effective nodal zone strength, $f_{ce} = 0.85 \cdot \beta_n \cdot f'_c$, where β_n is a factor to account for the effect of tie anchorage on the effective compressive strength of a nodal zone. The factor β_n is equal to 1.00 for nodes bounded by only compressive struts, 0.80 for nodes anchoring one tie, or 0.60 for nodes anchoring two or more ties.

Clause RA.2.3, which is part of the commentary, recognizes the possibility that a node may balance more than three forces. So, for the purpose of checking node strength, it is permissible to resolve adjacent force vectors into one resultant force vector so long as at least three force vectors remain and so long as those force vectors act over a definable node face.

2.3.3 "Strength Modelling of Concrete Deep Beams Reinforced with Internal Fiber-Reinforced Polymer" by Andermatt et al., 2013

This paper by Andermatt et al. (2013a) is the most recent paper on the topic of strut-and-tie modelling of FRP reinforced concrete beams. The authors treat this paper as a companion to another paper which is a summary of the results of experimental tests on 12 large scale FRP reinforced deep beams without shear reinforcing (Andermatt et al., 2013b); together they are a summary of Andermatt's master's thesis (2010).

Andermatt et al. open the paper by summarizing the state of FRP reinforced concrete design concerning deep beams. First, they note that transfer mechanisms of deep beams depend on the shear-span-to-effective-depth ratio, a/d, and that deep beams have a low ratio and thus transfer forces by arch action, while slender beams have a high ratio and transfer by beam action; a ratio of 2.5 is commonly regarded as the transition point between the two. Then the authors write that every major steel reinforced concrete design document recognizes this change in behaviour by directing designers to use different analytical methods depending on the a/d ratio; strut-and-tie models are commonly used to design deep beams and sectional methods are used to design slender beams.

However, at that time, as the authors point out, no FRP reinforced concrete design documents made that distinction, and they specifically reference CSA S6-06, CSA S806-02, ISIS-03-01, and ACI 440.R-06. Instead, these documents used sectional design methods for beams of any a/d ratio, and these

methods did not account for the arch action transfer mechanism of deep beams which increase their capacity. The authors note that a failure to observe the increase in capacity may lead to uneconomical designs with unnecessarily large cross-sections for beams without stirrups.

The authors then review current sectional design methods and provide a general overview of strut-and-tie modelling. They note that the basics of strut-and-tie modelling are similar across many design codes, and that most of the disagreement between them concerns the strut strength calculations. The authors then summarize the strut-and-tie modelling provisions for the CSA A23.3-04 standard and the ACI 318-08 code. The important portions of the two design documents were presented earlier in this section of the Literature Review, so the authors' summary is not repeated here.

However, in their summary of the CSA A23.3-04 standard Andermatt et al. make the salient observation that steel strut-and-tie models assume the tie strain is equal to the yield strain; an assumption which is not applicable to FRP reinforced concrete. So, the actual strain in the FRP tie must be considered when computing strut strength, see Equations 2.29 and 2.30.

The theory of extended nodal zones further complicates the matter. The CSA A23.3-04 standard allows designers to use either: the strain in the tie where it intersects the strut centreline, which is located inside the extended nodal zone, or the tie strain from the boundary of the node, which represents full tie strain. In this way, the strain used to compute the strut strength may be lower if the strain is taken from within the extended nodal zone since the code directs designers to linearly vary the strain in the tie as it crosses the node. Andermatt et al. investigated this further by considering two approaches for determining strut strength according to the CSA A23.3-04 standard: approach one used the full strain in the tie on the boundary of the extended nodal zone, and approach two used the reduced tie strain taken at the point where the strut and tie centrelines intersect within the extended nodal zone.

The paper presented a small database of FRP reinforced deep beams, twelve of which came from the companion paper, and none of which contained any transverse reinforcement. The database included a variety of effective depths, concrete strengths, a/d ratios, flexural reinforcement ratios, and FRP types. The authors used a traditional strut-and-tie truss for deep beams without reinforcement, which is a determinate structure with a simple solution to the force system.

However, use of the CSA A23.3-04 approaches necessitated that the load be applied incrementally to solve for the failure load. To simplify the solution Andermatt et al. assumed the depth of the compression stress block strut was constant and equal to $0.85 \cdot f'_c$. This locked the geometry of the strut-and-tie trusses, and kept the angle θ_s of Equation 2.30 constant on each load increment. However, the force, and thus strain, in the longitudinal tie would change with each increment and so would the strength of the diagonal strut. The analysis stopped if anyone of the strut-and-tie elements failed.

The authors checked the three approaches against their database of beams. The performance metric was equal to the experimental strength divided by the predicted strength. Approach one from the CSA A23.304 method had an average performance of 1.20 with a coefficient of variation of 0.21. Approach two had an average performance of 0.96 with a coefficient of variation of 0.22. And the approach from the ACI had an average performance of 1.02 with a coefficient of variation of 0.51. All of the strut-and-tie methods performed much better than the sectional methods. However, all the strut-and-tie methods provided poorer predictions for specimens with high strength concrete.

Andermatt et al. concluded that approach one of the CSA A23.3-04 method was the best. This approach had the lowest coefficient of variation, and tended to provide conservative results. The authors attributed the good performance of the CSA A23.3-04 approaches to their ability to account for the different moduli of elasticity of reinforcement types. The moduli of elasticity were vicariously accounted for in the strut strength calculation, since it is a function of tie strain which itself is a function of the elastic modulus of the reinforcement. The ACI method does not account for this because strut strength depends on a constant.

The authors conclude by acknowledging that FRP reinforced concrete design must rely on the deformation capacity of the concrete in order to achieve a ductile failure. They caution that the linear

elastic nature of FRP must be considered when a strut-and-tie model is used. The also caution that concrete can only provide limited deformation capacity, and that it may not be enough for complex truss models.

2.3.4 "Optimal efficiency factor in strut-and-tie model for FRP-reinforced concrete short beams with (1.5 < a/d <2.5)" by Nehdi et al., 2008

Nehdi et al. (2008) present equations for strut strength reduction factors for FRP reinforced concrete deep beams for use with the strut-and-tie provisions of the ACI code in this paper. The authors refer to the reduction factor as an efficiency factor in the paper.

The authors open the paper by noting that at the time research had not considered the strength and behaviour of FRP reinforced deep beams, and that strut-and-tie methods are a rational and powerful tool which could be adapted to analyze such beams. They acknowledge that FRP reinforcement elasticity influences slender beam behaviour, and suggest that it would also influence strut strength in an FRP strut-and-tie model. To further justify their investigation the authors reference another paper and write that, "…the efficiency factor, which accounts for variable stress distribution and limited ductility of concrete struts, is basically expressed to adjust the plasticity of the model to empirical data." (Nehdi et al., 2008).

The authors state that at the time of writing there was only one data point, beam test, which concerned the shear failure of an FRP reinforced deep beam. So, to provide data for their investigation they casted eight CFRP reinforced beams, seven GFRP reinforced beams, and four steel reinforced beams, all without shear reinforcement. The shear-span-to-effective-depth ratio, a/d, was between 1.5 and 2.5, concrete strengths ranged between 34.7 and 63.1 MPa, and different diameters of flexural reinforcements were used which provided a range of flexural reinforcement ratios. Both the effective depth and point of load application, in 4-point loading, were varied to affect change in the a/d ratio.

The authors' discussion of their results left a lot to be desired, and a commentary will follow the next few paragraphs.

Nehdi et al. observed that GFRP reinforced beams failed at lower loads than that of CFRP and steel reinforced beams for specimens with an effective depth of 150 mm or less, and that the GFRP beams produced cracks which were both more numerous and wider. The authors explain their observations by indicating that shear slip along the critical shear crack is reduced in the presence of wide cracks, and that without shear slip the aggregate interlock and dowel action shear transfer mechanisms cannot engage. They defend this explanation by citing another paper which noted a similar observation. The authors conclude that the reduced stiffness of FRP reinforcements produces wider cracks which decrease shear slip, and so the effect of axial stiffness must be considered by strut strength reduction factor.

The authors also observed that the cracking in CFRP reinforced beams was similar to that of steel beams and explain that this may be a result of the CFRP having an elastic modulus of 134 GPa, which is close to that of steel at 200 GPa, and far from that of GFRP at 40.8 GPa, for the reinforcements considered in their study.

The next few paragraphs of the paper become difficult to follow, even for someone who is well versed in the shear behaviour of FRP reinforced beams.

The authors observed that the strength of CFRP reinforced beams was higher than that of steel, and attribute that behaviour to the increased tensile strength of CFRP which increased aggregate interlock and dowel action. But this claim does not make sense because the tensile strength of CFRP reinforcement should only influence beam strength if the failure happens by way of longitudinal reinforcement rupture.

Nehdi et al then observe that GFRP reinforced beams with an effective depth of 350 mm failed at higher loads than similar steel reinforced beams but lower than similar CFRP reinforced beams. The explanation for this behaviour by the authors becomes unintelligible. They explain the behaviour by first noting that crack widths were smaller in the 350 mm GFRP reinforced beam than in the 150 mm beam,

and attribute the increase in strength to the shear slip mechanism which is improved with smaller cracks. Then they suggest that the increase in beam strength is not due to the improved aggregate interlock and dowel action of the GFRP because of its higher strength when compared to steel, which was the mechanism they suggested for CFRP beams with effective depths of 150 mm. Instead Nehdi et al. suggest that the increased tensile strength of GFRP improves the arch system, but they do not explain the means by which it is improved. However, this is all meaningless because, again, the tensile strength of the reinforcement should only influence beam strength if the failure happens by way of longitudinal reinforcement rupture.

The observed behaviour would have been better explained by considering bond mechanisms. The FRPs used in this investigation were sand coated and bonded to the concrete by adhesion and friction, whereas the steel was ribbed and bonded by adhesion, friction, and mechanical interlock. The amount of cracking and crack widths may be explained by failing bond mechanisms. The process of de-bonding leads to the development of an actual tied-arch mechanism, which is assumed to exist in deep beam strut-and-tie models as long as there is no slip past the supports. It is well known that the quality of sand coatings varies between FRP manufacturers, and the GFRP and CFRP in this study came from different manufacturers.

The differences in cracking, shear behaviour, and beam strength could be explained by the differences in the quality of bond between the different reinforcements. A better bond would delay the formation of the tied-arch mechanism as shear forces would transfer by way of simultaneous beam and arch action behaviours, and thus increase failure load. Technically, a poor bond increases the possibility of slip, and slippage destroys beam action which depends on load transfer across the concrete-reinforcement interface within the concrete teeth that form between cracks in the comb model for shear strength (Stratford et al., 2003).

The quality of the bond is also augmented by bar surface area. A beam with a larger number of smaller bars will have more surface-bond area than an equivalent beam with a small number of large bars. This was a factor in the experiments since the authors indicated that multiple sizes of bars were used to vary the flexural reinforcement ratios, but they were not clear on which beams were reinforced with which diameters. This is by far a more compelling explanation for their observed results than the discussion Nehdi et al. provided.

To be clear, a poor concrete-reinforcement bond in the GFRP reinforced specimens may have produced more and wider cracks than in their CFRP and steel reinforced counterparts for the beams with an effective depth of 150 mm or less. The poor bond would have allowed the beam action behaviour to diminish faster than in the beams with a better bond, and the tied arch mechanism would have formed and then failed at a lower load. In the case of the GFRP reinforced beam with an effective depth of 350 mm, it may have been the case that a larger number of smaller bars were used to reinforce the beam, thus increasing the quality of the bond when compared to its counterparts.

The works of Stratford et al. (2002)(2003) provide the best discussion on the influence of cracking, bond, and slippage on the shear strength of FRP reinforced beams. However, those articles are not summarized in this thesis.

In the next part of the paper Nehdi et al. noted that as the a/d ratio increased the flexural and shear capacity of the section decreased; they then note that a strut strength reduction factor should reproduce that observation. Their requirement fits well-established behaviour which indicates that strut strength decreases with decreases in the strut angle to the flexural reinforcement, and which is incorporated in the strut-and-tie methods of the CSA standards.

Surprisingly the authors reference two works to indicate that the strut strength reduction factor was not sensitive to concrete strength. This is, of course, at odds with every strut-and-tie design document, in that strut strength is always directly proportional to concrete strength.

The last passage of the experimental results section includes some unexpected discussion on the part of the authors. The paper includes plots which show that strains at failure increased with increases in

beam effective depth beyond 300 mm, and the authors suggest that the plots indicate an increase in flexural capacity. This observation is problematic because the authors never indicate the failure modes for any of the beams, and this statement calls into question their later analysis which concerns the strength of the diagonal strut and not the compression stress block strut, which is expected to crush in a flexural failure. Further, it contradicts previous discussion which implied that all beams failed by way of shear action.

Separately they note that increasing the effective depth increased the ultimate load of the FRP reinforced specimens, and conclude that the efficiency factor should account for increases in ultimate load with increases in section depth for the same a/d ratio. Then the authors write that both the effective depth and tensile strength of the reinforcement increase flexural capacity, and provide a very basic function for the moment capacity of concrete section as justification.

The next section of the paper is a passage on the concept of strut-and-tie modelling as it concerns the strut strength reduction factors and FRP reinforcements. The authors recognize that failure is traditionally assumed to take place when a compression strut crushes, or when a number of ties yield, and they note that it is inappropriate to assume that concrete is perfectly plastic. They also clearly state that FRP cannot yield, and so FRP reinforced members must fail by concrete crushing.

The authors then suggest that a larger compression stress block is needed to balance the force in the longitudinal tie because of the increased strength of the FRP, presumably when compared to a steel reinforced section. Their observation is true, but only if the FRP reinforced beam is designed to fail in by way of tensile rupture, which is generally not recommended. Then they suggest that if the depth of the compression stress block increases then so too will the diagonal strut since the size of the diagonal strut is a function of the size of the compression stress block and bearing plate at the load point.

The authors then acknowledge that confinement, by way of transverse reinforcement, influences strut strength and reference the ACI code for justification. Nehdi et al. then posit that confinement can be provided by way of having a large strut, and they note that since high strength reinforcement requires a deeper compressive stress block to balance the moment then large struts will be created. The authors conclude the section by noting that higher strength longitudinal reinforcement will vicariously confine the struts by way of making them large, and that this should be recognized by a strut strength reduction factor, but they offer no reference to justify these claims.

In the next section the authors reiterate their observations on the parameters which affect strut strength reduction factors: a/d ratio, reinforcement stiffness, and effective depth. The authors formulate their revised efficiency factors for use with the ACI 318-08 provisions, which were summarized earlier. The equations for the strut strength reduction factors follow:

$$\beta_s = 0.68 - 0.012\left(\frac{a}{d}\right)^4 \quad \text{for } \left(E_f \rho_f\right)^{1/3} \le 10 \tag{2.31}$$

$$\beta_s = 0.75 - 0.01\left(\frac{a}{d}\right)^4 \quad \text{for } \left(E_f \rho_f\right)^{1/3} > 10 \tag{2.32}$$

$$k = \frac{250 + d}{550} \tag{2.33}$$

where β_s is the reduction factor, a is the shear span length in mm, d is the effective depth in mm, E_f is the elastic modulus of the reinforcement in MPa, ρ_f is the flexural reinforcement ratio, and k is factor accounting for beam depth. The factor k is multiplies with β_s for sections which are deeper than 300 mm.

The authors present a figure to indicate that there is a linear relationship between β_s and the fourth power of the a/d ratio, and that two separate relationships exist for beams depending on the cubic root of the product of the reinforcement ratio and its modulus of elasticity. So, essentially Equation 2.31 applies to GFRP reinforced beams and Equation 2.32 applies to CFRP reinforced beams.

The paper then has another unusual inclusion: an equation for the stress in the flexural reinforcement from the ACI 440.R-06 guidelines, which are the ACI's guidelines for FRP reinforced concrete. The authors never refer to the equation beyond the sentences which introduce it, nor do they explain its variables, nor do they make reference to when they estimate tie stress or strain in their later strut-and-tie analysis. But, the equation is presented just after a sentence which directs readers to the strut-and-tie model truss. So, one might infer that this equation is used to calculate the depth of the flexural compression stress block, and thus the size of the inclined strut, but it would have been simpler and more direct to present the equation used to compute the depth of the flexural compression stress block if that were the intention.

The next part of the paper compares the performance of their strut strength reduction factors to the factors used in the strut-and-tie provisions of CSA A23.3-04, AS-3600-01, and ACI 318-08; they also compare the performance to that of sectional methods available at the time. The performance metric is equal to the ratio of the experimental strength over the predicted strength. Three figures are then presented, each with a separate plot for specimens with GFRP and CFRP bars. The figures plot the performance metric against the a/d ratio, flexural reinforcement ratio, and effective depth, respectively.

It is clear that strut-and-tie models with the proposed strut efficiency factors and the factors of ACI 318 & AS-3600 are all good predictors; the predictions of CSA A23.3-04 were more conservative. The sectional methods all made very conservative predictions, especially when d was large or the a/d ratio was small.

A closer examination of a table in the paper, which presents equivalent strut strength reduction factors for the four methods, indicated that the factors for the proposed method, and the ACI 318-08 & AS-3600 approaches are all very close to 0.60 for the data points shown in the figures, which explains the very similar predictions. However, the proposed method has efficiency factors which stray far from 0.60 and lead to good predictions for beams which were not included in the figures; as a result the proposed method by Nehdi et al. is overall the best predictor for the database of beams.

Predictions by the CSA A23.3-04 approach require the strain in the flexural reinforcement. The authors used a value of 0.002, which is the yield strain of common steel but is the only strain value suggested for use by the standard. The authors noted that the strain in the actual reinforcement was much larger, which would have led to smaller strength reduction factors, and even more conservative predictions. This contrasts with the findings summarized in the previous article by Andermatt et al. which found the CSA A23.3-04 method was a good predictor since the strut strength reduction equations accounted for a/d ratio and flexural stiffness through the strain and strut angle parameters.

2.3.5 "Shear Behavior of FRP-Reinforced Concrete Deep Beams without Web Reinforcement" by Farghaly et al., 2013

In this paper Farghaly et al. (2013) assess the strut strength factors given in the ACI 318-08 code and the CSA S806-12 standard. This paper is the first to publish an investigation which utilized the strut-and-tie modelling provisions of the CSA S806-12 standard.

The authors introduce the paper by noting that arch action is a function of the shear-span-to-effective-depth ratio, a/d ratio, the concrete compressive strength, and the properties of the longitudinal reinforcement, which are claims later supported by their observations. Note that Nehdi et al. (2008), which was summarized in the previous subsection, indicated that strut strength was not sensitive to concrete strength. The authors refer to Andermatt's thesis, which was noted as the primary source for the

first article on FRP strut-and-tie modelling that was summarized, to indicate that research on FRP-reinforced deep beams is very limited.

The authors note that the strut-and-tie provisions of both design documents are still subject to validation, and their main concern is the large discrepancy in the values of the strut strength factors between the ACI and CSA design documents. Their concerns stem from the provisions of the ACI which assume strut strength is independent of the longitudinal reinforcement, whereas the provisions of the CSA assume strut strength is independent of the stirrups. But this concern may belie a misunderstanding of the authors: if the stirrups are modelled as ties then strut strength may depend on them if the angle between the strut and stirrup-tie is the shallowest of all ties intersecting the strut.

The investigation tested 4 large scale, deep beams in 4-point loading. All beams shared a common a/d ratio of 1.13, and the effective depths were about 1.1 m but varied slightly for each specimen. Two of the specimens were reinforced with CFRP, and two were reinforced with GFRP, there was no transverse reinforcement. The concrete strength of the CFRP specimens was lower than that of the GFRP specimens. Each beam had a different reinforcement ratio, and the stiffness, a product of the elastic modulus and total reinforcement area, $E \cdot A$, between the beams within each GFRP and CFRP pair were made very different; however, the $E \cdot A$ term was made very similar for pairs with one GFRP and CFRP specimen each in an attempt to isolate concrete strength as a test variable from the influence of flexural reinforcement stiffness.

The failure of all specimens was by a brittle, diagonal shear failure. The critical failure crack formed first at mid-height of the beam, and then propagated to the load and support plates. Eventually concrete crushed at the top of the diagonal strut. The load level at which the initial flexural and diagonal shear cracks formed were very similar between beams with the same concrete strength. The authors observed that the reinforcement ratio had a clear impact on the width of the diagonal crack: an 80 percent increase in the reinforcement ratio caused a decrease in crack width of 43 percent and 51 percent at the same load level, for the GFRP and CFRP pairs, respectively.

The reinforcement ratio also had a clear impact on strut strength. Increasing the reinforcement ratio increased the diagonal strut strength, which was the governing failure. When the results were grouped by axial stiffness, the $E \cdot A$ term, it was clear that diagonal strut strength increased with increases in concrete strength. The authors also observed that the load-deflection response of beams with similar axial stiffness were different and further attributed this to differences in the concrete strength, and thus concrete elasticity.

Longitudinal reinforcement was outfit with strain gauges spaced evenly along the span. Plots included in the paper showed that the gauges all had similar strains at high load levels, which indicated arch action behaviour.

To consistently assess the strut-and-tie methods of the CSA and ACI design documents the authors made simplifying assumptions. First they assumed that the strut-and-tie model truss took the form of the most common truss for deep beams without transverse reinforcement. They assumed that the diagonal strut was prismatic, and defined by the size of the node at the support plate only, and referenced another paper as justification. They also approximated the strut angle by defining its vertical component as the distance between the effective depth and the mid-height of the compressive stress block strut and the horizontal component as the total shear span width, which spanned from the centres of the support and load plates.

Farghaly et al. justify their investigation into the strut strength factors by writing that, "…the approach has been to lump the effect of strut stress and strain conditions, reinforcement details, concrete strength, and uncertainties in the truss model into a single factor, referred to as the strut strength reduction factor $v \leq 1.0$" (2013). This statement is similar to the statement by Nehdi et al. cited in the previous subsection. The paper then presents a summary of the strut-and-tie modelling provisions of the CSA S806-12 standard and ACI 318-08 code.

The authors measured the performance of each model using a metric equal to the experimental strength divided by the predicted strength. Farghaly et al. found that the CSA method made conservative predictions with an average performance metric of 1.07 and a coefficient of variation of 0.01. The ACI method made un-conservative predictions with an average performance of 0.88 and a coefficient of variation of 0.17. But the database was limited to the four beams tested in the investigation.

The authors observed that the ACI method performed poorly because it will make the very similar predictions for beams with various reinforcement ratios or bar types, since the strut strength reduction factor is constant; it is a function of selecting the best factor from a table with qualitative strut descriptions. In fact, the predicted strength of the two beams in each GFRP and CFRP pair were different by only a few kilo-Newtons, whereas the experimental strengths were different by about 500 kN.

The CSA method was able to make better predictions, and the authors attributed the good predictions to the strength reduction factors which depend on tie strain, which is a function of tie stiffness. Increasing the axial stiffness by almost double, between beams in the same GFRP or CFRP pair, increased diagonal strut width by 3.0 to 4.0 percent, and increased strut strength by about 30 percent.

The increase in strut width and strength are so different because changes in the axial stiffness produce changes in both the strength calculation and the truss model geometry. First, the different reinforcement ratios were made possible by using different bar sizes which change the height of the node at the support plate; a parameter that was used to define the size of the strut. Second, strut strength simultaneously depends on longitudinal tie strain and the angle between the diagonal strut and longitudinal reinforcement, so in a non-linear fashion changing the axial stiffness will also change the depth of the compression stress block strut, and thus the strut angle, but it will also change the strain term since FRP strain is a function of the axial stiffness and the moment arm between compressive stress block and tensile tie. To address this non-linearity the authors iterated the strut angle until they found a maximum predicted strength. The relationships in the CSA method between the truss geometry, strut strength, and beam strength are complicated, but appear to offer the best predictions.

2.4 Dr. Young Mook Yun's Analysis Method for Indeterminate Strut-and-Tie Models with Steel Reinforcement

The papers reviewed in the previous subsection provide insight in to the many factors which must be considered to model FRP reinforced concrete deep beams with the strut-and-tie method. However, those papers only considered deep beams with determinate strut-and-tie trusses. This is a significant limitation to the method; it is not uncommon for strut-and-tie models with steel reinforcement to have indeterminate trusses that are made determinate by assuming the steel yields, but the same assumption does not apply to, and cannot simplify, strut-and-tie models with FRP reinforcements.

An effort was made to find strut-and-tie analysis solution methods which did not rely on the yield assumption. Two such methods were found, but only one is presented in this thesis. The method of Tae-Sung Eom and Hong-Gun Park in their 2010 paper, "Secant Stiffness Method for Inelastic Design of Strut-and-Tie Model" was found too late to be included in this thesis. Adaptation of this model may be a good alternative.

The Indeterminate Strut-and-Tie method presented later in this thesis is based on the analysis method of Dr. Young Mook Yun which was developed to analyze indeterminate strut-and-tie truss models for steel reinforced concrete. His method is a strut-and-tie modelling method, but his procedure for computing the failure load is cast in a stiffness formulation, which contrasts sharply with the strength formulation used by traditional methods.

Yun's method uses non-linear concrete material behaviour to model the struts, and a linear-elastic-to-perfectly-plastic material behaviour for ties. In the solution procedure, the global stiffness matrix is updated at each load increment to account for changes in the elastic moduli, and thus element stiffness. Yun's first paper on the topic was published in 1996 and his most recent, as the second author,

was published in 2011; relevant papers on the method and its evolution are cited here: (Yun, 1996), (Yun, 2000a), (Yun, 2000b), (Yun, 2000c), (Yun, 2006), (Yun, 2008), (Kim and Yun, 2011a), (Kim and Yun, 2011b).

Traditional strength formulations of strut-and-tie solutions do not consider the stiffness of elements explicitly. Instead, determinate force systems are sought, and the loss in stiffness of the elements is considered indirectly by assuming the steel yields, and by using strut strength reductions factors.

The remainder of this subsection will summarize the most important parts of Yun's suite of papers, highlighting aspects of its initial development and its most recent form.

The original method, presented in Yun's 1996 paper, modelled concrete struts and steel ties in addition to concrete only ties. The solution method was iterative, with modifications made to the strut-and-tie truss model to ensure the elements and nodes fit within the member geometry. The method was involved and had three distinct steps; the process is outlined below.

First, a linear elastic, plain concrete, finite element model of the structural member is analyzed. The results of the model are then used to create a strut-and-tie truss model according to common convention: concrete struts are aligned with principle compressive stress trajectories, and steel ties with principle tensile stress trajectories.

Second, the strut-and-tie model elements are assigned specific areas which are used later in the non-linear analysis. The areas are computed by dividing the element internal forces by their individual strengths. At this step element internal forces are determined by assuming the steel yields.

However, the process for computing the effective strength of the concrete struts is an involved process which makes use of a relationship by Kupfer et al. (1969). The statistic of Kupfer's relationship is the ratio of the concrete principle compressive stress over the principle tensile stress. Yun extracts this statistic from the results of the plain concrete finite element model from the first step, and his paper provides a graph of the relationship which can be used to look up effective strengths manually.

To determine the effective strength of the struts, the centre-line strut-and-tie model from the first step is superimposed over the linear elastic finite element results, also from the first step. Linear elastic elements from the plain concrete model which are intersected by the centre-line of a strut are then used to compute that strut's effective strength by averaging the results of Kupfer's relationship from all intersected elements. Yun provides some advice on modifying effective strengths for struts which have orientations that deviate from the principle compressive stress trajectories, and for confined struts. Steel areas are computed based on the assumption that steel yields.

Third, once the areas of the elements are defined the non-linear analysis method is implemented. Each concrete strut is given a unique peak stress and strain in the analysis. The discussion of the method for determining the peak strain leaves much to be desired, and the concrete material model used by Yun is not discussed in the paper. However, he uses a tangent modulus of elasticity to update material behaviour at each load increment. Yielded steel ties and crushed concrete struts were given a small, non-zero, stiffness to avoid issues with excessive deformation.

The paper provides an example of a deep beam to illustrate the method. Yun was able to show that his method could capture both truss and direct strutting action, and showed that the stirrups yielded first followed shortly by crushing of the main diagonal strut. The load at which the strut crushed was off of the experimental result by 20 percent.

A linear analysis of the strut-and-tie truss system was also conducted, where the initial tangent moduli were used for each strut. Element stresses were simply compared to the element strengths established in the second step. Yun found that the stirrups were predicted to yield at a load well ahead of the experimental load when the results of the linear analysis were compared to that of the experiment.

The paper spends an equal amount of space discussing an analysis method for the nodes; however, Yun's nodal zone analysis method is not used in this thesis.

In the year 2000 Yun published three papers (2000a)(2000b)(2000c) that present the analysis method in more detail. Each paper focuses on a different aspect of his work and illustrates the concept with different examples.

The analysis method for the year-2000 papers differs slightly from the 1996 paper and was programmed into a sophisticated non-linear, concrete focused, finite element analysis software package. The package allows a user to input the member geometry and loading, and the program outputs the principle compressive stress trajectories. The user then draws the strut-and-tie model overtop of the results. The software package then assigns areas to the strut-and-tie elements, and does a non-linear analysis on the strut-and-tie model to provide the user with the results. The solution still requires model iteration since the appropriate strut-and-tie truss geometry must still fit within the overall problem geometry. The program also requires a non-nodal zone failure mechanism, since a nodal failure fundamentally changes the load transfer paths assumed in the strut-and-tie truss.

The first step in the method from these papers differs slightly from the method in the 1996 paper: the initial finite element analysis uses a non-linear concrete material behaviour. The non-linear analysis is completed using software described best in the 2000b paper and uses a finite element formulation developed previously by Yun, which is also used in the analysis of the nodal zones. These results are then used to create the strut-and-tie model according to common convention, as in the 1996 paper.

The second step is now more involved. The areas are assigned by analysing the indeterminate strut-and-tie truss using the initial tangent moduli of the elements. The element strengths are assigned as in the 1996 paper: effective strut strengths are determined using Kupfer's relationship but with the results from the non-linear, plain concrete, finite element analysis instead, and, only for this step, the steel is assumed to yield before concrete crushes.

However, the strut-and-tie model is indeterminate and the stiffness of each element needs to be considered in the solution to the strut-and-tie truss system. Yun provides a follow chart which outlines a procedure for element area optimization in each paper. The procedure is iterative and assumes initially that each element has a unit area. The truss system is solved, and each element is checked to see if the difference between element strength and applied stress is less than a specific tolerance value, and a counter is checked to see if the number of iterations has exceeded a specific value. If neither of these conditions are satisfied then element areas are re-calculated by dividing element forces by element strengths, and the truss system is again solved. This optimization procedure is fundamentally flawed, and a discussion is provided in Chapter 5.

The third step is essentially the same as in the 1996 paper. In the 2000a paper by Yun, he provided a reference to the method by which concrete strut peak strain values are determined, but the referenced paper was inaccessible. In the 2000a and 2000b papers Yun provides the uniaxial stress-strain relationship for the concrete struts, which came from a 1964 discussion by Saenz of a paper submitted to the Journal of the ACI. This particular material model was obscure, was not used in this thesis, and is not reproduced here.

Each paper presents unique examples of the analysis method applied to concrete members such as deep beams, a shear wall with openings, and a pier structure. The two papers which present deep beams, 2000a and 2000c, show that the analysis method all but exactly predicts the capacity of the experimental specimens. The papers also present a more detailed discussion of Yun's nodal zone analysis method.

Yun's 2006 paper presents a very thorough review of the nodal zone analysis portion of his indeterminate strut-and-tie analysis method. This method was not used in this research programme because it is a complex two dimensional finite element analysis with a non-linear concrete material model.

The 2008 paper presents a novel and very unique strut-and-tie modelling approach to steel reinforced concrete. In this approach a concrete member is discretized into a grid of rectangular shapes with aspect ratios close to one. Each rectangular shape represents six one-dimensional truss elements, four which form the rectangle, and two inclined elements which cross from opposite corners. The grid is

superimposed over the entire member geometry, and elements are not assumed to be a strut or tie prior to the analysis.

As in the 1996 paper, a linear, plain concrete, finite element analysis is done to find the effective strength of compressive struts. The effective strength is determined as presented in a paper which Yun wrote and referenced, but which was inaccessible for this research programme, though the relationship appears to conform to Kupfer's relationship.

A linear analysis of the grid of strut-and-tie truss elements is conducted using unit areas. Elements defined as either a strut or tie only after the first force analysis is completed, depending on the sign of the internal force. Areas are updated by dividing the element force by the element strength. The process iterates, optimizing areas as outlined in the paper. If the number of iterations exceeds a specific number then it is assumed that the analysis will not converge to a solution. Otherwise, the iterations stop once the area of every element has been optimized, at which point elements with areas optimized below 1.0 mm^2 are set equal to 1.0 mm^2.

The optimization method is not significantly different from the earlier one, but in this case it is expected to perform adequately, and this is also discussed in Chapter 5.

The method does not check to see if element stresses exceed strengths, because element areas were optimized to make stresses equal to strength. Instead, adequacy of the strut-and-tie model is established through geometric compatibility. If the struts and ties can fit within the grid without overlapping then the truss model is assumed adequate. The method for checking this is best described by Yun in the paper. Nodal strengths are established according to ACI criteria, and are ultimately checked on the basis of geometric compatibility as well.

The power of the grid approach to strut-and-tie modelling is that it can be used to model several load cases with one grid. This is unlike traditional strut-and-tie modelling which requires a unique strut-and-tie truss model for each load case. The grid approach ultimately provides the maximum amount of steel tie area for each element in the grid. Designers can then use this information to detail the reinforcing for all load cases. Yun provides an example for how the approach, and his corresponding analysis software, can be used to design a multistory shear wall with openings, under several load cases, and the advantages it has over traditional approaches.

The 2011 papers by Kim and Yun are a companion pair. The first paper, 2011a, is a summary of an indeterminate strut-and-tie modelling method for deep beams which is similar in nature to the previous methods, but different in a few important ways. In the study of the first paper the method is used to solve a database of theoretical strut-and-tie models, and the results are used by Kim and Yun to develop a simple formula which predicts the portion of the applied load that is carried by the stirrup-truss mechanism; the formulae output is a simple ratio. In the study of the 2011b paper the authors validate the simple equation against current design methods for deep beams using a database of 234 steel reinforced concrete deep beam specimens.

The intent of the study in the 2011a paper was not to develop the indeterminate strut-and-tie analysis method, so steps one and two of the previous discussions on the 1996 and 2000 papers are forgone. In this paper a single model is used for all deep beams. It is composed of a direct-strut, and a stirrup-truss with only one vertical member located in the centre of the shear span. An example of the model is shown in Figure 2.1.

Strut element areas are based on the dimensions of the exterior, loaded nodes, nodes 1 and 4 in Figure 2.1. All nodes are assumed to be right angle triangles. The height of node 1 is determined from the location of the steel ties, and its width is determined from the required bearing area. The width of node 4 is also determined from the required bearing area, and the height is set equal to the depth of the equivalent flexural compression block. Strut areas are set equal to the width of the largest strut that can fit the node dimensions.

Internal nodes are dimensioned based on the size of the struts and ties that frame into their sides. The height of node 2 is based on the height of the top-chord strut, and the height of node 3 is based on the height of the bottom-chord tie. Internal node widths are calculated using the angle of the inclined strut element which frames into it. Further details on establishing the truss geometry are provided in the paper.

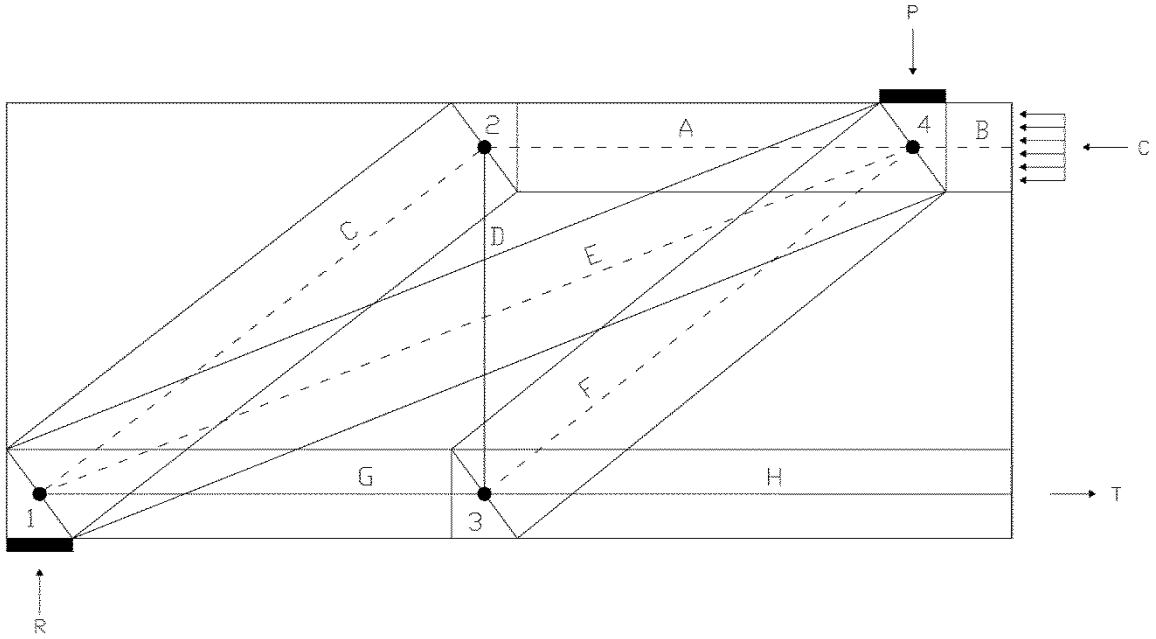

Figure 2.1: Strut-and-Tie Model Adapted from Kim and Yun (2011a)

Kim and Yun use a concrete material model that is different from the one used by Yun in his previous papers. The material model is a modified form of the Hognestad Parabola proposed in a 1995 paper by Pang and Hsu. In that paper the authors applied a softening coefficient to both the peak stress and strain at peak stress parameters. The softening coefficients are necessary because the unmodified Hognestad Parabola models the strength of concrete in uniaxial compression; however, concrete struts are subject to biaxial forces and transverse tensile strains which reduce their effective strength. The softening coefficients capture this reduction in strength. The equations from Yun's paper follow:

$$f_c = \zeta f'_c \left[2\left(\frac{\varepsilon_c}{\zeta\varepsilon_0}\right) - \left(\frac{\varepsilon_c}{\zeta\varepsilon_0}\right)^2 \right] \text{ for } \varepsilon_c / \zeta\varepsilon_0 \le 1 \tag{2.34}$$

$$f_c = \zeta f'_c \left[1 - \left(\frac{\varepsilon_c / \zeta\varepsilon_0 - 1}{2/\zeta - 1}\right)^2 \right] \text{ for } \varepsilon_c / \zeta\varepsilon_0 > 1 \tag{2.35}$$

where f_c is the concrete stress in MPa, ε_c is the uniaxial strain and independent variable, f'_c is the peak stress in MPa, ε_0 is the strain at peak stress, and ζ is the softening coefficient. The designer is free to specify values for f'_c, ε_0, and the initial tangent modulus of elasticity, E^t_c, as long as they satisfy the equation $\varepsilon_0 = 2 \cdot f'_c / E^t_c$.

The softening coefficients used by Kim and Yun were based on coefficients for the effective strength of concrete struts from the ACI 318-08 code. Prismatic, top-chord struts, were given a softening coefficient of 0.85 (= $0.85 \cdot \beta_s$, β_s = 1.00), and bottle shaped, inclined struts, were given a softening coefficient of 0.638 (= $0.85 \cdot \beta_s$, β_s = 0.75). Figure 5.3 shows an example of this stress-strain curve.

Analysis of the strut-and-tie model then proceeds as before, with load increments and stiffness matrix updating using the tangent moduli of the truss elements.

The load distribution ratio was found by dividing the force in the stirrups by the applied load at the point of balanced shear failure. A balanced shear failure occurs, according to Kim and Yun, at the simultaneous yielding of stirrups and crushing of a specific combination of struts. Further details and a descriptive flowchart may be found in the paper.

Kim and Yun performed a systematic study of deep beams by varying the flexural reinforcement ratio, concrete compressive strength, and shear-span-to-effective-depth ratio. The authors compared their results with that of literature on the load distribution ratio for deep beams and found that their model captured the reported behaviour, with respect to the aforementioned parameters. At the conclusion of the paper the authors present a formula that computes the ratio of the applied load that is assigned to the stirrup-truss portion of the strut-and-tie model. Ultimately designers will use that force to design the stirrups.

The companion paper by Kim and Yun (2011b) is a summary of an assessment on the ability of their model to adequately predict the ultimate load of real deep beams. They compare the ratio of predicted capacity to experimental strength for their model against that of commonly used design formulae.

In the 2011b paper the strength of beams is computed using the ACI 318-08 code procedure, modified to include the load distribution ratio predicted from the 2011a paper. The failure load was computed after the sequential failure of both the direct-strut and stirrup-truss mechanisms.

The geometry of the strut-and-tie elements was set using the reported bearing areas, reinforcing layout, and the load distribution ratio. The geometry looked similar to Figure 2.1. However, the nodal zone dimensions were provided, so the strut widths for both mechanisms were sized in proportion to the load distribution ratio, with respect to the bearing plates.

The force analysis was simplified because the load distribution ratio turns the indeterminate truss system into two determinate systems: the direct-strut system and the stirrup-truss system.

The first step of the analysis solved both truss systems individually by applying the full experimental load. Then the element with the lowest utilization ratio was identified, where the utilization ratio was defined as the strength, multiplied by element area, over the internal applied load in each element.

In the next step the mechanism with the identified element from the first step was then removed from the analysis. The elements of the remaining mechanism were reduced in size by subtracting from their total provided area the value of their required area from the first step multiplied by the lowest utilization ratio from that step. Then the analysis of the remaining, reduced area system, was done again as in the first step, by applying the experimental load. Again, the element with the lowest utilization ratio was identified.

In the last step, the final beam strength was calculated by summing the lowest utilization ratios from the identified elements from steps one and two, and then multiplying that sum by the applied experimental load. The process is not as involved as it may seem; in fact, any unit load should also work in place of the experimental load, as long as the same until load was applied in all steps.

The nodal analysis was simplified compared to Yun's previous papers. The strength of nodes were checked according to the method of the ACI 318-08 code. In this case Kim and Yun used vector addition to sum the forces from the direct and truss struts which framed into the critical nodes located at the bearing plate and load plate. The strength check was done on the basis of geometry by re-arranging the formulae from the ACI code to solve for the required bearing area.

Kim and Yun showed that their analysis method had an average experimental strength over predicted strength ratio of 1.11 with a coefficient of variation of 17.2 for all 234 specimens. It was in the top two of the nine models investigated. The paper also presents performance metrics on the ability of the model to accurately predict beam strength when specific ranges for the shear-span-to-effective-depth ratio, concrete strength, or flexural reinforcement ratio are considered.

2.5 Summary of Observations on Strut-and-Tie Modelling with FRP Reinforcements

The three papers on strut-and-tie modeling with FRP reinforcements were in general agreement on the following:

- Traditional strut-and-tie modelling methods are applicable to FRP reinforced deep beams; but the papers only investigated determinate strut-and-tie trusses.
- The strength of the diagonal strut is the most important concern.
- Failure of a strut-and-tie model should occur as a result of concrete failure. The fact that FRP should not rupture was largely taken for granted, and the failure of nodes was generally not considered in the papers.

The intent of the studies behind the three papers was to investigate the ability of traditional strut-and-tie modelling methods to predict the strength of FRP reinforced deep beams. The papers were summaries of experimental tests in which failure in the concrete was responsible for failure of the beam. The conclusions from the three papers were in general agreement that the following parameters influence the strength of the diagonal concrete strut:

- Transverse tensile strain acting across the strut: ε_1
- Concrete strength: f'_c
- Shear-span-to-effective-depth ratio: a/d
- Axial stiffness of the longitudinal reinforcement: $E_f A_f$

The fact that transverse tensile strains acting across the strut influence the strength of the strut is taken for granted; the strut strength reduction factors from the CSA and ACI exist to account for their influence. However, the strut strength reduction factors may also implicitly account for the influence of other factors as suggested by the quotes from Nehdi et al. (2008) and Farghaly et al. (2013) which were included in their summaries of their respective articles.

The shear-span-to-effective-depth ratio is an important parameter; however, in the case of the studies in the three papers this ratio was also an implicit measure of the angle between the diagonal strut and the longitudinal reinforcement, since the models were determinant and had only one diagonal strut. Two of the papers suggested that the CSA model was a better predictor of beam strength specifically because the strut strength reduction factor included this angle as an input.

The axial stiffness was considered differently by each paper, but they all accounted for it by some measure or another. This term includes the elasticity parameter which specifically accounts for different FRP types, which was considered influential on its own. But the axial stiffness term also includes the total flexural reinforcement area, and is an indirect measure of the flexural reinforcement ratio which was considered influential on its own too. More importantly the combination of the elasticity and area is effectively a measure of strain. The same two papers which suggested the CSA model was a better predictor because it accounted for the strut angle also suggested that the CSA model was a better predictor because the strut strength reduction factor also included strain as an input, and that strains were a function of axial stiffness which is a term that depends on flexural reinforcement properties.

The fact that the concrete strength is an influence parameter was, oddly, contested by one of the papers. However, this factor is included because it is the primary variable with which all concrete design provisions and analysis methods are concerned.

One of the papers also suggested that the effective depth, d, was an important parameter to strut strength as well. The other papers did not mention this as an influencing factor, but effective depth is used to compute the depth of the flexural compression stress block, which is used to compute strut width when

the bearing area of the load point is also considered. So the effective depth indirectly influences the total load carried by the diagonal strut, if not the strut strength specifically.

The strut-and-tie modelling method of Yun was thought to be a good method for analyzing FRP reinforced deep beams because it is capable of considering all of the factors on which the authors of the three papers were in general agreement.

The method treats all struts and ties equally by accounting for changes in their elasticity with each load increment, respective of their material models. As such, the failure of any one strut or tie is not assumed before the analysis begins.

The transverse tensile strains acting across the strut are considered in the method by way of softening coefficients applied to the concrete material model. And, of course, the concrete material model accounts for the concrete compressive strength.

The method indirectly and implicitly considers the influence of the a/d ratio, or the angle between a strut and tie, on strut strength by altering the amount of load carried by a strut as the analysis proceeds. Recall, from upper year courses on structural analysis, that the stiffness of an element relates the displacement at the ends of a truss element to the internal force of that element. Also recall that element stiffness depends on elasticity, cross-sectional area, length, and angular orientation. In an indeterminate truss system separate determinate load paths are made up of a collection truss elements that may be grouped together and given an equivalent stiffness, and the stiffness of load paths determine the amount of applied load they carry.

In Yun's method the elasticity, and thus stiffness, of struts change with each load increment, and thus so too does the stiffness of the load paths. So the proportion of the applied load carried by a load path will change as the elasticity of the struts change. In general, the proportion of load carried by stiffer load paths will increase with each load increment while the opposite will happen for more flexible struts. Ergo, the strength of a strut will not change, instead the proportion of the applied load carried by a strut at failure will be different than the proportion carried initially.

Lastly, Yun's method is a stiffness based method, and so the axial stiffness of reinforcement is considered with each load increment, every time the force system is solved. Consider two identical strut-and-tie models, but which have reinforcement with different elastic modulus values. Generally, the model with stiffer reinforcements will restrain the displacement of truss joints, which will decrease strain in the concrete struts, and thus decrease the rate at which the struts lose elasticity, and thus increase the strength of the beam.

This section will be clearer to the reader if they return here after reading Chapter 5 later.

2.6 Alternative Concrete Material Model

The section contains the summary of the compressive stress-strain curve for concrete by Thorenfeldt et al. (1987) as presented in Reinforced Concrete: Mechanics and Design by MacGregor and Bartlett (2000), which was used later to develop the IST method that is presented in Chapter 5.

The Thorenfeldt et al. material model captures the behaviour of concrete in uniaxial compression and is used in the analysis of this thesis for its ability to model concretes with strengths spanning 15 MPa to 125 MPa (MacGregor et al., 2000). The model is as follows:

$$f_c = \frac{f'_c \, n(\varepsilon_c / \varepsilon_0)}{n - 1 + (\varepsilon_c / \varepsilon_0)^{nk}} \tag{2.36}$$

where f_c is the concrete stress in MPa, ε_c is the uniaxial strain and independent variable, f'_c is the peak stress in MPa, ε_0 is the strain at peak stress, n is a curve fitting factor, and k is factor which controls the shape of the post-peak portion of the curve. Figure 5.3 shows a schematic plot of this function.

If a complete stress-strain curve is available from testing then the parameters may be readily established. The parameters f'_c, and ε_0 may be read from a graph of the test results. The parameters for n and k are determined as follows:

$$n = \frac{E_c^t}{E_c^t - E'_c} \tag{2.37}$$

$$k = 1.00 \text{ for } \left(\varepsilon_c / \varepsilon_0\right) \le 1.0 \tag{2.38}$$

$$k = 0.67 + \frac{f'_c}{62} \text{ for } \left(\varepsilon_c / \varepsilon_0\right) > 1.0 \tag{2.39}$$

where E^t_c is the initial tangent modulus in MPa, and $E'_c = f'_c/\varepsilon_0$

If a complete stress-strain curve is unavailable then the parameters may be estimated as follows, assuming that at least the value of f'_c is known.

$$E_c^t = 1.1\left(4500\sqrt{f'_c}\right) \text{ for concretes with a density close to 2300 kg/m}^3 \tag{2.40}$$

$$E_c^t = 1.1\left(3300\sqrt{f'_c} + 6900\right)\left(\frac{\gamma_c}{2300}\right)^{1.5} \tag{2.41}$$

$$n = 0.8 + \frac{f'_c}{17} \tag{2.42}$$

$$\varepsilon_0 = \frac{f'_c}{E_c}\left(\frac{n}{n-1}\right) \tag{2.42}$$

where γ_c is in kg/m^3. The parameter k is still estimated using Equations 2.37 & 2.38.

3 Experimental Design

This chapter is an explanation of the design, fabrication, instrumentation, test set-up, and test procedure for the specimens of this research programme.

3.1 Introduction

The research programme was originally an investigation into the shear strength of concrete beams reinforced with GFRP longitudinal bars and stirrups. Observations from literature suggested that a relationship may exist between the arrangement of longitudinal bars and the shear reinforcement that would better utilize the straight portion strength of the stirrups. The experimental design parameters were: stirrup diameters & spacings, and longitudinal bar diameters & configurations. Varying these parameters was expected to produce changes in: failure modes, peak load, and reinforcement strain.

Twelve concrete beams were cast and divided into three groups based on longitudinal reinforcing, four groups based on stirrups spacing, or two groups based on stirrup diameter. All specimens were cast using a single batch of concrete to unify the results.

Reinforcing bars and stirrups were instrumented with strain gauges, displacements were measured at mid- and quarter-span with linear variable displacement transformers (LVDTs), and a load cell recorded the applied load from the test frame actuator. The beams were tested to failure in displacement controlled 3-point loading.

3.2 Experimental Design Parameters

Specimens were designed so that the following parameters were intentionally varied: longitudinal bar diameters & configurations, and stirrup diameter & spacing. Specimens were also designed with a constant concrete compressive strength, effective depth to reinforcement, and shear-span-to-depth ratio. However, variation in the primary parameters also indirectly varied other design parameters. For instance, changes in longitudinal bar diameters and configurations produced changes the flexural reinforcement ratio. Likewise, as bar diameters change so do the anchorage lengths and total beam lengths. Beam width did not vary for beams that had stirrups of the same diameter, but did vary between groups of beams with different stirrup diameters. Table 3.1 below outlines how beam names are related to their intentionally varied parameters.

Table 3.1: Test Specimen Names

		Longitudinal Bar Effective Diameter (mm)			**Stirrup Effective Diameter (mm)**
		25	16	12	
Stirrup Spacing (mm)	INF*	BM25-INF	BM16-INF	BM12-INF	12
	150	BM25-150	BM16-150	BM12-150	
	220	BM25-220	BM16-220	BM12-220	
	230	BM25-s230	BM16-s230	BM12-s230	20

** Control specimen with no stirrups as stirrup spacing is infinite.*

A note on vocabulary: beams which are grouped by the same shear reinforcement spacing, the rows of Table 3.1, will be referred to as *beam series* in the remainder of this thesis, and beams with the

same diameter of longitudinal reinforcement, the columns of Table 3.1, will be referred to as *beam groups*.

A constraint on specimen strengths was imposed by limitations of available testing machines at the time. Shear strength predictions had to be well below 500 kN.

Stirrup rupture was necessary in order to test the original objective, and initial beam designs were large, which provided a reasonable certainty of beam-action shear-tension failures. However, these beams were far too strong for the testing machine, so beams with modest cross-sections were required. Beam designs also needed different longitudinal bar configurations, and it was difficult to find flexural reinforcement ratios that resulted in beams that were shear critical by way of beam-action, shear-tension failures.

The challenge of reducing the beam dimensions was rooted in the internal lever arm; as cross-section dimensions were decreased the chance of flexural compression failures increased. Several avenues to simultaneously or separately increase flexural strength and decrease shear strength tended to result in beam designs that: would not likely fail in shear, would likely fail in arch action / strut-crushing, or would exceed the capacity of the testing machine.

Eventually, the shear-span-to-depth ratio, a/d, was fixed at 2.5, which marks the border between beam- and arch-action failure modes. Preliminary designs with larger a/d ratios tended to increase the likelihood of flexural compression failures.

The effective depth of reinforcement, d, was fixed at 270 mm, which united the geometry of all test specimens. Fixing both d and a/d also fixed the shear span, a, at 675 mm, and one pedestal configuration could be used to test all specimens.

Beam width, b_w, differed depending on stirrup diameter: 200 mm for specimens with 12 mm stirrups, and 230 mm for specimens with 20 mm stirrups. Ideally all beams would have the same width. A width of 200 mm was satisfactory for the beams with 12 mm stirrups; but the beams with 20 mm stirrups would not fit in a 200 mm wide cross-section because of the minimum bend-radius-to-bar-diameter-ratio set by the manufacturer. However, a width of 230 mm risked approaching the limits of the testing machine, so the spacing of 20 mm stirrups was made large.

Longitudinal bar configurations were chosen to create three test groups which corresponded to having one, two, or three layers of reinforcing, though the lowest layer of reinforcing was detailed to conform to the curvature of the FRP stirrups. The size and number of bars in each layer were specified to keep the total resisting moment similar.

Concrete strength and stirrup spacing were chosen after a Monte-Carlo analysis, which is discussed in a later section of this chapter.

Table 3.2 identifies the as-designed test parameters for each specimen. Reinforcing bar properties were taken from the manufacturer's product literature. Figure 3.1 shows the elevation drawing for beam BM25-220 as well as the cross-sections for every beam. Elevation and cross-section drawings for each specimen may be found in Appendix E.

The specimens were designed primarily using the CSA S806-12 standard, which was presented in the Literature Review. The process of design will be discussed in the following section. The provisions for cover depth and bar spacing deviated from the requirements of the standard to keep beam strength low. These deviations were considered germane since this was an experimental investigation: cover spacing is mostly a durability concern, and equation 9-1 of the standard varies the bar development length as a function of bar spacing.

Table 3.2: Test Specimen Parameters *As-Designed*

Parameter	BM25-INF	BM25-220	BM25-150	BM16-INF	BM16-220	BM16-150	BM12-INF	BM12-220	BM12-150	BM25-s230	BM16-s230	BM12-s230
Beam Properties												
f'_c (MPa)		45			45			45			45	
b (mm)		200			200			200			230	
h (mm)		330			345			350		345	360	365
l (mm)		2470			1930			1810		2310	2110	1810
d (mm)		270			270			270			270	
a/d		2.5			2.5			2.5			2.5	
ρ_F (%)		1.82			2.23			2.51		1.58	1.94	2.18
ρ_v (%)	0.00	0.51	0.75	0.00	0.51	0.75	0.00	0.51	0.75		1.19	
Longitudinal Bar Properties												
f_{Fu} (MPa)		1000			1000			1000			1000	
E_F (GPa)		60			64			60		60	64	60
A_F (mm^2)		491			201			113		491	201	113
n_{Bar} (amnt)		2			6			12		2	6	12
ε_{Fu} (%)		2.61*			2.61			2.61*			2.61*	
Stirrup Properties												
$f_{Fu,straight}$ (MPa)		1000			1000			1000			900	
$f_{Fu,bent}$ (MPa)		700			700			700			550	
E_F (GPa)		50			50			50			50	
A_F (mm^2)		113.1			113.1			113.1			314.2	
r_{Bend} (mm)		42			42			42			70	

** Rupture strain was only provided for dia. 16 bars, this value was assumed valid for all bars.*

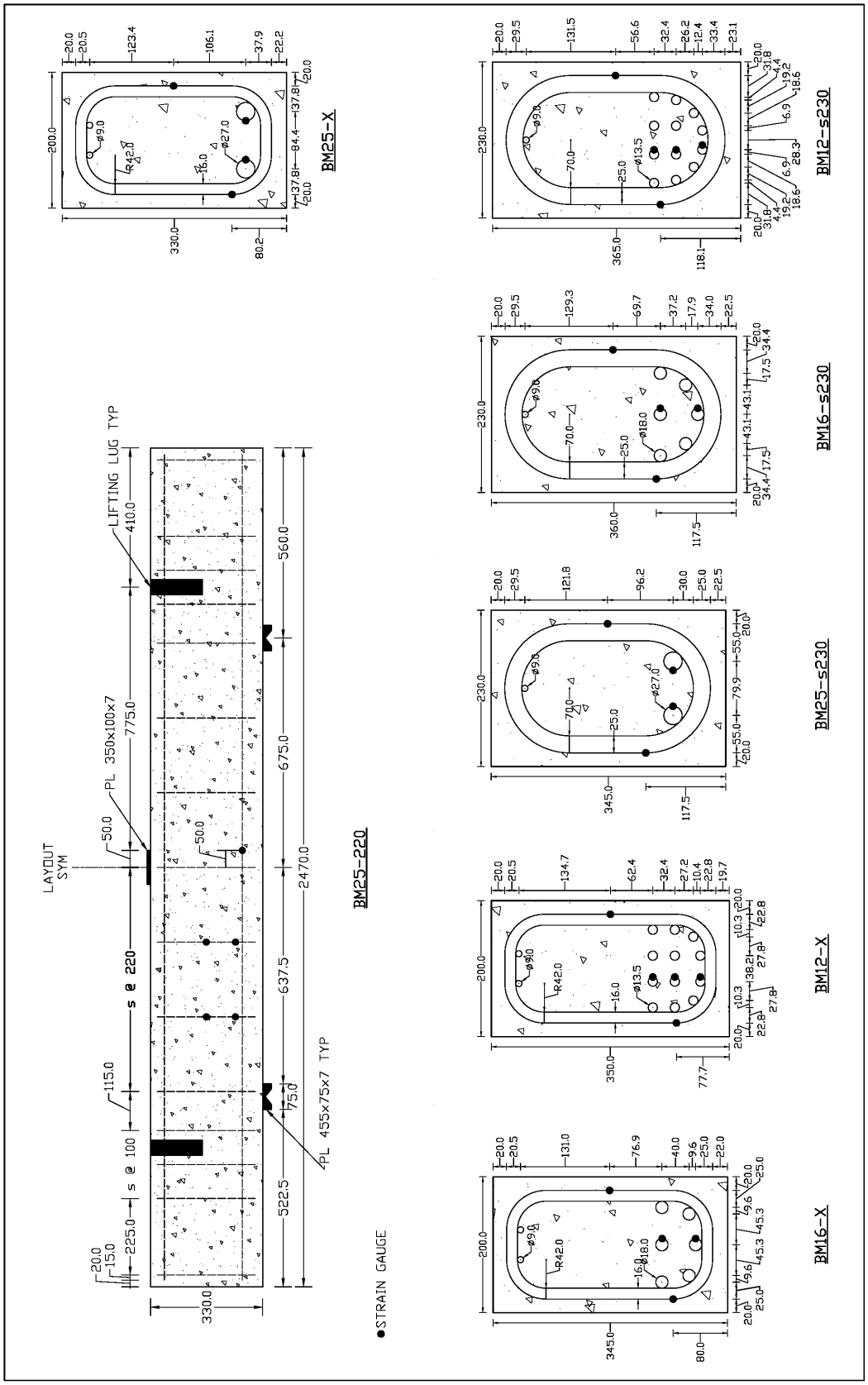

Figure 3.1: Elevation for Beam BM25-220 and Schematic Cross-Sections for All Beams

3.3 Shear and Flexural Strength Predictions

Shear strengths were predicted using the model of the CSA S806-12 standard, and the genetic algorithm model by Nehdi et al. (2007), both of which were presented in the Literature Review Chapter. Flexural compressive strength predictions came from the model of the CSA S806-12 standard, which uses a traditional equivalent stress block approach to the design of over-reinforced beams. For experimental design purposes all material factors of safety were set equal to 1.00.

At the time of design no academic articles had assessed the performance of the CSA S806-12 standard for shear design, so the author found it necessary to check the standard against another model. A paper by Machial et al. (2012), which was presented in the Literature Review Chapter, found that the Nehdi et al. model was the best performing shear model out of 11 for beams without stirrups, and the best performing model out of eight for beams with stirrups.

It is important to stress that beam designs were a highly iterative process. The models noted above produced estimates for preliminary designs assuming the concrete and reinforcing material inputs did not vary. Final designs were produced after conducting a Monte-Carlo analysis using the CSA S806-12 standard and Nehdi et al. model, which will be discussed in the next section.

In addition to material variability, the test specimens were also designed considering the potential for a wide range of realized stirrup strengths. Different realized stirrup strengths were examined because the original objective of this thesis investigated the possibility that the stirrup straight portion strength could be better utilized with different longitudinal bar configurations.

The ultimate strength of the GFRP stirrups in equation 8-22 of CSA S806-12 was set equal to the values provided by the manufacturer, which ignored the $0.005 \cdot E_f$ limitation of the standard. Different scenarios were investigated where the mandatory 0.4 reduction factor in the front of equation 8-22 of CSA S806-12 was varied up to and including a value of 1.00, which assumes full straight portion strength can be realized in the stirrups. Background on how equation 8-22 was developed may be found in a paper by Shehata et al. (2000), which was presented in the Literature Review Chapter, and provided a basis for the author to make changes to the reduction factor.

It is important to note that designers are implicitly directed to use the stirrup straight portion strength for design because of the mandatory 0.4 reduction factor in equation 8-22; this factor is intended to account for the bend strength of stirrups (Shehata et al, 2000). However, this could lead to confusion because the CSA S806-12 standard defines the stirrup strength, f_{Fu}, vaguely as, "the ultimate strength of FRP reinforcement", a definition which does not make distinction between the two ultimate strength definitions, for the bent and straight portions, that typical product literature provides.

The model by Nehdi et al. could not be modified to include the possibility of full straight portion strength because the model was derived using a genetic algorithm programming technique, and not from traditional mechanics. It was assumed that that database used to develop and verify the model included stirrup straight portion strengths instead of bend strengths, an assumption founded on the author's experience reviewing academic literature on beam tests where stirrup strengths are reported without qualification, or where stirrup strength testing conformed to the testing of straight bars as opposed to the testing of stirrup bends which are tested using the method noted in the paper by Ahmed et al. (2010c). Further, the paper is silent on the failure modes of specimens from the database used to create the model, and so the model likely does not make a distinction between shear-compression and shear-tension failures.

The application of the CSA S806-12 standard is straight forward for most design scenarios since the capacity check need only show that the shear capacity is greater than the applied shear, $V_r > V_f$.

However, it is difficult to solve for the scenario where the shear capacity equals the applied shear, $V_r = V_f$, because the shear capacity is a function of the applied moment and applied shear in three of the equations that comprise the shear capacity model. Iterations are required in order to solve for the design parameters where the shear capacity equals the applied load, as was the case for designing the experimental beam specimens. Microsoft Excel's goal seek feature was adequate in finding the proper solutions.

The maximum possible displacement for each beam specimen was also estimated using the CSA S806-12 standard. The maximum possible displacement was calculated using the 500 kN limit. Academic models for the displacement of FRP reinforced concrete beams were also investigated and it was found that the CSA model is based on, and in substantial agreement with, the model developed by Bischoff (Bischoff et al., 2011). The expected displacement values were used to select the operating ranges of LVDTs, and to estimate the displacement controlled load rate.

Table 3.3 shows the expected flexural and shear capacity in terms of the applied failure load, *P*. The capacities were calculated using the parameter values as presented in Table 3.2 and Figure 3.1. Table 3.3 also includes the estimated deflection for each specimen. The CSA S806-12 shear model was considered at a section located d_v from the applied load, and flexural failures & displacements were computed at mid-span. The Nehdi et al. model does not consider any specific section in a given shear span.

Table 3.3: Predicted Applied Failure Loads and Mid-Span Displacements

	Flexure kN	**Shear kN**				**Deflection mm**
Model →	**CSA S806-12**	**CSA S806-12**			**Nehdi et al.**	**CSA**
FRP Strength →	Longitudinal	0.4*	Bend**	1.0*	Straight	N/A
BM12-INF	385	238			143	8.5
BM16-INF	376	230			142	6.8
BM25-INF	339	224			133	6.5
BM12-220	385	396	472	537	327	8.5
BM16-220	376	380	452	523	326	6.8
BM25-220	339	346	426	513	317	6.5
BM12-150	385	446	545	677	367	8.5
BM16-150	376	427	531	660	365	6.8
BM25-150	339	393	520	647	357	6.5
BM12-s230	422	584	739	1028	467	8.3
BM16-s230	413	575	728	1013	465	6.6
BM25-s230	371	549	697	972	456	6.3

** Indicates the assumed value of the mandatory reduction factor of CSAS806-12 Equation 8.22.*
*** The equivalent factor was 0.7 and 0.61 times the straight strength for the 12 mm and 20 mm diameter stirrups, respectively.*
****Grey entries show strengths that are larger than the machine capacity.*

Several of the applied loads in Table 3.3 are greater than the testing machine limit of 500 kN. Note that specimens with identical flexural reinforcement ratios have the same flexural capacity. More importantly, Table 3.3 shows that most of the beams with stirrups are predicted to fail in flexure before shear. These results prompted the Monte-Carlo analysis.

For the INF beam series, the CSA S806-12 shear model predicts an almost uniform capacity regardless of the flexural reinforcement ratio. This occurs because, for these particular specimens, the concrete contribution, V_c, is greater than $V_{c,max}$. So, the strength of each specimen is set equal to $V_{c,max}$ which is a function of f'_c, b_w, and d_v; the slight variation in the strength is a results of slight variations in d_v which is a function of the beam height and not reinforcement effective depth for these specimens.

As expected, the CSA and Nehdi et al. models show that the predicted strength of the beams with larger shear reinforcement ratios are larger than that of the beams with lower ratios, regardless of stirrup diameter or spacing.

3.4 The Selection of Concrete Strength and Stirrup Spacing by Monte-Carlo Analysis

The preliminary design phase focused mainly on flexural design and was used to select workable longitudinal bar arrangements and overall beam dimensions. The concrete strength and stirrup spacing parameters had a significant effect on the shear strength and failure modes, such that a more thorough Monte-Carlo type analysis was warranted. All of the design parameters were confirmed once the analysis was completed, and were presented in Table 3.2.

The Monte-Carlo analysis was used to ascertain the likelihood of a shear failure, since the predictions in Table 3.3 indicated likely flexural failures. The analysis examined both the CSA S806-12 and Nehdi et al. models for shear, and the model for flexure. A more detailed discussion of the model and analysis may be found in Appendix A; it includes: an explanation on the choice of parameters to vary, an explanation on the choice of probability distributions, a print out of the code, etc. The analysis was conducted using MATLAB, a very sophisticated computer program and programming language used for, among other functionalities, the solution of computationally intensive mathematical models.

Briefly, the program determined the failure loads, *P*, resulting from the two shear models and the flexural compressive strength model. After all the failure loads for all trials were computed the program then identified the lowest failure load for each trial and sorted them by failure mode, or lack of failure if the loads were greater than the limit of the testing machine. The output included the number of trails from each of the following groups: shear failure, flexural compression failure, no failure, and possible tensile failures, as well as several plots.

The analysis was only performed on beams with both 12 mm diameter bars and stirrups due to the limited amount of available experimental test data for the manufacturer's products. It was assumed that the results extended to the other bar and stirrup arrangements.

The Monte-Carlo analysis was first used to determine an appropriate concrete strength. This was done by assigning a uniform distribution to the concrete strength which varied between 25.0 and 50.0 MPa. The analysis was run for several stirrup spacings and produced plots like Figure 3.2. Figure 3.2 shows a plot of failure load against concrete strength, with data points organized into flexural failures and shear failures; a very small number of trials indicated tensile failure, but no results exceeded the machine limit. The plot was made using the CSA S806-12 shear model with stirrups spaced at 150 mm, and included the mandatory 0.4 reduction factor.

Figure 3.2 was used to select a nominal concrete strength of 45 MPa, among other similar plots made with different assumptions. Later runs of the program would assume the concrete strength varied according to a normal distribution.

Initially, the smallest stirrup spacing was set to 84 mm, which was the maximum allowable spacing according to Cl.8.4.6 of the CSA S806-12 standard and would all but exclude shear failure entirety. Instead, several different spacings were considered, and each examined the impact of the mandatory reduction factor at values of 0.4, 0.7, and 1.0. Predictions according to the Nehdi et al. model were also considered. The results for relevant spacings are shown in Table 3.4.

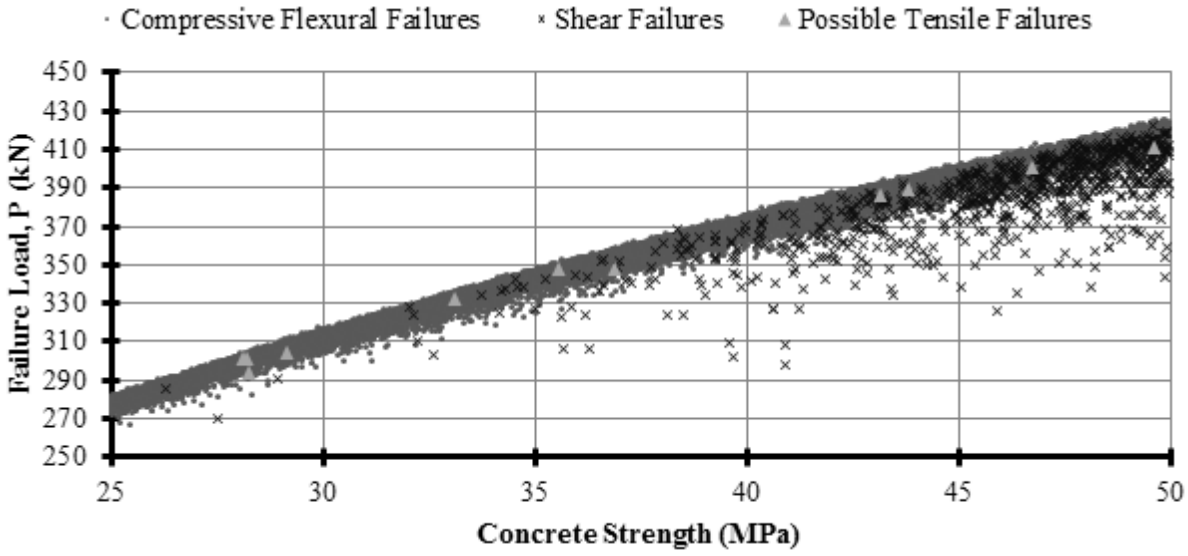

Figure 3.2: Scatter Plot of Predicted Failure Load against Concrete Strength

Table 3.4: Percent Probability of Shear Failure & (Flexural Failure)

Stirrup Spacing	CSA S806-12			Nehdi et al.
	Factor = 0.4	Factor = 0.7	Factor = 1.0	
INF	100.00 (Zero)			100.00 (Zero)
100	0.3 (99.7)	≈Zero (≈100.0)	Zero (100)	24.0 (76.0)
150	8.5 (91.5)	0.1 (99.9)	≈Zero (≈100.0)	84.7 (15.3)
220	70.3 (29.7)	2.2 (97.8)	0.1 (99.9)	99.3 (0.7)

The analysis showed that an under-reinforced failure was likely 0.02 to 0.04 percent of the time, and this was considered acceptable risk. The analysis also showed that CSA S806-12 model with the 0.4 mandatory reduction factor and the model by Nehdi et al. predicted similar probabilities for all stirrup spacings. And, as expected, the results show that as the stirrup spacing decreases so too does the probability of shear failure. The analysis also shows that as the coefficient on the CSA model increases from 0.4 to 1.0 the probability of a shear failure decreases significantly at all stirrup spacings.

At a minimum the results showed that beams specimens were likely to fail at a load under the 500 kN limit. They also showed that a range of possible failure modes existed, and while shear-tension failures were desired, a compressive flexural failure would also be acceptable because this could still indicate increased stirrup strength utilization. More realized stirrup strength utilization, which was the original objective, would increase the stirrup contribution to shear strength and could make the applied load at shear failure larger than the applied load at flexural failure.

Ultimately, the results of this analysis allowed the author to confidently specify the values for the concrete strength and stirrup spacing parameters which are found in Table 3.2.

3.5 Reinforcing Materials

The test specimens were designed using Schoeck ComBAR. The longitudinal bars were manufactured using a typical pultrusion. The relevant mechanical properties of the longitudinal bars were shown previously in Table 3.2.

The stirrups were manufactured using hand lay-up methods and the specifics of this process are not fully known. The FRP industry has yet to develop a uniform and robust method for manufacturing

bent bars. However, Schoeck uses a patented method for the manufacture of bent bars. This method involves threading the FRP bundle through corrugated, flexible plastic tubing. The tube with the GFRP bundle is bent into the desired shape and cured in an oven. This process allows the fibres to glide past one another as the tube is bent, lubricated by the polymer resin, to minimize the impact of fibre kinking and cross-sectional deformation in the bends. Material testing of the bars and stirrups was beyond the scope of this thesis; the relevant mechanical properties are presented in Table 3.2.

3.5.1 Stirrups and Closed Loop Detailing

The beam specimens were reinforced with closed loop GFRP stirrups. The detailing of closed loop GFRP stirrups should conform to good FRP stirrup design and manufacture practices, which limit the bend-radius-to-bar-diameter ratio to 3.5. In a typical steel stirrup, the closing of a loop occurs at a corner where the stirrup bar ends bend 135 degrees around a corner bar in a tight bend-radius-to-bar-diameter ratio. But tight bends are not practical for FRP bars. In this research programme the closed loops were formed by having the stirrup bar overlap itself at the two top corners and top side, where top refers to the flexural compression side of the beam. This is best illustrated in Figure 3.3.

Figure 3.3: Collection of Closed Loop GFRP Stirrup Photos

Figure 3.3 shows a good quality stirrup, but the figure also helps to show some potential complications of using closed loop FRP stirrups. These complications revolve around geometric inconsistencies from manufacturing. It is important to note that commenting on how these inconsistencies impacted stirrup strength, if at all, was outside of the scope of this research programme. Though a brief review how inconsistencies may impact stirrup strength, and therefore beam strength is provided.

It was observed that while constructing the reinforcing cage only one stirrup leg could hang vertically. The other must hang at a slight angle to accommodate the overlap at the top of the stirrup. This slight angle can be seen in Figure 3.3 and 3.4. However, this slight angle was seldom realized as the leg was often kinked to make the accommodation. This resulted in a more severe angle at the kinks than would be found with ideal geometry. Further, the angle, either ideal or kinked, was on occasion made too large such that the overlapping portions of the stirrup were not snug against one another, but instead

separated by a gap. Such angles are sources of unnecessary bending and may have a potential to introduce weakness into the unidirectional composites.

The original objective of this thesis was ultimately concerned with good detailing practices for beams reinforced with FRP stirrups, and it is important to note that other closed loop stirrup detailing schemes are also possible. Typically, these schemes involve taking two U-shaped stirrups, or C-shaped stirrups, and overlapping the legs on their free ends to form a closed loop. It is thought that these systems would be preferred by industry since all of the longitudinal reinforcement need not be pre-threaded through the closed loop stirrups.

However, papers that compare concrete shear models for FRP reinforced beams, which include the papers by Machial et al. (2012) and Nehdi et al. (2007) presented in the Literature Review Chapter, never account for the detailing of shear reinforcement. Experimental results for closed loop stirrups, and closed U- & C-shaped stirrups, and other closed and open stirrup arrangements are routinely lumped together; authors tacitly assume that these details have no impact on shear strength.

It is difficult to overcome that assumption though, because it likely stems from a lack of large datasets on which to perform a defensible analysis concerning the impact of FRP stirrup detailing. As a result of this lack, no statistical inferences can be made using the few existing publications. The issue is exacerbated when complicating factors are considered such as bend-radius-to-bar-diameter ratios, types of composites, surface preparations, etc. This is an area which needs further study within the broader field of FRPs as internal reinforcing for concrete structures.

Consider the complication further: the stirrup area of a common closed loop stirrup is twice the bar area, but the stirrup area of a closed loop stirrup constructed from two U-shaped stirrups is somewhere between twice and four times the bar area. Where cracks cross close to the bend of such stirrups the effective area may be as low as twice the bar area, since the free ends of one of the U-shaped stirrups may not be well anchored there. But for cracks which cross at the middle portion of the stirrup legs the effective area may vary between twice to four times the bar area depending on how well anchored, or bonded, the stirrup legs are to the concrete.

Whether or not closed loop stirrup detailing schemes actually influence the shear strength of FRP reinforced concrete beams is not well known. However, evidence indicates that stirrup detailing impacts behaviour.

One of the earliest studies on the shear strength of large pre-stressed, FRP reinforced, concrete bridge girder, bulb-T members was by Fam et al. (1997). The beams were reinforced with CFRP stirrups. One beam used a double legged stirrup which traced the outside profile of the beam. Another used a single legged stirrup, but the single leg of this stirrup dropped through the centre of the longitudinal reinforcement, and then looped around to enclose the longitudinal reinforcement. The beam with the first type of stirrup, when loaded, spalled off concrete at the re-entrant corner as the stirrups attempted to straighten, and the beam eventually failed by web crushing. The beam with the second type of stirrup, though it had half as much shear reinforcement area, failed without premature spalling at a larger load and by rupture of the longitudinal reinforcement. The authors concluded that the failure was significantly influenced by the stirrup configuration, and that the behaviour was not a characteristic the CFRP material.

A study by Hegger et al. (2011), investigated the shear strength of FRP reinforced I-girders. In their study stirrups were constructed using 4 types of overlapping bent FRP shapes. They were constructed and overlapped in such a way as to produce no re-entrant corners: the top and bottom flanges both contained a closed loop that essentially acted as framing bars, and the web was reinforced with two C-shaped pieces that over-lapped and were anchored in the flanges. In their study of four beams, only one beam failed by stirrup rupture, but the rupture occurred in the straight portion of the stirrup found in the beam web.

The important observation to take away from both of these studies is that in their large bridge girder beams, where stirrups were anchored in many rows of longitudinal reinforcement, the failure of

stirrups by rupture was either prevented, or occurred in the straight portion. These observations clearly support the original objective of this thesis.

Further, Nakamura et al. (2006) presented a paper on fractured steel stirrups. The experiment included three beams: a control specimen with un-fractured stirrups, N1, a specimen where stirrups were fractured at the bends on the flexural tension side, N2, and a specimen with stirrups fractured on the flexural compression side, N3. The strength of N2 and N3 was 25 and 20 percent less than that of the control, respectively. Specimen N2 was unable to sustain truss action as a result of ineffective confinement of the longitudinal bars; strain measurements showed that the progression of stirrup loading was very similar to that of the control specimen, and the loss in strength was attributed to a reduction of the concrete contribution. However, specimen N3 was unable to develop arch action; strain measurements showed that the progression of the concrete contribution was very similar the control specimen, while the stirrup contribution was reduced: stirrups only engage after they are crossed by shear cracks, so the stirrups near the applied load do not engage until the later part of testing, but they were unable to carry high loads due to short anchorage lengths. The paper contains a more detailed discussion of stirrup strains and yielding, but essentially stirrups were unable to yield when cracks crossed close to the fractured bends regardless of the location of the bend.

Varney et al. (2011) examined four beams with triple legged steel stirrups in a paper titled "Effect of Stirrup Anchorage on Shear Strength of Reinforced Concrete Beams". Their experiment included a control beam with properly anchored stirrups, a beam where the centre leg was not anchored around a longitudinal bar, another with small diameter framing bars for anchorage of the two exterior stirrup legs, and one with no bars for anchorage of the two exterior stirrup legs. Their findings indicated that anchorage around the longitudinal bar did not impact shear strength, and conclude that bond forces along the straight and bent portions of the stirrups were more important.

Lastly, Johnson et al. (2012) published test results on beams with two shear reinforcing schemes: one with conventional closed loop GFRP stirrups, and another with pairs of headed GFRP bars in the place of stirrup legs. Beams with headed bars failed at the theoretical flexural crushing load, while beams with closed loops stirrups showed two peaks: first at the theoretical flexural crushing load, and then again at a second higher load after significant post-peak ductility.

The purpose of this research programme was not to study stirrup detailing methods, but the above discussion serves to highlight the impact stirrup detailing has on the shear force transfer mechanisms, failure modes, peak loads, and ductility.

3.6 Specimen Fabrication

Specimens were fabricated in the concrete lab at the University of Waterloo. The fabrication process started with caging, which involved labelling each stirrup, placing them in order, and threading the longitudinal bars through the stirrups before lashing them together. Stirrup order was necessary to track strain instrumentation after casting.

An entirely non-metallic concrete beam philosophy guided the process of specimen fabrication, and thus non-metallic ties were used for caging to simulate real design and construction requirements. Common cable ties, which are meant to bundle cabling in office spaces, were used. The ties were Thomas & Betts 8.9 inch nylon ties, model number TY242M, and were installed with a cable tie installation tool, model number WT1TB, from the same manufacture. The tool, in one motion, both tensioned the ties so that they would hold tight and clipped the tails. The tool was ergonomic, and placed less stress on the hands when compared to tightening by hand or with pliers. Over 2000 ties were used and such a tool is recommended for researchers engaging in similar work.

Lastly, the author found that cable ties containing carbon black were too brittle to be used as rebar ties. They would often snap unexpectedly, both during installation and at random times after installation.

Carbon black is mixed with the nylon polymer of the cable tie to provide UV protection, so it is recommended to avoid UV-protected cable ties when they are being used as rebar ties.

However, it was also obvious that rebar caging with cable ties consumed more time than using traditional wire ties and tying tools. In practice, the strict non-metallic requirement could be relaxed. Plastic coated ties, similar to common wiring, or stainless steel ties could offer an effective alternative, since they could be installed with traditional tools and methods.

Figure 3.4 shows the assembled rebar cage for beam BM16-150.

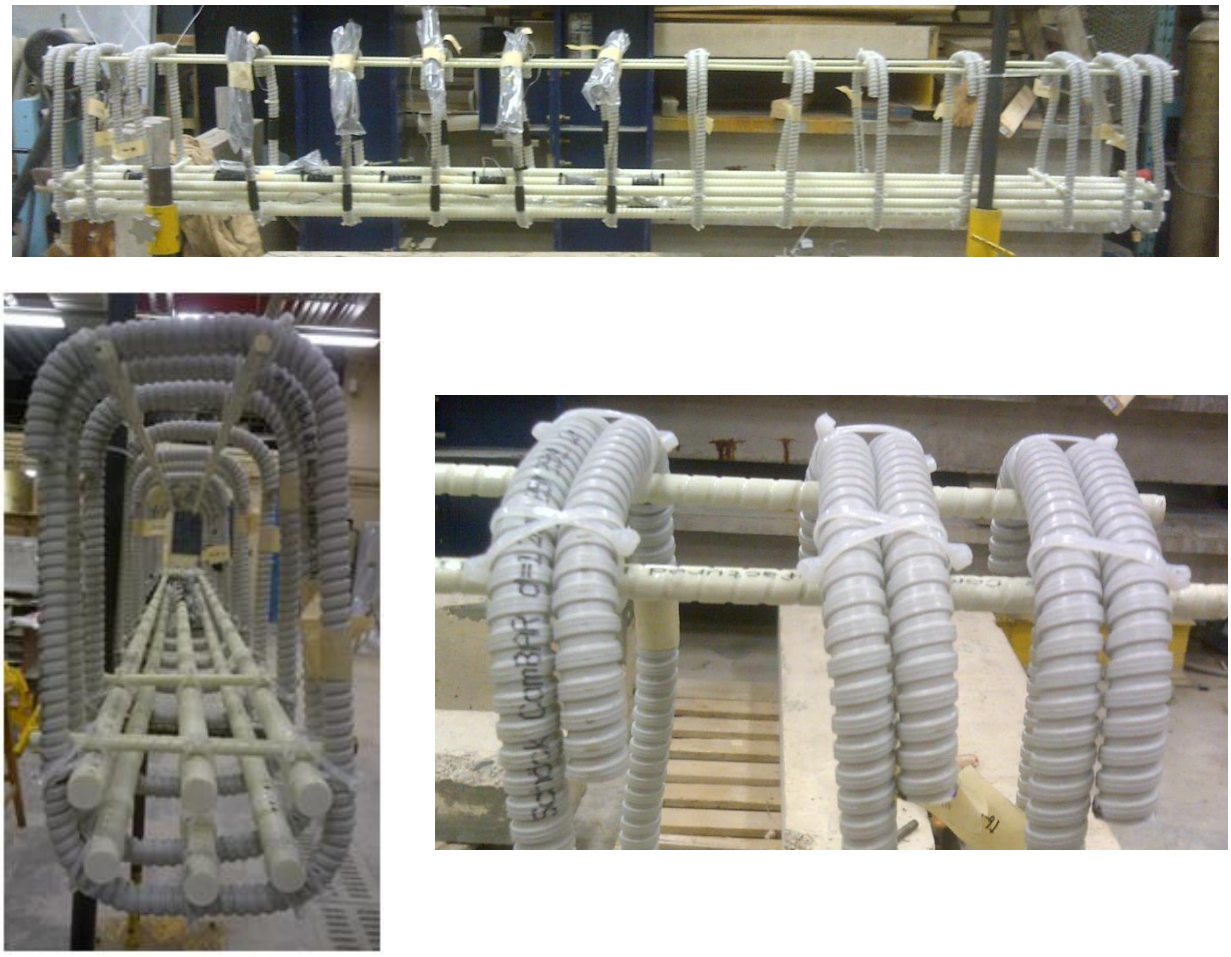

Figure 3.4: Collection Rebar Cage Photos for Beam BM16-150

Formwork for the concrete beams was constructed from ¾ inch plywood and ¾ inch form-ply. Under the advice of the lead lab technician, timber framing studs were formed by laminating two ¾ inch plywood boards together and cutting them into the required dimensions. To do so took advantage of the stricter dimensional tolerances of plywood over conventional timber framing studs. All laminating and cutting was contracted to the University of Waterloo's Engineering Machine Shop, where the work was carried out by an experienced carpenter. Assembly of the cut pieces was done by the author and other graduate students working in the concrete lab at the time. Pieces were assembled using either 2 inch or 2.5 inch wood screws. Pilot holes were pre-drilled for each screw. Over 2000 screws were used in the construction of the formwork.

The formwork was arranged into 4 modules each containing 3 beams. Beams of the same longitudinal reinforcement arrangement were grouped together since the outside dimensions of beams in these groups were identical. However, each beam of the s230 series had different heights and lengths, so one module included plywood risers and blocking to accommodate the differences.

In general, formwork contained 2 interior walls, 2 exterior walls, two end diaphragms, one large floor piece, strapping, bracing, and lifts. The interior walls were made up of two sheets of plywood connected by studs, which were connected to the floor piece and strapping to provide lateral resistance to sliding, overturning, and bowing; the gap in between studs provided a location to place strain gauge leads during the pour. The exterior walls were furnished with braces to provide lateral resistance. Lifts were also added to accommodate forklift tines, and to secure the braces. Strapping closest to the ends of the modules held lifting anchors in place during the pour. The formwork is pictured in Figure 3.5.

Figure 3.5: Collection of Formwork Module Photos for the Group 16 Beams

Rebar cages were hung in place from blocking. The blocks were cut to resemble an upside down pork pie hat with the brim resting on the edges of the formwork and the crown dropping down into the body of the beam. The rabar cages were lashed to the blocks from the top framing bars using wire ties, and the blocks were screwed into the formwork. This arrangement served three purposes: firstly, it held the cage up off the bottom of the forms to provide consistent concrete cover, secondly, it aligned the cages properly in the forms, and thirdly, it prevented potential floatation of the cages during concrete vibration. Strips of form ply were used to center the cages horizontally. This arrangement, and the hanging block, is shown in Figure 3.6.

Figure 3.6: Collection of Rebar Blocking Photos

The 500 kN capacity of the testing frame also indirectly placed restrictions on the concrete mix design. To fit reinforcement into the small beam width, the bar spacing requirements were relaxed, and the longitudinal bars in the group 12 beams were very congested. Some bars along the stirrup bend were a little over one bar diameter away from their neighbour. Thus, normal sized aggregates were precluded from the mix design.

Further, the hydraulic concrete needed to be workable to effectively place concrete around the very congested longitudinal reinforcement in the BM12 series of beams, while simultaneously providing a 28 day strength of 45 MPa. The concrete was specified as follows, and the mix design was prepared by the professionals at HOGG Ready Mix, a local supplier:

- 45 MPa 28-day strength
- 3/8 inch pea-stone aggregate
- 200 mm to 250 mm slump
- 2.5 m^3 volume

The concrete beams were cast in the morning of June 19, 2013, in the lower shed of the concrete lab of the University of Waterloo. The pour lasted 1.5 hours, and was prolonged because the concrete arrived with a very low slump. HOGG Ready Mix dispatched another driver to bring extra plasticizer and the pour did not begin until it was mixed in. The plasticiser was added before the pour actually started, and again midway through. Concrete was vibrated and tamped into place.

The rebar cage hanging blocks were removed from the formwork when each module was filled. Brief vibration was used to collapse the recesses left behind by the blocks with no cage movement observed. Strapping was removed at the end of the pour and revealed recesses deep enough to expose the top framing bars. A batch of concrete was mixed in a wheelbarrow on site to patch up these locations. The patched areas were outside of the test span and were not thought to have had any impact on later beam testing.

During the pour 50 concrete cylinders were cast, with dimensions of 100 mm x 200 mm, for later compression and tensile split testing. Concrete beams were left to cure for 7 days in the formwork under damp burlap and plastic sheeting. The formwork was then removed and the beams were stored in ambient conditions in the concrete lab. Test cylinders were de-moulded after 2 days. The cylinders were left to cure in the moist curing chamber of the concrete lab until testing.

Honeycombing was observed in some beams near the location of lifting lugs, towards the end of the beams. It's possible that this honeycombing and the recesses under the straps were related to insufficient vibration in these locations. The honeycombing was outside of the test span and was not considered to have impacted later test results. Figure 3.7 shows a typical example of the honeycombing.

Information on individual beam specimens may be found in Appendix E.

Figure 3.7: Typical Extent of Honeycombing

3.7 Instrumentation

In the experimental program the failure of GFRP reinforced concrete beams was explored through strains, displacements, crack widths, and load; instrumentation details follow.

Strain information was limited to longitudinal bars and stirrups and strain gauges were only affixed to reinforcing on the south half of the beam, the roller supported side. No concrete strain information was collected. The strain gauges used were supplied by Tokyo Sokki Kenkyujo Co., Ltd. and were of the FLA-5-11-5L type. They had a 5 mm gauge length and a gauge factor of 2.13 ± 1 percent. A thorough explanation of the procedure used to prepare the GFRP bar surface, affix the strain gauge, and protect the gauge and exposed fibres can be found in Appendix B. What follows is a very brief summary.

The GFRP bar surface was prepared by first cleaning away any obvious debris and surface contaminants. To provide a smooth surface on which to affix the gauge the shear ribs were filed off by hand; a powered grinder was not used for fear it would remove too much material from the cross section. The surface was ground to a uniform smoothness using ever finer grits of sand paper. Gloves, goggles, and dust masks were worn to minimize exposure to GFRP dusts.

The gauge location was marked with a burnishing tool and the surface was cleaned with isopropyl alcohol to remove any dusts or grease. A neutralizing solution was also used to balance the pH of the bar surface. The gauge was set in place with tape and cyanoacrylate adhesive was used to affix the gauge to the GFRP bar. The gauge and exposed glass fibres were protected with a surface coat of polyurethane, then later with SB Tape. SB Tape, manufactured by Tokyo Sokki Kenkyujo Co., Ltd., is a putty material known as buthyl which is kneaded in a thick layer over the gauges and exposed fibres. Finally, it was wrapped in electrical tape. This prevented the harsh environment of the hydraulic concrete and concrete pore solution from interfering with the strain gauge and exposed fibres. There are no photos of this process to share.

Strain gauges were attached to the flexural reinforcement on all beam specimens. The gauges were attached to both longitudinal bars of the group 25 beams, to the centre bar of both longitudinal layers of the group 16 beams, and to the centre most bar on all 3 layers of the group 12 beams. These strain gauges were placed 50 mm north of mid-span to avoid being damaged by the formation of mid-

span flexural crack. The group 16 beams with 12 mm diameter stirrups were also outfit with strain gauges spaced at 150 mm intervals along the centre bar of the upper most longitudinal layer.

Strain gauges were also affixed to stirrups in the south span of all beam specimens. Stirrups had one gauge attached to the straight portion, and the other attached to the bent portion on the opposite leg. The gauge on the straight portion was placed at mid-height of the stirrup leg, and the gauge on the bent portion was placed just above where the bend formed, which conforms to positioning used in other academic works.

The location of strain gauges is made clear in Figures 3.1, 3.3, and 3.4. Strain gauge leads were not protected inside the concrete, and several failed prematurely during testing, most likely by snapping. It is recommended that gauge leads be threaded through small diameter plastic tubing; doing so would allow the leads to move freely inside the tubes as cracks grow.

Displacements were recorded at mid-span, and the two quarter-span locations. Displacements were recorded using LVDTs. A Trans-Tek Inc. LVDT with a 4 inch operating range, model number 0245-0000, was used for quarter-span measurements, and one with a 6 inch operating range, model number 0246-0000, for mid-span. The LVDT gauges were installed upside down, so that the casing was above the bottom of the beam, to protect them from damage in the event of catastrophic failure. Doing so increased the risk of damage to the cores, which could fall out during failure, but minimized risk to the rest of the instrument. The cores of the LVDT rested on ¼ inch aluminium bars that were strapped to the beams using eyebolts and bungee cords. Bungee cords were occasionally cut by the sharp edges of cracking concrete and had to be replaced, but always survived the test. The LVDTs were held in place by test-tube holders with magnetic bases attached to steel blocking. Figure 3.8 shows a beam ready for testing and the set-up of the LVDTs.

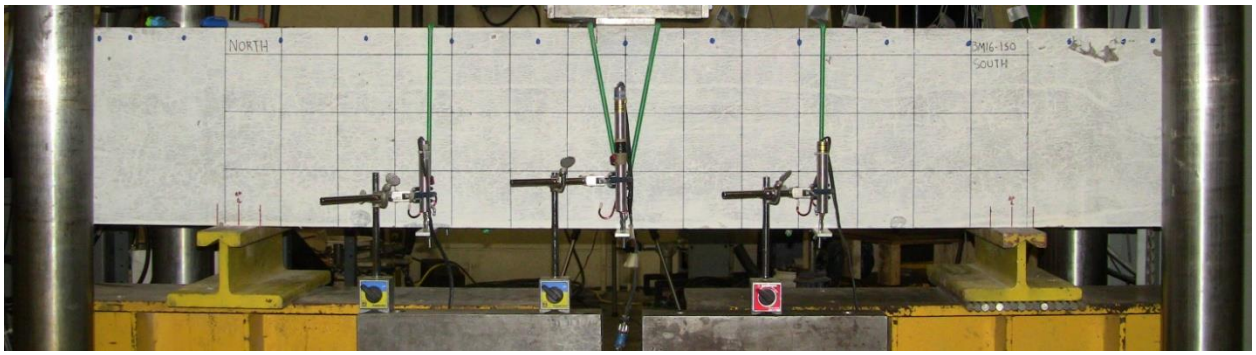

Figure 3.8: LVDT Gauge Set-up and Positioning

The load was measured using an MTS axial load cell, model number 661.23E-01, rated for 500 kN. The load cell was connected to a computer with MTS frame controller software, which relayed measurements to the data acquisition system (DAQ). The displacement of the frame actuator was also recorded through the MTS frame software.

No instrumentation was used to measure crack widths. Crack widths were measured with crack comparator card and a hand held optical loupe, microscope, with 20x magnification.

Otherwise, strain, displacement, and load measurements were recorded on a data acquisition system which ran Lab View version 8.

3.8 Beam Set-up and Test Procedure

The experimental program tested beams to failure in displacement controlled, 3-point loading. The procedure for testing may be found in Appendix C. Relevant details of the test set-up and procedure are outlined in this section. This section will also outline changes made to the test procedure to correct for issues as testing progressed.

Beam designs assumed simple supports for the specimens and the actual supports approximated that assumption. To ensure the applied load remained vertical a roller harness was attached to the pivoting load head. Figure 3.9, below, shows a schematic drawing of a typical beam ready for testing, the actual supports used, and the roller harness.

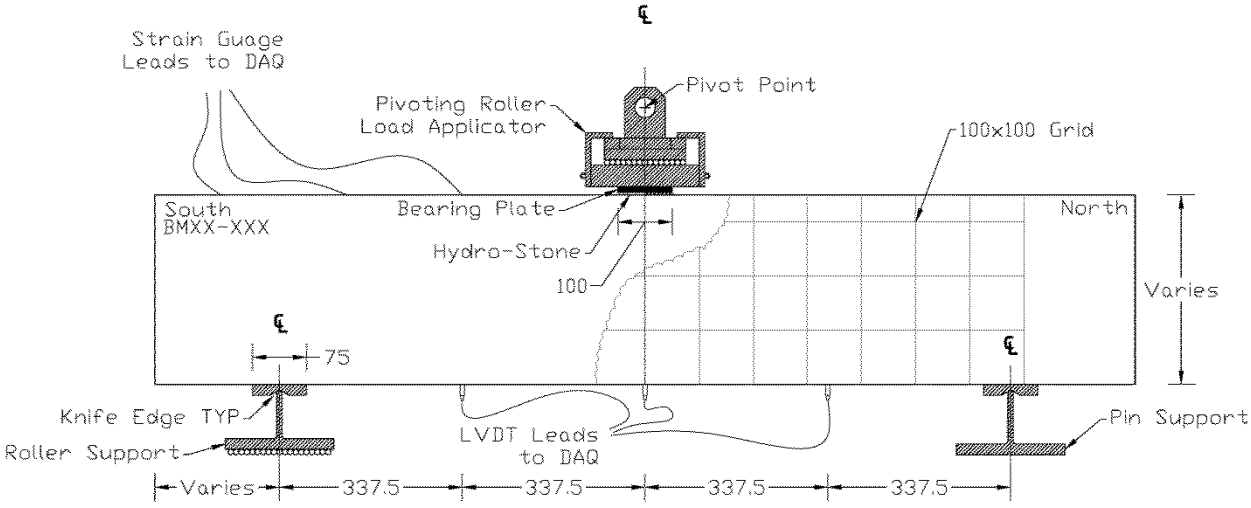

Figure 3.9: Schematic of Beam Ready for Testing

Specimens were prepared by painting both sides white. The first six beams were painted with a latex based primer diluted with 1 part water for every 2 parts primer, by volume. There were concerns about the elasticity of the latex primer, as it might span across small cracks obscuring their growth. So, the remaining six beams were painted with a traditional lime-wash, which is brittle and would likely not obscure small cracks. Lime-wash was made using 5 parts DAP Hydrated Lime, 1 part NaCl, and 5 to 8 parts water by volume. It is best to apply lime-wash in coats if necessary; thicker lime-wash mixtures may crack as they dry.

A 100 mm by 100 mm grid was drawn onto the beam to help track the growth of cracks. The grid was centred about mid-span, and started at the bottom of the beam. Instrumentation was connected to the DAQ in a particular order which will not be repeated here. The bearing plate was attached the day before testing with a product called Hydro-Stone, manufactured by USG.

The order of testing started with the beam BM25-INF. Testing then progressed, firstly, to beams with larger longitudinal reinforcement ratios, then, second, to beam series with higher shear reinforcement ratios. This order was chosen because it would proceed from weakest to strongest beam.

It is necessary to fail beams by stirrup rupture in order to make observations on the impact of longitudinal bar configurations on realized stirrup strength utilization. This had the potential for catastrophic failures, as shear failures are non-ductile in general, and because FRP rupture happens without warning. So, when approximately 70 percent of the lowest strength prediction by Table 3.3 was reached, crack measurements ceased, and barriers were put in place to protect people working in the area.

Three-quarter inch plywood was used on the west side, and a clear sheet of ¼ inch polycarbonate was used on the other.

The test procedure began by bringing the load frame actuator to just above the rollers in the roller harness. Displacement output from the MTS software was zeroed; load cell data was not zeroed because it always output a true load value. The data acquisition system was initialized, and all of the gauges were zeroed except the load. The data acquisition system was set to record samples three times per second.

The load was applied under a displacement controlled rate. The initial displacement rate was 0.272 mm/min. This rate was originally calculated by taking the largest expected single beam displacement and multiplying it by 1.5, because shear deflections are larger than flexural deflections, and then dividing by 45 minutes. Beams were expected to fail somewhere between 30 minutes and 60 minutes of uninterrupted test time. This rate was used for the first 4 tests, but BM25-220 exceeded the predicted displacement limits and took an excessive amount of time to fail, particularly when pauses for crack width measurements are considered.

Afterwards a variable rate was used for the remaining beams. The initial rate until cracking was still 0.272 mm/min for all beams, but was increased to 0.4 mm/min until the safe testing limit was reached. After the barriers were put in place the load rate increased to anywhere between 0.8 mm/min to 1.6 mm/min.

Crack growth was measured by visual inspection. Loading was halted and the displacement held constant while cracks were measured. Initially, loading was to be halted 10 times per test, but this was reduced to 7 to save time during tests. Load increments were evenly spaced between the anticipated cracking load and the safe testing limit.

All cracks were measured during the initial loading stage because it could not be known in advance which one may become the critical crack. However, as testing proceeded fewer cracks were measured; the author and helpers focused on what they believed to be the most critical cracks. Critical cracks included both flexural, flexural-shear, and shear cracks.

A copy of the crack tracking sheet is included in Appendix C. The tracking sheet includes a diagram of the grid onto which the cracks could be sketched. It also included fields for recording the load level, unique crack identifiers, locations of crack measurements, and the crack measurements. Cracks were measured at the crack mouth, crack tip, and any location where the crack crossed a gridline. Cracks were also traced on the side of the beam using permanent markers which alternated colour at each load level.

The author measured cracks using a 20x magnifying loupe on a linear scale with divisions equal to 0.05 mm. A lens for comparing line widths was not available. The author always measured on the east side of the beams.

4 Experimental Observations

This chapter is a presentation of the experimental results. The general observations from testing are presented first, followed by select results for each individual beam. The chapter finishes with a summary of important maximum values and beam load-deflection behaviours. Many observations were omitted from this chapter, but the complete results for each beam may be found in Appendix E.

4.1 Concrete

The concrete mix design was presented in the Experimental Design Chapter. The 8 day strength, based on one cylinder test, was 39.4 MPa. The 28 day strength, based on three cylinders, was 47.3 MPa. Tensile split tests were also conducted 102 days after casting on nine cylinders; the tensile split strength was 4.2 MPa, with 90 percent fractured aggregates. Other cylinders were tested at different times, and more information on concrete strength may be found in Appendix D.

4.2 General Observations

A note on the presentation of beam drawings and crack diagrams: all beam drawings and crack diagrams show the east side of the beam. So, when images on the pages of this document are viewed, the left-hand side of the image is the south end of the beam, and the right-hand side is the north end. Note that the South side of the beam contained the instrumentation Sensors.

4.2.1 Stirrups

No stirrups ruptured in any of the experimental specimens. As a result, no conclusions may be made on the original objective: to investigate the influence of longitudinal bar arrangement on the effective strength of GFRP stirrups.

Specimens which were likely candidates for stirrup failures, BM12-220, BM12-150, BM16-150, & BM16-s230, were investigated further. A jackhammer was used to carefully free the reinforcement from the concrete, and a hack saw was used to free the stirrups from the longitudinal bars. This particular bent GFRP reinforcement is formed inside corrugated plastic tubing, and box cutters were used to remove the tubing from the actual GFRP composite.

None of the stirrups showed any signs of rupture. Figure 4.1 shows the bend of stirrup 7 from BM12-220, which was the most distressed of any of the inspected stirrups. It also shows fibre waving over the bend as a result of the by-hand manufacturing process. The bend of stirrup 6 from BM12-150 showed similar cracking, and a photo of it is included in Appendix E.

Figure 4.1 shows a crack running through the middle of the stirrup bar perpendicular to the plane of the stirrup, and that this crack runs along a plane defined by a neutral axis. Stirrup bends are acted on by a combination of applied bond and bearing stresses that together change the global direction of the internal tensile force from vertical at the stirrup leg to horizontal along the bottom of the stirrup. The combination of applied stresses changes the internal shear stresses over the bend and thus an internal moment is developed. The fibres on the outside of the bend are loaded in tension, while the fibres on the inside of the bend are loaded in compression. Fibre delamination occurs at the neutral axis where the internal stresses switch from tensile to compressive.

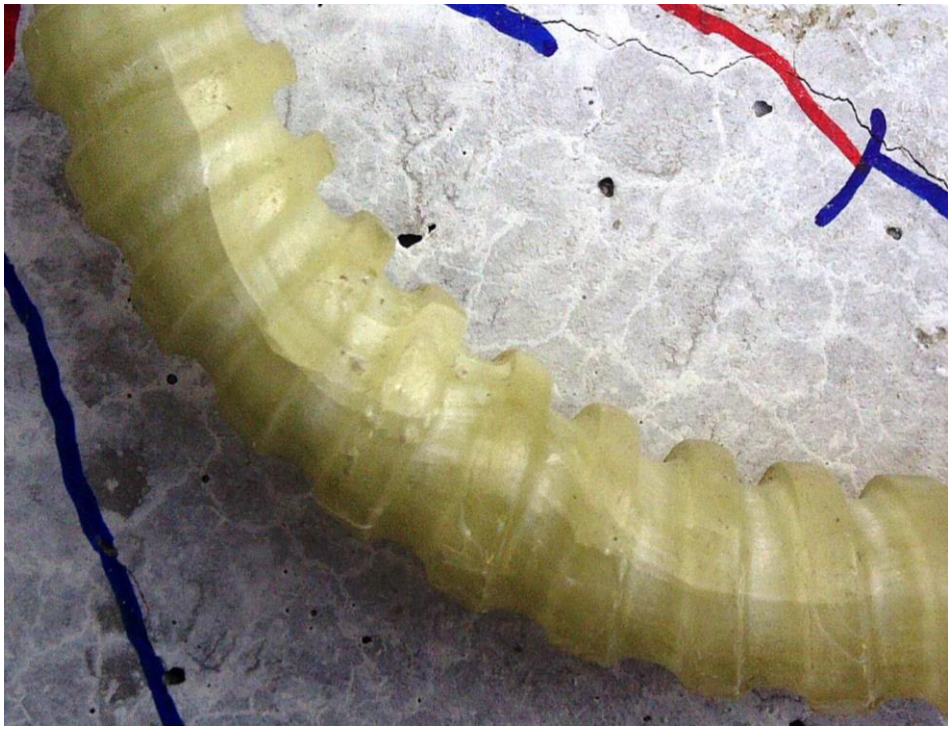

Figure 4.1: BM12-220 Bend of Stirrup 7

4.2.2 Failure Modes

The observed failure modes were separated into distinct categories: beams without stirrups failed in shear-tension, while beams with stirrups failed in shear-compression / strut-crushing.

The passage of peak load was generally unremarkable and was not accompanied by noises, movement, or the ejection of concrete pieces. Typically the only sign of distresses was an excessive amount of cracks, but overall crack widths were small. There are a few exceptions, and they are identified in the individual descriptions. Of course, within the vicinity of peak load beams would occasionally make popping noises consistent with the characteristic sound of concrete fracture, and occasionally small particles of concrete would fall from the sides of the beam. This is in direct contrast to the observations by Bentz et al. (2010), who noted that shear failures gave off more signs of distress leading up to failure than a compressive flexural failure.

Figure 4.2 shows photos of BM12-INF and BM12-s230 centred on the failed span when loading was stopped at a point sometime after peak load.

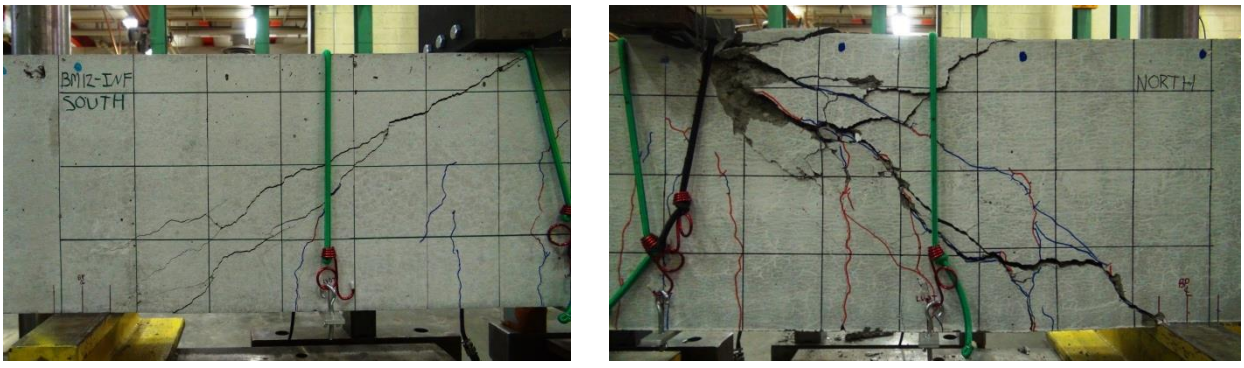

BM12-INF BM12-s230

Figure 4.2: Post-Peak Photos

The failure modes are made clear in Figure 4.2. The photo of BM12-INF shows a sparse number of cracks. The main shear crack developed fingers that tend to follow each layer of longitudinal reinforcement, which is typical of a shear-tension failure. The photo of BM12-s230 shows more cracks, a larger main shear crack, and a region of crushed concrete adjacent to the load plate which is typical of shear-compression failures.

4.2.3 Cracking

Cracking was typical: the mid-span flexural crack formed first followed by more flexural cracks. In beams with stirrups the flexural cracks formed at the location of the stirrups. Flexural cracks then grew into flexural shear cracks, and then shear cracks developed.

Beam BM25-INF failed along a crack which ran from quarter-span to the load plate. All other beams failed along a crack which ran from support plate to load plate.

In the BMX-INF series the crack along which the beams failed formed after crack measurements ceased. In beams with stirrups the main shear crack formed before crack measurements ceased, and often ran from load plate to support plate.

Maximum crack sizes at peak load tended to increase with increasing shear reinforcement ratio. The largest recorded crack was 1.65 mm on BM25-s230 measured near quarter-span along the bottom of the beam. The mid-span crack was typically obscured by the strapping for the mid-span LVDT gauge and was not measured. Shear cracks were typically wider at mid-depth than they were at the bottom face of the beam, as is typical of shear cracking.

Crack diagrams for each load stage for each beam may be found in Appendix E.

4.2.4 Longitudinal Strain

The results of longitudinal strain measurements were generally linear after cracking when plotted against applied load, as expected for GFRP reinforced beams. Figure 4.3 shows a plot of applied load against longitudinal strain for BM25-150. Recall that beams BM25-X had a mid-span strain gauge on both longitudinal bars.

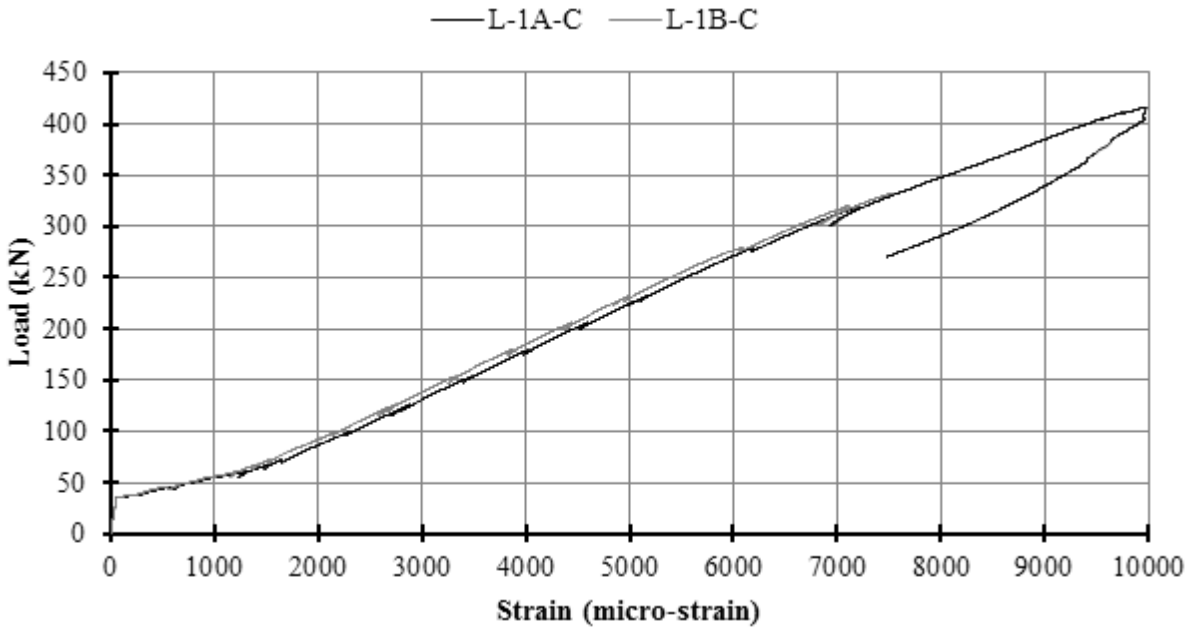

Figure 4.3: BM25-150 Plot of Load vs Mid-Span Strain

Figure 4.3 shows that the mid-span strain response of the longitudinal bars was initially stiff until the formation of the mid-span flexural crack. The response then softened, and at about 1750 micro-strain the stiffness recovered a slight amount. Nearing peak load the stiffness very gradually decreased, and after peak load the strain decreased with decreases in the applied load. The slight recovery of stiffness just after cracking, at 1750 micro-strain for this beam, was observed in all beams, but no explanation is given as to why this occurred.

In Figure 4.3, the two mid-span gauges recorded nearly identical behaviour; however, gauge L-1B-C failed prematurely.

Recall that beams BM16-INF, -220, & -150 included strain gauges along the centre most longitudinal bar in the south shear span, and served to observe changes in longitudinal bar strain with applied load at different sections. Figure 4.4 shows the development of longitudinal strain in each gauge respective to its location along the span. Each curve is a different percent of peak load.

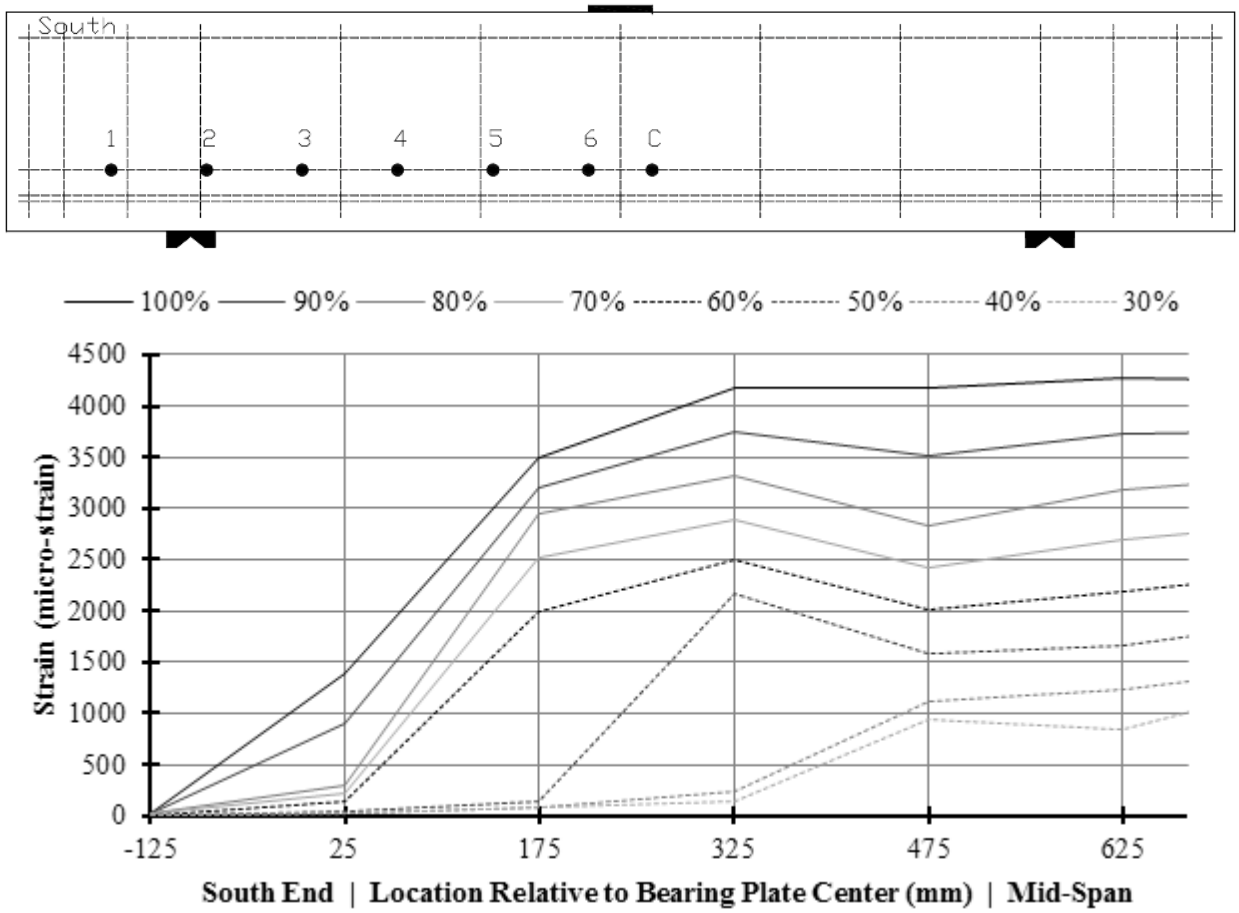

Figure 4.4: BM16-220 Arch Action Plot

At the top of Figure 4.4 is a layout of the strain gauges along the longitudinal bar; mid-span is located 675 mm from the centre of the support and gauge C is not shown on the plot. The plot of Figure 4.4 indicates that as the applied load increases so too does the strain at all points along the longitudinal bar. Initially the longitudinal strain is highest at mid-span with little strain registered in gauges closer to the support. As loading increases significant strain is recorded by gauges closer and closer to the support. The gauge located on the far side of the support never saw any significant strain which indicates that the bars were well anchored.

Most importantly Figure 4.4 shows that at peak load the three gauges closest to the centre of the support all recorded very similar strains. This indicates that the longitudinal bar has deboned in this region, and that a tied arch mechanism has formed. Such a mechanism is indicative of arch action behaviour. Arch action plots for beams BM16-INF, & -150 are found in Appendix E; BM16-150 shows similar behaviour, but BM16-INF failed in shear-tension well ahead of the development of a tied arch mechanism.

4.2.5 Stirrup Strain

The results of stirrup strain measurements are difficult to generalize. A number of gauges failed before peak load, and thus information on stirrup strains was lost. It was thought that the lead wires for the gauges snapped inside the concrete as they crossed growing cracks. Future researchers would be wise to protect the lead wires by threading them through thin plastic tubing so that the wires may move inside the tube as the beam deforms. In addition, most beams with stirrups failed in the un-instrumented north shear span, so the exact stirrup strain information for the failed span is not known.

Figure 4.5 shows a plot of applied load against stirrup strain and includes measurements for gauges on the straight and bent portions of the stirrups. In the figure, each stirrup is represented by one shade of grey; the dotted line represents the straight portion gauge, and the solid line represents the bent portion gauge.

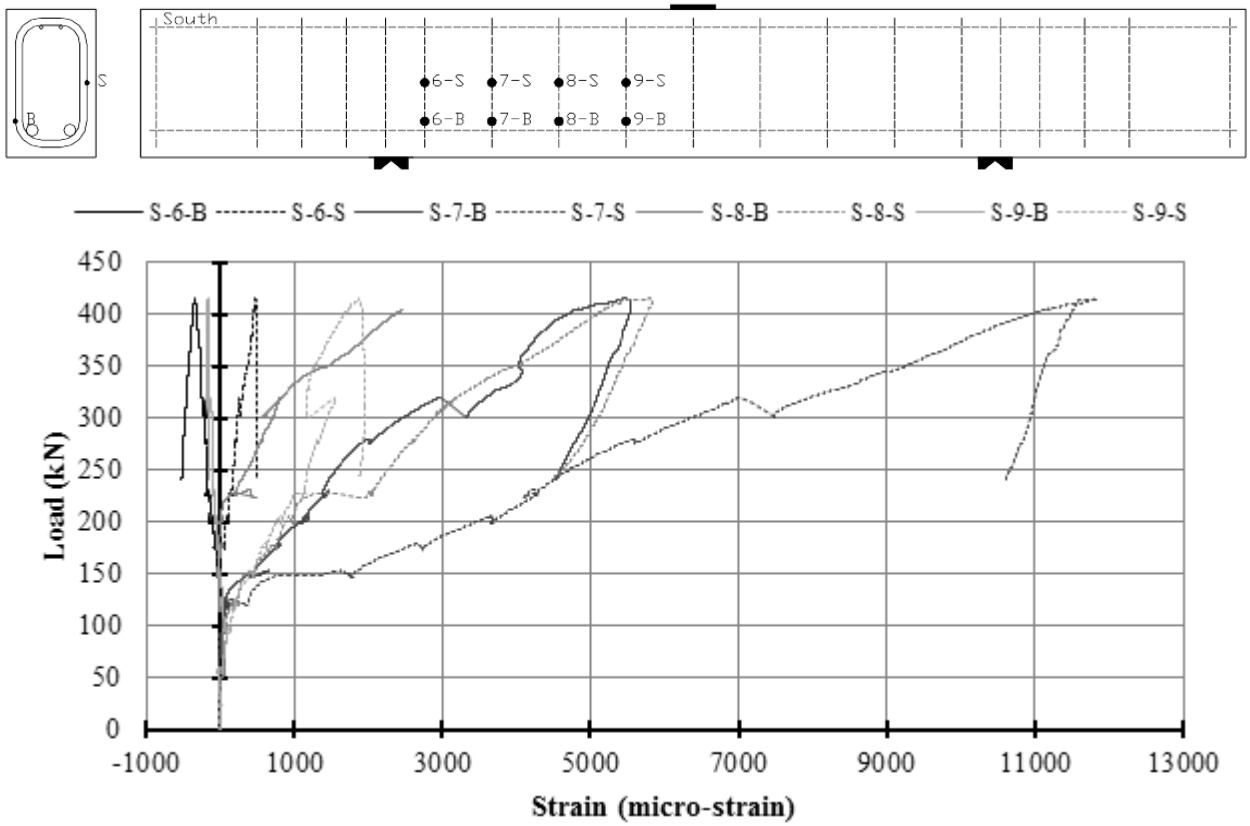

Figure 4.5: BM25-150 Plot of Load vs Stirrup Strain

Figure 4.5 shows results that are typical of most beams with stirrups regardless of the arrangement of longitudinal bars. It was typical for the strain in the straight portion of the stirrup leg to be larger than the strain at the bend portion for any given stirrup. Further, stirrups in the middle of the shear span showed the largest strains; stirrups closest to the support or load points strained much less, and as

Figure 4.5 shows, their bends experienced negative strain. Strain gauges S-7-B and S-8-S in Figure 4.5 were crossed by the same crack, and interestingly show very similar strain profiles. It is also important to note that neighbouring stirrups have the potential to be subjected to very different magnitudes of strain.

These observations are consistent with arch action behaviour; cracks tend to run from the point of load to the support and thus cross the middle most stirrups within the vicinity of mid-height. Concrete near the supports is expected to be in a general state of compression which explains why the gauge on the stirrup bend near the support may have a negative reading. No explanation is given for the negative strain measurements for stirrup bends near mid-span.

Figure 4.6 shows a stirrup action plot which was constructed in much the same way as the arch action plot of Figure 4.4. This plot shows the development of straight portion stirrup strain in each gauge respective to its location along the span. Each curve is a different percent of peak load.

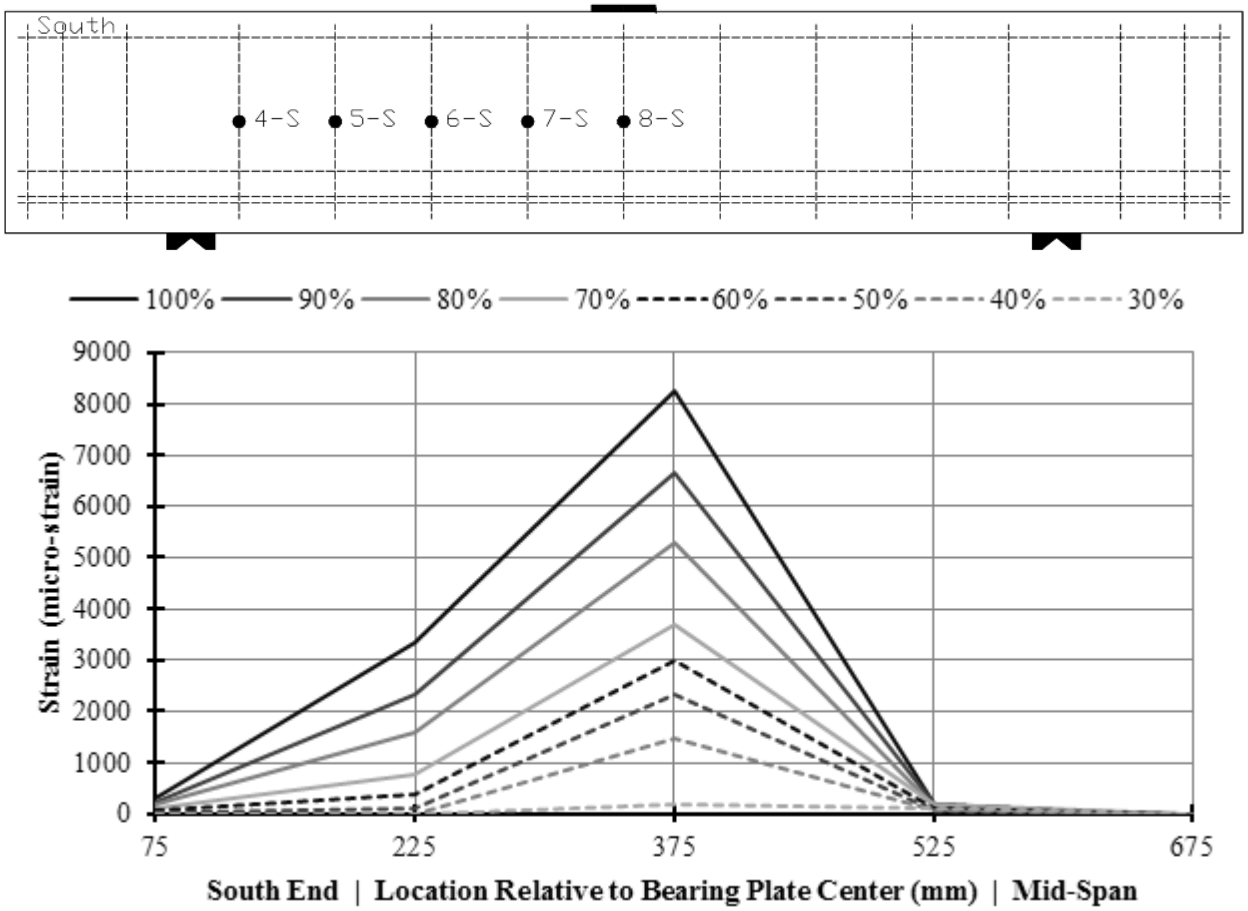

Figure 4.6: BM16-150 Straight Portion Stirrup Action Plot

Figure 4.6 generally confirms the discussion following Figure 4.5. The strain gauges in the middle most portion, and just south of the middle most portion, experience the largest strains. This occurs because the main shear cracks, which run from load plate to support plate, tend to have a more vertical slope near the support and a flatter slope near mid span, and generally form a flattened arching shape. So, the straight portion strain gauges are more likely to be engaged on stirrups near the support and in the middle of the shear span. This will become evident on peak load crack diagrams presented later in this chapter.

4.2.6 Other Observations

The top framing bars on all beams with stirrups ruptured along the plane of the main shear crack. These bars were not thought to have provided any strength and were used for rebar-cage framing.

4.3 Individual Beam Results

This section contains selected results for each beam to show the behaviour of individual beam specimens. Additional results and photos are included in Appendix E, which provides all data on the tested beams. Small dips in the load-displacement plots indicate pauses for crack measurements as displacement was held constant allowing the beams to relax; though dips are also indicative of crack formation.

The presentation of text and figures in this section makes use of several large intentional blank spaces.

4.3.1 BM12-INF

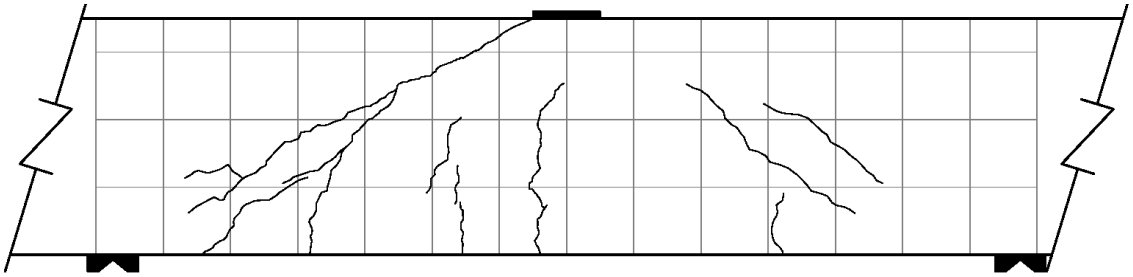

Figure 4.7: BM12-INF Peak Load Crack Diagram

This beam failed in shear-tension along a shear crack which formed after crack width measurements ceased. The crack ran diagonally from the load plate to the south bearing plate. The crack forked at failure and the fork tines tended to follow the three layers of reinforcement and are indicative of tensile splitting. At peak load, a loud noise characteristic of concrete fracture was heard and was accompanied by a slight jolting movement and a slight widening of the main shear crack; there was no ejection of concrete projectiles. Peak load occurred at 163.1 kN and 4.25 mm of displacement, and the failure took place in the south shear span 54 days after casting. All of the strain gauges functioned adequately during the test.

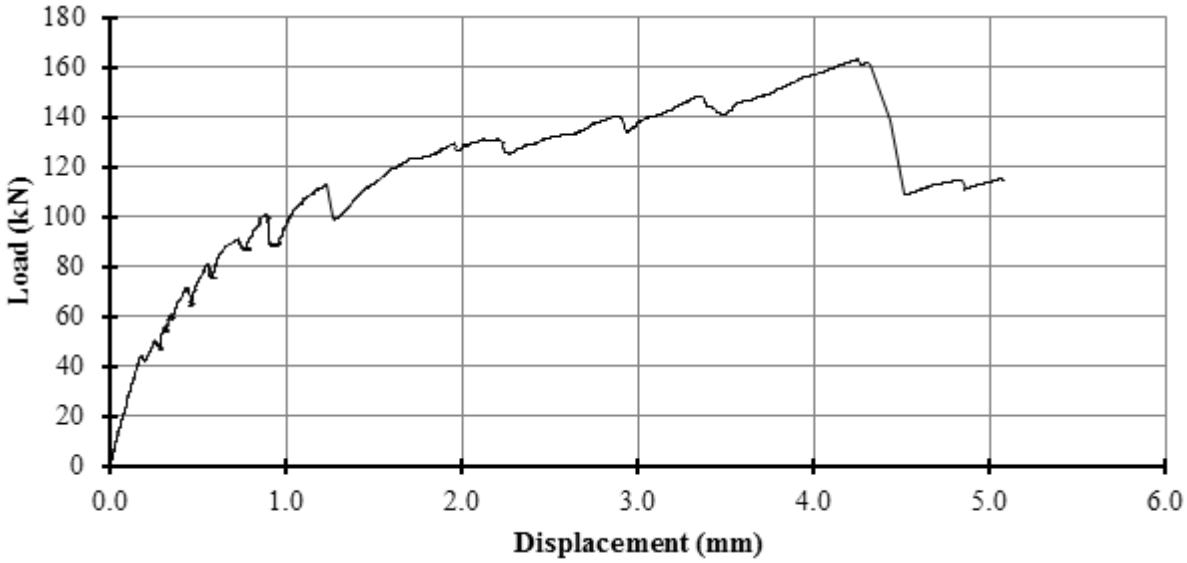

Figure 4.8: BM12-INF Plot of Load vs Displacement

4.3.2 BM16-INF

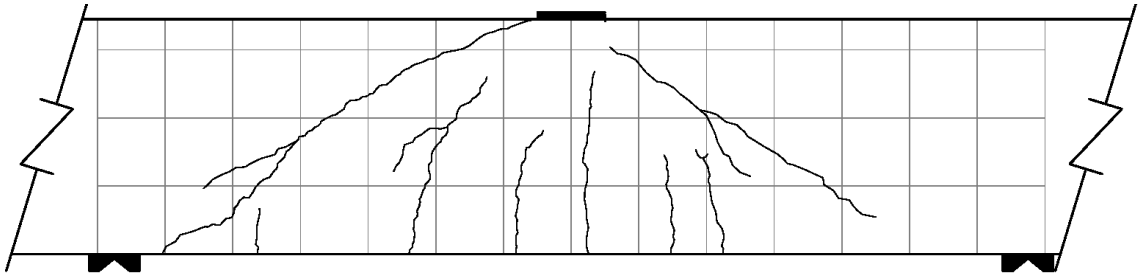

Figure 4.9: BM16-INF Peak Load Crack Diagram

This beam failed in shear-tension along a shear crack which formed after crack width measurements ceased. The crack ran diagonally from the load plate to the south bearing plate. The formation of the shear crack did not accompany peak load. The failure was unremarkable: it occurred at 150.2 kN and 4.21 mm of displacement, and failure took place in the south shear span 50 days after casting. Strain gauge L-2-4 failed shortly after peak load was reached; all other strain gauges functioned adequately during the test.

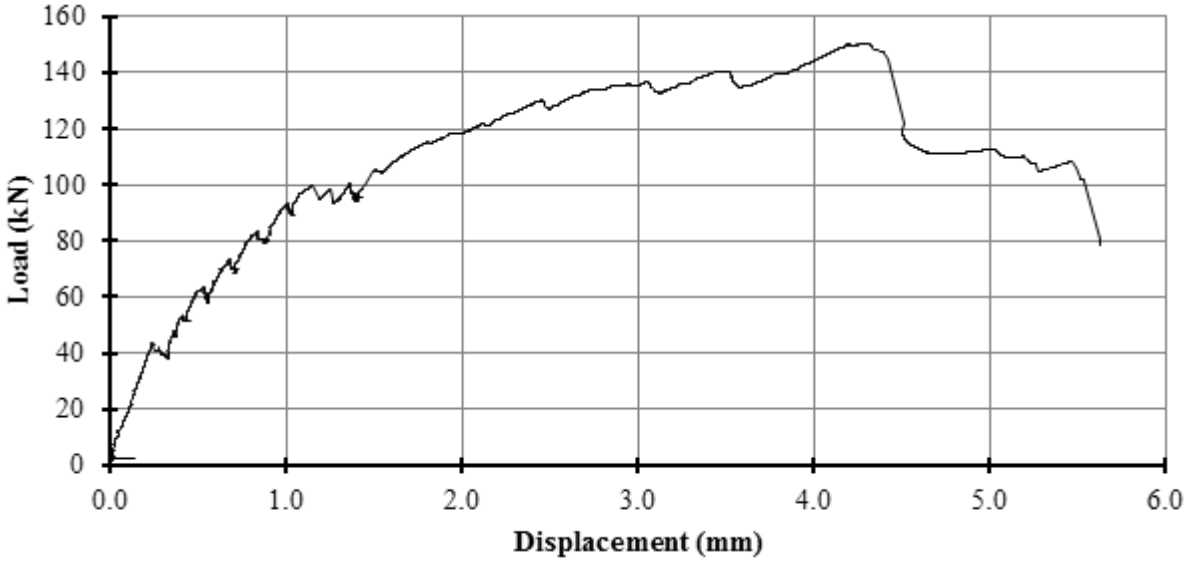

Figure 4.10: BM16-INF Plot of Load vs Displacement

4.3.3 BM25-INF

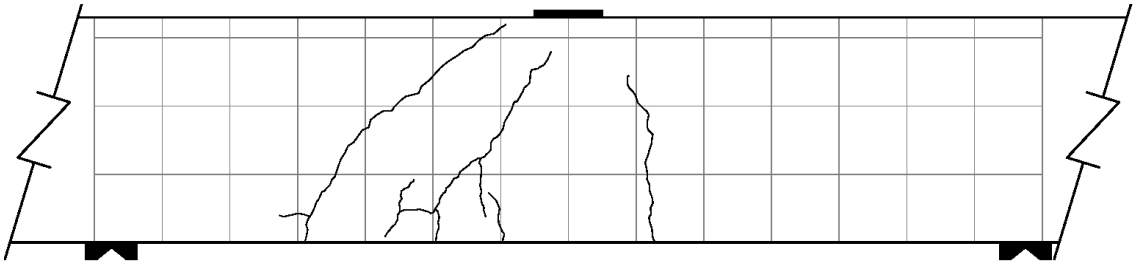

Figure 4.11: BM25-INF Peak Load Crack Diagram

This beam failed in shear-tension along a shear crack which formed after crack measurements ceased. Peak load was accompanied by the formation of the shear crack. Further increases in load resulted in the formation of tensile spitting cracks which coalesced into one crack with the main shear crack. Otherwise peak load was unremarkable: it occurred at 125.1 kN and 3.22 mm of displacement, and failure took place in the south shear span 43 days after casting. All of the strain gauges functioned adequately during the test.

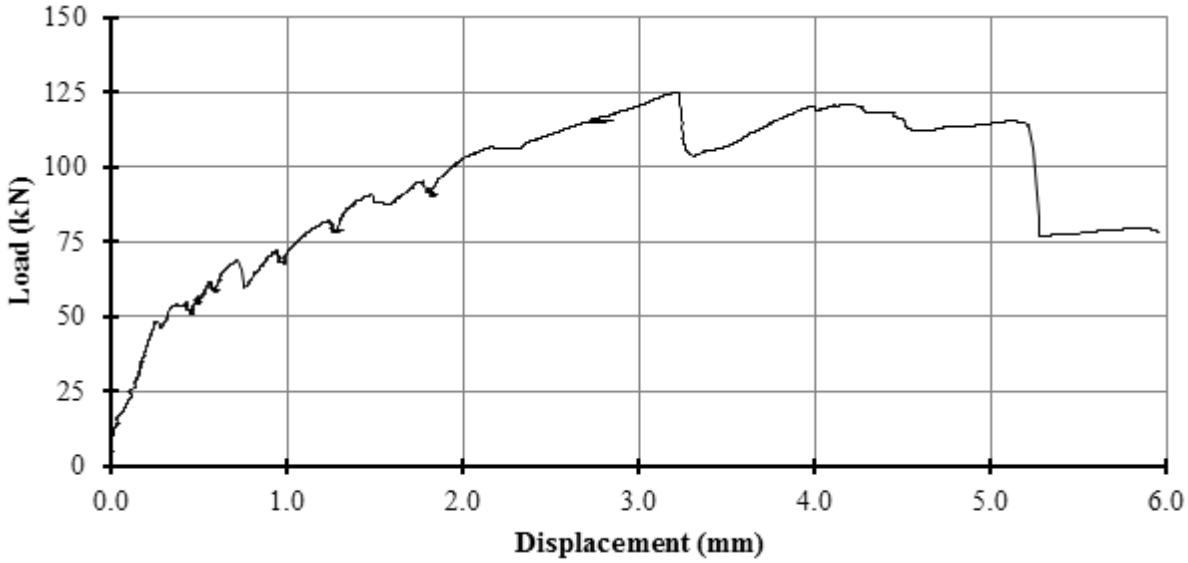

Figure 4.12: BM25-INF Plot of Load vs Displacement

4.3.4 BM12-220

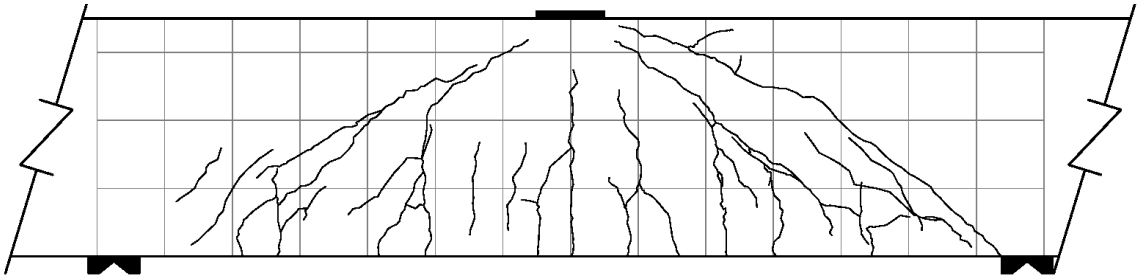

Figure 4.13: BM12-220 Peak Load Crack Diagram

This beam failed in shear-compression / strut-crushing along a plane which ran diagonally from the load plate to the north bearing plate. The failure was unremarkable, though shortly after peak load there was a popping noise characteristic of concrete fracture and a widening of cracks which accompanied a sudden drop in load. Peak load occurred at 382.4 kN and 11.96 mm of displacement, and failure occurred in the un-instrumented north shear span 72 days after casting. Strain gauge L-1-C failed before peak load, strain gauges L-2-C and L-3-C failed after peak load; all other strain gauges functioned adequately during the test.

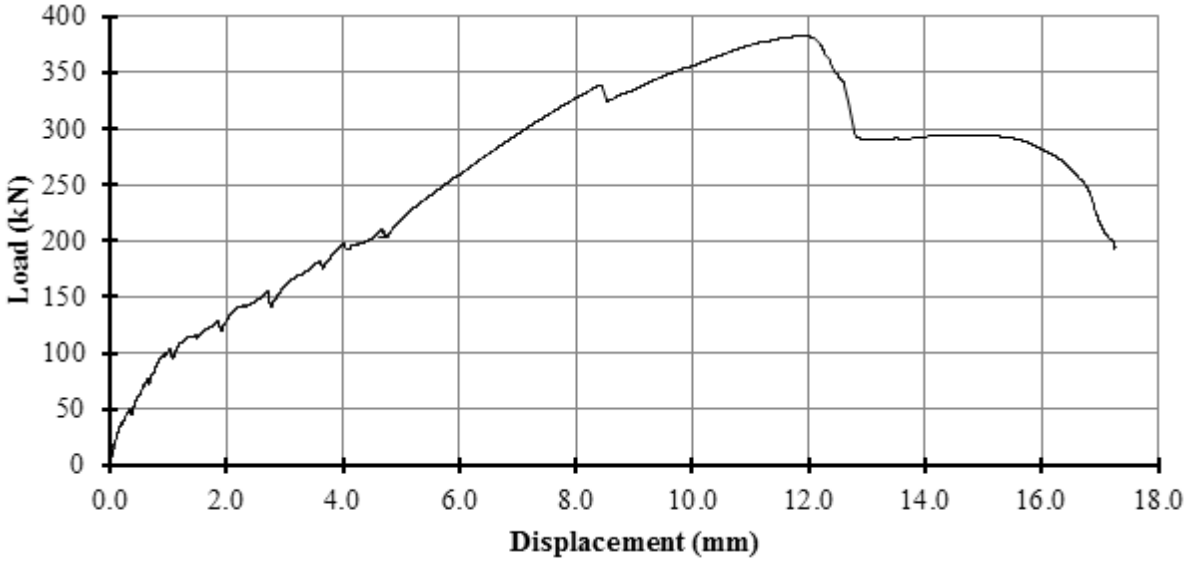

Figure 4.14: BM12-220 Plot of Load vs Displacement

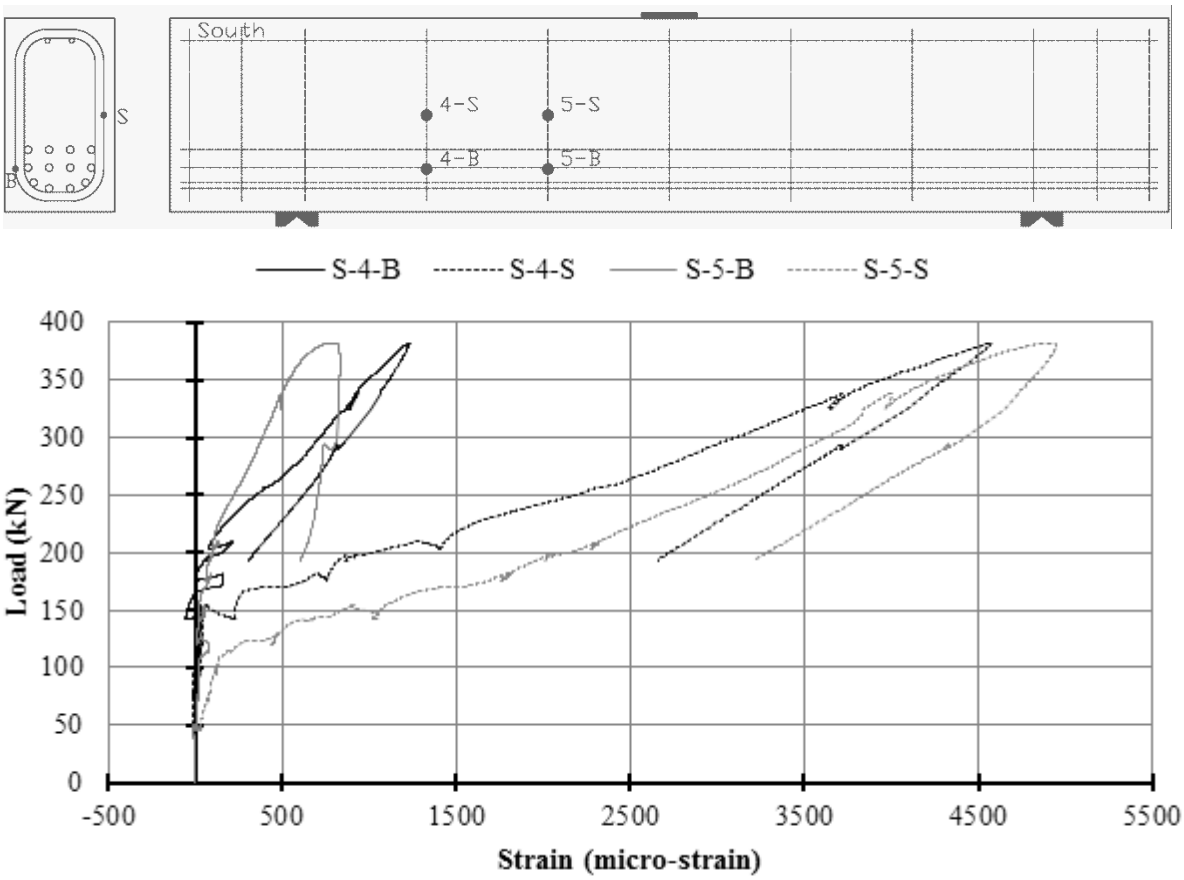

Figure 4.15: BM12-220 Plot of Load vs Strain on Stirrups

4.3.5 BM16-220

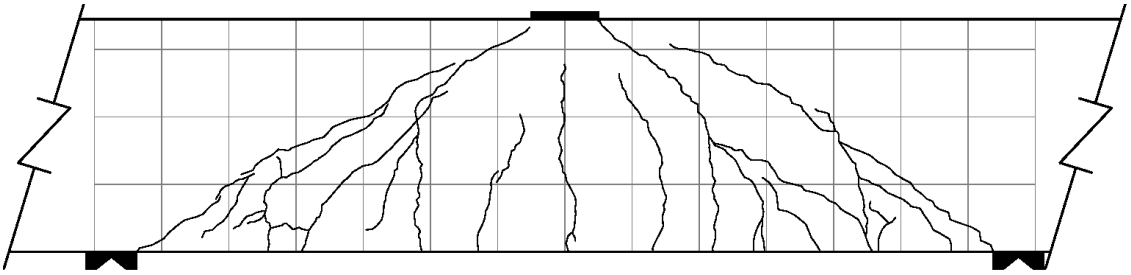

Figure 4.16: BM16-220 Peak Load Crack Diagram

This beam failed in shear-compression / strut-crushing along a plane which ran diagonally from the load plate to the north bearing plate. Peak load was accompanied by a slight popping noise characteristic of concrete fracture, but was otherwise not accompanied by perceptible movements or the ejection of concrete projectiles. Peak load occurred at 309.3 kN and 8.42 mm of displacement, and failure took place in the un-instrumented north shear span 68 days after casting. Strain gauges L-1-C and L-2-C failed after peak load; all other strain gauges functioned adequately during the test.

A blip in the power occurred during the test as a thunderstorm moved through the region. The blip caused the frame computer to shut off and knocked out the hydraulics to the entire structures lab. The data acquisition system survived the blip, but the gauges were re-zeroed when the test was restarted and information on permanent displacements and strains was lost. The power blip caused the beam to experience one load cycle that reached 43 percent of peak load, and calls into question the appropriateness of comparing these results to the results of other beam in this experimental program.

The inclusion of the results from this test in a database should be done with caution.

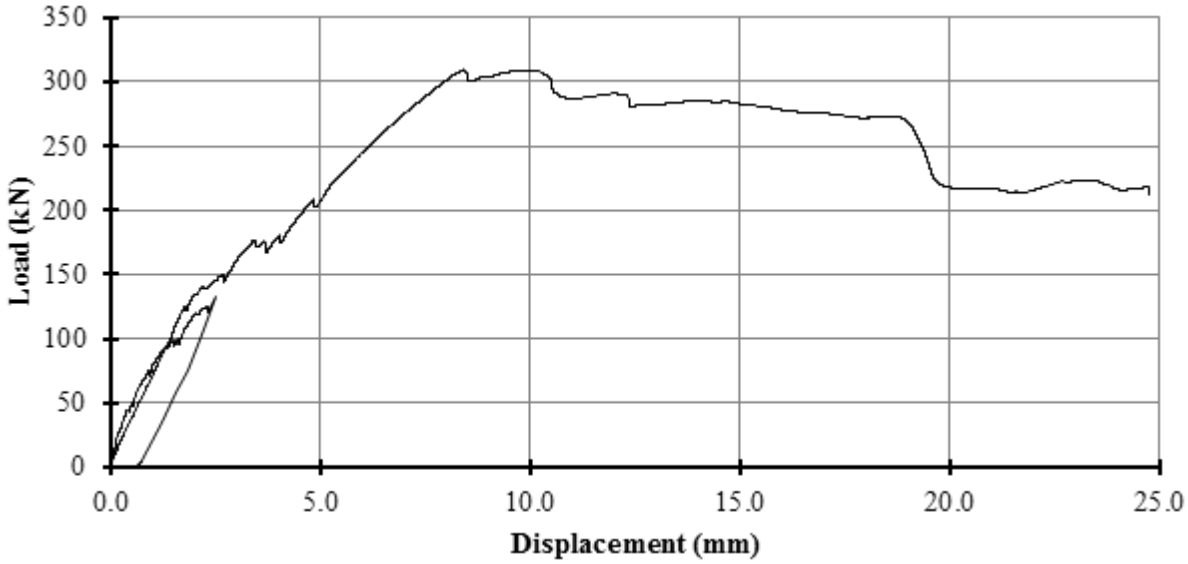

Figure 4.17: BM16-220 Plot of Load vs Displacement

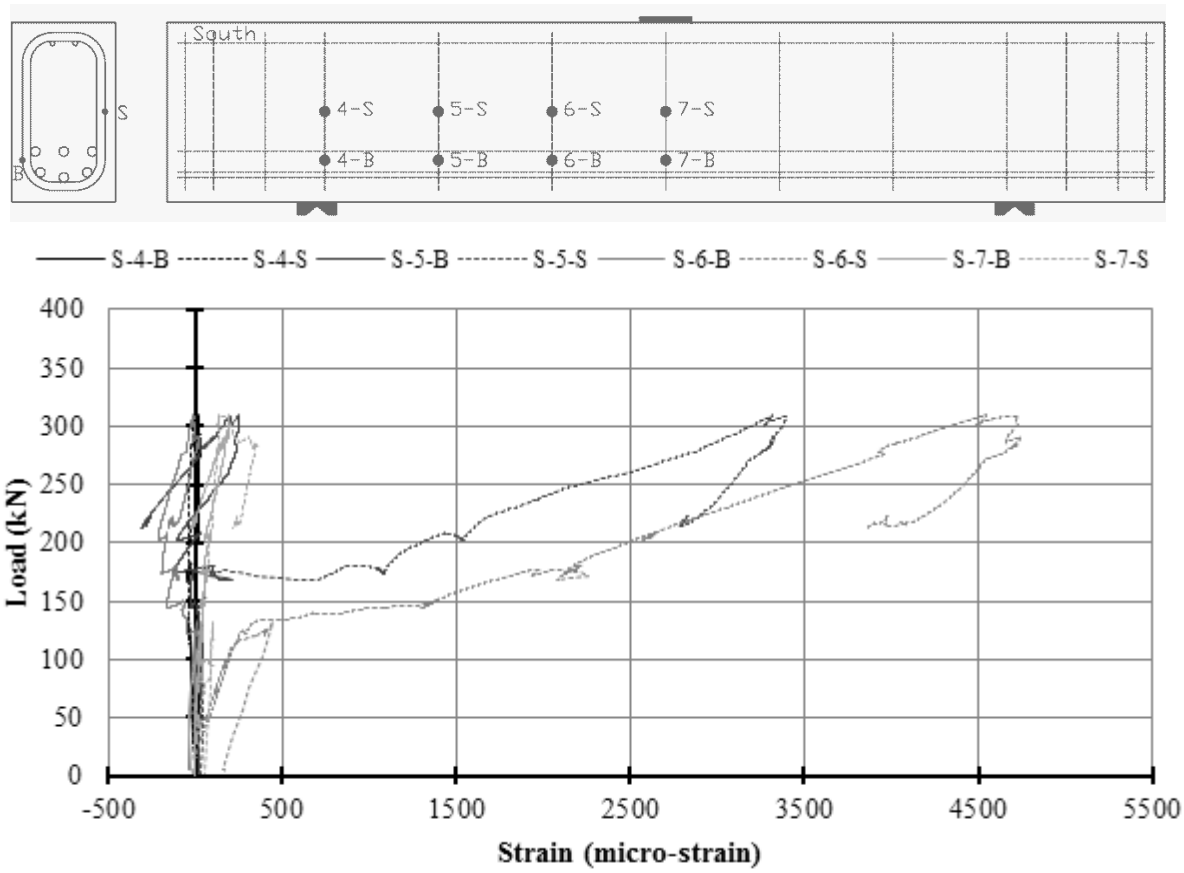

Figure 4.18: BM16-220 Plot of Load vs Strain on Stirrups

4.3.6 BM25-220

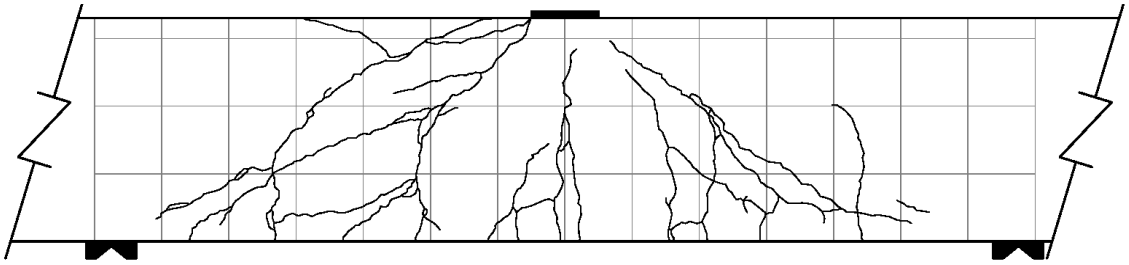

Figure 4.19: BM25-220 Peak Load Crack Diagram

This beam failed in shear-compression / strut-crushing along a plane which ran diagonally from the load plate to the south bearing plate. Peak load was reached and then followed by a plateau on the load displacement curve. The failure was unremarkable: peak load occurred at 360.1 kN and 24.01 mm of displacement, and failure took place in the instrumented south shear span 56 days after casting. Strain gauges S-7-B and S-7-S failed before peak load; strain gauge S-6-B failed after peak load; all other strain gauges functioned adequately during the test.

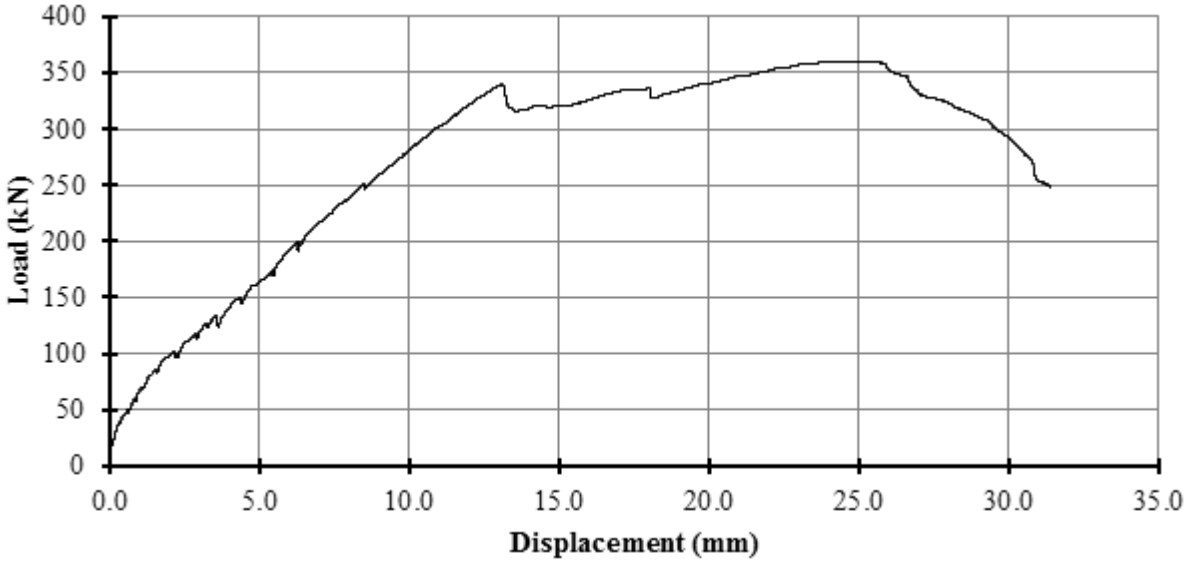

Figure 4.20: BM25-220 Plot of Load vs Displacement

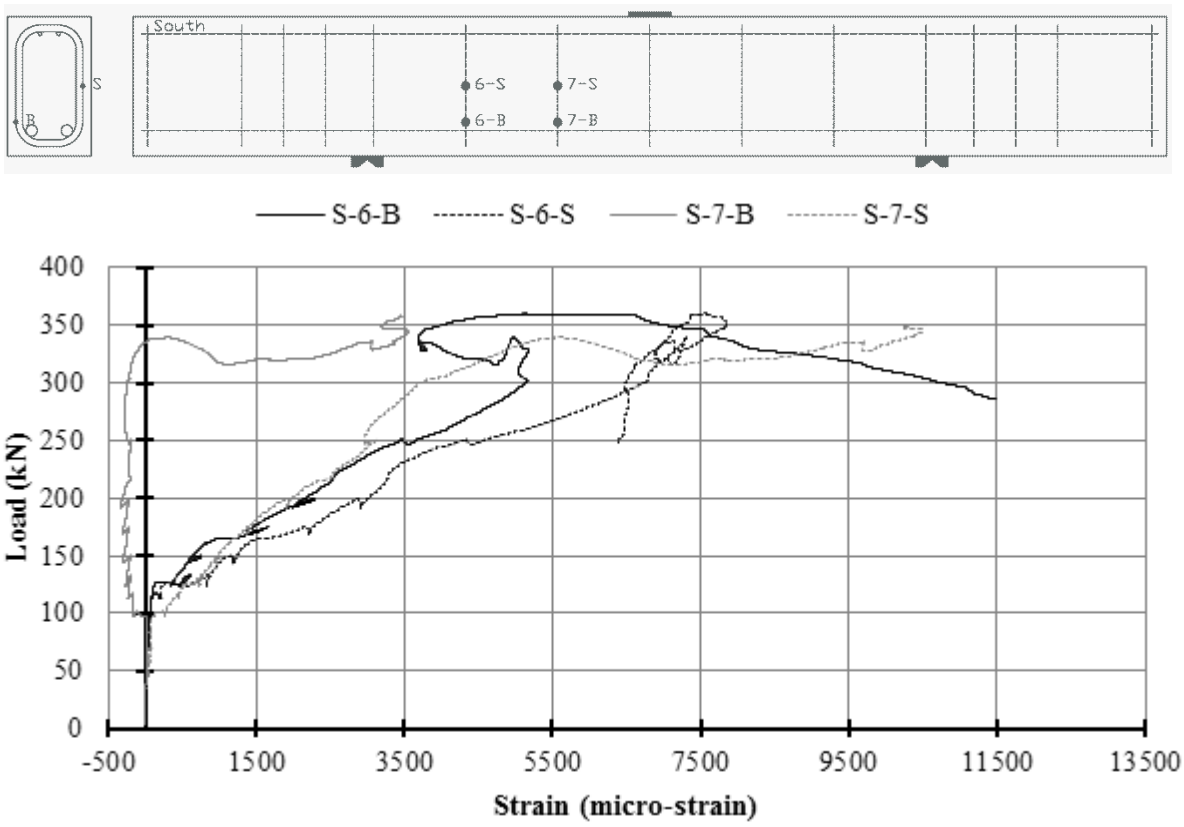

Figure 4.21: BM25-220 Plot of Load vs Strain on Stirrups

4.3.7 BM12-150

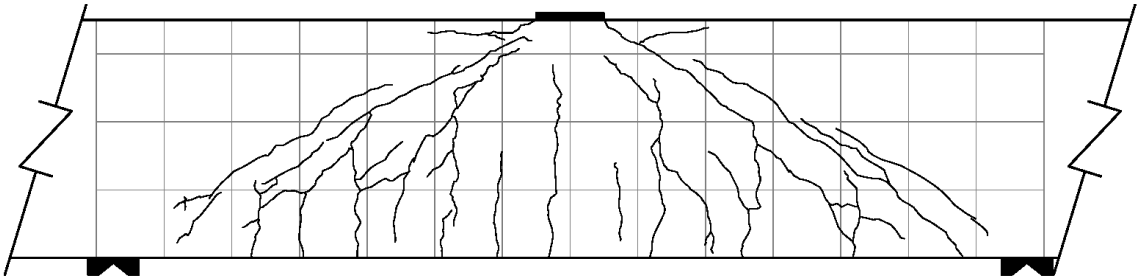

Figure 4.22: BM12-150 Peak Load Crack Diagram

This beam failed in shear-compression / strut-crushing along a plane which ran diagonally from the load plate to the south bearing plate. Peak load was accompanied by a slight popping noise characteristic of concrete fracture, but was not accompanied by perceptible movements or the ejection of concrete projectiles. Peak load occurred at 405.2 kN and 15.56 mm of displacement, and failure took place in the instrumented south shear span 91 days after casting. Strain gauges S-6-B and S-6-S failed before peak load; strain gauges S-5-B and S-5-S failed after peak load; all other strain gauges functioned adequately during the test.

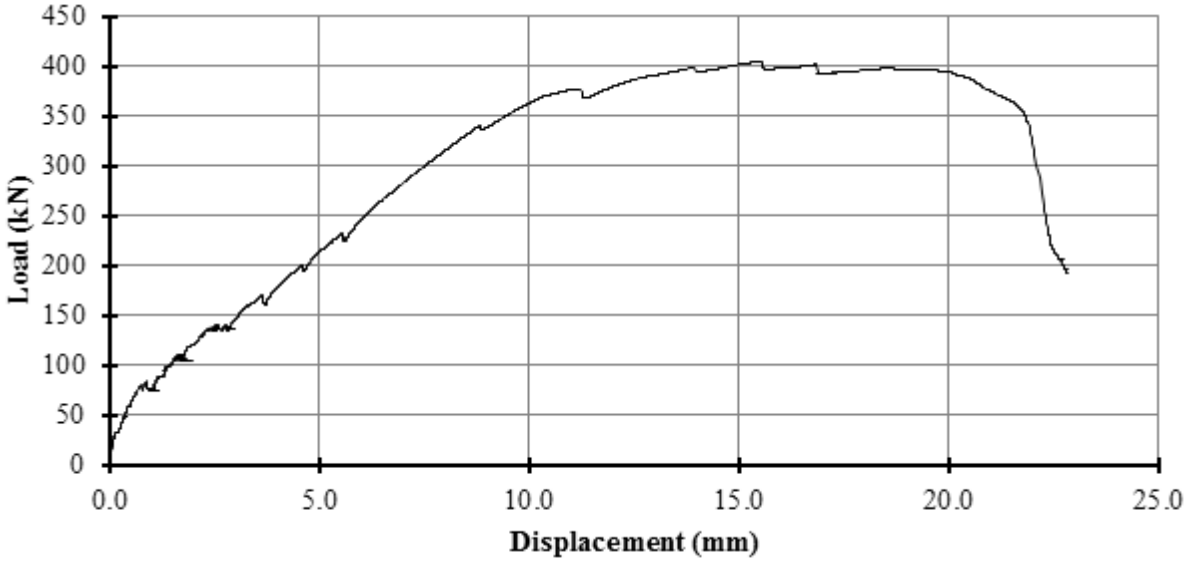

Figure 4.23: BM12-150 Plot of Load vs Displacement

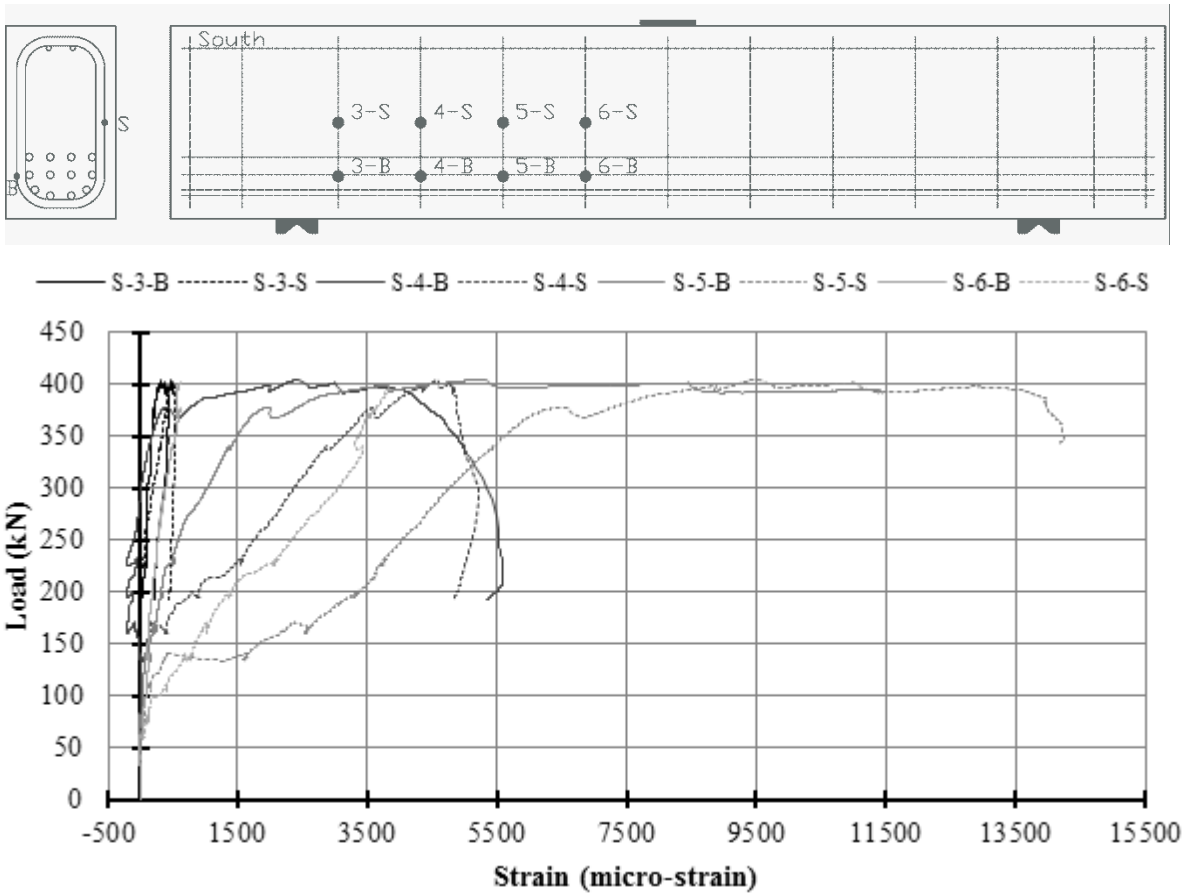

Figure 4.24: BM12-150 Plot of Load vs Strain on Stirrups

4.3.8 BM16-150

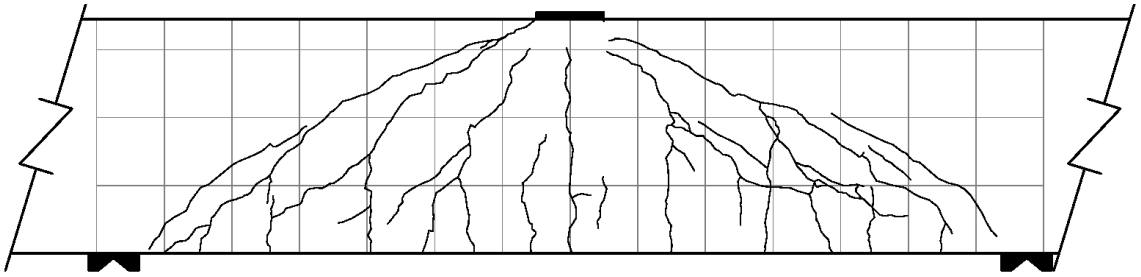

Figure 4.25: BM16-150 Peak Load Crack Diagram

This beam failed in shear-compression / strut-crushing along a plane which ran diagonally from the load plate to the north bearing plate. Peak load was accompanied by a slight popping noise characteristic of concrete fracture. Minutes later a sudden large drop in load occurred with only some flaking of concrete as warning. The drop in load was characteristic of a catastrophic failure and was accompanied by a loud banging noise, movement, and the ejection of large and small concrete projectiles. Peak load occurred at 416.5 kN and 14.44 mm of displacement, and failure took place in the un-instrumented north shear span 86 days after casting. Strain gauges L-1-C, L-2-C, L-2-6, and S-7-S failed before peak load; strain gauge S-7-B failed after peak load; all other strain gauges functioned adequately during the test.

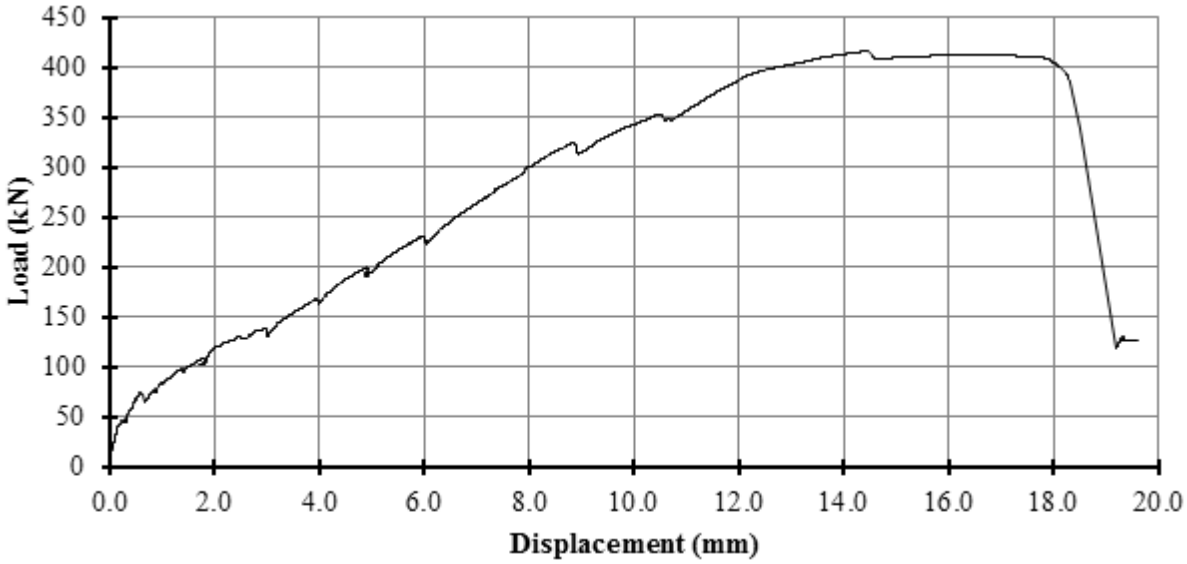

Figure 4.26: BM16-150 Plot of Load vs Displacement

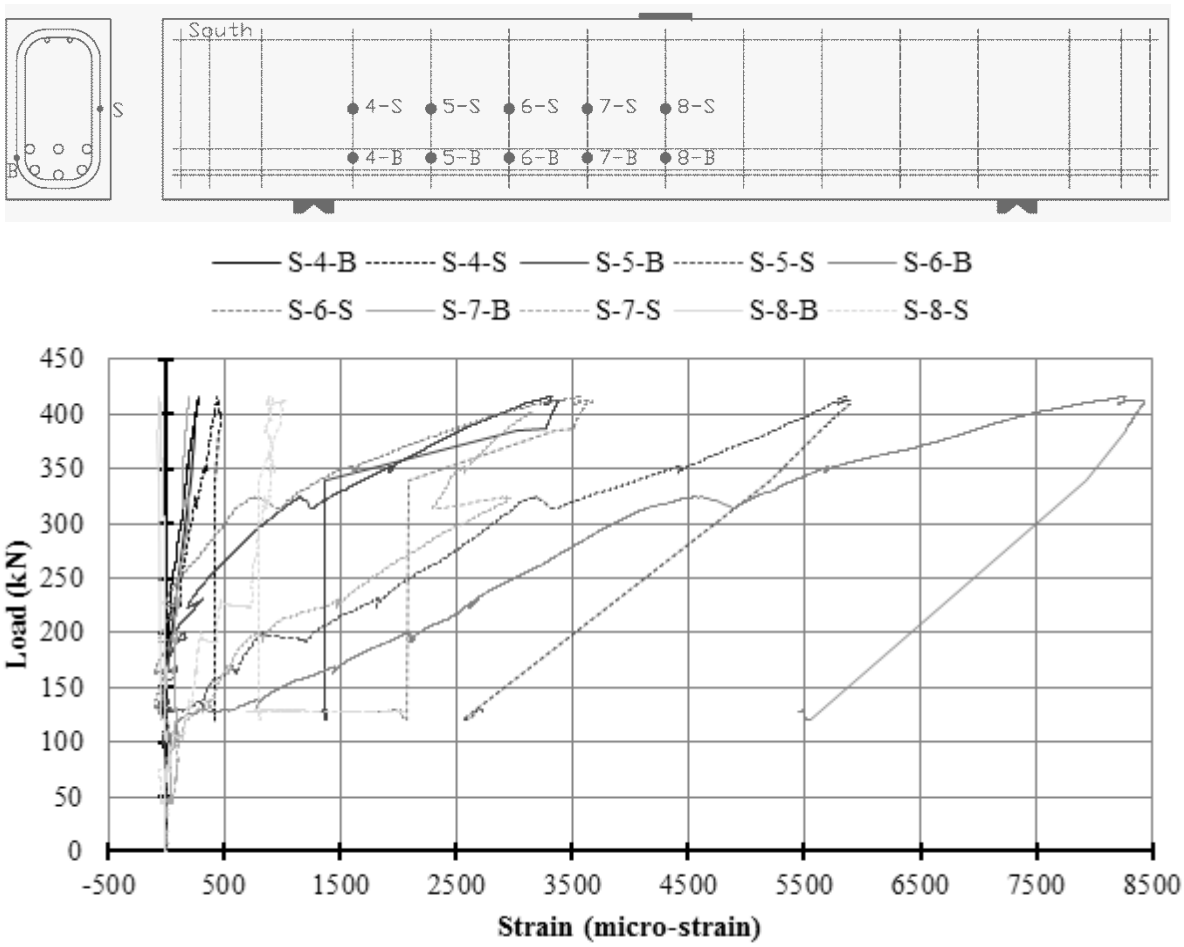

Figure 4.27: BM16-150 Plot of Load vs Strain on Stirrups

4.3.9 BM25-150

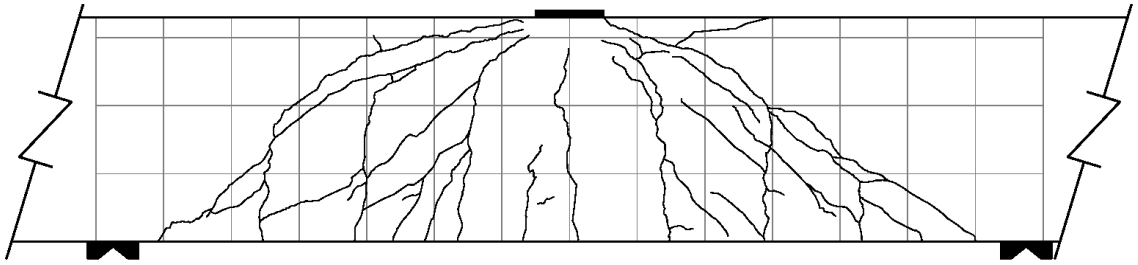

Figure 4.28: BM25-150 Peak Load Crack Diagram

This beam failed in shear-compression / strut-crushing along a plane which ran diagonally from the load plate to the north bearing plate. The failure was unremarkable: peak load was not accompanied by loud noises, perceptible movements, or the ejection of concrete projectiles. Peak load occurred at 415.8 kN and 22.07 mm of displacement, and failure took place in the un-instrumented north shear span 84 days after casting. Strain gauges L-1B-C and S-8-B failed before peak load; strain gauge L-1A-B failed after peak load; all other strain gauges functioned adequately during the test.

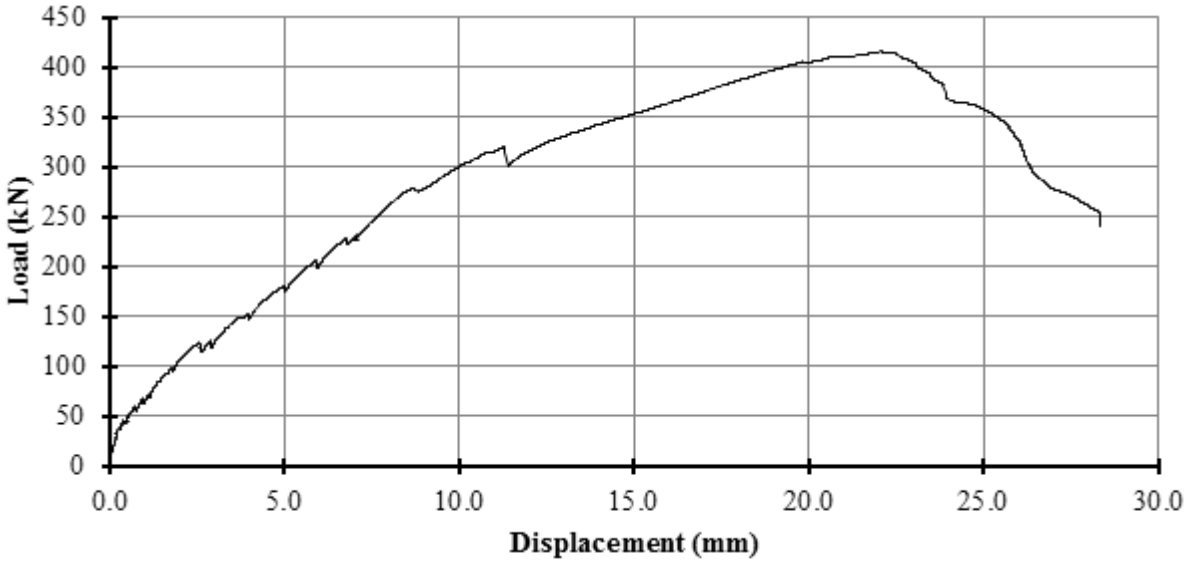

Figure 4.29: BM25-150 Plot of Load vs Displacement

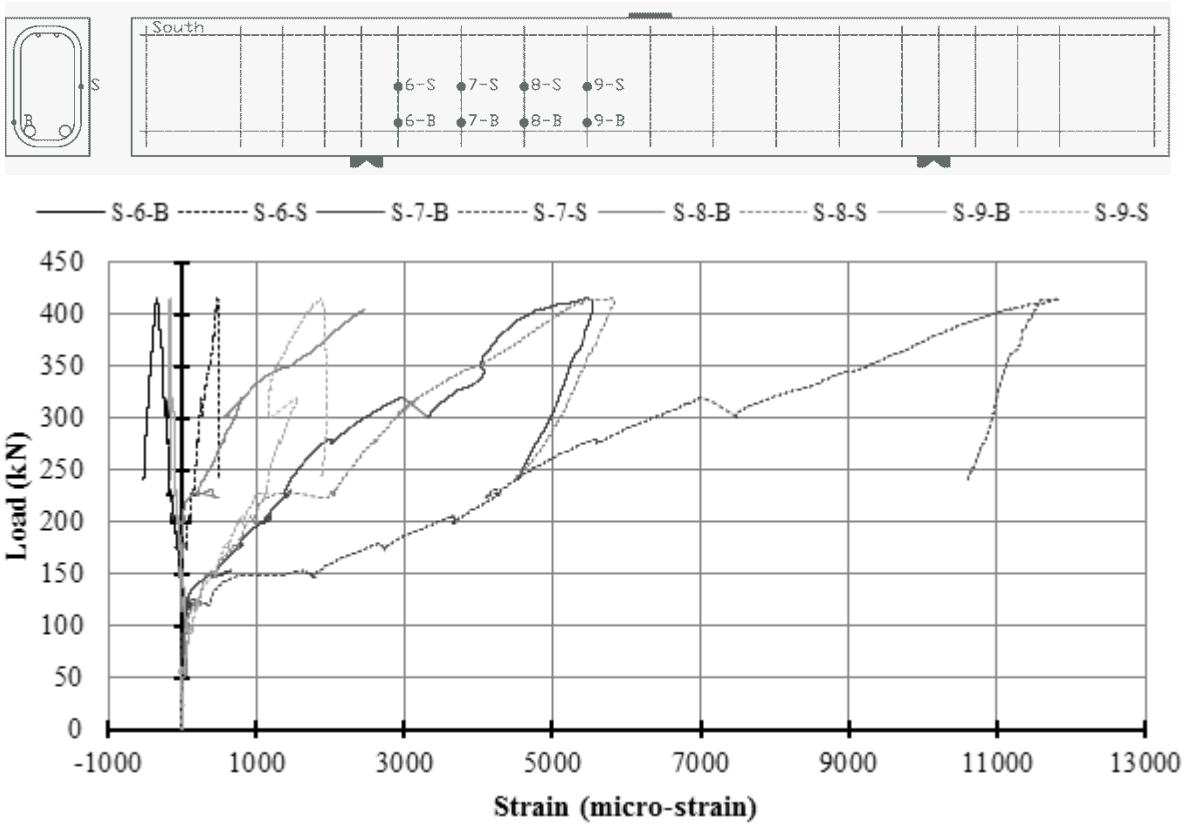

Figure 4.30: BM25-150 Plot of Load vs Strain on Stirrups

4.3.10 BM12-s230

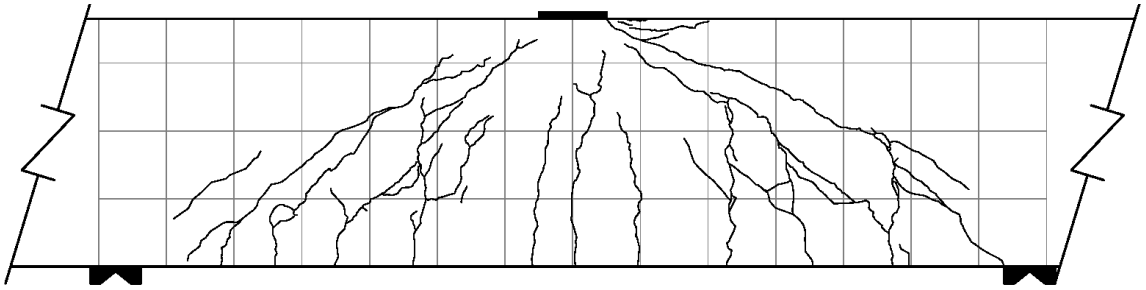

Figure 4.31: BM12-s230 Peak Load Crack Diagram

This beam failed in shear-compression / strut-crushing along a plane which ran diagonally from the load plate to the north bearing plate. The failure was unremarkable: peak load was not accompanied by loud noises, perceptible movements, or the ejection of concrete projectiles. Peak load was followed moments later by a large drop in load, which was accompanied by a popping noise characteristic of concrete fracture, widening of cracks, and the ejection of a few small concrete projectiles. Peak load occurred at 466.9 kN and 12.52 mm of displacement, and failure took place in the un-instrumented north shear span 98 days after casting. All strain gauges functioned adequately during the test.

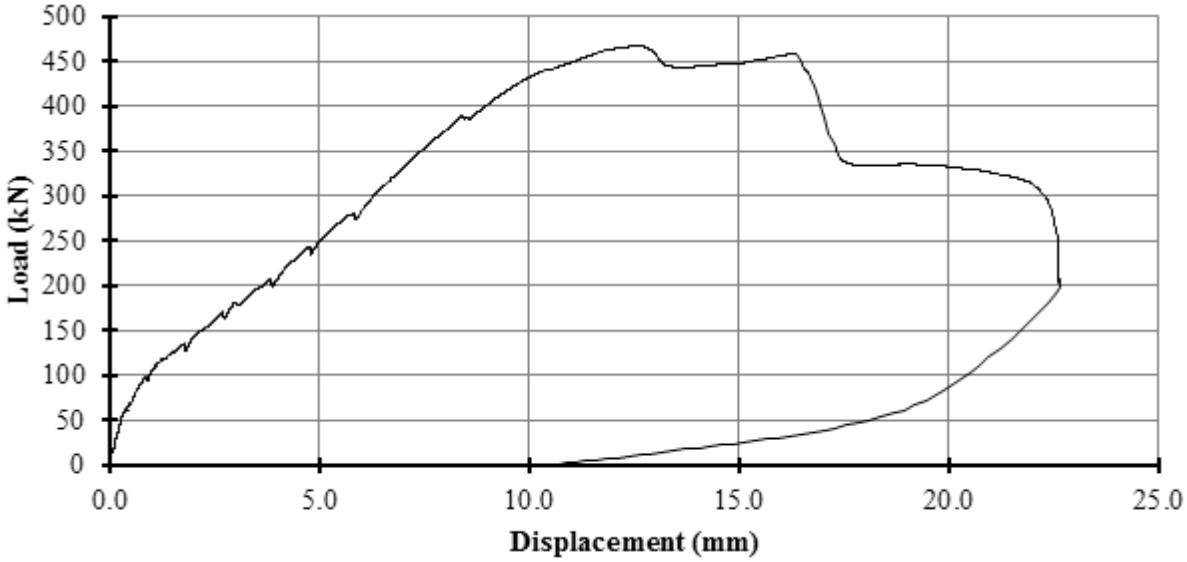

Figure 4.32: BM12-s230 Plot of Load vs Displacement

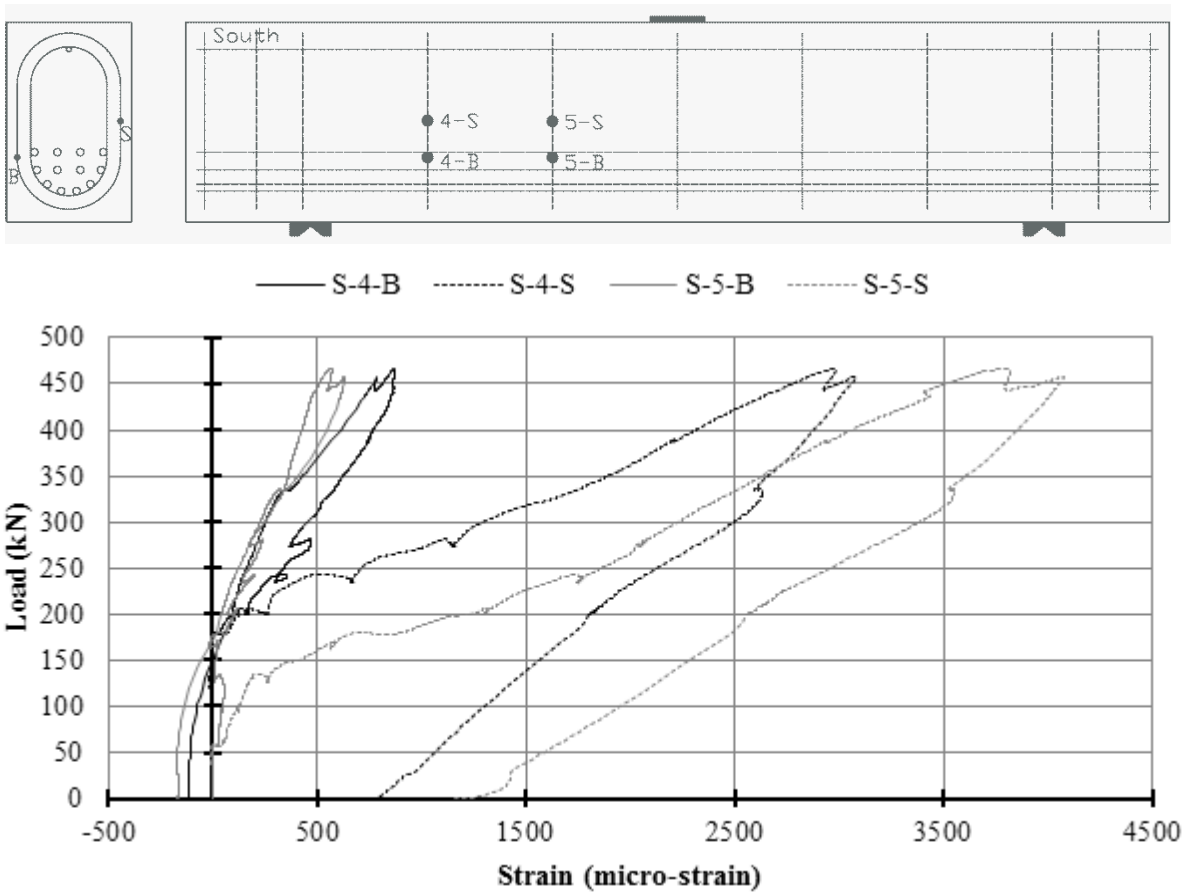

Figure 4.33: BM12-s230 Plot of Load vs Strain on Stirrups

4.3.11 BM16-s230

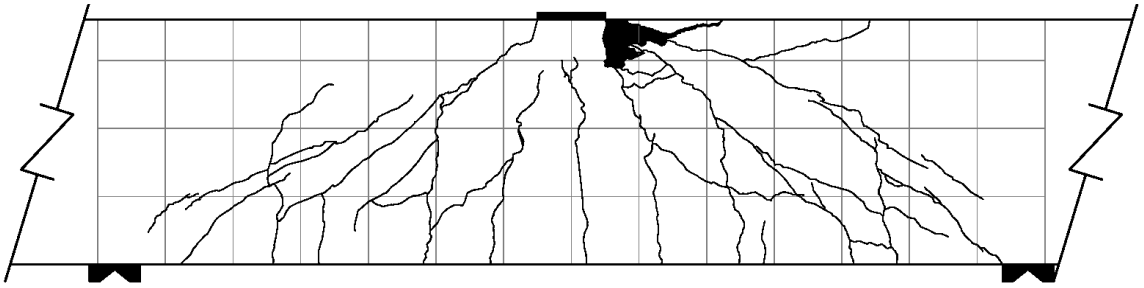

Figure 4.34: BM16-s230 Peak Load Crack Diagram

This beam failed in shear-compression / strut-crushing along a plane which ran diagonally from the loading plate to the north bearing plate. Peak load was unremarkable. A sudden large drop in load occurred a minute after peak load. The drop in load was preceded by flaking concrete and an occasional popping noise consistent with concrete fracture. The drop in load was accompanied by a loud banging noise, a jolting movement, and the ejection of large concrete projectiles. This was the most catastrophic failure witnessed in the testing program. Peak load occurred at 450.8 kN and 21.95 mm of displacement, and failure took place in the un-instrumented north shear span 96 days after casting. Strain gauges L-1-C and L-2-C failed before peak load; all other strain gauges functioned adequately during the test.

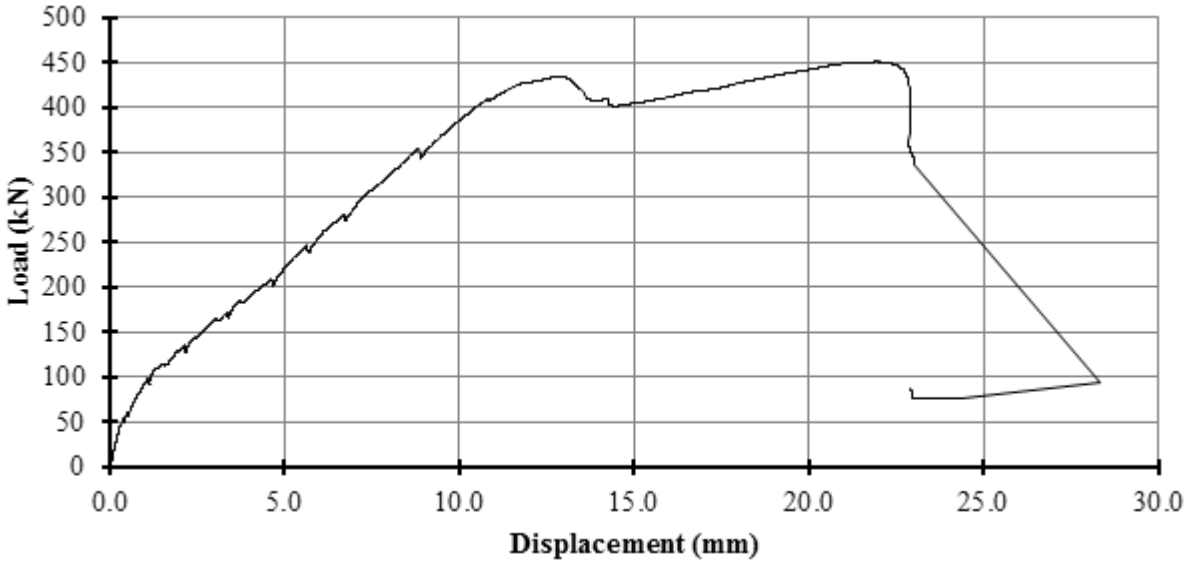

Figure 4.35: BM16-s230 Plot of Load vs Displacement

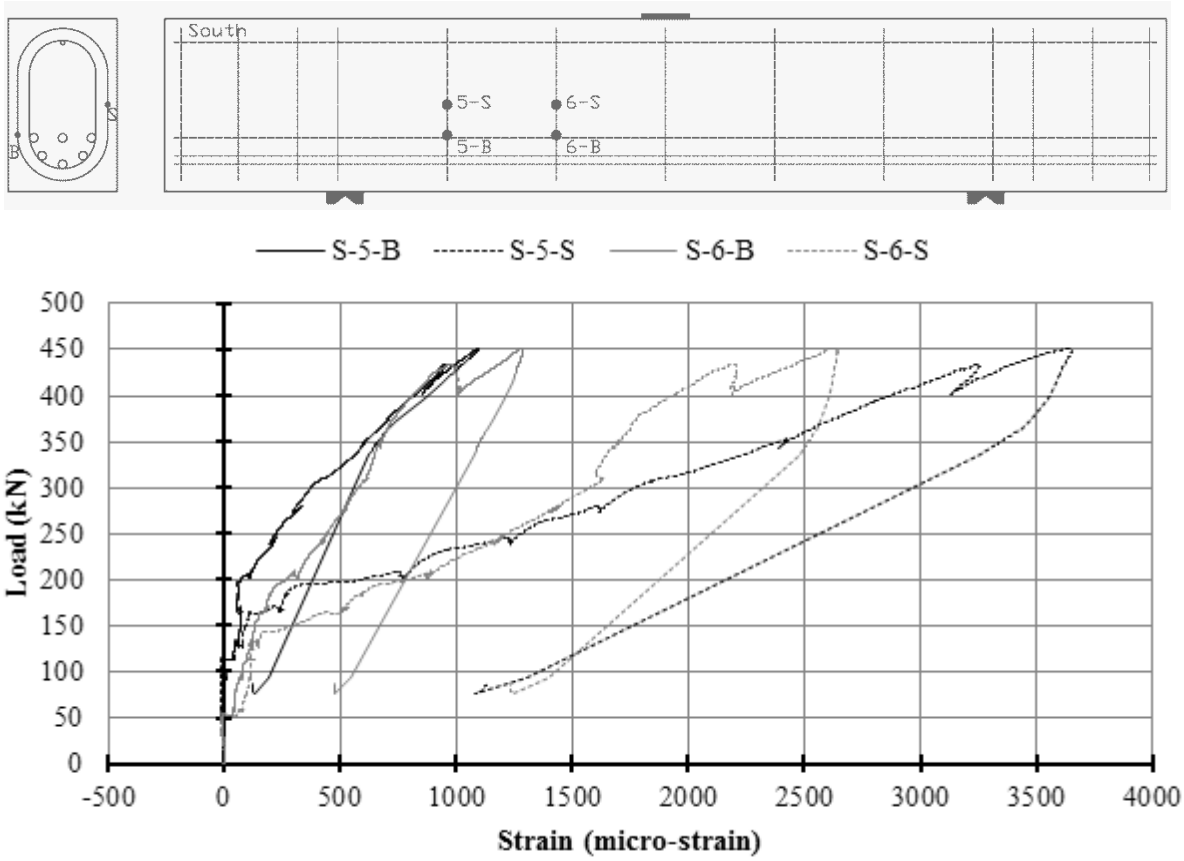

Figure 4.36: BM16-s230 Plot of Load vs Strain on Stirrups

4.3.12 BM25-s230

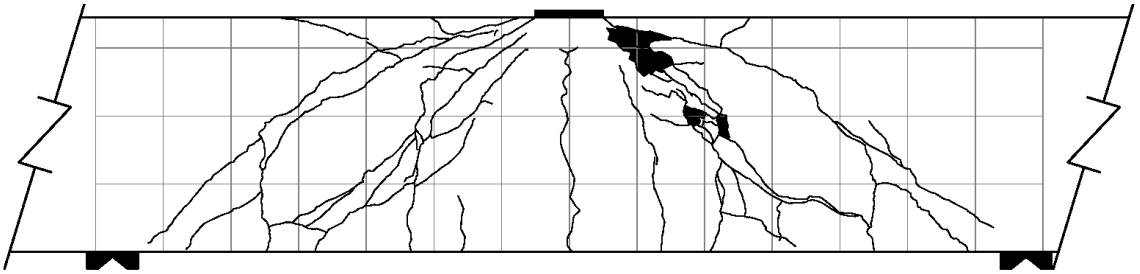

Figure 4.37: BM25-s230 Peak Load Crack Diagram

This beam failed in shear-compression / strut-crushing along a plane which ran diagonally from the load plate to the north bearing plate. Peak load was accompanied by some flaking of concrete, but was not accompanied by loud noises, perceptible movements, or the ejection of concrete projectiles. Peak load occurred at 444.0 kN and 35.65 mm of displacement, and failure took place in the un-instrumented north shear span 92 days after casting. Strain gauges L-1A-C, L-1B-C, and S-6-B failed before peak load; all other strain gauges functioned adequately during the test.

At different points during testing, each of the three LVDTs stopped recording data properly. After peak load the core of the mid-span LVDT fell out, so the mid-span displacement data was augmented by appending the relative displacement of the test frame actuator to the mid-span LVDT data. Since this occurred after peak load it is not expected to have a significant impact on the presentation of results.

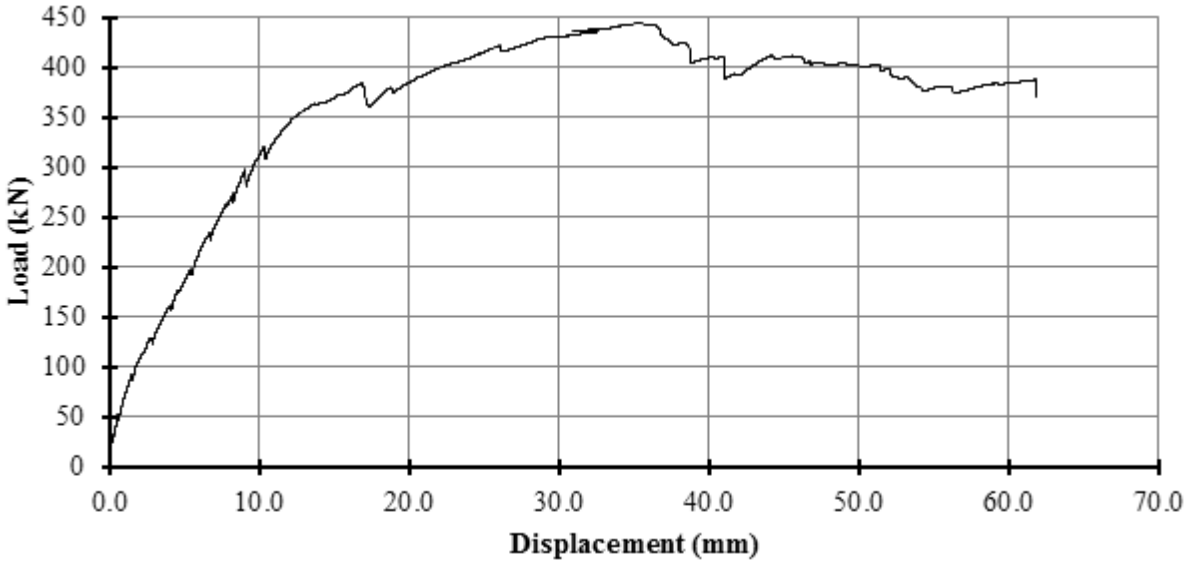

Figure 4.38: BM25-s230 Plot of Load vs Displacement

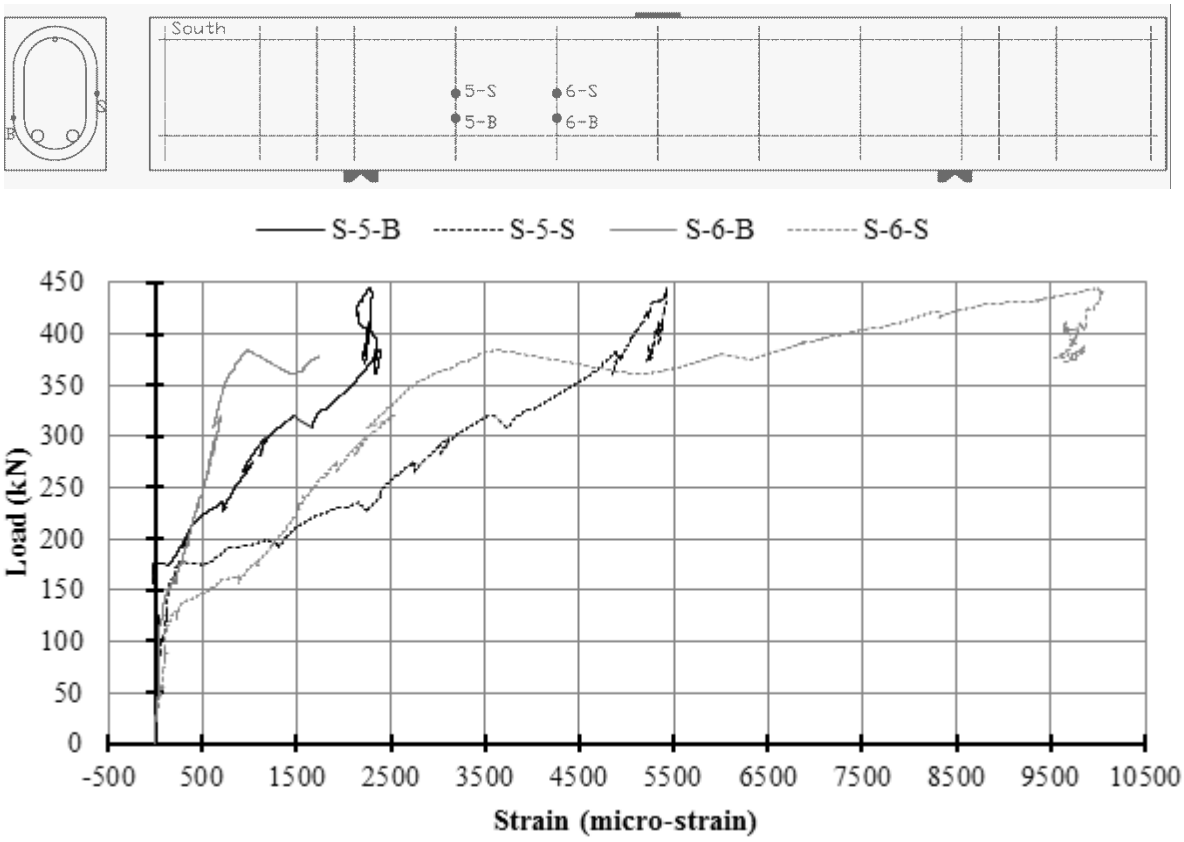

Figure 4.39: BM25-s230 Plot of Load vs Strain on Stirrups

4.4 Summary of Results by Beam Series

Table 4.1 presents a summary of the most important results from each beam. The longitudinal and shear reinforcement ratios are included for reference, P_E is the maximum load recorded during the test, and Δ_{mid} is the mid-span displacement.

Table 4.1: Results

Beam	ρ_f %	ρ_v %	P_E kN	Δ_{mid} at P_E mm	Longitudinal ε_{max} με	Stirrup Bend ε_{max} με	Stirrup Straight ε_{max} με
BM12-INF	2.5	-	163.1	4.25	2523	-	-
BM16-INF	2.2	-	150.2	4.21	2744	-	-
BM25-INF	1.8	-	125.1	3.22	2919	-	-
BM12-220	2.5	0.5	382.4	11.96	*7448*	1237	4952
BM16-220*	*2.2*	*0.5*	*309.3*	*8.42*	*5863*	*256*	*4742*
BM25-220	1.8	0.5	360.1	24.01	8783	11484	*10558*
BM12-150	2.5	0.8	405.2	15.56	8561	11425	14256
BM16-150	2.2	0.8	416.5	14.44	*10393*	8429	5904
BM25-150	1.8	0.8	415.8	22.07	9982	5546	11837
BM12-s230	2.2	1.2	466.9	12.52	9909	877	4081
BM16-s230	1.9	1.2	450.1	21.95	*9059*	1289	3652
BM25-s230	1.6	1.2	444.0	35.60	*11977*	2388	10035

**BM16-220 experienced one unintended 43% load cycle before failure.*
*** Italicised entries should be considered with caution for the reasons outlined in the following paragraph.*

There are a number of italicised entries in Table 4.1; in general, the italicised strain gauge entries represent entries where the actual maximum cannot be known because of premature gauge failures. Whereas the entire row for BM16-220 should be observed with caution since the beam experienced an unintended load cycle as a result of a power failure.

Otherwise, most beams with stirrups failed in the un-instrumented north shear span, so the exact stirrup strain information for the failed span is not known.

Table 4.1 indicates that beams with the same shear reinforcing ratio have similar strengths, and that as shear reinforcing ratio increased so did beam strength, where strength is equivalent to peak load.

For beams without stirrups, BMX-INF, there was a clear trend of increasing strength with increasing flexural reinforcement ratio. This trend was also clear in the BMX-s230 series of beams, but was less clear in the BMX-220 series because of the outlier. However, the strength of BMX-150 series beams did not show a correlation with flexural reinforcement ratio.

Beam series BMX-INF also showed a clear trend of increasing mid-span displacement at peak load with increasing flexural reinforcement ratio. However, this trend was not observed in any of the beam series with stirrups. Though, generally, mid-span displacement increased with increasing shear reinforcement ratio.

A number of beams showed a two peak load-deflection response, and of those beams there was no consistent trend in which peak was higher. The results presented in this thesis considered only the highest peak, and the mid-span deflection at that peak.

Table 4.1 also shows that the maximum longitudinal strain for the BMX-INF series of beams was correlated with the flexural reinforcement ratio. As the flexural reinforcement ratio increased the maximum longitudinal strain at mid-span decreased. This is because the load-deflection response is stiffer for beams with higher flexural reinforcement ratios. However, due to prematurely failed gauges on the longitudinal reinforcement, this same trend could not be identified in the beam series with stirrups.

The load deflection results were also considered together for each beam series, and plots of that comparison are shown in Figure 4.40. The scales were kept the same in each plot for the sake of comparison.

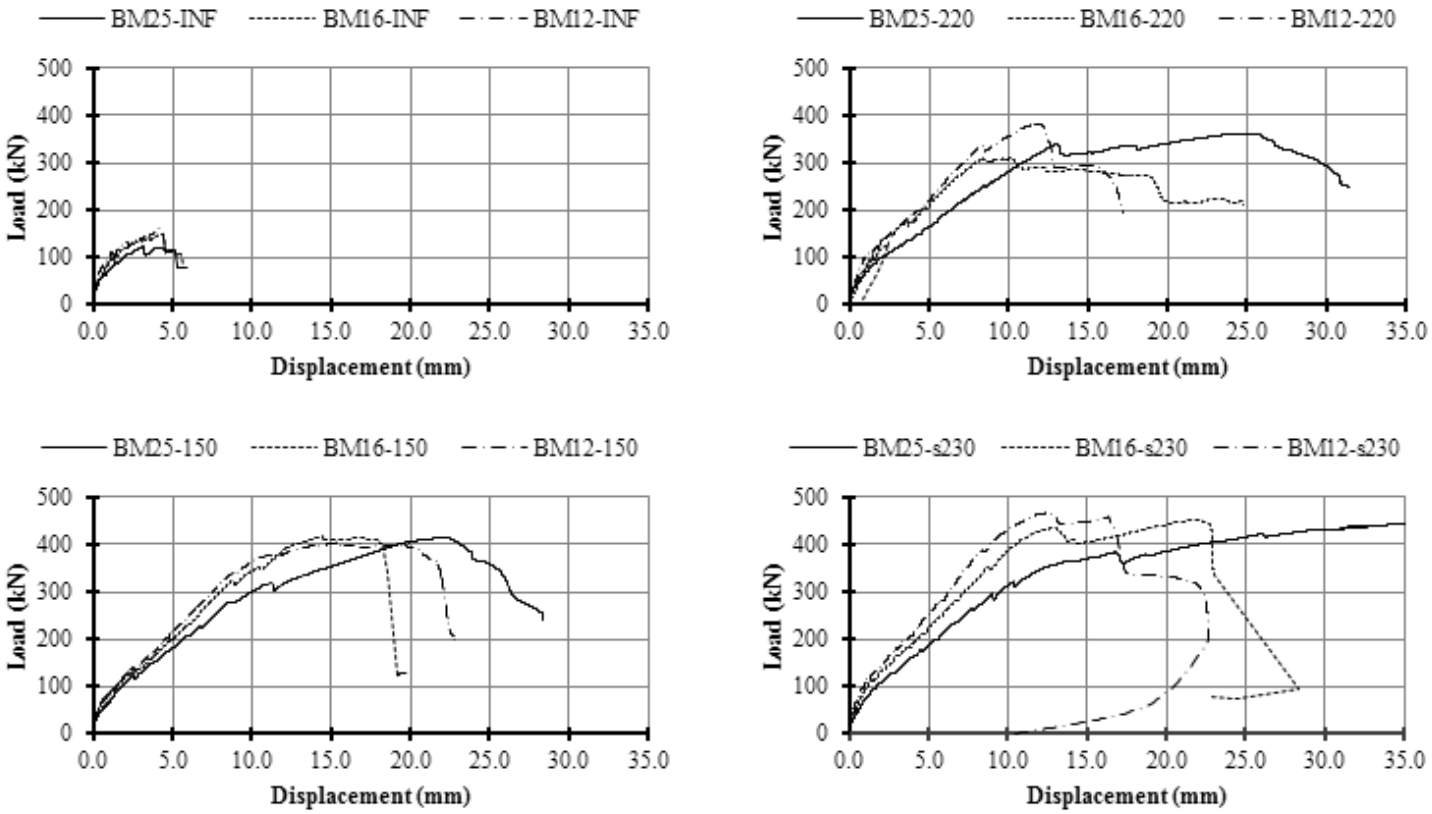

Figure 4.40: All Beam Comparison of Load vs Displacement

Figure 4.40 shows that as the longitudinal reinforcement ratio increased the post cracking response of a beam was stiffer, as expected; see the BMX-s230 series plot. The figure also shows that beams with stirrups are capable of post-peak ductility. Further, beams with lower reinforcement ratios tend to show more ductile behaviour when compared to beams with higher reinforcement ratios. However, that observation may be misleading: the beams with the lowest reinforcement ratio, BM25-X, had two large diameter bars, whereas the beams with the highest reinforcement ratio, BM12-X, had 12 small diameter bars. It is possible that the increase in ductility is related to bar surface area, which represents bond, between the concrete and reinforcement. So, beams BM25-X had less bar surface area available to bond to the concrete when compared to beams from other series.

Plots of beam groups, beams with the same longitudinal reinforcement arrangement, were also examined; however, those plots did not present any remarkable observations and have been omitted. In

general, beams of the same longitudinal reinforcement arrangement had very similar pre-cracking response, similar cracking loads, and similar post cracking stiffnesses.

5 Development of the Indeterminate Strut-and-Tie Analysis Method for FRP Reinforced Concrete

5.1 Motivation for the Development of the Indeterminate Strut-and-Tie Analysis Method for FRP Reinforced Concrete

The original objective of the research programme was to investigate the influence of longitudinal bar arrangement on the effective strength of GFRP stirrups.

In the most ideal scenario, all of the beams would have failed as a result of stirrup rupture. In which case the analysis would primarily investigate stirrup strains to determine stirrup strength and examine their influence on overall beam strength which might have confirmed or contradicted the influence of longitudinal bar arrangement on beam strength.

However, none of the beams failed as a result of stirrup rupture, and further, all of the beams with stirrups failed in the same shear-compression / strut-crushing failure mode. Without ruptured stirrups, or changes in failure modes, the influence of longitudinal bar arrangement on effective stirrup strength could not be known. Thus, it was not possible to make any conclusions on the original objective. Though, a basic investigation into the influence of stirrup and longitudinal bar arrangements on beam strength was still possible.

An alternative analysis method was required. The beams clearly showed arch action behaviour which suggested that strut-and-tie modelling could be used to predict beam strength. However, current practices for strut-and-tie modelling FRP reinforced deep beams, let alone other more complicated structural members, leave a lot to be desired.

The CSA S806-12 standard was the first FRP design standard to include provisions for strut-and-tie modelling of FRP reinforced members. However, a modest review of those provisions found that they lacked detail, and were generally inadequate for any reasonably complicated strut-and-tie model. Moreover, the clauses are nearly identical to the strut-and-tie modelling provisions from the CSA A23.3-04 standard for steel reinforced concrete design (Andermatt et al., 2013a).

The inadequacy of those provisions concern the determination of strut strength, see Equations 2.29 & 2.30, which are the same as those used for steel in CSA A23.3-04 Cl.11.4.2.3. In these equations the strain in the reinforcement is used to estimate the tensile strain acting across the strut, which is then used to estimate the compressive strength of the strut. The problem with the clause is not the equations themselves but the assumptions behind their inputs.

In the commentary of the CSA A23.3-04 standard, specifically entry N.11.4.2.3, designers are directed to take the reinforcement strain as either: the strain from a force analysis of the strut-and-tie model truss, or f_y/E_s, which is the yield strain.

The yield strain option is generally taught as the natural assumption in design classes for two reasons. First, this assumption typically makes an indeterminate strut-and-tie model truss into a determinate problem, and from a practical perspective this assumption is necessary for any indeterminate truss system; otherwise element stiffnesses would be required to solve the force system, which would be problematic because there is no design code or standard that provides guidance for estimating strut and tie stiffness values. Second, this assumption makes the most economical use of steel; if there is steel in the strut-and-tie model that does not yield then there is surplus.

There is no commentary to the CSA S806-12 standard and thus no guidance given to designers on how to establish a value for the reinforcement strain. It may not be obvious, but it is not appropriate to

assume a strain value for FRP reinforcement to establish strut strength. Assuming a uniform value for all FRP reinforcement blatantly ignores both the mathematics of a truss system and the results of the experimental investigation of this research programme, which demonstrated that strains can vary by orders of magnitude between reinforcement in the same system. Designers may be tempted to assume a value equal to the FRP rupture strain for all reinforcement, in a manner akin assuming the yield strain assumption for steel, but doing so ignores the fact that the first FRP tie to rupture will change the flow of forces in assumed the strut-and-tie truss system and render it obsolete. Further, this confuses FRP rupture with steel yielding, which is incorrect. The failure of steel only happens at the point of steel rupture, which is akin to steel rupture.

Overall the provisions of the CSA S806-12 standard for strut-and-tie modelling are adequate for a determinate strut-and-tie truss system where strain assumptions need not be considered to solve the force system. But the provisions are inadequate for any sufficiently complicated structural member, such as a deep-beam with stirrups, where an indeterminate analysis is necessary to solve the force system, and which requires truss element stiffness values.

Thus, a solution method for a strut-and-tie analysis which does not rely on the yield assumption was necessary. Only two such methods were found. The method of Kim and Yun (2011a), presented in the Literature Review Chapter, forms the basis for this chapter and the analysis method presented in it. The second method was referred to briefly in the opening paragraphs of Section 2.4.

5.1.1 The Indeterminate Strut-and-Tie Method in Brief

This chapter is a presentation of the development of the analysis method for the strut-and-tie modeling of FRP reinforced concrete, which will hereby be referred to as the Indeterminate Strut-and-Tie (IST) method. The method is a modified version of the indeterminate strut-and-tie analysis method developed by Kim and Yun (2011a), whose work was presented in the Literature Review Chapter.

Yun's method considered only steel reinforced concrete, so modifications to the method were necessary to accommodate the material behaviour of FRP reinforcement. This section focuses on the development of the IST method and is not intended to be a review of Yun's work, so the specifics of Yun's papers will only be discussed to justify modelling particulars.

To summarize the IST method briefly, it uses two dimensional finite element modelling of one dimensional truss elements with concrete material non-linearity. The analyst assumes a strut-and-tie truss geometry and assigns material behaviours to the elements. Load is applied incrementally, and the stiffness matrix is updated at each increment accounting for changes in strut elasticity. Failure is defined preferentially by truss instability as a result of strut crushing, as this is the preferred failure mode. The failure of nodes and ties are also considered.

The IST method is not optimised to find the point at which capacity is exactly equal to demand: a point which is sought by designers to make the most economical use of materials. Rather, it is appropriate for designers to use the IST method to check that the strength of the model is greater than the design loads. The process of design with the IST method is still iterative: unsatisfactory solutions will require changes to the strut-and-tie geometry, other inputs, or design assumptions until a satisfactory solution is found.

Implementation of the IST method is quite simple for anyone who has taken an introductory course on finite element analysis, and who has an elementary understanding of modelling material non-linearity in one dimension. However, the application of the method and interpretation of the results requires a solid background in reinforced concrete mechanics and experience with strut-and-tie modelling.

5.1.2 Chapter Organization

Ultimately this chapter is a presentation on modelling FRP reinforced members using the IST method so that with modest effort it may be reproduced by the interested reader.

The first part of this chapter is a review of the philosophy of traditional strut-and-tie modelling, and in particular the lower bound theory of plasticity. It includes an explanation of the way in which the theory is exploited by traditional strut-and-tie modelling with steel reinforcement, and the way in which the theory is exploited by strut-and-tie modelling with FRP reinforcement.

Then there is review of the relationship between the idealized truss model and the continuous cracked reinforced concrete medium it represents. The conventional assumptions behind strut-and-tie model components are explored, as is the means by which those assumptions impact an indeterminate analysis with brittle reinforcement.

A presentation on the methods for defining the geometry of the strut-and-tie model components for use with the IST method follows. The presentation explores the method presented in papers by Yun, and Kim & Yun, and highlights necessary differences.

Next is a presentation of the material models for the FRP reinforcement and concrete used by the IST method.

After which a step-by-step process for analysis and design using the IST method is introduced and discussed.

Then, an example of how the IST method is applied to beam BM25-220 of the experimental portion of this thesis is provided.

The last section is a brief investigation into the choice of material model and modelling parameters that are used later in the Analysis Chapter of this thesis.

Code for the IST method may be found in Appendix F and was written for the analysis of beam BM25-220 from the experimental portion of this thesis. The code may be easily modified to suit other beams in this thesis by making modifications to the *input function*, and the *failure check* function. The code was written for use with MATLAB.

5.2 Strut-and-Tie Modelling Philosophy

5.2.1 Design and Analysis with Steel Ties

The practice of strut-and-tie modelling with steel reinforced concrete cannot be directly applied to FRP reinforced concrete. The behavioural differences between steel and FRP reinforcements must first be recognized, as must the behaviour of the concrete-reinforcement composite.

Traditional strut-and-tie modelling with steel reinforcement relies on lower bound plasticity theory: if a postulated state of stress exists within a domain, which is internally consistent, and in equilibrium with externally applied loads, and the stresses do not exceed the strength of the materials, then the external loads are the lowest estimate of loads required to cause failure. The lower bound plasticity theory implicitly requires plastic behaviour from the material in which the postulated state of stress exists: the material must be able to undergo permanent deformation in response to an applied load.

Traditional design philosophies assume that plain concrete does not show plastic behaviour; however, common mild steel reinforcing bars do and, further, they undergo strain hardening past the point of yielding. The composite of the two materials is assumed to have plastic behaviour if the steel yields before concrete crushes, since the steel can undergo a significant change in shape under an applied load before rupture. Even though the concrete component of the composite can sustain some plastic defamation by way of cracking, which is actually necessary to engage the steel, it is not relied on in design.

Strut-and-tie modelling is an approximation of the flow of forces in a reinforced concrete element, and attempts to model the internal flow of forces using a simple truss system. The internal principle compressive stress fields are replaced by concrete struts conforming to the general orientation of the field, and the principle tensile stress fields are replaced with steel ties in the same way. As with any truss, the strut and tie elements must meet at joints and the force system must be in equilibrium.

The flow of forces in the reinforced concrete domain may be determined using conventional linear-elastic methods such as finite element modelling. However, this state of stress will only represent the flow of forces before cracking; the exact state of stress in a reinforced concrete element after cracking cannot be known. This is because the properties of concrete are affected by the formation of cracks, across which tensile forces cannot transfer, and which reduced shear forces transfer. So the state of stress becomes complicated as the flow of forces changes to accommodate cracking.

Thus, it is important that strut-and-tie models approximate the actual state of stress before cracking since cracks are assumed to occur near the location of the highest principle tensile stresses. The steel will carry the tensile load once cracks form, and the actual state of stress will start to conform to the strut-and-tie approximation. The steel tie will maintain the integrity of the principle tensile stress field and, thus, the rest of the stress field. It is assumed that as loading increases, more cracks will form in the locations of, and cross, the steel ties, and the actual state of stress will further conform to the truss approximation. It is possible that an inadequate representation of the flow of forces may lead to premature failure since cracks may not cross steel reinforcement, and the actual state of stress after cracking will not reasonably conform to the approximation.

Strut-and-tie modelling exploits the lower bound plasticity theory to estimate the lowest load required to cause failure. For steel reinforced concrete, failure occurs because of plastic flow from the yielding of steel. At this point the internal force system of the strut-and-tie truss is no longer consistent and the truss becomes unstable. The yield assumption is necessary to design for this failure mode, because only at the applied load which causes all steel ties to yield is the truss expected to become unstable. This load is the lowest estimate of loads required to cause failure. But as noted previously, the yield assumption is also necessary to make indeterminate systems into determinate problems, and to make the most economical use of steel.

Implicit in the yield assumption is that steel yields before any concrete struts crush. Strut crushing may lead to premature failure of the reinforced concrete member since alternative load paths may cease to exist; the forces may not be able to flow from the point of applied load to the supports.

The yield assumption, by way of making determinate problems, allows for the solution of internal strut-and-tie member forces so that struts can be designed to have a capacity which ensures they are not likely to crush.

In design, the strength of steel and concrete is reduced by material factors of safety; so the lowest estimate of loads required to cause failure in design, by way of the lower bound plasticity theory, will be smaller than the actual failure loads. It is possible that in a real member the design load may be reached before any tie actually yields.

Ultimately the purpose of using a strut-and-tie analysis for design is to provide designers with guidance on how much reinforcing is needed, and where it needs to be placed.

5.2.2 Exploiting Lower Bound Plasticity Theory when Modelling with FRP Ties

Many of the requirements of a strut-and-tie model with FRP reinforcements are the same as those with steel reinforcements. The model must still be a truss structure with FRP tie elements representing principle tensile stress fields, and concrete struts representing principle compressive stress fields. The strut-and-tie model truss must still be a good approximation of the flow of forces within the reinforced concrete element. Major cracks are still expected to intersect FRP ties, and the FRP ties are expected to maintain the integrity of the stress field in the reinforced concrete element.

Most importantly, the FRP reinforcements do not change lower bound plasticity theory, but instead change how it is exploited.

Fibre reinforced polymer reinforcement is a linear-elastic-to-brittle-rupture material in tension and does not show any plastic behaviour. It is not possible to use the lower bound plasticity theory on a composite with two brittle components, so the actual material behaviour of concrete must be reconsidered. In fact, concrete is best described as a quasi-brittle material in compression, and even the most common material models show non-linear stress-strain behaviour. Concrete, through the formation of cracks, changes shape in response to applied loads, and well confined concrete has a larger capacity for deformation than unconfined concrete. Strut-and-tie modelling of FRP reinforced concrete must make explicit use of concrete plasticity.

This modification to the nature of the concrete-reinforcement composite is not without precedent. Current design standards already require FRP reinforced concrete beams to fail in flexural crushing (CSA, 2012), because it is considered the more ductile failure mode. It is also assumed that the potential for large crack formation and spalling concrete will provide more warning before failure than if the FRP reinforcement were to rupture in a tensile flexural failure.

Consider further the experimental results of this research programme. Even though the beams were a composite of quasi-brittle concrete and brittle GFRP, all of the beams with stirrups were able to show some amount of post-peak behaviour. The post-peak behaviour was possible because the stirrups simultaneously restrained crack growth and confined the concrete. Beams with higher shear reinforcement ratios had larger failure loads owing to greater confinement. However, this discussion of beam ductility is mainly qualitative as no actual measurements of beam ductility were considered.

A quantitative analysis of GFRP reinforced beam ductility was presented in a paper by Vijay et al. (1996). The beams in that paper were reinforced in flexure and shear with GFRP bars and stirrups. The authors considered existing measures of beam ductility and made modification as necessary to account for the linear-elastic nature of FRP. They concluded that their measures indicate GFRP reinforced beam ductility is similar to that of steel reinforced beams. Though, they caution that further study is needed to consider parameters such as stirrup spacing, reinforcement ratio, load level, etc.

Strut-and-tie modelling of FRP reinforced concrete still exploits the lower bound plasticity theory to estimate the lowest load required to cause failure. In fact, the philosophy of failure for FRP strut-and-tie models is the same as that for steel: failure occurs when the internal force system is no longer consistent, when the truss is unstable. However, this instability is the result of the crushing and/or rupture of truss elements.

This is an important change in the philosophy because steel reinforced strut-and-tie models assume the individual elements of the model never fail: steel yielding is not failure until all steel yields. Further, indeterminate models with FRP ties may require more than one element to crush or rupture if valid load paths exist after the first element crushes or ruptures.

Yun's non-linear analysis method forms a basis for the strut-and-tie modelling of FRP reinforced concrete because it explicitly considers concrete behaviour in the solution of the force system: concrete is the plastic material and to satisfy lower bound plasticity theory its behaviour must be considered. However, even though this method emphasises the concrete portion, the ultimate purpose of this strut-and-tie analysis is to provide designers with guidance on how much FRP reinforcing is needed, and where it needs to be placed, just as with steel strut-and-tie modelling.

As an aside, it is possible that a non-linear analysis of the truss system is not necessary. A linear analysis may be possible if, at the failure load, the stiffness of the struts is reasonably approximated. However, doing so requires some advanced knowledge on the load paths at failure, and as such, a linear analysis is not recommended. In his research, Yun was able to show that the failure mode of a deep beam changed when a linear and non-linear analysis was performed and found the non-linear analysis to be a better representation of experimental results (Yun, 1996).

5.3 Failure Conditions for FRP Strut-and-Tie Models

5.3.1 System Failure

The system failure load is the largest possible load the strut-and-tie model may estimate according to the lower bound theory of plasticity. This failure condition occurs when a series of individual elements either crush or rupture leading to truss instability; this is the point when there no longer exists a stable load path through the strut-and-tie truss which connects the applied loads to the supports. This load may also be referred to as the ultimate load, or stability failure load at different points in this thesis.

The narrative of the previous subsection should make it obvious that good engineering practice for strut-and-tie modelling with FRP reinforcements requires concrete elements to crush before any other model element crushes or ruptures; stability failure should occur by changes in the stiffness of plastic elements.

5.3.2 Strut Crushing

For the purpose of this thesis the terms 'strut crushing' and 'strut rupture' are distinct. Strut crushing occurs at the point where the stiffness of a strut element becomes zero, and strut rupture occurs at the point where the strut breaks. The crushing strain is equal to the strain at peak stress on the stress-strain curve for concrete, which is also the point of zero tangent elasticity, and is identified as ε_0 in Figure 5.3. The rupture strain is the point where the strut is expected fail. In this sense, crushing precedes rupture in the same way that steel yielding precedes steel rupture. However, strut rupture is imminent once strut crushing has occurred for a beam under force controlled monotonic loading, generally.

Yun's analysis method is adapted in this chapter because it uses a stiffness approach which allows for a solution to the force system. With steel strut-and-tie models the designer can assume which strut-and-tie elements will lead to system failure prior to the force analysis: it will be by yielding of all the tie elements. But with FRP strut-and-tie models the designer cannot assume which elements will lead to system failure prior to the force analysis. Ideally it will be the strut elements, but which exact strut elements cannot be known in advance. It is inappropriate to assume that all concrete crushes simultaneously for the same reasons it is inappropriate to assume all FRPs rupture simultaneously, as outlined in Section 5.1 earlier.

To be clear, the external applied load level which causes crushing is unique to each strut, and is the root of the complication which requires Yun's method. The load level is unique because the amount of the externally applied load which is carried by each load path changes with changing strut stiffness. The proportion of load carried by each load path at system failure will not be the same proportion for load levels which precede it.

5.3.3 Tie Rupture

Tie elements fail when the stress exceeds the strength of material, or when the strain exceeds the rupture strain. This is straight forward for longitudinal elements; however, bent FRP elements have two strengths: one for the straight portion and one for the bend. In design, it is prudent to use the bend strength. In an analysis situation, such as an academic investigation, it is the analyst's choice.

The failure of ties is highly undesirable in design. The failure of FRP reinforcement is brittle and occurs without warning. Concrete cracking may be the only sign of distress for FRP bars encased in concrete, but crack patterns are open to interpretation.

In practice, current design codes and standards minimize the risk of tie failure. For example the CSA S806-12 standard limits the serviceability load in FRP reinforcement to a level which would induce a stress no greater than 25 percent of the tensile strength. Though this provision is intended to address creep rupture concerns, it also serves to keep FRP loads low even at ultimate.

5.3.4 Node Crushing

Nodal zones are regions of concrete that represent the joints of the strut-and-tie truss system. They will be discussed in more detail in a later section of this chapter.

It is possible for these regions of concrete to fail by way of concrete crushing. Each strut-and-tie element which intersects a joint has a face on the perimeter of the nodal zone region over which the element force is assumed to act. If the stress acting on the face of the nodal zone exceeds nodal zone design criteria then it is possible that the concrete in the nodal zone will fail.

These failures are highly undesirable, because some nodes form locations where separate determinate trusses of a larger indeterminate strut-and-tie model are likely to meet. If such a critical node fails then there is a possibility that no alternative load paths exist, and failure of the entire reinforced concrete element is likely as a result.

Further, nodal zone design criteria are sensitive to the amount of tension present in the nodal zone, since they are defined by a region of concrete. In general, nodal zones which are connected to only compression members, struts, are ascribed higher strengths than nodal zones which are connected to tension members, ties, and such nodes are ascribed decreasing strengths for an increasing number of tension members.

5.3.5 Other Considerations

Failure is defined differently when the IST method is used for design than when it is used for analysis. In design, the strut-and-tie truss would be made to fail exclusively as a result of strut crushing, since this is the most ductile failure mode. If a node or tie were found to fail before system failure then the designer would be required to revise the model by changing the amount of reinforcement or the size of bearing plates until a satisfactory solution was found.

Careful consideration must also be given to strut elements that overlap, or put differently, struts that intersect without forming nodes: the crushing of any one intersected element may weaken or crush the others. This notion may also be generally extended to any elements which intersect but do not form a node.

In practice, the design strength may be more conservatively taken as the load level at which the first strut crushes, but if that strut does not intersect any other struts then it would be modeller's choice as to whether or not to consider larger loads at which struts crush.

In analysis, the IST method openly considers every possible point of failure, and seeks to identify which element failure is closest to the recorded experimental load: the possibility that a beam failed as a result of node crushing, first strut failure, or system failure should be considered. The decision to assign beam strength to the load level of a particular element failure must consider experimental observations.

5.4 Idealizing Continuous Cracked Reinforced Concrete as Simple Truss Elements

Strut-and-tie models are trusses composed of two types of idealized structural components: members, which are struts and ties, and joints, which are called nodes. In the simplest form these components are represented with lines and dots which have no area or thickness, except where the mathematics of the solution of the force system is concerned. The members represent the flow of forces, and the joints are points where the forces abruptly change direction to maintain equilibrium. Force may only enter or leave the system at the joints in a truss analysis, so all members are implicitly constant axial force members.

However, in a strut-and-tie model, which represents a cracked reinforced concrete continuum, the elements have a finite geometry such as depth, width, and cross-section. Strut elements represent

compressive stress fields, tie elements represent tensile stress fields, and nodes represent a state of stress associated with the directional change of the flow of force between connected stress fields. In reality the reinforced concrete domain has one omnipresent stress field; compressive or tensile stress fields are just regions of the omnipresent stress field where one of the respective principle stresses is large. The state of stress each element represents is assumed to occur within the assigned geometry of each element, and each element must fit within the domain of the problem: stress fields cannot exist outside of the concrete.

5.4.1 Tie Elements

The ties are the simplest element in the model and they simultaneously represent the tensile stress fields and the reinforcing bars. As noted in the Strut-and-Tie Modelling Philosophy Section, cracks are expected to form in the vicinity of, and perpendicular to the orientation of, the principle tensile stress fields. The reinforcing bars maintain the integrity of the stress field by spanning crack faces so tensile force may continue to flow along the pathway assumed in the truss idealization.

The ties are also the most well-defined elements of the strut-and-tie model, with consistent geometry and reliable mechanical properties. The material behaviour of the reinforcement is also the simplest to model: FRP has a linear-elastic model.

The constant force phenomenon of a truss analysis implicitly assumes that ties are un-bonded between nodes. But this assumption is not representative of actual reinforcement behaviour because it ignores bond stresses as the primary force transfer mechanism. The development of tensile forces in the reinforcement spanning crack faces is achieved by the bearing of concrete lugs on the shear ribs of the reinforcement within the vicinity of the crack. Cracks form all along the reinforcement and thus bond stresses are present all along the reinforcement too. However, all force is assumed to transfer from the concrete to the reinforcement at the nodes for compatibility with the truss analysis simplification.

This assumption requires special consideration on anchorage and detailing of reinforcement at the nodes. The possibility that reinforcement may be subject to high loads as a result of cracks forming close to a node exists. If the reinforcement is not anchored well enough past the node to resist the loads then the reinforcement may slip or pullout of the concrete. Pullout would destabilize the force transfer mechanism at the node and lead to failure. Further, pullout failures are undesirable because they are difficult to reliably predict. Such failures are avoided by making conservative estimates on anchorage lengths as prescribed by design codes and standards. In the case of steel reinforcement, the steel is expected to yield before pullout even within the vicinity of a node. But in the case of FRP reinforcement neither pullout nor rupture is tolerable.

The constant force phenomenon and pullout failures are related to the process of de-bonding, and it is the primary mechanism by which reinforcement accommodates concrete cracking. The reinforcement within the immediate vicinity of the crack must de-bond to accommodate the opening of cracks. If not, the localized strain in the reinforcement between the crack faces would be very large and the reinforcement would yield or rupture. It is not uncommon for reinforcement to significantly de-bond from concrete at failure in the testing of deep beams (Andermatt et al., 2013b). In fact, such de-bonding occurred in the experimental beams, and evidence of this was presented as an arch action plot, see Figure 4.4.

It is also possible to assume that plain unreinforced concrete ties exist. Schlaich et al. noted, in their influential 1987 paper, that plain concrete ties may be essential to strut-and-tie models where ties are required but where reinforcement may not fit, and admonished overly conservative engineers from ignoring the existence of plain concrete ties. However, best design practices still ignore plain concrete ties because the actual loading on a structure over its lifetime cannot be known during the design phase; unexpected loading may cause cracking of plain concrete ties which will weaken them and may lead to premature failure in the structure under design loads.

In his analysis, Yun considered the effect of plain concrete ties on his strut-and-tie models. He even noted that two were necessary for stability of his assumed truss. In his analysis all ties were assumed to act as plain concrete ties until the non-linear analysis predicted tie failure, then they would act as steel only ties where steel was provided (1996)(2000a)(2000b)(2000c). It is possible to model the transition from concrete only tie to reinforcement only tie by considering the effect of tension stiffening, but that discussion is reserved for Section 5.6.1 and again later in the Analysis Chapter.

5.4.2 Struts Elements

The strut elements are more complicated, and represent both the concrete and the compressive stress fields. Compressive stress fields take on one of three forms: prismatic, bottle-shaped, or fan-shaped. The process of categorizing compressive stress fields by their shape helps designers understand their behaviour and is used to assign strength reduction factors in design with traditional strut-and-tie modelling techniques.

Unlike ties, the geometry of struts is not well-defined and certain simplifying assumptions are required. One major assumption is that each strut can be treated individually, even though each individual stress field is actually part of one omnipresent stress field. Further, their material behaviour is not as simple as that of the reinforcing, and that fact is the motivation for adopting Yun's analysis method. Concrete material models are discussed in a later part of this chapter.

Prismatic stress fields take on the shape of a rectangular prism and are found in the flexural compression zone of a reinforced concrete beam. The shape of the stress field is bound by the top and side faces of the beam, and the lower part of the prism is defined by the depth of the compressive stress block. This is the simplest type of stress field assumed in a strut-and-tie analysis.

Bottle-shaped stress fields are most common and take on a shape which is narrow at the ends and wide in the middle. This type of stress field is found in deep beams where compressive stresses are transferred from load plate to support plate. The middle of the stress field spreads out because there is no physical or mechanical boundary; however, the ends of the field narrow because they are bound by critical nodes, which are defined in the following subsection. The spreading of the stress field necessitates the development of tensile stresses and strains, and tensile strains reduce the strength of the concrete in the middle of the field.

Fan-shaped stress fields take on the shape of an opened paper fan. They develop from locations of concentrated loads which induce compression in the concrete. These types of fields are narrow at the critical node end, and load is gradually distributed to reinforcement through bond stresses at the fan edge.

For all intents and purposes every compressive stress field is modelled as a prismatic stress field and called a strut. In design, the shape of the strut is not assumed to change between nodes, but depending on the design code may be tapered if one end of the strut is stronger than the other. This assumption is made because the critical strut cross-section is found at the nodes where the stress field narrows causing the stresses to increase respective their middle portion. The change in cross-sectional shape is irrelevant when designing with traditional strut-and-tie modelling techniques.

Distinctions between the behaviour of the three types of stress fields are made by way of factoring strut strength. Bottle shaped-struts have their strength factored the most due to the significant tensile strains acting across their orientation. Fan-shaped stress fields are modelled using a number of prismatic struts radiating out from the critical node and which frame into nodes formed commonly by the intersection of longitudinal and transverse reinforcement.

The simplicity of strut shapes is a necessary part of an analysis as simple as modelling a continuous stress field with uniaxial truss elements. This discussion is included because element stiffness is a product of the elastic modulus and area: the shape, and thus cross-sectional area, of the strut is significant for the purposes of capturing concrete element the stiffness, a crucial parameter for the IST method.

5.4.3 Node Elements

Node elements are the least well-defined components of a strut-and-tie analysis. For the purpose of disambiguation the word ‘node’ will refer to the intersection of idealized truss elements, forces, or stress fields commonly called a truss joint; and the term ‘nodal zone’ will be used to describe a region of concrete with defined geometry which contains a critical state of stress associated with directional change of the flow forces.

Nodes function as joint mechanisms in strut-and-tie models; they are an approximation of the flow of forces which lay somewhere between the actual state of stress and the perfect joint assumed in the truss analysis. They are a better approximation than a perfect joint because they occupy a finite concrete region in which a state of stress may be assumed to exist. The actual state of stress in the node cannot readily be known, nor is it necessary to compute, since this state of stress would still be a simplification of the true and complicated state of stress in the cracked reinforced concrete continuum.

There are two types of nodal zones in a strut-and-tie model: singular and smeared. Singular nodal zones are locations where forces, from elements such as ties and bearing plates, change direction abruptly and within a small, well-defined area. A nodal zone with a bearing plate is singular because the forces from struts and ties which frame into the node must transmit their forces to the bearing plate directly within its vicinity, so the area over which the force is transferred can be no larger or no smaller than the bearing plate. Typically, singular nodal zones are found along the boundaries of the domain of a reinforced concrete element where force enters or leaves the truss system, and they are known as critical nodes.

Smeared nodal zones are locations where forces change direction gradually and over a large, poorly-defined area. They exist because the geometry of the strut-and-tie model suggests that they should. Smeared nodal zones are associated with fan-shaped stress fields, where the ends of prismatic struts on the open part of the fan intersect longitudinal and transverse reinforcement. They are typically found within the domain of a reinforced concrete element. Bond stresses are the mechanism by which the flow of forces change direction from fan-shaped stress fields, so the dimensions of these nodal zones are difficult to define since there is no tangible object, like a bearing plate, on which to prescribe the size of the nodal zone.

However, the state of stress at a node cannot readily be established. To simplify analysis it is possible to assume that a hydrostatic state of stress exists within the domain of the node if the stress fields which frame into the node are all equal in magnitude, and perpendicular to the face of the node (Schlaich et al., 1987). This assumption allows engineers to compare the hydrostatic state of stress directly to a factored form of the concrete strength, since the Morh’s circle for a hydrostatic state of stress is represented by a single point. To satisfy the hydrostatic assumption, tensile stress fields are rotated 180 degrees around the node and treated like a compressive stress field.

In practice this assumption is tremendously difficult to satisfy, and engineers assume a form of quasi-, or pseudo-hydrostatic state of stress exists. Schlaich et al. suggested that if the ratio of minimum nodal face stress over maximum was greater than 0.5 then the node would be acceptable by the criteria outlined in their paper (1987). Another method involves partitioning the node into a series of triangular hydrostatic parts and rectangular unidirectional stress field parts (Schlaich et al., 1990). However, this method is also not used in practice because it is not suitable for an iterative design procedure, as it may require extensive recalculation for changes in model geometry. Another form involves developing extended nodal zones (Schlaich et al., 1991), but this theory is more often used to reduce anchorage lengths.

Critical, singular nodes will typically have one or two node faces with well-defined geometry: a bearing plate will form the horizontal dimension, and the layout of flexural reinforcing or depth of the compression stress block will define the vertical dimension. To simplify analysis, one of two common approaches is used.

Designers may resolve the forces from all other struts and ties which frame into these nodes into one resultant force vector (ACI, 2008). In this case the node will take the form of a simple triangle balancing force from the bearing plate, the longitudinal reinforcing or compression stress block, and the resultant force vector. The nodal stresses are found by dividing the forces acting on each face by the dimension of the face, and those stresses are compared to nodal strength criteria.

Alternatively, designers may partition the nodes into two nodes, or they may partition the node faces in proportion to the forces of the various elements which frame into the node. In this way, it may be possible to assume that the vertical node face balances the force from one strut, the horizontal node face balances the force from another, and the interface between the two nodes or node partitions must be equal and opposite to satisfy statics of the system.

5.5 Defining the Geometry of Strut-and-Tie Elements for use with the Indeterminate Strut-and-Tie Method

The purpose of strut-and-tie modelling is to identify how much reinforcing is needed, and where to place it. So, locating the reinforcement defines the strut-and-tie truss geometry. The struts only come into existence to balance forces in the reinforcement, and they implicitly exist because the entire domain of the design problem is concrete. However, the choice of locating nodes is not arbitrary, as the strut-and-tie model must be a good approximation of the flow of forces. This section is an explanation of the development of a strut-and-tie truss geometry for deep beams, and the process may be generally extended to other geometries.

5.5.1 Defining the Geometry of Ties

The process of locating reinforcement is not affected by the material behaviour of the ties, and the process is generally consistent with that of steel reinforcement. For example, the required area of flexural reinforcement may be estimated from the flexural analysis of the beam. A designer will assume a stirrup diameter, a cover depth, and a reinforcement layout. Then the vertical location of the main longitudinal tie would be set to the effective depth of the reinforcement.

A common method for locating stirrups in deep beam design with steel is to assume that the truss has only one vertical member. Assumptions are made on load distribution between the direct-strut and truss mechanism of the strut-and-tie model, and the required area of stirrup reinforcement is determined. The number of stirrups is then found by dividing the required stirrup area by the area of one stirrup. Then these stirrups are distributed over the width of the shear span. This is appropriate for deep beam design with steel reinforcement because the failure plane is expected to span from load to support, thus crossing all stirrups.

The choice of strut-and-tie truss geometry is subject to several constraints which form best design practices. For example, design codes often limit the allowable angle between struts and ties, because struts become weaker as they are exposed to tensile strains which are expected to be large with in the vicinity of, and with respect to the orientation of, the tensile reinforcement. As the orientation of a strut and tie begin to align, the strut strength is expected to decrease. Stirrups are commonly distributed over a middle area of the shear span with respect to minimum allowable strut angles.

This exact same design philosophy cannot be used for FRP reinforced deep beams, since there is no research on how to compute the required load distribution ratio. However, the same stirrup design philosophy may still be useful for determining the area and locating the FRP stirrups; Section 6.3 of the Analysis Chapter will discuss this further.

Though, this philosophy should be used with some caution. Consider Figure 5.1; stirrups located closest to critical shear and flexural-shear crack mouths are expected to rupture before stirrups located further away (Zhao et al., 1995). This phenomenon is the result of cracks crossing close to the stirrup bend. Such a stirrup, like the second stirrup from the support in Figure 5.1, transfers a larger portion of

force by bearing on the bend than would a stirrup location further away, which transfers force by both bearing and by bond in the straight portion, like the second stirrup from the load plate in Figure 5.1. This is problematic because of the inherent weakness of FRP bends and because of loading across the cracks at this location, as noted in the Introduction Chapter.

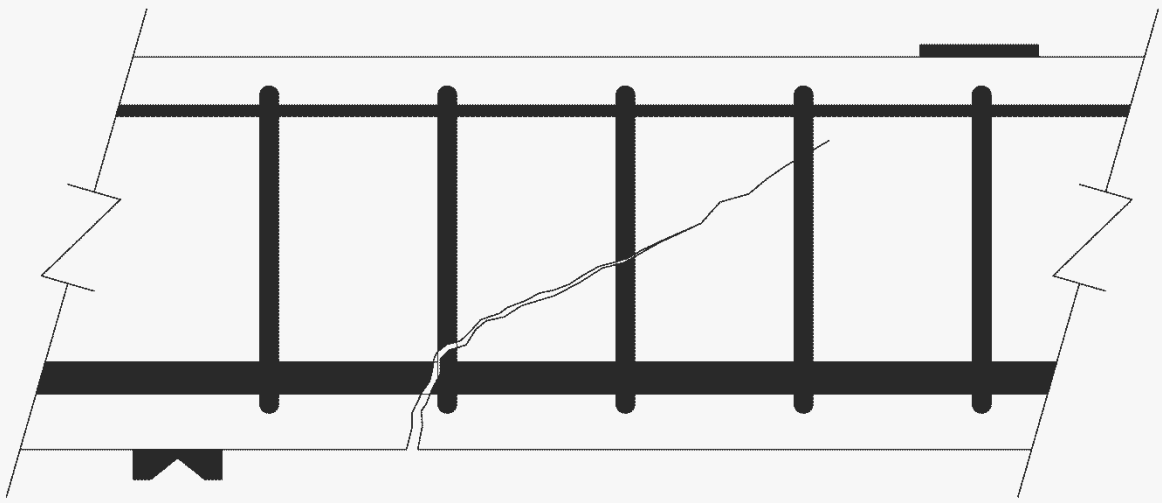

Figure 5.1: Considering the Location of a Critical Shear Crack with Respect to Stirrup Bends

In steel reinforced concrete, the fact that cracks cross near the bends is of little consequence because the steel is expected to yield, and when it yields it will strain harden and continue to transfer force. However, if an FRP stirrup ruptures then the load transfer mechanism of the reinforcement is lost.

Observations from the experimental portion of this research programme suggest that these concerns are more appropriate for slender beam design. Flexural cracks formed at the location of stirrups and then transitioned into flexural-shear cracks; however, ultimately the failure plane ran from the load plate to the support plate. So, stirrups located adjacent to the support plate, and thus main shear crack mouth, did not experience significant strain. Further, the observations found that the straight portion of the middle most stirrups strained the most.

Further, the IST method cannot address this potential issue anyway; the force analysis of a simple truss system under 3-point loading will find that all vertical members, the stirrups, carry identical loads. This is in contrast with the discussion from the previous paragraph which noted that the strain in neighbouring stirrups can be very different. So, best design practice would be to assume the stirrup strength is limited by the bend strength since the location of crack mouths cannot be known during design. There will be more discussion of the ability of the IST method to capture stirrup behaviour in the Analysis Chapter.

5.5.2 Defining the Geometry of Nodes

The location of the nodes will be defined by the location of the reinforcement. This section will not discuss strategies for locating the nodes, but will instead focus on defining the geometry of the nodal zone region.

The method used by Yun in his papers from 2000 and 2006 was not used in this thesis. In those papers he used a sophisticated non-linear, two dimensional, finite element analysis to model the behaviour of, and potential for, nodal failure in his indeterminate strut-and-tie models. The level of complexity used by Yun in that analysis is beyond the scope of a typical masters research programme such as this one.

Kim and Yun, in their 2011 papers, used much simpler design criteria from the ACI 318-08 code. In the 2011a paper the critical nodal zones were all right triangles, and their dimensions were defined by rearranging the formulae for nodal zone strength. The horizontal dimension was found from the required bearing area. The vertical dimension for bottom-chord nodes was found by assuming twice the clear cover, and for top-chord nodes the vertical dimension was equal to the depth of the compression stress block at flexural compression failure. The dimensions of the nodes, and subsequent geometry of the system, were updated on each load increment; so node dimensions were always made to satisfy load requirements.

However, the Kim and Yun, in their 2011b paper, did not update nodal geometry since the purpose of the study was to assess the performance of the 2011a model against a database of beam tests. The critical nodes were dimensioned using the parameters as prescribed in the specimen database. In those cases the horizontal dimension was defined by the actual bearing plate; the vertical dimension of the bottom-chord nodes was defined as twice the difference between the beam height and the effective depth, and for the top-chord nodes it was defined by the depth of compression stress block at flexural compression failure.

Then, as noted in the Literature Review, the strength of nodes were checked according to the method of the ACI 318-08 code. Kim and Yun used vector addition to sum the forces from the intersecting elements which framed into the hypotenuse of critical nodes. The strength check was done on the basis of geometry in the paper by re-arranging the ACI formulae to solve for the required bearing area and checking it against the provided area, but the check could also be done on the basis of stresses. The orientation of the resultant force vector acting on the hypotenuse was not perpendicular to the nodal zone face, but for simplicity and conservativeness it was assumed perpendicular.

Kim and Yun, in both 2011 papers, ignored strength checks on non-critical nodes entirely.

The method of the 2011b paper provided the most rational basis for determining the dimensions of the critical nodes in the analysis of this research programme. In the IST method critical nodes are assumed to be right-triangles. Their dimensions are assigned based on well-defined features or behaviours such as bearing plates, the effective width of the main longitudinal tie, or the depth of the flexural compression stress block.

The IST method also defines the dimension of smeared, internal, non-critical, nodes; however, the dimensions of internal nodes were tied to the dimensions of the struts and ties since non-critical nodes lack a physical object on which to base their dimensions. As such, the method for determining the dimension of internal nodes will be made clear at the end of the following part on determining strut areas.

5.5.3 Defining the Geometry of Struts and Internal Nodes for the Indeterminate Strut-and-Tie Method

The method by which strut areas are determined for FRP strut-and-tie models is entirely different than that for steel strut-and-tie models. The difference is one of the most complicating factors of the IST method.

In steel strut-and-tie modelling, the yield assumption is used to make problems determinate, and the solution of a determinate force system does not include element areas or elasticity. In fact, with traditional techniques, the area of a strut is only computed after the solution of the force system: the strut force is divided by the strut strength to compute area, and the formula for strut strength depends on the design code or standard. Once the strut area known, it is compared to the width of the node face into which it frames, and the strut area must be smaller than the node face. Then the geometry and specific orientation of the strut is also checked to ensure that the strut does not exceed the boundaries of the problem.

However, the solution of the force system in a stiffness based approach, such as the IST method, requires the area of each strut as an input. A method for determining strut area without first knowing the

internal load at which the strut crushes is necessary. Most importantly, the area of a strut must be appropriately approximated to ensure a reasonable estimate on the lowest load to cause failure by way of the lower bound theory of plasticity.

In Yun's 1996 paper he found the element internal forces by assuming the steel yielded, and used a rather involved process to compute strut strengths, and thus strut areas. The assumption that steel yields is no longer valid when FRP reinforcement is used.

In Yun's papers from 2000 he used an optimization routine to produce an estimate of the area of each element. The routine is explained in the literature review. The process was iterative, and stopped when either: 1) the difference between the strut strength and strut stress was less than a tolerance value, or 2) when the number of iterations reached a specific value. Otherwise all element areas were recalculated by dividing internal force by strength.

This method was fundamentally flawed. This routine will always add area to the elements in the stiffest load path and remove area from elements in more flexible load paths with each iteration. This occurs because, in linear force systems, more force is carried by the stiffest load path than by any other individual path.

Initially all elements have a unit area, and after the first force analysis the stiffest load path will carry the most load, and because it carries the most load the elements in this path will gain the most area, which makes the load path stiffer than any other paths which also initially gained some area, and thus the stiffest load path being made stiffer will carry more force in the subsequent iteration. After some number of iterations the elements in the flexible load paths will have virtually no cross-sectional area, and the elements in the stiffest load path will have some finite cross-sectional area. The rate at which the elements in flexible load paths approach zero area depends on the truss configuration, and on initial conditions.

Yun tries to overcome this problem in two ways. The first is by specifying a tolerance, and the second is limiting the number of iterations. Both of these limits are arbitrary; if the tolerance is specified low enough, or the number of iterations large enough, then the area of elements not part of the stiffest load path will always approach zero. This method will not produce strut areas that are in anyway a realistic approximation on the stress fields they intend to model: the actual flow of forces will not follow a load path which resulted from an arbitrary optimization routine.

Interestingly, Yun uses a slight modification of this approach in his 2008 paper on gird strut-and-tie modelling, and in that paper the fundamental flaw of the routine from the 2000 papers is exploited to form a necessary part of the 2008 analysis method.

The major difference is that the approach to design in the 2000 papers required a designer's judgement to prescribe truss geometry. In the 2008 paper, the strut-and-tie geometry is not prescribed using judgement because no assumptions are made about the grid of uniform, uniaxial elements prior to the analysis. The optimization routine ultimately defines the most direct load path through the grid, and does so by making that path the stiffest. The routine does this using the same principle as before, by adding more area to elements in the stiffest load path, and reducing area in elements in any of the more flexible load paths. Eventually, the method defines a truss for each load case investigated with the routine.

The analysis in the 2000 papers is predicated on the assumption that the load paths are known ahead of time by engineering judgement, while the analysis of the 2008 paper is predicated on the assumption that the load paths cannot reasonably be known ahead of time, especially when considering multiple load cases.

Though the above routine offers some hope for defining element areas, all of these methods are inappropriate for the average design engineer when defining the area of concrete struts in an FRP reinforced concrete region. The first method fundamentally changes the way load is carried in the truss model without any regard for manner in which the continuous medium actually carries the load. The

second is overly complicated and does not account for changes in concrete element stiffness under loading.

The 2011 companion papers by Kim and Yun offer a simpler and more rational method for establishing strut areas in deep beams: strut areas are based on the size of the critical nodes. The area of struts and nodal faces are, by convention, computed by multiplying their in-plane dimension, called a width, by the beam width. It is part of the parlance of conventional design to refer to the area of elements by width alone, since the beam width is a common factor to all elements. Further, strut widths are defined as the dimension perpendicular to the orientation of the strut which spans the strut boundary.

To define the width of the struts it is necessary to first define the geometry of the nodes, which was discussed in the previous subsection. In the 2011a paper, Kim and Yun assumed strut widths were defined by the full width of the nodal zone face into which they framed, regardless of the number of struts which framed into it. So, if a strut is perpendicular to the nodal face then the strut width is equal to the nodal face width. However, it is often the case that the strut is not perpendicular to the nodal face, so the width is computed using trigonometry to find the perpendicular dimension across the strut; this width will always be smaller than the nodal face.

The method by Kim and Yun is in sharp contrast to traditional methods, which compute the width of the struts and nodal faces separately. This is possible in steel strut-and-tie models because strut stiffness, and thus strut area, do not need to be computed before the force analysis. Further, traditional steel design practices require the strut widths to be smaller than the width of nodal faces, as failure in the node is less desirable than failure in the strut. But with the method of Kim and Yun this check is no longer necessary.

Internal nodal zone dimensions are, by extension, set equal to the dimension of the struts which frame into them, and they are assumed to take the form of right triangles as well. In this manner, the dimensions of all the strut-and-tie model elements are vicariously defined by the geometry of critical nodes. Implicitly this method assumes that all struts are prismatic, which is already assumed in traditional steel reinforced strut-and-tie models.

As a point of clarity, internal nodal zones are defined by struts which frame into them, and each of those struts may also frame into a critical node. So, it is possible that the dimensions of an internal node will be different depending on which strut is used to define the internal nodal zone geometry. To avoid this confusion in the later analysis, the dimensions of the nodes in the top chord of the deep beam truss were assumed to be defined by the depth of the compression stress block. The dimensions of the nodes in the bottom chord of the deep beam truss were assumed to be defined by the height of the tie element. Implicitly, this assumed that the dimension of inclined struts had the least reliable geometry. Indeed, the widths of inclined struts were set equal to the smaller of the two widths calculated for each end of the strut. This is made clearer in the design example later in this chapter.

While the process for defining strut widths, as outlined above, is simple, there is admittedly little evidence to suggest that this is an appropriate course of action to define the area of struts. This method does not explicitly take strut or concrete behaviour into account; instead the struts are defined vicariously by nodal geometry, which is vicariously tied to concrete material behaviour by way of nodal zone strength criteria. However, this method produces great results, as will be presented in the Analysis Chapter. It is possible that a more comprehensive, robust, or defensible method for defining strut areas could be developed.

The power of this method for defining strut areas is in its simplicity. The IST method is non-linear by way of making changes to the elasticity term of concrete elements, which ultimately makes changes to the stiffness term. So even though the method by which strut areas are defined is not held up by a compelling argument, it is possible to account for deficiencies in the method by making changes to the concrete material model alone, since the stiffness term is a product of the two parameters. The way in which the material models are modified is outlined in the following section.

5.6 Material Models

5.6.1 FRP Tension Ties

The stiffness of FRP tension ties is constant during an analysis. The stiffness is constant because the cross-sectional area of reinforcement is unambiguously defined, and because the material model for FRP tension ties is linear-elastic-to-brittle-rupture.

Figure 5.2 shows an example curve for the material behaviour using properties from the 25 mm diameter bars used in the experimental test specimens. The modulus of elasticity is 60 GPa and the guaranteed strength is 1000 MPa, as presented in Table 3.2.

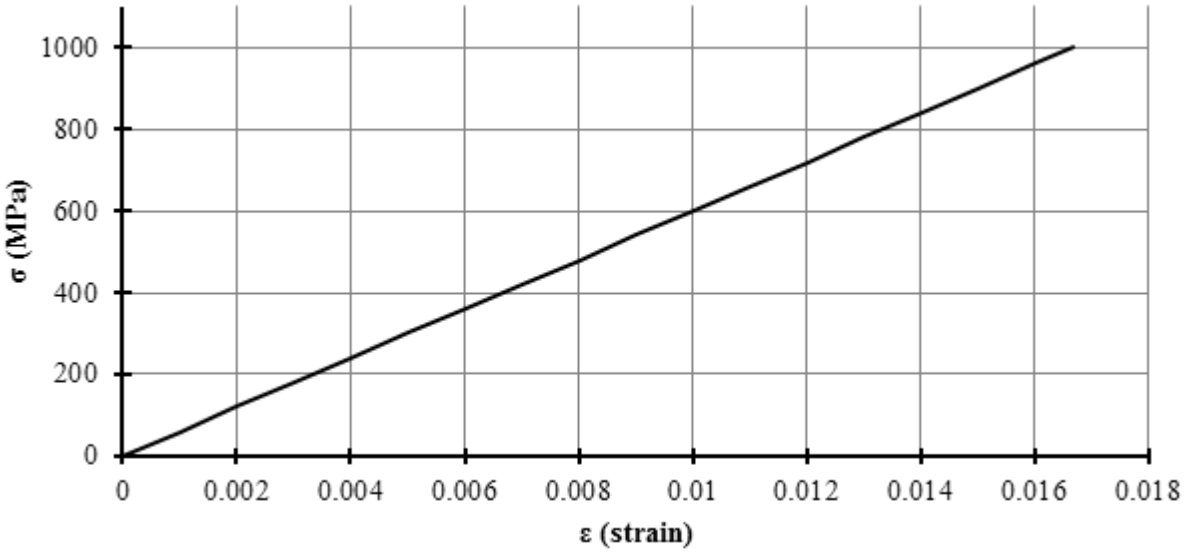

Figure 5.2: GFRP Stress-Strain Curve for the 25 mm Bars

It should be noted that it is possible to consider the effects of tension stiffening. Tension stiffening describes a process of tensile load sharing between the reinforcement and concrete. Before cracking tensile loads are carried by both concrete and reinforcement, and as cracking occurs more of the load is carried by the reinforcement and the tension stiffening effect diminishes.

However, it is unclear as to how much concrete contributes to the process of tensile load sharing, and the amount cannot be readily assumed at the time of design. This effect is ignored in steel reinforced concrete because the effect disappears at the point of yield. However, testing has shown that FRP reinforcement displays tension stiffening behaviour up to the point of rupture, though it is mostly diminished at that point (Bischoff et al., 2004). An investigation into tension stiffening is beyond the scope of this thesis and is left to others.

5.6.2 Concrete Struts

Two material models for concrete in uniaxial compression were used for verification and testing of the IST method: the Hognestad Parabola and the model by Thorenfeldt et al. (1987). Both models are presented later in this section.

In their original form neither of these models is appropriate for modelling concrete struts. These models predict the behaviour of concrete in uniaxial compression, which is a state of stress assumed in a truss analysis, but which is not representative of strut behaviour. A better approximation of reality assumes that struts are subjected to a biaxial state of stress with compression acting along their axis and tension acting across it. The strength of the strut is reduced in proportion to the magnitude of the tensile

strains. Uniaxial models are not capable of capturing this behaviour, two dimensional material models could, but they are not compatible with one dimensional elements.

The solution is to modify the uniaxial material model by artificially reducing the strength of the strut. This solution was devised by Kim and Yun in their 2011a paper where they used a modified form of the Hognestad Parabola to model concrete behaviour. Kim and Yun applied a softening coefficient to both the peak stress and strain at peak stress parameters of the parabola. The intent was to diminish the strength of the struts while retaining the ability to capture behaviour information from the uniaxial model, specifically the change in strut stiffness.

Kim and Yun took guidance from the ACI 318-08 code and used softening coefficients equal to the factors for effective strength of concrete struts. Prismatic top-chord struts were given a softening coefficient of $\zeta = 0.85$ ($= 0.85 \cdot \beta_s$, $\beta_s = 1.00$), and bottle-shaped inclined struts were given a softening coefficient of $\zeta = 0.638$ ($= 0.85 \cdot \beta_s$, $\beta_s = 0.75$). This solution was inspiring, and the modification was applied to the model by Thorenfeldt et al. as well, which is presented in the following subsection.

The choice of softening coefficients is not arbitrary, and this research programme used the values as presented by Kim and Yun. Other possible values for the softening coefficients could be considered based on available research and other design practices. However, the Analysis Chapter will show that Kim and Yun's coefficients were appropriate.

These material models are formulated in terms of a stress-strain curve, and so their slopes represent elasticity. The elastic modulus maybe found by using a line which is either tangent or secant to the point of interest. The tangent modulus is calculated from the determinant of the stress-strain curve, and the secant modulus is defined as the slope of a line intersecting both the origin and the point of interest. The method by which the modulus is calculated is modeller's choice.

The tangent modulus makes analytical sense since it is the slope of the stress-strain curve at the exact point of interest. But the drawback of using it to model concrete is that as the strain passes the point of peak stress the slope of the curve becomes negative which may lead to nonsensical solutions to the force system.

The secant modulus offers an advantage over the tangent modulus because it is always positive when modelling the compressive behaviour of concrete. However, the secant modulus is often more flexible for early stages of loading, and much stiffer for later stages; even at and past the point of peak load the elastic modulus will be unreasonably stiff for what would be described as crushed concrete.

The tangent modulus was used in the analysis of this research programme, and is in accordance with the method described by Yun in his papers. Further, the tangent modulus makes the most sense for this type of analysis since the point of strut failure is defined by the point at which the concrete crushes. And that point occurs at peak stress where the tangent modulus is zero, and thus the stiffness is zero.

However, an element with zero stiffness is also problematic for a truss analysis. So, if the elastic modulus of an element was calculated as less than one percent of the initial tangent modulus then it was reset to be equal to one percent of the initial tangent modulus in the later analysis in this research programme. From a structural perspective the load carried by a strut with only one percent of its initial stiffness was thought to be negligible. It was assumed to have insignificant impact on further solutions to the force system if alternative load paths still existed.

The stiffness modified concrete material models follow and are presented with the derivatives used to compute the tangent modulus in the IST method.

5.6.3 Softening Coefficient Modified Hognestad Parabola (Kim and Yun, 2011a)

The formulae for the softening coefficient modified Hognestad Parabola is presented as follows. The unmodified model may be found by setting the softening coefficient equal to one, $\zeta = 1.00$. This

model may be found in the section of the Literature Review Chapter on Yun's work, but is repeated here for convenience.

$$f_c = \zeta f'_c \left[2\left(\frac{\varepsilon_c}{\zeta\varepsilon_0}\right) - \left(\frac{\varepsilon_c}{\zeta\varepsilon_0}\right)^2 \right] \quad \text{for } \varepsilon_c / \zeta\varepsilon_0 \le 1 \tag{2.34}$$

$$f_c = \zeta f'_c \left[1 - \left(\frac{\varepsilon_c / \zeta\varepsilon_0 - 1}{2/\zeta - 1}\right)^2 \right] \quad \text{for } \varepsilon_c / \zeta\varepsilon_0 > 1 \tag{2.35}$$

The derivatives of the model, used to compute the tangent modulus of elasticity, follow:

$$E_c^t = \frac{2 f'_c}{\varepsilon_0}\left[1 - \frac{\varepsilon_c}{\zeta\varepsilon_0} \right] \quad \text{for } \varepsilon_c / \zeta\varepsilon_0 \le 1 \tag{5.1}$$

$$E_c^t = \frac{-2 f'_c}{\varepsilon_0}\left[\frac{\varepsilon_c / \zeta\varepsilon_0}{(2/\zeta - 1)^2} \right] \quad \text{for } \varepsilon_c / \zeta\varepsilon_0 > 1 \tag{5.2}$$

where f_c is the concrete stress in MPa, E^t_c is the tangent modulus in MPa, ε_c is the uniaxial strain and independent variable, f'_c is the peak stress in MPa, ε_0 is the strain at peak stress, and ζ is the softening coefficient.

The designer is free to specify values for f'_c, ε_0, and the initial tangent modulus of elasticity, E^t_c, as long as they satisfy the equation $\varepsilon_0 = 2 \cdot f'_c / E^t_c$. Often the only known design value is f'_c, and it is common to estimate E^t_c as a function of f'_c using design guides.

5.6.4 Softening Coefficient Modified Model by Thorenfeldt et al. (1987)

The formulae for the softening coefficient modified model by Thorenfeldt et al. is presented as follows. The unmodified model may be found by setting the softening coefficient equal to one, $\zeta = 1.00$. This model, without the softening coefficient, may be found in the Literature Review Chapter.

$$f_c = \frac{\zeta f'_c \, n(\varepsilon_c / \zeta\varepsilon_{'0})}{n - 1 + (\varepsilon_c / \zeta\varepsilon_{'0})^{nk}} \tag{5.3}$$

The derivative of the model, used to compute the tangent modulus of elasticity, follows:

$$E_c^t = \frac{(f'_c \, n / \varepsilon_{'0})}{n + (\varepsilon_c / \zeta\varepsilon_{'0})^{nk} - 1}\left[1 - \frac{nk(\varepsilon_c / \zeta\varepsilon_{'0})^{nk}}{n + (\varepsilon_c / \zeta\varepsilon_{'0})^{nk} - 1} \right] \tag{5.4}$$

where the parameters are defined identically to those in Softening Coefficient Modified Hognestad Parabola model above; and where n is a curve fitting factor, and k is factor which controls the shape of the post-peak portion of the curve.

The Thorenfeldt et al. model is slightly more complicated than the Hognestad Parabola. It is a common case that only f'_c is known at the time of design, so the concrete material model parameters must first be estimated without modifications for softening, specific calculations may be found in the Literature Review.

Once the parameters are defined for the concrete in general, then the initial tangent modulus for each individual strut must be computed considering the effect of softening coefficients on the parameters. To compute the initial tangent modulus for each strut, E^t_c, the parameter ε_c is set equal to zero and softening coefficient modified equations are used to compute parameters *n* and *k*. These modifications are as follows:

$$n = 0.8 + \frac{\zeta f'_c}{17} \tag{5.5}$$

$$k = 0.67 + \frac{\zeta f'_c}{62} \quad \text{for} \left(\varepsilon_c / \zeta\varepsilon_0\right) > 1.0 \tag{5.6}$$

The softening coefficient is also applied to the ratio of the Boolean function for determining which form of the equation for parameter *k* to use.

Figure 5.3 shows the curves for each model considering the two softening coefficients used in the IST method. All curves were plotted using the same values for f'_c and ε_0, but specific values were omitted from the plots for the sake of a general comparison.

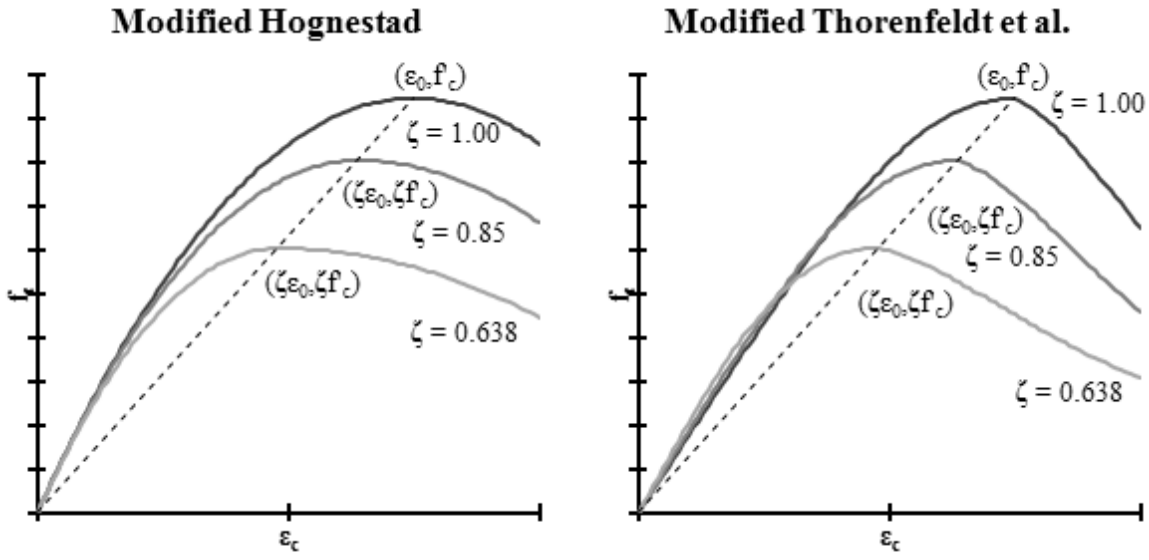

Figure 5.3: Material Model Comparison with Softening Coefficient Influence

It should be clear from Figure 5.3 that the softening coefficients reduce the strength and strain at peak stress parameters of both models linearly, see the dotted line. It may also be noted that the slope of the pre-peak portion of the modified model by Thorenfeldt et al. is fairly constant when compared to that of the modified Hognestad Parabola, which, in general, allows struts to carry more load with increasing strain. Finally, Figure 5.3 shows the post-peak portion of the stress-strain curves for completeness; however, these portions are never used since the IST method artificially limits the lowest allowable elasticity value to one percent of initial strut elasticity. However, when the shapes of the pre-peak and post-peak portions of the two models are compared it is obvious that the treatment of the post-peak portion markedly differentiates the two models, and in general, this can be said of any given compressive, uniaxial, concrete material models.

5.6.5 Nodal Zones

The nodal zones do not have a material model; however, they do represent a region of concrete which may crush as indicated in Section 5.3.4 earlier. The strength of a nodal face is checked by first resolving the forces acting on it into one resultant force, which is assumed to act perpendicular to the node face. The applied stress on the face is then equal to the resultant force acting over the area of the face, and assuming that the resultant acts perpendicular to the face will provide a conservative estimate on the applied stress. The applied stress is then checked against the nodal zone strength criteria from the CSA S806-12 standard.

5.7 Design and Analysis Process

A simplistic step-by-step form of the IST method is presented in this section. The details of calculations are omitted, and the input parameters are described in brief. This thesis is not a prescriptive design document. At all times it is the responsibility of the modeller to ensure their model is viable, and to confirm the appropriateness of the modelling results. It is still the responsibility of the designer to ensure that final designs are in accordance with the requirements of any relevant codes and standards required by the governing authority.

This process below is suitable for the design of deep beams in 3-point bending. It is possible to adapt this method to suit other design scenarios as necessary, taking into consideration the many concerns of working with FRP reinforcement outlined in this thesis and elsewhere.

The philosophy of the process is to record points where elements failed, but continue the algorithm until the strut-and-tie truss has become unstable as a result of strut failures. The purpose of recording points is to allow the modeller to use judgement in assessing strength, or making changes to the model.

1) Define the boundary of the deep beam, the location of the applied load, and the supports. Estimate the magnitude of applied loads and use code equations to estimate the required size of bearing plates. Use traditional moment design techniques to define the depth of the compression stress block and the layout of longitudinal reinforcement.
2) Locate the nodes and define the truss geometry. The critical nodes are located at the intersection of ordinates which extend from, and are perpendicular to the bearing plates and a face defined by the depth of the compression stress block, or the centroid of longitudinal reinforcement, depending on node location. The internal nodes will be located at the same vertical coordinate, but the horizontal coordinate depends on the modeller's choice for locating the stirrups. The analysis is appropriate for indeterminate trusses, so nodal connectivity is modeller's choice as long as the layout of struts and ties is a good approximation of the flow of forces.
3) Define all initial modelling parameters such as element length and element orientation. Define the material properties such as concrete compressive strength and FRP rupture strain. Define the geometry of nodal zones and compute nodal zone strength criteria. Define the width of strut elements, and the cross-sectional area of all elements. Define initial material behaviour for axial elements in terms of material elasticity. Define the boundary conditions in terms of joint fixity.
4) Compute the stiffness matrix.
5) Increment the applied load.
6) Solve the force system.
    a) Compute nodal displacements & reactions, and element internal strains, stresses, & forces.
    b) Update the elasticity term for strut elements using the strains from 6a. If the elasticity of an element is $0.01 \cdot E^t_c$ or less then this strut element has crushed; set the strut elasticity to $0.01 \cdot E^t_c$ for all remaining iterations. Record the strut and load.
7) Evaluate the failure conditions.

a) Check each node face to see if failure has occurred and if it has occurred then record the node, node face, and load.
b) Check each tie to see if failure has occurred and if it has occurred then record the tie and load.
c) Check to see if valid load paths still exist. If they do exist then return to step 4, and if they do not exist then move to step 8.

8) Stop the analysis. Review the results of all failed elements and use judgement to assess the strength.

The truss instability checks were hardcoded into the analysis used in this research programme since the indeterminate strut-and-tie model consisted of only two truss mechanisms, which are identified in the next section. Instability was the result of the crushing of at least one strut from both mechanisms. Hard coding stability checks may not be feasible for more complicated indeterminate trusses.

5.8 Design Example Applied to BM25-220

This section will apply the design and analysis procedure to beam BM25-220 from the experimental portion of this thesis. This is done to illustrate the procedure and to show how the IST method is later applied to all of the beams in the Analysis Chapter of this thesis. This example will also highlight considerations which were difficult to describe without an example. The code for this design example is included in Appendix F.

5.8.1 Model Geometry

The IST method was not researched until well past the design of the experimental beams, which were designed according to the CSA S806-12 standard, as explained in the Experimental Design Chapter. The model geometry is taken from the beam drawings which are found in Appendix E.

The node locations were defined as outlined in steps 1 & 2 of the design process from the previous section, and considered the actual placement of reinforcement as well as the actual size of the bearing plates. Figure 5.4 shows the assumed strut-and-tie truss and the x- and y-coordinates of the nodes. The truss model is symmetric so only half of the strut-and-tie model was needed for analysis. Note that the location of nodes 4 and 7 are not at the exact centre of the beam, but are instead positioned at a location that is half of half the bearing plate width.

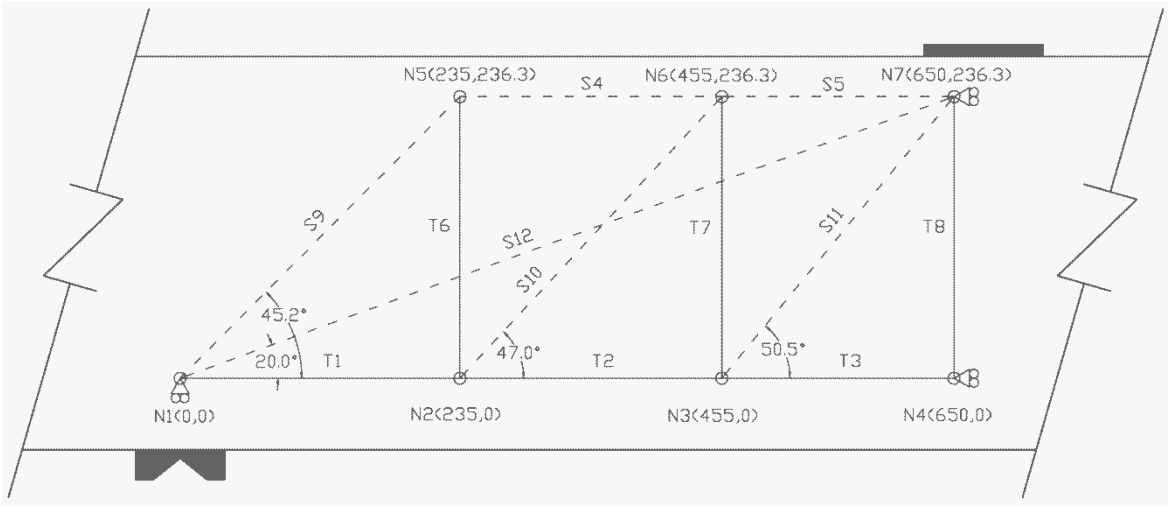

Figure 5.4: Centre-Line Geometry of the Strut-and-Tie Truss for beam BM25-220

The stirrup-truss mechanism of the strut-and-tie model will treat each stirrup as an individual tie. The y-coordinate of the top-chord nodes was computed based on the depth of compression stress block at the point of a flexural crushing failure, and the longitudinal tie is located at the effective depth. The nodes and axial elements are numbered for later reference.

This strut-and-tie truss model has two load transfer paths called load transfer mechanisms. One is called the direct-strut mechanism, and the other is the stirrup-truss mechanism. The direct-strut mechanism is the determinate truss composed of elements T1, T2, T3, T8, & S12, and is called such because it contains the only strut which spans directly from load point to support point. The stirrup-truss mechanism is the determinate truss composed of elements T1, T2, T3, S4, S5, T6, T7, T8, S9, S10, & S11, and is called such because it contains all of the ties that represent stirrups. Note that these two load transfer mechanisms both contain the elements T1, T2, T3, & T8. The super-position of the two determinate trusses produces the indeterminate strut-and-tie truss used to model the flow of forces in this beam. Note that T8 is a zero force truss member.

The geometry of the elements, specifically element widths, was assigned according to the size of the critical nodes and shown in Figure 5.5. Example calculations follow to make clearer the means by which strut and node dimensions were computed.

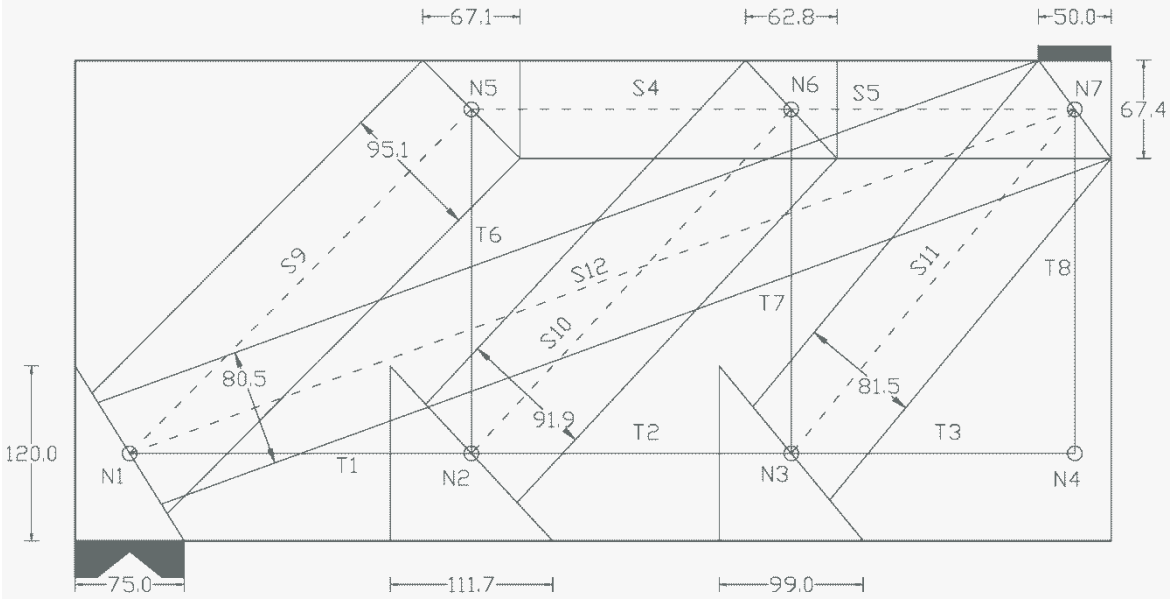

Figure 5.5: Centre-Line Geometry of the Strut-and-Tie Truss for beam BM25-220

The generalized calculation for the width of a strut is as follows:

$$w = d_{node,x} \sin(\theta_{strut}) + d_{node,y} \cos(\theta_{strut}) \tag{5.7}$$

where w is the strut width perpendicular to the strut orientation in mm, $d_{node,x}$ is the x-dimension of the node in mm, $d_{node,y}$ is the y-dimension of the node in mm, and θ_{strut} is the strut angle. When this equation is applied to strut 11 the width of the strut at each node would be computed as follows:

$$w_{strut11@node7} = (50.0\text{mm}) \times \sin(50.5°) + (67.4\text{mm}) \times \cos(50.5°) = 81.5\text{mm}$$
$$w_{strut11@node3} = (99.0\text{mm}) \times \sin(50.5°) + (120.0\text{mm}) \times \cos(50.5°) = 152.7\text{mm}$$

And the width of the strut would be the smaller of the two widths, 81.5 mm.

The generalized calculation for the horizontal dimension of an interior node, based on the strut angle and vertical node dimension is as follows:

$$d_{node,x} = d_{node,y} / \tan(\theta_{strut}) \tag{5.8}$$

When this equation is applied to node 6 the horizontal dimension would be computed as follows:

$$d_{node6,x} = (67.4\text{mm}) / \tan(47.0°) = 62.8\text{mm}$$

And the horizontal dimension would be 62.8 mm.

5.8.2 Commentary on Node Geometry

The joints of the truss coincide with the orthocentre of the right-triangles that makes up the nodal zones. The orthocentre was chosen because it conforms to the analysis method of Kim and Yun (2011a), and because it is very easy to define, particularly for the critical nodes that have two well-defined faces.

However, the choice of using the orthocentre for interior nodes is born of necessity and simplicity. Consider an interior top-chord node: the dimension of the vertical face is defined by the depth of the compression stress block, but the dimension of the remaining faces cannot be defined based on any object or well-known concrete behaviour. Ergo, to define the shape of the node it is necessary to make assumptions.

If the nodal zone is assumed to take the form of a right-triangle then the dimension of the horizontal face can be found using trigonometry and the angle of the strut which frames into the node. The dimension of the hypotenuse is found using Pythagorean Theorem. If multiple struts frame into the face of the hypotenuse then it may be necessary to consider some form of resultant on which to base the angle. The resultant is not necessary for critical nodes since the two well defined faces are all that is necessary to define the dimension of the hypotenuse.

Further, it has been the author's experience that design guides are reluctant to clearly define the relationship between the location of the truss model joint and the location of the centroid of the nodal zone. Even more, it can be maddeningly impossible to make the two coincide, and it is not clear that coincidence is even appropriate.

Nodal zones were originally intended to be zones of hydrostatic stress, so the location of the truss joint was irrelevant as long as a state of hydrostatic stress could be formed at the intersection of the stress fields, and as long as the nodal zone resided inside the domain of the concrete. Creating a hydrostatic state of stress in an iterative design procedure was unrealistic, and the requirements were relaxed to allow pseudo- and quasi-hydrostatic states of stress as was noted in a previous section. However, when this was done there were no conditions placed on the relationship between the location and geometry of the nodal zone and the location of the truss joint. The following documents may be used for further consideration: (Schlaich et al, 1987)(Schlaich et al, 1990)(Schlaich et al, 1991).

It is assumed that as long as the truss joint is located within a reasonable proximity to the location and geometry of the nodal zone then the solution of the force system, and the forces used to assess the capacity of the nodal zones will be appropriate.

Indeed, consideration of the strength of non-critical nodes is presented because it is convention to do so. Recall that Kim and Yun (2011a)(2011b) do not assess the strength of non-critical nodes in their analysis.

5.8.3 Clarification on Assigning Node and Strut Dimensions

The process of assigning node and strut dimensions is described here to make clear the generalized processes mentioned in subsections 5.5.2 and 5.5.3.

Consider first node 7. The horizontal dimension of node 7 was set equal to half the bearing plate width, since the model is symmetric, and the vertical dimension was set equal to the depth of the compression stress block at flexural compression failure. Once those two node faces were determined the remaining face was calculated using trigonometry.

Once the dimension of the hypotenuse face of node 7 was computed the width of struts 5, 11, & 12 were computed using Equation 5.7.

Once the dimension of strut 5 was determined, it was then possible to define the geometry of node 6. The vertical face was set equal to the width of strut 5. The dimension of the horizontal face was calculated using Equation 5.8. Once those two node faces were determined the remaining face was calculated using trigonometry.

Now consider node 1. The horizontal dimension of node 1 was set equal to the bearing plate width. The vertical dimension was set equal to twice the difference between beam height and effective depth of reinforcement, which is consistent with assumptions used in steel strut-and-tie modelling. Once those two node faces were determined the remaining face was calculated using trigonometry.

The vertical dimension of node 2 is the same as that of node 1 since the longitudinal reinforcing bars run across all of the bottom-chord nodes. The dimensions of node 2 were determined in the same manner as those for node 6.

The width of strut 10 was determined by considering the dimensions of the nodes at either end of the strut and selecting the smallest width.

Now, to be clear, the dimension of node 2 was not determined using the width of strut 10 because strut 10 is a less well-defined dimension than the height of tie 1. That is to say that strut 10 is vicariously defined by node 6 which is vicariously defined by strut 5 which is defined by node 7, whereas node 2 is defined by tie 1.

5.8.4 Define Material Properties and Element Strengths

The next step in the analysis is to define the material properties and design strengths of the elements. The material properties may be found in Table 3.2 of the Experimental Design Chapter. The strength of nodes was defined as per Cl.8.4.4 in the CSA S806-12 standard. Concrete material behaviour for this example was described by the Softening Coefficient Modified Thorenfeldt et al. model. The initial tangent elastic modulus was calculated using Equation 2.41. The softening coefficients were defined and applied to the struts as explained in the Material Models Section.

5.8.5 Results and Discussion on General Model Behaviour

Table 5.1 and Figure 5.6 illustrate how the elastic moduli of the concrete struts change as the analysis progresses. The load values have been doubled from the model output to account for symmetry. The table includes only a few load levels for illustration purposes to highlight important points in the analysis. The actual analysis proceeded in increments of 10 N and ran less than 20 seconds on a typical office computer.

The strut failure checks are done after strain computations, and after the elastic modulus values are updated for the next iteration. So, the row for 413980 N shows the elastic modulus values computed at the end of the previous load level, where Strut 12 had crushed. The next strut that crushed, strut 5, occurred at 414040 N, and is the system failure load. The next load level is included in the table to show the failure of strut 5 in terms of the value of the elastic modulus only.

The initial tangent modulus values are the same for struts which have the same softening coefficients. Struts 4 and 5 were prismatic with a softening coefficient of 0.85, while struts 9 through 12 were reinforced and bottle-shaped with a softening coefficient of 0.638.

Table 5.1 also shows that node 7 is predicted to fail prematurely; the pressure acting on the vertical face exceeded the strength of the node. However, the analysis continues until the load which causes a loss of stability as a result of struts crushing. If this example were a true design example then

modifications to the strut-and-tie model would need to be made to ensure that truss instability was exclusively the result of strut failures.

Table 5.1: Evolution of Strut Elasticity with Load Increments

Load	Elastic Moduli (MPa)						
N	**Strut 4**	**Strut 5**	**Strut 9**	**Strut 10**	**Strut 11**	**Strut 12**	**Comments**
Zero	36947	36947	41318	41318	41318	41318	Initial Modulus Values
100000	36945	36935	41295	41295	41291	41139	
200000	36933	36840	41181	41180	41153	40208	
300000	36898	36545	40916	40913	40833	37799	
394260	36823	35868	40435	40429	40249	31556	Node 7 Fails
400000	36815	35798	40390	40384	40194	30679	
413960	36719	34872	39846	39835	39527	4817	Strut 12 Crushes
413980	36527	33108	38901	38884	38378	*413*	Next Iteration
414040	35994	12406	35679	35627	33969	*413*	Strut 5 Crushes - Stability Failure
414060	35994	*369*	35609	35554	33737	*413*	Next Iteration

The change in strut elasticity over the analysis is clearly illustrated in Figure 5.6.

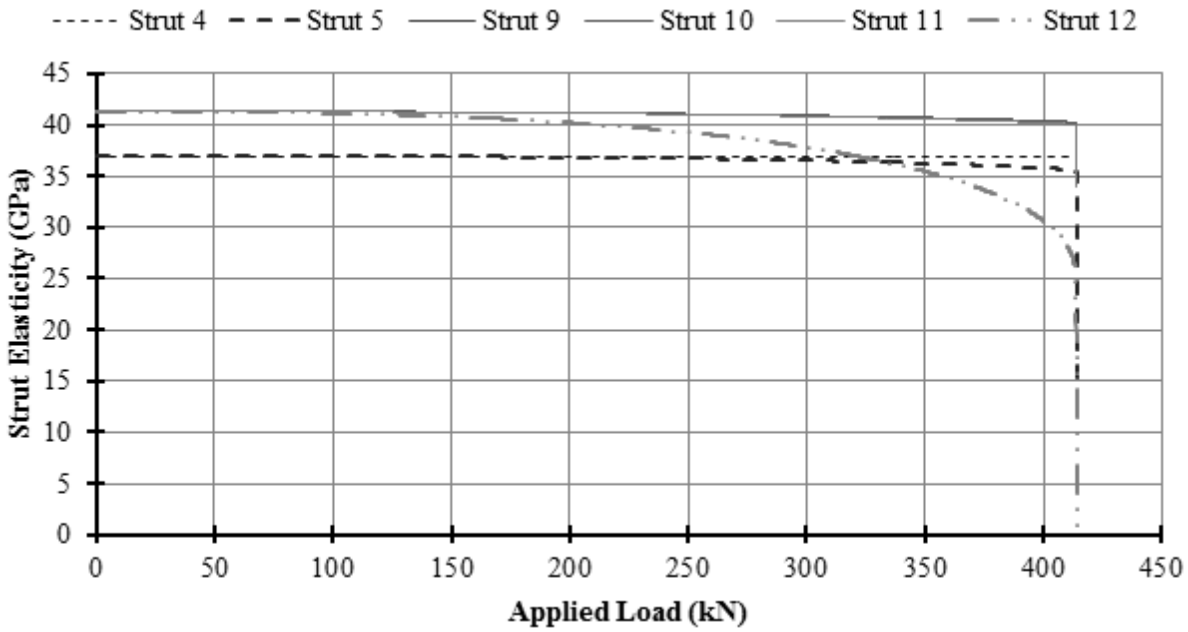

Figure 5.6: Evolution of Strut Elasticity

In Figure 5.6 the curves for struts 5 and 12 have been made thicker for convenience, further the curves for struts 9, 10, and 11 almost entirely overlap. Strut 12 crushed first and shows a very gradual loss of elasticity over the course of the analysis. The crushing of strut 12 occurs quickly over a few iterations at the very end of the curve, and within these iterations the force carried by the direct-strut mechanism is transferred to the stirrup-truss mechanism. The curves for the remaining struts show a very, very short decrease followed by an abrupt drop in elasticity when strut 12 actually crushes. The abrupt drop is the result of the remaining stirrup-truss mechanism having to carry the entire load, and very shortly thereafter strut 5 also crushes and the analysis stops because the truss is now unstable.

Figure 5.7 shows the percentage of load transferred by each load carrying mechanism at each load increment. As before, the load values have been doubled from the model output to account for symmetry.

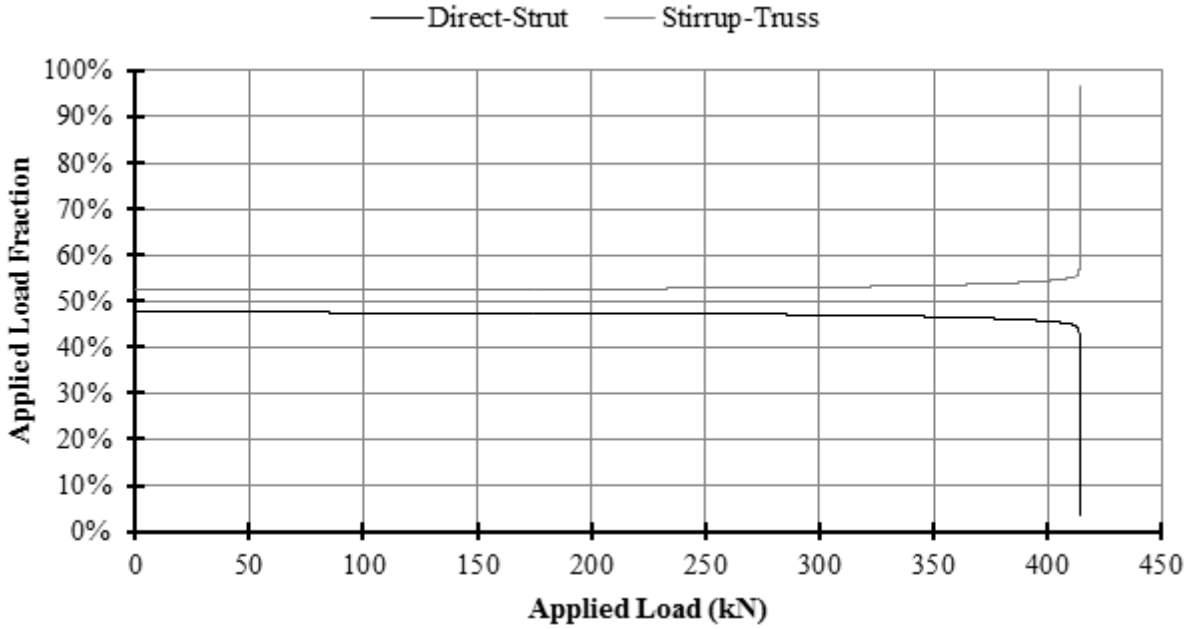

Figure 5.7: Applied Load Carried by Each Load Transfer Mechanism

Figure 5.7 shows that the percentage of load carried by each mechanism does not change much over most of the analysis. It is only towards the very end of the curves that an abrupt change occurs. The observations gleaned from this figure also reinforce the observations from Figure 5.6. As load increases the direct-strut mechanism, strut 12, carries less load, and it carries less load because it is losing stiffness faster than any other strut, or more generally, faster than the other mechanism.

The particular orientation of these curves is unique to this beam. It is possible that another strut-and-tie model would have the direct-strut curve start above the stirrup-truss curve, or the stirrup-truss mechanism decrease its load fraction. It all depends on the geometry and material properties of the specific strut-and-tie model.

Failure of the stirrup reinforcement was also potentially indicated, but ignored since the experimental results never produced a stirrup failure. The maximum stirrup stress from the analysis reached 883 MPa, which exceeds the 700 MPa bend strength, but not the 1000 MPa straight portion strength indicated by the manufacturer. Further, the strains in the stirrups were always well below the rupture strain.

Figure 5.8 is included to clarify the process by which stresses on the nodal faces are determined. In this figure the force values were not doubled to account for symmetry, and were taken from node 7 at an applied load of 197130 N, the point at which node 7 was predicted to fail.

The three force vectors from struts 5, 11, and 12 are summed using vector addition, and the magnitude of the resultant force is divided by the area of the hypotenuse face of the nodal zone. That stress is then compared to the nodal zone strength criteria for a node with only compression faces. Again, the fact that the resultant does not act perpendicular to the face is ignored, because the analysis conservatively assumes that it does.

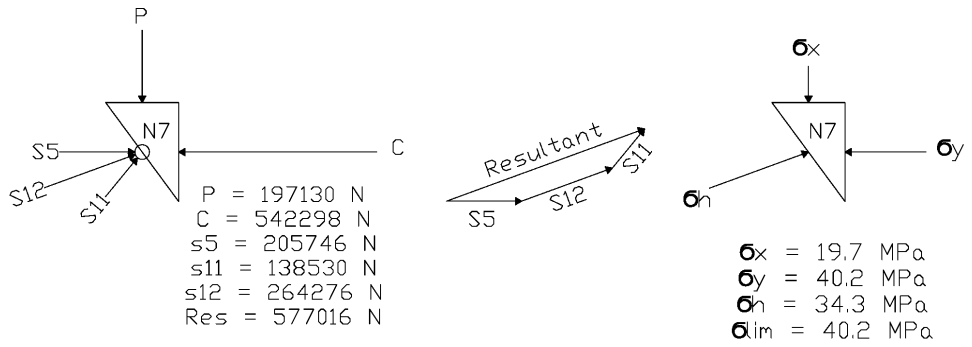

Figure 5.8: Diagram for the Clarification of the Process by which Nodal Stresses are Determined

5.8.6 Other Observations

There are other interesting observations to be made from the analysis, some of which may not be immediately obvious.

One observation comes from Figure 5.8; the resultant force could have been determined from the vector sum of force P and C instead of S5, S11, and S12. Recall that force C is directly proportional to force P, since force C represents part of the internal moment force couple developed by P alone. The direct proportionality means that the orientation of the resultant will never change even though the fraction of load carried by the direct-strut, S12, and stirrup-truss, S5 and S11, change over the course of the analysis.

Another observation is that the force carried by the members within each determinate truss of an indeterminate system will always be in direct proportion to the load carried by any of the other members in that determinate truss, with the caveat that this does not apply to members of the determinate truss which are shared with other determinate trusses. For example, the force carried by elements S4, S5, T6, T7, S9, S10, & S11 of the stirrup-truss mechanism will always be proportionate to one another, but not to the force in elements T1, T2, & T3 because those elements are also part of the direct-strut mechanism. Element T8 is excluded because it is a zero-force member. So, even though the elasticity of the struts in the stirrup-truss are not in the same proportion to one another, or to the elasticity of the ties, from one iteration to the next they still maintain proportionate internal forces.

5.9 On the Choice of Material Model and Initial Parameters

This section presents the results of an investigation into which combination of concrete material model and parameters best predicted the experimental results of BM25-220. And it is assumed that the best combination would be appropriate for modelling the rest of the test specimens from the research programme, which are presented later in the Analysis Chapter of this thesis.

This section is by no means a presentation of a comprehensive sensitivity analysis; a formal sensitivity analysis is beyond the scope of this research programme since this research programme was originally intended to be an experimental investigation. A more thorough sensitivity analysis is left to others.

The concrete material models are sensitive to two parameters: the peak stress, f'_c, and the strain at peak stress, ε_0. Unfortunately, the IST method was not yet established at the time of experimental testing, so concrete cylinder tests conformed to the minimum required by the CSA A23.2-9C “Compressive Strength of Cylindrical Concrete Specimens” test method, and thus data which would describe the complete stress-strain curve was never recorded. It is necessary to estimate ε_0, which is commonly done by first estimating the initial tangent modulus, E^t_c. The method by which each model estimates ε_0 is presented in the Material Model Section of this chapter.

There exist several methods by which E^t_c may be estimated, and it is common for different design codes to have different equations. This investigation examined three such equations: one used by Kim and Yun, and two from the CSA A23.3-04 standard. The three equations follow:

$$E_c = 3300\sqrt{f'_c} + 7700 \quad \text{(Kim and Yun, 2011a)} \tag{5.8}$$

$$E_c = 4500\sqrt{f'_c} \quad \text{CSA A23.3-04 Equation 8-2} \tag{5.9}$$

$$E_c = \left(3300\sqrt{f'_c} + 6900\right)\left(\frac{\gamma_c}{2300}\right)^{1.5} \quad \text{CSA A23.3-04 Equation 8-1} \tag{5.10}$$

where E_c is the secant modulus in MPa, f'_c is the peak stress in MPa, and γ_c is in kg/m^3. The secant modulus describes the elasticity of concrete stressed within a range of 0.4 to 0.5 of f'_c (MacGregor et al., 2000); however, to properly define the parameters of the material models in the IST method an estimate on the value of the initial tangent modulus is required. To estimate E^t_c, MacGregor et al. recommend multiplying the secant modulus by a factor of 1.10.

The investigation involved varying the value of the initial tangent modulus, applying or not apply the softening coefficients, and changing the material model. The rest of the parameters were as specified in the Design Example Section. Table 5.2 shows the result of such an analysis, and includes the computed modulus, strain at peak stress, and the ratio of experimental load, P_E = 360.1 kN, over predicted load, P_P. Several values for the initial tangent modulus were used to help define model behaviour, some of which are unrealistic.

Table 5.2: Results of the Investigation into Modelling Parameters

	Thorenfeldt et al. Material Model			**Hognestad Material Model**		
		Ratio P_E/P_P			**Ratio P_E/P_P**	
E^t_c	**ε_0**	**With Softening**	**Without Softening**	**ε_0**	**With Softening**	**Without Softening**
10000	0.0066	0.717	*0.515*	0.0095	0.806	0.652
20000	0.0033	0.806	*0.494*	0.0047	0.813	0.628
30396[1]	0.0022	0.855	0.493	0.0031	0.867	**0.615**
30949[2]	0.0021	0.857	0.494	0.0031	0.870	0.615
31873[3]	0.0021	0.860	0.495	0.0030	0.874	0.614
33435[4]	0.0020	0.865	0.497	0.0028	0.881	0.613
34044[5]	0.0019	0.867	0.498	0.0028	0.884	0.612
35060[6]	0.0019	**0.870**	**0.500**	0.0027	**0.888**	0.612
45000	0.0015	0.892	0.512	0.0021	0.923	0.608
70000	0.0007	0.943	0.540	0.0014	0.976	*0.626*

[1]ACI equation; [2]CSA equation 8-2; [3]CSA equation 8-1
[4,5,6]Same as notes [1,2,3] but multiplied by 1.1 to estimate on the initial tangent modulus
**__Bold__ indicates results closest to unity, $P_E = P_P$., within the range of reasonable E^t_c values.*

It is clear from Table 5.2 that the softening coefficients have the most significant impact on the ability of the IST method to predict the experimental results of BM25-220. The prediction ratio values are closer to unity by a value between 0.15 and 0.40 when compared to those without softening coefficients, depending on initial tangent modulus and material model. Whereas varying the value of the initial tangent

modulus by 5000 MPa, within the range of defensible estimates, changes the ratio values by no more than 0.02, depending on the material model and the application of softening coefficients. So, if the softening coefficients are reasonably estimated then the choice of initial tangent modulus is almost irrelevant, as long as it, too, is reasonable. Interestingly, the results show that there is no realistic value for the initial tangent modulus which would predict the strength of BM25-220 exactly.

Note that the trend lines for ratio values is, generally, reversed for model trials with softening coefficients when compared to those without. This may be clearer in Figure 5.9 which shows a plot of the data in Table 5.2.

Regardless of material model strut 12 crushed first followed by strut 5, when softening coefficients were used. However, the opposite was true when softening coefficients were not used. As a point of interest, the second strut failure typically occurred within 3 iterations after the first strut failure.

The reversal of the order in which struts 12 and 5 failed occurred because strut 12 has a softening coefficient of 0.638, whereas strut 5 has a coefficient of 0.85. For the specific geometry of the strut-and-tie model for BM25-220, the application of softening coefficients reduces the strength of strut 12 such that it fails before strut 5.

There are exceptions to the trends identified above which may be seen in Figure 5.9, and which were italicised in Table 5.2. These values do not follow the trend and are the result of the failure of struts 12 and 5 occurring in the opposite order than predicted by the other trials in each column. However, they occur at trials which included unrealistic values of the elastic modulus, though it is possible that this may be an important observation for a different design problem.

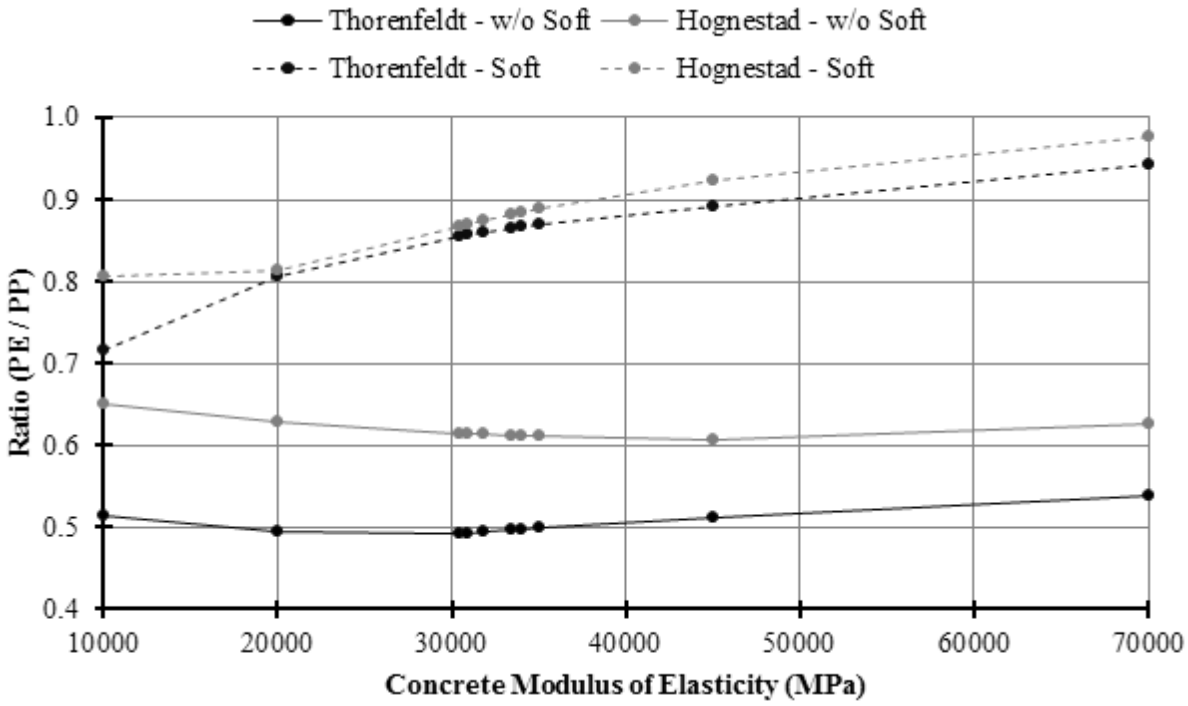

Figure 5.9: Plot of the Results of the Investigation into Modelling Parameters

5.9.1 A Comment on the Choice of Softening Coefficients

The results of the investigation found that the model was most sensitive to the value of the softening coefficients; however, the investigation was not rigorous in finding the 'best' softening coefficient values. Such an undertaking is beyond the scope of this research programme; it would require significant effort to justify a different choice of softening coefficient values.

The most natural assumptions are to either set the softening coefficients equal to unity, thus providing an unmodified form of the concrete material model, or to assume the same values as that of Kim and Yun (2011a) upon which the IST method is based.

Kim and Yun (2011a) never justify their choice of softening coefficients because the results of their investigation speak for themselves. Their 2011b paper finds that their modelling method makes remarkably good predictions on the strength of a large database of steel reinforced deep beams. Indeed, their assumption is not entirely unreasonable either: setting the softening coefficients equal to the strut strength reduction factors of the ACI 318 code relies on the body of research used to justify those reduction factors.

There was an attempt to use the formulas from the CSA S806-12 standard, which are identical to those of CSA A23.3-04, to predict the value of the softening coefficients. However, those formulas assume that the strain in the reinforcement at failure is known before the strength of the struts are determined, which is the same problem as trying to define the strut areas as discussed earlier. The strain in the reinforcement at failure cannot be known until after the analysis, which requires the softening coefficients as an input. Attempts to update the softening coefficients using the reinforcement strain with each iteration were not productive.

Recall that updating strut strength reduction formulae of the CSA S806-12 standard on each iteration worked well for Andermatt et al. in their 2013a paper presented in the Literature Review Chapter. In their case, they were not actually performing a finite element analysis; rather, they were engaging in a form of optimization. Specifically, their analysis did not require any information from a previous load level to arrive at a solution for the next load level. However, the IST method uses strut strains from a previous load level to compute the elastic moduli for the next load level. If the softening coefficients were revised on each iteration then the entire concrete material model would be different, and it would be improper to use strain from a previous load level to compute the elastic moduli for the next.

The strut strength reduction factors recommended by Nehdi et al. (2008) were also examined as potential softening coefficients, see Equations 2.31 and 2.32. However, they computed softening coefficients which were about half the value of those used by Kim and Yun (2011a) and did not lead to good predictions, the struts were too soft.

5.9.2 Input Parameters Used in the Analysis Presented in Chapter 6

As a result of this investigation the following assumptions will be used by the IST method in the Analysis Chapter of this thesis: the material model will be that of the Softening Coefficient Modified Hognestad Parabola, and the elastic modulus will be calculated using the equation 8-1 of CSA A23.3 modified by a factor of 1.1.

6 Analysis

This chapter is a presentation of two three analyses. The first is a comparison between the experimental results and the predictions from the CSA S806-12 standard, the academic model by Nehdi et al., and the IST method. The second is an investigation into the behaviour of the FRP reinforced deep beam specimens done by decomposing the results into separate concrete and stirrup shear strength contributions. Finally, the third is an investigation into the ability of the IST method to capture FRP reinforced beam behaviour other than ultimate strength.

A note on vocabulary: the remainder of this chapter will refer to the CSA S806-12 shear model and the Nehdi et al. model as methods, since the IST method is performed on several different strut-and-tie truss models. This clarification is made to avoid possible confusion in later text.

6.1 Comparing Predictions to Experimental Results

In this section, the results from the experimental tests are compared to the predictions from the CSA S806-12 standard, the Nehdi et al. method, and the IST method developed in Chapter 5. These methods have been explained in previous sections of this thesis and their details are not repeated here.

6.1.1 Truss Models for the Indeterminate Strut-and-Tie Method

This subsection is an exploration of possible truss models, some of which are then used in the comparison of the next subsection.

The IST method is performed on a specific truss model with geometry unique to each experimental test specimen. Figure 6.1 shows four types of models which were chosen for consideration. Other models are possible, but these were the only ones investigated in this research programme. An investigation into the use of alternative models is left to others.

Figure 6.1 shows four models types. Models of Type I, III, IV are hereby called analytical models, while models of Type II are hereby called design models. As noted in Chpater 5, design models avoid assumptions on the specific location of stirrup reinforcing: stirrups are lumped into one location to first find the required area of stirrups, and then designers distribute the required amount of stirrups evenly over the shear span. The analysis of Type II models will provide insight into this design technique. The analytical models represent the specific reinforcement geometry by placing tie elements at the location of stirrup reinforcing as indicated on beam drawings from Appendix E. In the case of Type II models, the stirrup was located midway between N1 and N3.

Further, models of Type I represent deep beams with no transverse reinforcing. As per the discussion of Chapter 5, all inclined struts were assumed to have a softening coefficient of ζ =0.638; a value equal to the strut effective strength factor from the ACI 318-08 code for struts which are both bottle-shaped and reinforced. However, models of Type I are unreinforced, so the analysis will also consider applying a softening coefficient of ζ = 0.51 (= 0.85·β_s, β_s = 0.60), which represents the strut effective strength factor for unreinforced bottle-shaped struts.

Even further, models of Type IV will consider the truss as shown, but will also consider a similar truss with elements N2, N7, T1, T10, S6, and S15 removed, and with elements T2 and S16 extended from N2 to N1. This was done to address the premature failure of S15, as Table 6.2 will later show. The angle between S15 and T10 is quite small and does not comply with best practices for strut-and-tie modelling.

The stirrup area of tie T10 was evenly distributed to ties T11, T12, and T13 so that the modified truss would still have a representative stiffness. There was no real justification for doing the redistribution, and doing so may very well have had insignificant influence on the result.

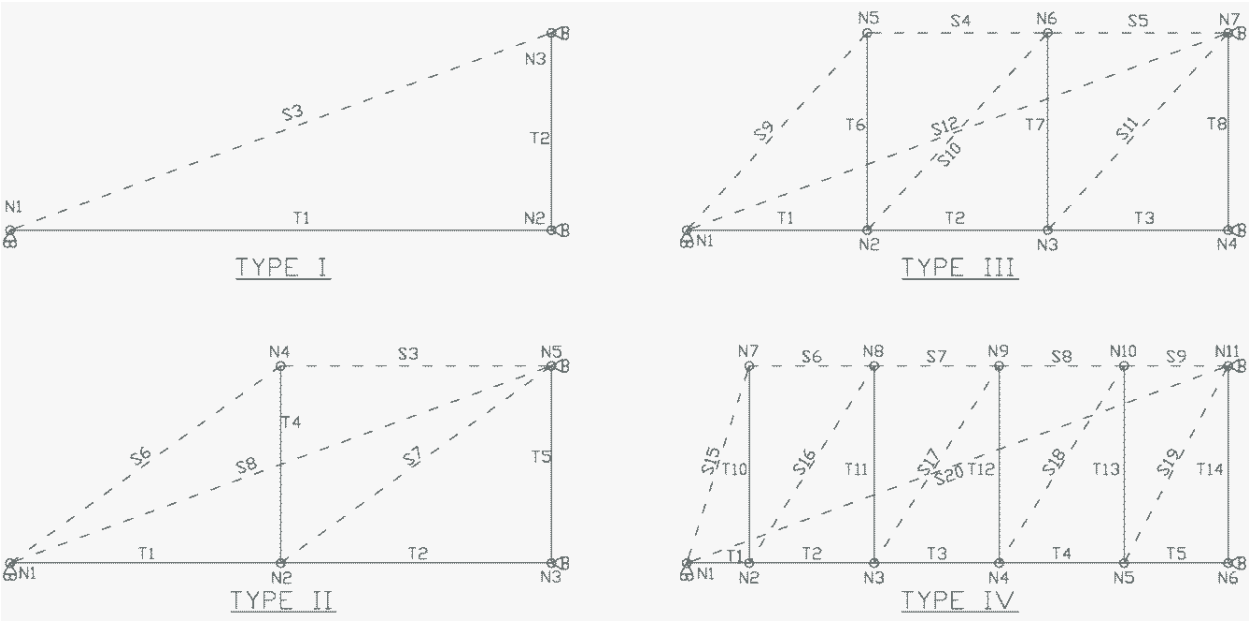

Figure 6.1: Strut-and-Tie Model Truss Types for Analysis

Table 6.1 clarifies which beams will be analyzed with which model types. The grouping of beams in Table 6.1 represents 27 different models when each beam is considered.

Table 6.1: Association of Model Types with Experimental Beam Specimens

Model Type	Beam Series	Comments
Ia	INF	Analytical model with a softening coefficient of 0.638
Ib	INF	Analytical model with a softening coefficient of 0.51
II	150, 220, s230	Typical design model
III	220, s230	Analytical model
IVa	150	Analytical model including T10
IVb	150	Analytical model excluding T10

Specifics of the geometry and material properties for each model are not reproduced here, but may be readily determined from information in Appendix E. Appendix E contains a beam diagram and table with various parameter values for each experimental beam. The modelling parameter values come from the beam diagrams and the as-designed column of the table. There are two exceptions: 1) the concrete strength used the 28 day as-constructed value, and 2) the elastic modulus of the longitudinal reinforcing for beams BM16-X was assumed to be 60 GPa instead of 64 GPa. The geometry of each model was established in the same manner as outlined in the Design Example part of Chapter 5; the node underneath the applied load considered only half the width of the bearing plate. Load was iterated using 10 N increments. The code used for the analysis is found in Appendix F; the functions "initialInput" and "failureCheck" were modified for each model.

Table 6.2 shows the results of the IST method applied to models of Types I, III, and IV, representing 18 different models. The heading "Elem" is short for element, P_E is the experimental applied load at failure, and P_P is the predicted applied load from the IST method at the point of element failure.

Table 6.2: Summary of Results for Models of Type I, III, and IV

Beam	P_E (kN)	Model Type	System Failure			Alternative Failures					
			Elem	P_P (kN)	Ratio (P_E/P_P)	Elem	P_P (kN)	Ratio (P_E/P_P)	Elem	P_P (N)	Ratio (P_E/P_P)
BM12-INF	163.1	Ia	S3	181.66	**0.90**						
		Ib	S3	145.34	1.12						
BM16-INF	150.2	Ia	S3	176.18	0.85						
		Ib	S3	140.96	**1.07**						
BM25-INF	125.1	Ia	S3	166.84	0.75						
		Ib	S3	133.48	**0.94**						
BM12-220	382.4	III	S5	391.18	0.98	S12	391.08	**0.98**			
BM16-220*	*309.3*	*III*	*S5*	*395.16*	*0.78*	*S12*	*395.08*	***0.78***			
BM25-220	360.1	III	S5	405.52	0.89	S12	405.46	0.89	N7	394.26	**0.91**
BM12-150	405.2	IVa	S15	295.10	1.37	S20	286.60	1.41			
		IVb	S9	375.82	**1.08**	S20	375.74	1.08			
BM16-150	416.5	IVa	S15	285.60	1.46	S20	285.24	1.46			
		IVb	S9	379.30	**1.10**	S20	379.24	1.10			
BM25-150	415.8	IVa	S15	284.52	1.46	S20	284.38	1.46			
		IVb	S9	388.30	**1.07**	S20	388.26	1.07			
BM12-s230	466.9	III	S12	484.48	0.96	S5	484.44	0.96	N7	483.28	**0.97**
BM16-s230	450.8	III	S12	450.78	**1.00**	S5	450.74	1.00			
BM25-s230	444.0	III	S12	395.18	**1.12**	S5	395.12	1.12			
Average* of System Failure Ratios Closest to Unity =					1.01						

**Outlier not included in average, see the Results Section for more information.*
*** **Bold** entries highlight ratios closet to unity for each specimen.*

Table 6.2 presents the results in two groups: system failure and alternative failures. System failure is the load at which the truss becomes unstable exclusively as the result of strut crushing, and represents the highest possible strength using the IST method. Models of Type Ia & Ib were determinate, with only one strut, so system failure occurred at the crushing of that single strut. The remaining model types are all indeterminate trusses each composed of two determinate truss mechanisms: the direct-strut and the stirrup-truss; system failure required the crushing of at least one strut from each mechanism. The alternative load columns show the failure of other strut-and-tie components in order of decreasing load. By chance the first column of alternative failures are all composed of the first struts to crush, and the second column are all composed of nodal failures. A third set of alternative failures was not necessary as no other failures were indicated.

The alternative failures are included in Table 6.2 because it is possible that beam failure may take place at one of these points instead of at the point of truss instability. Consider a general deep beam truss, if the direct-strut were to crush first then one could reasonably argue that the inclined struts of the stirrup-truss mechanism also crushed since these struts represent overlapping regions of concrete. Likewise, if an inclined strut were to crush then one could also argue that the direct-strut has crushed. Nodal failures were also considered since this was an analysis of potential causes of failure.

In Table 6.2 individual beams are grouped by alternating row shading. Comments on possible tensile failures are provided after Table 6.3. Recall that the models only represent half of the experimental beams because of symmetry, and so the output of the code in Appendix F was doubled when shown in Table 6.2.

The analysis of beams BMX-INF did not consistently indicate the most appropriate softening coefficient for unreinforced deep beams. However, since two of the three beams were better represented by Type Ib models, and since the description of the strut effective strength factor on which the Type Ib softening coefficient is based better describes the actual state of strut reinforcing, it was decided that the choice of model type for later comparison would be Type Ib.

The analysis of beams BMX-150 consistently indicated that models of Type IVb were better suited for predicting beam strength. These models failed first by crushing of the direct-strut S20, followed closely by the crushing of the compression stress block strut S9. Models of Type IVa predicted strengths much lower than the experimental values; failure occurred first by crushing of the direct strut S20, followed closely by the crushing of inclined strut S15. S15 crushed before any other strut in the stirrup-truss mechanism because it was the smallest, and it was the smallest because of the severe angle of S15 relative to the hypotenuse face of N7; recall that the widest strut which will fit into a node face will be a strut perpendicular to the face.

The magnitude of the difference between the applied load level at which the direct-strut crushes, in Models IVa & IVb, is remarkable. Consider Figures 5.5 & 5.6 in addition to the following passage.

A review of the analysis results found that the stirrup-truss mechanism of both model types carried less applied load then the direct-strut mechanism until the load at which the direct-strut crushes. And, that the stirrup-truss mechanism of Type IVa models carried much less applied load than those of Type IVb, which implies that the stirrup-truss mechanism of Type IVa models were less stiff than those of Type IVb.

This is initially counter intuitive: common knowledge on the behaviour of linear elastic trusses suggests that trusses with more vertical members are stiffer than those with fewer. But this is only applicable to uniform trusses composed of members with identical cross-sections respective to the member configuration in the truss. In this case, the cross-sectional area of members S17 through S20 are identical between models of Type IVa & IVb, so the members with the most influence on the stiffness of the stirrup-truss mechanism are elements S15 in Type IVa models and S16 in Type IVb models. Type IVa models are more flexible because element S15 has much less cross-section compared to element S16 from Type IVb models. Further, Type IVb models may also be stiffer because the stirrup area of tie T10 was evenly distributed to the remaining non-zero force stirrups.

So, the direct-strut of Type IVa models failed at a lower applied load, when compared to Type IVb models, because the direct-strut mechanism of Type IVa models carried a larger portion of the applied load, compared to Type IVb models; however, to dispel possible confusion it should be noted that crushing of the direct-strut occurs as a result of the force internal to S20. Since the direct-strut from both models had the exact same geometry and material behaviour, they also had the exact same crushing load, but they carried different proportions of the applied load when they crushed.

What is also remarkable about the difference in predicted failure load between the two model types is that a poor, but reasonable, choice on the approximation of the flow of forces predicted a more conservative strength.

The analysis of beams BMX-220 does not indicate a consistent trend. Specimen BM16-220 is an outlier and is not considered. The results show that beam BM12-220 is expected to fail as a result of the crushing of the first strut since it is closest to the experimental strength; however, this load is not significantly different from the final failure load in structural terms, so failure may still be considered to take place at the system failure load.

Beam BM25-220 is predicted to fail as a result of the failure of the critical node where the load is applied. This failure is the result of crushing of the vertical face of the node, which is indicative of a flexural-compression failure. The failure load closest to unity, for each specimen, will be used for later comparison in Table 6.4.

The analysis of beams BMX-s230 does not indicate a consistent trend. Beams BM16-s230 and BM25-s230 are both expected to fail as a result of the crushing of the compression stress block strut S5 followed closely by the crushing of the direct-strut S12. However, beam BM12-s230 is expected to fail as a result of the crushing of the vertical face of the N7, the critical node where load is applied. This is indicative of a flexural compression failure. The failure load closest to unity, for each specimen, will be used for later comparison in Table 6.4.

Table 6.3 shows the results of the IST method applied to models of Type II, representing 9 different models. Again, the heading "Elem" is short for element, P_E is the experimental applied load at failure, and P_P is the predicted applied load from the IST method at the point of element failure.

Table 6.3: Summary of Results for Models of Type II

Beam	Model Type	P_E	System Failure			Alternative Failures		
			Elem	P_P (N)	Ratio (P_E/P_P)	Elem	P_P (N)	Ratio (P_E/P_P)
BM12-220	II	382.4	S8	431.98	0.89	S7	431.94	**0.89**
BM16-220*	*II*	*309.3*	*S8*	*409.02*	*0.76*	*S7*	*408.98*	***0.76***
BM25-220	II	360.1	S8	370.52	0.97	S7	370.48	**0.97**
BM12-150	II	405.2	S8	375.76	**1.08**	S7	375.72	1.08
BM16-150	II	416.5	S8	356.26	**1.17**	S7	356.22	1.17
BM25-150	II	415.8	S8	324.08	**1.28**	S7	324.02	1.28
BM12-s230	II	466.9	S8	394.5	**1.18**	S7	394.44	1.18
BM16-s230	II	450.8	S8	374.04	**1.21**	S7	373.98	1.21
BM25-s230	II	444.0	S8	340.52	**1.30**	S7	340.46	1.30
Average* of System Failure Ratios =					1.14			

**Outlier not included in average, see the Results Section for more information.*
*** **Bold** entries highlight ratios closet to unity for each specimen.*

Most of the comments directly following Table 6.2 apply to Table 6.3 and are not repeated.

Models of Type II lumped the area of all stirrup reinforcement into one tie to be representative of typical design techniques; only the area of non-zero force ties were considered.

The results of the analysis on models of Type II show uniform behaviour. The procession of strut failures for all beams occurred first by crushing of inclined strut S7, followed by crushing of the direct-strut S8; and the two crushing loads were only separated by a few load increments, so either crushing load may be considered the system failure load.

The analysis of beams BMX-220, excluding BM16-220, predicted un-conservative failure loads when using this traditional technique for deep beam design. Further, beams BM25-220 and BM12-s230 were not predicted to fail in flexural compression as they were by the analytical models. In general, models of Type II have ratios which are further away from one than those of the analytical model types for the same beam. It is possible that the strut-and-tie approximation of the design models is not as good of an approximation of the flow of forces in the beam as those of the analytical models.

6.1.2 Tensile Failures

The IST method analysis indicated the *possibly* of stirrup tensile failure in the Type III model applied to the BMX-220 series. Recall that the FRP manufacturer provided two design strengths for bent FRP: the bend strength and the straight portion strength. Each of the models which indicated the possibility of stirrup tensile failure computed a maximum stirrup stress which was greater than the bend

strength, but less than the straight portion strength. The author is reluctant to comment how well stirrup failure is predicted when two design strengths are recognized, as no stirrup failures occurred in the experimental program, though some were damaged.

More discussion on the ability of the IST method to predict stirrup behaviour is presented later in this chapter.

6.1.3 The Comparison

Table 6.4 is a comparison of the experimental results to the predicted strengths from the CSA S806-12 methods for compressive flexure and shear, from the Nehdi et al. shear design method, and from the IST method models of this research programme. The parameters used as input into each modelling method were the same for the sake of comparison. Specifics of the geometry and material properties for each method are not reproduced here, but may be readily determined from information in Appendix E. Appendix E contains a beam diagram and table with various parameter values for each experimental beam. The modelling parameter values come from the beam diagrams and the as-designed column of the table. There are two exceptions: 1) the concrete strength used the 28 day as-constructed value, and 2) the elastic modulus of the longitudinal reinforcing for beams BM16-X was assumed to be 60 GPa instead of 64 GPa in the models used by the IST method only. The heading P_E is the experimental applied load at failure, and P_P is the predicted, equivalent applied load at failure calculated from the method directly or indirectly from shear or moment strength predictions using statics or beam diagrams depending on the method and context.

The discussion of the results examines each beam series, moving across Table 6.4 from left to right. It will be followed by brief discussions on the averages and on the beam groups. Recall that beams BM25-X have the lowest longitudinal reinforcing ratio and beams BM12-X have the highest.

The shear strength predictions of CSA S806-12 in Table 6.4 are significantly different from the predictions of Table 3.3 because the calculations of Table 6.4 include a stirrup strength limit of $0.005 \cdot E_f$ as required by the standard. This was omitted from Table 3.3 because the original objective was to investigate the possibility of large stirrup strengths.

For beams BMX-INF, the CSA S806-12 standard predicted shear strengths that were significantly greater than experimental strengths. This is a very significant observation. Such highly un-conservative predictions are unexpected from a design standard. Recall that the CSA S806-12 standard uses the common $V_c + V_s$ approach to compute shear strength, the same equation found in most steel reinforced design standards such as CSA A23.3-04. In fact, Cl.11.2.7(a) of that standard indicates stirrups are necessary when $V_f > V_c$, which implicitly directs designers to assume that V_c is representative of the shear strength of a span without stirrups. However, the equivalent clause in CSA S806-12, Cl.8.4.5.1, indicates that shear spans must include minimum stirrups where $V_f > 0.5 \cdot V_c$. It cannot be known with certainty if this is tacit admission by the Technical Committee that their calculation for V_c doubles the strength of shear-unreinforced spans. Certainly the V_E/V_P ratios in Table 6.4 support this assertion, but a review of available literature suggests that this is not the case at all. The technical committee might be entirely unaware of this behaviour.

It is common for design standards and codes to be overly conservative where the shear design of concrete beams reinforced with FRP stirrups is concerned. The reasons for this should be obvious from reviewing Chapters 1 and 2 of this thesis. This observation on conservativeness is supported by the findings of Machial et al. (2012).

In that paper, Machial et al. (2012) found that the CSA S806-02 standard was generally conservative for beams without stirrups, and so some change to the 2012 edition caused the standard to make un-conservative predictions. More importantly, Cl.8.4.5.1 is identical between the two editions of the standard. It follows that the requirements of Cl.8.4.5.1 in the 2012 edition were rooted in an attempt to

be overly conservative in 2002, and not because of a tacit admission on the un-conservative prediction on V_c.

Table 6.4: Experimental Results and Predicted Strengths

Beam	P_E kN	CSA S806-12 Flexure P_P kN	CSA S806-12 Flexure Ratio (P_E/P_P)	CSA S806-12 Shear P_P kN	CSA S806-12 Shear Ratio (P_E/P_P)	Nehdi et al. Shear P_P kN	Nehdi et al. Shear Ratio (P_E/P_P)	The Analysis Method: Analytical Models Model	Analytical Models P_P kN	Analytical Models Ratio (P_E/P_P)	Design Model (II) P_P kN	Design Model (II) Ratio (P_E/P_P)
BM12-INF	163.1	395.5	0.41	243.7	0.67	144.9	1.13	Ib	145.3	**1.12**	-	-
BM16-INF	150.2	386.4	0.39	235.7	0.64	143.1	**1.05**	Ib	141.0	1.07	-	-
BM25-INF	125.1	348.0	0.36	229.8	0.54	134.5	0.93	Ib	133.5	**0.94**	-	-
BM12-220	382.4	395.5	0.97	292.4	1.31	329.1	1.16	III	391.1	**0.98**	431.9	0.89
BM16-220*	*309.3*	*386.4*	*0.80*	*282.3*	*1.10*	*327.3*	***0.94***	*III*	*395.1*	*0.78*	*409.0*	*0.76*
BM25-220	360.1	348.0	1.03	268.6	1.34	318.7	1.13	III	394.3	0.91	370.5	**0.97**
BM12-150	405.2	395.5	**1.02**	312.4	1.30	368.8	1.10	IVb	375.8	1.08	375.8	1.08
BM16-150	416.5	386.4	**1.08**	301.4	1.38	367.1	1.13	IVb	379.3	1.10	356.3	1.17
BM25-150	415.8	348.0	1.20	283.9	1.46	358.5	1.16	IVb	388.3	**1.07**	324.1	1.28
BM12-s230	466.9	433.6	1.08	404.7	1.15	469.1	**1.00**	III	483.3	0.97	394.5	1.18
BM16-s230	450.8	423.7	1.06	394.1	1.14	467.1	0.97	III	450.8	**1.00**	374.0	1.21
BM25-s230	444.0	380.5	1.17	356.0	1.25	457.5	**0.97**	III	395.2	1.12	340.5	1.30
Average* =			0.89		1.11		1.07			**1.03**		1.14

**Outlier not included in averages, see the Results Section for more information.*

However, it is possible that the experimental results for beam BMX-INF are outliers, but this is generally contraindicated by the good predictions of the Nehdi et al. method and the IST method. Further, if the method of the CSA S806-02 standard for shear strength is applied to beams BM12-INF, BM16-INF, and BM25-INF it predicts strengths of 135.0 kN, 132.1 kN, and 120.3 kN, and P_E/P_P ratios of 1.21, 1.14, and 1.04, respectively. So, the very un-conservative nature of the predictions from the CSA S806-12 code are almost certainly born of the calculation for V_c, and Cl.8.4.5.1 does not likely reflect the fact that the calculation of V_c significantly over predicts the strength of beams without stirrups.

The exact reason for this over prediction is the subject of a paper that the author and his supervisor intend to write shortly after the publication of the experimental results in a yet to be determined journal.

The method by Nehdi et al. is a better predictor of shear strength for beam BMX-INF, though it is neither consistently conservative nor un-conservative in its predictions for the INF series of beams. The Nehdi et al. method was the closest predictor for the strength of beam BM16-INF.

The analytical models of the IST method were the best predictors of beam strength for this beam series. These models most closely predicted the experimental strength of beams BM12-INF and BM25-INF. The models were neither consistently conservative nor un-conservative.

Beams BMX-220 show less clear trends because this beam series contains the outlier BM16-220. The possibility of flexural compression failure was higher for this beam series, but it was never the closest predictor. The S806-12 shear method preformed much better with this series of beams than the previous series. It was the closest predictor for BM25-220, but the predictions were neither consistently conservative nor un-conservative.

The method of Nehdi et al. was the best predictor of strength for the outlier BM16-220. Recall that the outlier is thought to have failed at a much lower strength than anticipated because of an unintended load cycle. If the beam had instead failed at a load between that of the other two beams in the series as expected, then it would be reasonable to say that for this series of beams the Nehdi et al. method was a consistently conservative predictor of beam strength by a margin of 10 percent or more.

The analytical models of the IST method were also good but slightly un-conservative predictors of beam strength; the model for BM12-220 was the closest predictor. The design models of the IST method were also good but slightly un-conservative predictors of beam strength.

The keen observer will note that the analytical models of the IST method do not follow the trend which shows increasing strength with increasing longitudinal reinforcement ratios, but this is because the failure mode for beam BM25-220 was different from the other two beams in the series, see Table 6.2.

Beams BMX-150 were predicted to fail in flexural compression, but this failure mode was the closest predictor for only beam BM12-150. In general, flexural compression failures were probable given the closeness of the stirrup spacing. The S806-12 shear method was the closest predictor for beams BM16-150 and BM25-150, making this the best method for this series. However, this method was neither consistently conservative nor un-conservative.

The method by Nehdi et al. is a conservative predictor of beam strength for this series by a margin of 10 percent or more.

The analytical models of the IST method are good but slightly conservative predictor of beam strength. However, the design models of the IST method under predict the experimental strength by the widest margin of all, and are thus the most conservative predictors.

Beams BMX-s230 were also generally predicted to fail in flexural compression. The S806-12 shear method was a very conservative predictor of shear strength.

The Nehdi et al. method is the best predictor of strength for this series, being the closest predictor for beams BM12-s230 and BM25-s230. However, the Nehdi et al. method is neither a consistently conservative or un-conservative predictor, but did closely predict the strength of the beams.

The analytical models of the IST method were also good predictors of beam strength, but were neither consistently conservative nor un-conservative. The model for beam BM16-s230 was the closest strength predictor. The design models of the IST method under predict the experimental strength by the widest margin of all, and are thus the most conservative predictor.

The bottom of Table 6.4 shows averages for the prediction ratios of each method, which excludes BM16-220. By this metric the analytical models from the IST method are the best predictors overall, with this column containing 5 of the 12 closest predictors. The second best predictor is the method by Nehdi et al., which has 4 of the 12 closest predictors including the outlier beam. The CSA S806-12 model would appear to be the third best predictor according to averages, but the average is just the middle point of two extremes; the method was never the best predictor for any specimen. The CSA S806-12 shear model was very un-conservative for beams without stirrups, and overly conservative for beams with stirrups. The design models of the IST method are the worst predictors of shear strength based on the average; the method was the best predictor for only one beam. The design models are neither constantly conservative nor un-conservative, but its extremes are milder than those of the CSA S806-12 shear method. The CSA S806-12 compressive flexural model was the best predictor for 2 of the 12 specimens, but none of the beams failed in flexural compression.

The results and predictions were also examined by placing them into groups with the same longitudinal reinforcement.

The CSA S806-12 shear method and the Nehdi et al. method both indicate increases in strength with decreases in stirrup spacing, which conforms to expected beam behaviour. However, models of the IST method do not show this same trend, instead they show a large increase in strength when going from

no stirrups to some stirrups, and a decrease in strength when going from stirrups spaced at 220 mm to stirrups spaced at 150 mm. It is possible that a strut-and-tie model that better approximates the flow of forces may better reproduce the expected behaviour. Beams BMX-s230 had the largest expected strengths overall, but this may be due to their larger cross-sections and thicker stirrups. As expected, the compressive flexure model was identical for beams with identical cross-sections.

An examination of the ability of the prediction methods to closely predict beam strength did not show any useful trends when beams were grouped by longitudinal reinforcement. Three of the analysis methods were equally the closest predictors, each being the closets predictor for 2 beams.

6.2 Analysis of Beam Behaviour

In this section of the Analysis Chapter, the experimental strength of each beam is decomposed into two components to seek further insight into beam behaviour: the concrete contribution, V_c, and the stirrup contribution, V_s. This exercise was insightful despite the specimens behaving like deep beams. Those results are then plotted alongside the flexural and shear reinforcement ratios; many other comparisons were made, but ultimately the most informative comparisons came from the reinforcement ratios.

6.2.1 Determining the Concrete Contribution to Shear Strength

The shear strength of slender beams, V_r, in design methods is found by summing the shear strength contributions from the concrete, V_c, and from the stirrups, V_s. This method is common to the vast majority of design codes and standards the world over, though methods for calculating V_c and V_s are unique to each. The rationale for this equation will not be discussed here, and an explanation may be found in any modern text on the design of concrete members, such as MacGregor et al. (2000).

This method is useful for slender beam design but is generally not recommended for the design of deep beams. Deep beams transfer forces directly from the load point to support points through a direct-strut in some proportion to the shear-span-to-effective-depth ratio. The closer this ratio approaches zero the more the element will behave like a column, and the further it tends to infinity the more it will behave like a slender beam.

This approach differs from the state-of-the-art, where the increasing strength of the deep beams with increasing shear reinforcement ratio is attributed to the effects of confinement. That is, the stirrups act to confine the core of the concrete beam and restrain the opening of cracks while simultaneously decreasing the tensile strains acting perpendicular to the principle compressive stress field after initial cracking. Since the compressive strength of concrete is proportional to these tensile strains, the presence of stirrups increases the concrete strength. Unfortunately, confinement based methods are still being developed, and most apply to concrete columns (Montoya et al., 2004). Confinement based methods for the shear strength design of deep beams are not readily available in literature.

There are three methods for defining V_c: 1) the load at which the first shear or flexural-shear crack forms, 2) the strength of an equivalent beam without stirrups, or 3) back calculating from the strain in the stirrups.

The first method may be done by recording the load at which shear cracks formed during the experiment, but this was not done. Photographs of the cracking pattern for the beams were taken each time loading was paused for crack width measurements, but there is no good method for using those photographs to interpolate the value of V_c. Instead, plots of applied load against stirrup strain, found in Appendix E, were used.

The shear cracking load may be reasonably estimated from the points where the stirrup strain curves dogleg, and then selecting the point with the lowest load. In this case, a dogleg is defined as a sharp increase in strain with little increase in load. The choice of specific V_c value requires judgement;

other observers may have chosen a different value, but they would likely all be similar. Figure 6.2 shows the four points where V_c is measured, and the point with the lowest load value defines V_c.

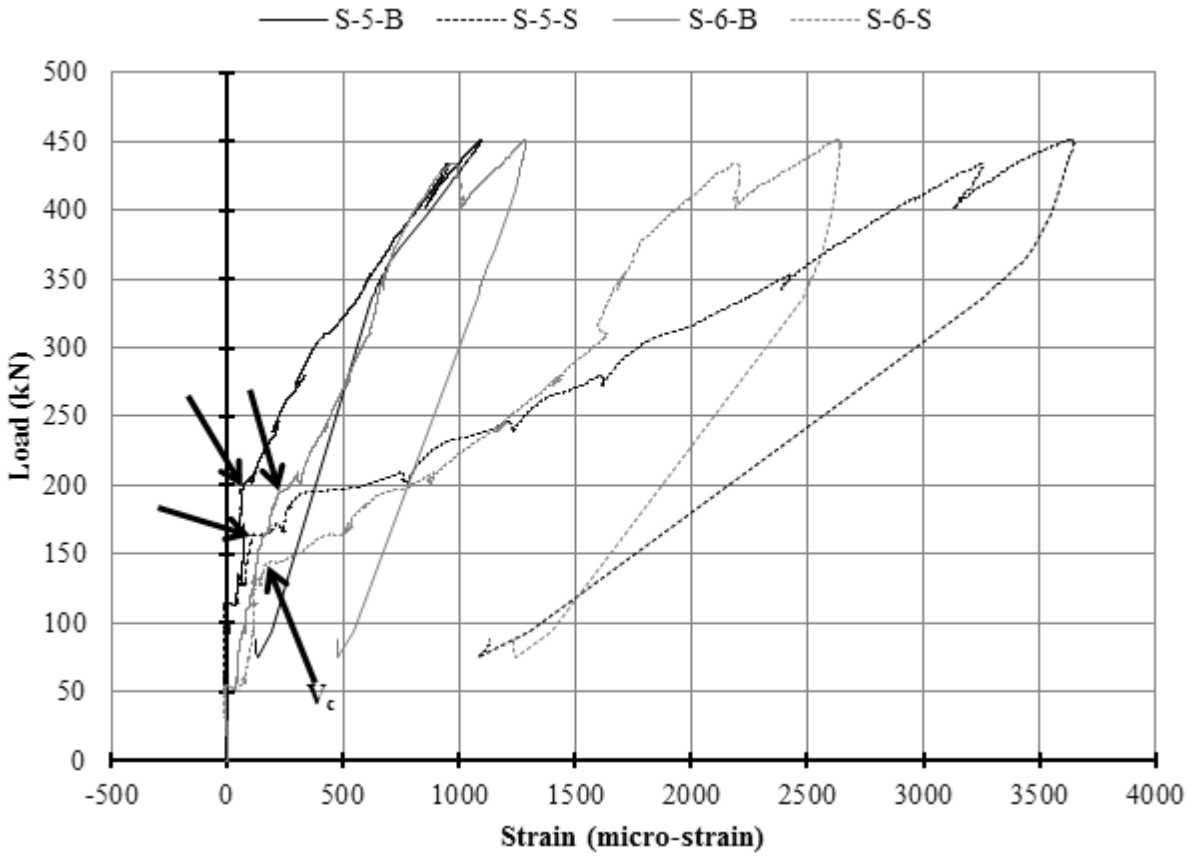

Figure 6.2: Determining V_c from load vs stirrup strain plots for BM16-s230

This method relies on the assumption that cracking started with flexural cracks forming at the location of the stirrups and then progressing into flexural-shear cracks before the formation of shear cracks, which was generally the case with the experimental beams. The load at which a crack moves from a flexural crack to a flexural-shear crack was assumed to be associated with the dogleg in the strain curve.

The second method is simpler; the value of V_c is set equal to the peak load of the respective BMX-INF beam. Beams BMX-s230 were taller and wider than their counterparts, so the V_c load for those beams was estimated by multiplying the peak load for the respective BMX-INF beam by the ratio of the area of the BMX-s230 beam over the area of the BMX-INF beam. This was thought justified since the BMX-s230 beams were not significantly taller than their counterparts and the influence of size- and strain-effects would be minimal.

The third method was inspired by the paper of Nakamura et al. (2006) discussed earlier in the Experimental Design Chapter, and is possible because all of the beams with stirrups failed along a plane that intersected every stirrup. The load carried by the stirrups, V_s, was computed from the stirrup strains and thus the concrete contribution, V_c, was computed by subtracting the stirrup contribution from the applied shear, V_A, at each data point along the stirrup strain curves ($V_c = V_A - V_s$). The concrete strength is then set equal to the data point with the largest concrete contribution.

Certain assumptions are necessary to apply this method. Recall that stirrups were instrumented in two locations; one gauge was located at the lower bend of one stirrup leg, and another was located on the

straight portion of the opposite leg. The gauge data used in this method was from the one with the largest strains overall, which assumes that it was closest to the crack. Recall from the Results Chapter that straight portion gauges had the largest strains most often; only one beam used data from a stirrup bend. Further, it was assumed that the strain in one stirrup leg was representative of the strain in both stirrup legs.

The method considers shear strength, so the applied shear, V_A, was assumed to be equal to one-half the applied load since the supports were symmetric about the load point. Though, this assumption becomes less appropriate with significant deformation and crushing.

Application of this method would seem problematic, since the only beams to fail in the instrumented span were BM25-220 and BM12-150, and these beams also had stirrup strain gauges which failed before peak load. However, consider Figure 6.3, which shows shows the results of this method applied to beam BM25-150, a beam without strain gauge failures but which failed in the un-instrumented span.

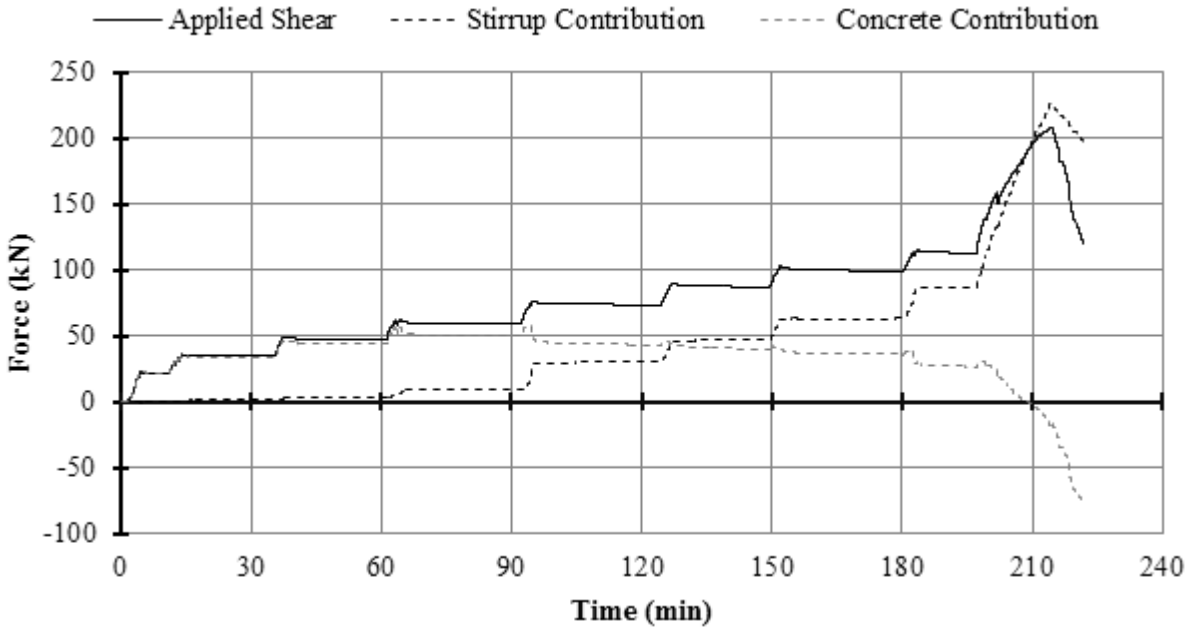

Figure 6.3: V_A, V_s, &V_c curves for BM25-150

According to this method the V_c curve reached a maximum value of 57.9 kN, at a time of 91.24 min, when the applied load was approximately 35 percent of the peak load. This implies that peak concrete contribution is reached well in advance of problematic points. At this load, flexural-shear and shear cracks had formed on both spans, but significant deformation had not taken place. It is reasonable to assume that both spans still have similar stiffnesses and thus draw a similar amount of the applied load.

However, the curves indicate that the stirrup contribution exceeds the applied load as loading approaches peak load, which is unexpected. Further, this curve is generally representative of all the specimens with stirrups, which requires some explanation for beams which did and which did not fail in the instrumented span.

One explanation for why beams which failed in the instrumented span might show this behaviour is that the stirrups had to accommodate geometric compatibility arising from significant deformation and crushed concrete. Whereas this behaviour in the non-failed span past peak load occurs because that span is stiffer and thus draws more than 50 percent of the applied load. This plot for other specimens may be found in Appendix E.

The results from each of the methods are shown in Table 6.5. The peak shear load, V_E, is half the peak load of the specimen. The stirrup contribution is found by subtracting the concrete contribution from the peak shear load, $V_s = V_E - V_c$. In all beam specimens, the peak concrete contribution occurred at a load level so low that no strain gauges had yet failed.

Table 6.5: Estimates on the Concrete Contribution, V_c

Beam	V_E kN	Method 1 V_c kN	Method 1 V_s kN	Method 1 (V_c/V_E)	Method 2 V_c kN	Method 2 V_s kN	Method 2 (V_c/V_E)	Method 3 V_c kN	Method 3 V_s kN	Method 3 (V_c/V_E)
BM12-220	191.2	60.0	131.2	0.31	81.5	109.7	0.43	84.8	106.4	0.44
BM16-220*	*154.6*	*56.5*	*98.1*	*0.37*	*75.1*	*79.5*	*0.49*	*95.5*	*59.2*	*0.62*
BM25-220	180.0	63.5	116.5	0.35	62.6	117.5	0.35	53.8	126.2	0.30
BM12-150	202.6	70.0	132.6	0.35	81.5	121.1	0.40	57.6	145.0	0.28
BM16-150	208.3	58.5	149.8	0.28	75.1	133.2	0.36	58.4	149.9	0.28
BM25-150	207.9	73.5	134.4	0.35	62.6	145.4	0.30	57.9	150.0	0.28
BM12-s230	233.5	67.0	166.5	0.29	97.8	135.7	0.42	68.5	165.0	0.29
BM16-s230	225.4	70.5	154.9	0.31	90.1	135.3	0.40	66.3	159.1	0.29
BM25-s230	222.0	69.5	152.5	0.31	75.2	146.8	0.34	55.5	166.5	0.25

**Outlier, see the Results Section.*

Table 6.5 shows that Method 2 tends to predict the highest values of V_c, with Method 1 predicting the second highest, and Method 3 predicting the lowest. Further, the ratio of V_c over V_E is never different by more than 0.13 per specimen, and some specimens have similar predictions according to all three methods.

The problem with Method 2 is that it provides no information on changes in the concrete contribution when it is compared to any of the other parameters, because the concrete contribution is constant. The results of Method 2 are also interesting when compared to the other methods because confinement effects should increase V_c when compared to an equivalent beam with no stirrups; but Methods 1 and 3 do not predict concrete contributions larger than the strength of the BMX-INF counterparts, with one exception and excluding the outlier. Further consideration of the concrete contribution is provided following Figure 6.4, which shows a comparison of Methods 1 and 3.

Figure 6.4 shows that the concrete contribution is generally constant for Method 1. Beams BM12-X are the tallest beams and should show larger V_c values, and beams BMX-s230 are widest and should also show larger V_c values. However, the differences in the experimental parameters may have been too slight to show up in the concrete contribution when experimental error is considered. Also worthy of note is that the V_c value for BM16-220 from Method 1 is accurate because the stirrup strain curve doglegged before the power failure.

Much the same can be said about Method 3, which shows a constant concrete contribution from each beam with beams BM12-220 and BM16-220 excepted. BM16-220 is the outlier; however, no explanation is offered for the V_c value of BM12-220 as it is simply born out of the data.

The choice of method to represent the concrete contribution, V_c, is Method 1. This choice is though justified since the results of Method 1 are consistent, unlike Method 3, but are capable of accounting for some amount of experimental variability, unlike Method 2, and since they are capable of capturing the behaviour of the outlier. The values for V_c used in the remainder of this section will come from Method 1.

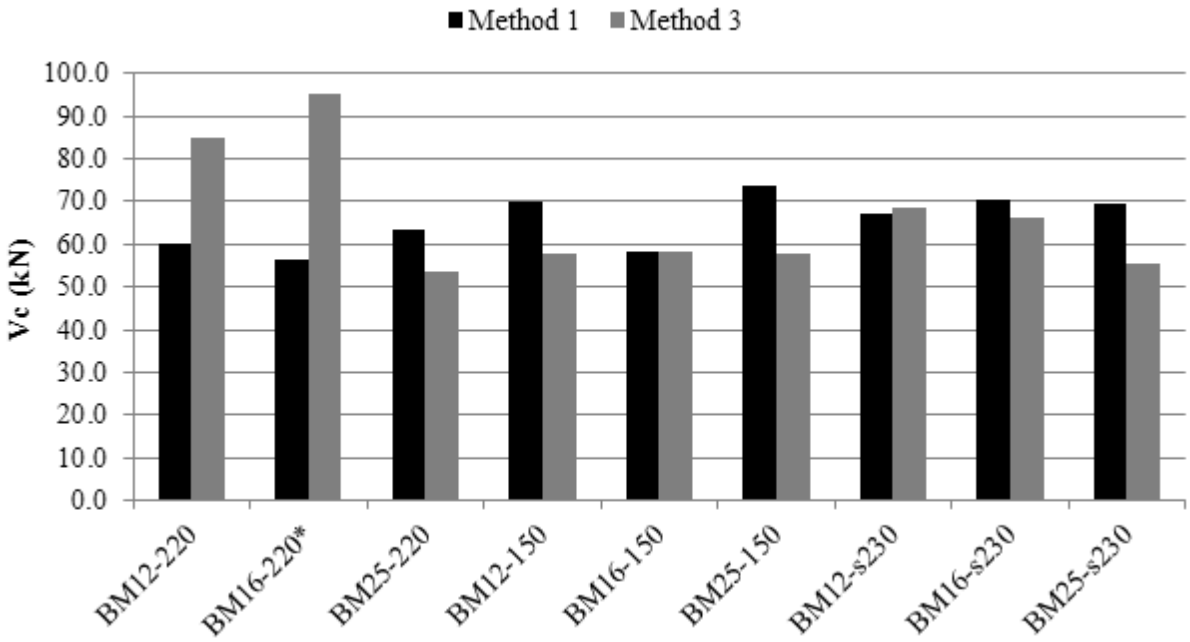

Figure 6.4: Concrete Contribution Comparison Chart

6.2.2 Experimental Beam Behaviour

The reason for considering the concrete contribution was that they might show insight into beam behaviour, even if these methods are inaccurate predictors of the concrete contribution. In general, all three methods indicate that the concrete contribution is effectively constant for beams with similar cross-sections and flexural reinforcement ratios, regardless of shear reinforcement ratio.

However, this observation allows the increase in shear strength to be attributed entirely to the stirrup contribution, V_s, which is simply the portion of the shear strength that may be attributed to the presence of stirrups; all beam failures were concrete controlled.

Figures 6.5 and 6.6 show the variation in V_c, computed using Method 1, against the flexural and shear reinforcement ratios of the beam specimens, respectively.

The plots of Figures 6.5 and 6.6 suggests no correlation between V_c and the main input parameters. Beams BMX-INF were included in Figure 6.5 using their experimental shear strengths for comparison; however, it is well known that beams without stirrups show a strong correlation between shear strength and flexural reinforcement ratio.

An investigation into the variation of the stirrup contribution was more promising. Stirrup contribution values were computed as indicated in Table 6.5 using values from Method 1. Figure 6.7 shows the variation in V_s against the shear reinforcement ratio of the beam specimens.

Figure 6.7 shows a clear trend of increasing stirrup contribution with increasing reinforcement ratio, but with diminishing returns for larger reinforcement ratios. This observation suggests that each stirrup is utilized less as more stirrup area is added to the span, even as beam strength increases with more stirrup area. Figure 6.8 clarifies this observation by plotting the variation in average stirrup stress against the shear reinforcement ratio of the beam specimens.

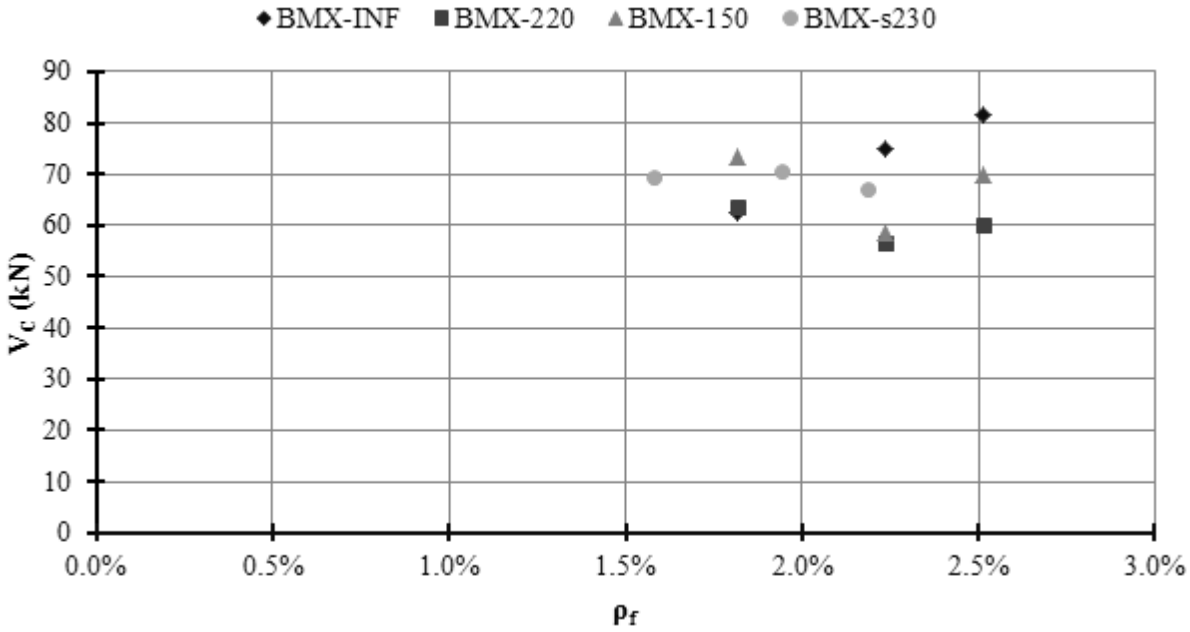

Figure 6.5: Variation in V_c with Flexural Reinforcement Ratio

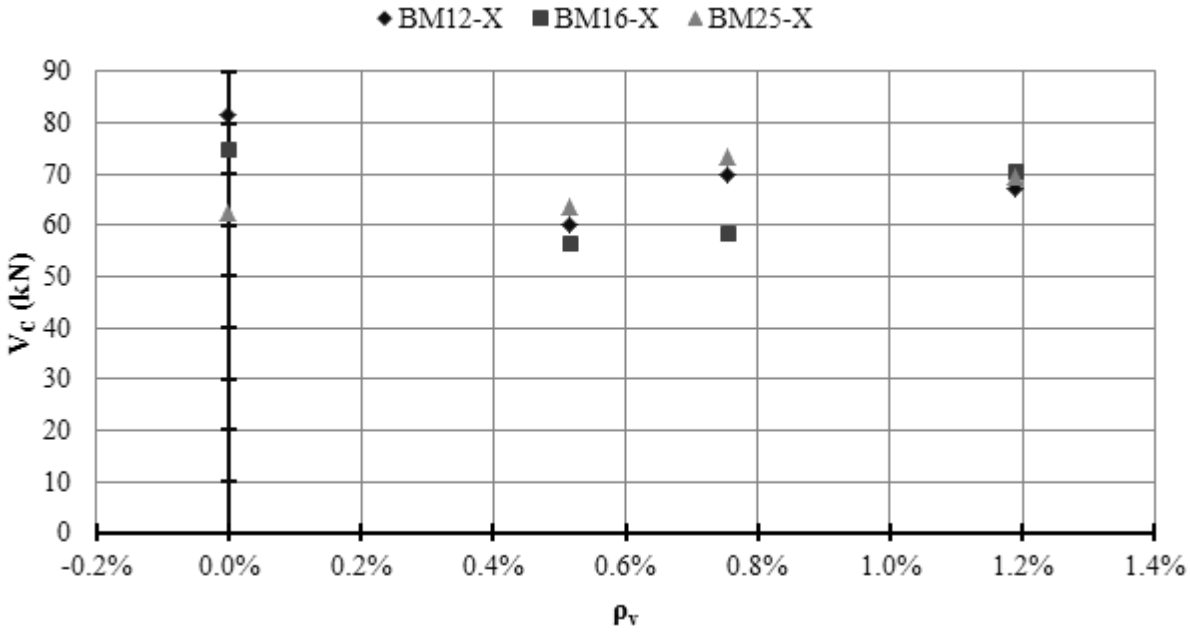

Figure 6.6: Variation in V_c with Shear Reinforcement Ratio

The average stress was calculated by dividing V_s by the total area of stirrups in one span. This plot clearly shows that as the area of stirrups in the span becomes large the force in the stirrups decreases even as beams become stronger. If this were steel then this observation would be called load redistribution or load sharing.

However, this is not the reality of the experiments: stirrup strain plots, found in the Results Chapter, clearly show that some stirrups will have significantly larger strains than their neighbours, and because FRP stirrups rupture there is no possibility of load redistribution wherein stirrups may be

assumed to bear an equal portion of the load. Further, the method by which V_s was calculated does not actually represent average stirrup strains, stress, or forces; it is simply the difference between the peak experimental load and the assumed concrete contribution.

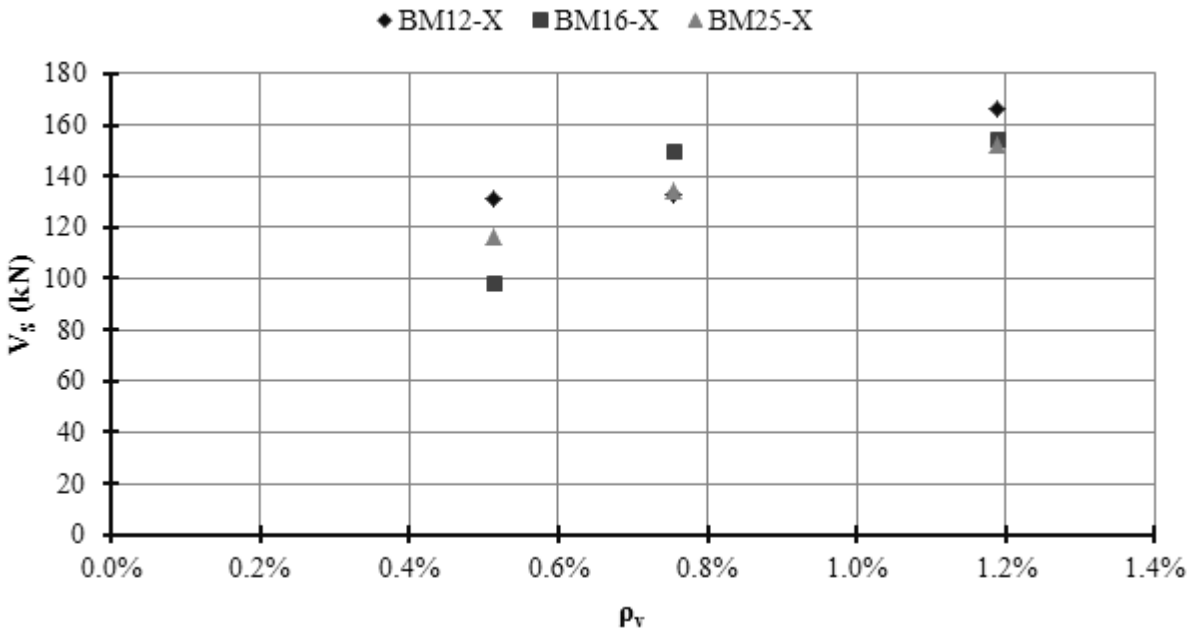

Figure 6.7: Variation in V_s with Shear Reinforcement Ratio

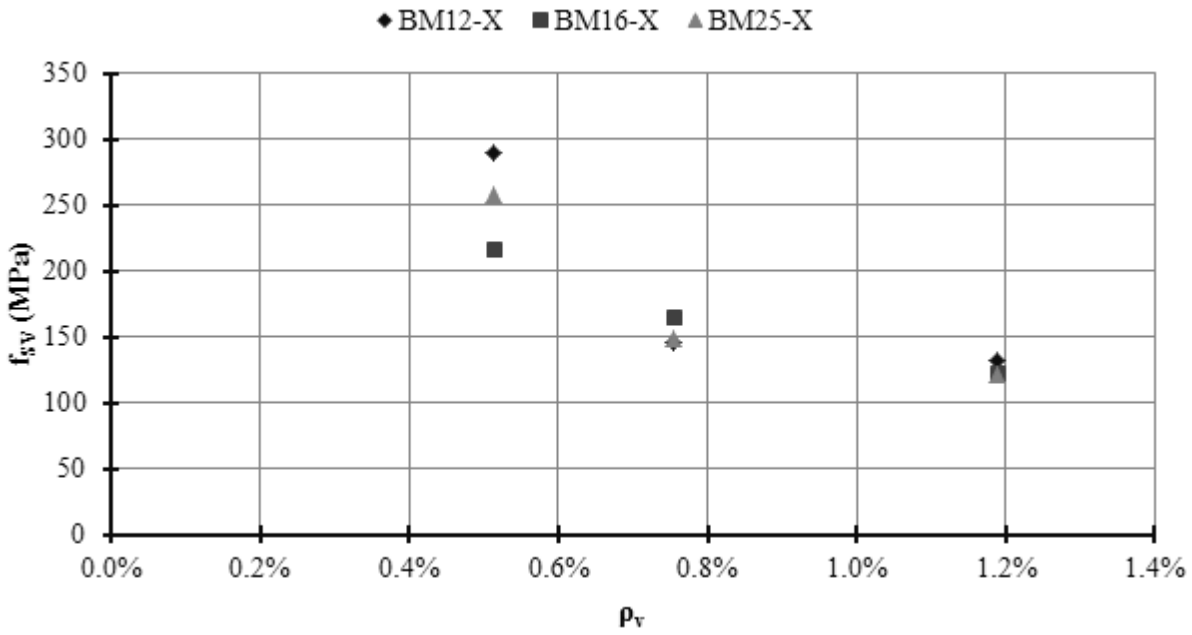

Figure 6.8: Variation in V_s with Shear Reinforcement Ratio

Rather, this plot shows that when failure nucleates in the concrete, the confinement affected shear strength increase has diminishing returns with increases in confinement, where confinement is provided by way of closed loop stirrups.

No stirrup contribution correlations were present when compared with the flexural reinforcement ratio.

A plot of the full experimental strength against the shear reinforcement ratio is not included because the plot is very similar to Figure 6.7, since the strength values are increased by the effectively constant value of V_c. Further, a plot of the full experimental strength against the flexural reinforcement ratio is not included because only beams BMX-INF show any correlation with this parameter. However, Figure 6.9 shows a plot of the product of the peak load and flexural reinforcement ratio against the shear reinforcement ratio. Curves produced using the Nehdi et al. method were included to clarify observations.

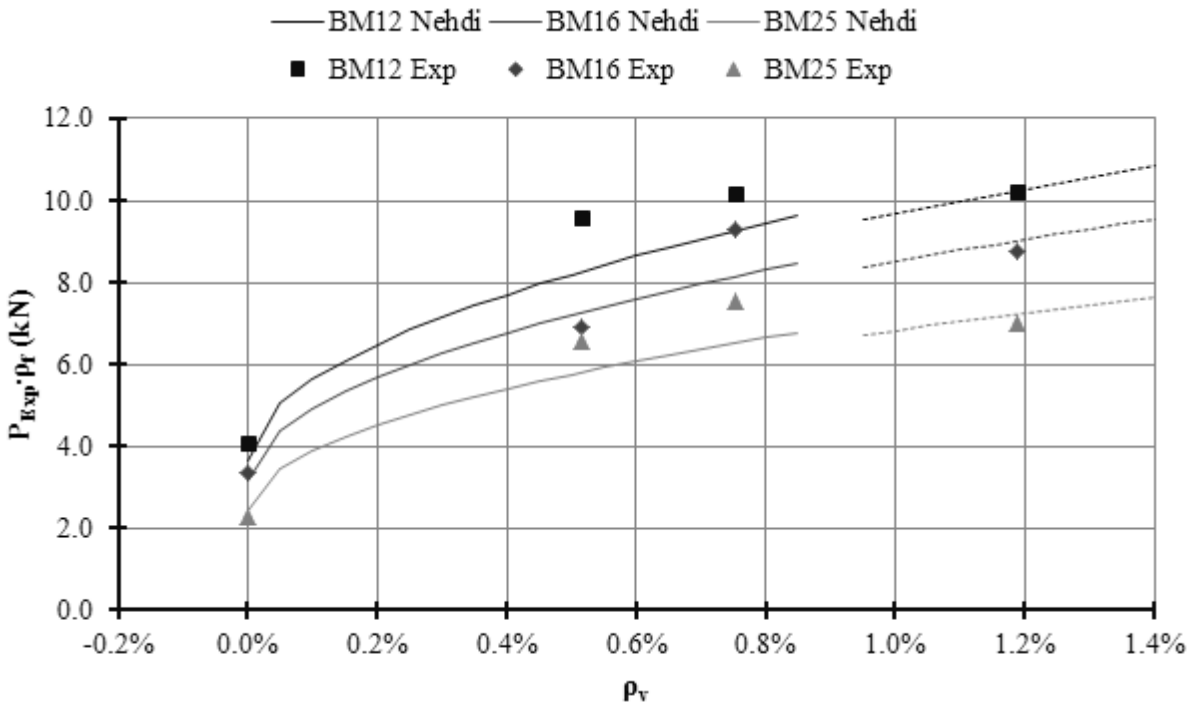

Figure 6.9: Variation the Product of Peak Load and Flexural Reinforcement Ratio against Shear Reinforcement Ratio

Figure 6.9 effectively shows the primary experimental result plotted against all of the primary experimental parameters, except for beam width which is present in the denominator of both the shear and flexural reinforcement ratios. The plot shows that beam shear strength is correlated with both the flexural and shear reinforcement ratios, and strength increases with an increases in either ratio. This plot, and the trend highlighted by the curves, also shows diminishing returns with increases in the amount of shear reinforcement.

The curves from the method by Nehdi et al. are included to clarify the experimental trends. Recall that beams BMX-s230 have larger cross-sections than their counterparts but the same amount of flexural reinforcement, so their flexural reinforcement ratios are lower. If one were to assume the same curve for all beams of the same longitudinal reinforcement size then one may incorrectly suspect a peak and subsequent decrease in shear strength when flexural and shear reinforcement ratios are simultaneously considered. Similar curves for the method of the CSA S806-12 standard and the IST method are not included because of the intense amount of computation required to produce them.

6.3 Investigation into the Ability of the Indeterminate Strut-and-Tie Method to Model Beam Behaviour

In this section the output from the IST method is compared to other experimental data to investigate the ability of the method to capture beam behaviour, such as strains in the longitudinal bars and stirrups, and mid-span displacement. The investigation examines plots in terms of the applied load against the particular characteristic, and then tables to examine the characteristic at peak load.

Recall that the IST method is predicated on the lower bound theory of plasticity. This theory only requires equilibrium and an admissible stress-field, but neither requires, nor expects, displacement compatibility or admissible strain-fields. The upper bound theory of plasticity is the corollary, which requires displacement compatibility and admissible strain-fields, but not equilibrium or admissible stress-fields. T. J. Stratford (2001) wrote a very thorough thesis on the application of the upper bound theory to concrete beams with brittle reinforcements, with a specific shear focus, which serves as a counterpoint to the IST method.

6.3.1 Capturing Strain and Displacement Behaviour

The beams in the plots of this behaviour were chosen because they did not have any premature instrumentation failures which would affect the presentation of data, though some may have had failures occur after peak load. Only a select few beams are shown, but similar plots for all beams may be found alongside the experimental results in Appendix E.

Figures 6.10 and 6.11 are plots of the applied load against the longitudinal strain at mid-span. The plots include the experimental data from gauge readings, and output of the IST method. The strain from the IST method comes from the tie connected to the mid-span node in the tension chord of the strut-and-tie models.

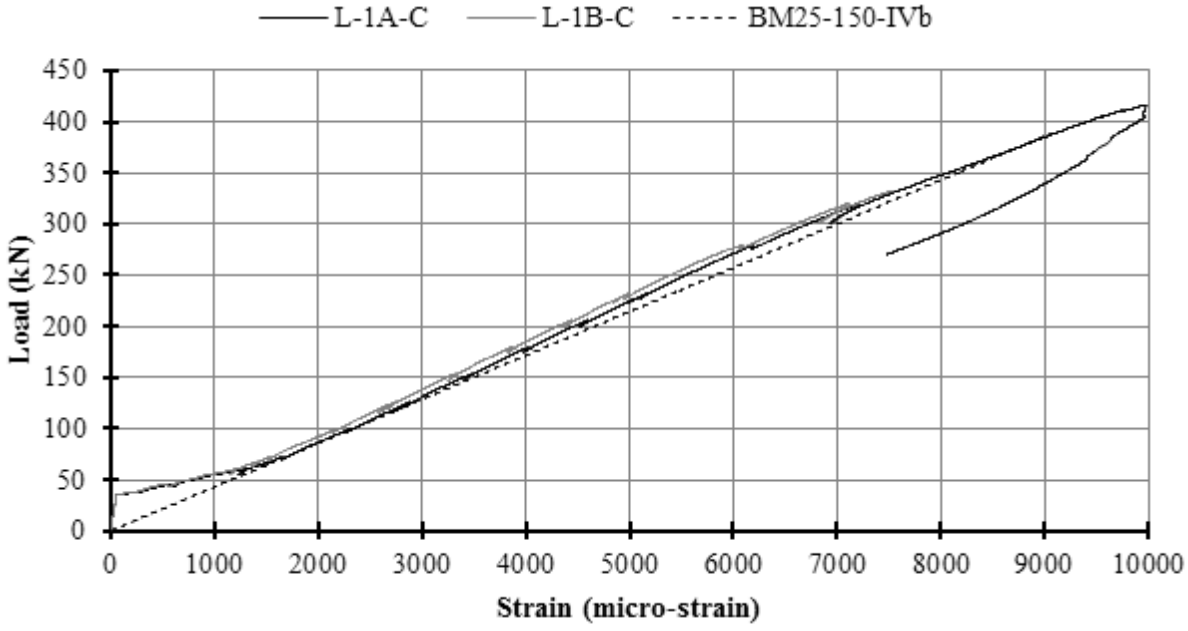

Figure 6.10: Longitudinal Strain at Mid-Span for BM25-150 with the IST Method Prediction

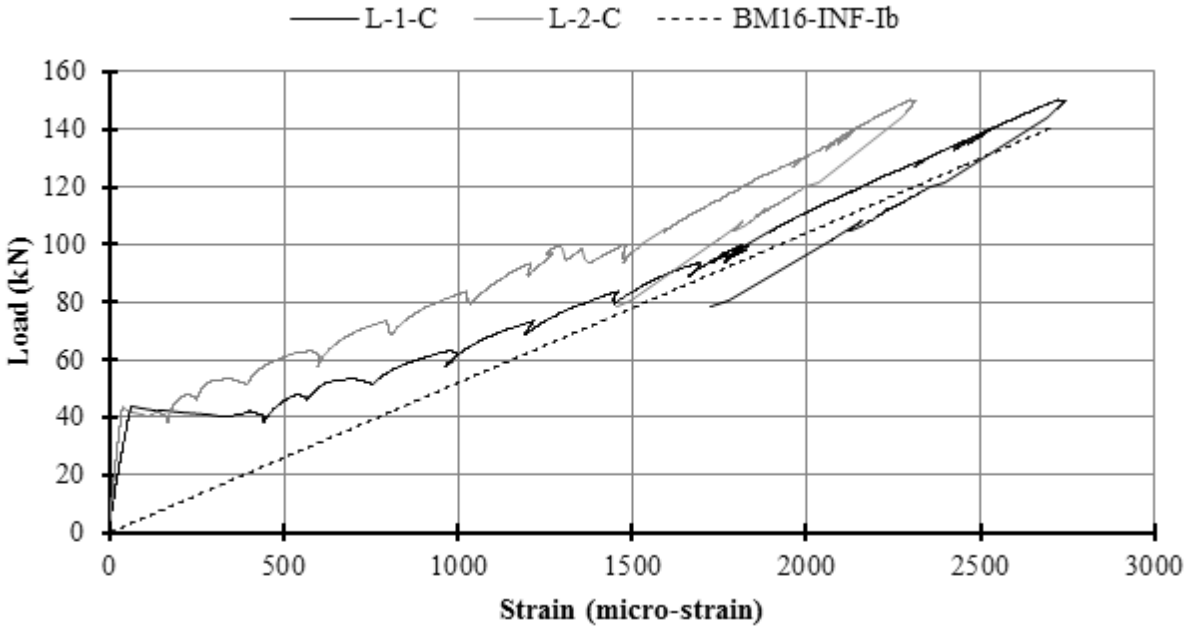

Figure 6.11: Longitudinal Strain at Mid-Span for BM16-INF with the IST Method Prediction

Figure 6.10 shows that after cracking, the experimental curves and prediction curve converge and maintain a fairly similar slope until failure, and this behaviour was observed for all test specimens. In general, the IST method is capable of capturing mid-span longitudinal strain behaviour after cracking.

Three key observations should be made about the prediction curve. First, the prediction curve is linear. Neither the location of the compression stress block strut, nor the longitudinal tie, change during analysis, and so the moment arm between them remains constant. Simple sectional analysis shows that, under a point load, the internal force couple is linearly related to the applied load; ergo, the strain at mid-span is in linear proportion to the applied load.

Second, the slope and location of the prediction line matches very closely the slope of the experimental curves after cracking. This is because the depth of the compression stress block strut was set equal to the depth of the compression stress block at flexural compression failure; a metric which is a good predictor of the actual neutral axis of a beam at flexural failure. However, the depth of the neutral axis is reflected in the growth of the mid-span crack, which slows with loading. The analysis suggests that the depth of the experimental compression stress block appears to be established well ahead of any failure, be it shear or flexural. For these reasons, the IST method captures the behaviour of longitudinal reinforcing strains at mid-span.

Third, the ability of the IST method to capture the behaviour of longitudinal reinforcing strains at mid-span could be improved by incorporating tension stiffening behaviour in the longitudinal reinforcement, as suggested in Chapter 5. Tension stiffening would make the stiffness dependant on the elasticity and area of concrete around the reinforcement up to the point of cracking, this stiffness would be quite large. After cracking, the stiffness of the tie would soften over a period until it was essentially equal to that of the longitudinal bars alone.

Figure 6.11, which presents the results of a beam without any stirrup reinforcement, shows a better focus on the strain region where tension stiffening would occur. So, if tension stiffening were incorporated then the prediction curve would potentially follow the steepness of the experimental curve initially, and then gradually soften just like the experimental curve.

Such work would require the incorporation of another non-linear material model into the IST method, and is beyond the scope of this research programme, and that work is left to others.

Figures 6.12 and 6.13 are plots of the applied load against the stirrup strain. The plots include the experimental data from gauge readings, and output of the IST method. The readings were taken from the same gauges used to determine the concrete contribution, V_c, values by Method 3 in the previous section. Recall that the force analysis of a typical truss will indicate that all vertical members have the same internal load, assuming the vertical members are identical; so it is only necessary to show the strain in one stirrup for the analysis.

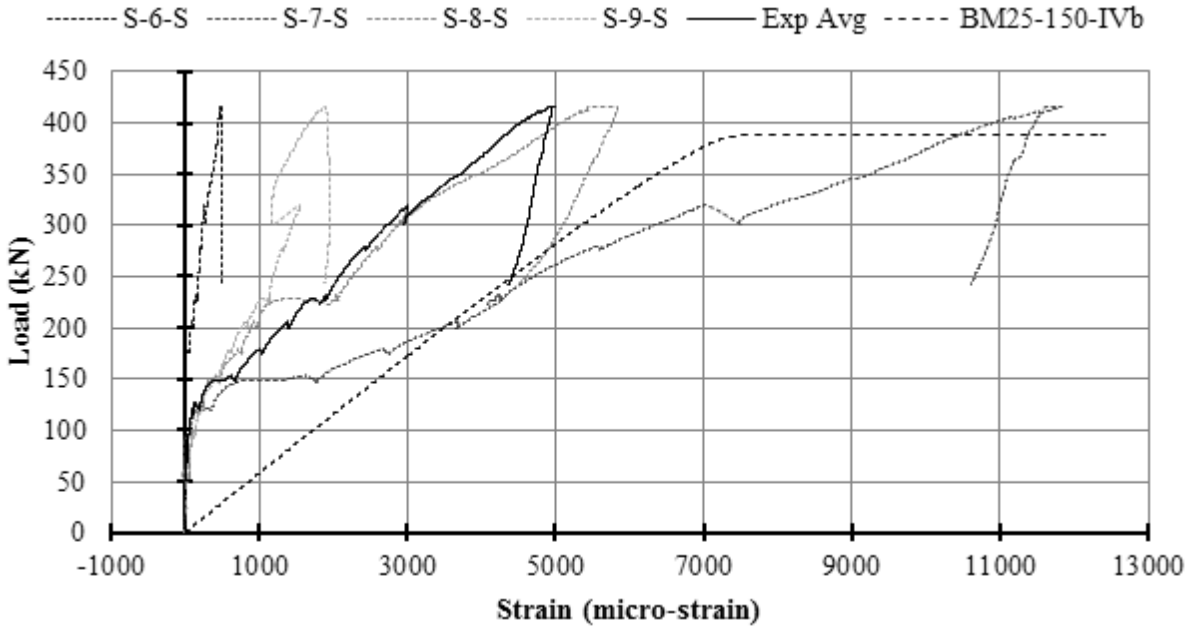

Figure 6.12: Stirrup Strain for BM25-150 with the IST Method Prediction

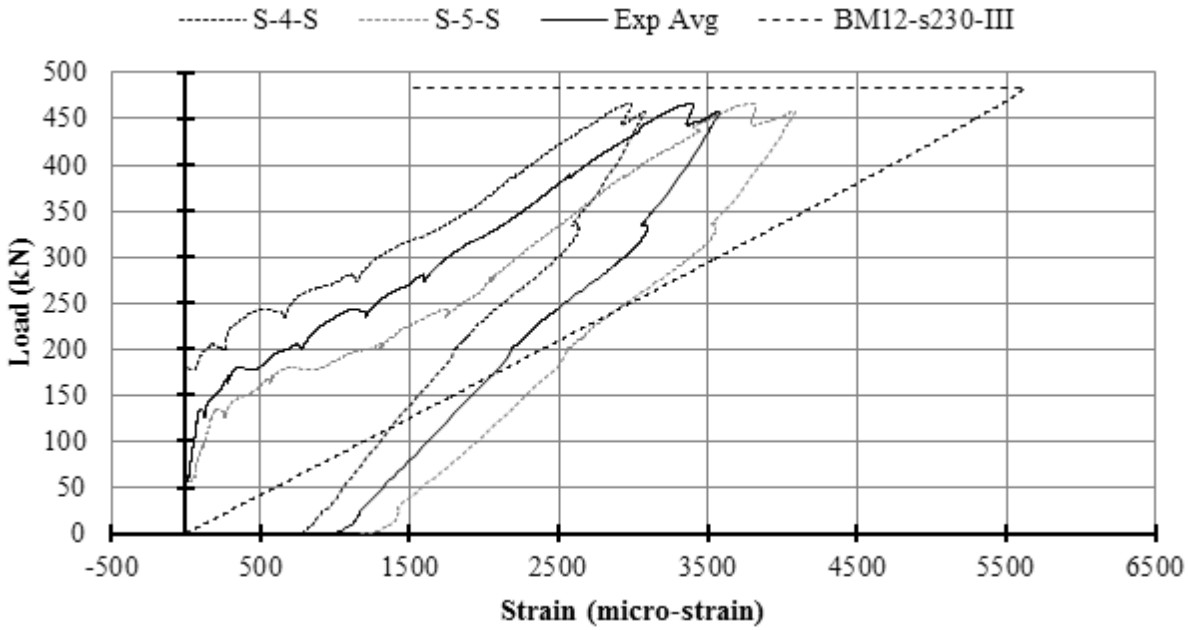

Figure 6.13: Stirrup Strain for BM12-s230 with the IST Method Prediction

Figures 6.12 and 6.13 both include individual curves for each strain gauge, but also include a curve which is an average of the readings. This average curve was the one used to compute the stirrup contribution, V_s, in the previous section according to Method 3. The plots also include the stirrup strain prediction according to the IST method.

The figures indicate that the IST method does not capture the behaviour of the strains in individual stirrups. However, the slope of the prediction tends to match the slope of the average strain curve. It is possible that incorporating tension stiffening in the stirrup tie elements will improve the ability of the model to predict the average stirrup strain in a manner similar to that which was described for longitudinal strains. However, the nature of the cracking which softens the response of the stirrups is not entirely similar to that which softens the response of longitudinal bars.

The prediction curves in Figure 6.12 and 6.13 show a very sharp change in slope, which is associated with the crushing of the first strut. When the first strut crushes the model loses a force transfer mechanism, and so the force going through the remaining mechanism effectively increases to the total applied load. In the case of Figure 6.12 the first mechanism to fail was the direct-strut and thus stirrup strains increase quickly; whereas in Figure 6.13 the first mechanism to fail was the stirrup-truss, and thus stirrup strains decrease quickly. Recall that the IST method sets the elasticity of crushed struts to one percent of their initial elasticity, so some load is still transferred through the failed mechanism.

Figures 6.14 and 6.15 are plots of the applied load against the mid-span displacement. The plots include the experimental data from LVDT readings, and output of the IST method. The IST method displacement comes from the mid-span node in the tension chord of the strut-and-tie models.

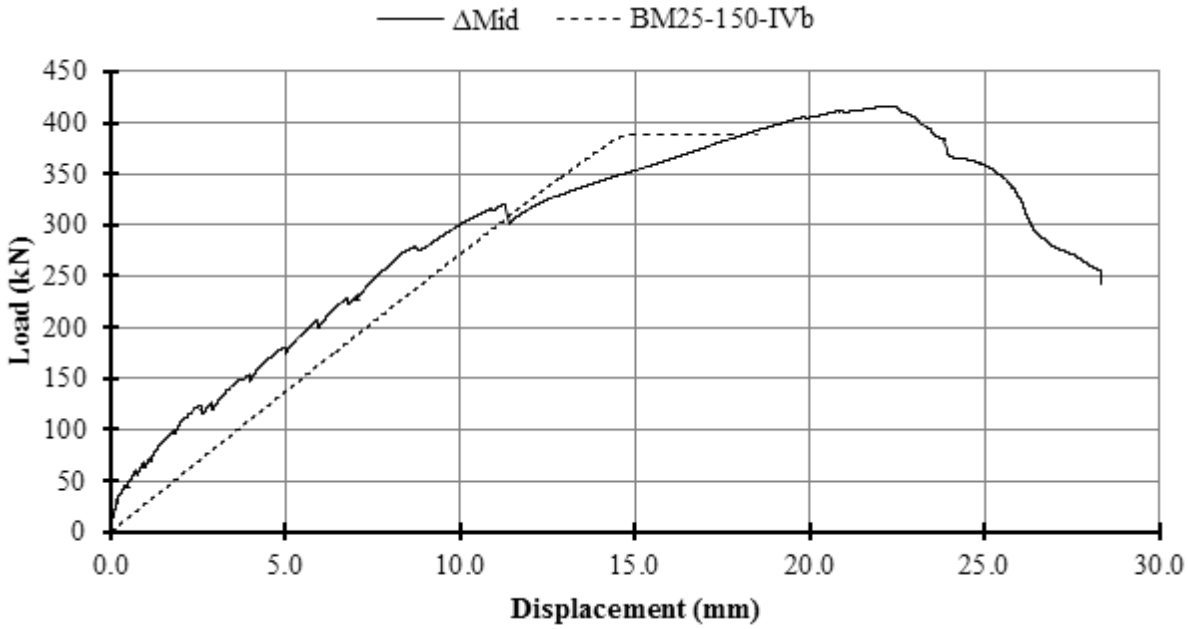

Figure 6.14: Mid-Span Displacement for BM25-150 with the IST Method Prediction

Figures 6.14 and 6.15 show that, in a very general sense, the IST method captures mid-span displacement behaviour. However, the values of displacement at peak load do not coincide. The initial slope of the prediction curve tends to match the slope of the experimental curve after cracking and up to just before peak load. The prediction curve appears to capture the post-peak ductility of beam BM12-s230 in Figure 6.15, but this is coincidence; recall that the data recorder continued to record information as load was removed to capture the amount of permanent displacement. The IST method cannot capture post-peak ductility because the IST method can never provide a negative slope to the prediction curve of

this plot, and so it is not able to capture post-peak behaviour like that shown by the LVDT readings in Figure 6.14.

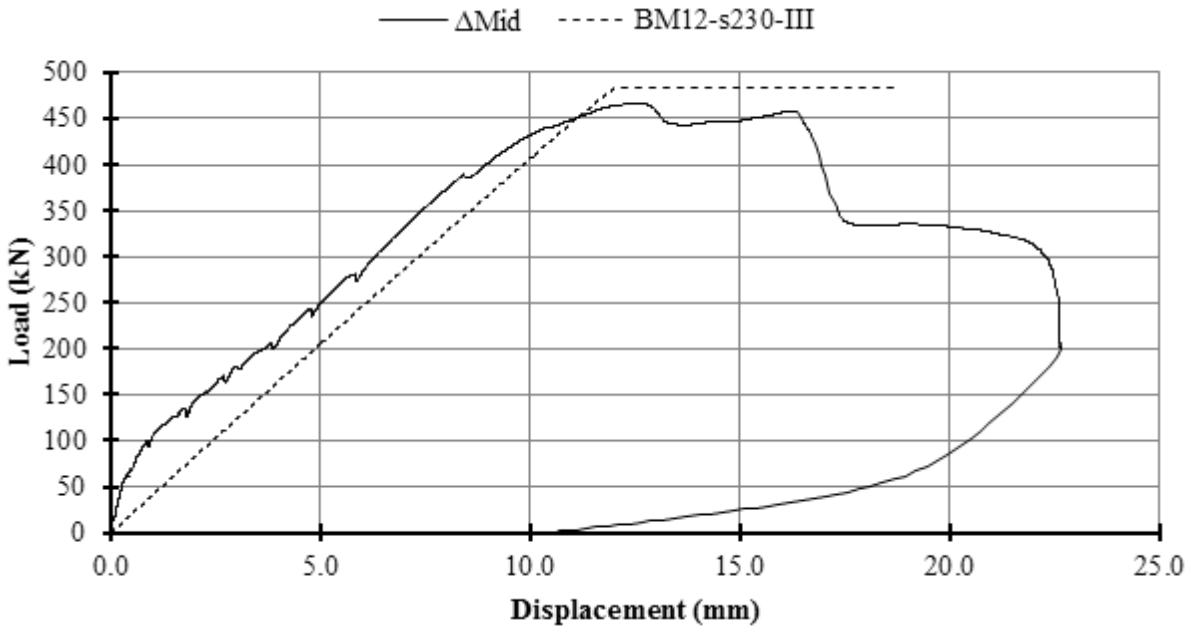

Figure 6.15: Mid-Span Displacement for BM12-s230 with the IST Method Prediction

The incorporation of tension stiffening behaviour in the longitudinal reinforcement would likely improve the ability of the model to capture mid-span deflection behaviour. The predicted response would be stiffer initially, thus reproducing the initially steeper slope of the experimental results.

It should be noted that the prediction curves in Figure 6.14 and 6.15 only appear bi-linear; however, they are actually made of a single non-linear curve, albeit with highly linearized portions. The initial linearity is related to the longitudinal strains, which as noted previously, are linear for these models. The second linear portion is made up of the very few data points which lie between the crushing of the first strut and stability failure.

It is remarkable that a strut-and-tie modelling method, which is founded in the lower bound theory of plasticity, is capable of capturing the behaviour of the beam specimens as well as it has.

6.3.2 Strains and Displacements at Peak Load

Tables 6.6 through 6.8 show a summary of the experimental results and the output of the IST method models used in constructing Table 6.4. The experimental results are taken from the point of peak load and the results from the IST method are taken at the crushing of the first strut and the point of system failure.

Table 6.6 shows all of the strain gauge readings for each mid-span longitudinal gauge at the point of peak load. Recall that gauges with a higher label number were placed in reinforcing layers which were higher in the beam. Beams BM25-X had only one layer of reinforcing comprised of two bars, so gauges 1A and 1B were at the same depth, but were placed on opposite bars.

The table also shows the strain in the longitudinal tie at mid-span for models of the IST method; only one strain value is predicted for all layers because the tie lumped all layers of reinforcement together and was centred at the effective depth of the beam. Strains at the crushing of the first strut are nearly

identical to those at the point of system failure, so adjacent to the predicted strain values is the ratio of the experimental strain over the predicted strain at system failure.

Table 6.6: Summary of the Ability of the IST Method to Predict Longitudinal Strains at Mid-Span

		Experimental	The IST Method					
			Analytical Models			Design Models		
Failure Condition →			1st Strut	System		1st Strut	System	
Beam	Gauge	Strain (micro)	Strain (micro)	Strain (micro)	Ratio ($\varepsilon_E/\varepsilon_A$)	Strain (micro)	Strain (micro)	Ratio ($\varepsilon_E/\varepsilon_D$)
BM12-INF	1	2494	-	2507	**0.99**	-	-	-
	2	2316	-	2507	0.92	-	-	-
	3	1803	-	2507	0.72	-	-	-
BM16-INF	1	2725	-	2714	**1.00**	-	-	-
	2	2297	-	2714	0.85	-	-	-
BM25-INF	1A	2919	-	3116	**0.94**	-	-	-
	1B	2519	-	3116	**0.81**	-	-	-
BM12-220	1	fail	6747	6749	-	7452	7452	-
	2	6391	6747	6749	0.95	7452	7452	0.86
	3	5573	6747	6749	0.83	7452	7452	0.75
BM16-220*	*1*	*5364*	7605	*7607*	*0.71*	7873	*7874*	*0.68*
	2	*4246*	7605	*7607*	*0.56*	7873	*7874*	*0.54*
BM25-220	1A	8727	9465	9467	**0.92**	8649	8650	**1.01**
	1B	7856	9465	9467	**0.83**	8649	8650	**0.91**
BM12-150	1	8384	6482	6484	**1.29**	6482	6483	**1.29**
	2	7007	6482	6484	1.08	6482	6483	1.08
	3	5827	6482	6484	0.90	6482	6483	0.90
BM16-150	1	fail	7300	7302	-	6857	6858	-
	2**	6410	7300	7302	0.88	6857	6858	0.93
BM25-150	1A	9958	9064	9065	**1.10**	7564	7566	**1.32**
	1B	fail	9064	9065	-	7564	7566	-
BM12-s230	1	9064	8282	8283	**1.09**	6743	6744	**1.34**
	2	7242	8282	8283	0.87	6743	6744	1.07
	3	6468	8282	8283	0.78	6743	6744	0.96
BM16-s230	1	fail	8602	8603	-	7137	7138	-
	2	fail	8602	8603	-	7137	7138	-
BM25-s230	1A	fail	9150	9152	-	7884	7886	-
	1B	fail	9150	9152	-	7884	7886	-
Average* =					0.93			1.04
Average* for Extreme Layer (**Bold**) =					1.00			1.17

**Outlier not included in averages, see the Results Section for more information.*
***Value from gauge L-2-5*
**** **Bold** entries highlight ratios from gauges on the most extreme layer of reinforcement.*
***** "fail" refers to strain gauges which failed before peak load.*

When the averages are considered, the IST method would appear to be a good predictor of the longitudinal strain at mid-span. However, predictions show that the analytical models over predicted one layer by 29 percent and under predicted another by 28 percent, while the design models had over predicted by 29 percent and under predicted by 25 percent, when the outlier is ignored. As such, it does not seem that the IST method is capable of predicting the mid-span longitudinal strain at failure.

Figures 6.10 and 6.11 show that the analytical models of the IST method best predict the behaviour of the most extreme layer of reinforcement, which is the layer marked as 1 in Table 6.6. So, when only the most extreme fibres are considered, the average of the predictions using the analytical models improves, but the same improvement is not seen in the design models. The extreme layer data still includes the 29 percent over prediction. Longitudinal strains in the BMX-INF series of beams are best predicted when only the extreme fibres are considered.

The predicted strain values from the table follow the same trends as seen in the predicted failure loads presented earlier in this chapter. That is, predicted longitudinal mid-span strain at failure increases with increasing flexural reinforcement ratio, but a clear trend in predicted longitudinal strains is not present when compared to the shear reinforcement ratio.

Table 6.7 shows the average of the stirrup strain gauge readings at the point of peak load. The readings were taken from the same gauges used to determine the concrete contribution, V_c, values in the previous subsection. The table also shows the predicted stirrup strain for models of the IST method at crushing of the first strut and at system failure. Adjacent to the predicted strain values is the ratio of the experimental strain over the predicted strain. Recall that when a typical truss is analyzed the results will show all vertical members have the same internal load, assuming the vertical members are identical; so it is only necessary to show one value for the stirrup strain for the models of the IST method.

Table 6.7: Summary of the Ability of the IST Method to Predict Average Stirrup Strains

	Experimental	**The IST Method**							
		Analytical Models				**Design Models**			
Failure Condition →		**1st Strut**		**System**		**1st Strut**		**System**	
Beam	**Strain (micro)**	**Strain (micro)**	**Ratio ($\varepsilon_E/\varepsilon_A$)**	**Strain (micro)**	**Ratio ($\varepsilon_E/\varepsilon_A$)**	**Strain (micro)**	**Ratio ($\varepsilon_E/\varepsilon_D$)**	**Strain (micro)**	**Ratio ($\varepsilon_E/\varepsilon_D$)**
BM12-220	4756	13085	0.36	16576	0.29	5325	0.89	2350	2.02
BM16-220*	*1997*	*13111*	*0.15*	*16791*	*0.12*	*5990*	*0.33*	*1787*	*1.12*
BM25-220	7576	13575	0.56	17104	0.44	5612	1.35	1563	4.85
BM12-150	4870	8589	0.57	11672	0.42	2200	2.21	768	6.34
BM16-150	4859	10351	0.47	11861	0.41	2263	2.15	707	6.87
BM25-150	4995	8982	0.56	12379	0.40	2636	1.89	940	5.31
BM12-s230	3387	4833	0.70	2040	1.66	2178	1.56	925	3.66
BM16-s230	3138	4628	0.68	1804	1.74	2270	1.38	729	4.31
BM25-s230	7716	4253	1.81	2541	3.04	2289	3.37	593	13.01
Average* =			0.71		1.05		1.85		5.80

**Outlier not included in average, see the Results Section for more information.*

Table 6.7 shows that the predictions are non-sense. Figures 6.12 and 6.13 showed that the predicted strain curves increased in a highly linearized fashion immediately while the experimental curves only showed increases in strain after cracking, but were otherwise parallel to the predicted curve. The intent of the comparison in this table was to examine if the stirrup strains at the crushing of the first strut would provide a conservative estimate on stirrup strains. This is the case for 10 of the beams, excluding

the outlier, but not for beam BM25-s230, in which the experimental strain far exceeded the predicted strain. Table 6.7 does not show any other trends, there is no consistent correlation between stirrup strains at either failure condition when compared to changes in flexural or shear reinforcement ratio.

Table 6.8 shows the mid-span displacement of the beams at the point of peak load, and also shows the predicted displacement for models of the IST method at crushing of the first strut and stability failure. Adjacent to the predicted displacements is the ratio of the experimental displacement over the predicted displacement.

Table 6.8 shows that mid-span deflections predictions increase with increasing flexural reinforcement ratio at the crushing of the first strut for the analytical models. Otherwise the predictions are non-sense. This is not unexpected; strut-and-tie models have never been used to predict displacements because, as noted earlier, the lower bound theory of plasticity does not require kinematically admissible solutions.

Table 6.8: Summary of the Ability of the IST Method to Mid-Span Displacements

	Experimental	**The IST Method**							
		Analytical Models				**Design Models**			
Failure Condition →		**1st Strut**		**System**		**1st Strut**		**System**	
Beam	Δ_E **mm**	Δ_A **mm**	**Ratio** (Δ_E/Δ_A)	Δ_A **mm**	**Ratio** (Δ_E/Δ_A)	Δ_D **mm**	**Ratio** (Δ_E/Δ_D)	Δ_D **mm**	**Ratio** (Δ_E/Δ_D)
BM12-INF	4.3	-	-	9.5	0.45	-	-	-	-
BM16-INF	4.2	-	-	11.3	0.37	-	-	-	-
BM25-INF	3.2	-	-	9.1	0.36	-	-	-	-
BM12-220	12.0	13.6	0.88	16.5	0.72	12.9	0.92	20.3	0.59
BM16-220*	*8.4*	*14.6*	*0.58*	*17.3*	*0.49*	*12.8*	*0.66*	*18.5*	*0.45*
BM25-220	24.0	16.8	1.43	21.5	1.12	13.5	1.77	18.7	1.28
BM12-150	15.6	12.8	1.21	19.6	0.80	11.3	1.38	15.3	1.02
BM16-150	14.4	14.8	0.98	19.6	0.74	11.5	1.26	15.4	0.94
BM25-150	22.1	15.7	1.41	18.5	1.19	11.5	1.91	18.5	1.19
BM12-s230	12.5	12.9	0.97	18.7	0.67	10.7	1.17	18.7	0.67
BM16-s230	21.9	13.0	1.68	18.2	1.21	10.8	2.03	17.3	1.27
BM25-s230	35.6	13.3	2.68	22.5	1.58	11.3	3.15	17.0	2.10
Average* =			1.13		0.84		1.70		1.13

**Outlier not included in average, see the Results Section for more information. Beams BMX-INF are included in both Analytical Model averages.*

6.4 On Analytical and Design Models of the IST Method

Two general model types for use with the IST method were investigated for analyzing FRP reinforced deep beams: analytical models and design models. The analytical models placed the tie elements at the actual location of the longitudinal and stirrup reinforcement; the design models lumped all the area of transverse reinforcement into one stirrup tie located at the centre of the span; after the necessary amount of reinforcing was confirmed it was assumed that a designer would evenly distribute the reinforcement over the shear span.

The results presented in this section indicate that the analytical model types were much better predictors, subject to the caveat that the arrangement of strut-and-tie elements conform to best design

practices. That is, Type IVb models were better representations of the flow of forces in the beams than Type IVa models.

The ratios of predicted strength over experimental strength for analytical models were typically closer to unity than they were for design models, and the average was the best of the 5 analysis methods as presented in Table 6.4. And the analytical models were the best predictor of beam capacity for 5 of the 12 beams in the test program.

Conversely, the ratios for the design models were further from unity, and the average of those ratios was the worst of the 5 analysis methods in Table 6.4. Further, the predictions were never consistently conservative. The design model truss works well for steel since the yielding of steel actually redistributes forces to other stirrups by allowing large deformations in the concrete which activate other steel stirrups.

In general, this discussion underscores the importance of using a strut-and-tie model truss which reasonably approximates the flow of forces in the beam.

6.4.1 On Designing with the IST Method

In practice, most governing authorities require the use factors of safety with design models. This research programme has not included any factors of safety. Use of the IST method for design, and the application of any factors of safety, is done at the practitioner's own risk.

Non-linear strut-and-tie modelling methods, including the work of Yun, Kim & Yun, or this IST method, should still make use of best design practices for strut-and-tie modelling with steel reinforcement for now, or until other practices are developed for use with these methods or designing with FRP reinforcements. For example, the minimum angle between a strut-and-tie should be 25 degrees, as recommended in the definition of a D-Region from commentary clause RA.1 of ACI 318-08, a practice which is supported by the investigation of Type IVa and IVb models in Subsection 6.1.1.

For a general strut-and-tie problem, it is recommended to develop and iterate a few possible truss solutions. As with steel strut-and-tie design, a fully elastic finite element analysis of the D-Region could be used as a starting point to develop a reasonable approximation of the follow of forces. The IST method is a lower bound method, so it should be appropriate to design with the model that predicts the largest applied load at failure.

Recall that it is important for a strut-and-tie model with FRP reinforcement to fail exclusively by way of instability resulting from the crushing of concrete struts, as this is the most ductile failure mode. Any other potential failure, or other element failures, should be designed-out by changing the geometry of the strut-and-tie model or other design parameters. Also recall that the practitioner must exercise judgement in design when one overlapping strut crushes, for struts which intersect without forming nodes, as to whether the overlapped struts have also crushed. The IST method is not capable of making this determination.

For deep beams, no single design model truss is here recommended since the beams in this research programme were few in number and all similarity sized, despite difference in reinforcement arrangements. Ergo, the investigation is not robust enough to recommend a single design model.

As a starting point, it may be helpful to use the Nehdi et al. (2007) or CSA S806 (2012) methods to estimate the size and spacing of stirrups. Then an analytical model truss could be used to predict the strength of the deep beam with more accuracy. No rules of thumb currently exist for developing the initial layout out of FRP reinforcement.

Also, recall that the term 'design model' used in this thesis is such in name only; it was used to make reference to a method of steel reinforced deep beam design, and that these models were thought to be a poor representation of the flow of forces in FRP trusses since the results were more scattered than the analytical models and not always conservative.

7 Conclusions and Recommendations

A brief review the entire thesis is presented in this chapter. Then summaries of all the key observations on beam behaviour and the IST method are listed. Recommendations for future research work follow.

7.1 Review of Thesis

The original intent of this research programme was to assess the influence that longitudinal bar arrangements have on the effective strength of FRP stirrups. Bent FRP reinforcement, such as shear stirrups, commonly ruptures at the bend at a stress lower than the strength of the straight portion; however, there have been noted exceptions presented in literature. The analysis of a beam with multiple layers of flexural reinforcement in Bentz et al. (2010) found that the stirrup bend was protected from large shear stresses, and during the experiment the stirrup had ruptured in the straight portion instead. This observation served as motivating factor for the research.

Unfortunately, no stirrups ruptured during the course of this research programme. Failures were always concrete controlled, occurring in a form of shear-compression and/or strut-crushing for beams with stirrups. So, two new objectives were devised after testing. The first was to observe the influence that FRP flexural and transverse reinforcement arrangements have on the shear strength of concrete beams, so as to make use of the experimental data. And the second was to investigate a method of strut-and-tie modelling for beams with brittle reinforcements and indeterminate strut-and-tie trusses in order to provision a proper analysis of the results.

The literature review for this thesis was extensive and covered aspects relevant to the original hypothesis, and the two modified hypotheses. It also presented literature on the parameters which influence FRP bend strength, presented the most modern model for the shear strength of FRP reinforce beams, CSA S806-12, as well as the most accurate, Nehdi et al. (2007). The review also presented the state of the art of strut-and-tie modelling for FRP reinforce beams and highlighted its deficiencies. The Literature Review Chapter concluded by summarizing a suite of papers on a method of strut-and-tie modelling for steel reinforced structures that does not require the yield assumption to find a lower bound solution, literature which formed the basis for the IST method presented in this thesis.

The design of the experimental specimens was driven by the original intent of this thesis. Twelve beams were cast and separated into three groups by longitudinal bar size and arrangement, or four series based on transverse reinforcement spacing. One series used thicker stirrups with beam widths slightly larger than the others. The effective depth was kept constant, at 270 mm, and the longitudinal reinforcement ratios were kept similar, between 1.58 and 2.51 percent, thus forcing more longitudinal layers as longitudinal bar sizes decreased. Beam widths were kept constant, at 200 mm, for three series and the fourth was 230 mm. The shear-span-to-effective-depth ratio was kept constant at 2.5. To diminish the effect of concrete variability, all beams were cast at the same time with the same batch of concrete. The 28 day concrete strength was 47.3 MPa.

Beams were tested in 3-point loading in a machine with a 500 kN capacity. Shear-tension failures were desired; however, the capacity of the test machine constrained the dimensions of the specimens. A detailed Monte Carlo analysis using two shear models was used to assess the likelihood of different failure modes. In general, shear failures were likely, but not guaranteed. Observations on the results of testing are summarized in the following conclusions section.

The specimens behaved like deep beams during tests, which warranted a strut-and-tie analysis. However, strut-and-tie methods for steel reinforced concrete are not directly applicable to FRP reinforced concrete. The problem is the yield assumption, which is necessary to solve a strut-and-tie truss with any amount of indeterminacy. The assumption fixes the stress in the tie to the yield stress, which is then used to solve for forces in the system. This solution method naturally presumes that failure of the reinforced concrete is the result of plastic flow by yielding of all steel ties. This assumption does not apply to FRP reinforcements because they cannot yield, and without that assumption a particular failure mechanism cannot be presumed. A more detailed analysis, which does not presume the elements that will comprise the failure mechanism, is necessary to solve for a lower bound solution. State-of-the-art strut-and-tie modelling methods for FRP reinforced concrete have not overcome this problem. Literature on the topic has focused exclusively on beams without stirrups and determinate strut-and-tie trusses, because the force system may be solved without having to make force or strain assumptions.

Work by Dr. Young Mook Yun, on the solution of strut-and-tie truss models for steel reinforced beams which do not require the yield assumption, served as a basis for the IST method developed in this research programme. The method was not directly applicable to FRP reinforced concrete; both the reinforcement material behaviour and failure criteria had to be modified, as well as other aspects including element geometry.

Failure is still defined by instability of the strut-and-tie truss, but instead it preferably results exclusively from crushing of concrete struts as this is the most ductile failure mode. In this case, crushing is defined as the point on the concrete stress-strain curve where the tangent modulus of elasticity is zero, commonly known as the point of peak load; however, this is not considered failure, instead the point of strut rupture is considered strut failure. Strut crushing is akin to steel yielding. Other element failures are also considered in the analysis, but are not desirable in design.

As is best described in Chapter 5, the IST method is the solution to a finite element system comprised of truss elements. One dimensional concrete material non-linearity, modified by softening coefficients, is used to model strut behaviour, which requires an incremental non-linear solution method.

The analysis compared the experimental results to the CSA S806-12 standard, a shear model for FRP reinforce beams by Nehdi et al. (2007), and the IST method. The IST method was the best predictor of beam strength. The experimental data from the beam tests were examined further as was the ability of the IST method to predict behaviour other than capacity, and the results are summarized in a following section.

7.2 Conclusions

7.2.1 Experimental Observations and Beam Behaviour

- Beams without stirrups failed in shear-tension. Beams with stirrups failed in a form of shear-compression or strut-crushing. Often peak load passed without noise, movement, or the ejection of particles, though there are individual exceptions. Within the vicinity of peak load beams would occasionally make popping noises consistent with the characteristic sound of concrete fracture. Only one beam showed a catastrophic failure, but it occurred sometime after peak load.
- No stirrups ruptured during the tests. Specimens which indicated the possibility of stirrup rupture were investigated further by freeing them with a jackhammering. Two stirrups showed cracks running along the neutral axis of the flexural tension zone bend, and those cracks ran perpendicular to the plane of the stirrup.
- Beam cracking was typical: the mid-span flexural crack formed first followed by more flexural cracks. In beams with stirrups the flexural cracks formed at the locations of the

stirrups. Flexural cracks then grew into flexural shear cracks, and then shear cracks developed. Maximum crack sizes at peak load tended to increase with increasing shear reinforcement ratio.

- Mid-span longitudinal reinforcement strains were linear after cracking up to the point of peak load when plotted against applied load. Response was initially quite stiff, then softened after cracking, and became just slightly stiffer after some initial amount of strain.
- Specimens with strain gauges equally spaced along the longitudinal reinforcement showed the development of a tied arch mechanism on arch action plots. These curves confirmed deep beam behaviour.
- Stirrup strains were difficult to summarize because several gauges failed prematurely, or because failure occurred in the un-instrumented shear span. Almost exclusively, the strain in the straight portion of the stirrup was larger than the strain at the flexural tension zone bend. Otherwise, strain for stirrups located in the middle of the shear span showed the largest strains compared to those closer to mid-span or the support. This was consistent with arch action behaviour, as the main shear crack tends to run from the load point to the support point and cross the middle most stirrups near mid height of the stirrup where the straight portion strain gauges were located.
- Beams of the same series, which have the same shear reinforcing ratio, all had similar strengths when compared to other series. As the shear reinforcing ratio increased, so too did beam strength, and in general, so too did mid-span displacement at peak load.
- Beams without stirrups clearly showed increases in mid-span displacement and strength with increases in the flexural reinforcement ratio; they also showed a clear decrease in mid-span longitudinal strain. However, such trends were less clear in the case of beams with stirrups; in the case of longitudinal strains, premature gauge failures precluded any conclusions.
- Beams with higher flexural reinforcement ratios had stiffer load-displacement responses than those with lower flexural reinforcement ratios.
- A number of beams showed a two-peak load-deflection response; however, the second peak was not always higher than the first peak and there was no indication on how to predict which peak would be higher based on the design parameters.
- All beams with stirrups showed some amount of post-peak ductility on a plot of load against displacement. Beams with lower flexural reinforcement ratios tended to show more post-peak ductility; though this may have been related to bond-quality as beams with lower reinforcement ratios used the smallest diameter bars, and thus had the most surface area for bonding.
- Beams with the same longitudinal reinforcing ratios showed similar pre-cracking and post-cracking responses and similar cracking loads.
- Three methods were used to estimate the concrete contribution to beam shear strength in Chapter 6, and Method 1 was the best. Method 1 assumed the concrete contribution was equal to the lowest load from the curves on the load vs stirrup strain plots at the point where the curves doglegged. The stirrup contribution was computed by subtracting the concrete contribution from the shear load at failure.
- The concrete contribution was effectively constant for all twelve beams. Though there was some variation, it was not correlated with design parameters. The differences that may be caused by variation in specimen design parameters may have been too slight to show up when experimental error is considered.
- The stirrup contribution increases with increasing shear reinforcement ratio; even as the average stirrup stress decreases. However, increases in stirrup contribution diminish with

increases in shear reinforcement ratio. Specifically, when the failure is concrete controlled, the confinement affected shear strength increase shows diminishing returns with increases in confinement, where confinement is provided by way of closed loop stirrups.

- Ultimately the results show that shear strength is correlated with both flexural and shear reinforcement ratios for the case where beams fail by way of shear-compression / strut-crushing.

7.2.2 The Indeterminate Strut-and-Tie Method

- The strut-and-tie analysis method developed by Dr. Yong Mook Yun for steel reinforced concrete was successfully adapted to predict the strength of the FRP reinforced concrete deep beam specimens of this research programme. The specific adaptation presented in this thesis is referred to as the Indeterminate Strut-and-Tie (IST) method.
- The IST method is now a new tool, which provides researchers and practitioners with a way to analyze FRP reinforced concrete members that could, theoretically, be applied to any D-region. This is significant, as there is no strategy or method that could be used to design complicated FRP reinforced concrete D-regions such as shear walls with multiple openings, corbels, dapped-end beams, the flanges of T-beam, etc. However, the research in this thesis was limited to only deep beams of a very similar size.
- A thorough sensitivity analysis was not conducted on the IST method. However, preliminary work found that the IST method was most sensitive to the choice of softening coefficients used in the one-dimensional concrete material models. The softening coefficients were set equal to the same values used by Yun in his work, which he set equal to the strut strength efficiency factors of the ACI318-08 code; these unaltered values worked remarkably well.
- The IST method was not very sensitive to the choice of one-dimensional concrete material model; most concrete material models are differentiated by their post-peak behaviour, which is ignored in the IST method.
- The IST method was not very sensitive to the value of the initial concrete tangent modulus.
- The beam designs were analyzed with the IST method using different types of strut-and-tie model trusses. The truss models fell into two categories: analytical models and design models. The analytical models placed tie elements at the location of each stirrup, whereas the design models lumped the area of all stirrups into one tie in the centre of the shear span. Overall the analytical models were better predictors of beam strength than the design models.
- A proper strut-and-tie model truss configuration still requires judgement. Two similar analytical models for the BMX-150 beams were analyzed. One included a stirrup tie located very close to the support, which produced an adjoining strut that formed a small angle with the stirrup tie. The other omitted that stirrup tie and thus the adjoining strut. The models which included the strut with the small angle were much poorer predictors of beam strength, erring on the conservative side, than those that omitted it. Omitting the tie was supported by experimental observations which showed that the stirrup closest to the support never developed any appreciable strains. Further, the conservative predictions of a bad, but still reasonable, choice of strut-and-tie model truss configuration reinforces the power of this method and its basis in the lower bound theory of plasticity.
- The design models were neither consistently conservative nor un-conservative in their predictions; they simply tended to make predictions which were further from the experimental strength than the predictions by the analytical models. It is possible that the design model trusses were not reasonable approximations of the flow of forces, and thus did not provide consistently conservative predictions.

- The strength predictions for the beams without stirrups were better when the softening coefficient was set equal to the value of the strut strength efficiency factor for unreinforced bottle shaped struts from the ACI 318-08 code. However, in beams with stirrups all inclined struts were modelled using a softening coefficient equal to the value of the strut strength efficiency factor for reinforced bottle shaped struts because the stirrups still act to confine the concrete even when struts do not cross a stirrup tie.
- The analytical models of the IST method were found to be the best predictors of beam strength when compared to predictions made by the shear strength method of Nehdi et al. (2007), and the shear strength method of the CSA S806-12 standard.
- The IST method uses the finite element method to find solutions, and is thus capable of producing information beyond the lowest estimate of loads required to cause failure.
- The IST method was used to model longitudinal mid-span strain behaviour, but it was not capable of predicting the longitudinal mid-span strain at either the crushing of the first strut or system failure with any accuracy. However, plots of mid-span strain superimposed over experimental observations suggest that, in general, the IST method is capable of capturing this behaviour after cracking.
- The IST method was also used to model average stirrup strain behaviour, but it was not capable of predicting the average stirrup strain at either the crushing of the first strut or system failure. Plots of predicted stirrup strain superimposed over stirrup strain observations suggest that, in general, the slope of the stirrup strain prediction curve matches that of the average stirrup strain after shear cracking when the stirrups are engaged.
- The IST method was used to model mid-span displacement as well, but it was not capable of predicting the mid-span displacement at either the crushing of the first strut or system failure. Plots of predicted mid-span displacement superimposed over experimental observations suggest that, in general, the IST method can reproduce the behaviour after cracking but before peak-load.

7.2.3 CSA-S806-12

- The CSA S806-12 shear method dangerously over-predicted the strength of the experimental test specimens without stirrups. The reason for this will be the subject of a future paper.

7.3 Recommendations

- The original objective of this research programme should be investigated again since the experimental results precluded making any conclusions. Future investigations should design specimens with a larger shear-span-to-effective-depth ratio to avoid deep beam behaviour. A robust investigation should also consider both CFRP and GFRP reinforcements, and possibly high strength steel. The motivating observations for the original objective are compelling, and protecting the bend with multiple layers of reinforcement should be readily satisfied since FRP beams must be over reinforced. It is possible that a simple design detail could eliminate premature rupture of stirrup bends that discourages adoption of the reinforcing material, especially considering the stirrup detailing discussion of Subsection 3.5.1.
- A study on the influence of different methods for creating closed loop FRP stirrups should be investigated. The study could be made more robust by including a parallel study using steel stirrups. Such a study could put to rest concerns about the influence of different stirrup detailing methods, and recommend a practicable detailing method to be used by researchers and industry.

- Though the IST method produced good results using softening coefficients equal to the strut strength efficiency factors of the ACI 318-08 code, a more thorough study should be done to confirm the appropriateness of using those values. The brief investigation into setting the softening coefficients equal to the equivalent strut strength factors according to the provisions of the CSA methods, as noted at the end of Chapter 5, was very basic and a more thorough investigation is certainly possible. Though, doing so should consider the discussion of Section 2.5. Such an investigation should occur simultaneously with tests on beams of many and varied design parameters, sizes, and shear-span-to-effective-depth ratios.
- A study on the impact of calculating the tangent modulus of elasticity of struts from strains that approach and surpass peak load should be conducted. Kim and Yun allowed this behaviour in their two 2011 papers on which the IST method was based. By doing so, a more thorough study on the impact of one-dimensional concrete material models may be conducted. Further, a study on the use of a secant modulus of elasticity could also be conducted.
- A study on alternative strut-and-tie truss model configurations should be investigated to see if there are better choices than the ones used in this research programme. For example, a truss model where struts fan out to every node opposite the critical nodes at the load and support points. Such a study would need to further contemplate the geometry and strength of the nodes.
- A study on the application of the IST method to other design and analysis problems, such as corbels, dapped-end beams, shear walls, or structures with openings reinforced with FRP should be conducted. At this time there does not appear to be any published literature concerning these types of experiments, and that is likely because there was no robust method for analyzing the results; however, those results can now be analyzed with the IST method. A study on the application of the IST method to slender beams is also warranted.
- A database analysis should be conducted on other FRP reinforced deep beams to verify the IST method against independent experimental observations.
- A study on the impact of incorporating a tension stiffening model into the longitudinal reinforcement behaviour should be conducted, as this will likely improve the ability of the IST method to model beam behaviour. Further, the study should also investigate similar tension stiffening like behaviours for the stirrup reinforcement.
- A more robust sensitivity analysis should be conducted to confirm that the IST method produces expected results for a range of probable inputs and design scenarios.

References

Ahmed, E. A., El-Salakawy, E. F., Benmokrane, B., "Performance Evaluation of Glass Fiber-Reinforced Polymer Shear Reinforcement for Concrete Beams", ACI Structural Journal, 107(1), (January/February) 2010a, pp 53-62.

Ahmed, E. A., El-Salakawy, E. F., Benmokrane, B., "Shear Performance of RC Bridge Girders Reinforced with Carbon FRP Stirrups", Journal of Bridge Engineering, 15(1), (January/February) 2010b, pp 44-54.

Ahmed, E. A., El-Sayed, A. K., El-Salakawy, E. F., Benmokrane, B., "Bend Strength of FRP Stirrups: Comparison and Evaluation of Testing Methods", Journal of Composites for Construction, 14(1), (February) 2010c, pp 3-10.

Alqam, M., Bennett, R. M., Zureick, A., "Three-Parameter vs. Two-Parameter Weibull Distribution for Pultruded Composite Material Properties", Composite Structures, 58(4), (December) 2002, pp 497-503.

American Concrete Institute (ACI), "Building Code Requirements for Structural Concrete and Commentary (ACI 318-08)", American Concrete Institute, Farmington Hills, Michigan, 2008.

American Concrete Institute (ACI), "Building Code Requirements for Structural Concrete and Commentary (ACI 318-11)", American Concrete Institute, Farmington Hills, Michigan, 2011.

Andermatt, M. F., Lubell, A. S., "Strength Modeling of Concrete Deep Beams Reinforced with Internal Fiber-Reinforced Polymer", ACI Structural Journal, 110(4), (July-August) 2013a, pp 595-606.

Andermatt, M. F., Lubell, A. S., "Behaviour of Concrete Deep Beams Reinforced with Internal Fiber-Reinforced Polymer—Experimental Study", ACI Structural Journal, 110(4), (July-August) 2013b, pp 585-594.

Andermatt, M. F., "Concrete Deep Beams Reinforced with Internal FRP", Master's Thesis, Department Civil and Environmental Engineering, University of Alberta, Edmonton, Alberta, Canada, Fall 2010.

Baena, M., Torres, L., Turon, A., Barris, C., "Experimental Study of Bond Behaviour between Concrete and FRP Bars Using a Pull-Out Test", Composites Part B: Engineering, 40(8), (December) 2009, pp 784-797.

Batdorf, S. B., Ghaffarian, R., "Size Effect and Strength Variability of Unidirectional Composites", International Journal of Fracture, 26(2), (October) 1984, pp 113-123.

Bentz, E. C., Massam, L., Collins, M. P., "Shear Strength of Large Concrete Members with FRP Reinforcement", Journal of Composites for Construction, 14(6), (November/December) 2010, pp 637-646.

Bischoff, P. H., Gross, S. P., "Design Approach for Calculating Deflection of FRP-Reinforced Concrete", Journal of Composites for Construction, 15(4), (July/August) 2011, pp 490-499.

Bischoff, P. H., Paixao, R., "Tension Stiffening and Cracking of Concrete Reinforced with Glass Fiber Reinforced Polymer (GFRP) Bars", Canadian Journal of Civil Engineering, 31(4), (August) 2004, pp 579-588.

Canadian Standards Association (CSA), "Design and Construction of Building Structures with Fibre-Reinforced Polymers (CAN/CSA S806-12)", Canadian Standards Association, Mississauga, Ontario, Canada, March 2012.

Canadian Standards Association (CSA), "Test Methods and Standard Practices for Concrete (CAN/CSA A23.2-09)", Canadian Standards Association, Mississauga, Ontario, Canada, December 2009.

Canadian Standards Association (CSA), "Design of Concrete Structures (CAN/CSA A23.3-04)", Canadian Standards Association, Mississauga, Ontario, Canada, December 2004.

Canadian Standards Association (CSA), "Design and Construction of Building Structures with Fibre-Reinforced Polymers (CAN/CSA S806-02)", Canadian Standards Association, Mississauga, Ontario, Canada, May 2002.

Cosenza, E., Menfredi, G., Realfonzo, R., "Behavior and Modeling of Bond of FRP Rebars to Concrete", Journal of Composites for Construction, 1(2), (May) 1997, pp 40-51.

Currier, J., Fogstad, C., Walrath, D., Dolan, C., "Bond Development of Thermoplastic FRP Shear Reinforcement Stirrups", *Proceedings of the ASCE Third Material Engineering Conference "Infrastructure: New Materials and Methods of Repair"*, San Diego, California, United States, (November) 1994, Ed. Basham, K. D., American Society of Civil Engineers, New York, New York, United States, pp 592-597.

Ehsani, M. R., Saadatmanesh, H., Tao, S., "Bond of Hooked Glass Fiber Reinforced Plastic (GFRP) Reinforcing Bars to Concrete", ACI Materials Journal, 92(4), (July/August) 1995, pp 391-400.

El-Maaddawy, T., Biddah, A., "Monitoring of Tensile Tests Performed on ComBar Glass Fiber Reinforced Polymer Reinforcing Bars", UAE University Center for Externally Funded Projects (EFORS), Department of Civil & Environmental Engineering, United Arab Emirates University, United Arab Emirates, June 2008.

Eom, T., Park, H., "Secant Stiffness Method for Inelastic Design of Strut-and-Tie Model", ACI Structural Journal, 107(6), (November/December) 2010, pp 689-698.

Erki, M. A., Rizkalla, S. H., "FRP Reinforcement for Concrete Structures: A Sample of International Production", Concrete International, 15(6), (June) 1993, pp 48-53.

Fam, A. Z., Rizkalla, S. H., Tadros, G., "Behavior of CFRP for Prestressing and Shear Reinforcements of Concrete Highway Bridges", ACI Structural Journal, 94(1), (January) 1997, pp 77-86.

Farghaly, A. S., Benmokrane, B., "Shear Behaviour of FRP-Reinforced Concrete Deep Beams without Web Reinforcement", Journal of Composites for Construction, 17(6), (December) 2013, pp N/A.

HBMa, "HBM Strain Gauge Installation Video" [Motion Picture] Retrieved from https://www.youtube.com/watch?v=WJokJqlS50k, n.p., n.d., pp N/A.

HBMb, “Strain gage installation on fiber-reinforced plastics” Retrieved from http://www.hbm.com/en/menu/tips-tricks/experimental-stress-analysis/strain-gage-installation-on-fiber-reinforced-plastics/, n.p., n.d., pp N/A.

Hegger, J., Kurth, M., “Shear Capacity of Concrete Beams with FRP Reinforcement”, Special Publication of the ACI, 275, (March) 2011, pp 1-14.

Hoffmann, K., “Practical Hints for the Installation of Strain Gages”, 4th ed., HBM, 1979.

Imjai, T., Guadagnini, M., Pilakoutas, K., “Mechanical Performance of Curved FRP Rebars - Part I: Experimental Study”, *Proceedings of the First Asia-Pacific Conference on FRP in Structures, APFIS 2007, by the International Institute for FRP in Construction (IIFC)*, Hong Kong, China, (December) 2007a, Ed. Smith S. T., University of Hong Kong, Hong Kong, China, pp 333-338.

Imjai, T., Guadagnini, M., Pilakoutas, K., “Mechanical Performance of Curved FRP Rebars - Part II: Analytical Study”, *Proceedings of the First Asia-Pacific Conference on FRP in Structures, APFIS 2007, by the International Institute for FRP in Construction (IIFC)*, Hong Kong, China, (December) 2007a, Ed. Smith S. T., University of Hong Kong, Hong Kong, China, pp 339-344.

Johnson, D. T. C., Sheikh, S. A., “Performance of Bent Stirrup and Headed Glass Fibre Reinforced Polymer Bars in Concrete Structures”, Canadian Journal of Civil Engineering, 40(11), (November) 2013, pp 1082-1090.

Kanematsu, H., Sato, Y., Ueda, T., Kakuta, Y., "A Study on Failure Criteria of FRP Rods Subject to Tensile and Shear Force", *Proceedings of FIP Symposium ’93 “Modern Prestressing Techniques and Their Applications”*, Kyoto, Japan, (October) 1993, Japan Prestressed Concrete Engineering Association, pp 743-750.

Kara, I. F., “Prediction of Shear Strength of FRP-Reinforced Concrete Beams without Stirrups Based on Genetic Programming”, Advances in Engineering Software, 42(6), (June) 2011, pp 295-304.

Kiefer, D., “Monitoring of the tensile tests performed on ComBAR GFRP reinforcement”, Institute for Concrete Construction and Building Material Technology, University of Karlsruhe, August 1, 2006.

Kim, B. H., Yun, Y. M, “An Indeterminate Strut-Tie Model and Load Distribution Ratio for RC Deep Beams – (I) Model & Load Distribution Ratio”, Advances in Structural Engineering, 14(6), (December) 2011a, pp 1031-1041.

Kim, B. H., Yun, Y. M, “An Indeterminate Strut-Tie Model and Load Distribution Ratio for RC Deep Beams – (II) Validity Evaluation”, Advances in Structural Engineering, 14(6), (December) 2011b, pp 1043-1057.

Kupfer, H., Hilsdorf, H. K., Rusch, H., “Behavior of Concrete Under Biaxial Stresses”, ACI Journal, 66(8), (August) 1969, pp 656-666.

MacGregor, J. G., Bartlett, F. M., “Reinforced Concrete Mechanics and Design”, First Canadian ed., Pearson Education Canada Inc., Toronto, Ontario, Canada, 2000.

Machial, R., Shahria Alam, M., Rteil, A., "Revisiting the Shear Design Equations for Concrete Beams Reinforced with FRP Rebar and Stirrup", Materials and Structures, 45(11), (November) 2012, pp 1593-1612.

Maruyama, T., Honma, M., Okamura, H., "Experimental Study on Tensile Strength of Bent Portion of FRP Rods", Special Publication of the ACI, 138, (September) 1993, pp 163-176.

Maruyama, T., Honma, M., Okamura, H., "Experimental Study on the Diagonal Tensile Characteristics of Various Fiber Reinforced Plastic Rods", Transactions of the Japan Concrete Institute, 11, 1989, pp 193-198.

Montoya, E., Vecchio, F. J., Sheikh, S. A., "Numerical Evaluation of the Behaviour of Steel- and FRP-Confined Concrete Columns Using Compression Field Modelling", Engineering Structures, 26(11), (September) 2004, pp 1535-1545.

Nagasaka, T., Fukuyama, H., Tanigaki, M., "Shear Performance of Concrete Beams Reinforced with FRP Stirrups", Special Publication of the ACI, 138, (September) 1993, pp 789-812.

Nakamura, H., Higai, T., "Evaluation of Shear Strength of Concrete Beams Reinforced with FRP", (English Translation) Concrete Library International of Japanese Society of Civil Engineers (JSCE), 26, (December) 1995, pp 111-123.

Nakamura, E., Watanabe, H., "Shear Resisting Mechanism in RC Beams with Fractured Stirrups", *Proceedings of the 22nd UW – Japan Bridge Engineering Workshop*, Seattle, Washington, USA, (October) 2006.

Nehdi, M., Omeman, Z., El-Chabib, H., "Optimal Efficiency Factor in Strut-and-Tie Model for FRP-Reinforced Concrete Short Beams with ($1.5 < a/d < 2.5$)", Materials and Structures, 41(10), (December) 2008, pp 1713-1727.

Nehdi, M., El Chabib, H., Aly Said, A., "Proposed Shear Design Equations for FRP-Reinforced Concrete Beams Based on Genetic Algorithms Approach", Journal of Materials in Civil Engineering, 19(12), (December) 2007, pp 1033-1042.

Nowak, A. S., Rakoczy, Anna M., Szeliga, E. K., "Revised Statistical Resistance Models for R/C Structural Components", Special Publication of the ACI, 284, (March) 2012, pp 1-16.

Pahn, M., Schnell, J., "Report 07030/1/Pa/528: Monitoring of the tensile tests performed on ComBAR GFRP reinforcement Ø8, Ø12, Ø16", BAUINGENIEURWESEN, Fachgebiet Massivbau und Baukonstruktion, Technische Universität Kaiserslautern (Civil Engineering, Institute of Concrete and Building Construction, Technical University Kaiserslautern), July 4, 2007.

Pang, X. D., Hsu, T. T. C., "Behavior of Reinforced Concrete Membrane Elements in Shear", ACI Structural Journal, 92(6), (November/December) 1995, pp 665-679.

Schlaich, J., Schafer, K., "Design and Detailing of Structural Concrete Using Strut-and-Tie Models", The Structural Engineer, 69(6), (March) 1991, pp 113-125.

Schlaich, J., Schafer, K., Jennewein, M., "Towards a Consistent Design of Reinforced Concrete Structures", PCI Journal, 32(3), (May-June) 1987, pp 74-150.

Schlaich, M., Anagnostou, G., "Stress Fields for Nodes of Strut-and-Tie Models", Journal of Structural Engineering, 116(1), (January) 1990, pp 13-23.

Shehata, E., Morphy, R., Rizkalla, S., "Fibre Reinforced Polymer Shear Reinforcement for Concrete Members: Behaviour and Design Guidelines", Canadian Journal of Civil Engineering, 27(5), (October) 2000, pp 859-872.

Shehata, E. F. G., "Fibre-reinforced Polymer (FRP) for Shear Reinforcement in Concrete Structures", PhD Thesis, Department of Engineering Civil and Geological Engineering, University of Manitoba, Winnipeg, Manitoba, Canada, March 1999.

Stratford, T., Burgoyne, C., "Shear Analysis of Concrete with Brittle Reinforcement", Journal of Composites for Construction ASCE, 7(4), (November) 2003, pp 323-330.

Stratford, T., Burgoyne, C., "Crack-Based Analysis of Concrete with Brittle Reinforcement", Magazine of Concrete Research, 54(5), (October) 2002, pp 321-332.

Stratford, T. J., "The Shear of Concrete with Elastic FRP Reinforcement", PhD Thesis, Department of Engineering, Jesus College, University of Cambridge, Cambridge, England, 2000, revised 2001.

Thorenfeldt, E., Tomaszewicz, Jensen, J. J., "Mechanical Properties of High-Strength Concrete and Application in Design", Proceedings of the Symposium "Utilization of High-Strength Concrete", Stavanger, Norway, (June) 1987, Tapir, Trondheim, pp 149-159.

Ueda, T., Sato, Y., Kakuta, Y., Imamura, A., Kanematsu, H., "Failure Criteria for FRP Rods Subjected to a Combination of Tensile and Shear Forces", *Proceedings of the Second International RILEM Symposium on Non-Metallic (FRP) Reinforcement for Concrete Structures*, Ghent, Belgium, (August) 1995, Ed. Taerwe, L., E & FN Spon, London, United Kingdom, pp 26-33.

Varney, J. C., Brown, M. D., Bayrak, O., Poston, R. W., "Effect of Stirrup Anchorage on Shear Strength of Reinforced Concrete Beams", ACI Structural Journal, 108(4), (July/August) 2011, pp 469-478.

Vijay, P. V., Kumar, S. V., GangaRao, H. V. S., "Shear and Ductility Behavior of Concrete Beams Reinforced with GFRP Rebars", *Proceedings of the 2nd International Conference on Advanced Composite Materials in Bridges and Structures, ACMBS-II, by the Canadian Society for Civil Engineering (CSCE),* Montreal, Quebec, Canada, (August) 1996, Ed. El-Badry, M. M., pp 217-226.

Yun, Y. M, Kim, B. H., "Two-Dimensional Grid Strut-Tie Model Approach for Structural Concrete", Journal of Structural Engineering, 134(7), (July) 2008, pp 1199-1214.

Yun, Y. M, "Strength of Two-Dimensional Nodal Zones in Strut-Tie Models", Journal of Structural Engineering, 132(11), (November) 2006, pp 1764-1783.

Yun, Y. M., "A Refined Strut-Tie Model Approach and Its Application Tool", Proceedings of the Institution of Civil Engineers Structures and Buildings, 140(1), (February) 2000a, pp 13-24.

Yun, Y. M., "Computer Graphics for Nonlinear Strut-Tie Model Approach", Journal of Computing in Civil Engineering, 14(2), (April) 2000b, pp 127-133.

Yun, Y. M., “Nonlinear Strut-Tie Model approach for Structural Concrete”, ACI Structural Journal, 97(4), (July-August) 2000c, pp 581-590.

Yun, Y. M., Ramirez, J. A., “Strength of Struts and Nodes in Strut-Tie Model”, Journal of Structural Engineering, 122(1), (January) 1996, pp 20-29.

Zhao, M., Maruyama, K., Suzuki, H., “Shear Behavior of Concrete Beams Reinforced by FRP Rods as Longitudinal and Shear Reinforcement”, *Proceedings of the Second International RILEM Symposium “Non-metallic (FRP) Reinforcement for Concrete Structures”*, Ed. Taerwe, L., 1995, E & FN Spon, London, pp 352-359.

Appendices

A: Monte Carlo Analysis of Probable Shear Failure

This appendix contains information related to the Monte Carlo analysis used to select specimen design parameters, which are referred to in Chapter 3. Specifically, the appendix includes a brief description of the analysis procedure, an explanation on the assignment of certain parameters as random variables, an explanation on the choice of probability distributions and their parameters, and a copy of the MATLAB Code.

A.1 Description of Analysis Procedure

The intent of the program is to compute the applied load at failure. Four outcomes were assumed: shear failure, compressive flexural failure, tensile flexural failure, or no failure; no failure, because the testing machine had a capacity of 500 kN and there was a possibility that the beam strength could be larger than the machine capacity.

The program starts by assigning values to the constant variables, and using probability distribution functions to assign values to the random variables for each trial. Then the compressive flexural capacity of the beam for each trial is computed. The computation, as described in Chapter 3, used a traditional rectangular stress-block approach for an over reinforced beam. Simple beam diagram equations were used to compute the applied load at compressive flexural failure.

The tensile flexural capacity of the beam was not computed; instead the possibility of a tensile flexural failure was assessed by comparing the ratio of the depth the neutral axis over effective depth, c/d ratio, against the limit from the CSA S806-12 standard for each trial. If the ratio was less than the limit then a flexural failure was suspected. In addition, the strain in the most extreme tensile reinforcing bar was checked against the rupture strain of the reinforcement. An index was used to keep track of which trials indicated that the beam was suspected of tensile flexural failure. Tensile flexural failure was assessed in this manner because it was an undesirable failure mode. Had a significant number of trials indicated a tensile flexural failure was likely then the beams would have been redesigned to minimize that likelihood.

The flexural compressive capacity was computed first, since the CSA S806-12 model is a sectional shear strength model, and requires the applied moment and shear at the section of interest in several of the model equations. The flexural compressive capacity for each trial was set equal to the applied moment, and simple beam diagram equations were used to estimate the applied shear from that moment.

Then the shear capacity was computed using the CSA S806-12 model, as was presented in the Literature Review Chapter. Once the shear strength at the critical section was determined it was compared to the assumed applied shear at the critical section. If the two shear values were different then the process was repeated, and the computed shear strength was used as the assumed applied shear on the next iteration. The applied moment was computed using simple beam diagram equations. This process iterated until the difference between the assumed applied shear and computed shear strength was very small. Then the applied load at shear failure was computed using simple beam equations. Convergence often happened in less than 15 iterations for any given trial.

The failures were indexed once the shear capacity for each trial was computed. If the applied load at shear failure was less than the applied load at compressive flexural failure for a trial, then the failure was recorded in an index for shear failures; otherwise it was indexed as a flexural failure.

Finally, the applied loads at failure for any given trial were compared to the capacity of the testing machine. If both loads were higher than the limit then that was recorded in an index, and the other indices were modified to reflect that.

To be clear, the outcome for each trial was recorded in only one of the indices for shear failure, compressive flexural failure, or no failure. Any trials which indicated tensile failure were recorded in one of the indices previously mentioned as well as the tensile failure index.

The outcome was then presented in several plots. Regardless, each plot had four data markers, one for each of the indices, and was used to make the separate failures modes visually distinct. This was very useful for identifying trends.

The first set of plots display the applied load at failure against the random variables. Then, each random variable was plotted against one another, but data points were still separated by failure mode marker. Finally, the program outputs the portion of trials from each outcome as a percentage of the total trials. To create the plot in Chapter 3, relevant data was then output to an excel file.

However, the program continues and computes the shear strength according to the Nehdi et al. (2007) model. The calculations for the Nedhi et al. model are quite simple and need no discussion; they were presented in the Literature Review Chapter. The program then repeats much of what was written earlier in terms of recording indices, sorting results by marker, plotting the results, and outputting the outcomes as percentages.

A.2 Assignment of Random Variables

The capacity models for either compressive flexure, or shear by the CSA S806-12 or Nehdi et al models, all contain a great number of parameters. To assess the probability of a particular failure mode and strength, it was not necessary, or even possible, to assign a random distribution to them all. The random variables of this investigation were limited to: the concrete compressive strength $f_c^{'}$, longitudinal bar strength f_{Fu}, longitudinal bar rupture strain ε_{Fu}, longitudinal bar elastic modulus E_F, and stirrup strength f_{Fu_bent}.

The assessment concerning which parameters would be constant variables and which would be random variables considered aspects such as: impact of the parameter on the outcome of the model, previous experience with the physical properties that the parameters represent, how likely those parameters were to vary, and the ability to find information on which to make an informed decision on the distribution if they were a random variable.

For example, the concrete strength parameter is very influential as it may be found in several of the equations of the different strength models. Past experience has shown that the concrete strength is highly influential, and aspects of the Introduction and Literature Review Chapters support this observation. It is also well known that the strength of concrete varies from the assumed design strength, and depending on quality of placement may vary from cylinder strength as well. Further, there is ample literature on the strength distribution of concrete strength.

However, parameters such shear span length, effective depth, and beam width were not assessed as random variables. In general, shear span length and beam width are not as influential as other parameters. Previous experience has shown that these design elements are not expected to vary by more than a few millimeters because they are carefully controlled when the formwork is constructed, when the rebar cage is assembled, and when the beam is positioned in the loading machine. Further, there is no literature which would be used to make an informed decision on the distribution of any of these variables.

Other parameters, such as stirrup spacing, were not varied. Though stirrup spacing is very influential in shear strength calculations, the nature of the variability is not readily accounted for in the calculations. Shear strength calculations assume a constant spacing between each and every stirrup, and though a random value could be assigned to that spacing, in reality the variation in distance between a

pair of adjacent stirrups is not identical for every pair of adjacent stirrups. So, this form of variation could not be readily modelled.

The Monte Carlo analysis, as described in Chapter 3, made changes to some of the constant variables in order to make informed choices on concrete strength, and stirrup spacing, and assess probable failure load and failure modes. To do this, the analysis method was run several times and the parameters of the random distributions were modified as necessary as were the values of some of the constant variables, such as stirrup spacing.

A.3 Probability Distributions

It is very important to use representative probability distributions when performing a Monte Carlo analysis; otherwise the results of the analysis are meaningless. Attempts were made to find data, or previous work, on which to make an informed choice of the specific type of probability distribution, and the choice of parameters of those distributions.

A.3.1 Concrete Strength

Two different probability distributions were used to model the concrete strength. At first a uniform distribution was used to find the probability space in which shear failures were likely. Once that region of concrete strength was identified, a normal distribution was used to assess probable failure modes and failure loads.

The uniform distribution was $f'_c \equiv U(a = 25, b = 50)$, where a was the lower bound limit and b was the upper bound limit, and values are in MPa. This range was intended to represent a region of normal strength concretes available from a typical ready mid plant.

The normal distribution was $f'_c \equiv N(\mu = ((40 \cdot 1.15), \sigma = (40 \cdot 1.15 \cdot 0.125))$, where μ is the mean in MPa, and σ is the standard deviation. The use of a normal distribution and the values of the mean and standard deviation came from a paper by Nowak et al. (2012), which examined compressive strength distributions for ready mix concretes. The value of 40 in the mean represents the nominal compressive strength of concrete in MPa, and the value of 1.15 represents the bias factor. The bias factor is the ratio of mean and nominal strength and was taken from Table 3 of Nowak et al. (2012), along with the value of the standard deviation, for a concrete with a strength of 6000 psi, or 41.4 MPa equivalent.

A.3.2 GFRP Parameters

The current state of GFRP reinforcement is such that the properties and behaviours differ with manufacturers. So, there are no papers which provide recommendations on the distribution types and parameters for a generic GFRP reinforcing bar. Therefore, a more rigorous investigation was necessary to determine how the GFRP properties would be modelled.

There are two distinct aspects to the investigation: determining probability distribution type, and determining the parameters for the distribution. If a significantly large amount of data is available then these two aspects could be investigated simultaneously; however, this was not the case.

The determination of probability distribution type was made after an amount of literature review. A paper by Alqam et al. (2002) investigated the use of Weibull distributions to model the properties of pultruded GFRP composites. The authors noted in their paper that the Weibull distribution was often used by other authors, and concluded that the two-parameter Weibull distribution was recommended to characterize the tensile strength and elastic modulus.

So, the strength and elastic modulus random variables were modelled with a Weibull distribution. However, a recommendation on the probability distribution type for the tensile strain of GFRP composites could not be found, so a normal distribution was assumed.

The choice of model parameters was much more involved. Raw data on tests of Schoeck Ltd. reinforcing bars was needed. At the time the analysis in Chapter 3 was done, about December 2012, Schoeck Ltd. had published three independent laboratory test reports on their website for view by the general public. These results reported in those documents were used to compute the necessary distribution parameters. Those reports were: (El-Maaddawy & Biddah, 2008)(Kiefer, 2006)(Pahn & Schnell, 2007).

In general, the reports presented observations on the tensile testing of different bar sizes and presented results for several parameters. The exact results are not reproduced here, as reproduction requires permission. Regardless, there were complications in using the results to compute distribution parameters.

First, GFRP reinforcing bars show a tensile size effect, which is based in fracture mechanics for bundled brittle fibres. Essentially, as the bundle diameter gets larger for a fixed length of bar, or as the bar length gets larger for a fixed bundle diameter, the stress that the material holds at failure will decrease, even though the force increases; interested readers are directed to the work of Batdorf et al. (1984). Therefore, different distribution parameters were necessary for each bar size, and thus only a few test results from each report were available to compute the distribution parameters for each bar size.

Second, each report also observed several tests in which the tensile test specimen did not fail by rupture of the bar; instead, the specimens would fail by way of the bar pulling out of the anchor. The anchor is a steel tube in which the bar is secured, by epoxy or grout, and to which the testing machine grips grasp; otherwise the machine grips would easily crush the GFRP reinforcing bar. These pullout failures could not be used to assess bar strength, so even fewer tests results were available from each report on which to compute the distribution parameters.

Each of the reports tested bars of size 8, 12, and 16 mm. As the size of the bar increased so too did the number of pullout failures. So, size 8 bars had the most data points on which to compute distribution parameters; however, this thesis only used size 12 and 16 mm bars. Further, the amount of data points for each parameter also varied because of test method, and because one report did not include strain measurements. So, the number of data points available for size 12 mm bars for the elastic modulus, rupture strength, and rupture strain were 11, 8, and 8, respectively. However, there were only 4 data points for rupture strain on which to base the strength of size 16 mm bars. So, as noted in Chapter 3, only specimens with size 12 mm bars were analyzed.

There was another complication: there are no publicly available test results or databases for bent bars manufactured by Schoeck Ltd. So, the probability distribution parameters for the strength of the stirrups were estimated based on the results for the straight pultruded bars; however, there is little to suggest this is an appropriate course of action given the difference in manufacturing methods. Regardless, the stirrup strength value for the straight portion, as reported in Schoeck Ltd. technical literature, was assumed to represent the average strength. There is no indication by Schoeck Ltd. that these values are the average strength, they simply refer to the values as the bar strength. However, to determine the distribution parameters it was assumed that the straight portion of the bent bars would have the same variance as the pultruded straight bars.

The probability distribution for 12 mm bar longitudinal strength in MPa was a Weibull distribution of $f_{Fu} \equiv \mathrm{W}(\alpha = 11.5159, \beta = 1398.6)$ where α is the shape parameter, and β is the scale parameter.

The probability distribution for 12 mm bar longitudinal elastic modulus in MPa was a Weibull distribution of $E_F \equiv W(\alpha = 44.8330, \beta = 65784.3)$ where α is the shape parameter, and β is the scale parameter.

The probability distribution for 12 mm bar longitudinal rupture strain as a percent was a normal distribution of $\varepsilon_{Fu} \equiv N(\mu = 2.689, \sigma = 0.552)$, where μ is the mean, and σ is the standard deviation.

The probability distribution for 12 mm stirrup straight portion strength in MPa was a Weibull distribution of $F_{Fu,bent} \equiv W(\alpha = 8.4570, \beta = 1059.0)$ where α is the shape parameter, and β is the scale parameter.

A.4 MATLAB Code

```
%Copyright: Martin D. Krall
%This is the MATLAB code for the monte-carlo procedure of
%Martin D Krall's master's thesis, "Tests on Concrete Beams
%with GFRP Flexural and Shear Reinforcements & Analysis Method for
%Indeterminate Strut-and-Tie Models with Brittle Reinforcements",
%University of Waterloo, 2014.

clc, clear all, close all

%This MATLAB file computes the shear and flexural strength of a GFRP
%reinforced concrete beam according to the CSA S806-12 standard, and the
%model by Nehdi et al. The analysis within is used to compute the likely
%failure outcomes for cases noted in the thesis. The output is the
%likelihood of a certain type of failure (shear, flexural compression,
%flexural tension, and no failure). The output also compares all of the
%input variables to one another and compares the input variables to the
%failure load.

% Variables for the Monte Carlo Analysis
n = 2^16 %Number of Monte Carlo trials
np = 5; %Number of Random Variables

%Arrays to keep track of failure modes.
URFailure = zeros(n,1); %UR - Under Reinforced failure (flexural tension).
%The code does not compute the value of a tension failure, but notes where
%the check indicate a tension failure is likely to occur.
BendingFailure = zeros(n,1); %Flexural Compression
ShearFailure = zeros(n,1);
NoFailure = zeros(n,1); %When the lowst failure load is above the capcity
%of the testing machine.

%User Defined Constant Variables
%==============================
%These variables are assumed invariant in the analysis. Attempts have been
%made to use variables names that conform to standard beam design notation,
%and descriptors have been added to variable names where necessary.
machineLimit = 500000; %N, capacity of testing machine.
phi_c = 1.0; % FOS for concrete, assumed for experimental design.
phi_F = 1.0; % FOS for FRP, assumed for experimental design.

%Concrete Material Properties
epsilon_cu = 0.0035; %concrete crushing strength Cl. 8.4.1.2.

%Cross-sectional Properties
b_w = 200; %mm, assumed constant, the formwork will not vary significantly.
d = 270; %mm, assumed constant, this is one of the main test parameters.
d_top = 237.6; %mm, effective depth to the top layer of reinforcement, used
%for computation of moment capacity.
n_top = 4; %No. of bars in top layer
d_middle = 270.0; %mm, for computation of moment capcity.
n_middle = 4; %No. of bars in middle layer.
d_bottom_outer = 297.2; %mm, for computation of moment capacity.
n_bottom_outer = 2; %No. of bars in bottom outer layer.
d_bottom_inner = 307.6; %mm, for computation of moment capacity.
n_bottom_inner = 2; %No. of bars in bottom inner layer.
h = 350; %mm, total height of beam.
n_bar_l = 12; %total number of specified longitudinal bars in beam.

%Member Properties
```

```
a_over_d = 2.5; %assumed constant.
a = 675; %mm, length of shear span.
l = 2 * a; %mm, length between simple supports.
l_bearing = 100; %mm, assumed bearing length at the supports.

%Reinforcement Properities
dia_eff_l = 12.0; %mm, effective longitudinal reinforcement diameter.
dia_eff_s = 12.0; %mm, effective stitrrup diameter.

%Stirrup Spacing
% Only one value is specified for a given model run, and it is asusmed
% constant since it is one of the main test parameters.
%s = 100; %mm, assumed constant, one of the main test variables.
s = 150;
%s = 220;
%s = 100000; %for beam with no shear reinforcement.

%CSA S806-12 Shear Model Mandatory Reduction Factor Value
% This factor of equation 8-22 was given a specific value for each model
% run, and is assumed constant since it is one of the main parameter of
% interest in the experimental design.
coefficient = 0.4; %coefficient in computation of stirrup contribution to shear strength.
%coefficient = 0.7;
%coefficient = 1.0;

%User Defined Random Variables
%============================
%Conrete
% Only one distribution was chosen per model run.
% f_prime_c = 25 + (50-25).*rand(n,1); %MPa, Concrete Strength, Uniform
%Distribution
Nom = 40; %MPa, Approx. Nominal Strength, 1.14 bias factor, 0.12 COV;
f_prime_c = normrnd((Nom*1.15),(Nom*1.15*0.125),n,1); %MPa, Concrete
%Strength, Normal distribution

%Longitudinal Bars
f_Fu_l = wblrnd(1398.6,11.5159,n,1); %MPa, Uniaxial Longitudinal Bar
%Strength, Weibull Distribution
epsilon_Fu_l = normrnd(2.680,0.552,n,1) / 100; %Rupture Strain of Longitudinal
%Bar, Normal Distribution
E_F_l = wblrnd(65784.3,44.8330,n,1); %MPa, Elastic Modulus of Longitudinal,
%Bar, Weibull Distribution

%Stirrups
f_Fu_s = wblrnd(1059.05,8.4570,n,1); %MPa, Uniaxial Stirrup Straight
%Portion Strength, Weibull Distribution

%Arrays for Plotting Data
Graphscale = {'Concrete Strength, f`c, MPa','Uniaxial Longitudinal Bar Strength, f_F_u-l, MPa',
'Longitudinal Bar Rupture Strain, epsilon_F_u, unitless','Uniaxial Longitudinal Bar Elastic
Modulus, E_F, MPa', 'Uniaxial Stirrup Bar Strength, f_F_u-s, MPa'};
GraphMatrix = [f_prime_c, f_Fu_l, epsilon_Fu_l, E_F_l, f_Fu_s];

%Computed Beam Design Parameters
%==============================
%Concrete Material Properties
alpha_1 = 0.85 - 0.0015 .* f_prime_c;
beta_1 = 0.97 - 0.0025 .* f_prime_c;

%Cross-sectional Properties
A_F_bar = pi * (dia_eff_l / 2)^2; %mm2, longitudinal bar area.
A_F_total = n_bar_l * A_F_bar; %mm2, total longitudinal bar area for beam.
A_V_doubleLegged = 2 * pi * (dia_eff_s / 2)^2; %mm2, stirrup area.
%A_V_doubleLegged = 0; %mm2, for beam with no shear reinforcing.
d_v = min((0.9 * d),(0.72*h)); %mm, effective shear depth of beam.
rho_Fw = A_F_total / (b_w * d); %mm, reinforcement ratio.

%Computation of Mr by CivE 313 Course Notes
%=========================================
alpha = alpha_1 .* phi_F .* f_prime_c * b_w;
beta = phi_F .* A_F_total .* E_F_l * epsilon_cu;
gamma = -phi_F .* A_F_total .* E_F_l .* beta_1 * d * epsilon_cu;
positive_root_a = (-beta + (beta.^2 - 4 .* alpha .* gamma).^0.5) ./ (2 .* alpha); %mm, depth of
compression block
c = positive_root_a ./ beta_1; %mm, depth to neutral axis.
epsilon_F_top = ((d_top - c) ./ c) * epsilon_cu; %strain in longitudinal FRP
epsilon_F_middle = ((d_middle - c) ./ c) * epsilon_cu; %strain in longitudinal FRP
epsilon_F_bottom_outer = ((d_bottom_outer - c) ./ c) * epsilon_cu; %strain in longitudinal FRP
epsilon_F_bottom_inner = ((d_bottom_inner - c) ./ c) * epsilon_cu; %strain in longitudinal FRP
M_r = phi_F .* E_F_l .* A_F_bar .* ((n_top .* epsilon_F_top .* (d_top - 0.5.*positive_root_a)) +
(n_middle .* epsilon_F_middle .* (d_middle - 0.5.*positive_root_a)) + (n_bottom_outer .*
```

```
epsilon_F_bottom_outer .* (d_bottom_outer - 0.5.*positive_root_a)) + (n_bottom_inner .*
epsilon_F_bottom_inner .* (d_bottom_inner - 0.5.*positive_root_a))); %N.mm, resisting moment.

%Confirm Compression Failure
%============================
limit = 7 / (7 + 2000 .* epsilon_Fu_l); %Cl.8.4.1.4
c_over_d = c ./ d; %for comparison to limit
for i = 1:n
    if c_over_d(i) <= limit(i)
        URFailure(i) = 1;
    end
end
%Additional FRP strain check
for i = 1:n
    if (epsilon_F_bottom_inner(i) >= epsilon_Fu_l(i))
        URFailure(i) = 1;
    end
end

%Compute Vf from Beam Diagrams
%============================
M_f = M_r; %N.mm, obvious assumption.
P_m = M_f * l / a^2; %N, failure load due to moment.
P_vCSA = P_m; %N, initial assumption for assessing shear failure mode.
V_f = P_vCSA * a / l; %N, assumed shear in each span for assesing shear failure mode.


%Compute Vr as per CSA S806-12 and Iterate to Find Failure Load
%==============================================================
V_c = zeros(n,1); %N, Concrete contribution
V_sF = zeros(n,1); %N, Stirrup Contribution
V_r = zeros(n,1); %N, V_r = V_c + V_sF, Total Shear Capacity

%Compute ks as per Cl.8.4.4.7 - Constant.
k_s = 750 / (450 + d); %modification factor

for i = 1:n
    endCounter = 0; %to stop iterating once V_r = V_f.
    while endCounter == 0
        %Compute Vc as per Cl.8.4.4.5
        k_m = ((V_f(i) * d) / M_f(i))^0.5; %modification factor
        if k_m > 1.0
            k_m = 1.0;
        end

        k_r = 1 + (E_F_l(i) * rho_Fw)^(1/3); %modification factor

        V_c(i) = 0.05 * phi_c * k_m * k_r * (f_prime_c(i) ^ (1/3)) * b_w * d_v; %N, computed
concrete shear strength
        V_c_max = 0.22 * phi_c * f_prime_c(i)^0.5 * b_w * d_v; %N, maximum concrete shear
strength allowed by standard
        V_c_min = 0.11 * phi_c * f_prime_c(i)^0.5 * b_w * d_v; %N, minimum concrete shear
strength allowed by standard
        if (V_c(i) > V_c_max)
            V_c(i) = V_c_max;
        elseif (V_c(i) < V_c_min)
            V_c(i) = V_c_min;
        end

        %Apply Cl. 8.4.4.6 as per experimental design
        %Compute ka as per Cl.8.4.4.6
        k_a = 2.5 / (M_f(i) / (V_f(i) * d)); %modification factor
        if k_a < 1.0
            k_a = 1.0;
        elseif k_a > 2.5
            k_a = 2.5;
        end
        V_c(i) = V_c(i) * k_a;

        %Cl. 8.4.4.7 does not apply.

        %Compute V_sF as per Cl.8.4.4.9
        if M_f(i) < (V_f(i)*d_v)
            Mtemp = (V_f(i)*d_v);
        else
            Mtemp = M_f(i);
        end
        epsilon_1 = ((Mtemp / d_v) + V_f(i)) / (2 * E_F_l(i) * A_F_total); %strain at mid-depth
of beam.
        theta = 30 + 7000 .* epsilon_1; %deg, angle of diagonal compressive stress.
        if theta > 60
```

```
            theta = 60;
        elseif theta < 30
            theta = 30;
        end

        V_sF(i) = (coefficient * phi_c * A_V_doubleLegged * f_Fu_s(i) * d_v) / (s * tan(theta *
pi / 180)); %N, shear strength of stirrups.

        %Compute Vr as per Cl.8.4.4.4
        V_r(i) = V_c(i) + V_sF(i);
        V_r_max = 0.22 * phi_c * f_prime_c(i) * b_w * d_v;
        if V_r(i) > V_r_max
            V_r(i) = V_r_max;
        end

        %Iteration Decisions
        ratio = V_f(i) / V_r(i);

        if abs(1-ratio) > 0.000001
            P_vCSA(i) = P_vCSA(i) + 1.33 * (V_r(i) - V_f(i)); %1.33 was found to a good value for
quickly convering to a solution.
            V_f(i) = P_vCSA(i) * a / l; %recompute the applied shear value using beam diagram
formulae.
            M_f(i) = P_vCSA(i) * (a - d_v) / 2; %recompute the applied moment value using beam
diagram formulae.
        else
            endCounter = 1; %terminates iteration if converance is acheived
        end
    end
end

%Block of code for seperating shear failures and compressive flexural failures.
P_temp = P_m;
for i = 1:n
    if P_vCSA(i) < P_m(i) %P(i) represents the converged failure loads in shear
        ShearFailure(i) = 1;
        P_temp(i) = P_vCSA(i);
    else
        BendingFailure(i) = 1;
    end
end

%Block of code for determining if no failure is expected.
for i = 1:n
    if P_temp(i) > machineLimit
        NoFailure(i) = 1;
        ShearFailure(i) = 0;
        BendingFailure(i) = 0;
    end
end

%This section of code is for creating plots.
%These variables are indicies that will be used to match failure modes to
%their respective failure loads in the array P_temp.
indShear = find(ShearFailure);
indBending = find(BendingFailure);
indNone = find(NoFailure);
indUR = find(URFailure);

PShear = P_temp(indShear);
PBending = P_temp(indBending);
PNone = P_temp(indNone);
PUR = P_temp(indUR);

%This block of code is used to create the legend for the plots. Multiple
%runs found that for these particular specimens the cases of no failure and
%flexural tension failure would not happen and as such including them in
%the legend cause problems with the plots.
legendString = {'Shear Failure' 'Bending Failure' 'No Failure Expected' 'Under Reinforced / FRP
Rupture Failure'};
indLegend =zeros(4,1);
if sum(ShearFailure) > 0
    indLegend(1) = 1;
end
if sum(BendingFailure) > 0
    indLegend(2) = 1;
end
if sum(NoFailure) > 0
    indLegend(3) = 1;
end
if sum(indUR) > 0
```

```
    indLegend(4) = 1;
end

fig = 0;

%Block of code to plot the failure load VS the RV.
if n < (2^16 + 1)
    for i = 1:np
        fig = fig + 1;
        figure(fig)
        hold on
        scatter(GraphMatrix(indShear,i),PShear(:),1,'.','cdata',[(81/256),(81/256),(81/256)])
%dark grey

scatter(GraphMatrix(indBending,i),PBending(:),1,'.','cdata',[(191/256),(191/256),(191/256)])
%light grey
        scatter(GraphMatrix(indNone,i),PNone(:),25,'x','cdata',[(235/256),(235/256),(235/256)])
%very light grey
        scatter(GraphMatrix(indUR,i),PUR(:),25,'+','cdata',[(125/256),(125/256),(125/256)])
%black
        ylabel('Load, P, N')
        xlabel(Graphscale(i))
        title('Uncertainty Analysis')
        legend(legendString(find(indLegend)))
    end
end

RatioShearFailureCSA = 100 * sum(ShearFailure) / n
RatioBendingFailureCSA = 100 * sum(BendingFailure) / n
RatioNoFailureCSA = 100 * sum(NoFailure) / n
RatioURFailureCSA = 100 * sum(URFailure) / n

%Block of Code to Export Data to Excel for Thesis Plot
fileName = strcat('MonteCarloForThesis.xlsx');
titleRow{1} = sprintf('fc for PShear');
titleRow{2} = sprintf('PShear');
titleRow{3} = sprintf('fc for PBending');
titleRow{4} = sprintf('PBending');
titleRow{5} = sprintf('fc for PNone');
titleRow{6} = sprintf('PNone');
titleRow{7} = sprintf('fc for PUR');
titleRow{8} = sprintf('PUR');
xlswrite(fileName, titleRow, 'Sheet1')
fcPShear = f_prime_c(indShear);
fcPBending = f_prime_c(indBending);
fcPNone = f_prime_c(indNone);
fcPUR = f_prime_c(indUR);
if isempty(fcPShear) == 0
    xlswrite(fileName, fcPShear, 'Sheet1','A2')
    xlswrite(fileName, PShear, 'Sheet1','B2')
end
if isempty(fcPBending) == 0
    xlswrite(fileName, fcPBending, 'Sheet1','C2')
    xlswrite(fileName, PBending, 'Sheet1','D2')
end
if isempty(fcPNone) == 0
    xlswrite(fileName, fcPNone, 'Sheet1','E2')
    xlswrite(fileName, PNone, 'Sheet1','F2')
end
if isempty(fcPUR) == 0
    xlswrite(fileName, fcPUR, 'Sheet1','G2')
    xlswrite(fileName, PUR, 'Sheet1','H2')
end

%==========
%M Nehdi
%==========
%Compute Vr as per M. Nehdi et al. "Proposed Shear Design Equations for FRP-Reinforced Concrete
Beams Based on Genetic Algorithmys Approach"
%=================================================
% This block of code recycles the variables from before, and redoes the
%Monte-Carlo analysis for the M.Nehdi et al. shear model.
V_c = zeros(n,1);
V_sF = zeros(n,1);
V_r = zeros(n,1);

V_c = 2.1 * (((f_prime_c .* rho_Fw * d .* E_F_l) / (a * 200000)).^0.23) * b_w * d;
V_sF = 0.74 * (((A_V_doubleLegged / (b_w * s)) .* f_Fu_s).^0.51) * b_w * d;
V_r = V_c + V_sF;

P_vMN = V_r * l / a;
```

```
%Reset arrays to keep track of failure modes.
BendingFailure = zeros(n,1); %Flexural Compression
ShearFailure = zeros(n,1);
NoFailure = zeros(n,1);

%Block of code for seperating shear failures and compressive flexural failures.
P_temp = P_m;
for i = 1:n
    if P_vMN(i) < P_m(i) %P(i) represents the converged failure loads in shear
        ShearFailure(i) = 1;
        P_temp(i) = P_vMN(i);
    else
        BendingFailure(i) = 1;
    end
end

%Block of code for determining of no failure is expected.
for i = 1:n
    if P_temp(i) > machineLimit
        NoFailure(i) = 1;
        ShearFailure(i) = 0;
        BendingFailure(i) = 0;
    end
end

%Block of code for plots
indShear = find(ShearFailure);
indBending = find(BendingFailure);
indNone = find(NoFailure);
indUR = find(URFailure);

PShear = P_temp(indShear);
PBending = P_temp(indBending);
PNone = P_temp(indNone);
PUR = P_temp(indUR);

legendString = {'Shear Failure' 'Bending Failure' 'No Failure Expected' 'Under Reinforced / FRP
Rupture Failure'};
indLegend =zeros(4,1);
if sum(ShearFailure) > 0
    indLegend(1) = 1;
end
if sum(BendingFailure) > 0
    indLegend(2) = 1;
end
if sum(NoFailure) > 0
    indLegend(3) = 1;
end
if sum(indUR) > 0
    indLegend(4) = 1;
end

%Block of code to plot the failure load VS the RV.
if n < (2^16 + 1)
    for i = 1:np
        fig = fig + 1;
        figure(fig)
        hold on
        scatter(GraphMatrix(indShear,i),PShear(:),1,'.','cdata',[(81/256),(81/256),(81/256)])
%dark grey

scatter(GraphMatrix(indBending,i),PBending(:),1,'.','cdata',[(191/256),(191/256),(191/256)])
%light grey
        scatter(GraphMatrix(indNone,i),PNone(:),25,'x','cdata',[(235/256),(235/256),(235/256)])
%very light grey
        scatter(GraphMatrix(indUR,i),PUR(:),25,'+','cdata',[(125/256),(125/256),(125/256)])
%black
        ylabel('Load, P, N')
        xlabel(Graphscale(i))
        title('Uncertainty Analysis')
        legend(legendString(find(indLegend)))
    end
end

%Block of code to plot the RV against one another.
if n < (2^16 + 1)
    for i = 1:(np-1)
        for j = (i+1):np
            fig = fig + 1;
            figure(fig)
```

```
            hold on

scatter(GraphMatrix(indShear,i),GraphMatrix(indShear,j),1,'.','cdata',[(81/256),(81/256),(81/256)
]) %dark grey

scatter(GraphMatrix(indBending,i),GraphMatrix(indBending,j),1,'.','cdata',[(191/256),(191/256),(1
91/256)]) %light grey

scatter(GraphMatrix(indNone,i),GraphMatrix(indNone,j),25,'x','cdata',[(235/256),(235/256),(235/25
6)]) %very light grey

scatter(GraphMatrix(indUR,i),GraphMatrix(indUR,j),25,'+','cdata',[(16/256),(16/256),(16/256)])
%black
            ylabel(Graphscale(j))
            xlabel(Graphscale(i))
            title('Uncertainty Analysis')
            legend(legendString(find(indLegend)))
        end
    end
end

RatioShearFailureNedhi = 100 * sum(ShearFailure) / n
RatioBendingFailureNehdi = 100 * sum(BendingFailure) / n
RatioNoFailureNehdi = 100 * sum(NoFailure) / n
RatioURFailureNehdi = 100 * sum(URFailure) / n
```

B: Procedure for Affixing Strain Gauges to GFRP Surface

This appendix contains a description of the procedure used to prepare the surface of GFRP reinforcing bars and stirrups for strain gauges, the procedure for affixing strain gauges to those surfaces, and the procedure for protecting the gauges.

This procedure was written by the author based on the review of the following sources: (HBMa, n.d.)(HBMb, n.d.)(Hoffmann, 1979). None of the sources were directly related to the specific combination of materials used in the procedure and were never directly cited..

B.1 Required Materials and Supplies

Safety

- This procedure does not purport to address all possible safety concerns. Discuss any and all safety concerns with an appropriate authority before starting.
- Disposable latex gloves
- Goggles
- Dust mask

Chemicals

- Cyanoacrylate adhesive
- Chemically pure isopropyl alcohol
- Neutralizing agent
- Polyurethane

Supplies

- Strain gauges: Tokyo Sokki Kenkyujo Co. Ltd. type FLA-5-11-5L
- Magnifying lamp
- Coarse hand file
- 240, 320, and 400 grit sand paper / emery paper
- Burnishing tool / pen
- Cellophane film
- Sterile lab tissues
- 2 pairs of tweezers
- Clear adhesive tape which will not deposit mastic
- Scissors
- Teflon sheets
- Minute timer
- Electrical tape
- Tokyo Sokki Kenkyujo Co. SB Tape (a.k.a. Buthyl)
- Stiff working surface approximately 1 ft by 1 ft
- Temporary dish for holding a small amount of solvent
- Desk mounted vice with rubber grip inserts

B.2 Preparation of Bonding Surface

A magnifying lamp is necessary at several points in this procedure; it will be necessary to closely inspect the GFRP surface in step 2, to marking the surface in step 3, and to position the gauge in step 6. A desk mounted vice with rubber grip inserts will be very useful for holding the bar during this procedure.

Step 1) Perform a coarse clean of the GFRP surface.

Inspect the bars and clean off any obvious deleterious materials and debris such as paints, lubricants, dirt, etc. Remove any cleaning agents by thoroughly rinsing the area with clean water. Note that water film on a degreased surface will be unbroken. Use appropriate personal protective equipment for the type of cleaning being done.

Step 2) Smooth the surface on to which the strain gauge will be affixed.

Wear appropriate protective gear including a dusk mask and goggles for this step. Filing and sanding will create FRP dust which includes glass fibres.

A hand file should be used to remove the mechanical and frictional bonding components of the GFRP bars such as shear ribs or sand particles. Removing these components will provide a smooth, unobstructed surface on which to affix the strain gauge. The use of a hand file is recommended in order to avoid excessive cross-sectional loss which may occur with a mechanical grinder. File the surface to conform to the curvature of the bar if the intended strain gauges are compatible with curved surfaces.

Once an area large enough to fit the strain gauge is exposed, use sand paper to smooth out the roughness left on the surface by the file. Start with sand paper of 240 grit and move the sand paper in circling motions to avoid creating preferential stress directions. Proceed to finer grits and stop after sanding with a 400 grit sand paper. The actual purpose of the sand paper is to create a surface with a very fine and uniform roughness which will increase the bond between the FRP and adhesive.

Step 3) Mark the exact position of the gauge.

A burnishing tool should be used to make marks, such as a dry ballpoint pen. Avoid using any marking tool which will leave residue or which will damage the surface. Do not make marks which will be covered by the gauge as these marks may affect both adhesion and the distribution of stresses directly underneath the gauge. However, when completed the marks should be visible after the final cleaning in step 5. Strain gauges come with alignment markings on their backs, consider these when making marks on the bar.

B.3 Affixing the Strain Gauge

Steps 1 to 3 can be done in advance, though it may be more convenient to do step 3 in the same session as steps 4 through 8. The following steps should be done in one sitting and may take anywhere between 20 to 30 minute to complete.

Step 4) Prepare the working area.

Don the necessary protective gear including goggles and clean disposable latex gloves. The gloves serve a dual purpose to protect skin from solvent exposure and to prevent tools and surfaces from being contaminated with natural oils present on the hands. This equipment should remain on until the end of the procedure. Replace gloves if they become contaminated.

Prepare a clean working surface by wrapping a stiff flat object, such as a 1 ft by 1 ft piece of plywood or cutting board, in cellophane. Assemble all necessary items for the cleaning of the GFRP surface, and for affixing the strain gauges which may include: tweezers, scissors, solvents, adhesives, neutralizing agent, tape, tissues, etc.

Pour a portion of the solvent from the stock bottle in to a clean dish. The solvent should be chemically pure, non-reactive, and should not dissolve the polymer of the FRP material or the protective

latex gloves. Standard isopropyl alcohol has been suggested as a cleaning and degreasing agent, though mild soap and water has also been suggested.

Clean all instruments by dipping tissues into solvent and whipping down both the working surfaces and handles of tools.

Step 5) Clean the smoothed GFRP surface.

The surface needs to be free from impurities and dirt which will interfere with the ability of the adhesive to bond with the GFRP surface. To clean the GFRP surface use a clean tissue wrapped around the tines of a pair of tweezers and held in place by the tip of the finger. Dip the tissue in the solvent and clean the surface by moving the tissue in circling motions. Replace soiled tissues and continue cleaning until a fresh solvent dipped tissue shows no signs of dirt after wiping. Two final cleaning swipes are recommended and each motion should be done with a fresh tissue dipped in solvent. The first swipe should start at one edge and proceed to the other, and the second should proceed in the opposite direction.

Once the GFRP surface has been cleaned with the solvent, the solvent residue must be removed as it may interfere with the adhesive. Use a tissue dipped in neutralizing agent to clean the surface. The agent provides two functions, to remove residue and to balance the pH of the GFRP surface. Follow the same cleaning instructions outlined in the previous paragraph including the two final swipes.

Further notes on the preparation of the GFRP surface:

- Avoid spreading natural oils, wash hands and wear protective gloves.
- Never use a solvent directly from the stock bottle, place a small amount in a clean temporary vessel.
- Use solvents in well ventilated space, cover solvents when not in use.
- Use cleaning materials which are free from soluble particles.
- Avoid contaminating the solvents, never double dip a tissue.

Step 6) Position the strain gauge on the GFRP surface.

Only handle the strain gauge with the tweezers, the bonding surface of the gauge when it first comes out of the package will be free from contamination. The bond side of the gauge will not have any markings. Place the strain gauge with the bond side down on the clean surface. Using tweezers and scissors, cut a small piece of adhesive tape off the roll and place it on the back of the strain gauge. The purpose of the tape is to hold the gauge in position during the adhering process in step 7. Place the tape on the gauge so that it extends outwards from one of the longer edges of the gauge, though it is okay if a small amount of tape overlaps the other sides.

To position the gauge, hold it from the strain gauge lead with the hand or between the soldier terminals with tweezers, and hold the edge of the tape with a second pair of tweezers. Align the gauge with the marked location on the GFRP surface. This step may take some time depending on how precisely the gauge must line up with the markings. Care should be taken to avoid damaging the gauge and leads when lifting and repositioning. It is best to use the tweezers, both pairs, during this process. Avoid grasping the gauge directly, and use the tweezers to grasp the edges and corners of the tape. Avoid subjecting the gauge to any folding motions.

Once the gauge is positioned in needs to be rolled back so that the adhesive may be applied. Roll the tape back along itself leaving a length of tape 1 to 2 millimeters wide between the gauge and the GFRP surface.

Step 7) Adhering the strain gauge.

Do this part quickly! You will need to have ready the adhesive, a teflon foil, and the timer.

The gauge will be set in a quick rolling motion of the finger, or thumb, which will lay the tape and gauge flat and simultaneously apply a smooth and even pressure. First, position the finger behind the

tape and gauge with a teflon foil between the surface of the glove and the surface of the tape. The teflon will prevent adhesive from getting on the glove. Place just a drop of adhesive in the gap described at the end of Step 6.

Then in one smooth motion roll the finger over and then keep a constant and firm pressure on the gauge for 1 minute. The rolling motion will spread the drop of adhesive evenly between the gauge and GFRP surface. The adhesive layer should be as thin as possible; constant firm pressure ensures that excess adhesive is pushed out while it cures. The curing of the cyanoacrylate adhesive is accelerated by heat from the finger will be sufficiently cured within 1 minute.

After the minute has passed remove the finger, teflon foil, and tape from atop the strain gauge. Pull the tape back on itself, almost horizontally, such that the angle it forms between itself is very small. The cyanoacrylate adhesive cures to a matte finish, any areas which appear shiny or glistening can be cured by placing the teflon foil over the area and applying pressure with the finger for a brief period of time.

If the gauge was damaged in the process then return to step 2 but skip coarse filing. Using good judgement, sand until the gauge and adhesive are removed, and finish with 400 grit sandpaper.

B.4 Protecting the Strain Gauge

The gauge is delicate and needs to be protected from handling of the bars, and from the caustic environment of hydraulic concrete and concrete pore solution.

Step 8) Surface coating.

Use a small applicator brush and apply a thin coat of polyurethane shortly after the tape is removed in step 6. Apply the polyurethane atop the gauge, exposed portion of the leads, and exposed glass fibres. The polyurethane coating takes 24 hours to cure, though an accelerant may be brushed on top of the coating a few moments after it is applied.

Step 9) Final protective layers.

Apply a putty material known as SB Tape after a 24 hour period to further protect the gauges and exposed GFRP fibres. Place the putty material in the centre of the gauge and knead & roll it out with the fingers until it covers the gauge, lead wires, and exposed glass fibres. Take electrical tape and wrap it over top of the SB Tape and around the bar to prevent the putty from being worked out of place during handling or later concrete compaction.

Further notes on the protection of the strain gauge:

- Avoid manhandling the lead wires, as they may rip free from the gauge. Add a margin of safety by looping an inch or two of lead wire back on itself immediately adjacent to the gauge. Then use a cable tie or tape to hold the loop in place. If the lead wire is tugged on, it will pull from the excess in then loop before pulling on the gauge connection.

C: Experimental Procedure for GFRP Shear Critical Beam Tests

This appendix contains the procedure for the set-up of experimental test specimens in the load frame, and the procedure for experimental testing.

C.1 Required Materials and Supplies

Safety

- This procedure does not purport to address all possible safety concerns. Discuss any and all safety concerns with an appropriate authority if using this as a guide for future testing.
- Shatter resistant safety glasses / goggles
- Steel toed safety boots (or equivalent)
- Durable work gloves
- Latex gloves
- 1 – 4'x8' plywood barrier
- 1 – 4'x6' polycarbonate (Lexan) barrier

Equipment

- 1 – 500 kN load frame (Uniroyal Frame) and load frame controlling computer with MTS software
- 1 – Forklift
- 1 – 'pin-support' with knife edge
- 1 – 'roller-support' with knife edge and roller bars
- 1 – 'roller-support' pivoting load applicator
- 1 – Data acquisition system with a minimum of 18 channels (running LabView v8)
- 1 – 5 inch LVDT
- 2 – 3 inch LVDT
- 1 – Optical crack comparator
- 1 – 20x magnification optical loupe
- 2 – HD Cameras & Tripods
- 3 – ¼" aluminum bars

Materials and Supplies

- 12 experimental beam specimens
- 1 – 100mm x 350mm x ¼inch bearing plate
- 1 – 100mm x 360mm x 25mm bearing plate
- USG Hydro-Stone
- Assorted colours of permanent marker
- Latex based primer
- DAP hydrated lime, NaCl salt, water
- Paint tray, mixing container, roller paint applicator assembly
- Straight edge

- Rubber mallet and plumb bob
- Test tube holders with magnetic bases
- Bungee cords or small diameter steel cables, eye-bolts and wing-nuts
- Shunt box for testing strain gauges
- USB drive

C.2 Procedure for Test Set-up

Beam Preparation

Test specimens were painted white on both sides to make crack identification easier. Initially, a latex based primer was used, diluted with one part water for 2 parts primer by volume. Beam series BMX-INF and BMX-220 were painted with this dilution; however, there were concerns about the elasticity of latex obscuring crack tips. Beam series BMX-150 and BMX-s230 were painted with a traditional white wash using 8 to 5 parts DAP hydrated lime, to 1 part NaCl salt, to 5 parts water by volume. White wash was thought to be as brittle as concrete. White wash is caustic, so appropriate protection such as latex gloves were used. Beams were painted with a roller brush.

The sides of test specimens were overlaid with a 100 mm x 100 mm grid drawn on using permanent markers and a straight edge. The grid was centred at mid-span with the first 100 mm row starting at the base of the beam. The grid was to facilitate observations on crack growth for later testing. The locations of other important elements were also marked, including support points, load points, bearing plate locations, and displacement transducer locations. Beams were labelled at the south end; the south end encased the strain gauges.

Specimen Set-up in Test Frame

Test specimens were forklifted into place and set to rest on the roller and pin supports which rested on level pedestals. Beams were centred with the use of a plumb bob and forceful pushing. Supports were aligned by tapping with a rubber mallet for small modifications, and larger movements involved jacking the beam off the supports.

The bearing plate was positioned at the top centre of the beam as indicated by markings. Most beams used the thinner bearing plate, but concerns about the roller support load harness coming in contact with both the beam and bearing plate after significant deformation arose. Later beams used the thicker bearing plate. Bearing plates were set in place with the application of Hydro-Stone. Hydro-Stone was prepared by the careful addition of water to the powdered product until the mixture reached the consistency of a thick syrup or honey. The hydro-Stone was left to set overnight.

Specimens which were ready to test resembled the figure below.

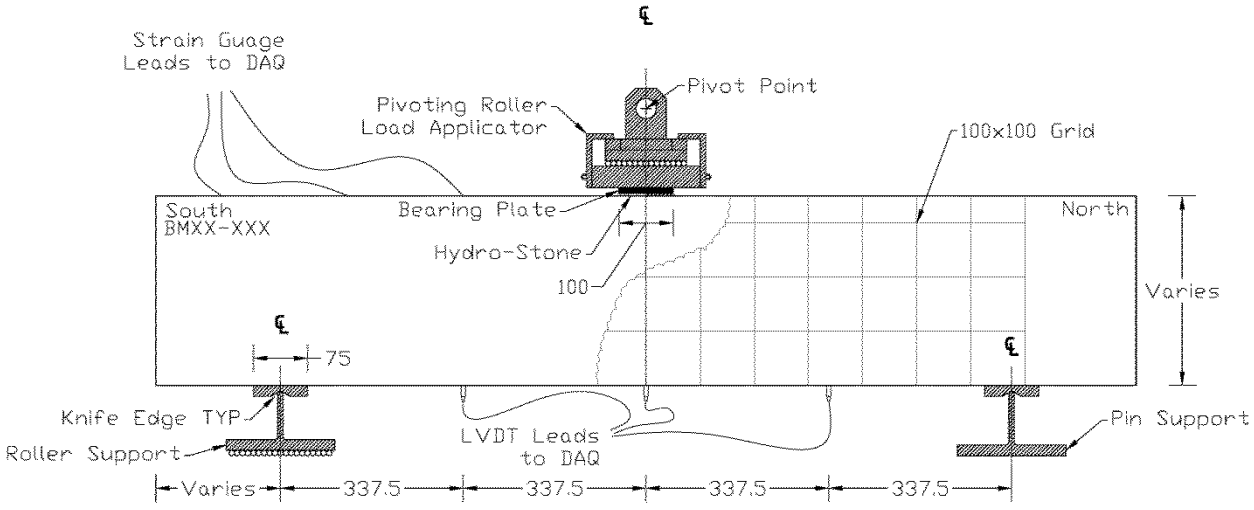

Instrumentation Preparation

Strain gauges were connected to the data acquisition system in the following order:

Longitudinal Bars

- First: gauges at mid-span, starting with the closest to the tension face (L-1-c, L-2-c, etc…), for specimens with 25M bars, starting with gauges labeled A, then B.
- Second: gauges on longitudinal bars in increasing order (L-2-1, L-2-2, etc…)

Stirrups

- Third: gauges located on bends, in increasing order (S-4-B, S-5-B, etc…)
- Fourth: gauges located on straight portions, in increasing order (S-4-S, S-5-S, etc…)

The LVDTs were held in place by laboratory test-tube holders attached to magnetic bases. The bases rested on firm steel blocking. Aluminum bars ¼" thick were strapped to the bottom of the beams at the measuring points and held in place initially by steel cabling, and later by common bungee cords. Eye-bolts and wing-nuts were threaded through drilled holes on either end of the bars to connect the bars to the cords. The LVDTs were hung upside down to minimize the risk of the LVDT casing from being damaged in the event of catastrophic failure. The displacement transducers were connected to the data acquisition system in the following order: north quarter point, midspan, south quarter point. The LVDTs were calibrated prior to the first test.

The load cell was connected to the computer running the MTS software, which was relayed to the data acquisition system. The load frame actuator displacement data was routed similarly.

Tests were performed to confirm that the system was recording data before each test. A shunt box simulated strain, LVDT cores were manually displaced.

C.3 Testing

The test started by positioning the load applicator such that it was just touching the rollers in the roller harness. The displacement in the MTS software was zeroed, but the load cell output was not zeroed as it outputs true measurements of load. The data acquisition system was initialized and the strain and displacement gauges were zeroed; gauges were sampled three times every second.

The load was applied at a displacement controlled rate of 0.272 mm/min until the predicted cracking load was reached. After first cracking the load rate was increased to 0.400 mm/min for all beams in BMX-220, -150, -s230 except BM25-220. Loading was halted at predetermined intervals to measure cracks. The first crack measurements were taken at the predicted cracking load, and the final crack measurement was taken at approximately 70 percent of the lowest predicted failure load. Initially, 9 load

increments, 10 measurements, were specified, but this was reduced to 6 increments, 7 measurements, after the BM25-220 test.

Measurements ceased after the approximate 70 percent lowest predicted failure load level because of safety concerns, and protective barriers were then erected around the specimen. A GFRP reinforced concrete beam, by the virtue of its constituent materials, is brittle in nature as are shear failure modes. Two barriers were erected to address the risks of concrete projectiles, which may be ejected at failure. One barrier was made of polycarbonate, allowing those involved to see and photograph the beam specimen, and the other made of plywood. The barriers were situated between the test specimen and the test frame columns and held in place by wire ties. The barriers were prevented from moving outwards by the test frame columns.

Crack measurements were always made on the east side of the beam with a 20x magnification optical loupe, and when helpers were available they were also made on the west side with a crack comparator card; however, the measurements made by helpers were not included in this thesis. Crack measurements were made at the crack mouth and at any location where a crack crossed a gridline. Crack data was recorded on a crack tracking sheet, which is included at the end of this procedure. The sheet contains a diagram, onto which cracks are traced, and includes fields to record the date, beam identifier, load level, and general comments. The body of the tracking sheet includes fields for recording crack growth data and includes a way to identify the crack, the point and location of measurement, and the crack width value.

Initially all cracks were measured as it was not possible to tell which crack would be the most critical crack. Towards the end, only cracks of concern were measured. Measurements included flexural cracks, flexural shear cracks, and shear cracks. New cracks and crack growth were traced on the side of the beam with permanent marker, which alternated colours at each load level. No markings were made to identify closing or closed cracks as the test proceeded.

High definition cameras on tripods captured images at several points: before testing, at each load level after cracks were traced, after failure before the load actuator was retracted, after the load actuator was retracted, and after spalled and loose concrete was removed. The camera on the east side recorded high definition video starting after the barriers were erected and ending after failure.

Data from both the data acquisition system and MTS frame software were saved to a USB drive.

Date:_____ Beam:_____ Load Level:_____

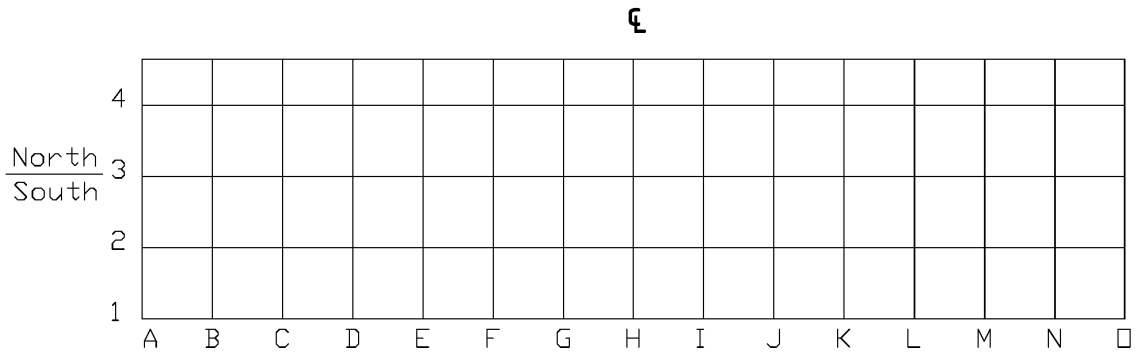

General Comments:

Crack	Location			
	Label	X (mm)	Y (mm)	Width (mm)

Figure C.1: Crack Tracking Sheet

D: Compressive Strength and Tensile Strength Testing

Fifty 100 mm x 200 mm test cylinders were cast alongside the beam specimens. Forty of the cylinders were used to test compressive strength as per CSA A23.2-9C Compressive Strength of Cylindrical Concrete, and ten were used to test tensile strength as per CSA A23.2-13C Splitting Tensile Strength of Cylindrical Concrete Specimens. The data and results are presented at the end of this appendix.

The cylinders were cast on June 19, 2013, and after 2 days they were removed from their molds and left to cure in a moisture room until they were tested. Half were placed high up on a shelf and were not kept constantly wet by the spray in the room, while the other half were placed low on the shelf and were kept wet.

Details of the concrete mix design were outlined in the Experimental Design Chapter.

D.1 Compressive Strength

The 8 day strength, computed using one test cylinder, was 39.4 MPa. The 28 day strength, computed using the average of 3 cylinders, was 47.3 MPa. The cylinder diameters for these first four tests were not measured correctly, so the strengths were corrected as outlined in the following paragraphs.

The remaining cylinders were tested at later dates, the majority of which were tested when the beam tests finished. Sixteen cylinders were tested 100 days after casting with an average strength of 58.3 MPa, and another 12 cylinders were tested 102 days after casting with an average strength of 57.8 MPa. Combined, the 100 and 102 day cylinders represent an average strength of 58.1 MPa.

The cylinder testing machine output both the peak load and peak stress. The peak stress output from the machine assumed a perfect 100 mm diameter cross-section, and would over predict strength. The proper strength is determined using an average of two cylinder diameters measured at mid-height and perpendicular to one another.

The 8 and 28 day test results were corrected by multiplying them by a ratio of the proper stress over the machine output, which was computed using averages of the results of the 100 and 102 day tests.

An aside investigation was done to see if the storage location in the moist curing room impacted cylinder strength. Thirteen of the cylinders from the 100 and 102 day tests came from the lower part of the shelf, and fifteen came from the upper part. The average strength of the cylinders from the lower part of the shelf was 57.8 MPa with a coefficient of variation of 0.06. The average strength of the cylinder from the upper part of the shelf was 58.3 MPa with a coefficient of variation of 0.07. So it would appear that storage location in the moist curing chamber does not impact strength.

D.2 Tensile Strength

Tensile strength tests were performed 102 days after casting on ten specimens; but the data recorder malfunctioned during one test. The average tensile strength was 4.2 MPa. Inspection of the fracture plane showed 90 percent fractured aggregate.

Table D.1: Compression Test Results

Day	Heights (mm)			Diameters (mm)		Mass	Cross-section	Density	Specific Weight	Failure Load	Comp. Strength (machine)	Comp. Strength (calc.)	Failure Type
(d)	h1	h2	h3	d1	d2	(g)	(mm2)	(kg/m3)	(kN/m3)	(kN)	(MPa)	(MPa)	
8	-	-	-	-	-	-	-	-	-	322.238	41.031	-	-
28	200	200	200	-	-	3971	-	-	-	395.718	50.387	-	Cone / Type 1
28	199	200	199	-	-	3981	-	-	-	387.649	49.360	-	Cone-Shear / Type 2
28	201	200	201	-	-	3981	-	-	-	378.170	48.153	-	Shear / Type 4
43	200	200	200	102.0	101.5	3969	8131.3	2441	23.9	378.713	48.222	46.6	Cone / Type 1
43	199	199	199	101.5	102.0	3971	8131.3	2454	24.1	392.088	49.925	48.2	Cone-Shear / Type 2
54	199	199	199	102.0	102.0	3978	8171.3	2446	24.0	470.702	59.930	57.6	Cone-Shear / Type 2
54	201	201	201	102.0	102.0	3993	8171.3	2431	23.8	260.461	33.164	31.9	Cone-Shear / Type 2
57	197	197	197	102.2	107.1	3926	8601.4	2317	22.7	488.148	-	56.8	Cone-Shear / Type 2
57	198	198	198	101.9	102.3	3196	8187.3	1972	19.3	437.824	-	53.5	Cone / Type 1
100	201	200	200	101.4	102.4	4002	8155.3	2450	24.0	471.943	60.008	57.9	Shear / Type 4
100	204	203	203	102.3	102.1	4046	8203.4	2426	23.8	464.074	59.088	56.6	Shear / Type 4
100	197	199	199	103.2	100.5	3932	8147.3	2433	23.9	469.274	59.750	57.6	Cone / Type 1
100	200	200	200	102.5	102.2	3946	8227.5	2398	23.5	459.933	58.558	55.9	Cone / Type 1
100	199	199	200	101.0	102.5	3948	8131.3	2436	23.9	374.496	47.684	46.1	Shear / Type 4
100	200	201	199	101.6	101.7	3945	8115.3	2431	23.8	488.850	62.239	60.2	Cone-Shear / Type 2
100	198	199	198	102.1	102.2	3930	8195.3	2418	23.7	510.095	64.949	62.2	Cone / Type 1
100	201	201	201	101.7	102.5	3994	8187.3	2427	23.8	490.826	62.994	59.9	Cone-Shear / Type 2
100	199	199	199	102.4	101.5	3934	8163.3	2422	23.8	477.774	60.833	58.5	Cone / Type 1
100	197	197	198	102.4	101.5	3930	8163.3	2440	23.9	506.617	64.508	62.1	Shear / Type 4
100	200	202	201	101.2	101.1	3976	8035.7	2462	24.1	507.569	64.625	63.2	Cone-Shear / Type 2
100	202	202	202	101.7	102.5	4013	8187.3	2426	23.8	499.331	63.577	61.0	Cone / Type 1
100	197	198	198	102.6	102.3	3936	8243.5	2416	23.7	467.486	59.523	56.7	Cone-Shear / Type 2
100	200	199	199	102.5	101.5	3955	8171.3	2428	23.8	460.315	58.613	56.3	Cone-Shear / Type 2
100	201	200	200	101.7	101.4	3958	8099.3	2439	23.9	488.450	62.191	60.3	Cone / Type 1
100	200	200	200	101.7	103.0	3995	8227.5	2428	23.8	481.658	61.329	58.5	Cone / Type 1
102	196	196	195	101.5	102.7	3928	8187.3	2452	24.1	520.331	66.252	63.6	Cone-Shear / Type 2
102	202	202	202	101.8	101.7	4034	8131.3	2456	24.1	474.585	60.426	58.4	Cone / Type 1
102	201	202	202	102.5	102.4	4019	8243.5	2418	23.7	450.107	57.310	54.6	Cone / Type 1
102	200	201	201	102.8	102.1	4030	8243.5	2436	23.9	494.090	62.908	59.9	Cone / Type 1
102	197	198	198	101.2	102.0	3943	8107.3	2460	24.1	460.996	58.695	56.9	Cone / Type 1
102	199	200	199	102.3	103.2	4017	8291.9	2430	23.8	519.561	66.156	62.7	Cone / Type 1
102	201	201	201	101.8	101.5	4011	8115.3	2459	24.1	505.509	64.363	62.3	Cone-Shear / Type 2
102	199	199	199	102.7	102.5	3983	8267.7	2421	23.7	487.609	62.088	59.0	Cone / Type 1
102	198	197	198	102.5	102.6	3935	8259.6	2410	23.6	465.106	59.219	56.3	Cone / Type 1
102	198	198	199	103.1	102.3	3980	8283.8	2422	23.8	-	-	-	Cone-Shear / Type 2
102	200	200	199	102.3	101.2	3966	8131.3	2443	24.0	459.635	58.523	56.5	Cone / Type 1
102	198	199	199	101.1	102.5	3936	8139.3	2434	23.9	447.108	56.930	54.9	Cone-Split / Type 2
102	198	199	199	103.0	101.8	3933	8235.5	2404	23.6	423.431	53.910	51.4	Cone-Shear / Type 2
102	198	198	198	102.7	102.1	3934	8235.5	2413	23.7	454.871	57.916	55.2	Cone-Shear / Type 2

Table D.2: Tensile Split Test Results

Day (d)	Heights (mm)		Diameters (mm)			Mass (g)	Failure Load (kN)	Strength (MPa)	Percent Fractured Aggregate
	h1	h2	d1	d2	d3				
102	198	198	102.3	102	101.9	3977	120.471	3.80	90 %
102	201	201	102.3	101.1	101.4	4019	-	-	90 %
102	199	199	102.3	101.7	101.5	3982	113.252	3.56	90 %
102	200	200	100.8	100.6	101.1	3981	114.986	3.63	90 %
102	196	196	102.4	102.1	101.8	3908	159.162	5.06	90 %
102	200	200	101.7	102	102.8	3982	126.801	3.95	90 %
102	199	199	102.7	102.3	101.8	3968	156.462	4.89	90 %
102	199	199	102.1	102.1	101.8	3976	149.522	4.69	90 %
102	199	200	101.7	102.3	103.1	3961	136.035	4.24	90 %
102	198	198	101.9	101.6	101.2	3939	138.989	4.40	90 %

E: Individual Beam Descriptions

This appendix contains all of the results of from individual beam tests, and selected results referenced in Chapter 6 section "Investigation into the Ability of the Indeterminate Strut-and-Tie method to Model Beam Behaviour". The specific strut-and-tie model use by the IST method is indicated in the legend of the plot.

Testing started with the INF series of beams and beam BM25-INF was tested first, then BM16-INF, and BM12-INF. This same pattern was used on subsequent beam series, going from series with the lowest shear reinforcement ration to highest. However, this thesis always showed beams in the order of BM12-X, then BM16-X, followed by BM25-X, and this order is maintained in this appendix.

E.1 A Note on the Presentation of Diagrams & Photographs

All beam drawings, crack diagrams, and photographs show the east side of the beam, and any exceptions are noted in the photograph captions. So, when the reader looks at these images the left-hand side of the image is the south end of the beam, and the right-hand side is the north end. As the reader considers these diagrams and the results they should recall that the South side of the beam contained the instrumentation Sensors.

A number of photographs were included for the results of each beam. These images were taken with a high definition camera, but the quality was reduced to avoid the problem of large file sizes in completing this document. The failure of each beam was recorded on video by the same camera, but the image at failure was taken from a single still / frame from the video and is of lesser quality. In general, testing continued until well past peak load to ensure all beams had failed. Photographs taken after testing show deformation in excess of what would have been seen at peak load, but are included to confirm failure modes. Images which indicate that spalled concrete was removed show the beams after loose bits of concrete were removed by hand only; no mechanical device was used to further remove concrete.

E.2 A Note on Bar, Stirrup, and Gauge Nomenclature

Details of the gauge nomenclature are included in Appendix C, but they are presented here for convenience. Gauges were labeled in the following manner: X-Y-Z, where X indicated to which type of bar the gauge was attached, Y indicated the longitudinal layer or stirrup to which the gauge was attached, and Z indicated their location on the bar. Longitudinal bars were labeled starting with the bottom most layer of bars being numbered 1. Stirrups were labeled starting with the stirrup at the south most end being numbered 1.

For example, a gauge on the bend of stirrup number 5 would be labeled: S-5-B (Stirrup-#5-Bend), and a gauge at the mid-span of a longitudinal bar in the second layer would be labeled: L-2-C (Longitudinal-2nd layer-Centre).

E.3 Generalized Observations

This section repeats, in brief, the discussion of the General Observations Section of the Experimental Observations Chapter.

No stirrups ruptured in any beam. Beams BM12-220, BM12-150, BM16-150, & BM16-s230, showed sharp drops in load after peak load and were more thoroughly examined to investigate the possibility of stirrup rupture. The stirrups were freed from the concrete carefully with a jackhammer. A hacksaw was used to cut the stirrups loose from the longitudinal bars, and a box cutter was used to remove the corrugated plastic tubing around the actual GFRP composite. After extracting the stirrups no obvious signs of stirrup rupture were present; however, some cracking was indicated on stirrup 6 of BM12-150, and stirrup 7 of BM12-220. The cracks formed along the axis of the bar through the bend perpendicular to the plane of the stirrup. It is not known if the cracks formed before or after peak load. Images of the stirrups also show some scoring marks from the box cutter.

The failure of beams can be separated in to two groups: shear-tension failures and shear-compression / strut-crushing failures. The shear-tension failures all occurred in beams without stirrups, beams BMX-INF. The failure plane for these beams formed after crack measurements ceased. In two of the beams the main shear crack ran from load plate to support plate.

The shear-compression / strut-crushing failures occurred in all beams with shear reinforcement. Generally, the shear behaviour was dominated by arch action and the failure plane ran from the load plate to the support. The main shear crack formed before crack measurements ceased, but the exact crack path changed as cracks coalesced.

The majority of beams tested showed few signs of distress as peak load was reached and passed: peak load was not accompanied by loud noises, movement, or the ejection of concrete projectiles. Typically, the only indication of beam distress at peak load was excessive cracking and the formation of cracks which ran from bearing plate to support.

Though, as noted in the individual beam sections, beams with large shear reinforcement ratios showed other signs of distress such as the flaking-off of small bits of concrete, popping noises consistent with the characteristic sound of sudden concrete fracture, and occasionally slight movement. Two beams were noted to have violently ejected concrete.

As a result of this, film stills used to show the condition of beams at failure are approximate; the only indication that peak load was reached was indicated on the load-displacement curve during testing, but it could not have been known a priori that peak load had been reached and was not announced on the video. However, given the very gradual progression of failure for most beams, the stills should be adequate.

Cracking was typical: the mid-span flexural crack formed first followed by more flexural cracks. In beams with stirrups the flexural cracks formed at the location of the stirrups. Flexural cracks then grew into flexural shear cracks, and then shear cracks developed.

Longitudinal strain observations showed a stiff early response up until cracking. This was followed by a much softer response for some small amount of strain, which then stiffened slightly. Near the very end of the test the stiffness gradually softened. Overall the response was highly linearized, as expected since the GFRP longitudinal reinforcement is characterized by linear elastic behaviour.

The observations from the BM16-X series of beams, which included strain gauges along the length of the longitudinal reinforcement in the south shear span, indicated arch action behaviour. The strain at peak load was constant for gauges closest to mid-span. The readings also indicated that bars were well anchored past the bearing plate.

Stirrup strain observations were difficult to generalize since so many of the gauges lead wires snapped across crack faces during testing. Each stirrup in the south shear span included a strain gauge on the stirrup bend in the flexural tension zone of the beam, and on the middle most part of the straight portion of the stirrup on the opposite leg.

Generally, the straight portion of the stirrups in the middle most portion of the shear span strained the most. Stirrup bends strained much less, and stirrups nearest to the support or mid-span strained less as well. Some of the gauges closest to the support or mid-span actually showed small amounts of negative strain.

After testing the top framing bars on all beams with stirrups had ruptured along the plane of the main shear crack. These bars were not thought to have provided any strength and were used for rebar-cage framing.

Small dips in the load-displacement plots indicate pauses for crack measurements as displacement was held constant allowing the beams to relax; though, some dips are indicative of crack formation.

In the photos of the beams with stirrups, blue dots along the top side of the beam indicate the approximate location of stirrups.

E.4 BM12-INF

This was the third beam tested. It was tested at a constant displacement rate of 0.272 mm/min. This beam was the first to use common bungee-cord to hold aluminum bars snug against the bottom of the beam. This was the best system for attaching the aluminum bars for deflection measurements and was used on all subsequent beam specimens. The cords were attached to eye-bolts using bungee-cord hooks.

The beam failed in shear-tension along a shear crack that formed after crack width measurements ceased. The crack ran diagonally from the load plate to the south bearing plate. The crack forked at failure and the fork tines tended to follow the three layers of reinforcement and are indicative of tensile splitting. At peak load a loud noise characteristic of concrete fracture was heard and was accompanied by a slight jolting movement and a slight widening of the main shear crack; there was no ejection of concrete projectiles.

Peak load occurred at 163.1 kN and 4.25 mm of displacement, and the failure took place in the south shear span 54 days after casting.

All of the strain gauges functioned adequately during the test.

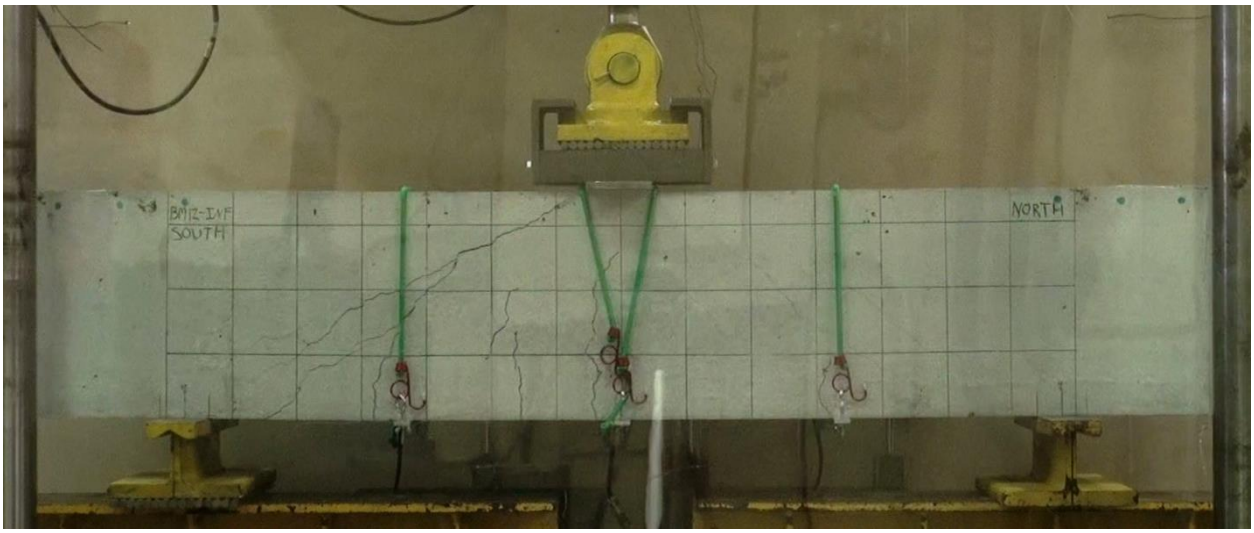

Figure E.1: BM12-INF At Peak Load

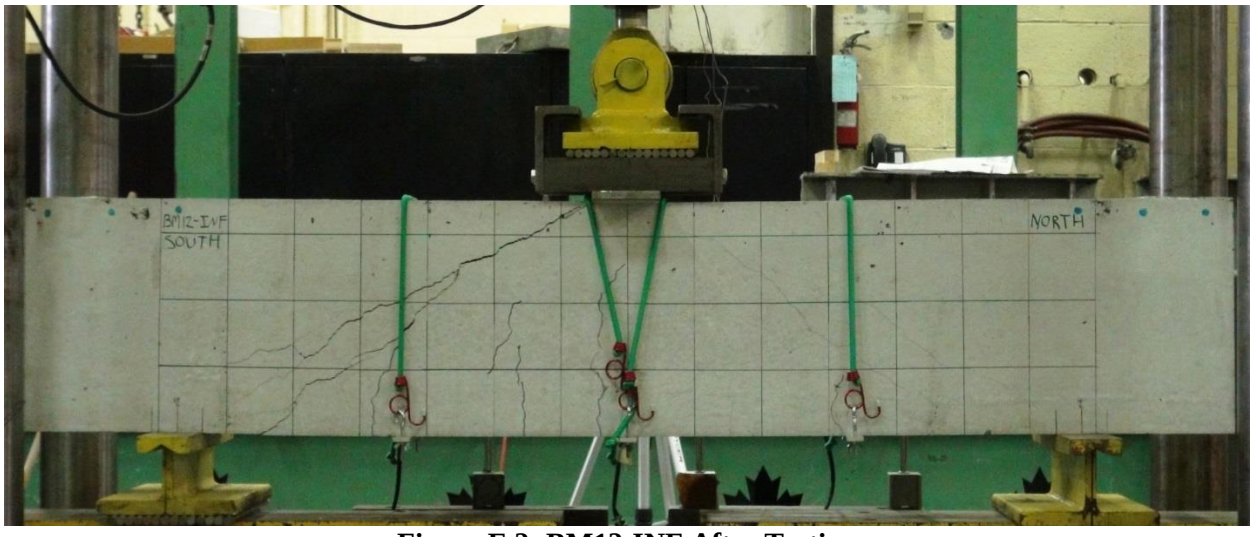

Figure E.2: BM12-INF After Testing

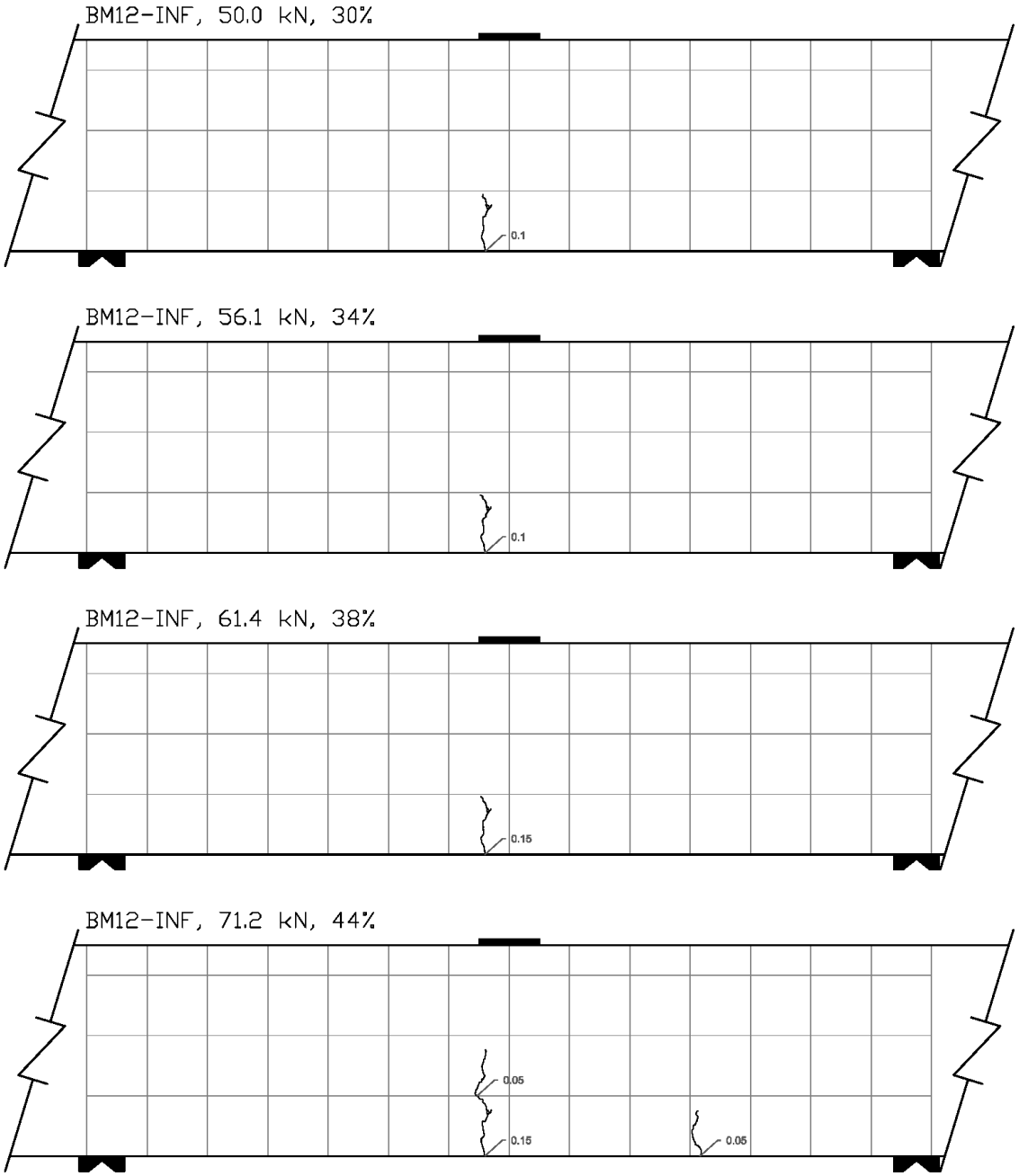

Figure E.3: BM12-INF Crack Diagram 1

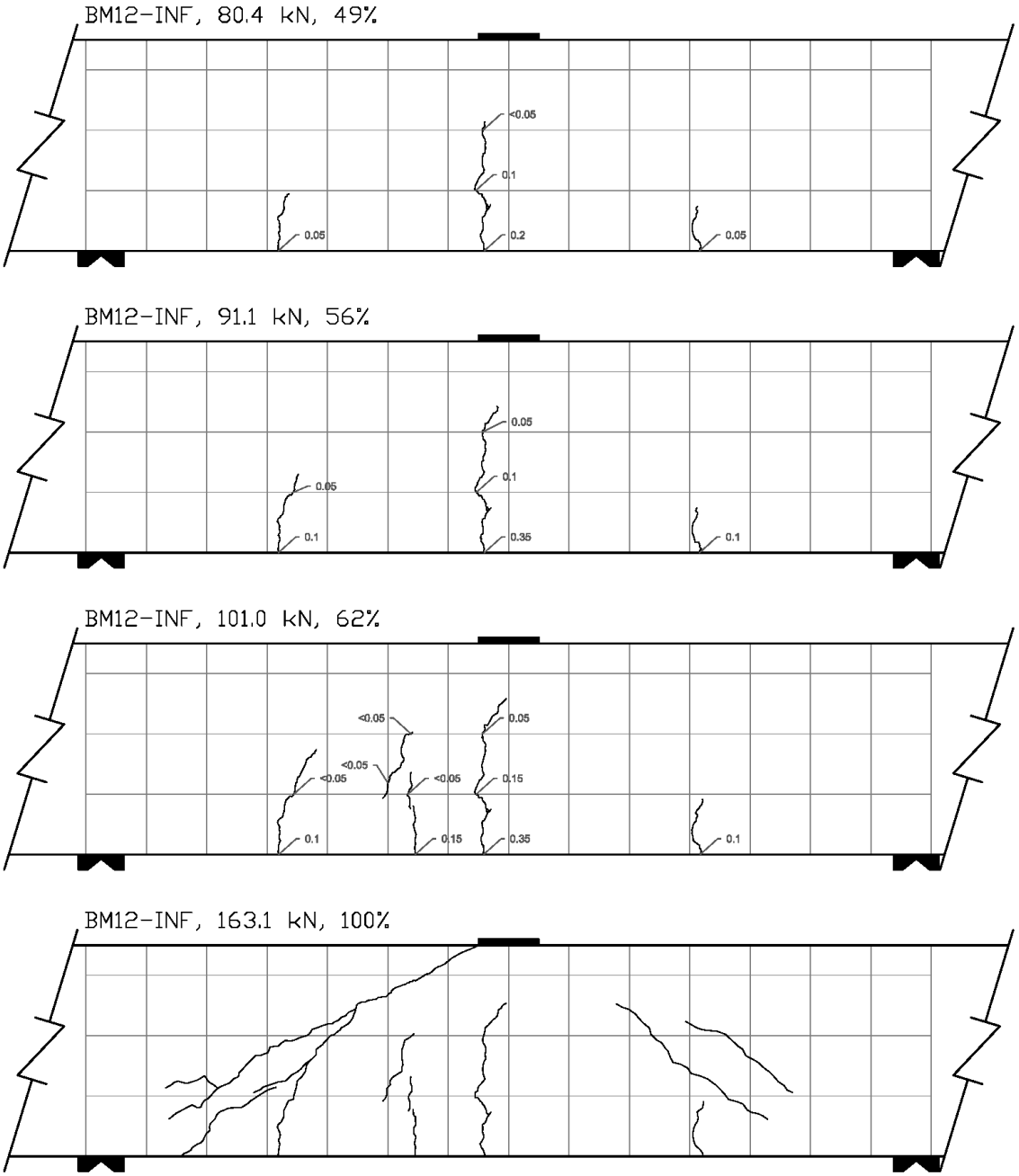

Figure E.4: BM12-INF Crack Diagram 2

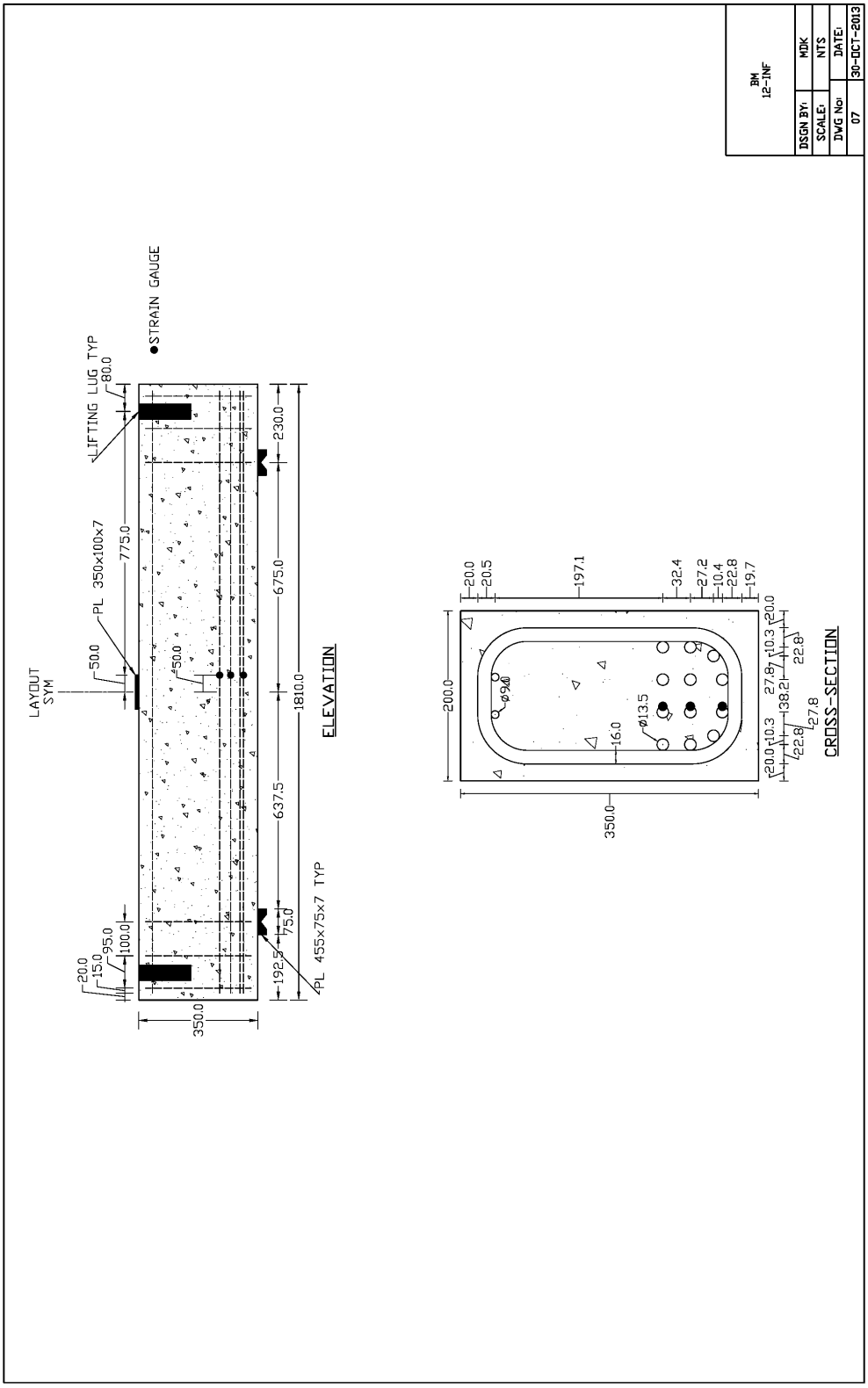

Figure E.5: BM12-INF Schematic Drawing

Table E.1: As-Designed and As-Constructed Parameter Chart for BM12-INF

Parameter	As-Designed	As-Constructed
Beam Properties		
f'_c (MPa)	45	47.3 (28 day)
b (mm)	200	198.0**
h (mm)	350	351.0**
l (mm)	1810	-
d (mm)	270	263.8***
a/d	2.5	-
ρ_F (%)	2.51	-
ρ_v (%)	0.00	-
Longitudinal Bar Properties		
f_{Fu} (MPa)	1000	-
E_F (GPA)	60	-
A_F (mm^2)	113	-
n_{Bar} (amnt)	12	-
ε_{Fu} (%)	2.61*	-
Stirrup Properties		
$f_{Fu,straight}$ (MPa)	1000	-
$f_{Fu,bent}$ (MPa)	700	-
E_F (GPA)	50	-
A_F (mm^2)	113.1	-
r_{Bend} (mm)	42	-

** Rupture strain was only provided for dia. 16 bars; this value was assumed valid for all bars.*
*** Measured at midpoint of the failed shear span before testing, width is an average of top and bottom.*
**** Based on an average from measured bar depths before pour on north and south ends.*

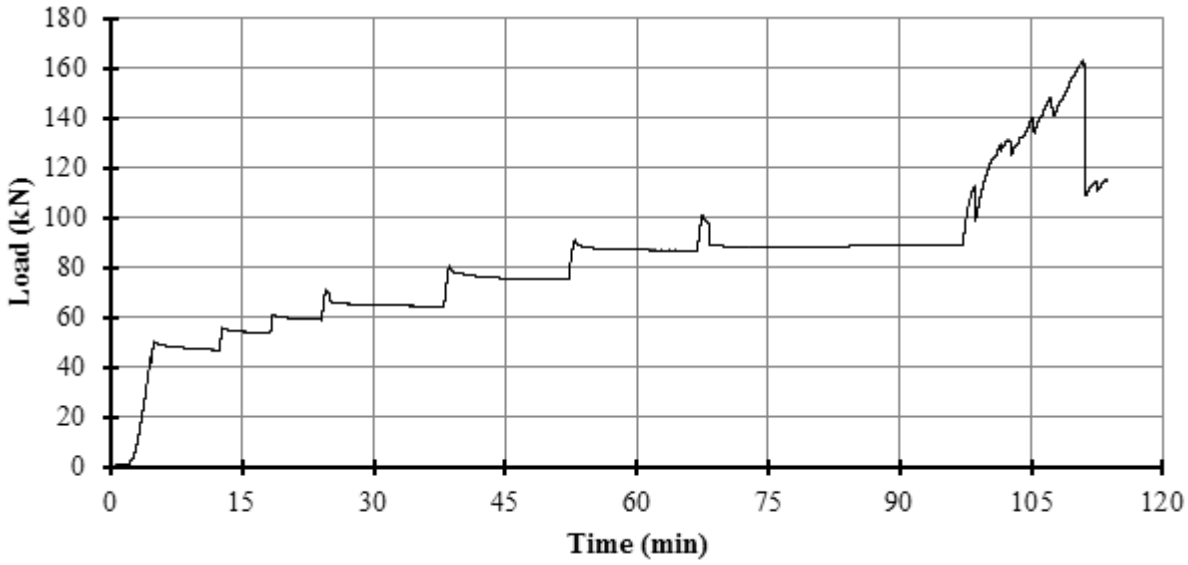

Figure E.6: BM12-INF Plot of Load vs Time

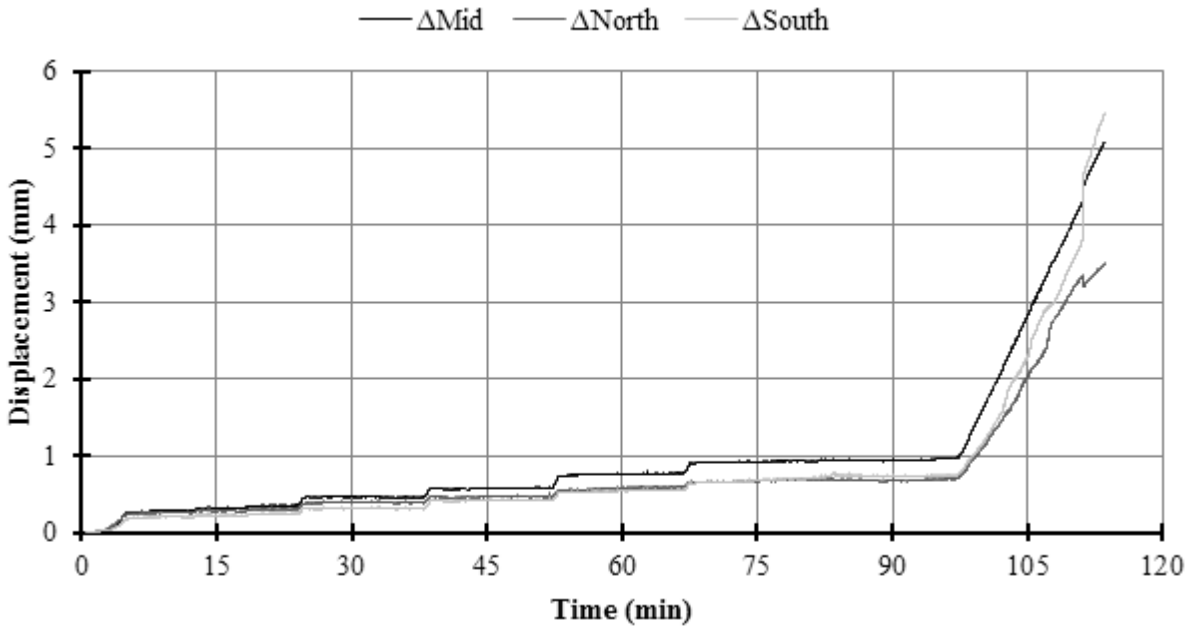

Figure E.7: BM12-INF Plot of Displacement vs Time

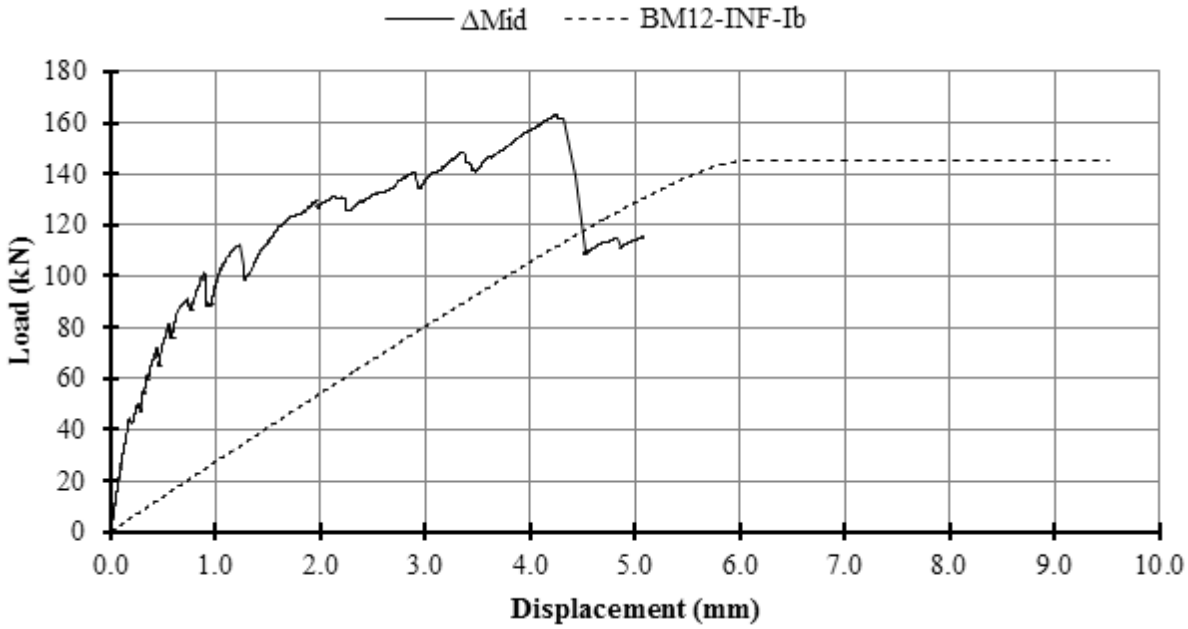

Figure E.8: BM12-INF Plot of Load vs Displacement

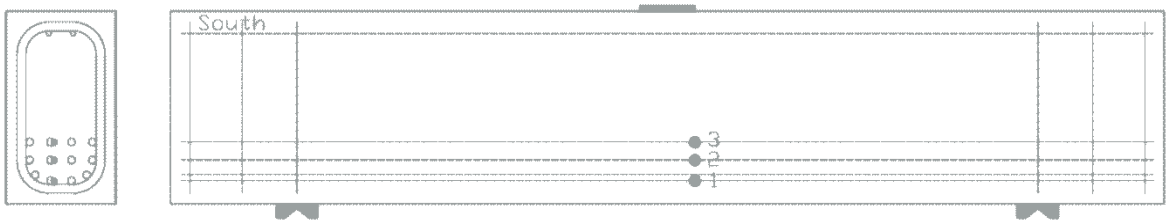

Figure E.9: BM12-INF Schematic of Mid-Span Strain Gauge Locations

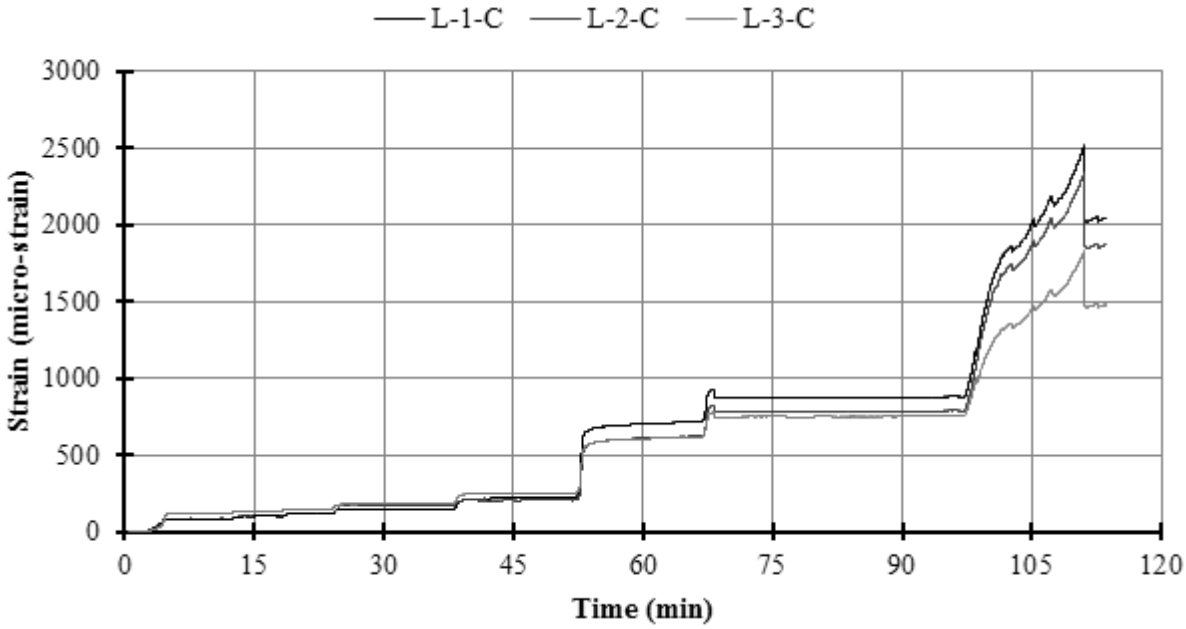

Figure E.10: BM12-INF Plot of Strain vs Time on Longitudinal Bars at Mid-Span

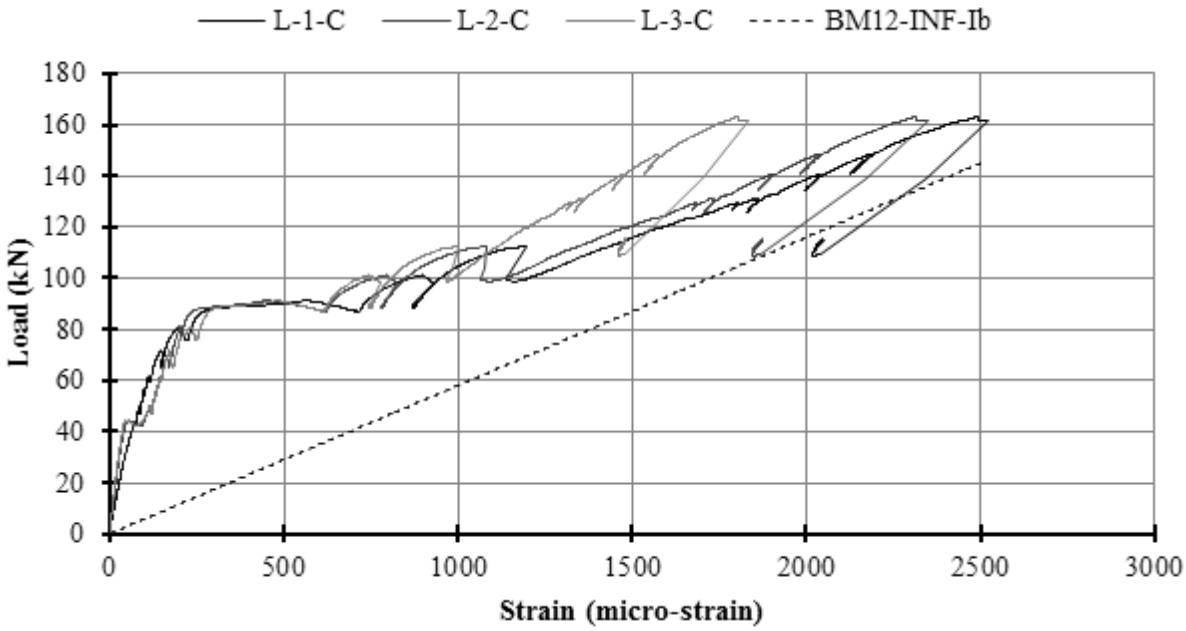

Figure E.11: BM12-INF Plot of Load vs Strain on Longitudinal Bars at Mid-Span

E.4.1 BM12-INF Photographs

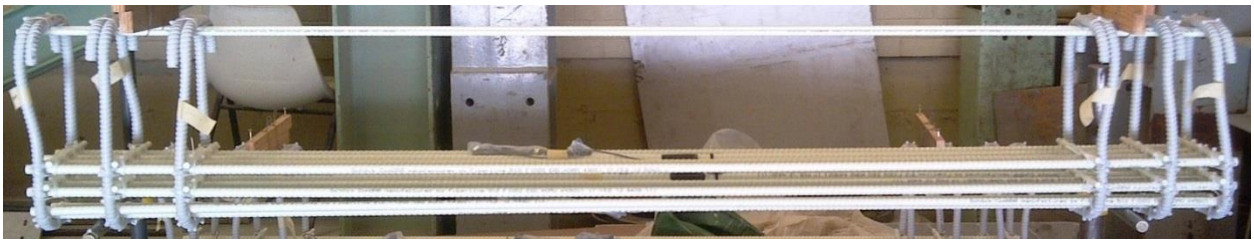

Figure E.12: BM12-INF Rebar Cage Elevation Photo

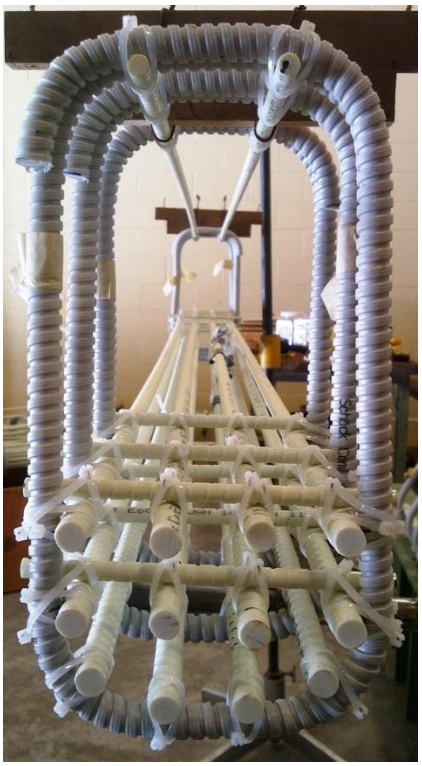

Figure E.13: BM12-INF Rebar Cage Cross-Section Photo

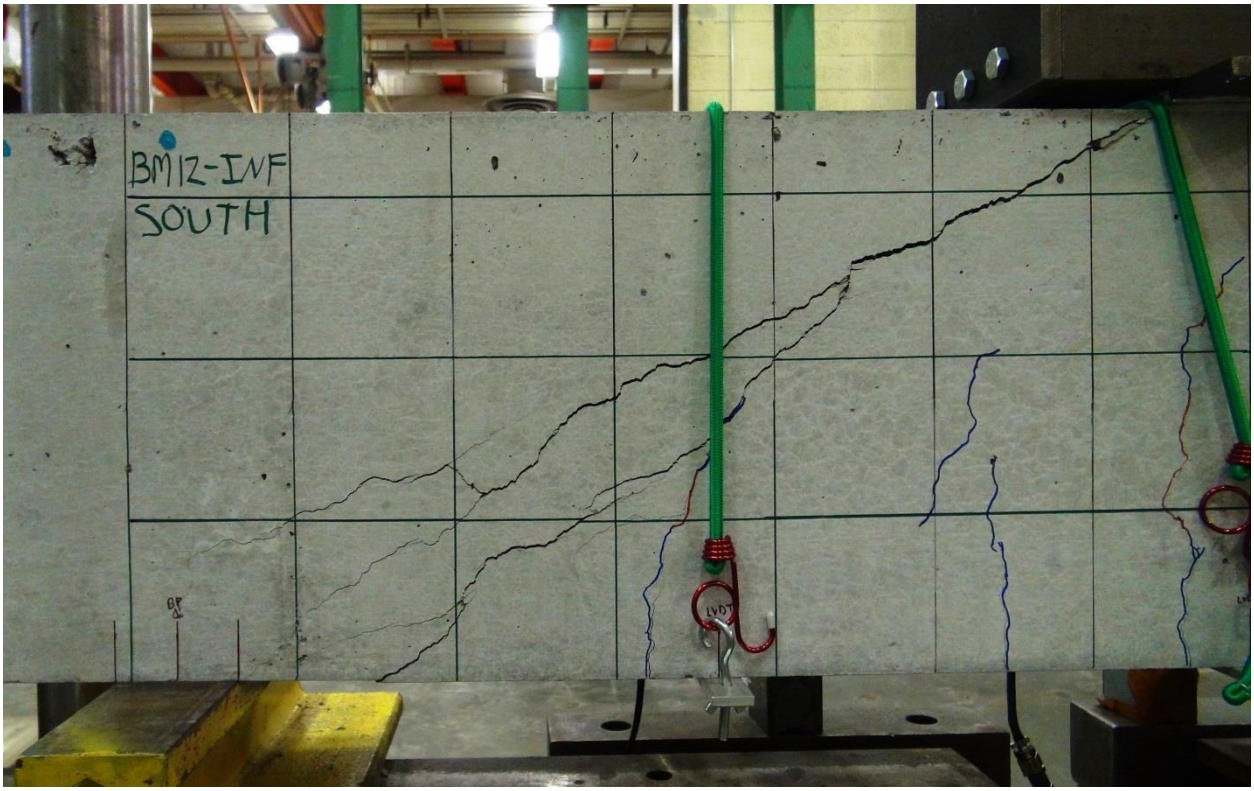

Figure E.14: BM12-INF Close-up Photo of Failure

E.5 BM16-INF

This was the second beam tested. It was tested at a constant displacement rate of 0.272 mm/min. Steel cable straps held the aluminum bars, which were used for displacement measurements, snug against the bottom of the beam. The cables were connected to the eye-bolts by stiff springs; the springs were used to allay concerns about the steel cables being deformed as shear cracks grew wider.

The beam failed in shear-tension along a shear crack that formed after crack width measurements ceased. The crack ran diagonally from the load plate to the south bearing plate. The formation of the shear crack did not accompany peak load. The failure was unremarkable: peak load was not accompanied by loud noises, perceptible movements, or the ejection of concrete projectiles.

Peak load occurred at 150.2 kN and 4.21 mm of displacement, and failure took place in the instrumented south shear span 50 days after casting.

Strain gauge L-2-4 failed shortly after peak load was reached; all other strain gauges functioned adequately during the test.

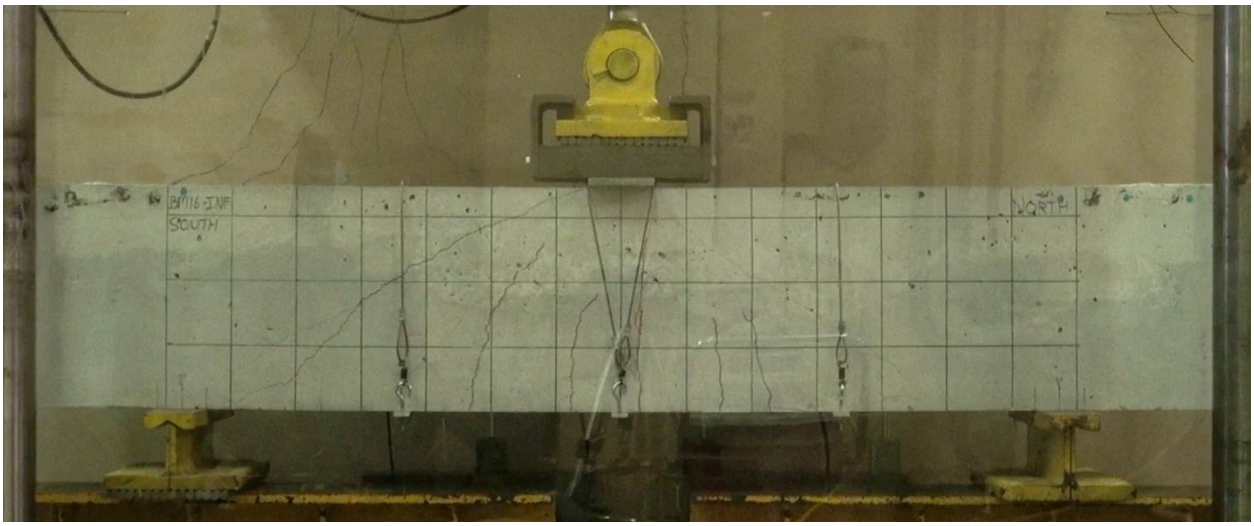

Figure E.15: BM16-INF At Peak Load

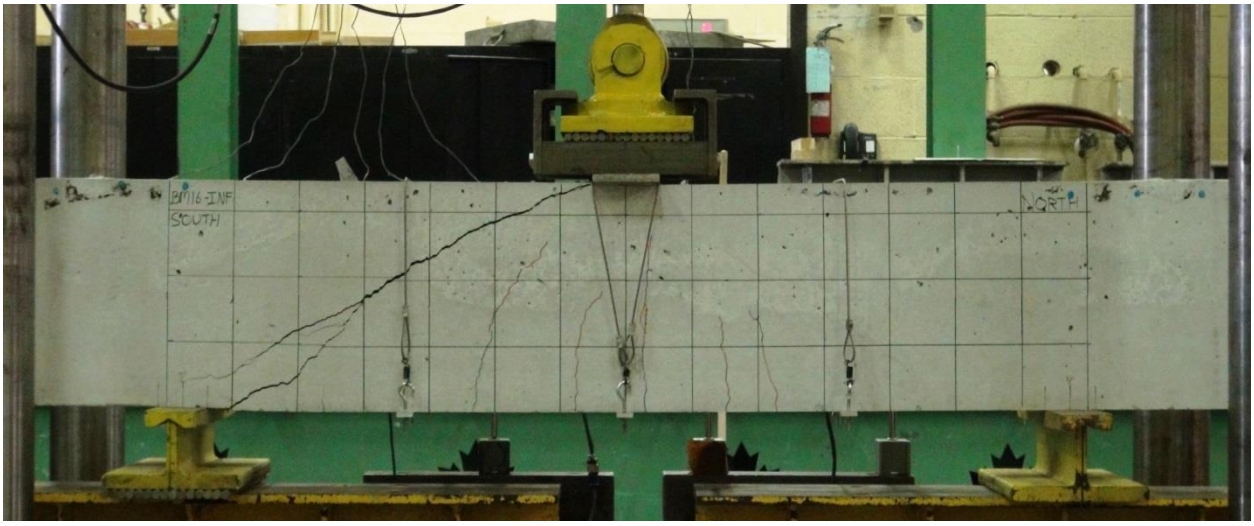

Figure E.16: BM16-INF After Testing

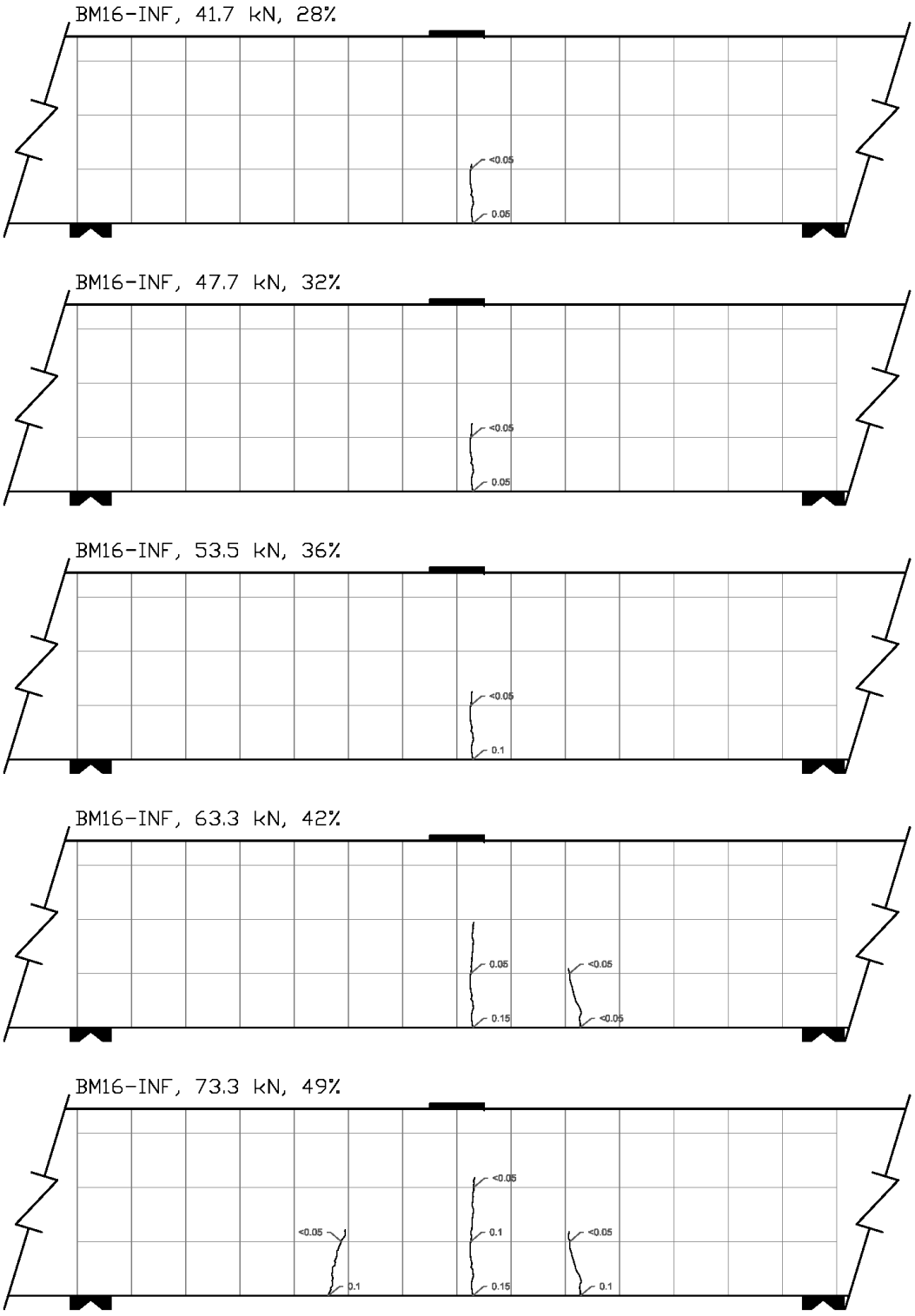

Figure E.17: BM16-INF Crack Diagram 1

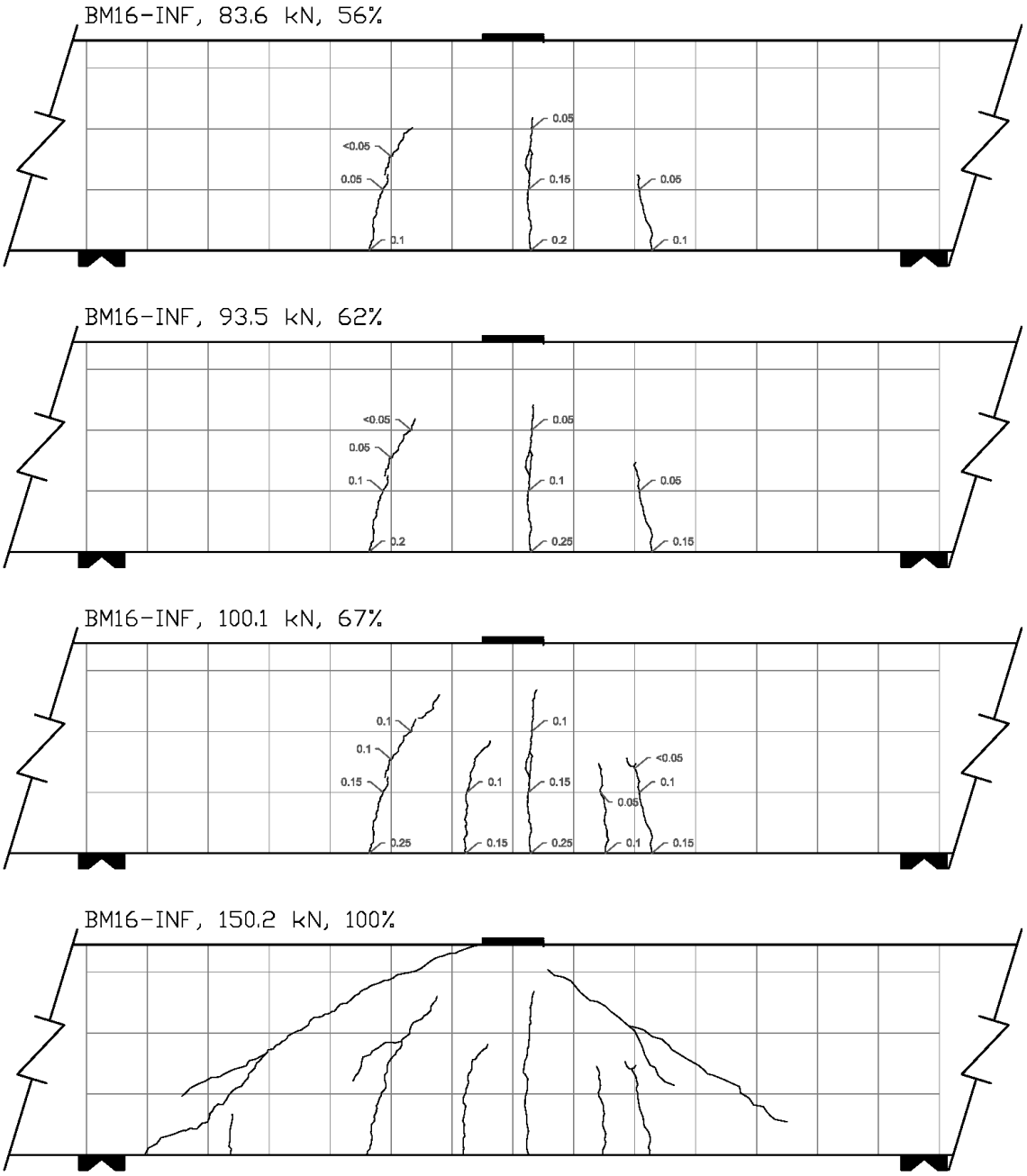

Figure E.18: BM16-INF Crack Diagram 2

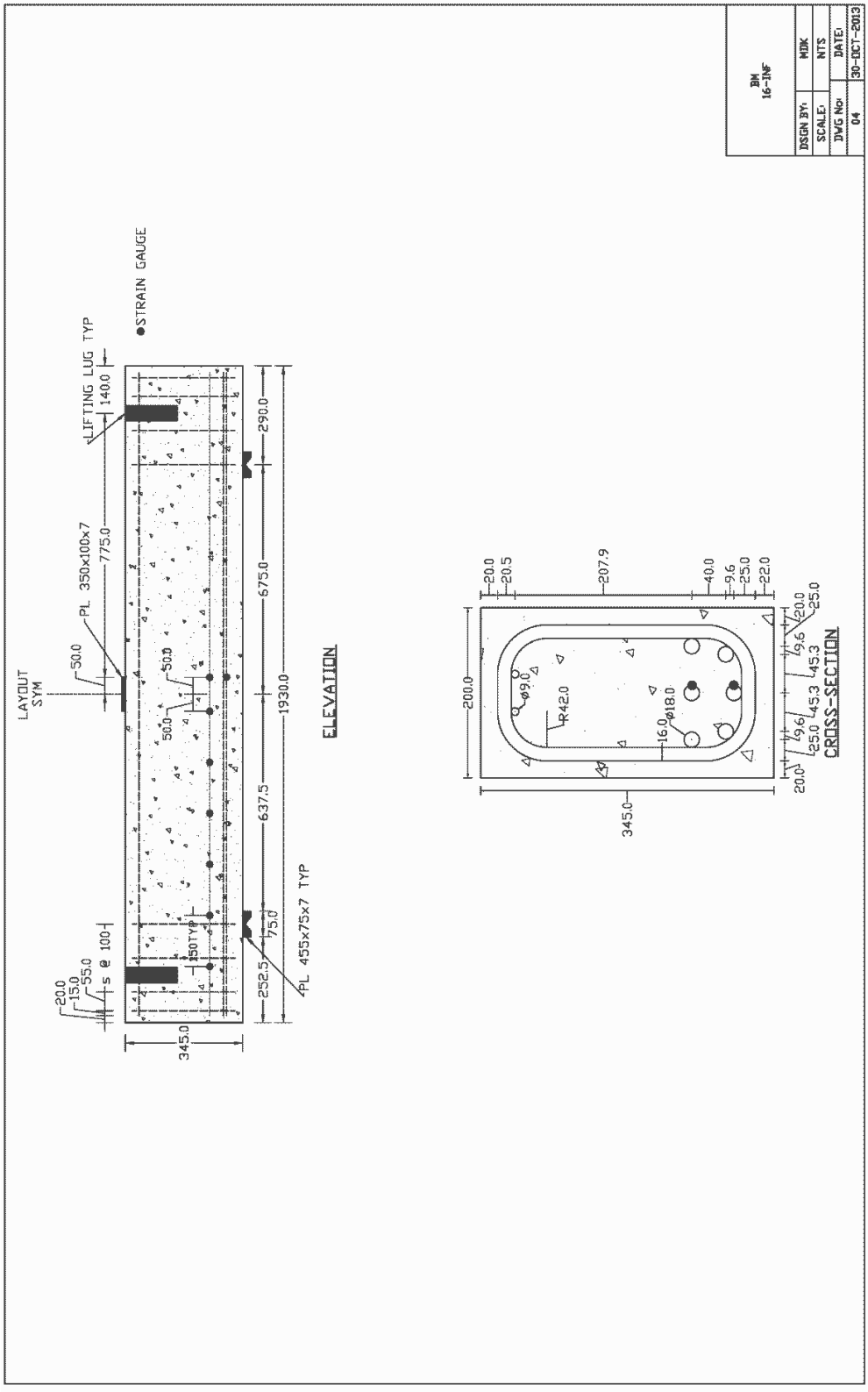

Figure E.19: BM16-INF Schematic Drawing

Table E.2: As-Designed and As-Constructed Parameter Chart for BM16-INF

Parameter	As-Designed	As-Constructed
Beam Properties		
f'_c (MPa)	45	47.3 (28 day)
b (mm)	200	202.0**
h (mm)	345	346.0**
l (mm)	1930	-
d (mm)	270	267.7***
a/d	2.5	-
ρ_F (%)	2.23	-
ρ_v (%)	0.00	-
Longitudinal Bar Properties		
f_{Fu} (MPa)	1000	-
E_F (GPA)	64	-
A_F (mm^2)	201	-
n_{Bar} (amnt)	6	-
ε_{Fu} (%)	2.61*	-
Stirrup Properties		
$f_{Fu,straight}$ (MPa)	1000	-
$f_{Fu,bent}$ (MPa)	700	-
E_F (GPA)	50	-
A_F (mm^2)	113.1	-
r_{Bend} (mm)	42	-

** Rupture strain was only provided for dia. 16 bars; this value was assumed valid for all bars.*
*** Measured at midpoint of the failed shear span before testing, width is an average of top and bottom.*
**** Based on an average from measured bar depths before pour on north and south ends.*

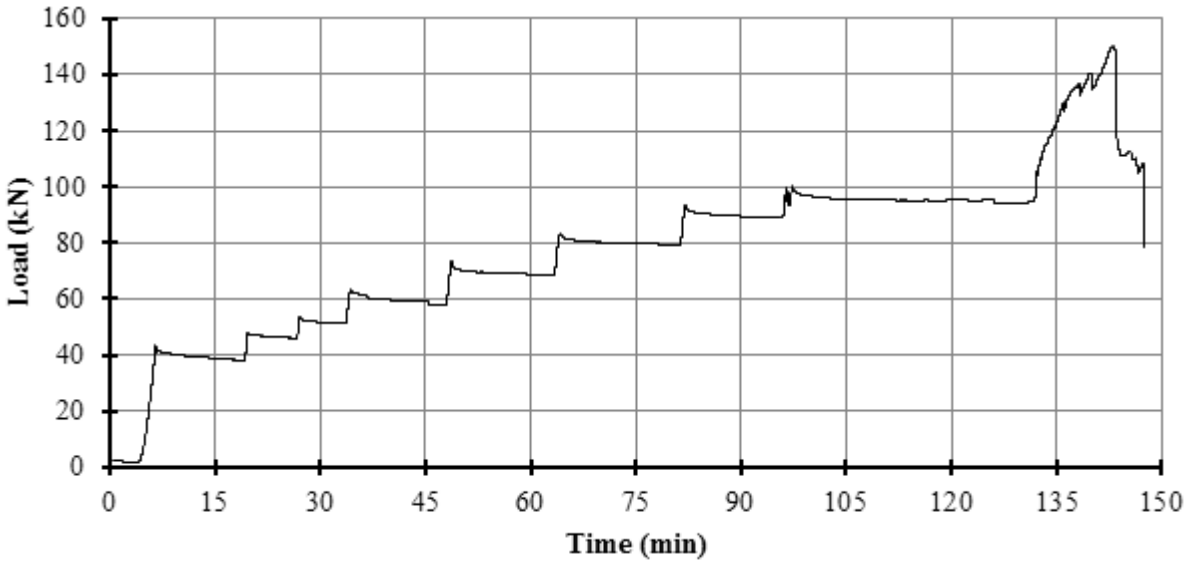

Figure E.20: BM16-INF Plot of Load vs Time

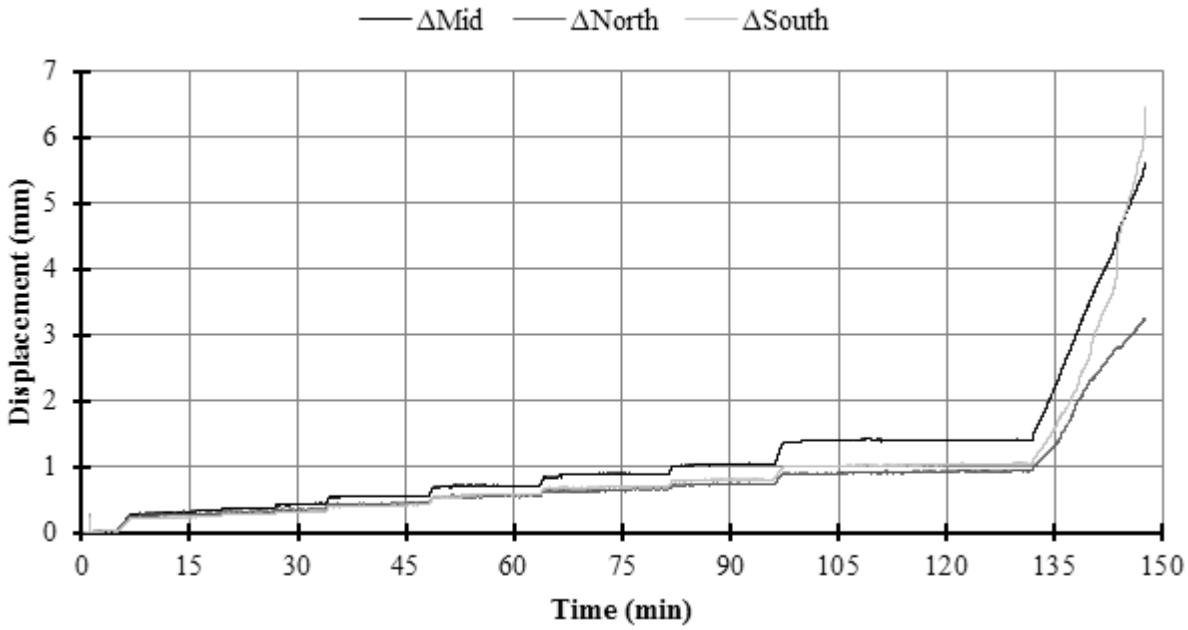

Figure E.21: BM16-INF Plot of Displacement vs Time

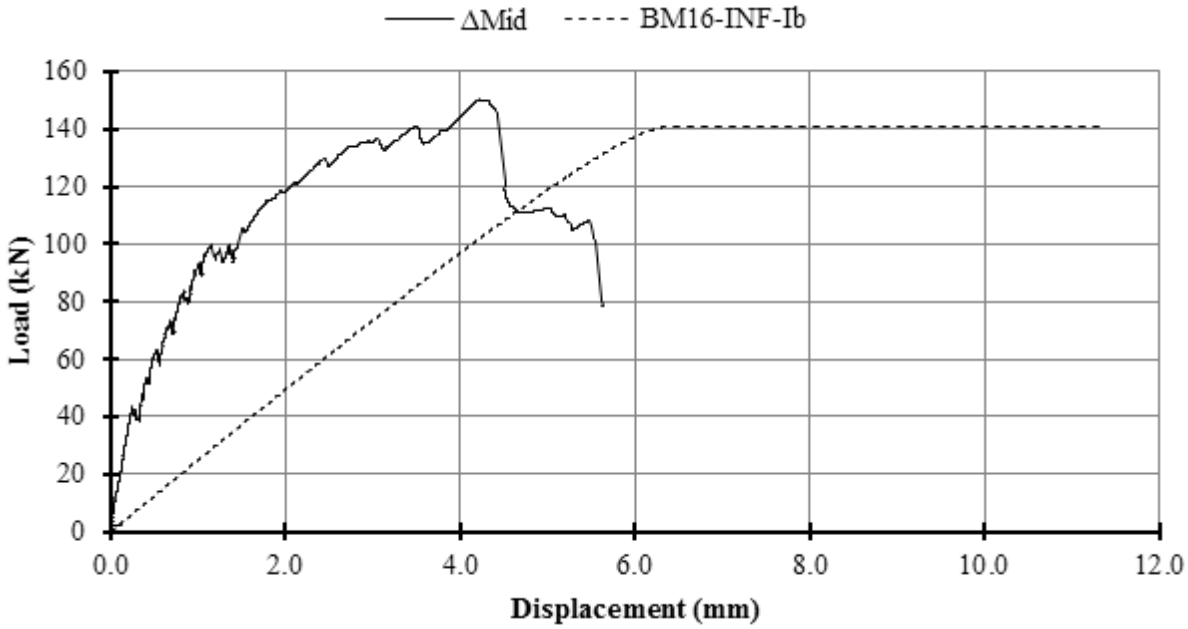

Figure E.22: BM16-INF Plot of Load vs Displacement

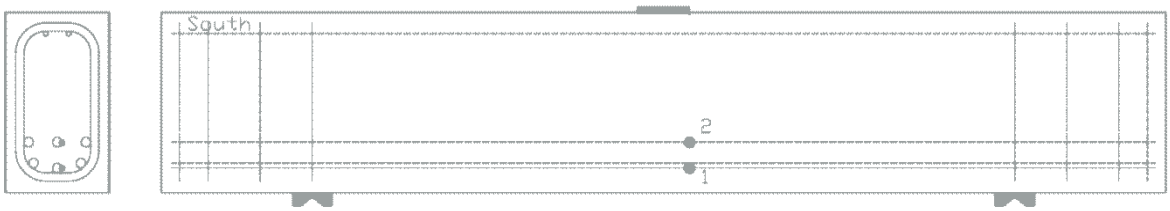

Figure E.23: BM16-INF Schematic of Mid-Span Strain Gauge Locations

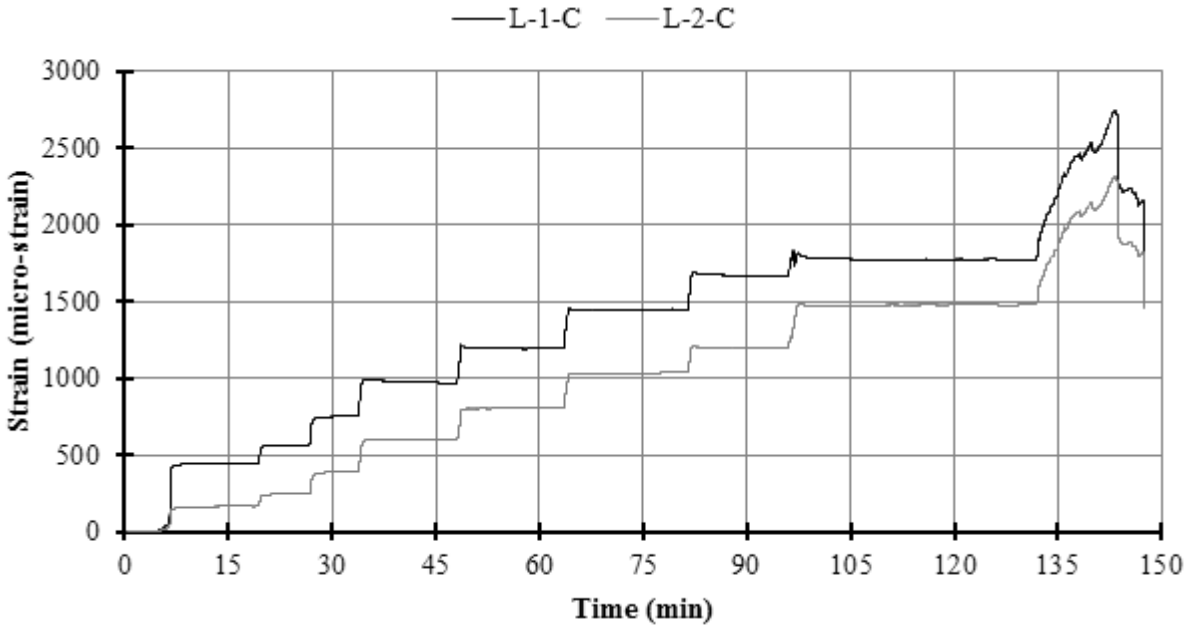

Figure E.24: BM16-INF Plot of Strain vs Time on Longitudinal Bars at Mid-Span

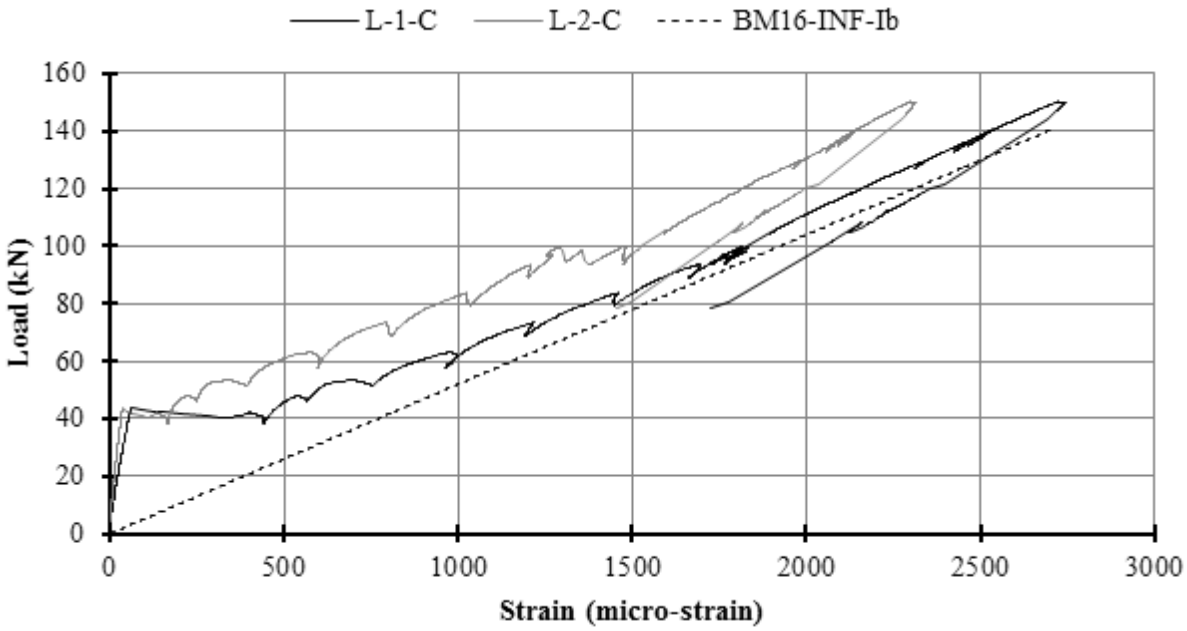

Figure E.25: BM16-INF Plot of Load vs Strain on Longitudinal Bars at Mid-Span

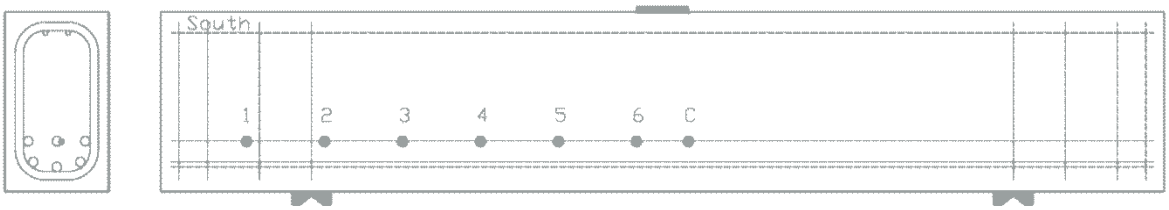

Figure E.26: BM16-INF Schematic of Longitudinal Strain Gauge Locations

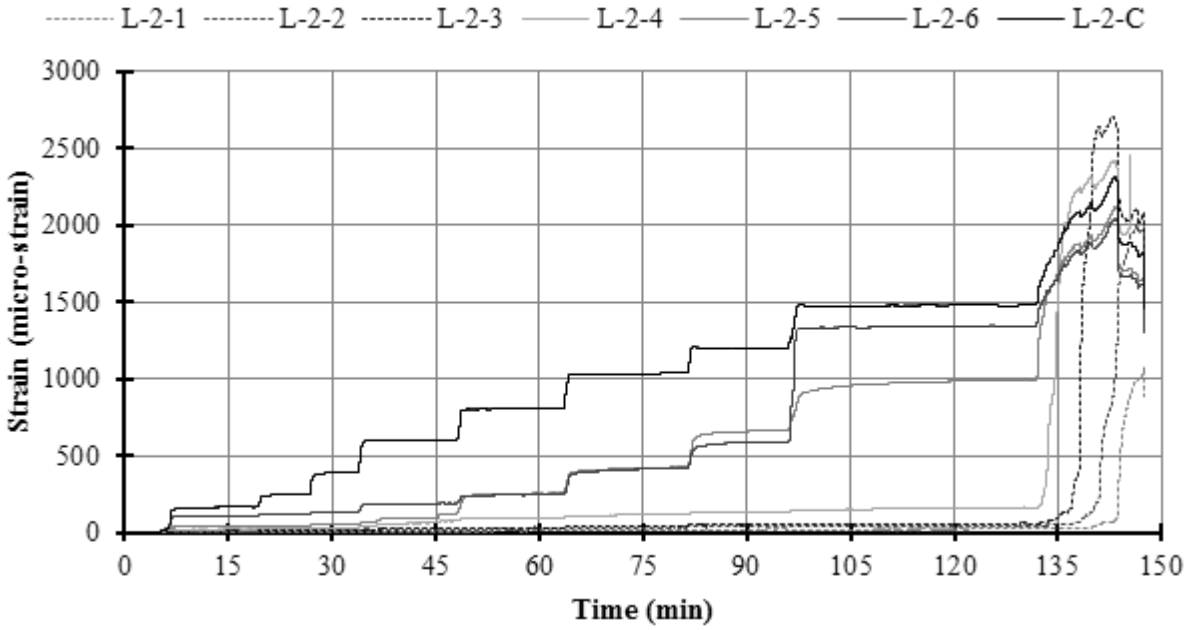

Figure E.27: BM16-INF Plot of Strain vs Time from Gauges along the Top Longitudinal Bar

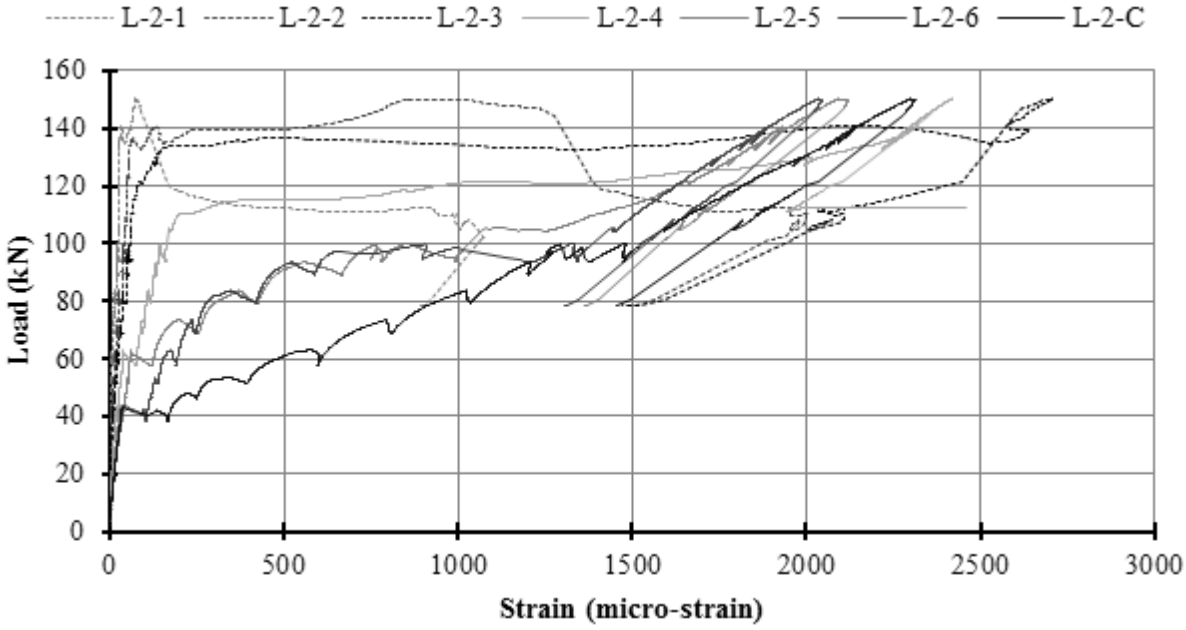

Figure E.28: BM16-INF Plot of Load vs Strain from Gauges along the Top Longitudinal Bar

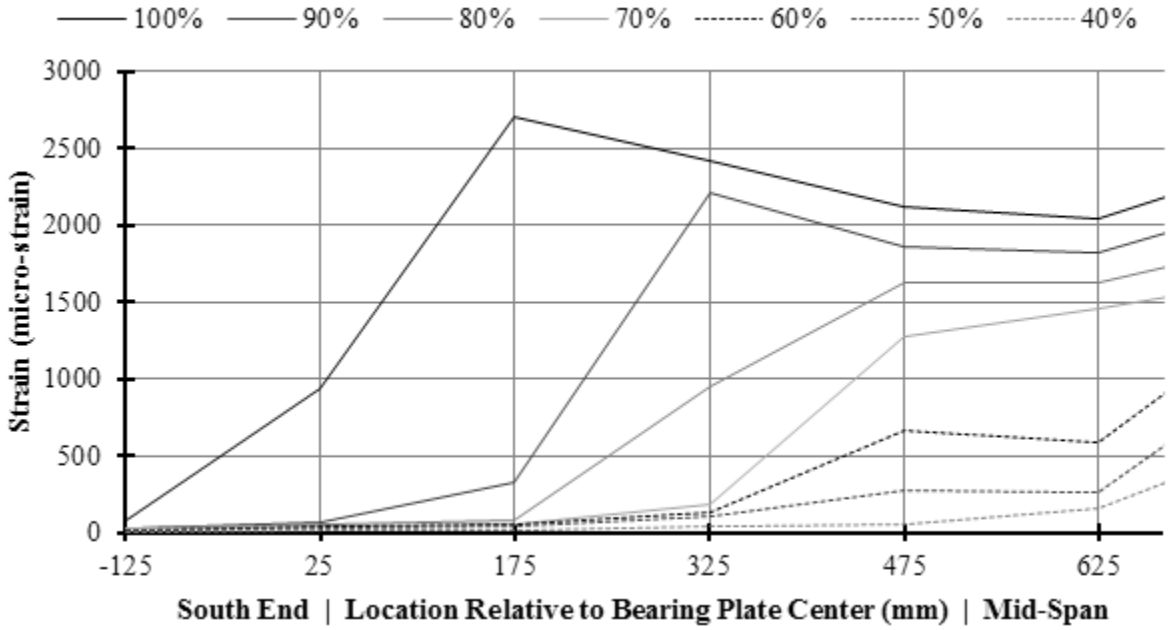

Figure E.29: BM16-INF Plot of Longitudinal Strain vs Gauge Location with Increasing Load

E.5.1 BM16-INF Photographs

Figure E.30: BM16-INF Rebar Cage Elevation Photo

Figure E.31: BM16-INF Rebar Cage Cross-Section Photo

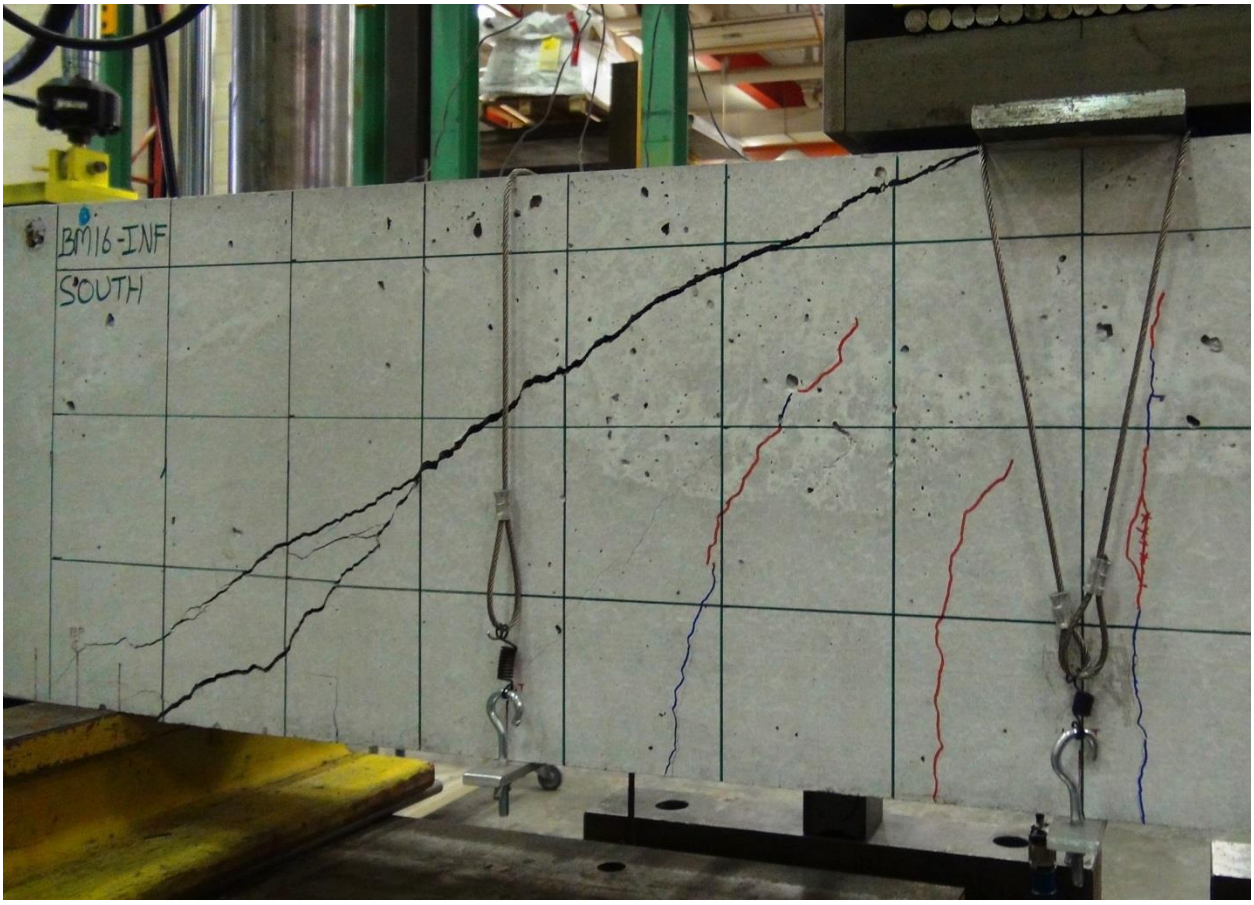

Figure E.32: BM16-INF Close-up Photo of Failure

E.6 BM25-INF

This was the first beam tested. It was tested at a constant displacement rate of 0.272 mm/min. Unlike specimens tested after this one, this beam used steel cables to hold aluminum bars snug against the bottom of the beam. The cables were attached directly to eye-bolts, which were tightened by turn of nut to provide sufficient tension to prevent movement of the bars. The bars were used as measurement points for beam deflections.

The beam failed in shear-tension along a shear crack that formed after crack width measurements ceased. Peak load was accompanied by the formation of the shear crack. Further increases in load saw the formation of tensile spitting cracks which coalesced into one crack with the main shear crack. The failure was unremarkable: peak load was not accompanied by loud noises, perceptible movements, or the ejection of concrete projectiles.

Peak load occurred at 125.1 kN and 3.22 mm of displacement, and failure took place in the south shear span 43 days after casting.

All of the strain gauges functioned adequately during the test.

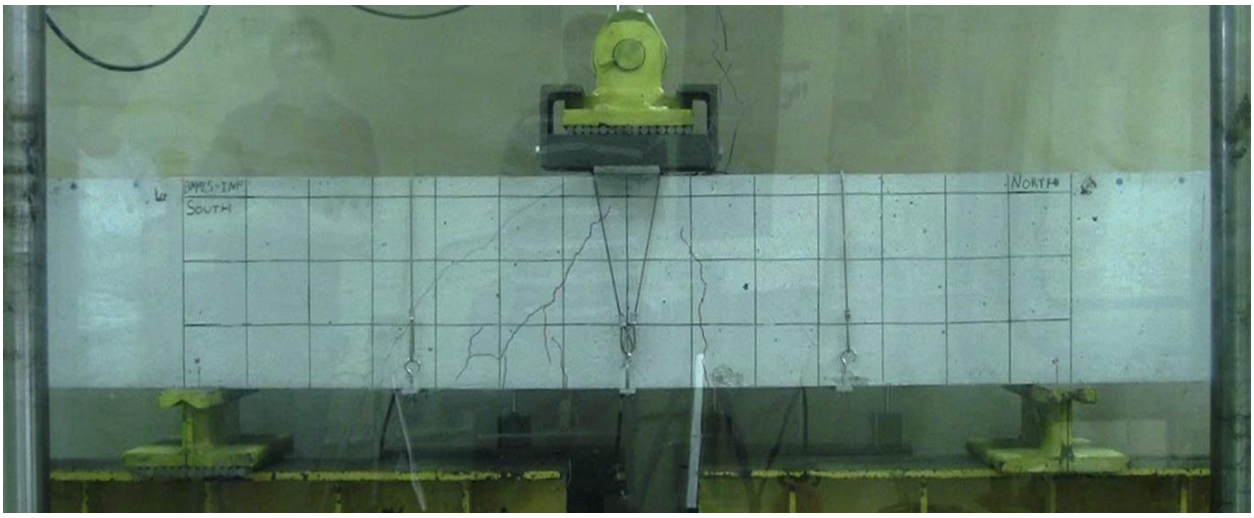

Figure E.33: BM25-INF At Peak Load

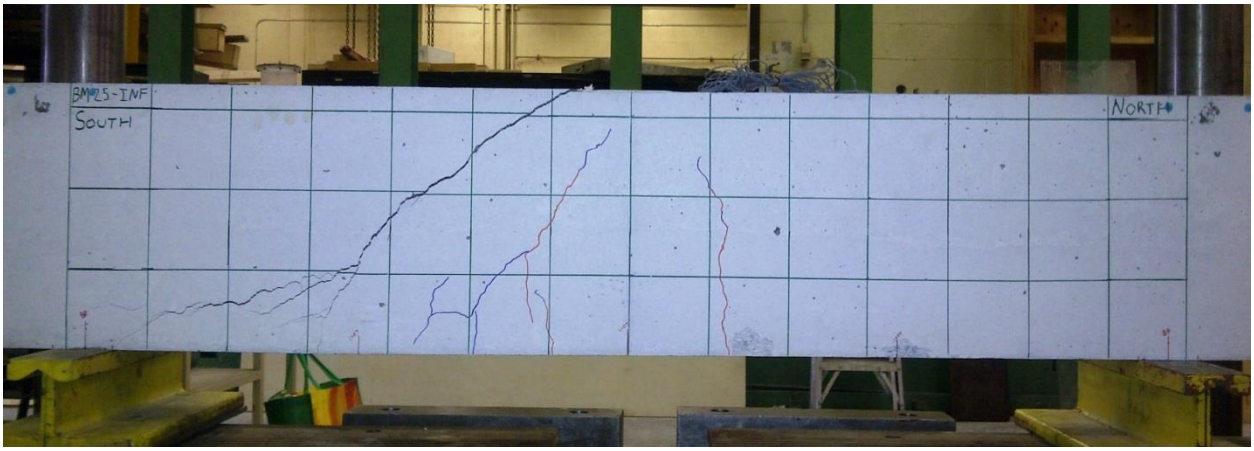

Figure E.34: BM25-INF After Testing

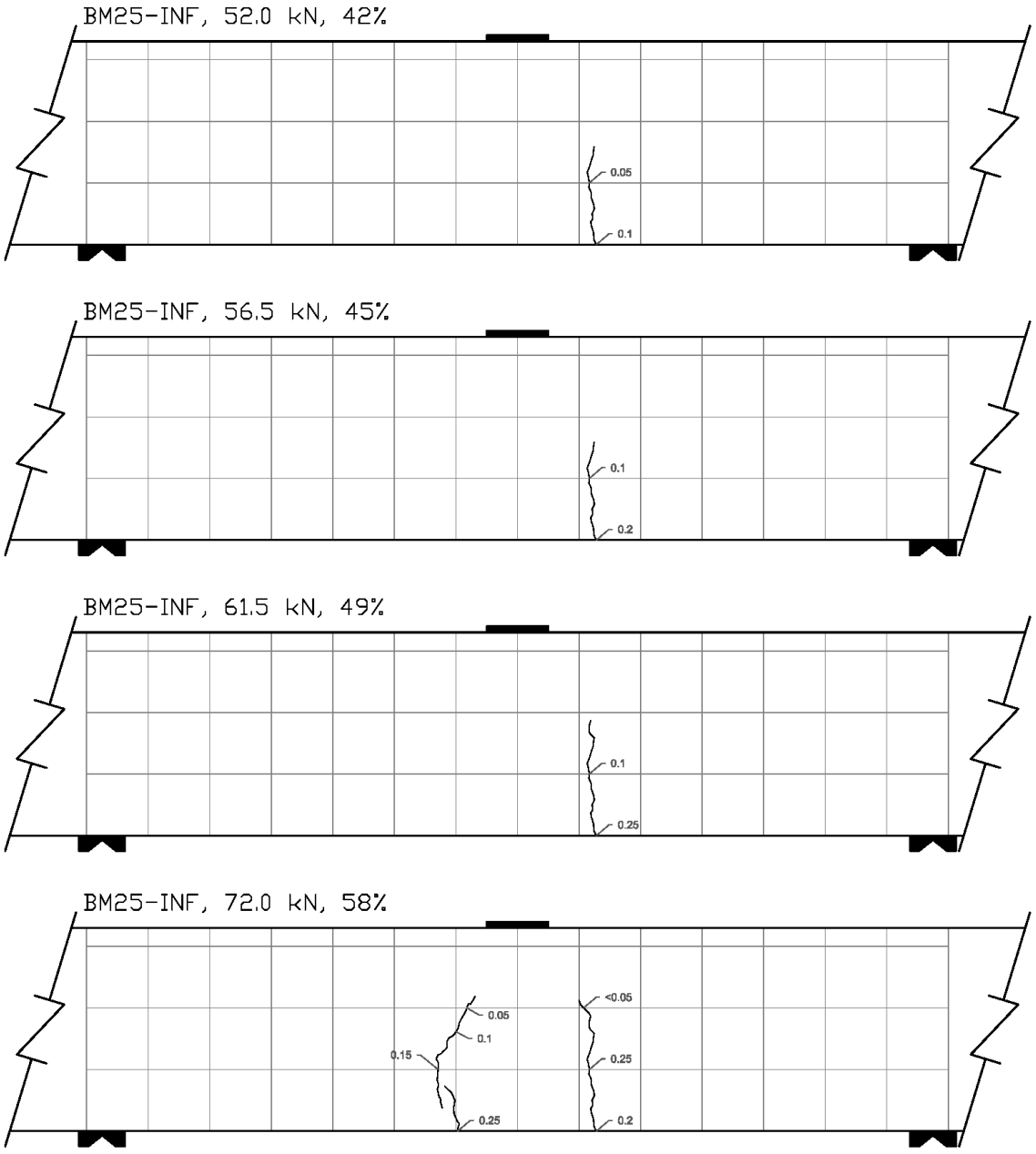

Figure E.35: BM25-INF Crack Diagram 1

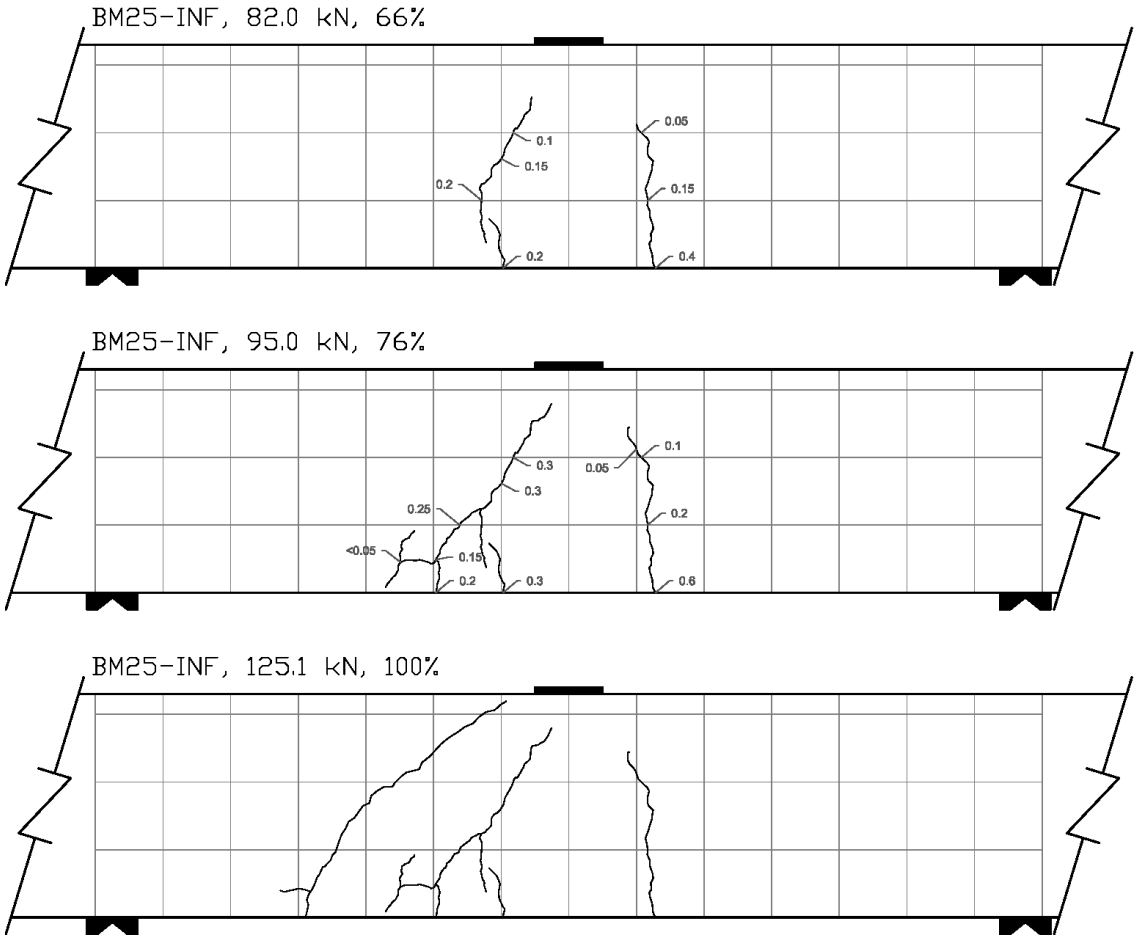

Figure E.36: BM25-INF Crack Diagram 2

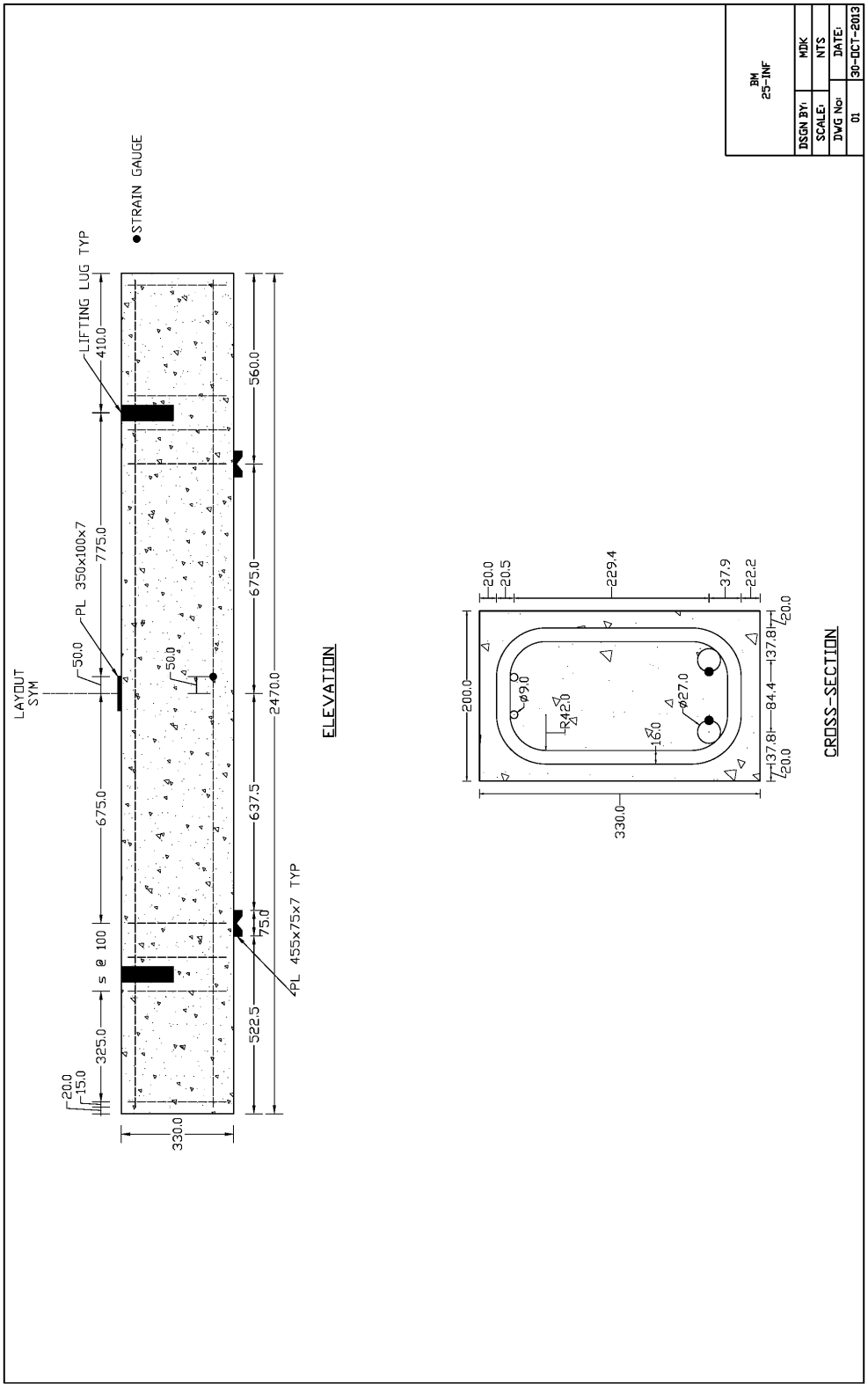

Figure E.37: BM25-INF Schematic Drawing

Table E.3: As-Designed and As-Constructed Parameter Chart for BM25-INF

Parameter	As-Designed	As-Constructed
Beam Properties		
f'_c (MPa)	45	47.3 (28 day)
b (mm)	200	198.0**
h (mm)	330	331.0**
l (mm)	2470	-
d (mm)	270	272.5***
a/d	2.5	-
ρ_F (%)	1.82	-
ρ_v (%)	0.00	-
Longitudinal Bar Properties		
f_{Fu} (MPa)	1000	-
E_F (GPA)	60	-
A_F (mm^2)	491	-
n_{Bar} (amnt)	2	-
ε_{Fu} (%)	2.61*	-
Stirrup Properties		
$f_{Fu,straight}$ (MPa)	1000	-
$f_{Fu,bent}$ (MPa)	700	-
E_F (GPA)	50	-
A_F (mm^2)	113.1	-
r_{Bend} (mm)	42	-

** Rupture strain was only provided for dia. 16 bars; this value was assumed valid for all bars.*
*** Measured at midpoint of the failed shear span before testing, width is an average of top and bottom.*
**** Based on an average from measured bar depths before pour on north and south ends.*

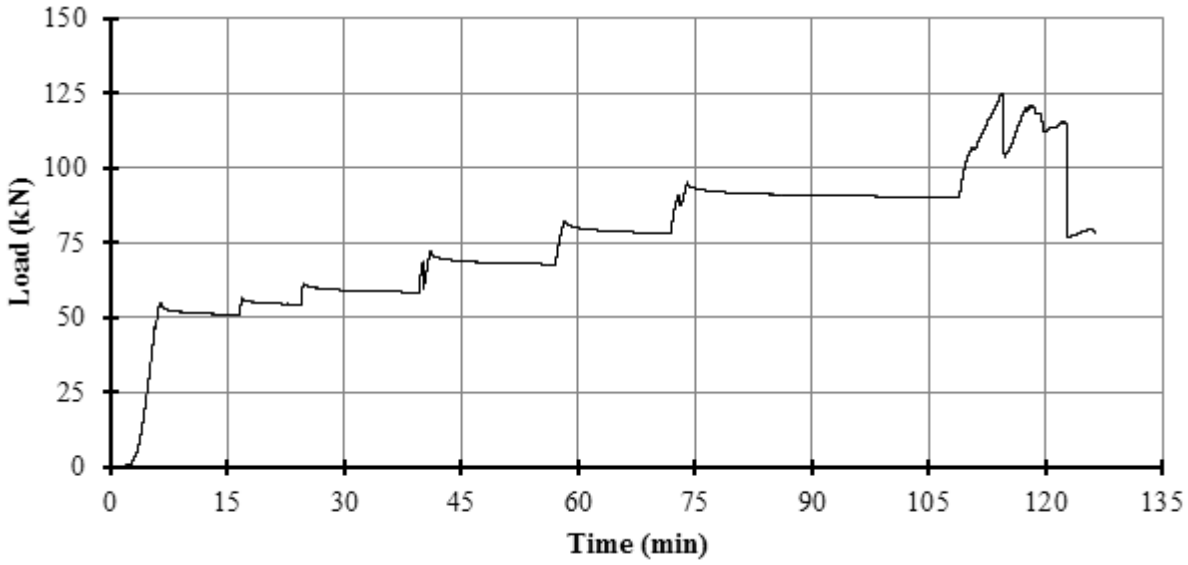

Figure E.38: BM25-INF Plot of Load vs Time

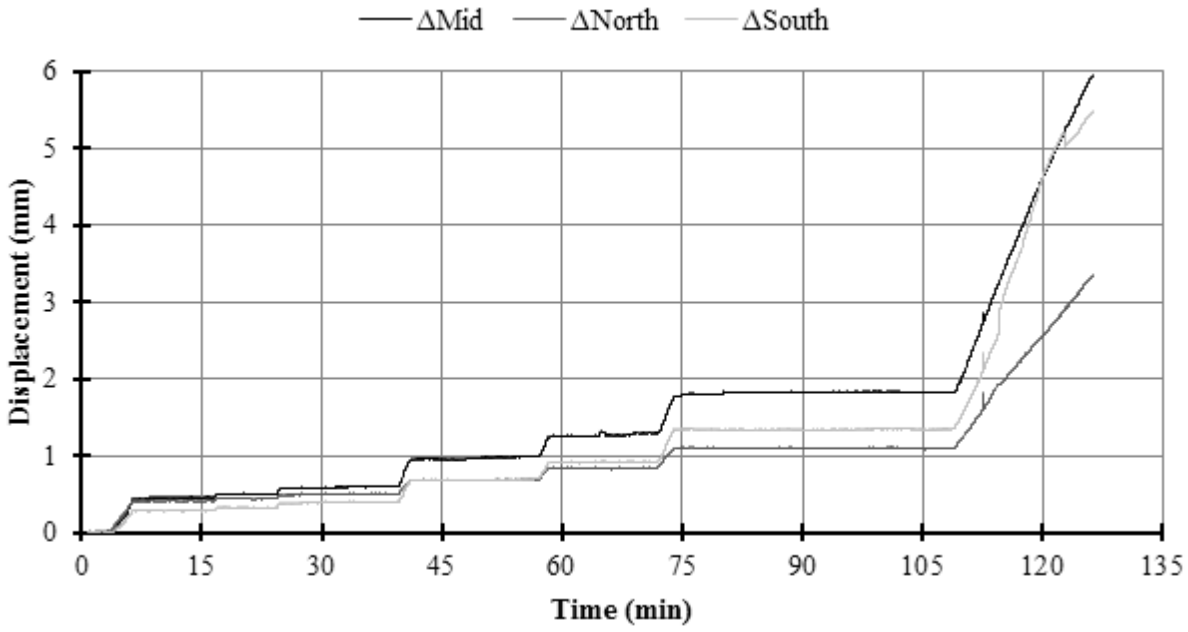

Figure E.39: BM25-INF Plot of Displacement vs Time

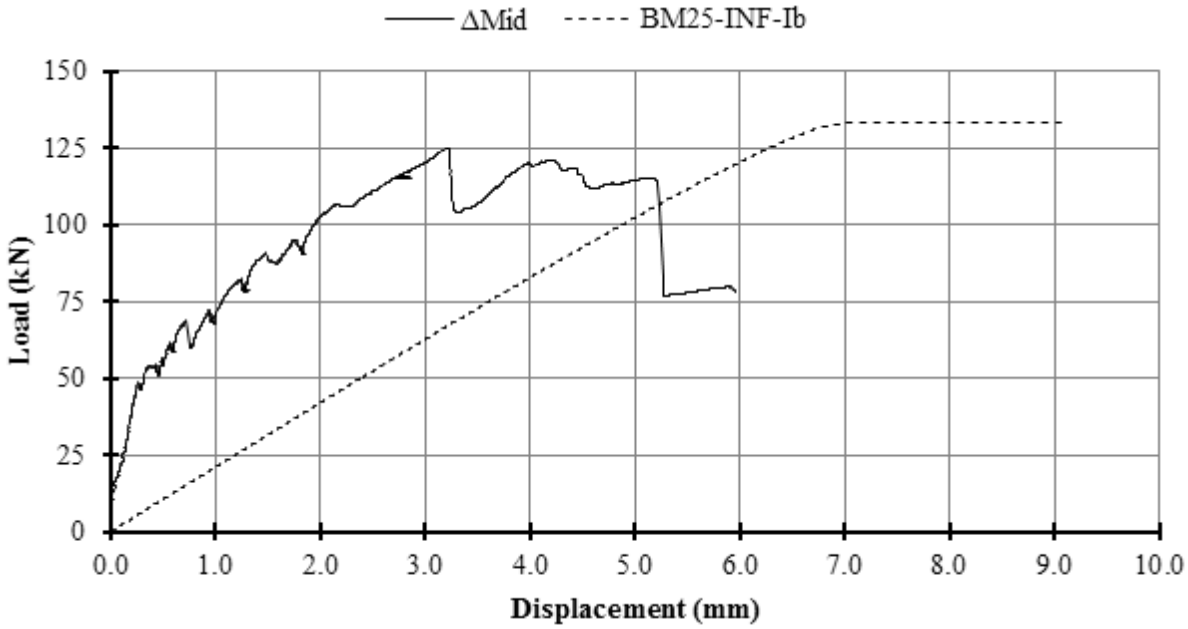

Figure E.40: BM25-INF Plot of Load vs Displacement

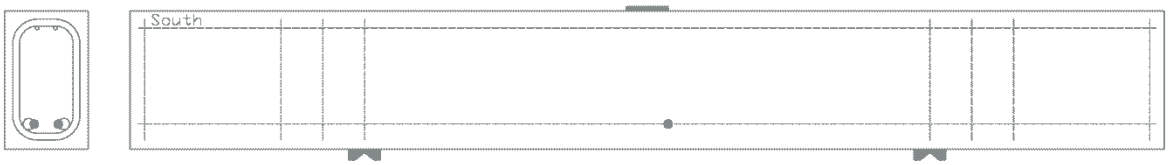

Figure E.41: BM25-INF Schematic of Mid-Span Strain Gauge Locations
A record of the specific longitudinal bar to which gauge A and B were attached was not kept.

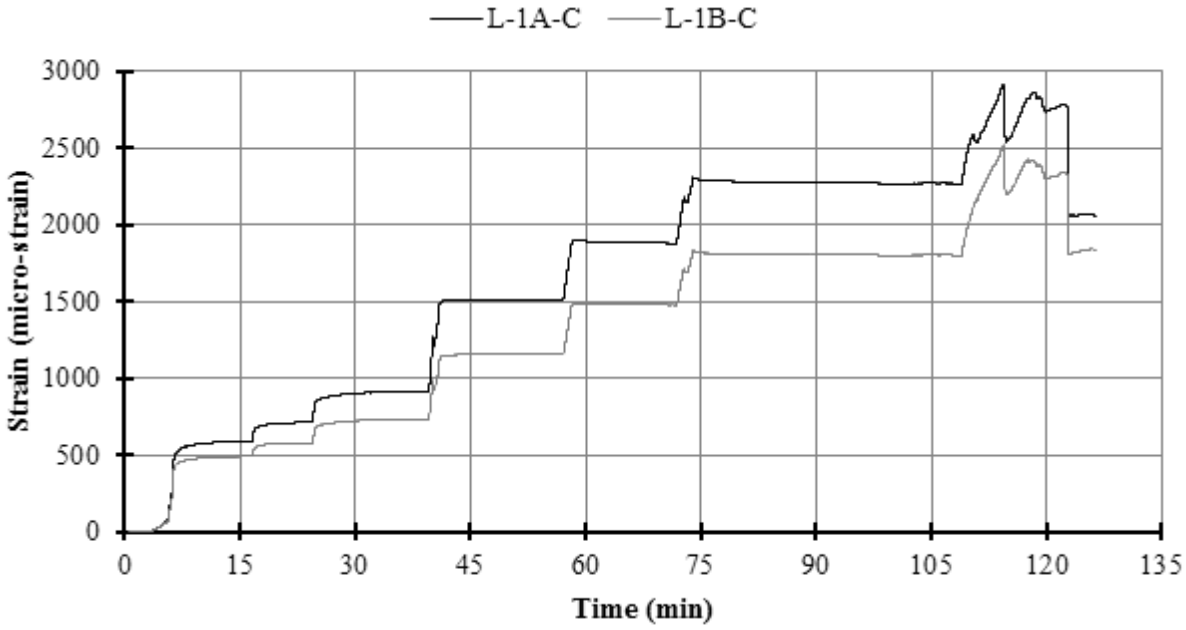

Figure E.42: BM25-INF Plot of Strain vs Time on Longitudinal Bars at Mid-Span

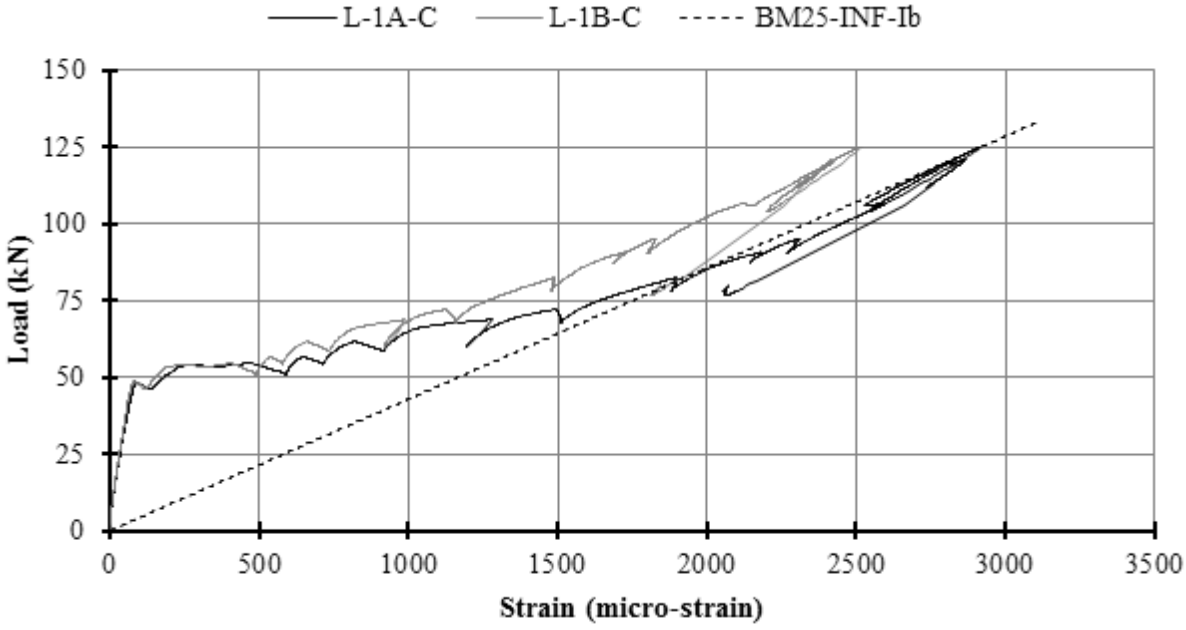

Figure E.43: BM25-INF Plot of Load vs Strain on Longitudinal Bars at Mid-Span

E.6.1 BM25-INF Photographs

Figure E.44: BM25-INF Rebar Cage Elevation Photo

Figure E.45: BM25-INF Rebar Cage Cross-Section Photo

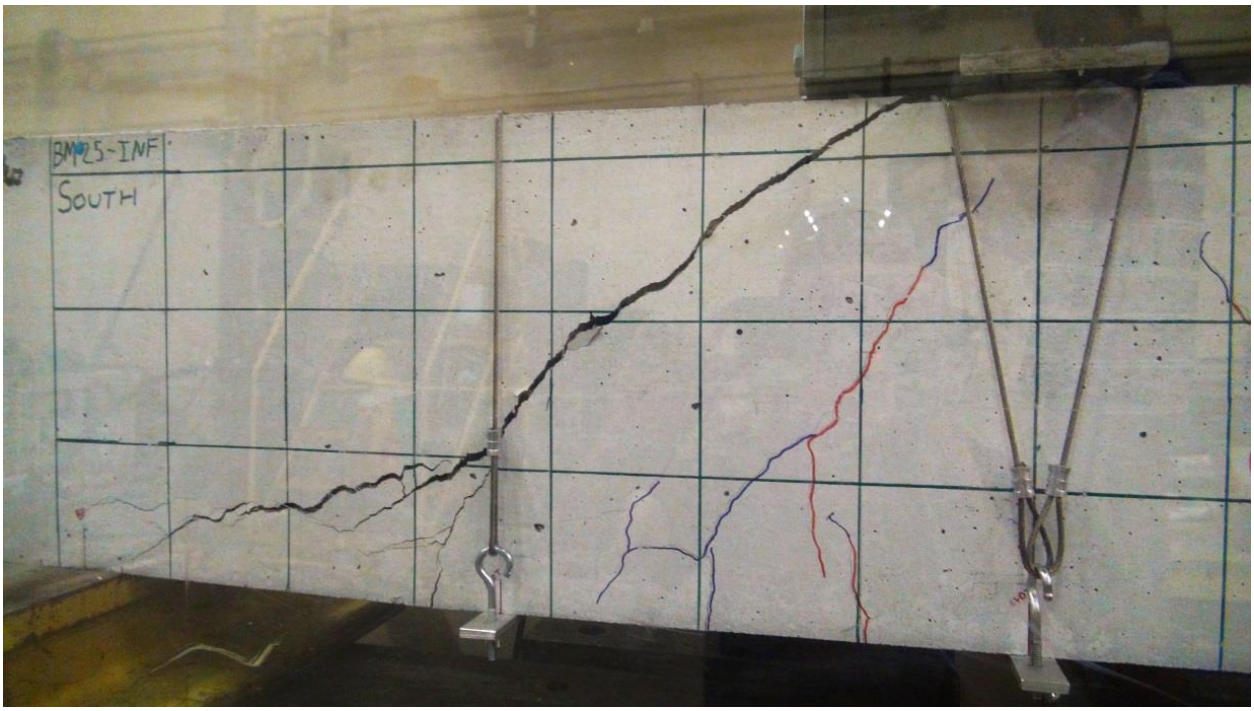

Figure E.46: BM25-INF Close-up Photo of Failure

E.7 BM12-220

This was the sixth beam tested. The displacement rate was 0.272 mm/min until the first crack measurement. The rate was then increased to 0.4 mm/min until after the final crack measurement at which point the rate was increased to 0.9 mm/min.

The beam failed in shear-compression / strut-crushing along a plane that ran diagonally from the load plate to the north bearing plate. The failure was unremarkable: peak load was not accompanied by loud noises, perceptible movements, or the ejection of concrete projectiles. Shortly after peak load there was a popping noise characteristic of concrete fracture and widening of cracks that accompanied a sudden drop in load.

Peak load occurred at 382.4 kN and 11.96 mm of displacement, and failure occurred in the un-instrumented north shear span 72 days after casting.

Strain gauge L-1-C failed before peak load, and strain gauges L-2-C and L-3-C failed after peak load; all other strain gauges functioned adequately during the test.

The stirrups in the failed shear span of this beam were extracted to investigate if the stirrups had failed at all. Stirrup 7 was found to have a large crack running along one of the bends found in the flexural tension zone of the beam. The crack followed the undulating geometry of the glass fibres through the bend, and was closely aligned with the neutral axis of the bend. Two photos are included at the end of this section. The condition of the rest of the stirrup, and that of another stirrup was unremarkable.

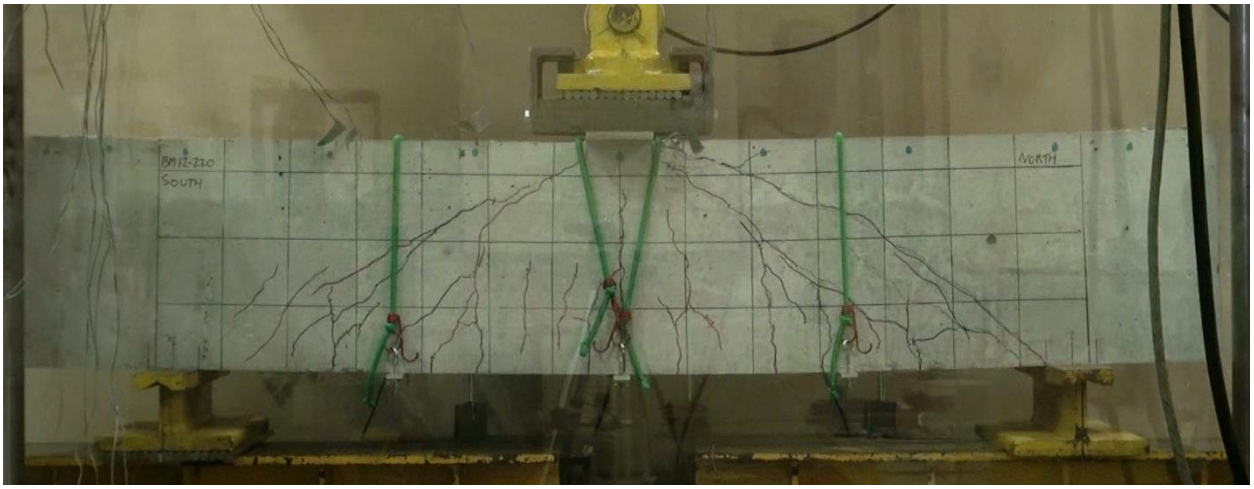

Figure E.47: BM12-220 At Peak Load

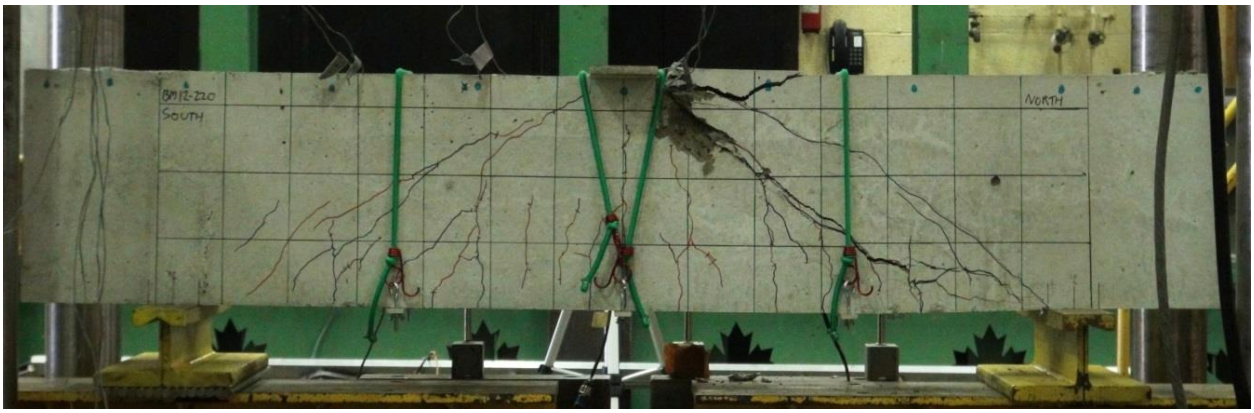

Figure E.48: BM12-220 After Testing

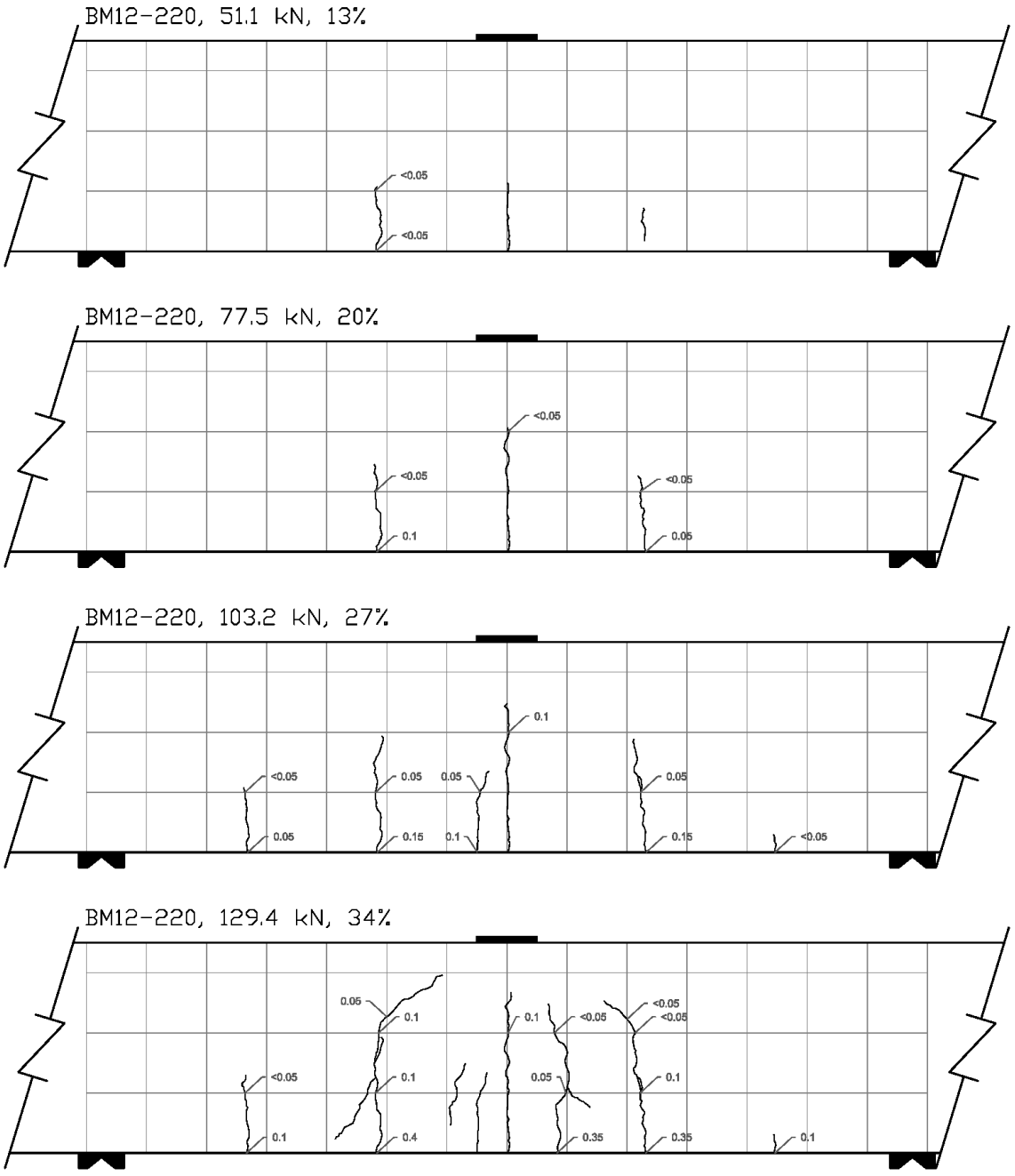

Figure E.49: BM12-220 Crack Diagram 1

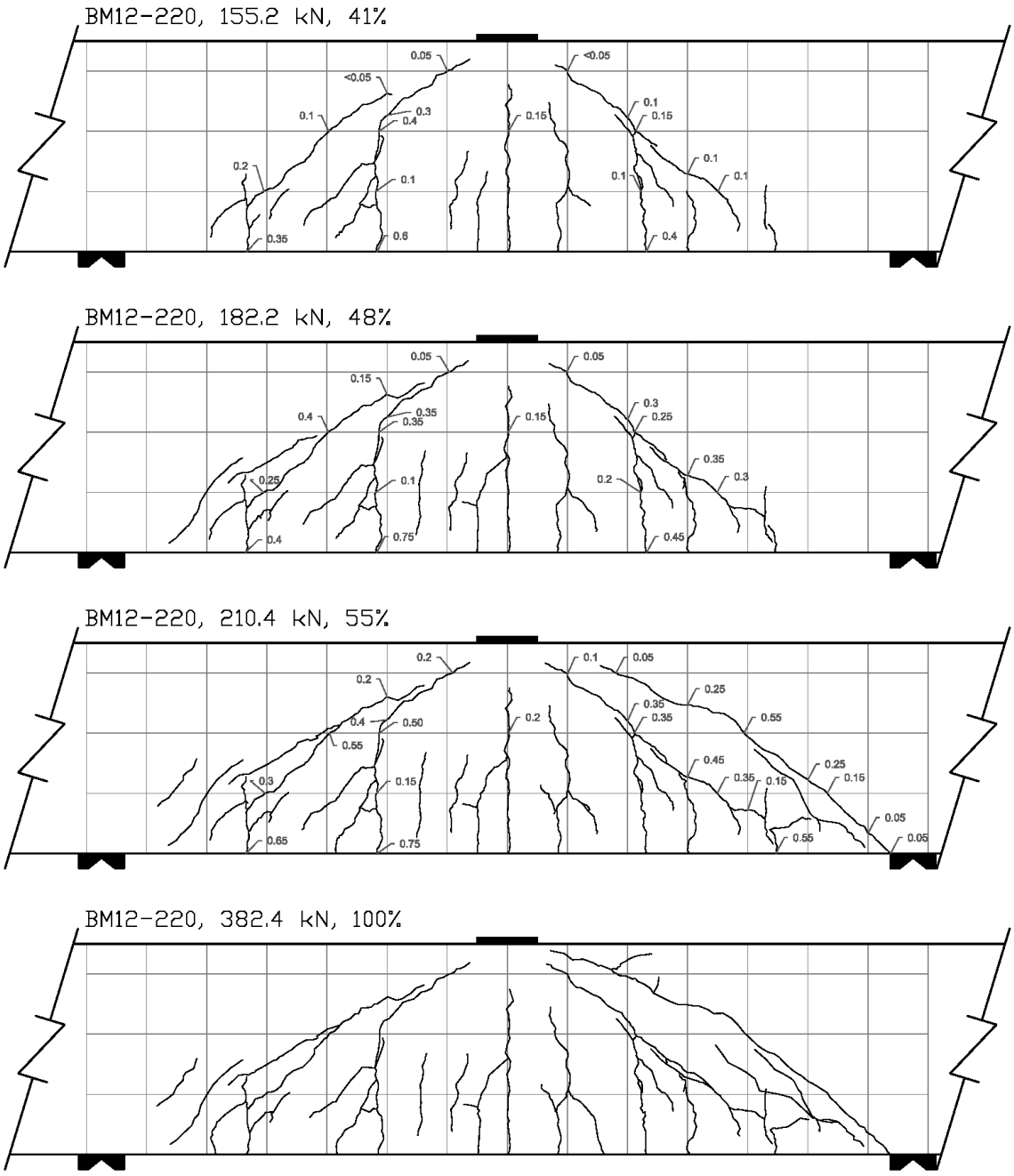

Figure E.50: BM12-220 Crack Diagram 2

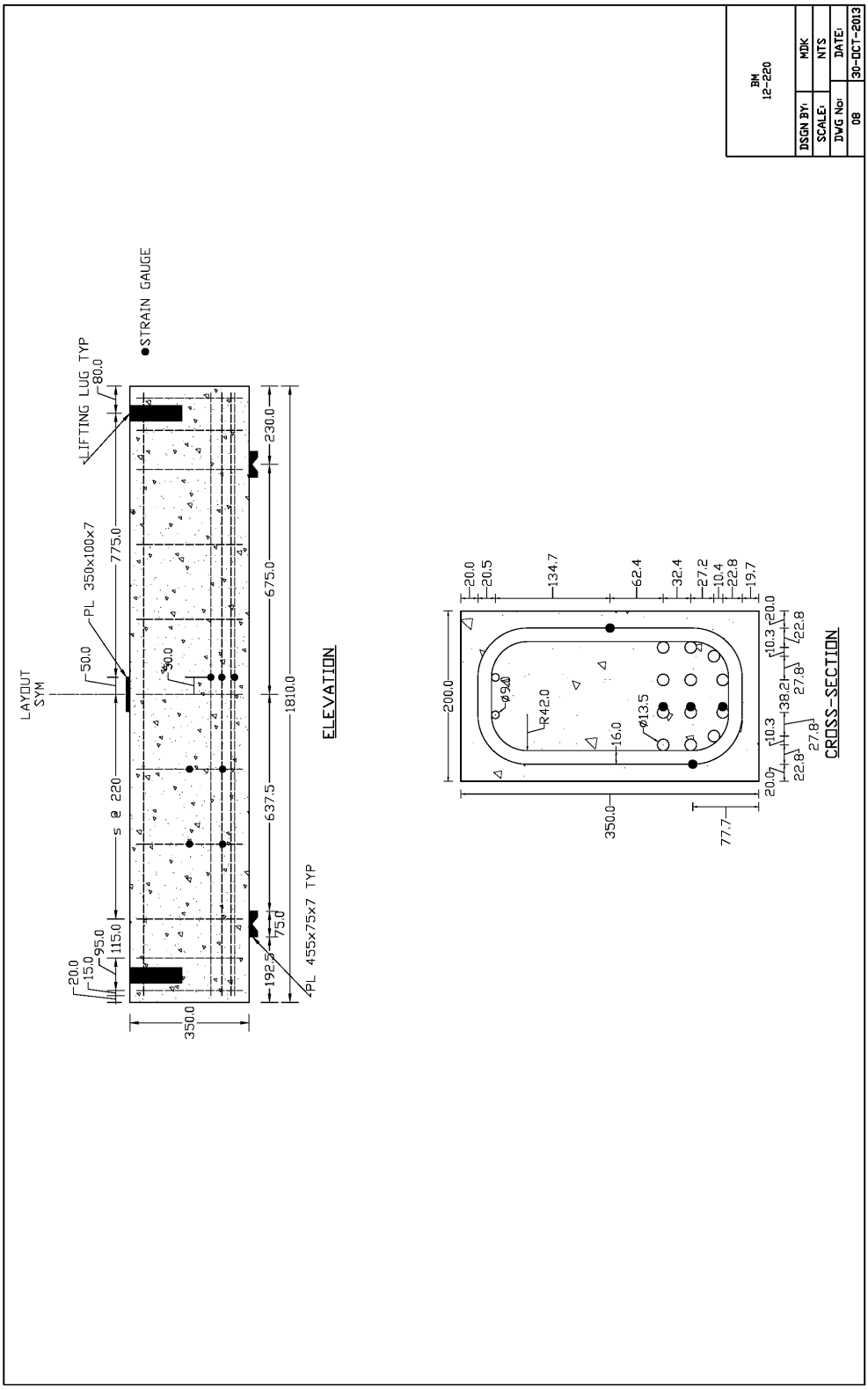

Figure E.51: BM12-220 Schematic Drawing

Table E.4: As-Designed and As-Constructed Parameter Chart for BM12-220

Parameter	As-Designed	As-Constructed
Beam Properties		
f'_c (MPa)	45	47.3 (28 day)
b (mm)	200	198.0**
h (mm)	350	351.0**
l (mm)	1810	-
d (mm)	270	263.8***
a/d	2.5	-
ρ_F (%)	2.51	-
ρ_v (%)	0.51	-
Longitudinal Bar Properties		
f_{Fu} (MPa)	1000	-
E_F (GPA)	60	-
A_F (mm^2)	113	-
n_{Bar} (amnt)	12	-
ε_{Fu} (%)	2.61*	-
Stirrup Properties		
$f_{Fu,straight}$ (MPa)	1000	-
$f_{Fu,bent}$ (MPa)	700	-
E_F (GPA)	50	-
A_F (mm^2)	113.1	-
r_{Bend} (mm)	42	-

** Rupture strain was only provided for dia. 16 bars; this value was assumed valid for all bars.*
*** Measured at midpoint of the failed shear span before testing, width is an average of top and bottom.*
**** Based on an average from measured bar depths before pour on north and south ends.*

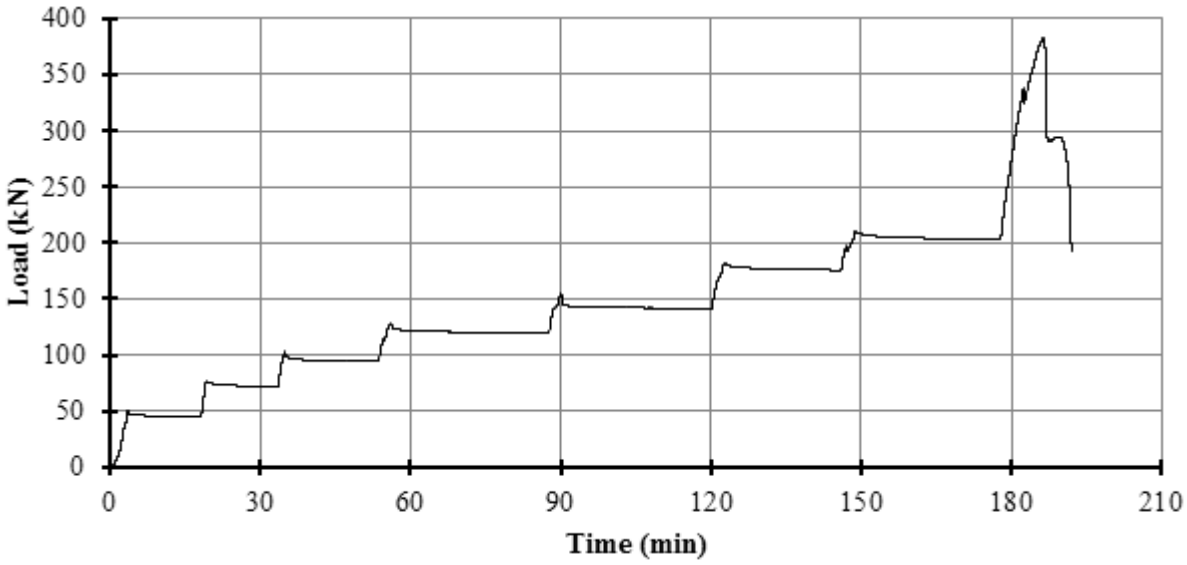

Figure E.52: BM12-220 Plot of Load vs Time

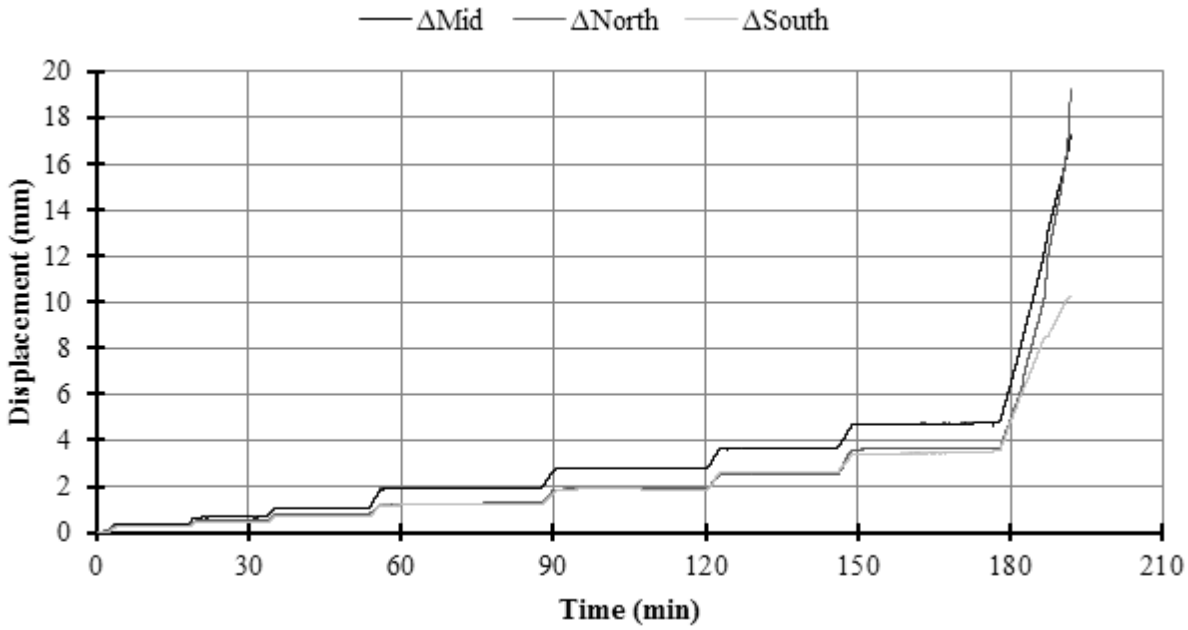

Figure E.53: BM12-220 Plot of Displacement vs Time

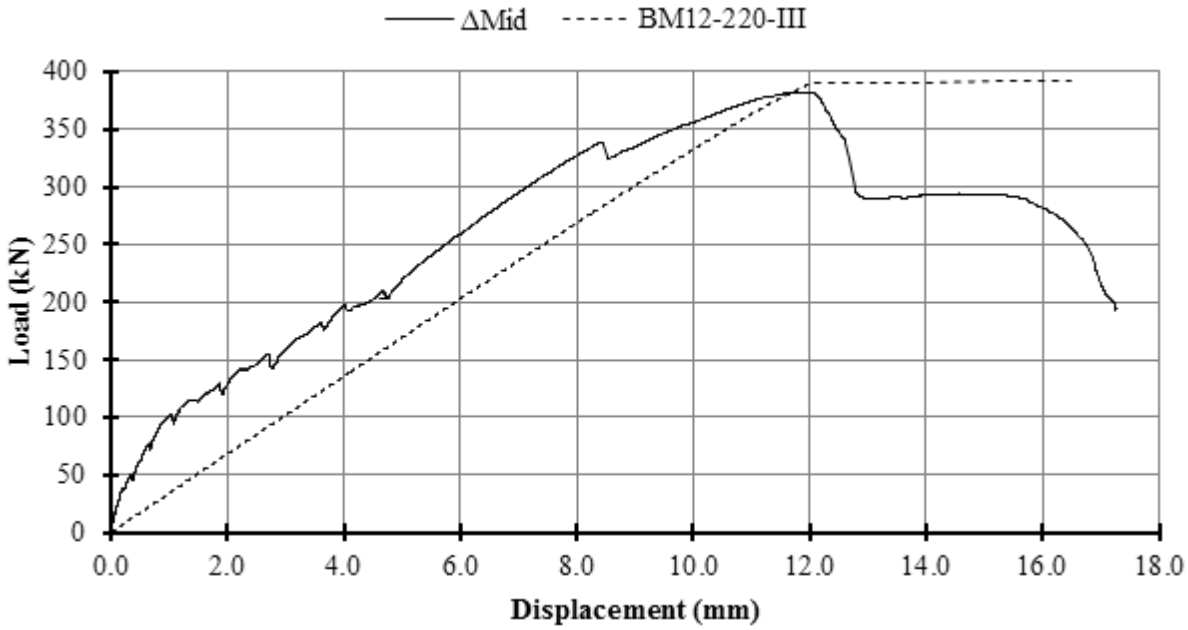

Figure E.54: BM12-220 Plot of Load vs Displacement

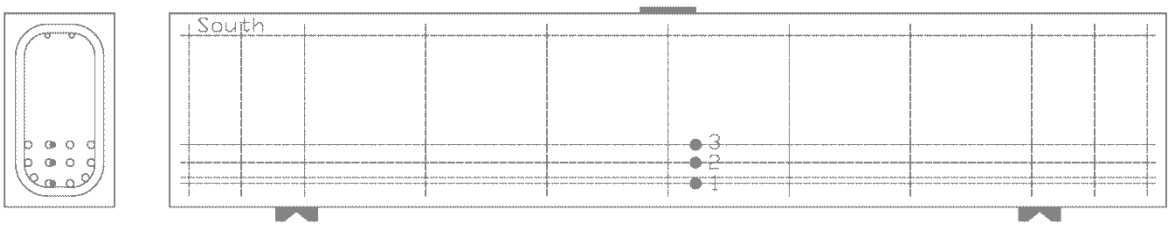

Figure E.55: BM12-220 Schematic of Mid-Span Strain Gauge Locations

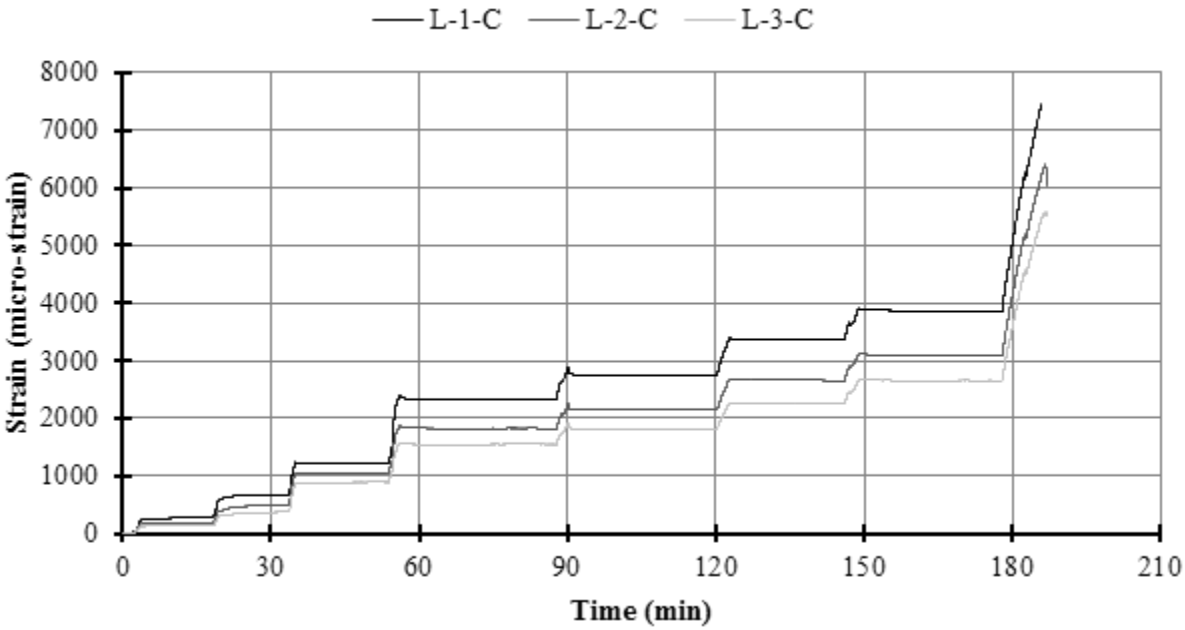

Figure E.56: BM12-220 Plot of Strain vs Time on Longitudinal Bars at Mid-Span

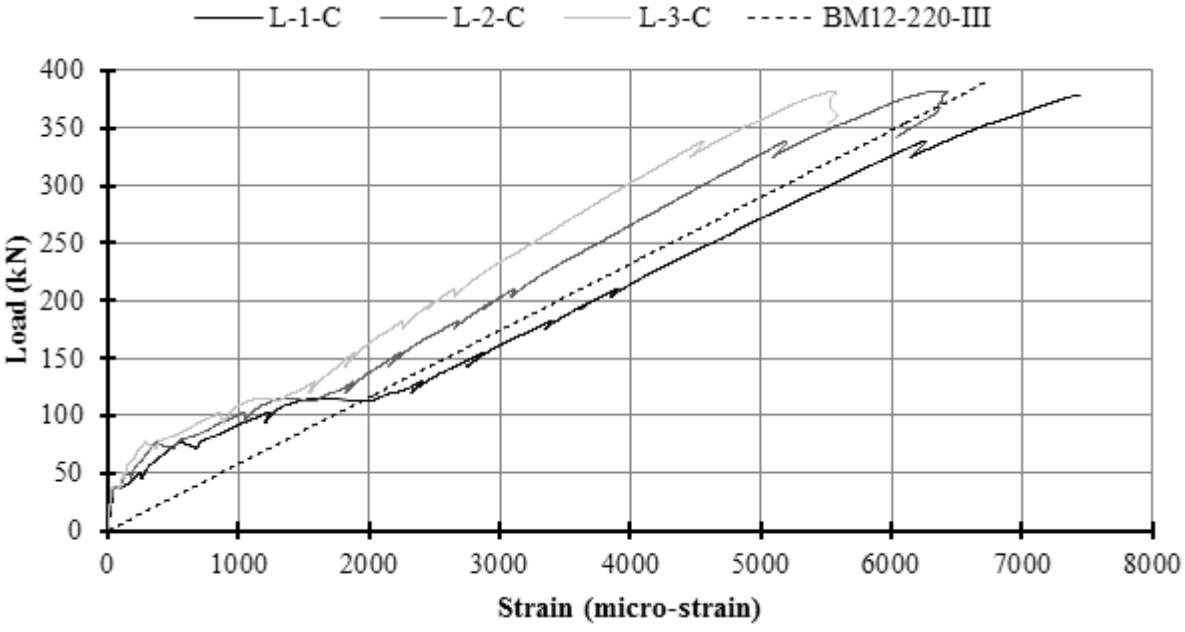

Figure E.57: BM12-220 Plot of Load vs Strain on Longitudinal Bars at Mid-Span

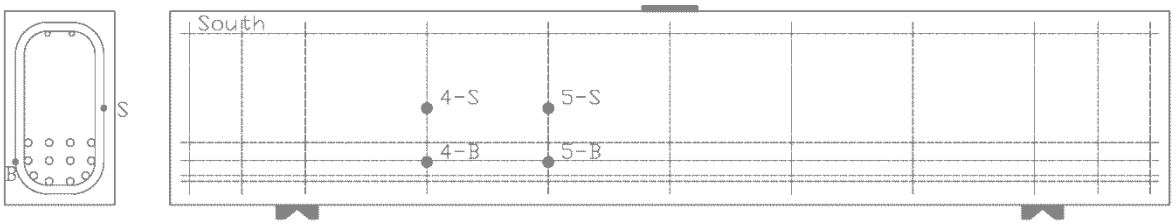

Figure E.58: BM12-220 Schematic of Stirrup Strain Gauge Locations

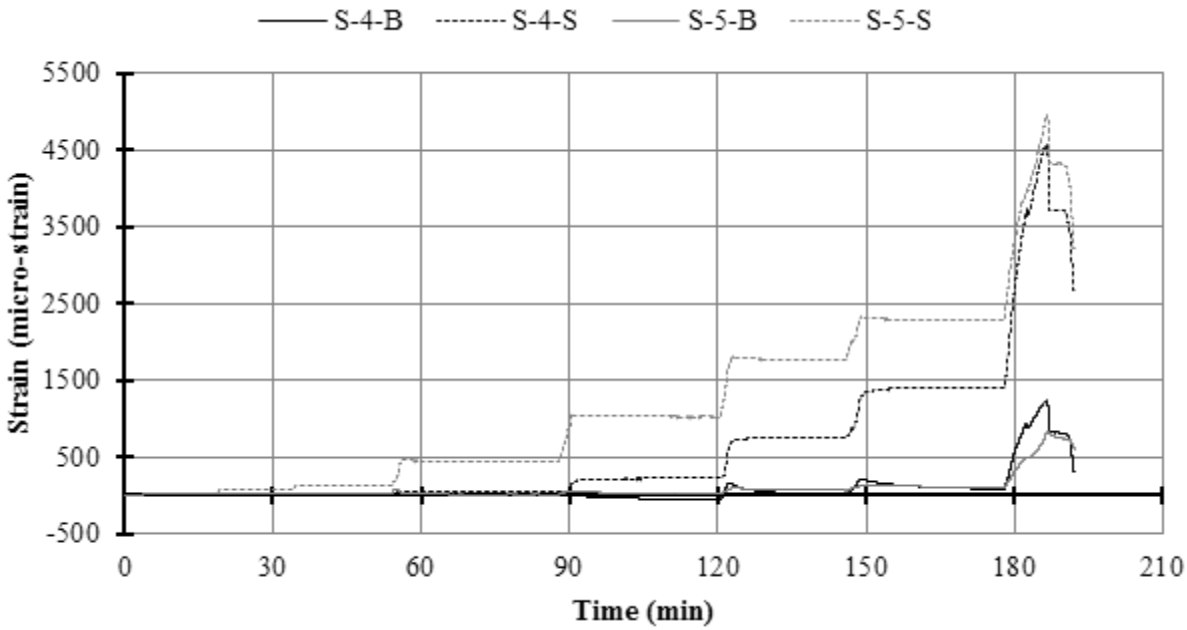

Figure E.59: BM12-220 Plot of Strain vs Time on Stirrups

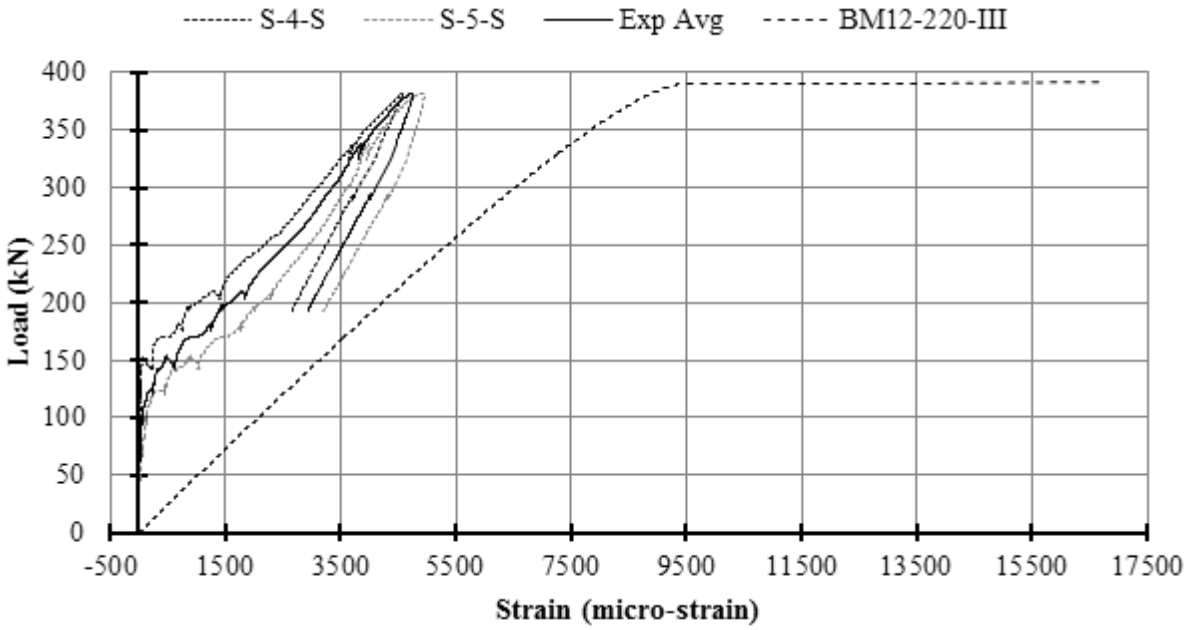

Figure E.60: BM12-220 Plot of Load vs Strain on Stirrups

A plot with all stirrup strain gauges may be found in the Results Chapter.

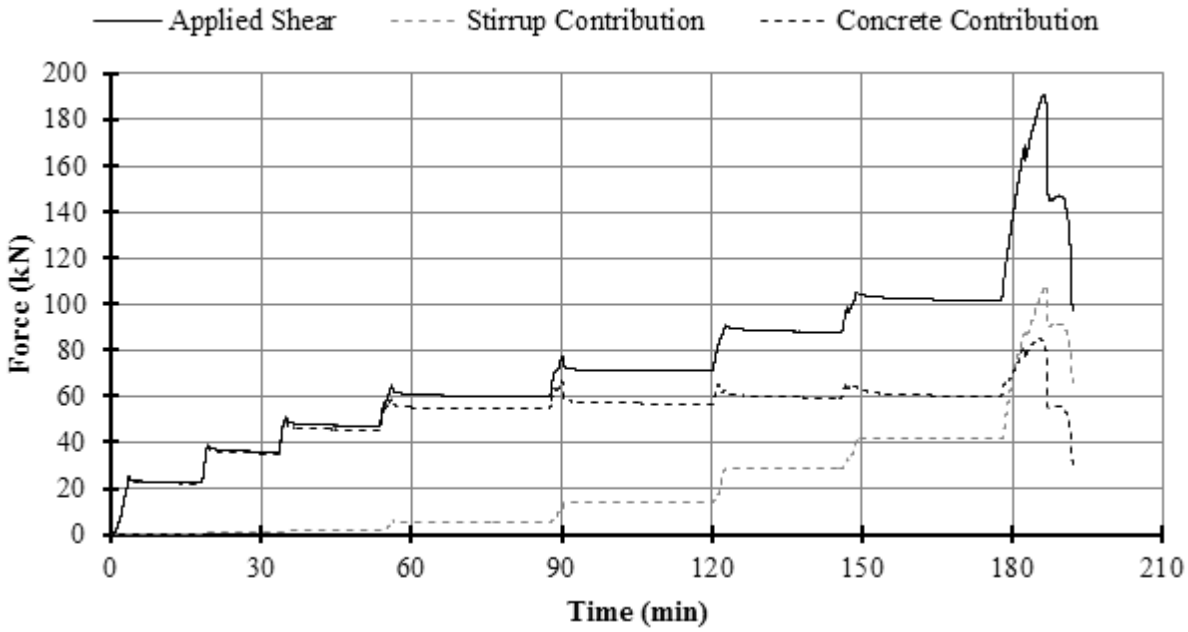

Figure E.61: BM12-220 Plot of Shear Contribution vs Time

E.7.1 BM12-220 Photographs

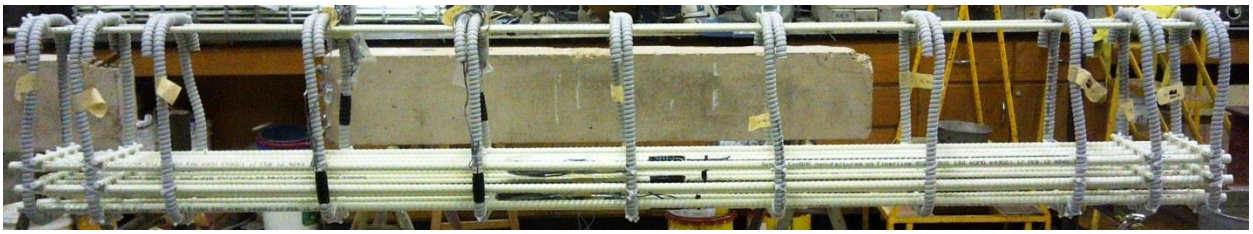

Figure E.62: BM12-220 Rebar Cage Elevation Photo

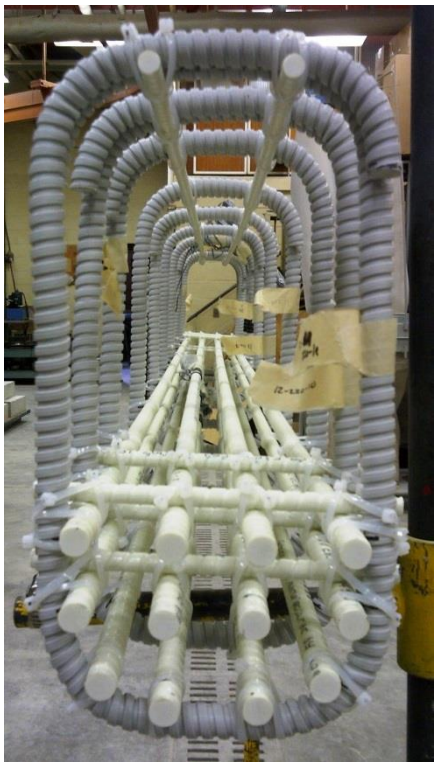

Figure E.63: BM12-220 Rebar Cage Cross-Section Photo

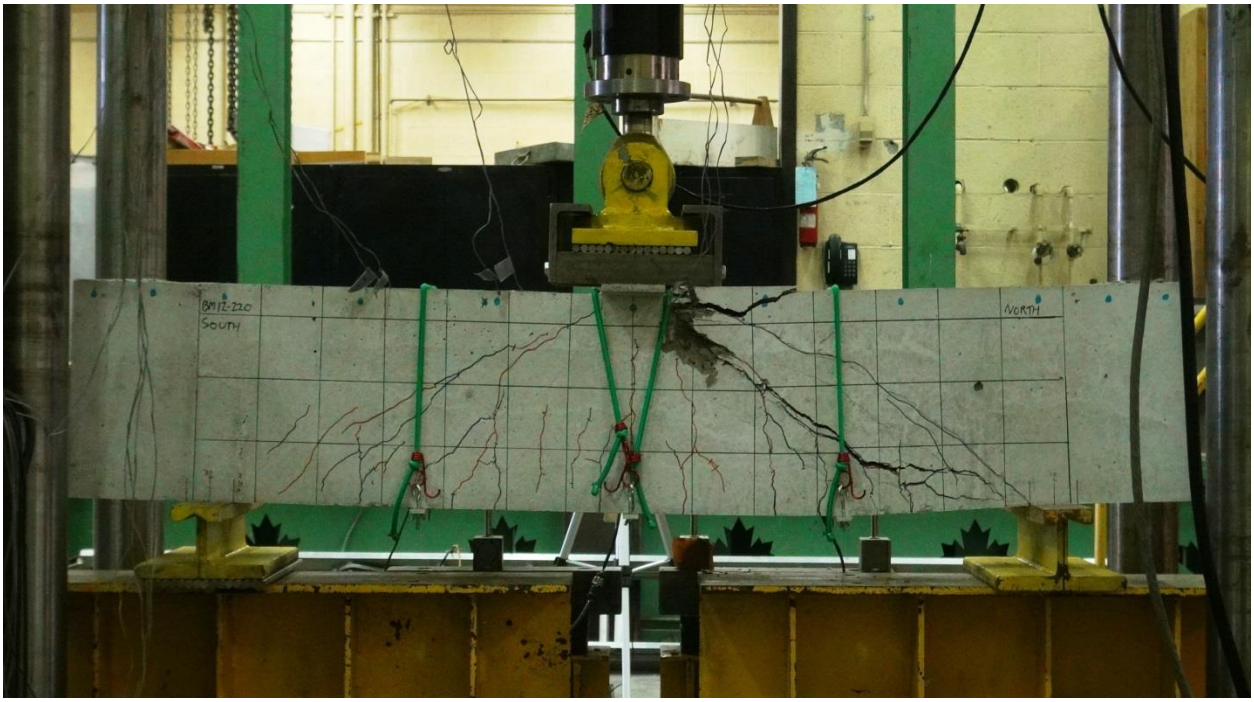

Figure E.64: BM12-220 Alternative Photo of Entire Beam Under Load After Testing

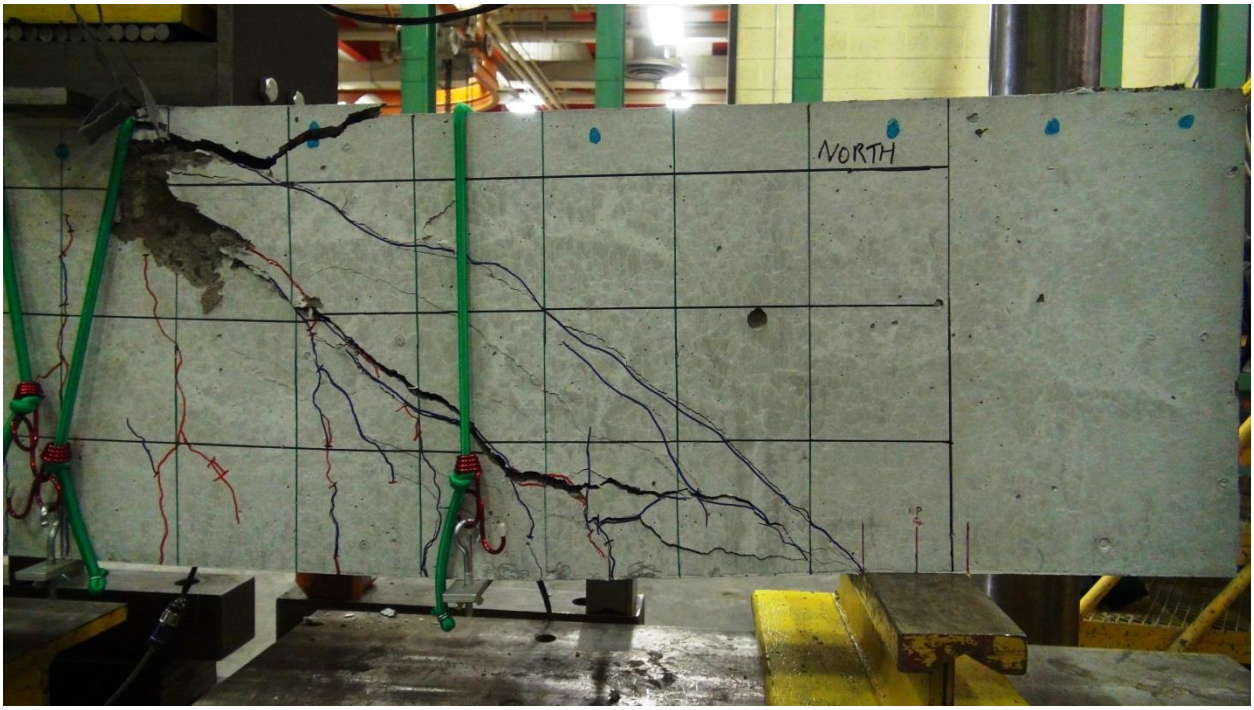

Figure E.65: BM12-220 Close-up Photo of Failure

Figure E.66: BM12-220 Photo of Exposed Stirrup 7 after Testing

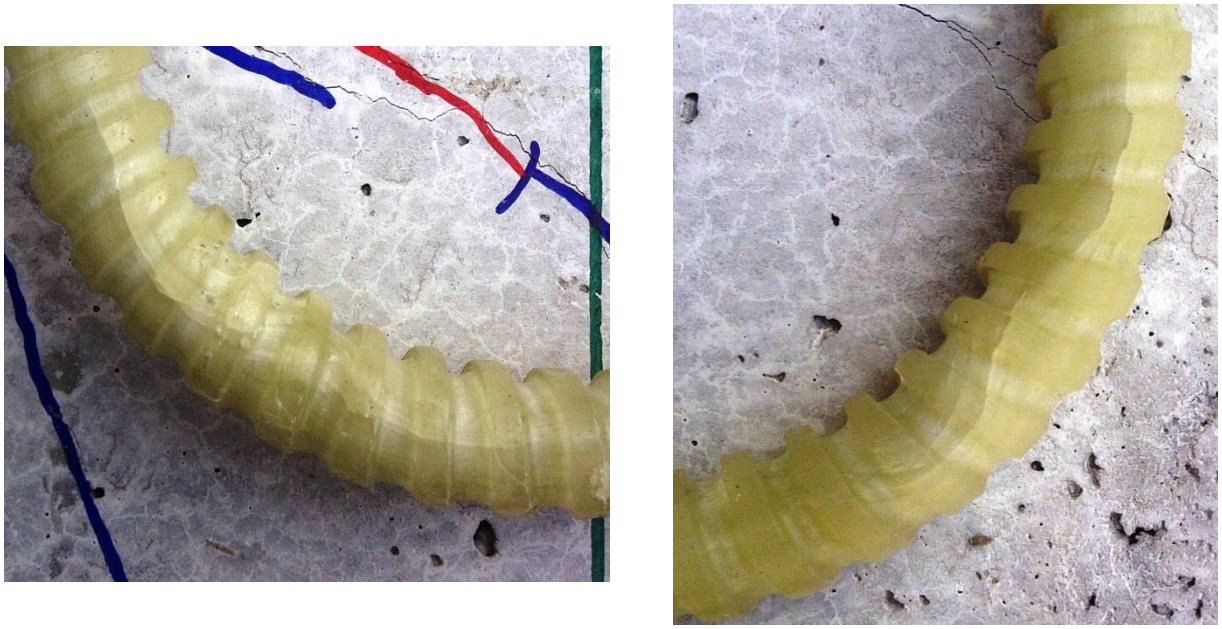

Figure E.67: BM12-220 Bend of Stirrup 7 Front and Back

This stirrup bend comes from the part of the stirrup in the flexural tension zone.

E.8 BM16-220

This was the fifth beam tested. The displacement rate was 0.272 mm/min until the first crack measurement. The rate was then increased to 0.4 mm/min until after the final crack measurement after which the rate was increased to 0.8 mm/min.

The beam failed in shear-compression / strut-crushing along a plane that ran diagonally from the load plate to the north bearing plate. Peak load was accompanied by a slight popping noise characteristic of concrete fracture, but was otherwise not accompanied by perceptible movements or the ejection of concrete projectiles.

Peak load occurred at 309.3 kN and 8.42 mm of displacement*, and failure took place in the un-instrumented north shear span 68 days after casting. (* See *Issues* below.)

Strain gauges L-1-C and L-2-C failed after peak load; all other strain gauges functioned adequately during the test.

Issues

A thunderstorm moved through the region and a power blip interrupted the test. The blip caused the computer controlling the load frame to shut off and knocked out the hydraulics to the entire structures lab. The power blip affected the test results in two important ways.

The beam was loaded to 43 percent, 132.0 kN, of its ultimate load, 309.3 kN, at the time of the power blip before quickly returning to no load. The 132.0 kN load was the result of a spike in load caused by the blip. At the time the data acquisition system was sampling once per second and may not have captured the true peak. The blip occurred during the fourth pause for crack measurements and several flexural shear cracks had formed at the time. Ergo, this beam went through a load cycle and it is difficult to take this load cycle into account when considering the results.

The author stopped recording data shortly after the power blip because the possibility of another power failure precluded further testing until the storm passed. When the data acquisition system restarted, all of the gauge readings were zeroed. The residual displacement and strains in the beam after the 43 percent load cycle were not included in the measurements taken when testing restarted. The applied load is always measured accurately, and is never zeroed.

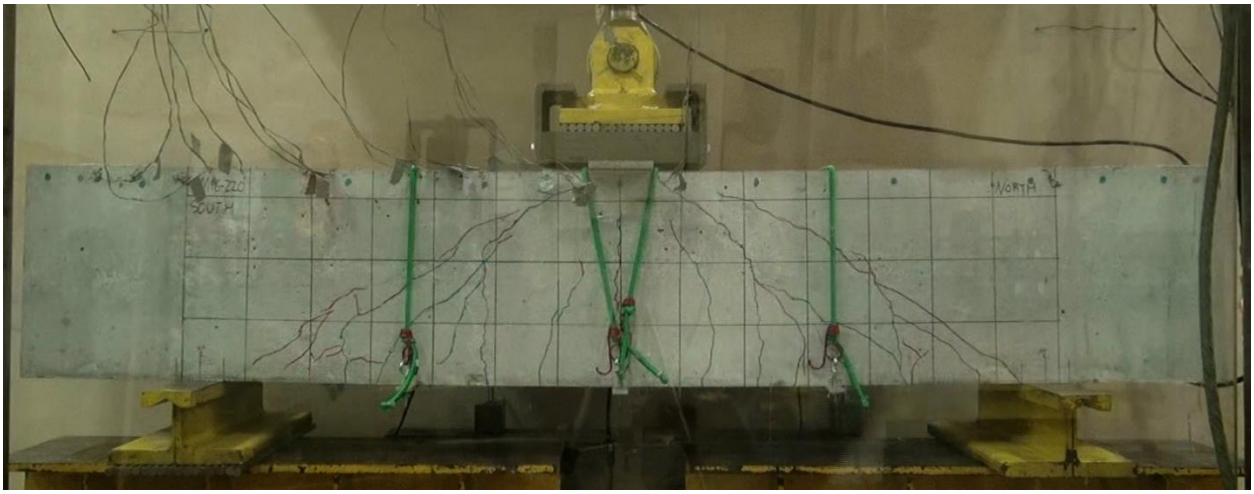

Figure E.68: BM16-220 At Peak Load

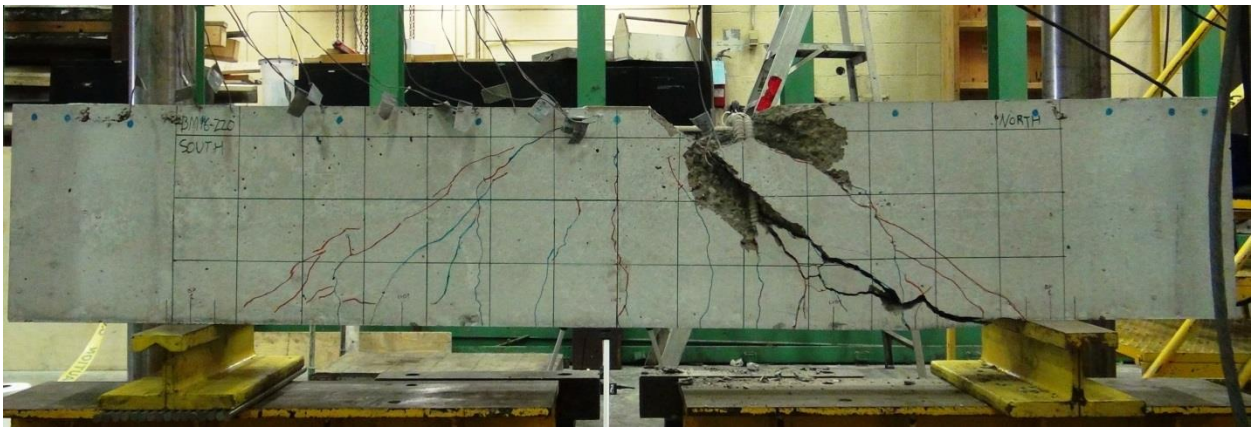

Figure E.69: BM16-220 After Testing

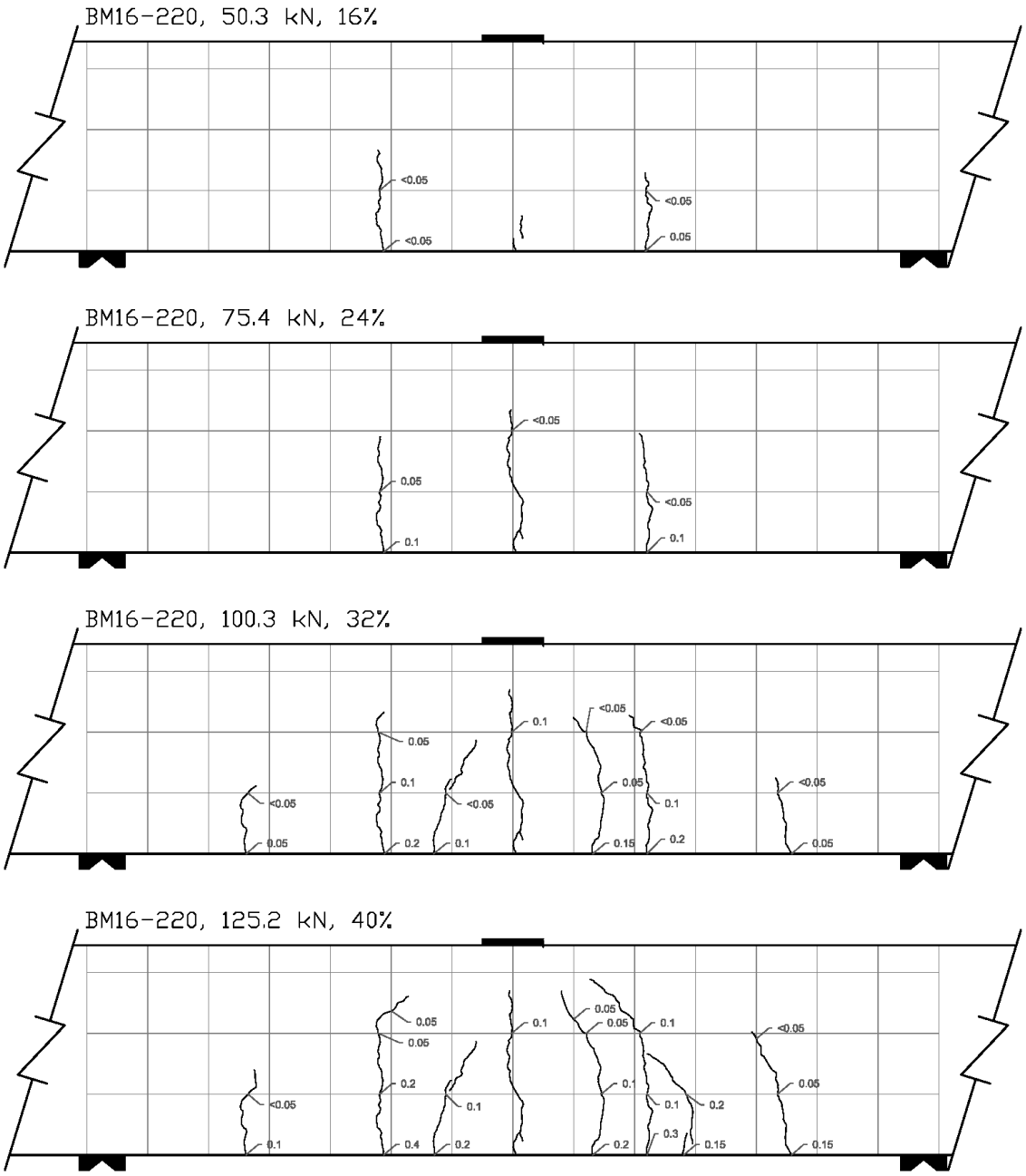

Figure E.70: BM16-220 Crack Diagram 1

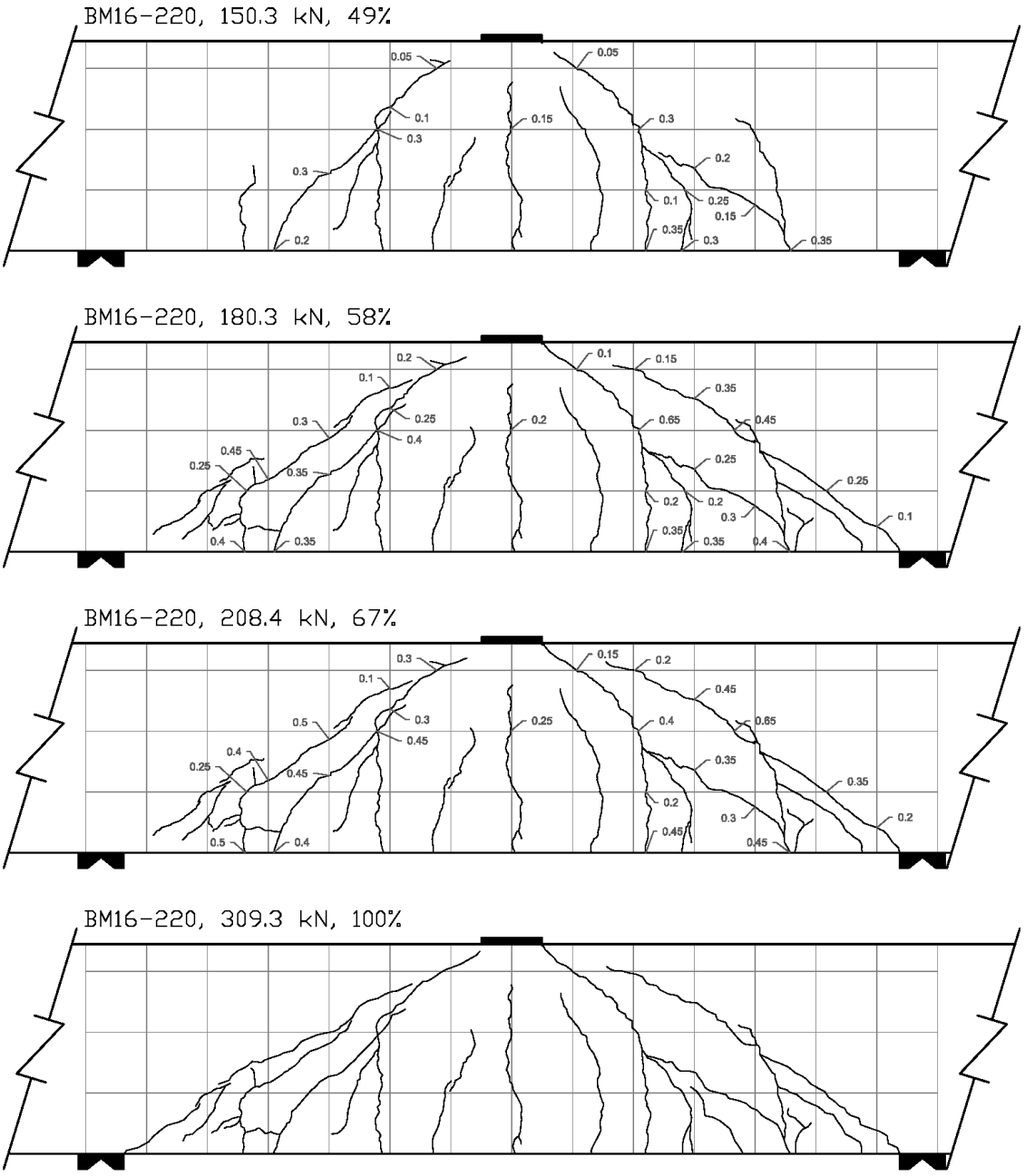

Figure E.71: BM16-220 Crack Diagram 2

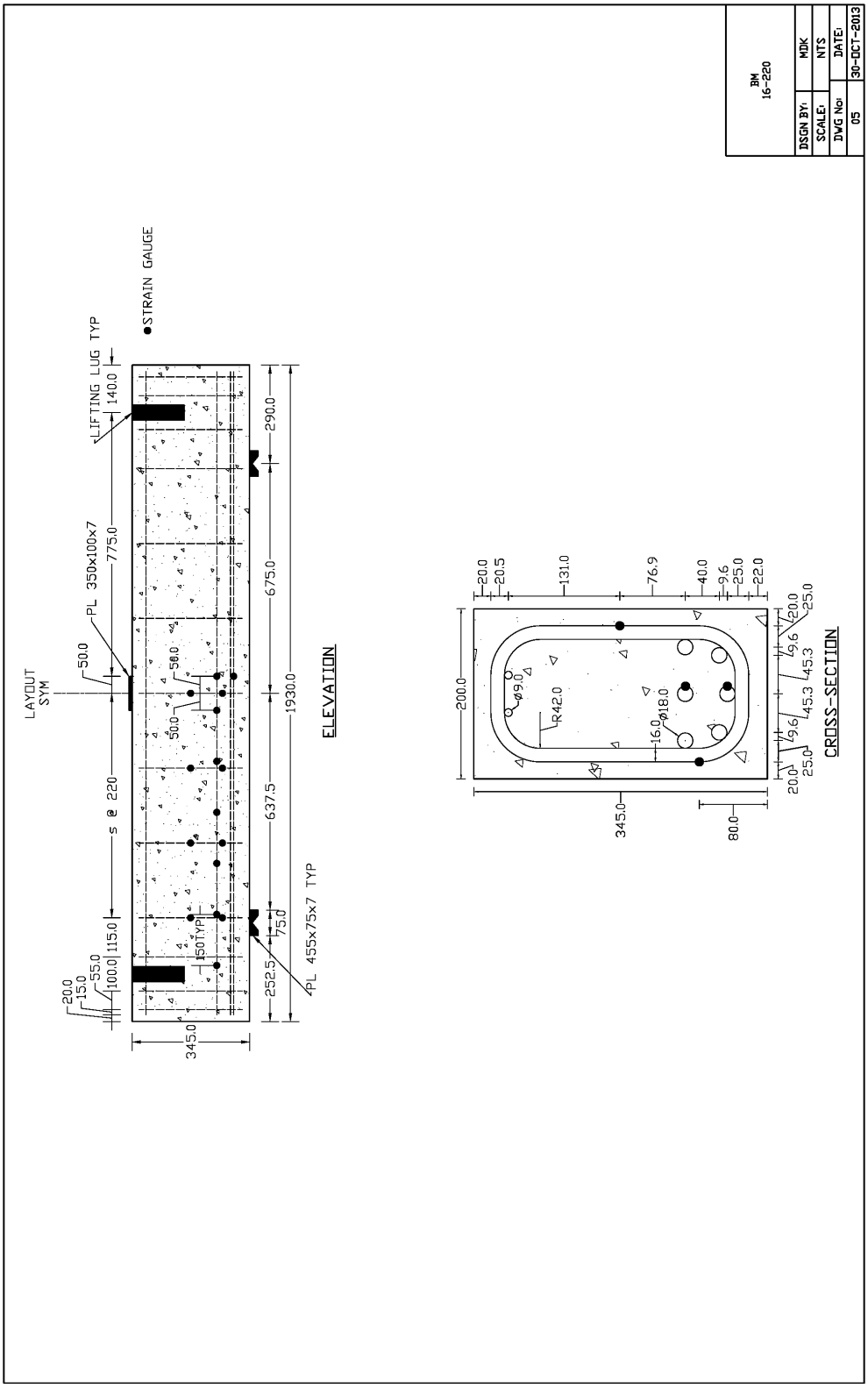

Figure E.72: BM16-220 Schematic Drawing

Table E.5: As-Designed and As-Constructed Parameter Chart for BM16-220

Parameter	As-Designed	As-Constructed
Beam Properties		
f'_c (MPa)	45	47.3 (28 day)
b (mm)	200	201.0**
h (mm)	345	346.0**
l (mm)	1930	-
d (mm)	270	264.1***
a/d	2.5	-
ρ_F (%)	2.23	-
ρ_v (%)	0.51	-
Longitudinal Bar Properties		
f_{Fu} (MPa)	1000	-
E_F (GPA)	64	-
A_F (mm^2)	201	-
n_{Bar} (amnt)	6	-
ε_{Fu} (%)	2.61*	-
Stirrup Properties		
$f_{Fu,straight}$ (MPa)	1000	-
$f_{Fu,bent}$ (MPa)	700	-
E_F (GPA)	50	-
A_F (mm^2)	113.1	-
r_{Bend} (mm)	42	-

** Rupture strain was only provided for dia. 16 bars; this value was assumed valid for all bars.*
*** Measured at midpoint of the failed shear span before testing, width is an average of top and bottom.*
**** Based on an average from measured bar depths before pour on north and south ends.*

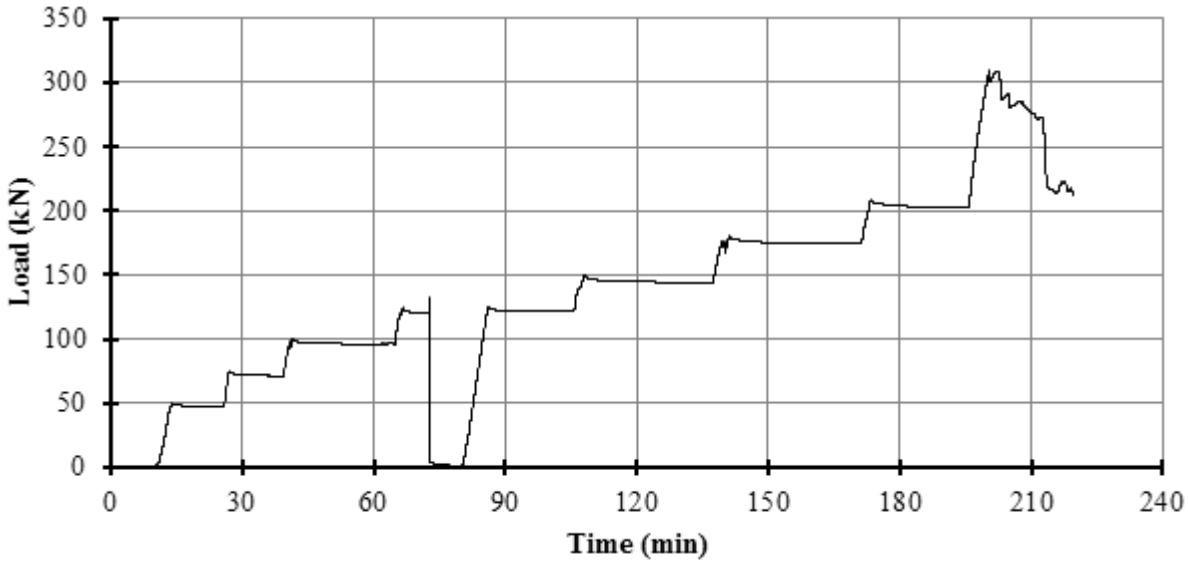

Figure E.73: BM16-220 Plot of Load vs Time

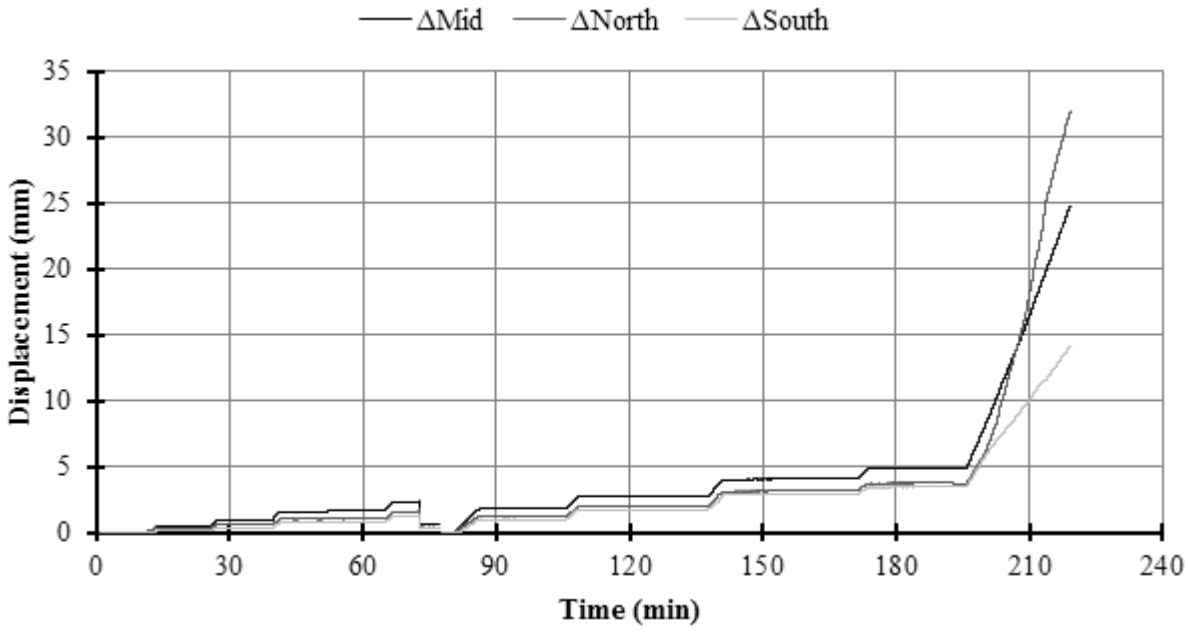

Figure E.74: BM16-220 Plot of Displacement vs Time

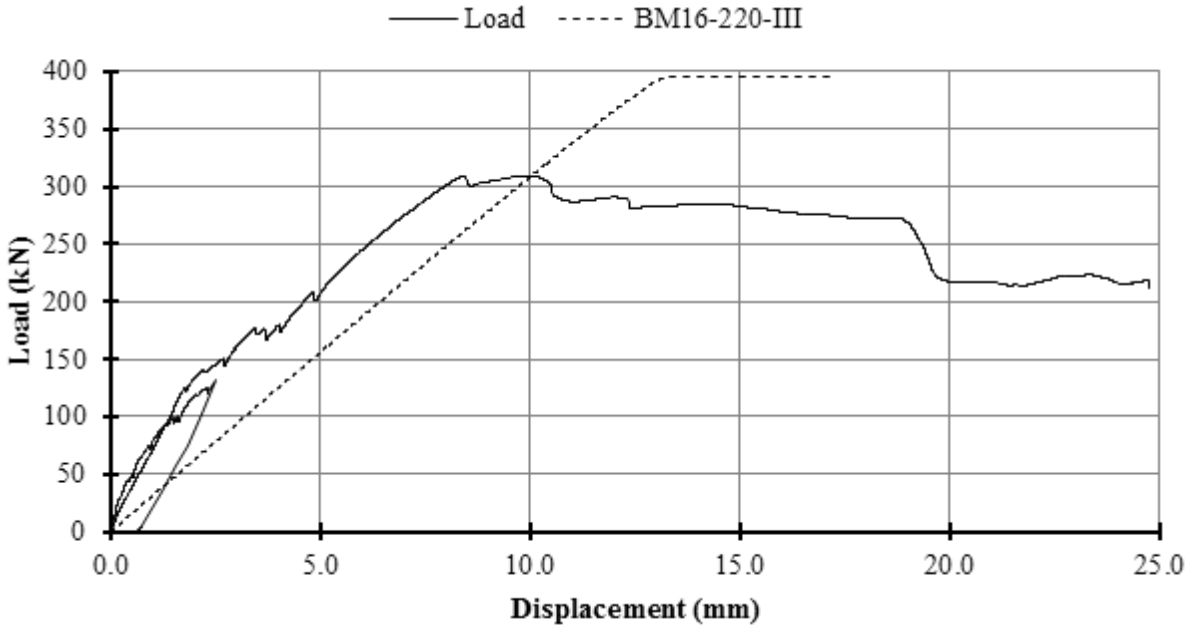

Figure E.75: BM16-220 Plot of Load vs Displacement

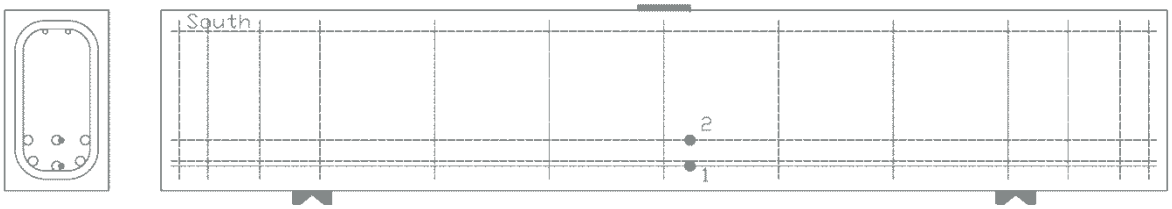

Figure E.76: BM16-220 Schematic of Mid-Span Strain Gauge Locations

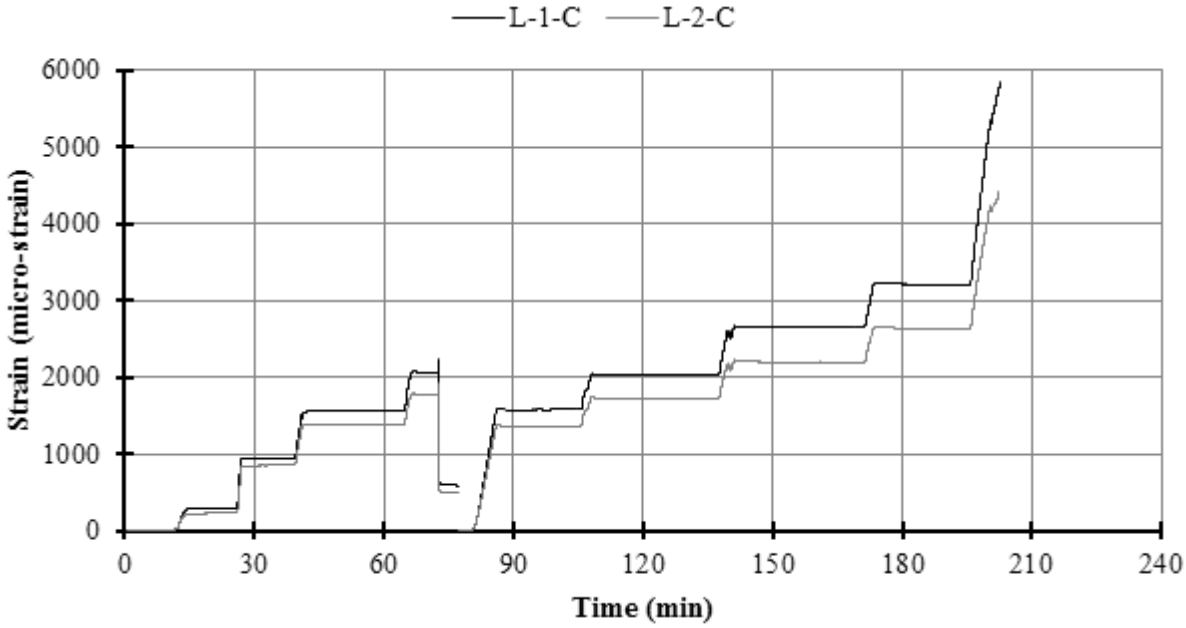

Figure E.77: BM16-220 Plot of Strain vs Time on Longitudinal Bars at Mid-Span

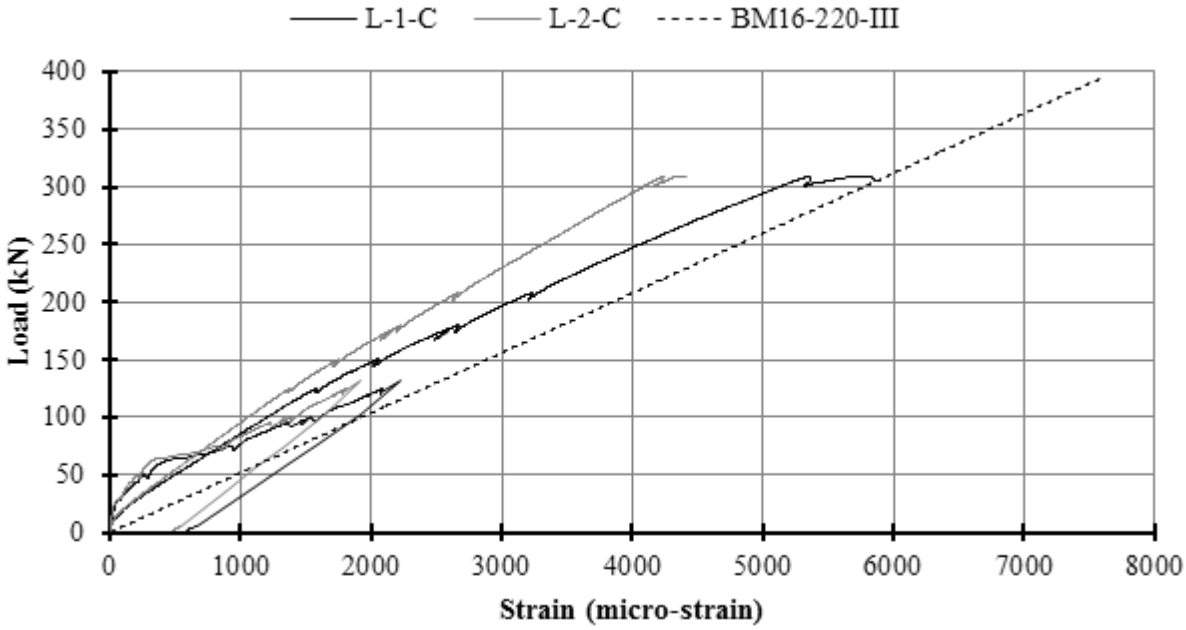

Figure E.78: BM16-220 Plot of Load vs Strain on Longitudinal Bars at Mid-Span

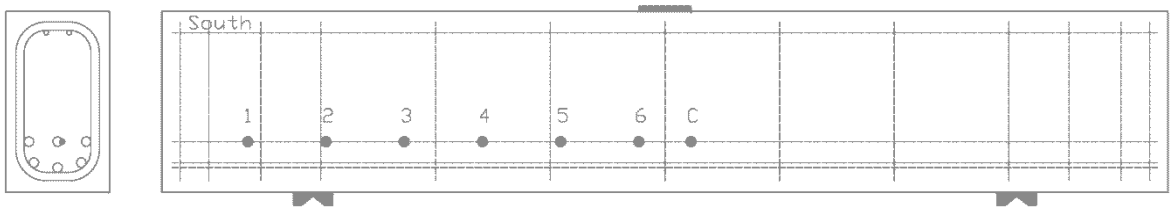

Figure E.79: BM16-220 Schematic of Longitudinal Strain Gauge Locations

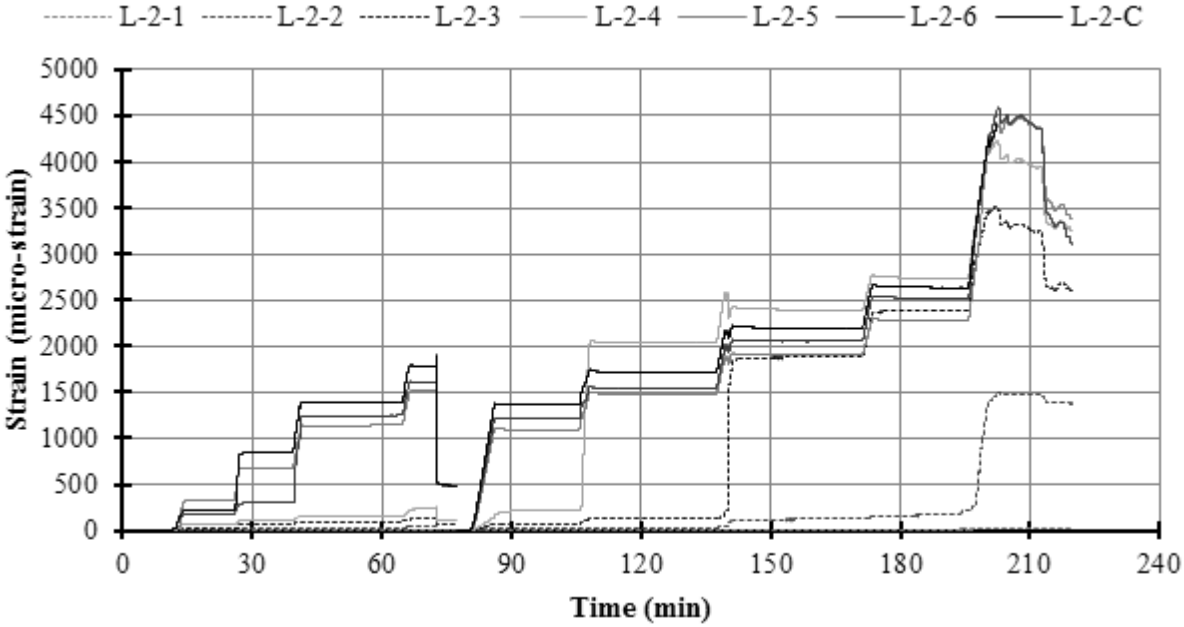

Figure E.80: BM16-220 Plot of Strain vs Time from Gauges along the Top Longitudinal Bar

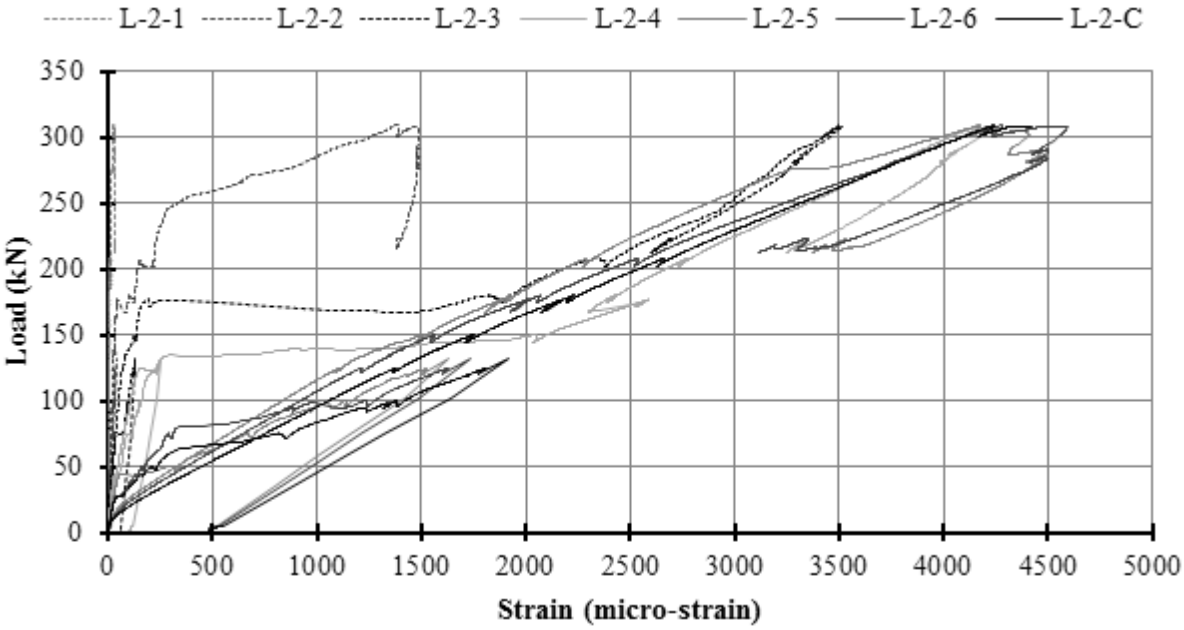

Figure E.81: BM16-220 Plot of Load vs Strain from Gauges along the Top Longitudinal Bar

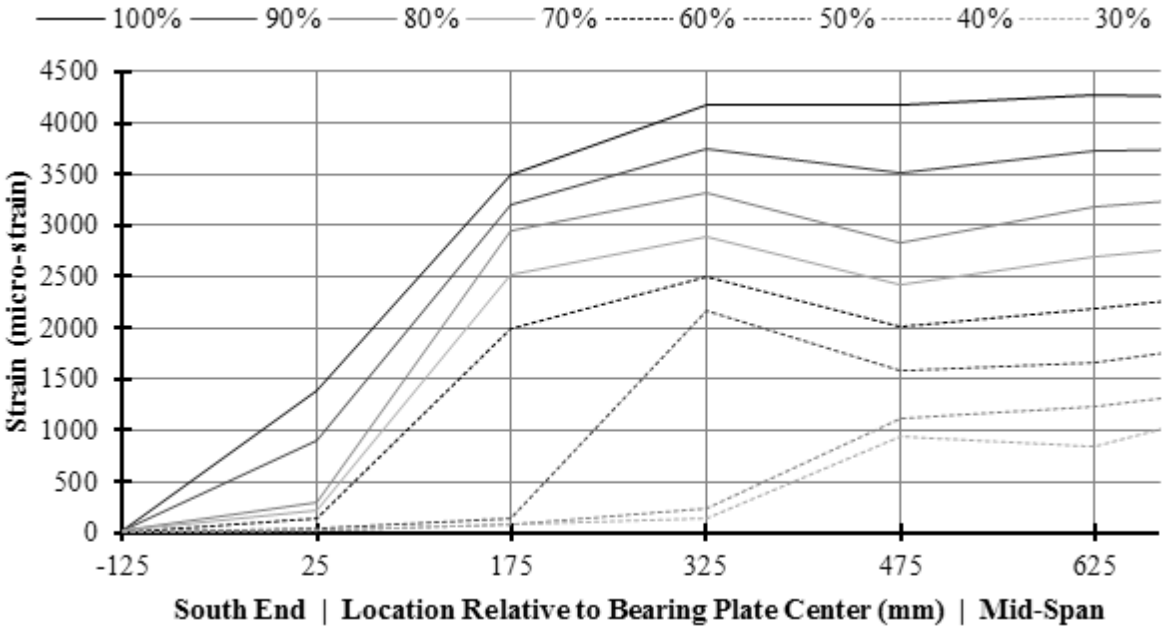

Figure E.82: BM16-220 Plot of Longitudinal Strain vs Gauge Location with Increasing Load

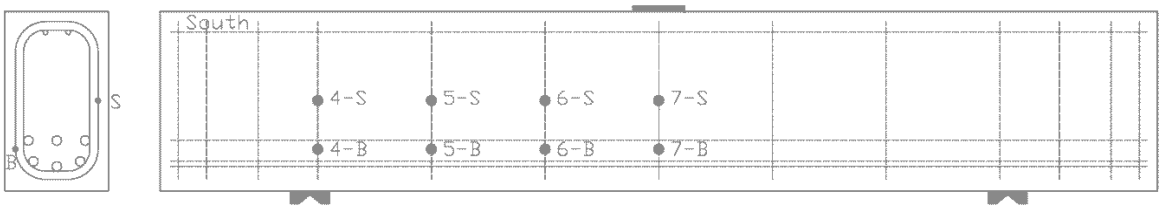

Figure E.83: BM16-220 Schematic of Stirrup Strain Gauge Locations

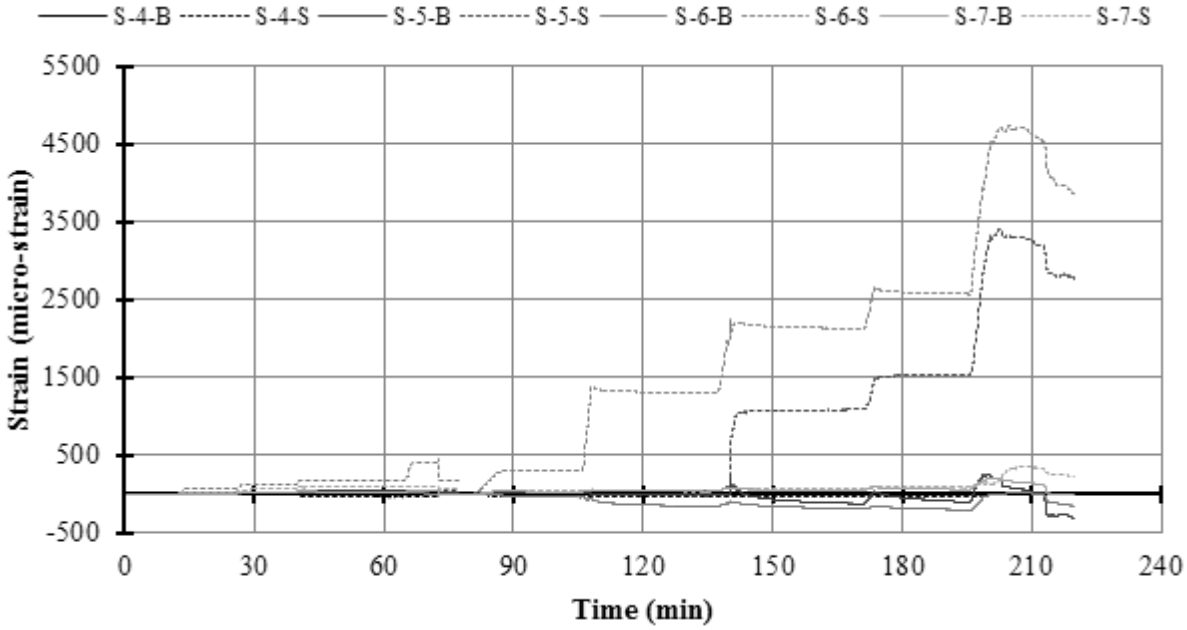

Figure E.84: BM16-220 Plot of Strain vs Time on Stirrups

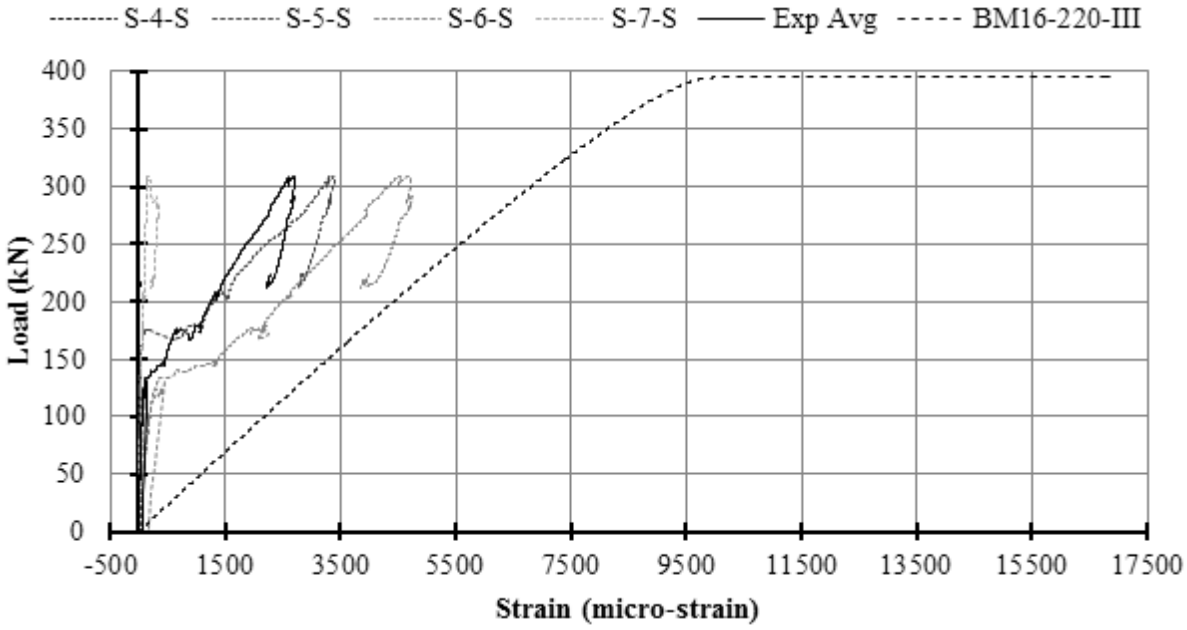

Figure E.85: BM16-220 Plot of Load vs Strain on Stirrups

A plot with all stirrup strain gauges may be found in the Results Chapter.

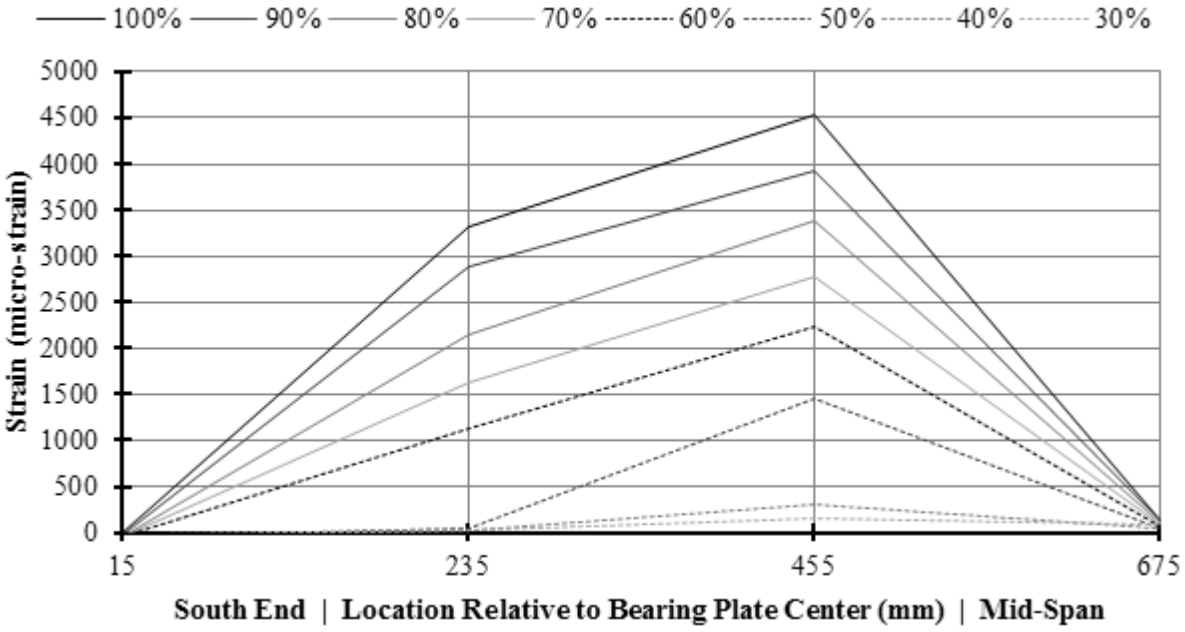

Figure E.86: BM16-220 Plot of Stirrup Strain vs Gauge Location with Increasing Load

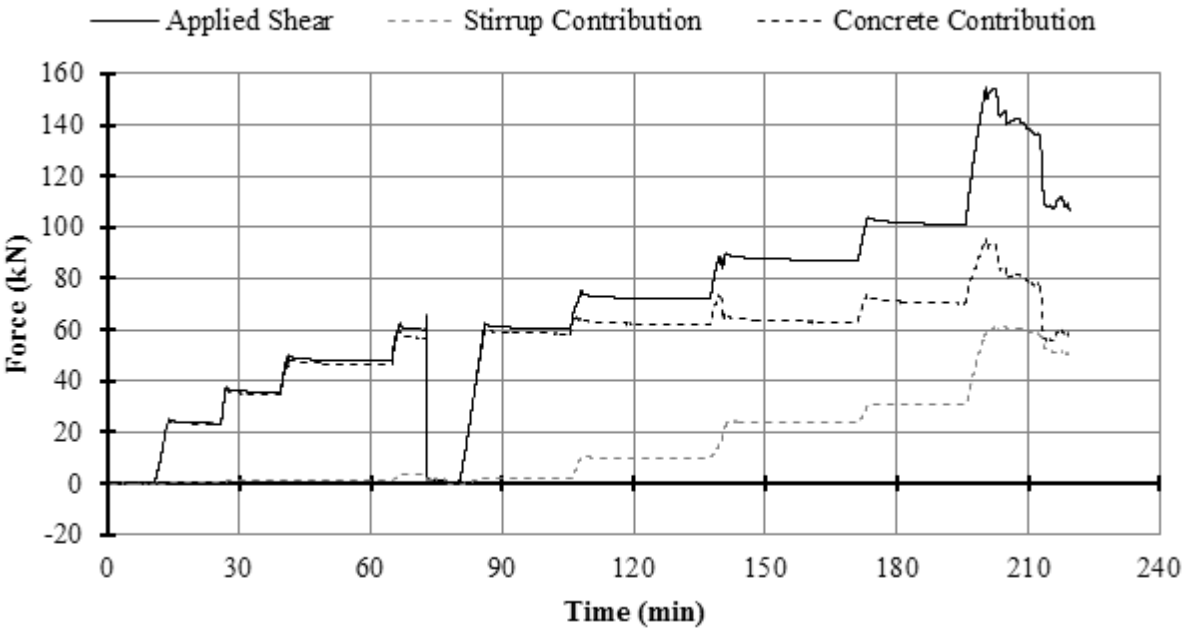

Figure E.87: BM16-220 Plot of Shear Contribution vs Time

E.8.1 BM16-220 Photographs

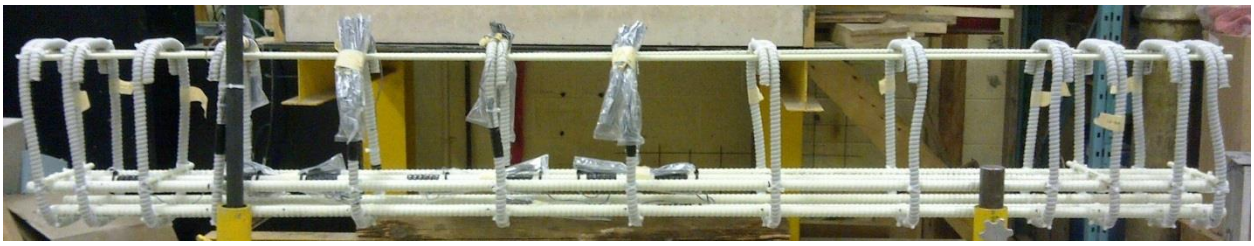

Figure E.88: BM16-220 Rebar Cage Elevation Photo

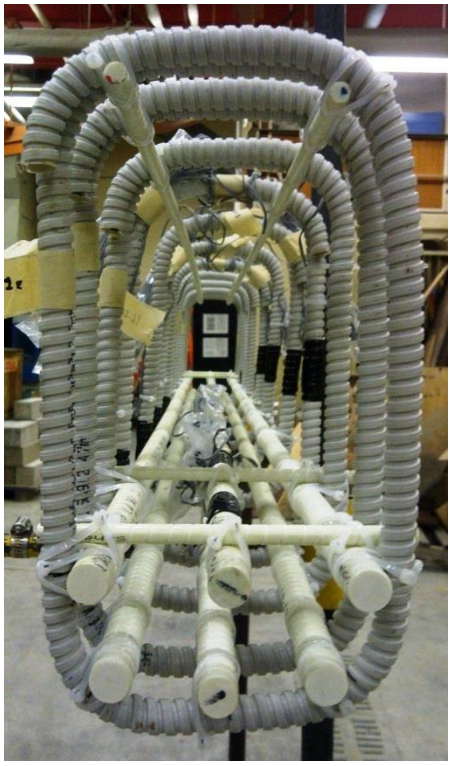

Figure E.89: BM16-220 Rebar Cage Cross-Section Photo

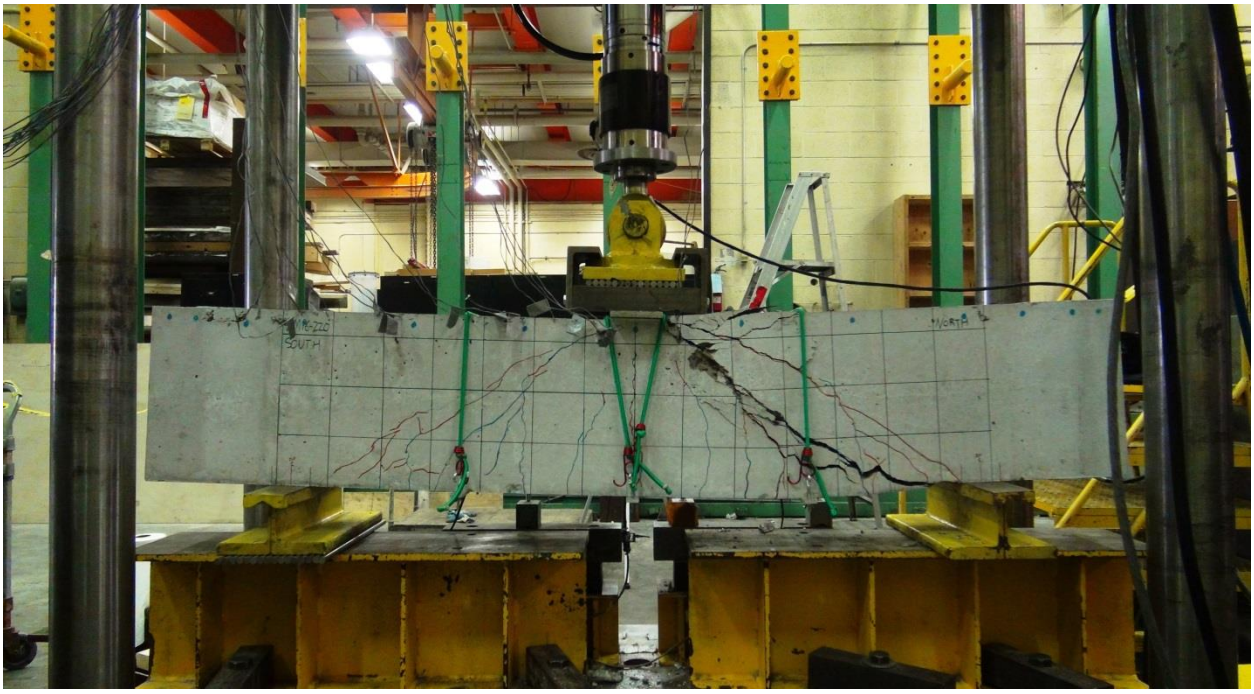

Figure E.90: BM16-220 Alternative Photo of Entire Beam Under Load After Testing

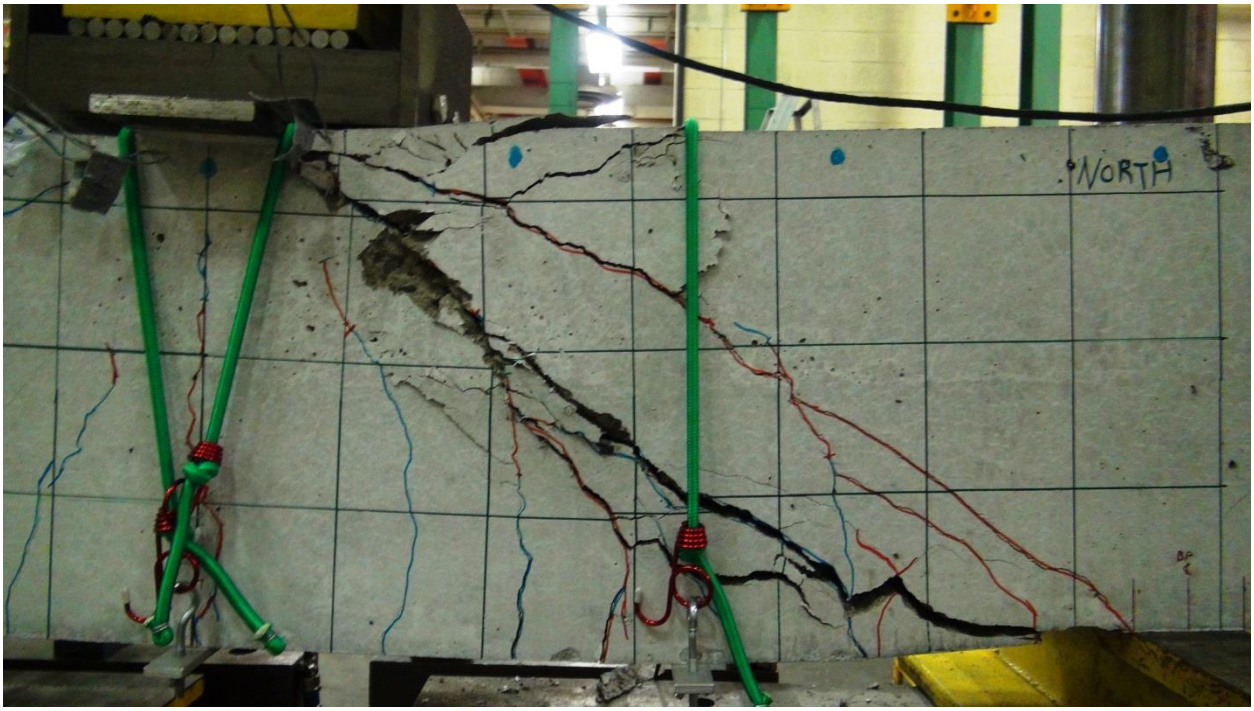

Figure E.91: BM16-220 Close-up Photo of Failure

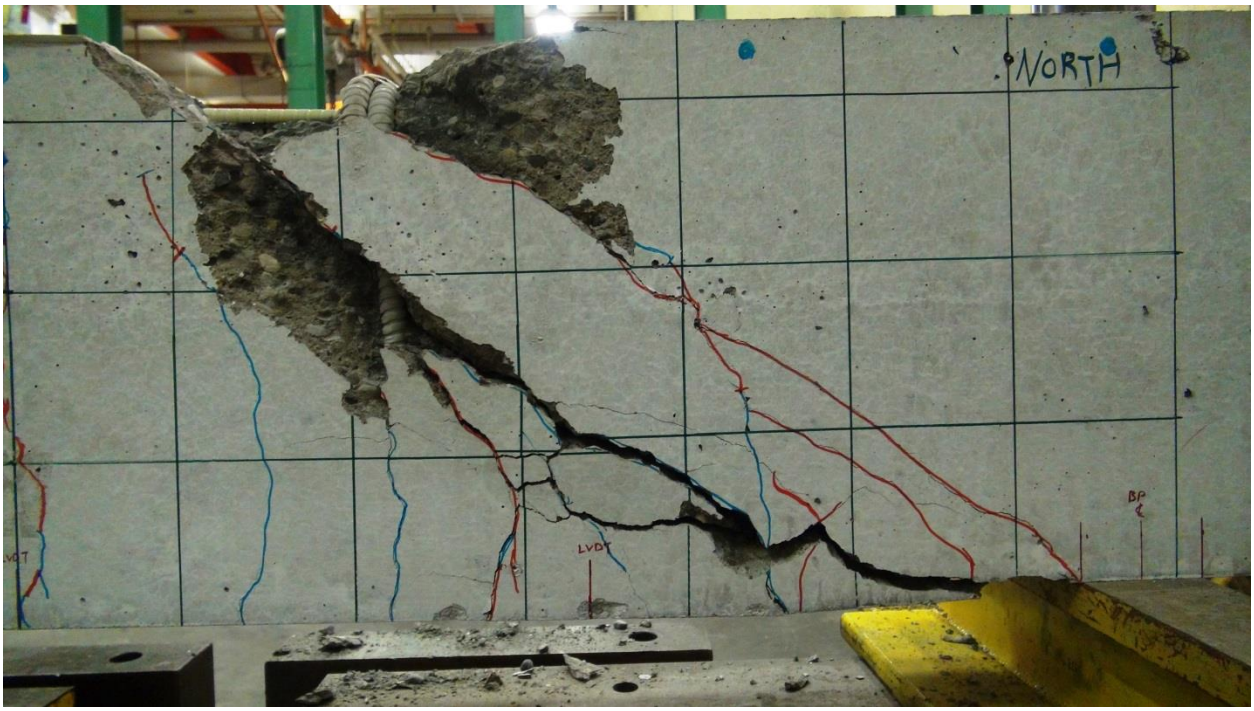

Figure E.92: BM16-220 Close-up Photo of Failure with Spalled Concrete Removed

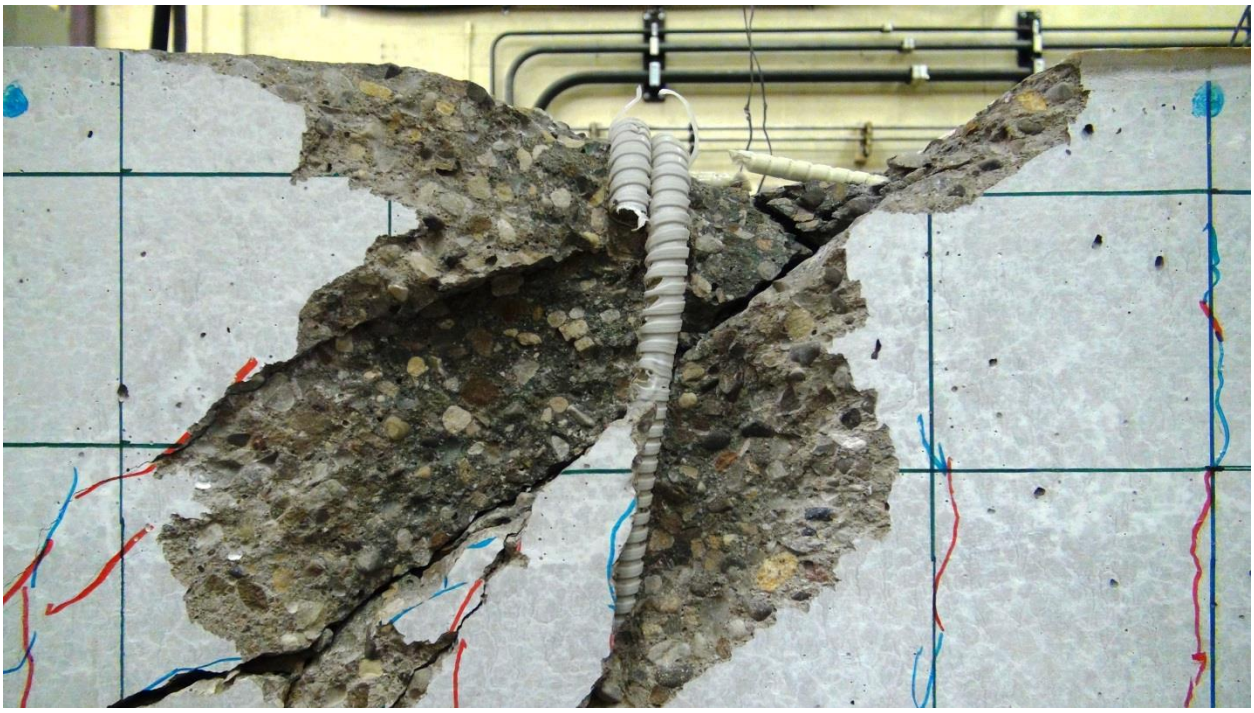

Figure E.93: BM16-220 Photo of Exposed Stirrup and Failure Plane after Loading from Reverse

E.9 BM25-220

This was the fourth beam tested. It was tested at a constant displacement rate of 0.272 mm/min. This rate was exceedingly slow for beams with stirrups and subsequent beam tests were done with higher rates of displacement. Crack widths were measured at 10 different intervals during the test; however, future beam tests were done with fewer intervals to shorten test time.

The beam failed in shear-compression / strut-crushing along a plane that ran diagonally from the loading plate to the south bearing plate. A bottle shaped section of deformed concrete was located along the failure plane. Peak load was reached and then followed by a plateau on the load displacement curve. The failure was unremarkable: peak load was not accompanied by loud noises, perceptible movements, or the ejection of concrete projectiles.

Peak load occurred at 360.1 kN and 24.01 mm of displacement, and failure took place in the instrumented south shear span 56 days after casting.

Strain gauges S-7-B and S-7-S failed before peak load; strain gauge S-6-B failed after peak load; all other strain gauges functioned adequately during the test.

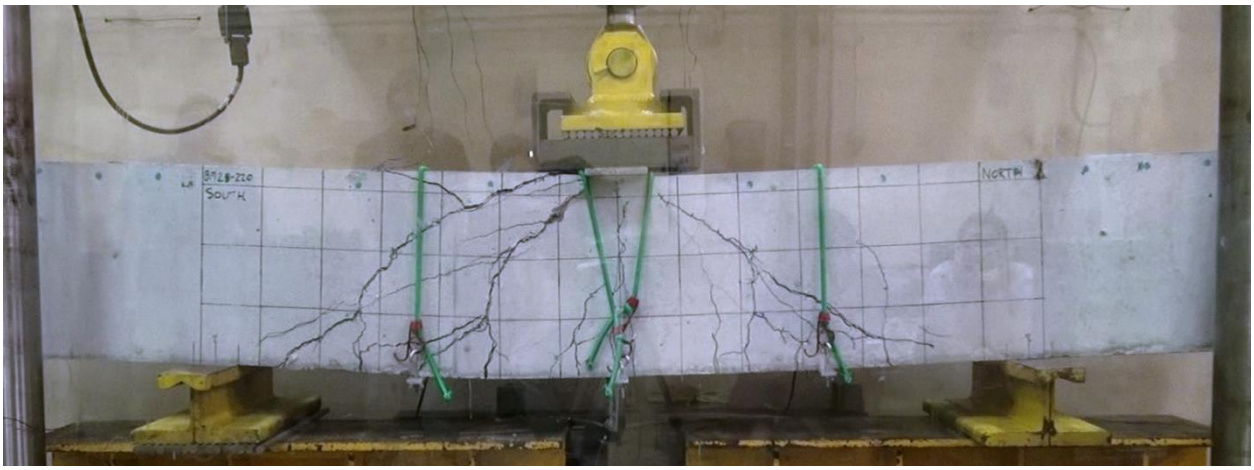

Figure E.94: BM25-220 At Peak Load

Figure E.95: BM25-220 After Testing

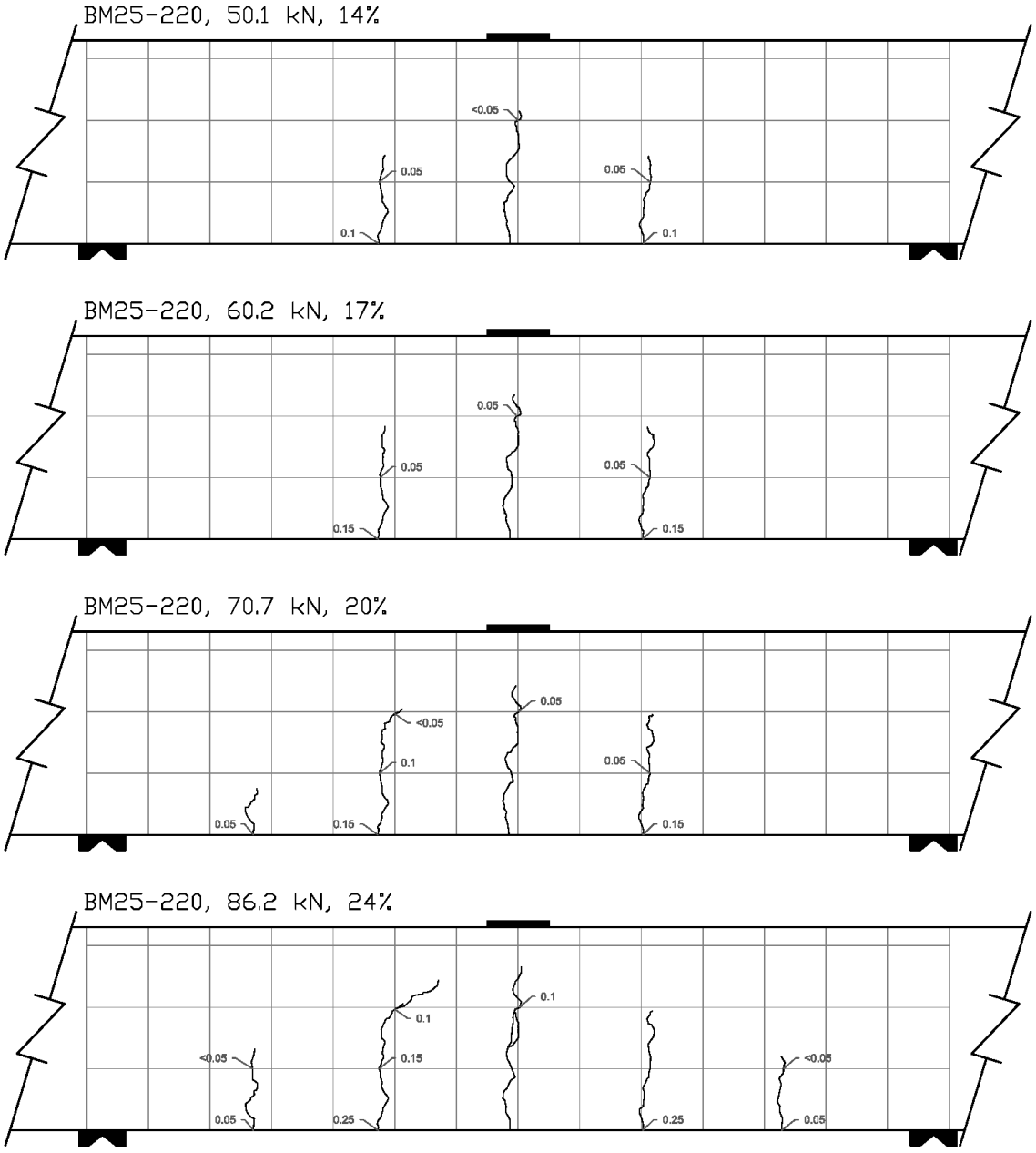

Figure E.96: BM25-220 Crack Diagram 1

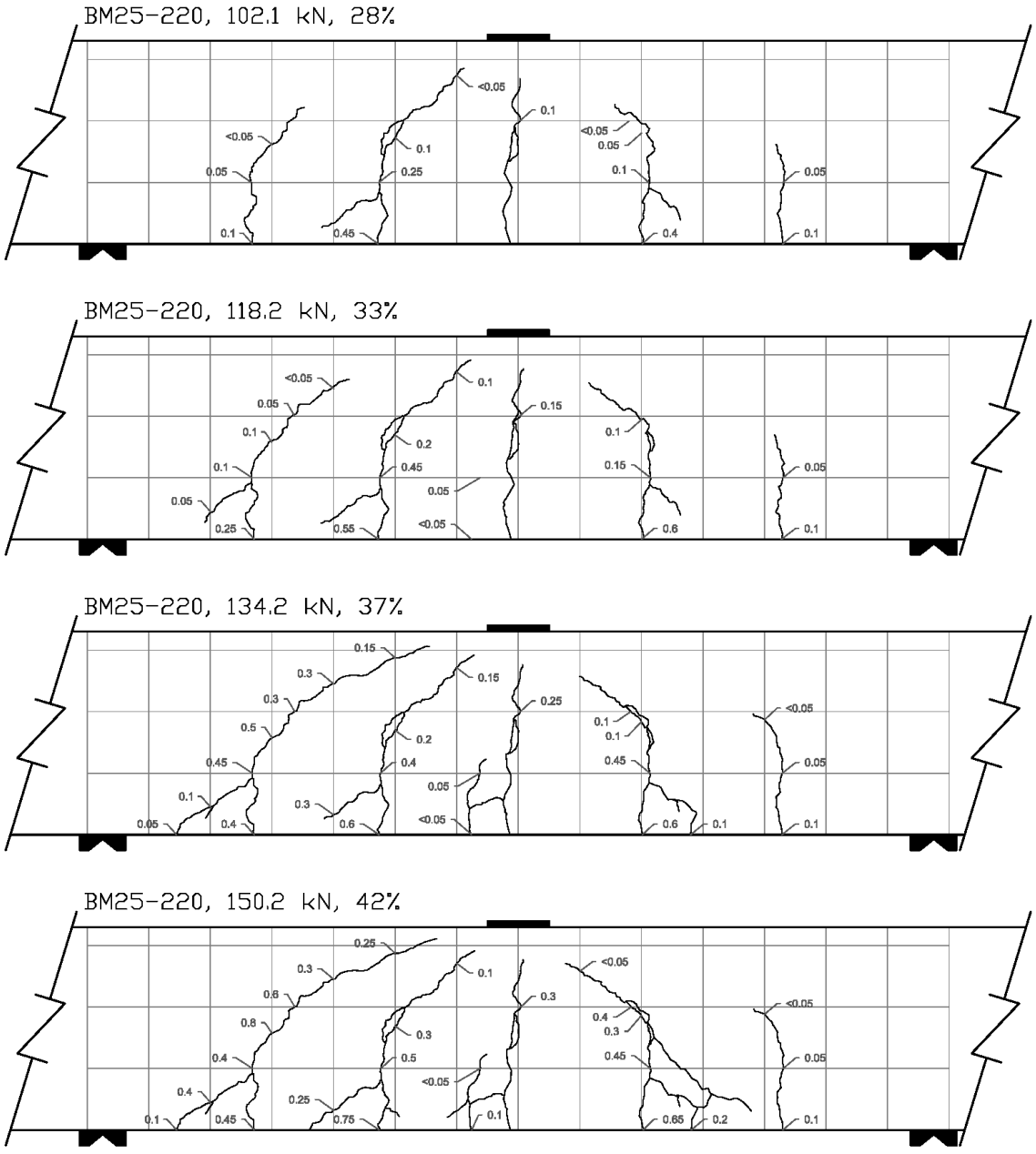

Figure E.97: BM25-220 Crack Diagram 2

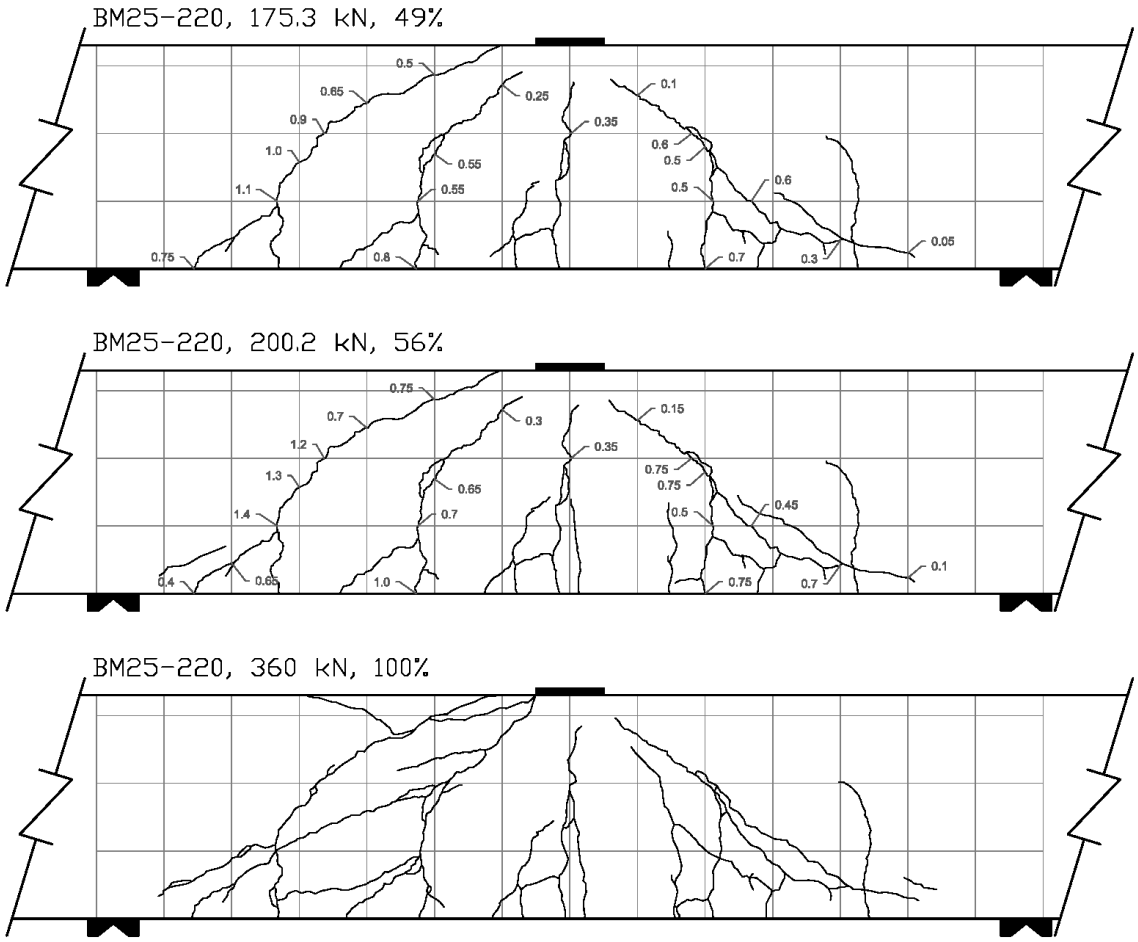

Figure E.98: BM25-220 Crack Diagram 3

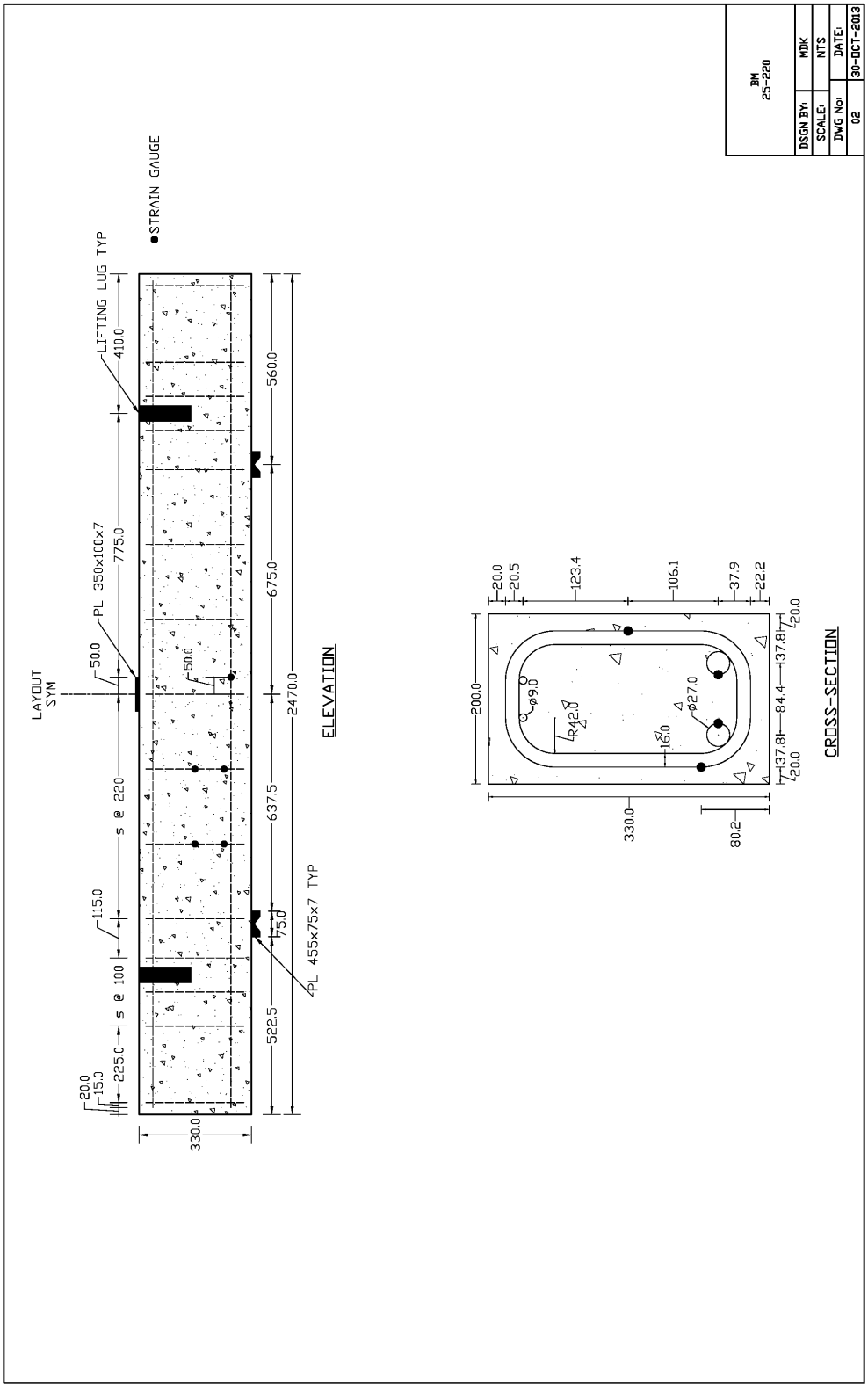

Figure E.99: BM25-220 Schematic Drawing

Table E.6: As-Designed and As-Constructed Parameter Chart for BM25-220

Parameter	As-Designed	As-Constructed
Beam Properties		
f'_c (MPa)	45	47.3 (28 day)
b (mm)	200	200.8**
h (mm)	330	333.0**
l (mm)	2470	-
d (mm)	270	272.8***
a/d	2.5	-
ρ_F (%)	1.82	-
ρ_v (%)	0.51	-
Longitudinal Bar Properties		
f_{Fu} (MPa)	1000	-
E_F (GPA)	60	-
A_F (mm^2)	491	-
n_{Bar} (amnt)	2	-
ε_{Fu} (%)	2.61*	-
Stirrup Properties		
$f_{Fu,straight}$ (MPa)	1000	-
$f_{Fu,bent}$ (MPa)	700	-
E_F (GPA)	50	-
A_F (mm^2)	113.1	-
r_{Bend} (mm)	42	-

** Rupture strain was only provided for dia. 16 bars; this value was assumed valid for all bars.*
*** Measured at midpoint of the failed shear span before testing, width is an average of top and bottom.*
**** Based on an average from measured bar depths before pour on north and south ends.*

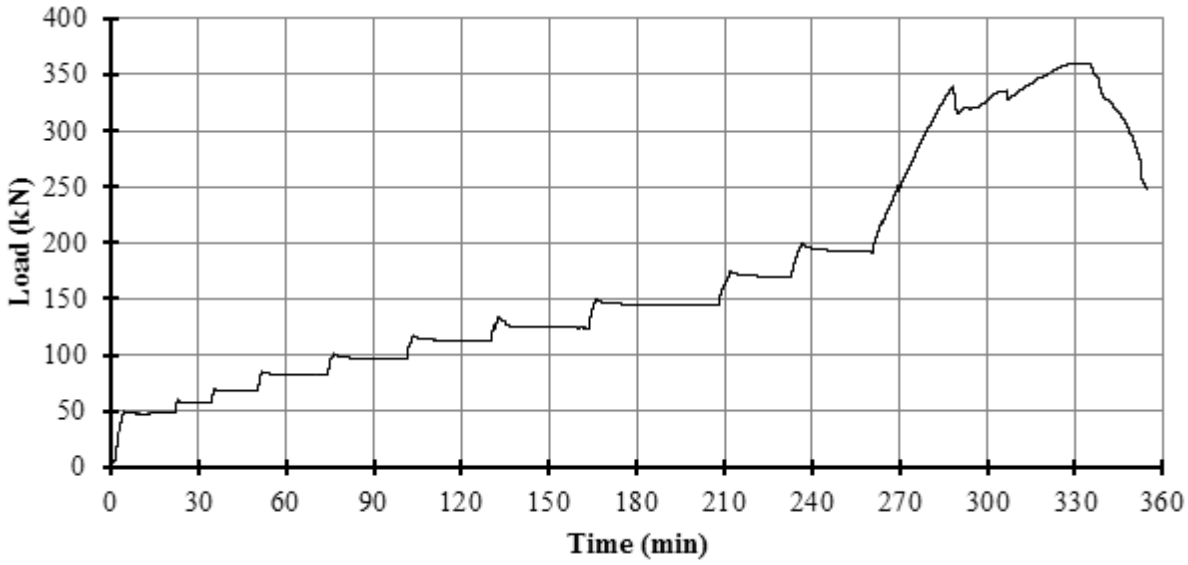

Figure E.100: BM25-220 Plot of Load vs Time

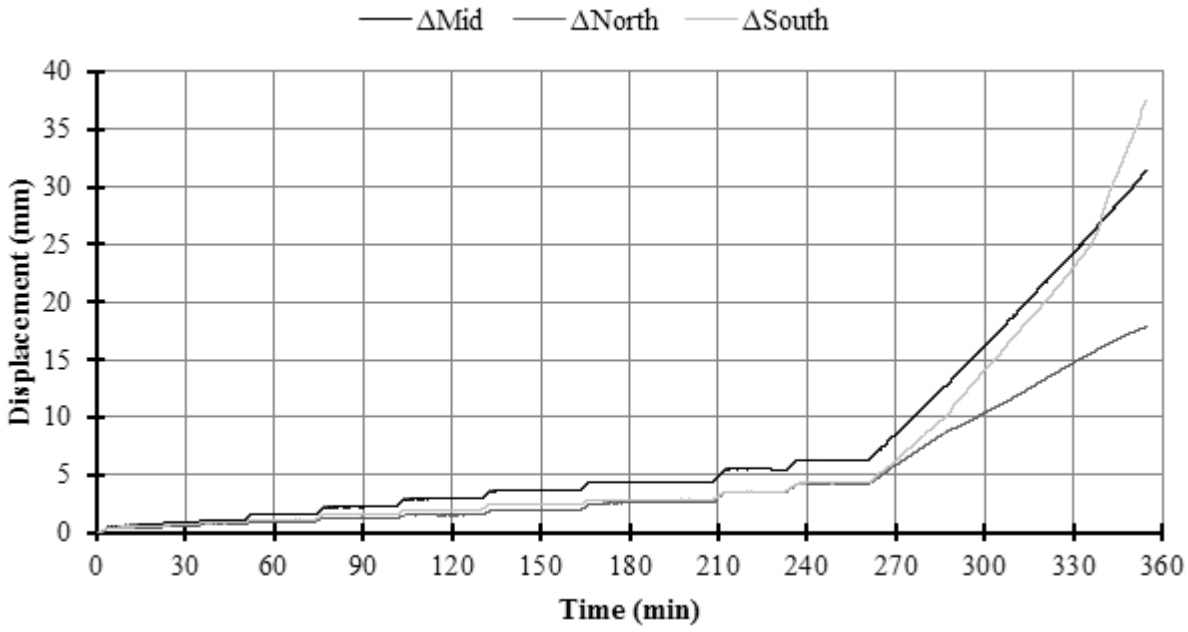

Figure E.101: BM25-220 Plot of Displacement vs Time

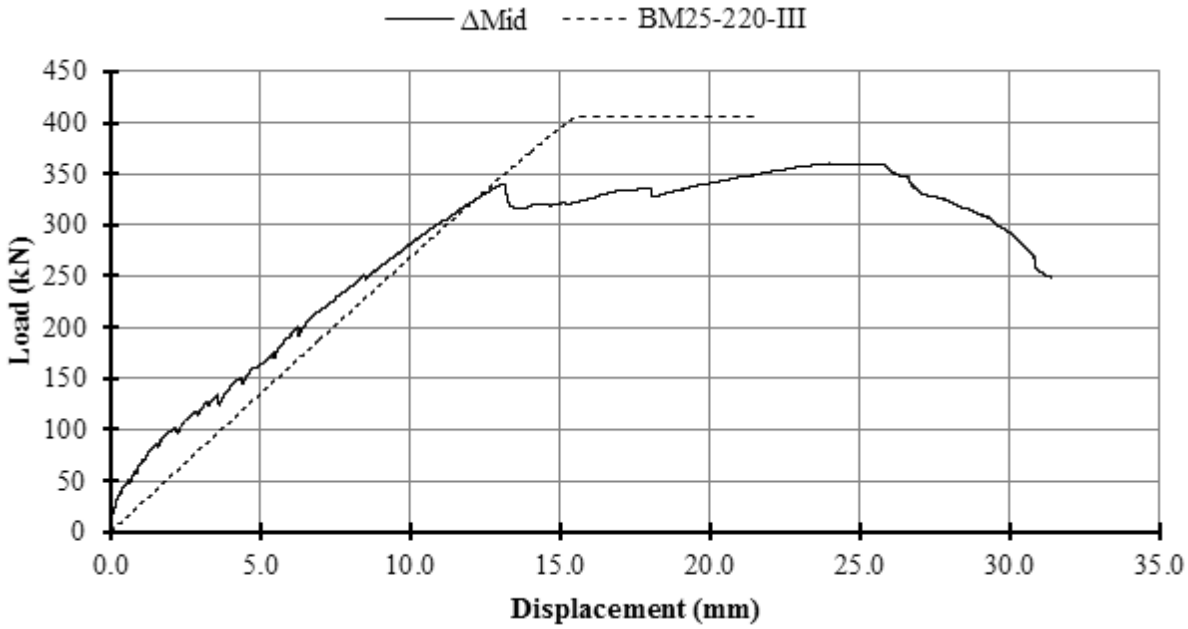

Figure E.102: BM25-220 Plot of Load vs Displacement

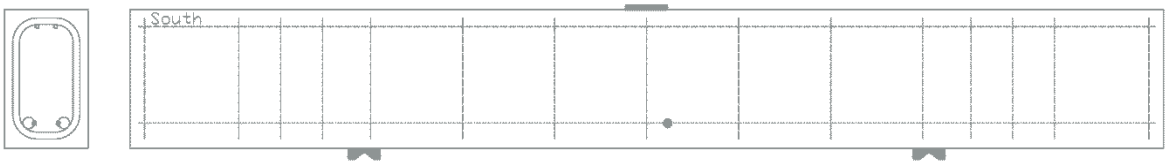

Figure E.103: BM25-220 Schematic of Mid-Span Strain Gauge Locations

A record of the specific longitudinal bar to which gauge A and B were attached was not kept.

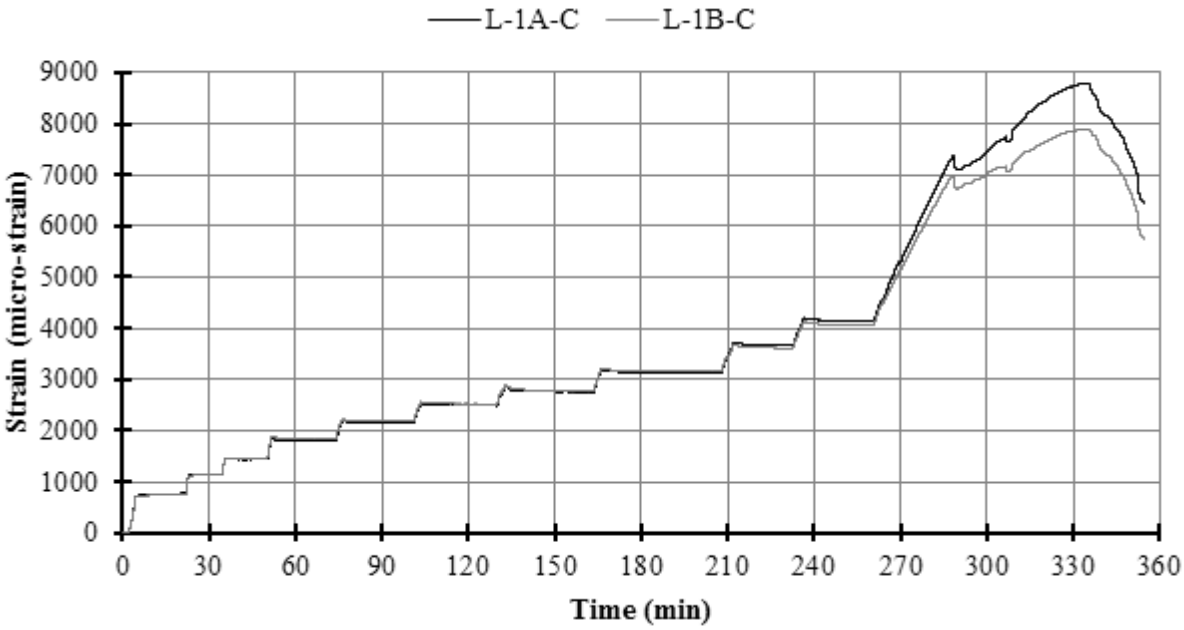

Figure E.104: BM25-220 Plot of Strain vs Time on Longitudinal Bars at Mid-Span

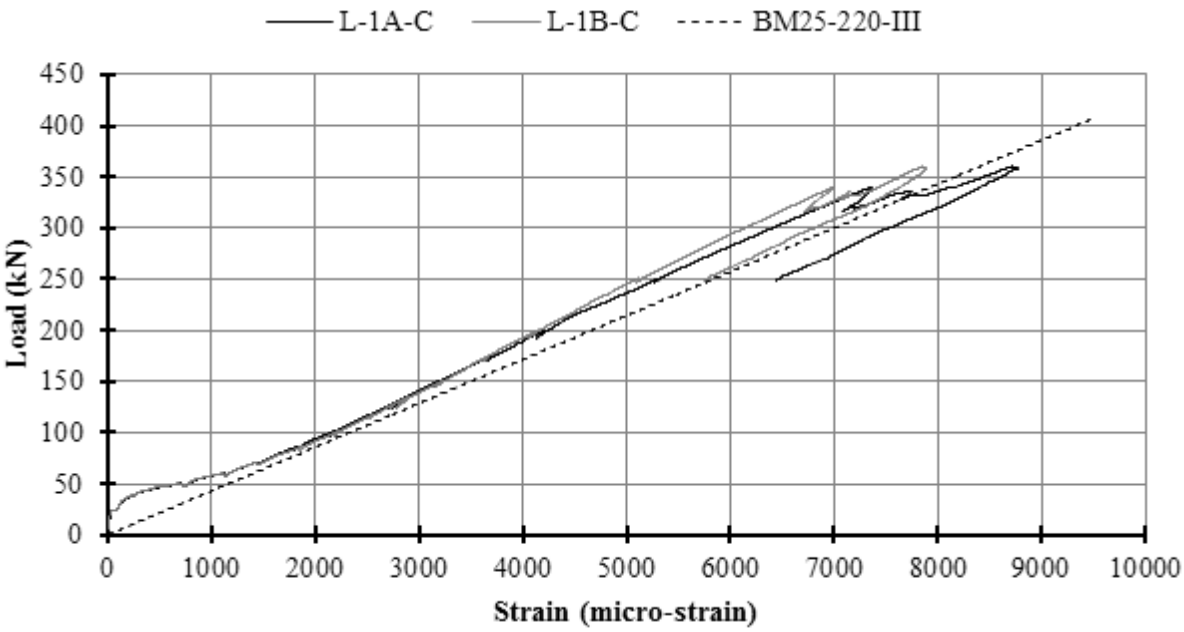

Figure E.105: BM25-220 Plot of Load vs Strain on Longitudinal Bars at Mid-Span

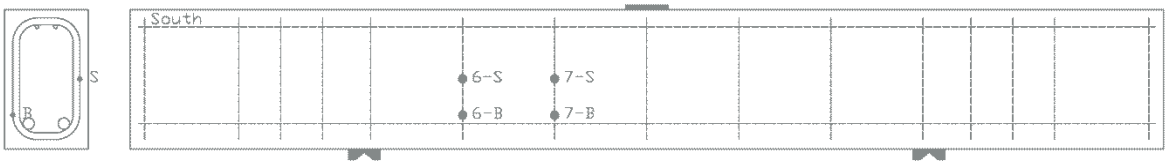

Figure E.106: BM25-220 Schematic of Stirrup Strain Gauge Locations

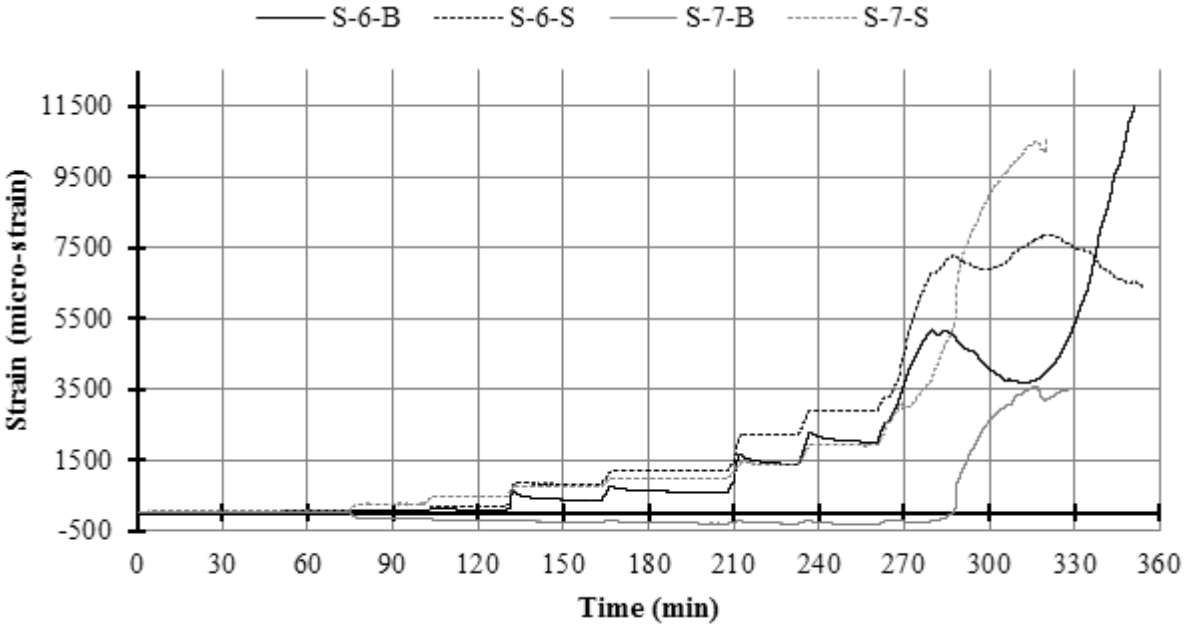

Figure E.107: BM25-220 Plot of Strain vs Time on Stirrups

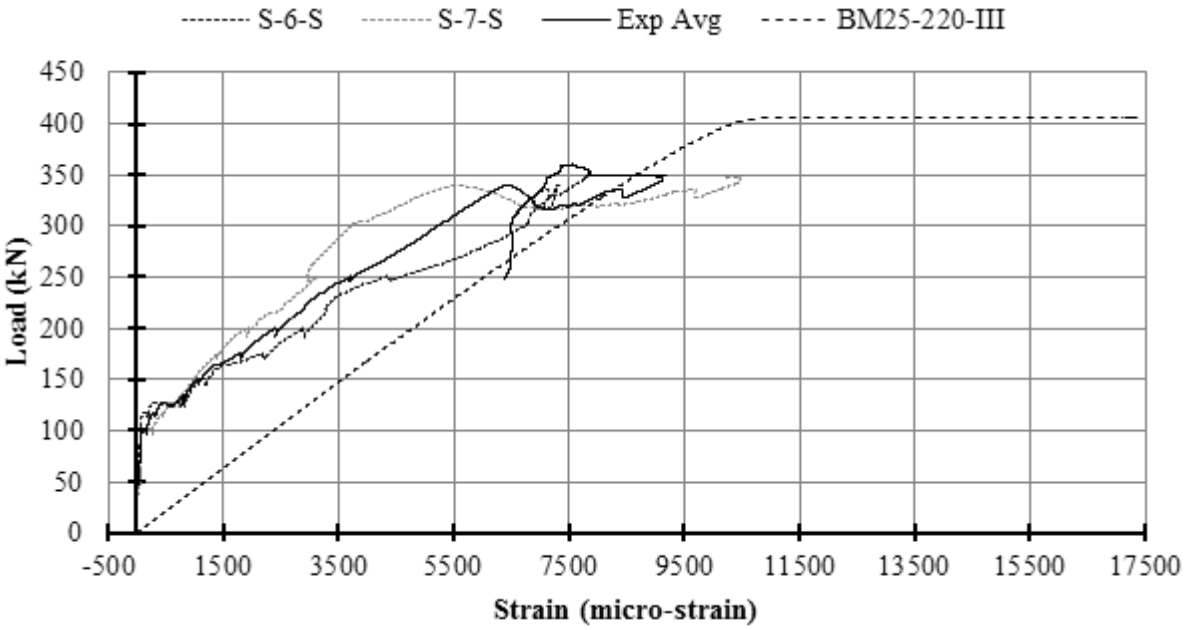

Figure E.108: BM25-220 Plot of Load vs Strain on Stirrups

A plot with all stirrup strain gauges may be found in the Results Chapter.

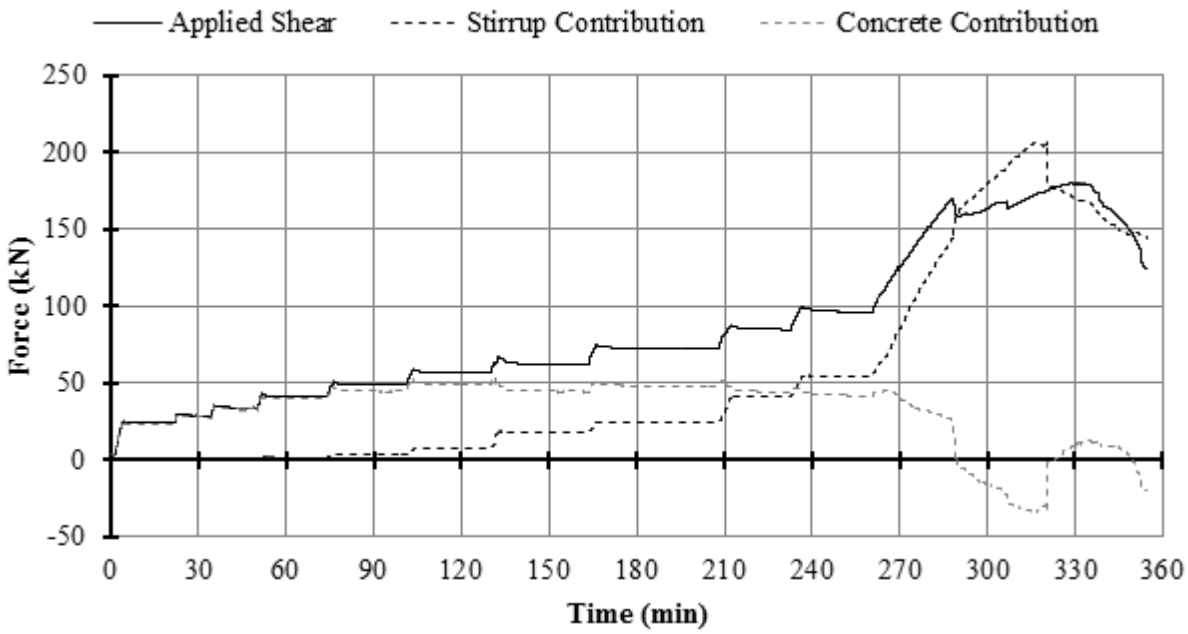

Figure E.109: BM25-220 Plot of Shear Contribution vs Time

E.9.1 BM25-220 Photographs

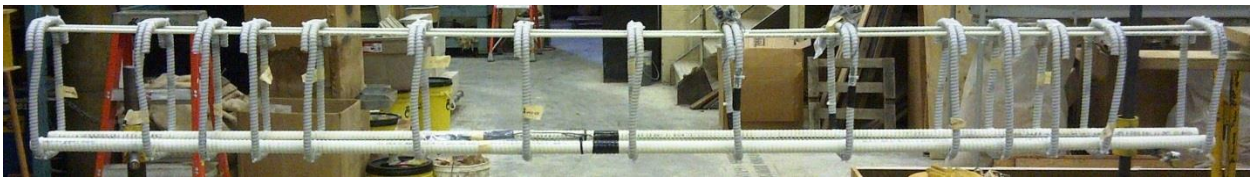

Figure E.110: BM25-220 Rebar Cage Elevation Photo

Figure E.111: BM25-220 Rebar Cage Cross-Section Photo

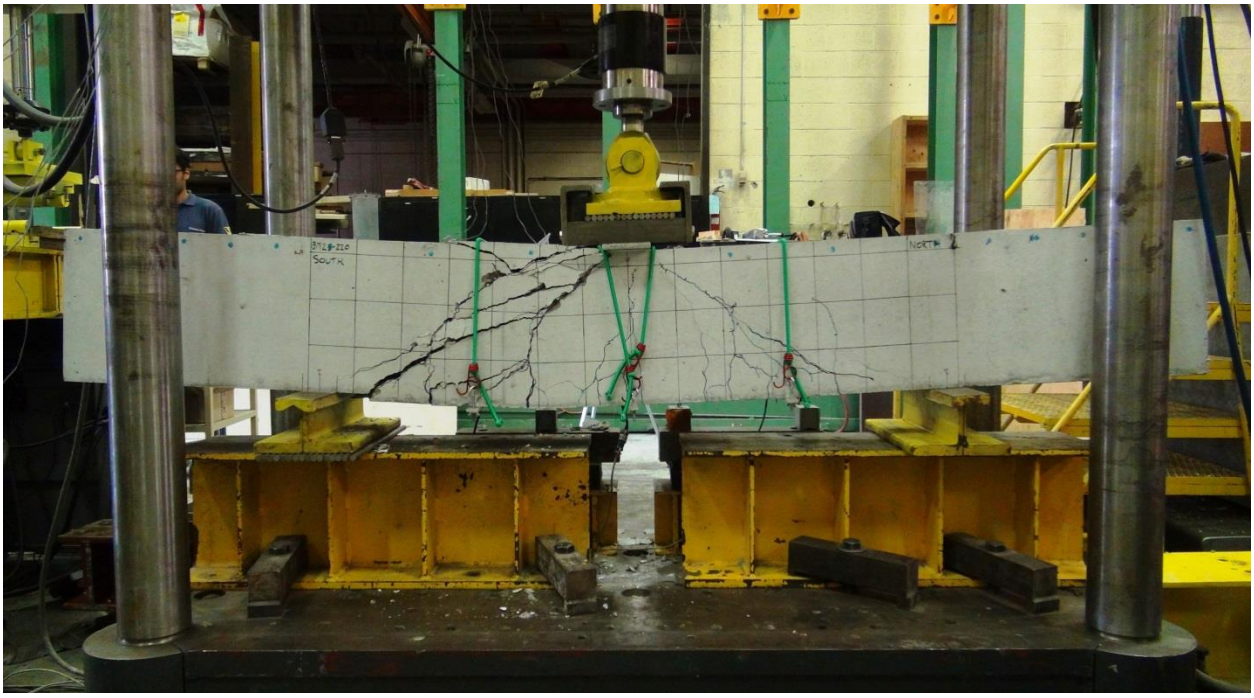

Figure E.112: BM25-220 Alternative Photo of Entire Beam Under Load After Testing

Figure E.113: BM25-220 Close-up Photo of Failure

Figure E.114: BM25-220 Photo of Exposed Stirrup after Loading 1

Figure E.115: BM25-220 Photo of Exposed Stirrup after Loading 2

E.10 BM12-150

This was the ninth beam tested. The displacement controlled loading rate was 0.272 mm/min until the first crack measurement. The rate was then increased to 0.4 mm/min until after the final crack measurement at which point the rate was increased to 0.9 mm/min.

The beam failed in shear-compression / strut-crushing along a plane that ran diagonally from the load plate to the south bearing plate. Peak load was accompanied by a slight popping noise characteristic of concrete fracture, but was not accompanied by perceptible movements or the ejection of concrete projectiles.

Peak load occurred at 405.2 kN and 15.56 mm of displacement, and failure took place in the instrumented south shear span 91 days after casting.

Strain gauges S-6-B and S-6-S failed before peak load; strain gauges S-5-B and S-5-S failed after peak load; all other strain gauges functioned adequately during the test.

The stirrups in the failed shear span were extracted to investigate if they had ruptured. Stirrup 6 was found to have a large crack running along a bend in the flexural tension zone. The crack followed the geometry of the glass fibres through the bend, and was closely aligned with the neutral axis of the bend. Two stirrup photos are included at the end of this section.

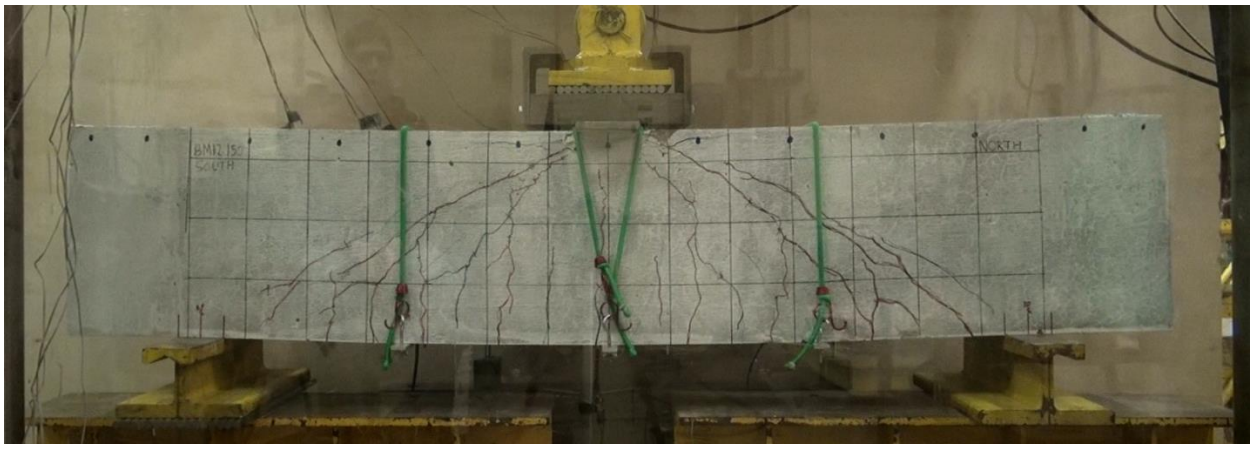

Figure E.116: BM12-150 At Peak Load

Figure E.117: BM12-150 After Testing

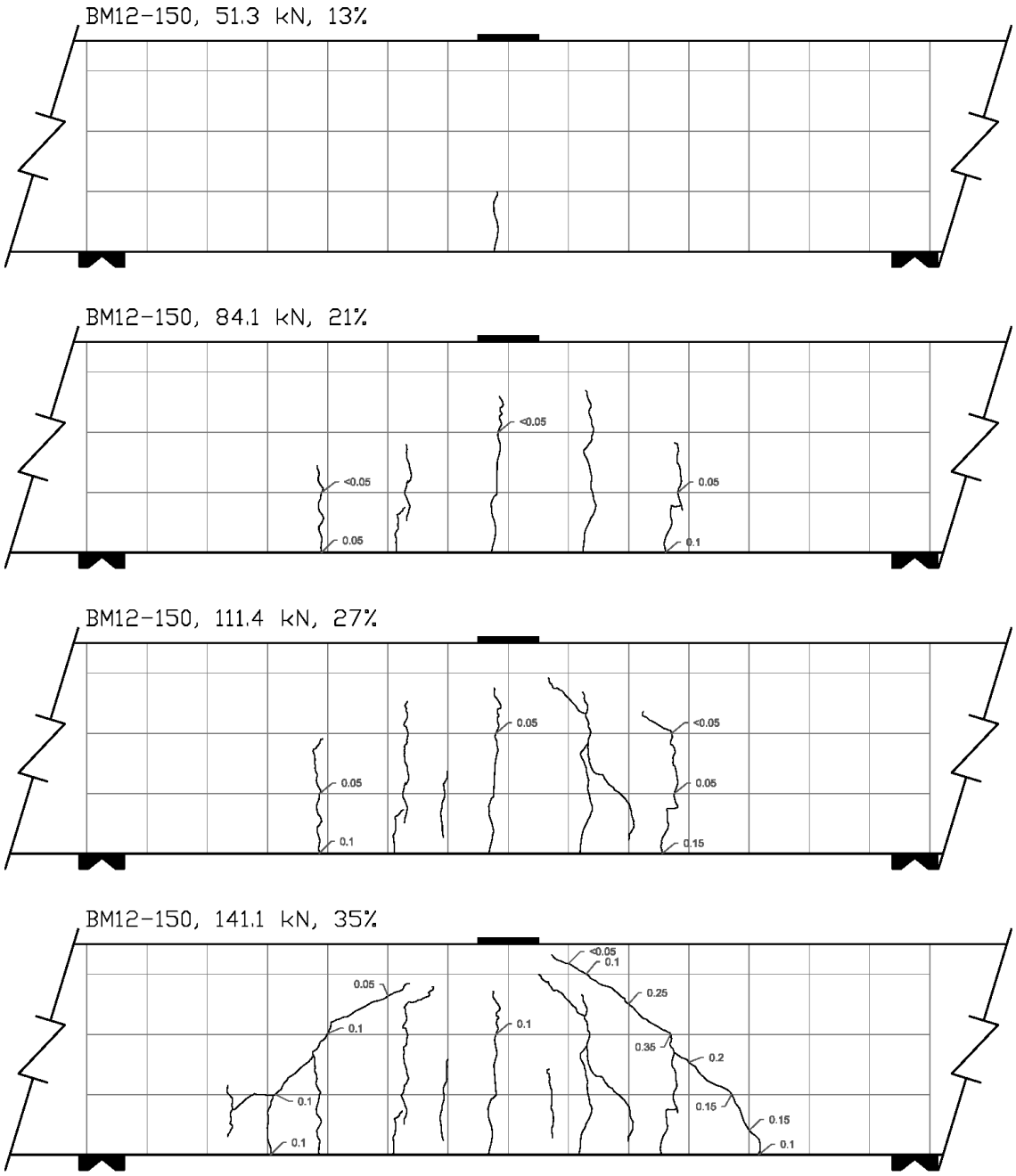

Figure E.118: BM12-150 Crack Diagram 1

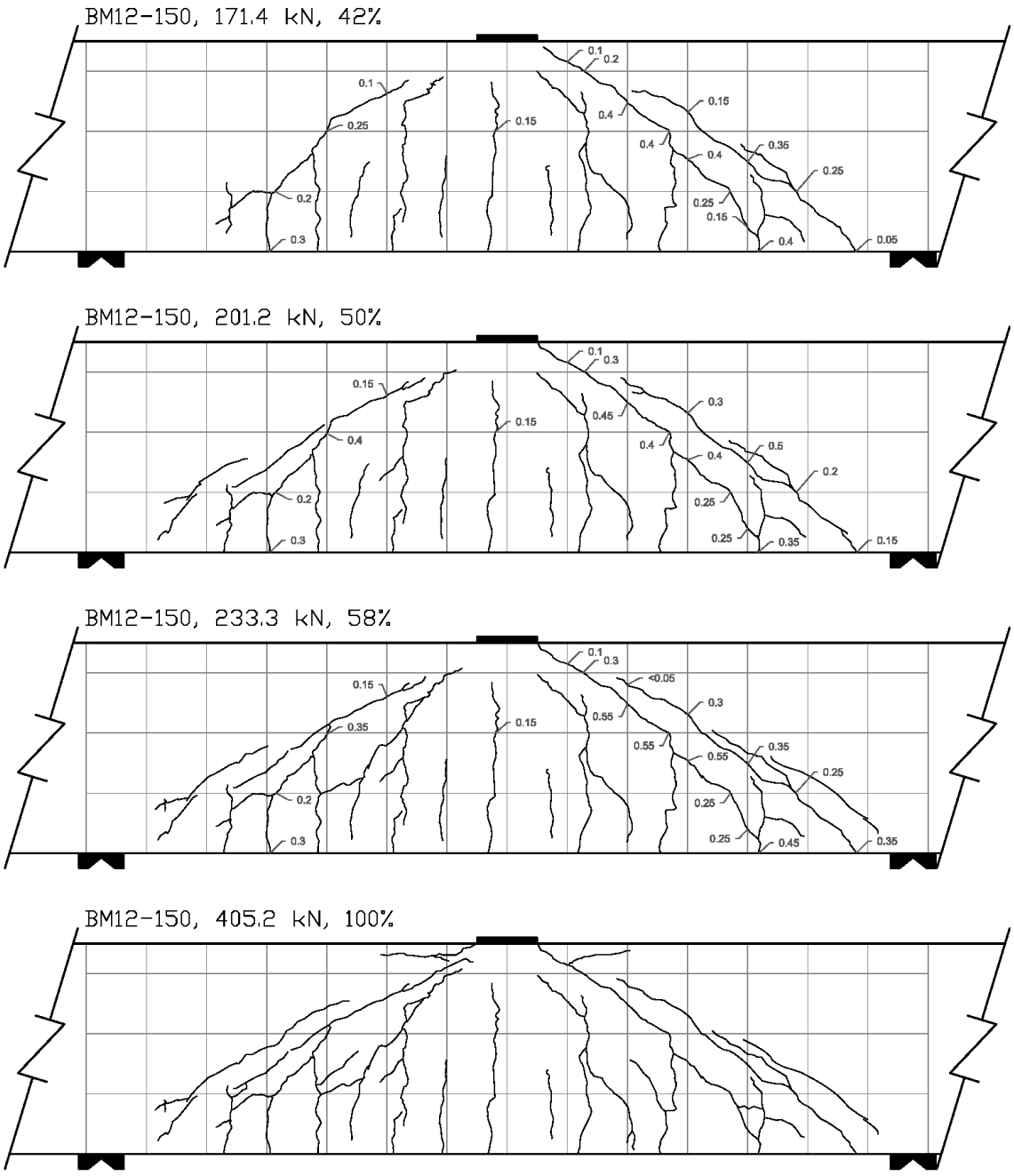

Figure E.119: BM12-150 Crack Diagram 2

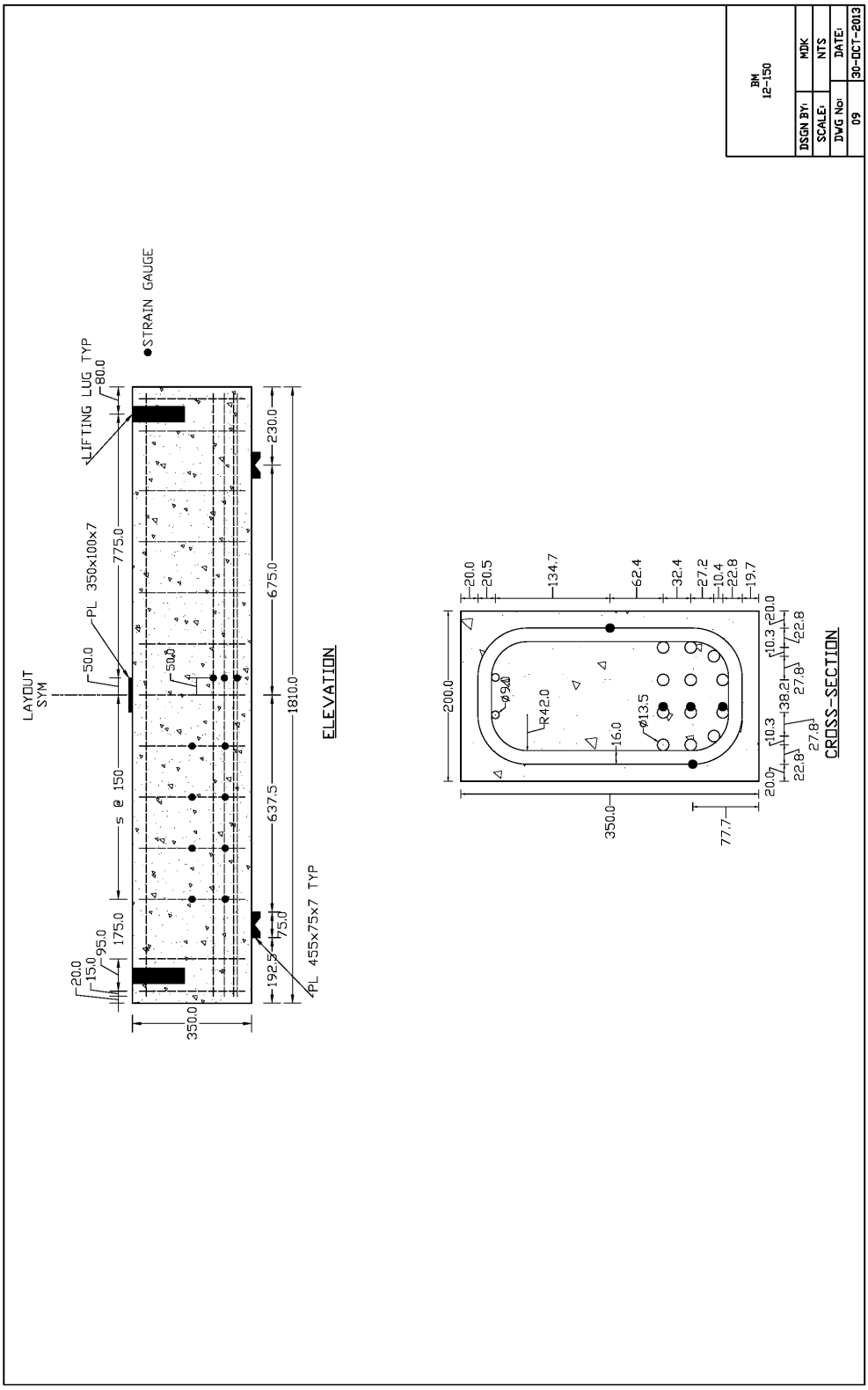

Figure E.120: BM12-150 Schematic Drawing

Table E.7: As-Designed and As-Constructed Parameter Chart for BM12-150

Parameter	As-Designed	As-Constructed
Beam Properties		
f'_c (MPa)	45	47.3 (28 day)
b (mm)	200	200.0**
h (mm)	350	351.0**
l (mm)	1810	-
d (mm)	270	264.4***
a/d	2.5	-
ρ_F (%)	2.51	-
ρ_v (%)	0.75	-
Longitudinal Bar Properties		
f_{Fu} (MPa)	1000	-
E_F (GPA)	60	-
A_F (mm^2)	113	-
n_{Bar} (amnt)	12	-
ε_{Fu} (%)	2.61*	-
Stirrup Properties		
$f_{Fu,straight}$ (MPa)	1000	-
$f_{Fu,bent}$ (MPa)	700	-
E_F (GPA)	50	-
A_F (mm^2)	113.1	-
r_{Bend} (mm)	42	-

** Rupture strain was only provided for dia. 16 bars; this value was assumed valid for all bars.*
*** Measured at midpoint of the failed shear span before testing, width is an average of top and bottom.*
**** Based on an average from measured bar depths before pour on north and south ends.*

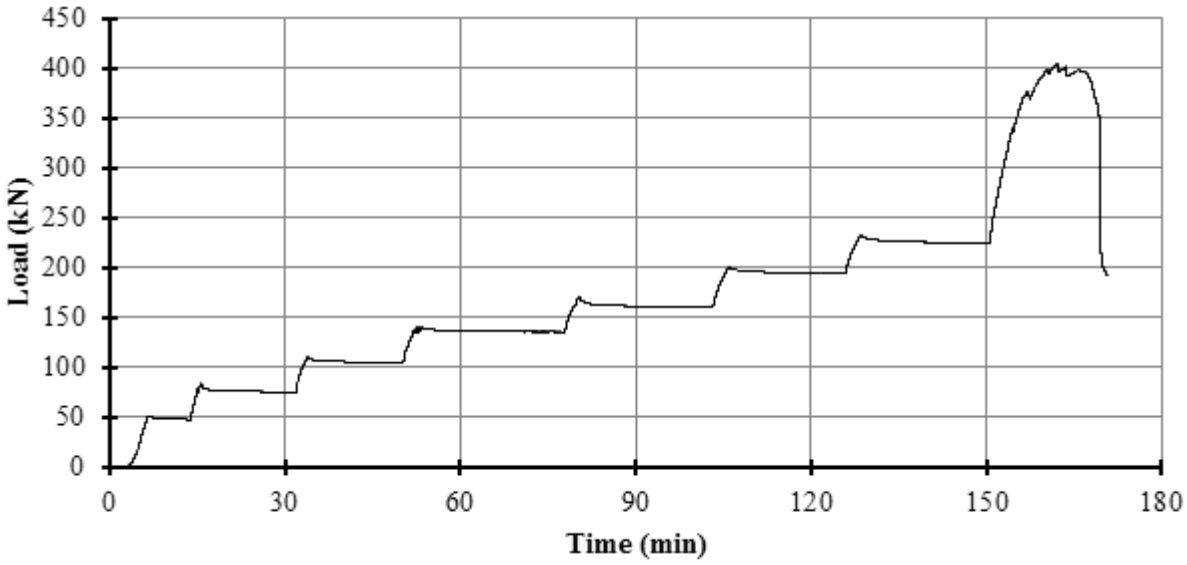

Figure E.121: BM12-150 Plot of Load vs Time

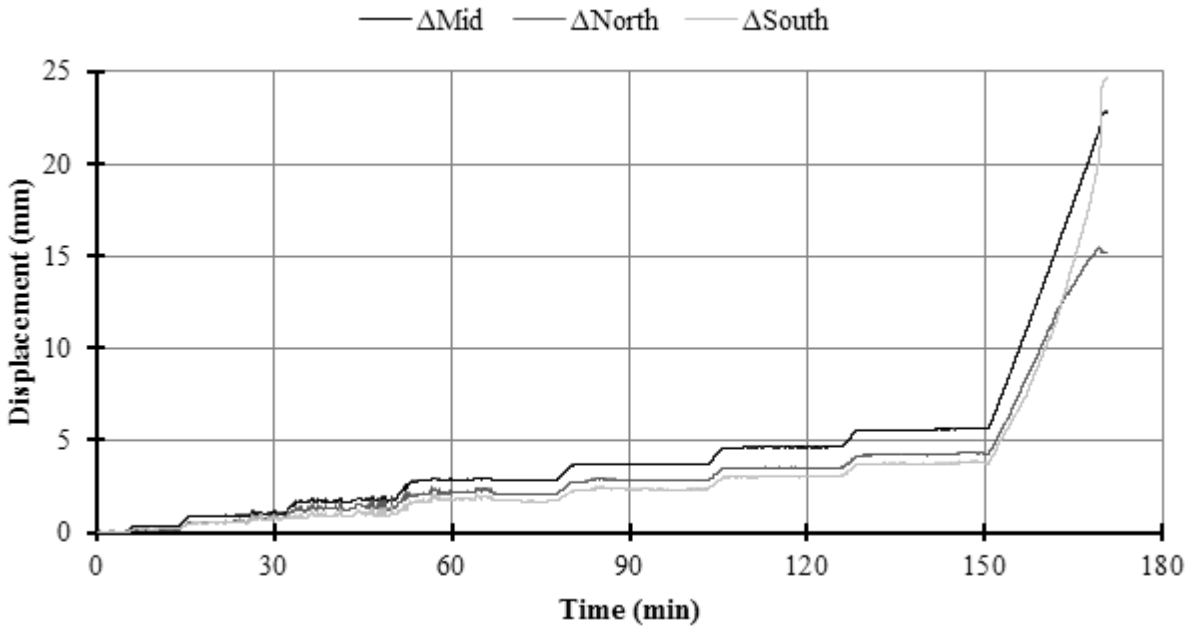

Figure E.122: BM12-150 Plot of Displacement vs Time

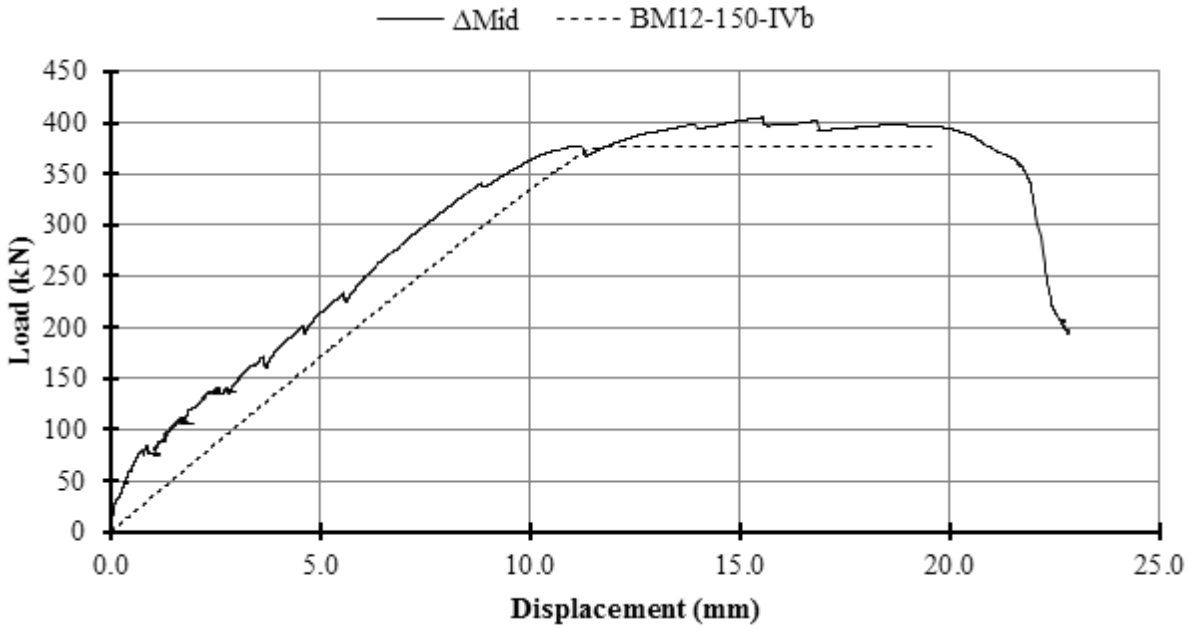

Figure E.123: BM12-150 Plot of Load vs Displacement

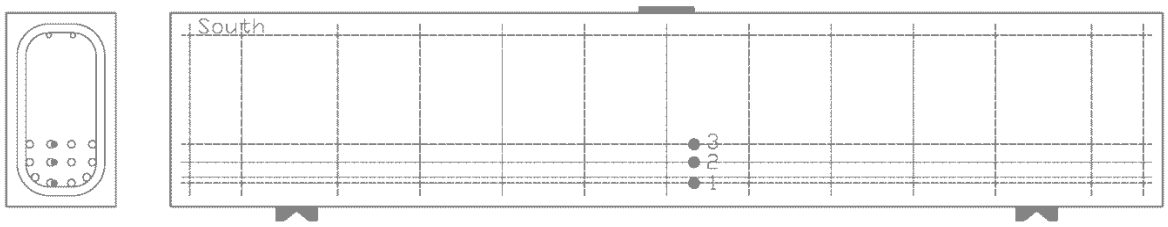

Figure E.124: BM12-150 Schematic of Mid-Span Strain Gauge Locations

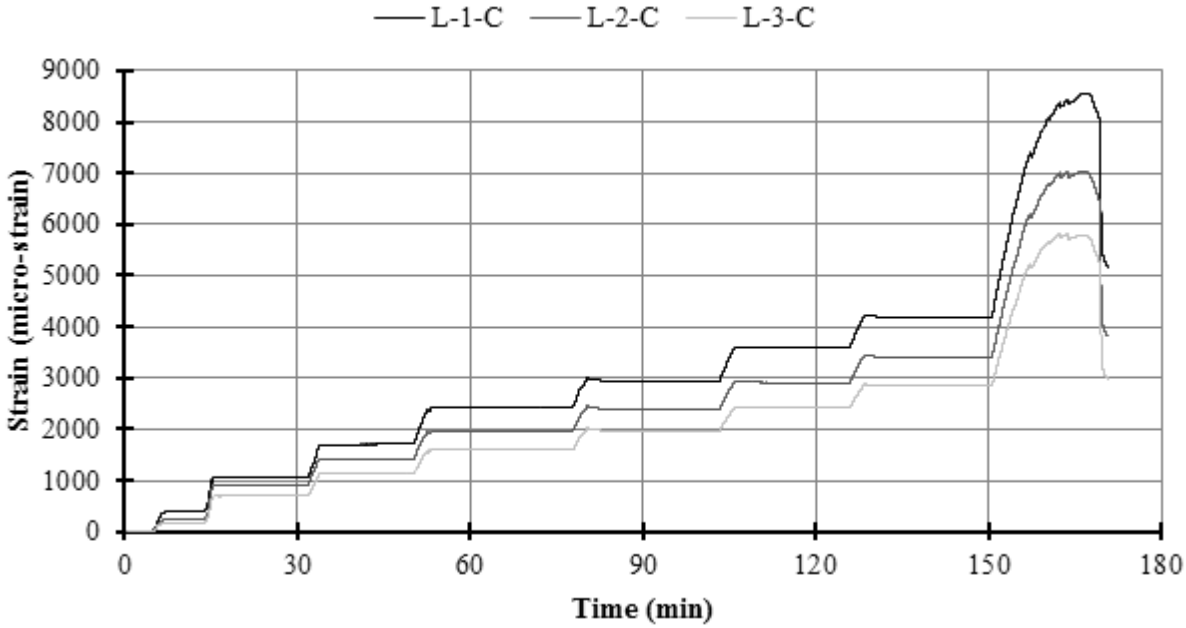

Figure E.125: BM12-150 Plot of Strain vs Time on Longitudinal Bars at Mid-Span

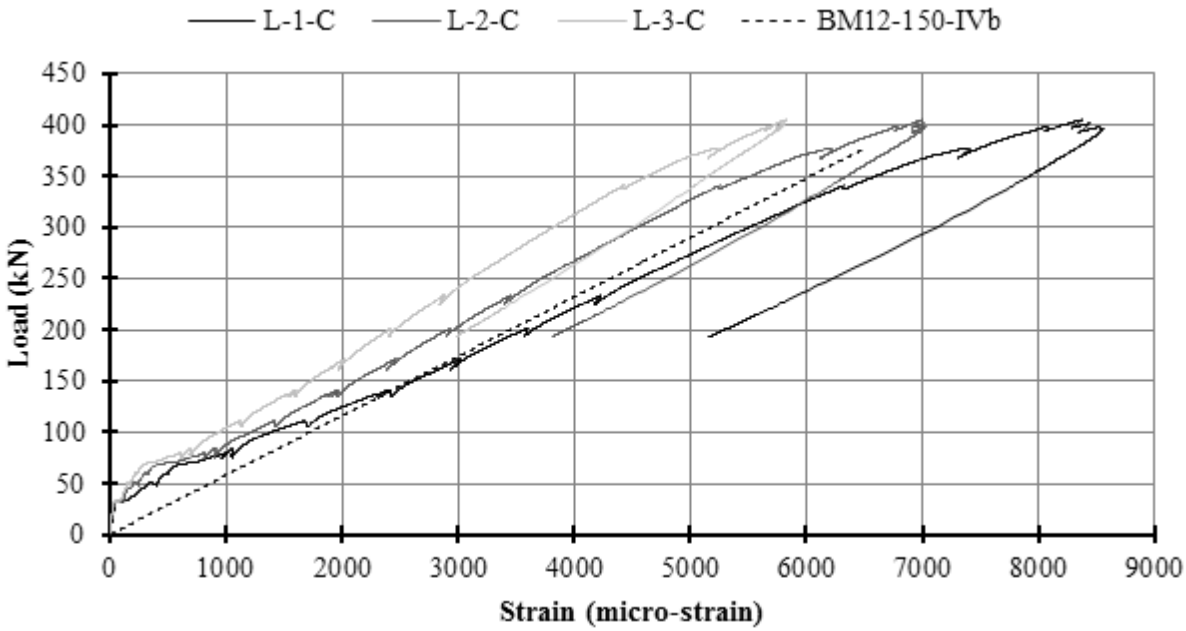

Figure E.126: BM12-150 Plot of Load vs Strain on Longitudinal Bars at Mid-Span

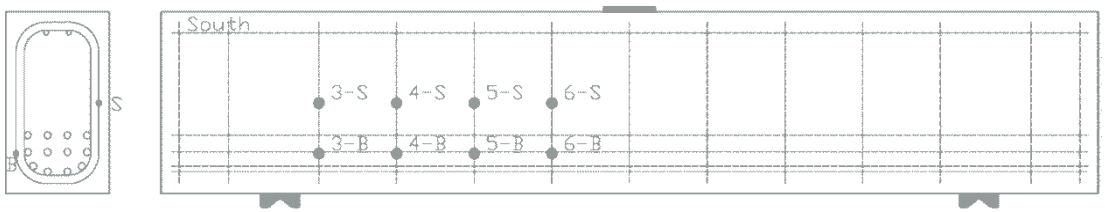

Figure E.127: BM12-150 Schematic of Stirrup Strain Gauge Locations

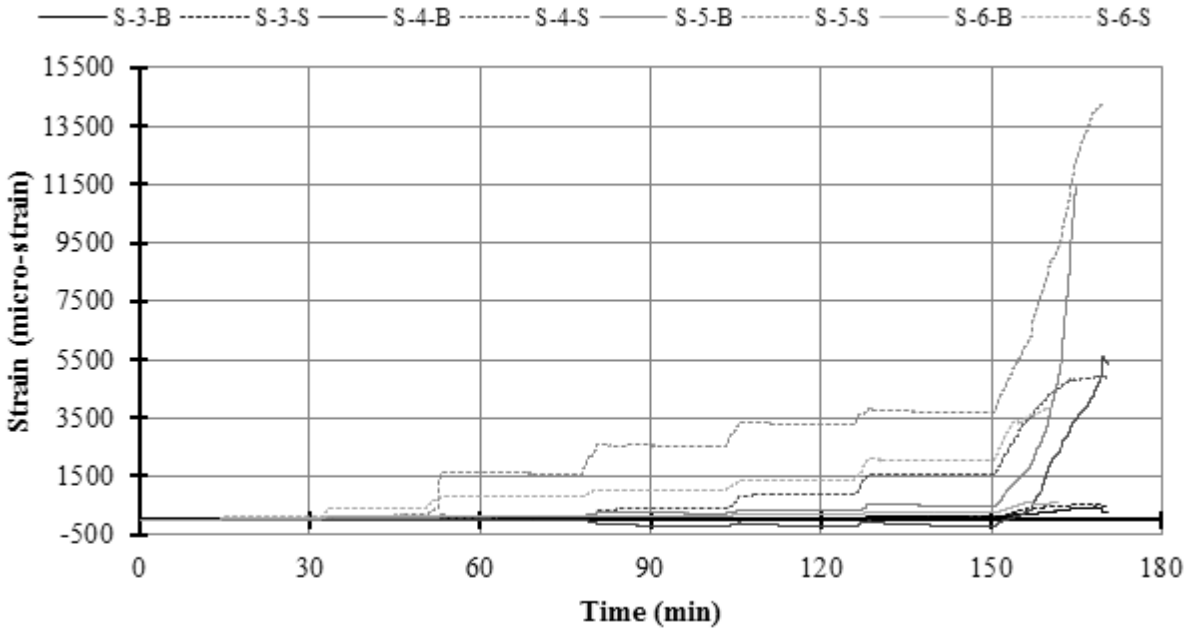

Figure E.128: BM12-150 Plot of Strain vs Time on Stirrups

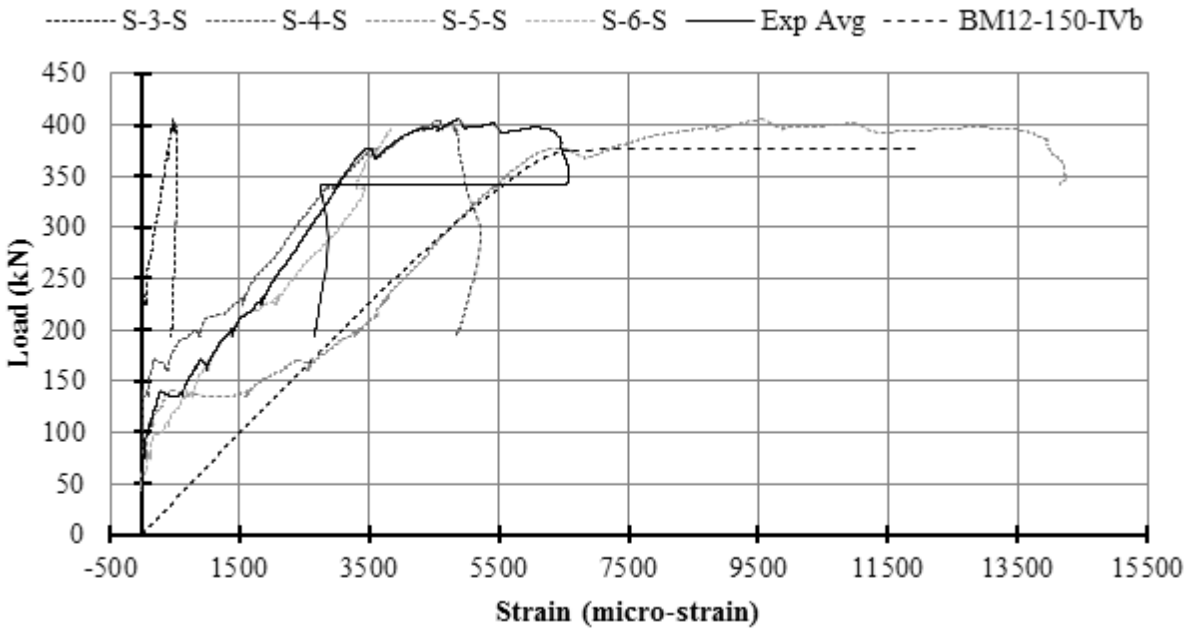

Figure E.129: BM12-150 Plot of Load vs Strain on Stirrups

A plot with all stirrup strain gauges may be found in the Results Chapter.

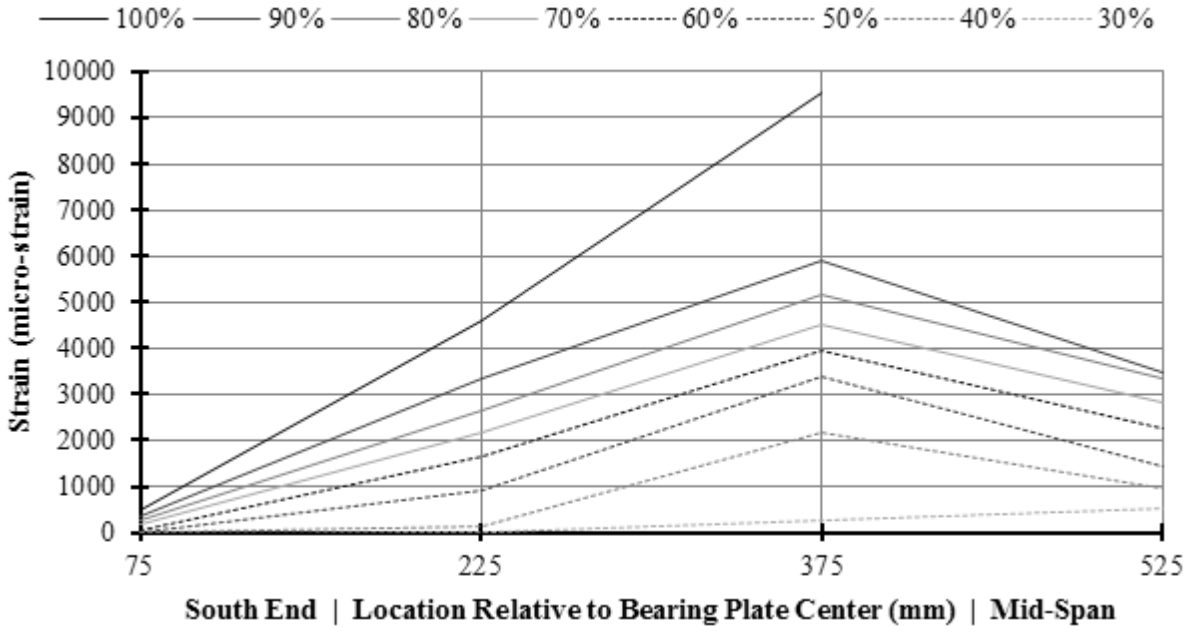

Figure E.130: BM12-220 Plot of Stirrup Strain vs Gauge Location with Increasing Load

Gauge S-6-S failed after 90 percent load.

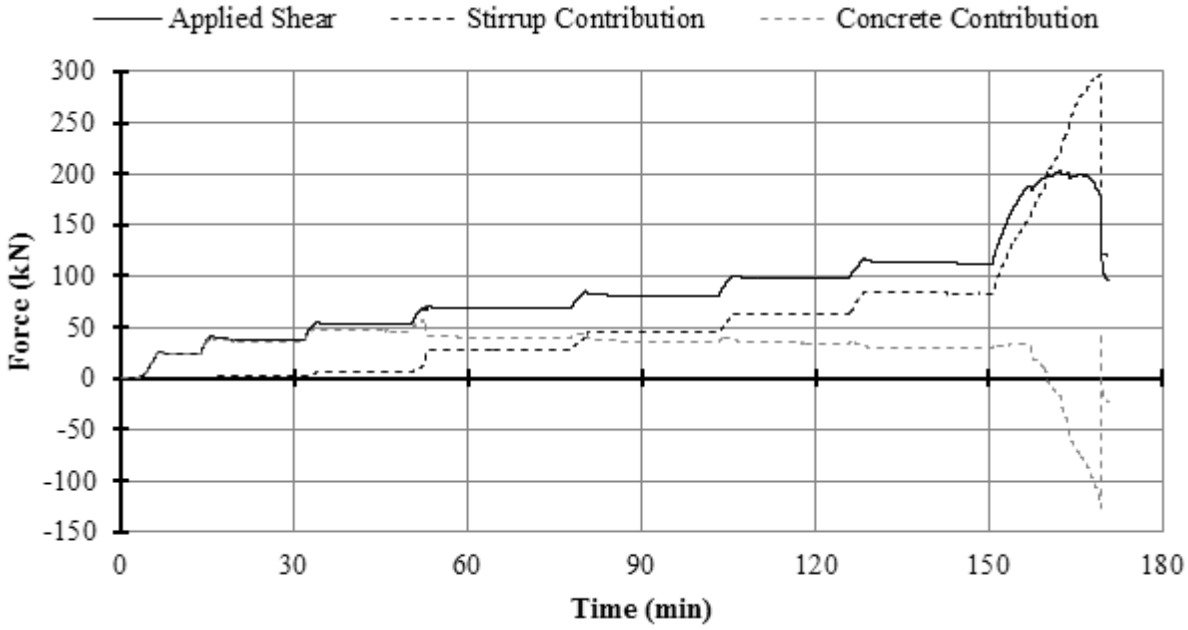

Figure E.131: BM12-150 Plot of Shear Contribution vs Time

E.10.1 BM12-150 Photographs

Figure E.132: BM12-150 Rebar Cage Elevation Photo

Figure E.133: BM12-150 Rebar Cage Cross-Section Photo

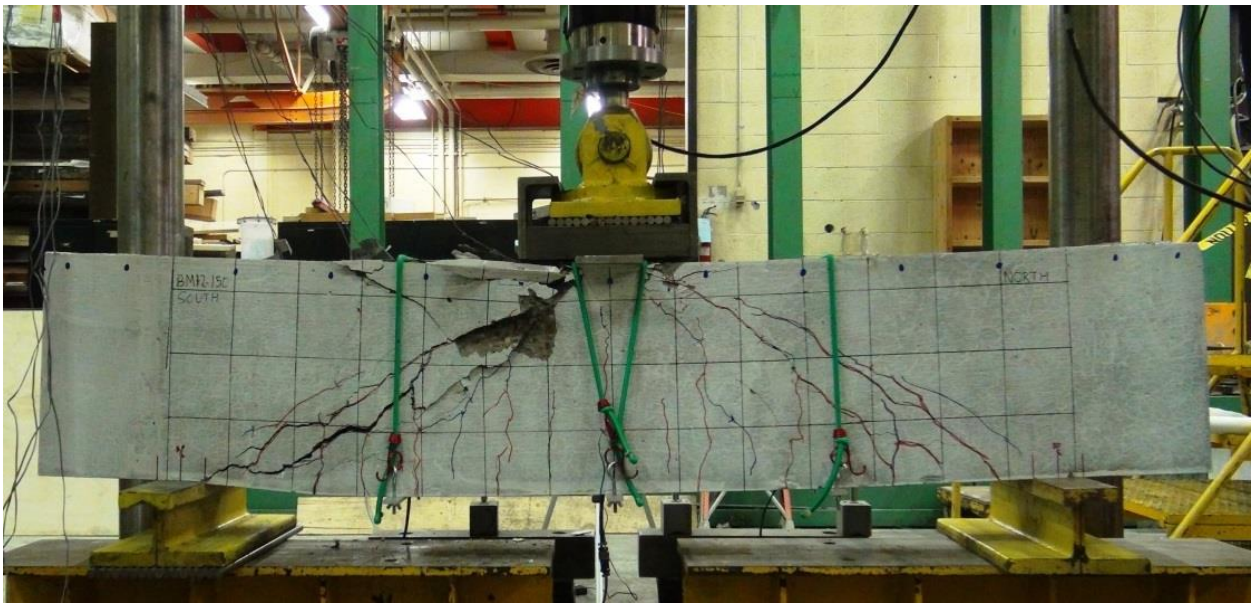

Figure E.134: BM12-150 Alternative Photo of Entire Beam Under Load After Testing

Figure E.135: BM12-150 Close-up Photo of Failure

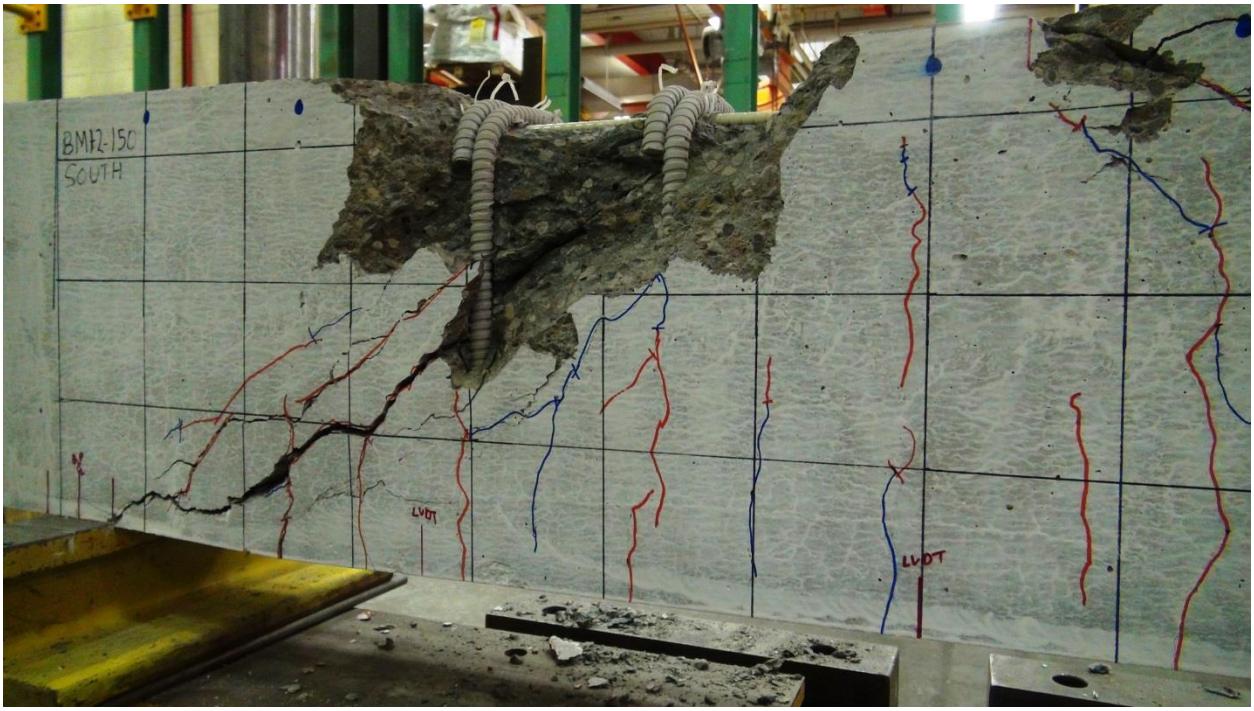

Figure E.136: BM12-150 Close-up Photo of Failure with Spalled Concrete Removed with Stirrups 5 and 6 Exposed

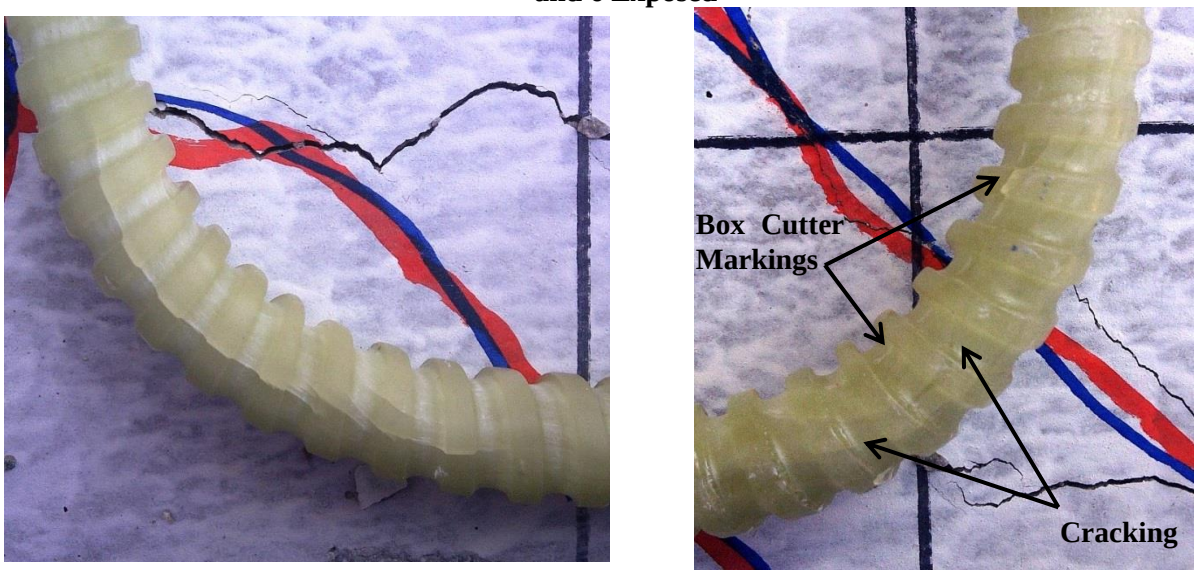

Figure E.137: BM12-150 Bend of Stirrup 6 Front and Back

This stirrup bend comes from the part of the stirrup in the flexural tension zone.

E.11 BM16-150

This was the eighth beam tested. The displacement controlled rate was 0.272 mm/min until the first crack measurement. The rate was then increased to 0.4 mm/min until after the final crack measurement after which the rate was increased to 0.9 mm/min.

The beam failed in shear-compression / strut-crushing along a plane that ran diagonally from the load plate to the north bearing plate. Peak load was accompanied by a slight popping noise characteristic of concrete fracture. Minutes later a sudden large drop in load occurred with only some flaking of concrete as warning. The drop in load was characteristic of a catastrophic failure and was accompanied by a loud banging noise, movement, and the ejection of large and small concrete projectiles.

Peak load occurred at 416.5 kN and 14.44 mm of displacement, and failure took place in the un-instrumented north shear span 86 days after casting.

Strain gauges L-1-C, L-2-C, L-2-6, and S-7-S failed before peak load; strain gauge S-7-B failed after peak load; all other strain gauges functioned adequately during the test.

Two stirrups in the failed shear span were extracted to investigate if the stirrups had ruptured, but condition of the two stirrups was unremarkable.

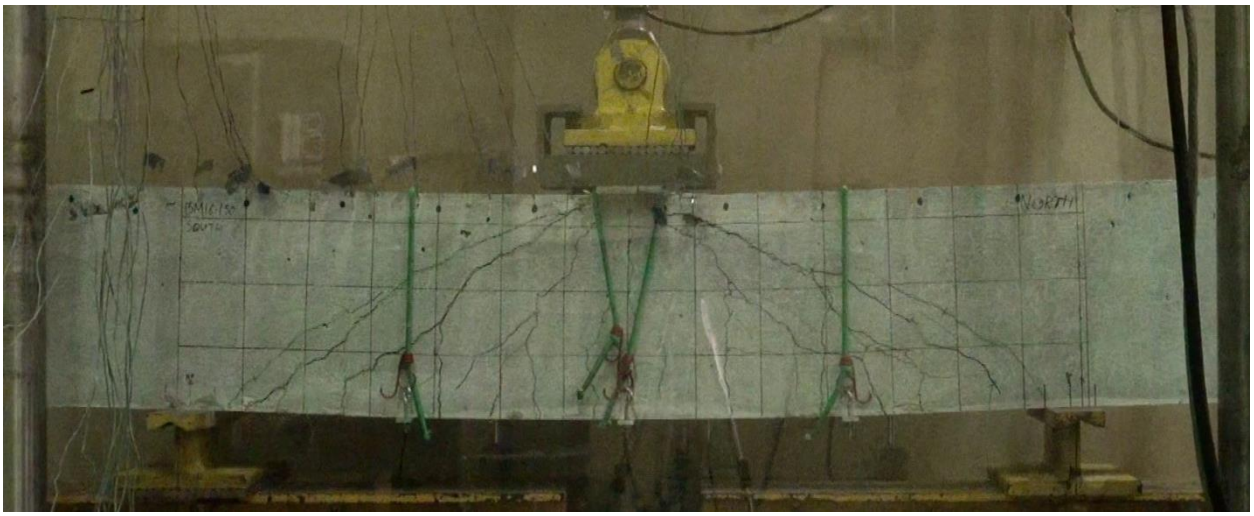

Figure E.138: BM16-150 At Peak Load

Figure E.139: BM16-150 After Testing

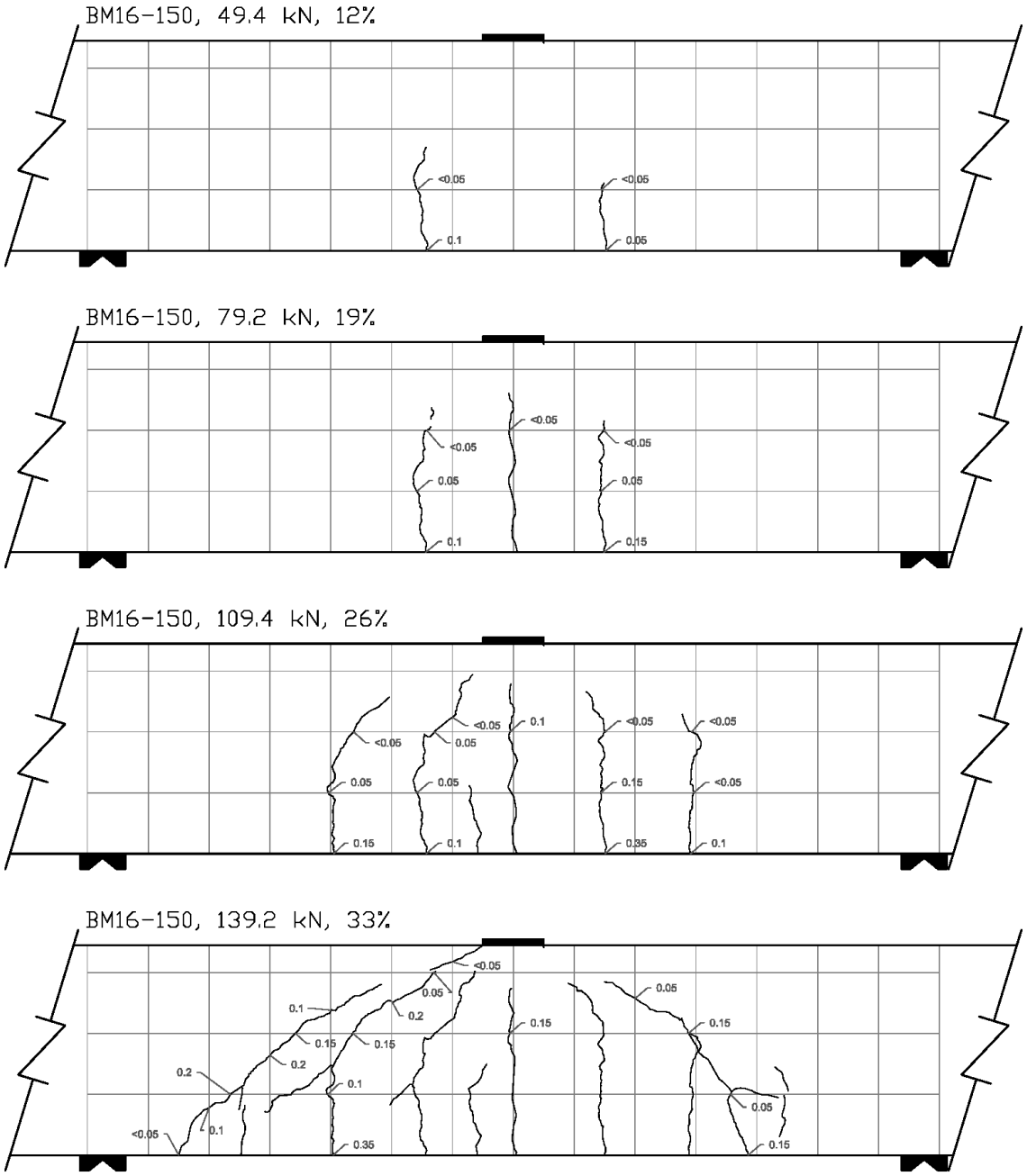

Figure E.140: BM16-150 Crack Diagram 1

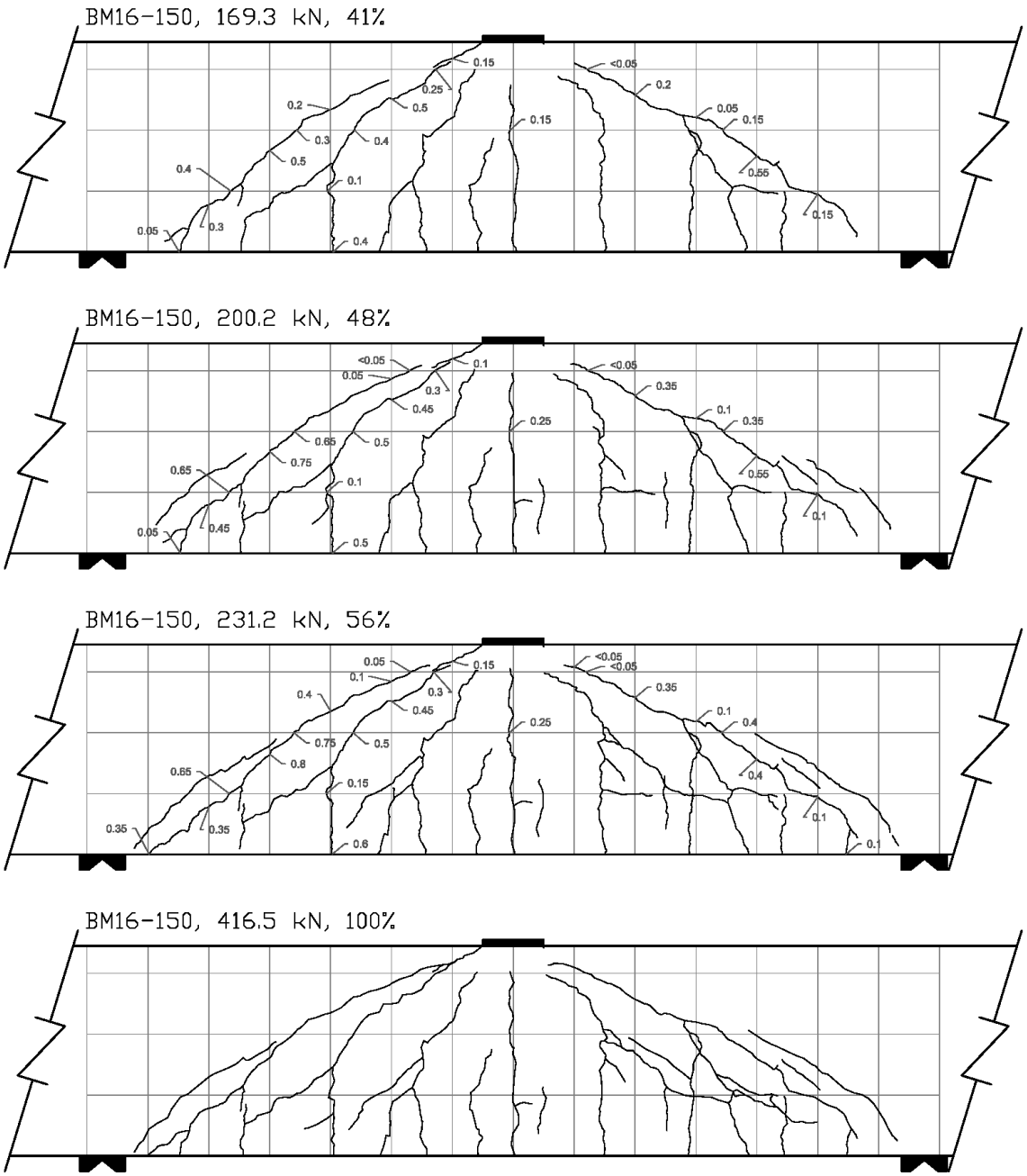

Figure E.141: BM16-150 Crack Diagram 2

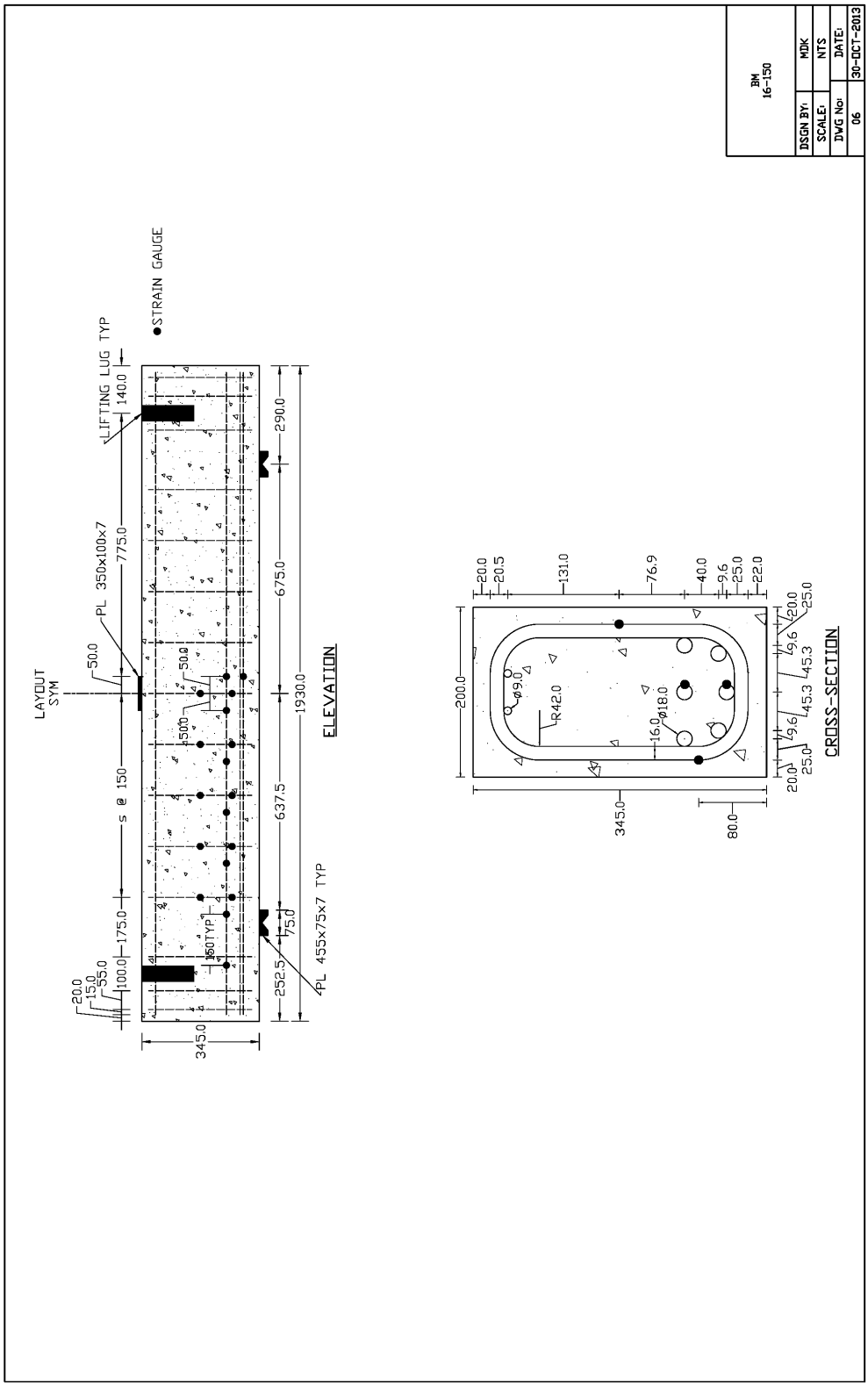

Figure E.142: BM16-150 Schematic Drawing

Table E.8: As-Designed and As-Constructed Parameter Chart for BM16-150

Parameter	As-Designed	As-Constructed
Beam Properties		
f'_c (MPa)	45	47.3 (28 day)
b (mm)	200	202.5**
h (mm)	345	346.0**
l (mm)	1930	-
d (mm)	270	265.6***
a/d	2.5	-
ρ_F (%)	2.23	-
ρ_v (%)	0.75	-
Longitudinal Bar Properties		
f_{Fu} (MPa)	1000	-
E_F (GPA)	64	-
A_F (mm^2)	201	-
n_{Bar} (amnt)	6	-
ε_{Fu} (%)	2.61*	-
Stirrup Properties		
$f_{Fu,straight}$ (MPa)	1000	-
$f_{Fu,bent}$ (MPa)	700	-
E_F (GPA)	50	-
A_F (mm^2)	113.1	-
r_{Bend} (mm)	42	-

** Rupture strain was only provided for dia. 16 bars; this value was assumed valid for all bars.*
*** Measured at midpoint of the failed shear span before testing, width is an average of top and bottom.*
**** Based on an average from measured bar depths before pour on north and south ends.*

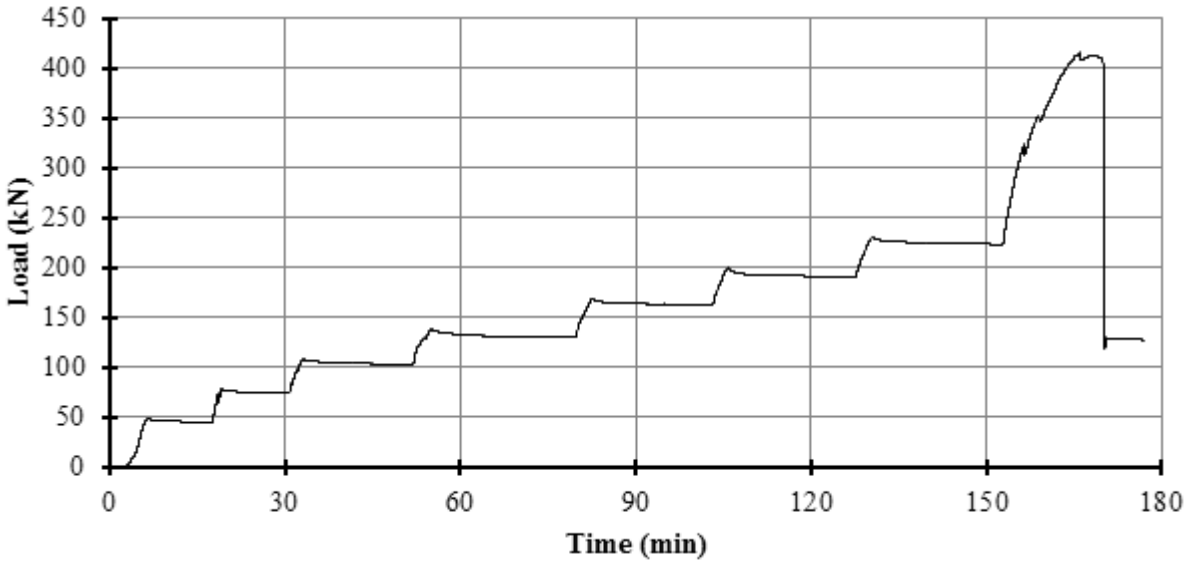

Figure E.143: BM16-150 Plot of Load vs Time

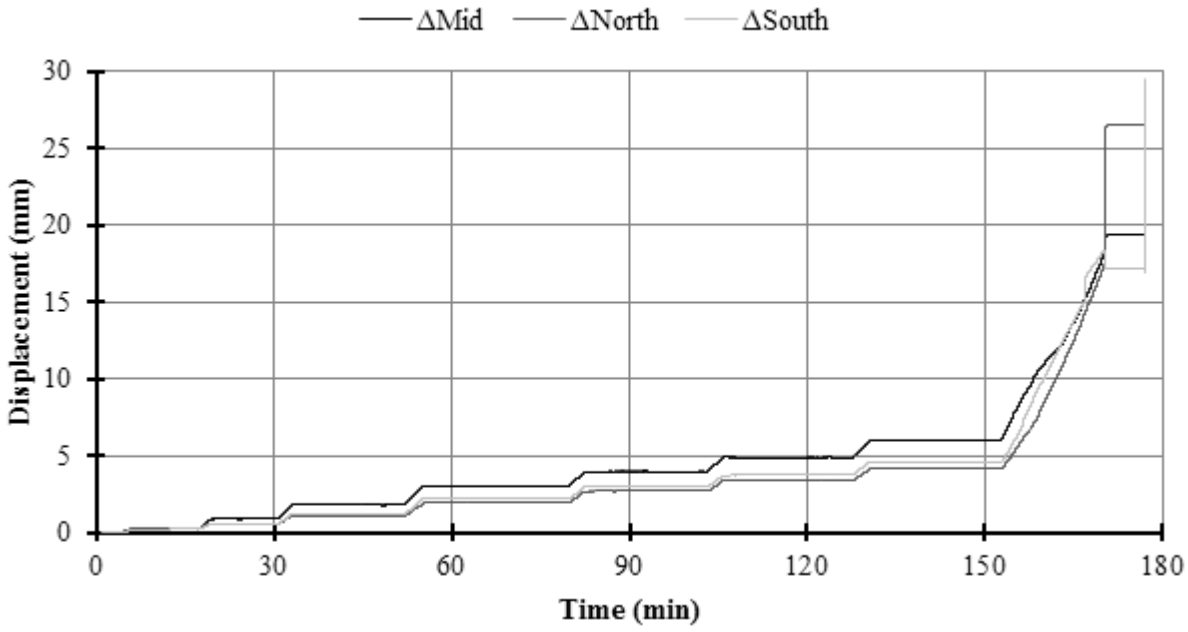

Figure E.144: BM16-150 Plot of Displacement vs Time

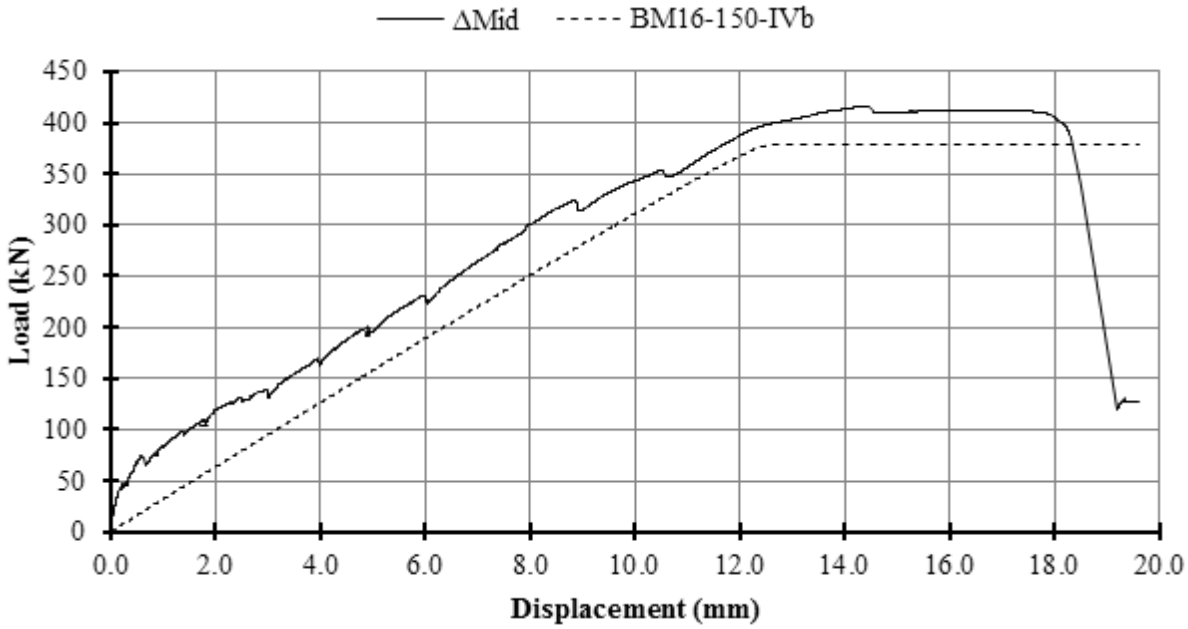

Figure E.145: BM16-150 Plot of Load vs Displacement

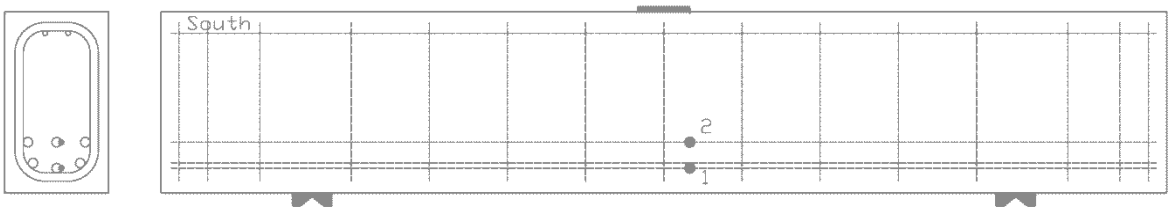

Figure E.146: BM16-150 Schematic of Mid-Span Strain Gauge Locations

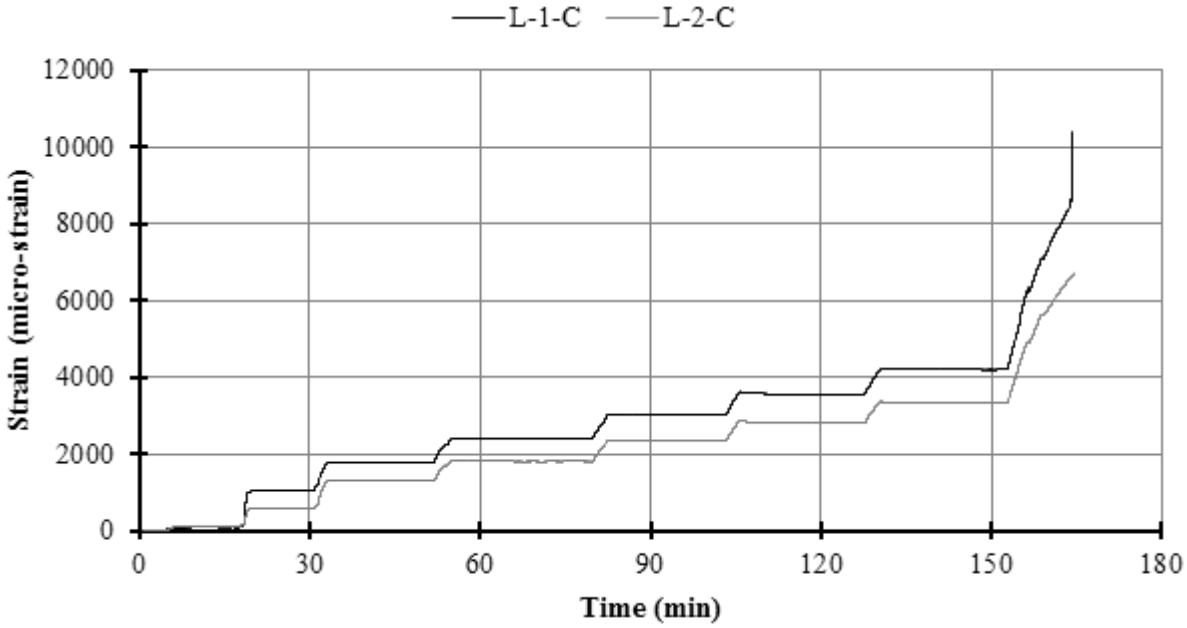

Figure E.147: BM16-150 Plot of Strain vs Time on Longitudinal Bars at Mid-Span

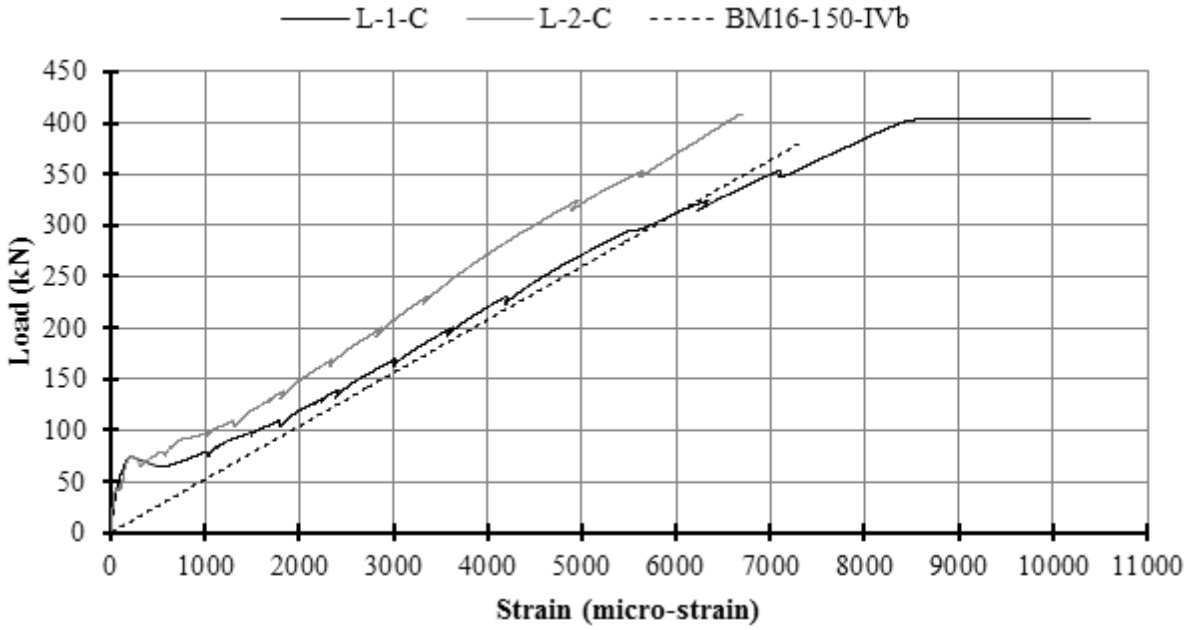

Figure E.148: BM16-150 Plot of Load vs Strain on Longitudinal Bars at Mid-Span

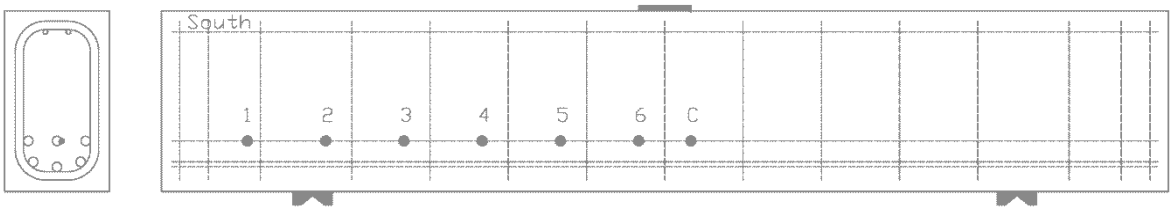

Figure E.149: BM16-150 Schematic of Longitudinal Strain Gauge Locations

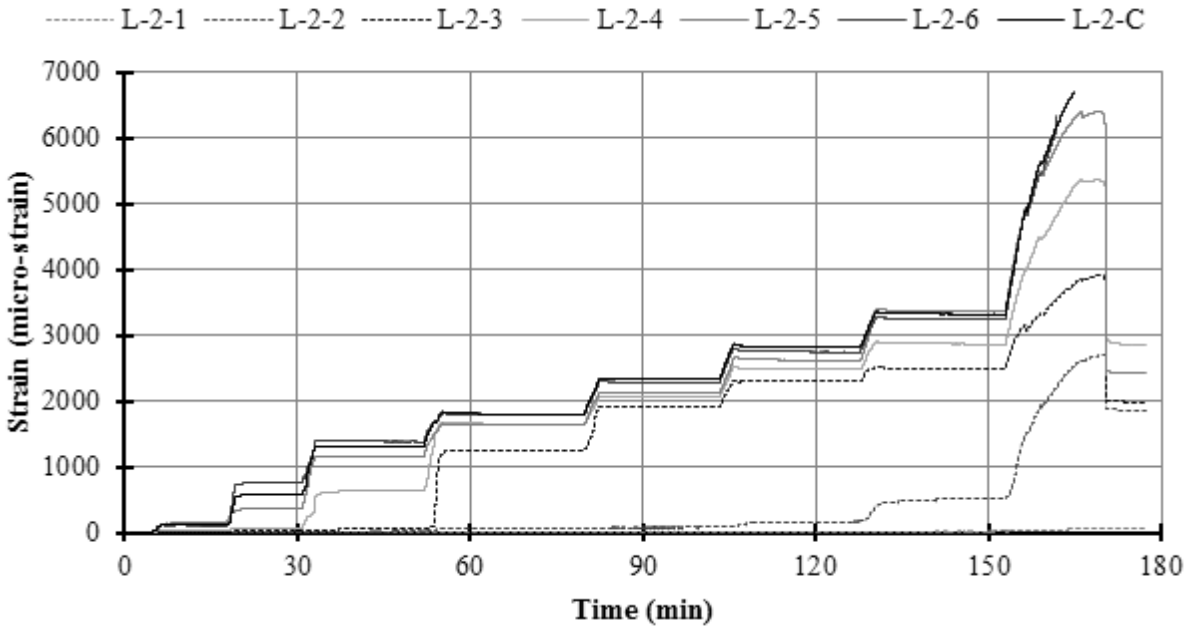

Figure E.150: BM16-150 Plot of Strain vs Time from Gauges along the Top Longitudinal Bar

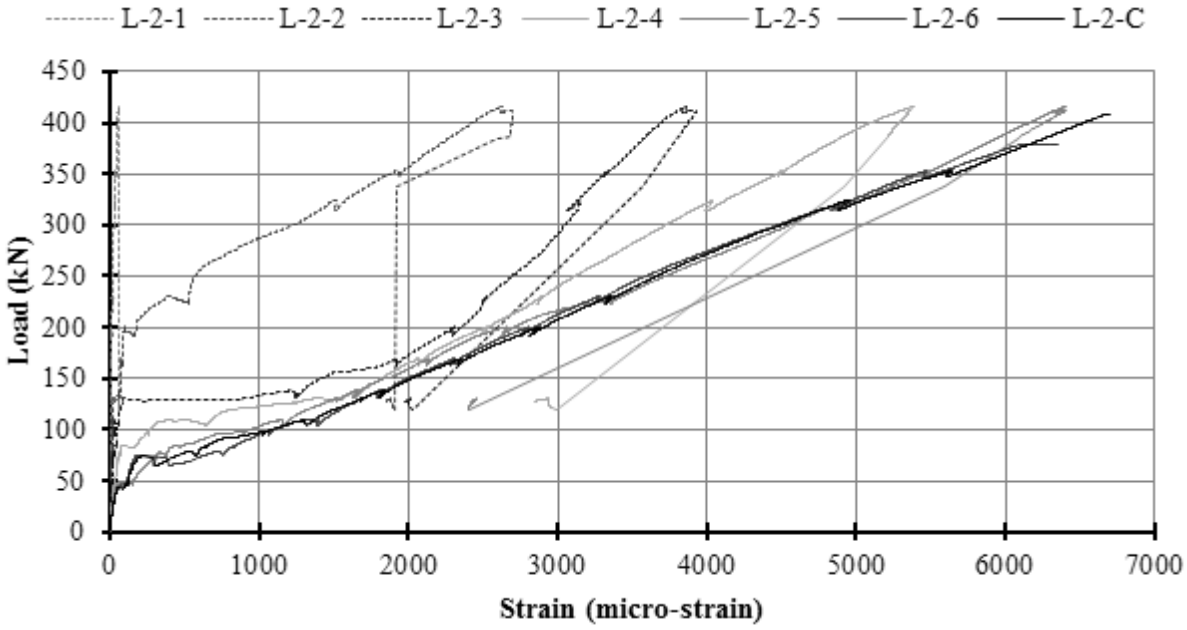

Figure E.151: BM16-150 Plot of Load vs Strain from Gauges along the Top Longitudinal Bar

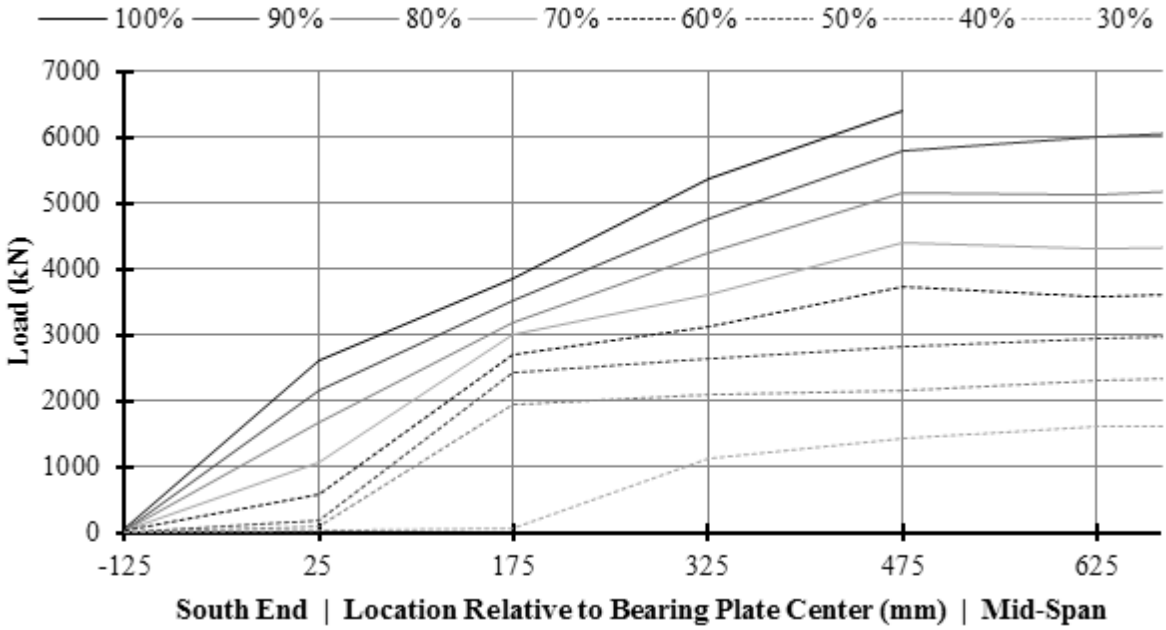

Figure E.152: BM16-150 Plot of Strain vs Gauge Location with Increasing Load
Gauges L-2-6 and L-2-C failed after 90 percent load.

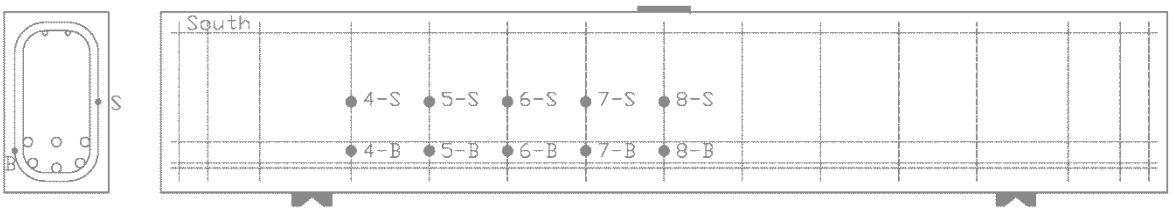

Figure E.153: BM16-150 Schematic of Stirrup Strain Gauge Locations

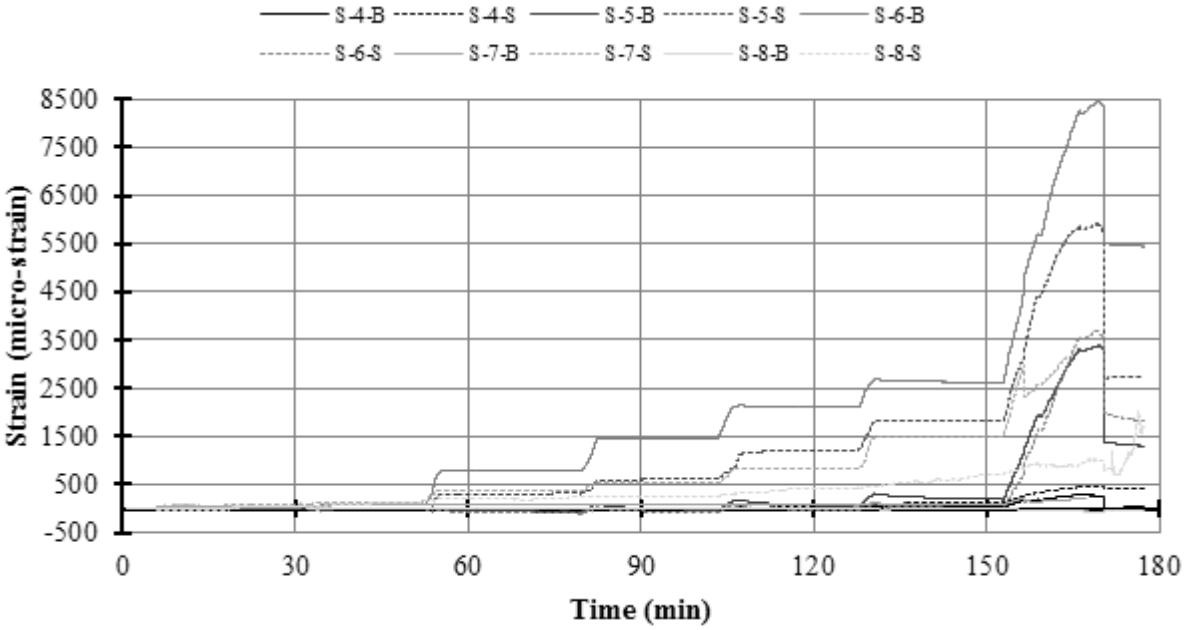

Figure E.154: BM16-150 Plot of Strain vs Time on Stirrups

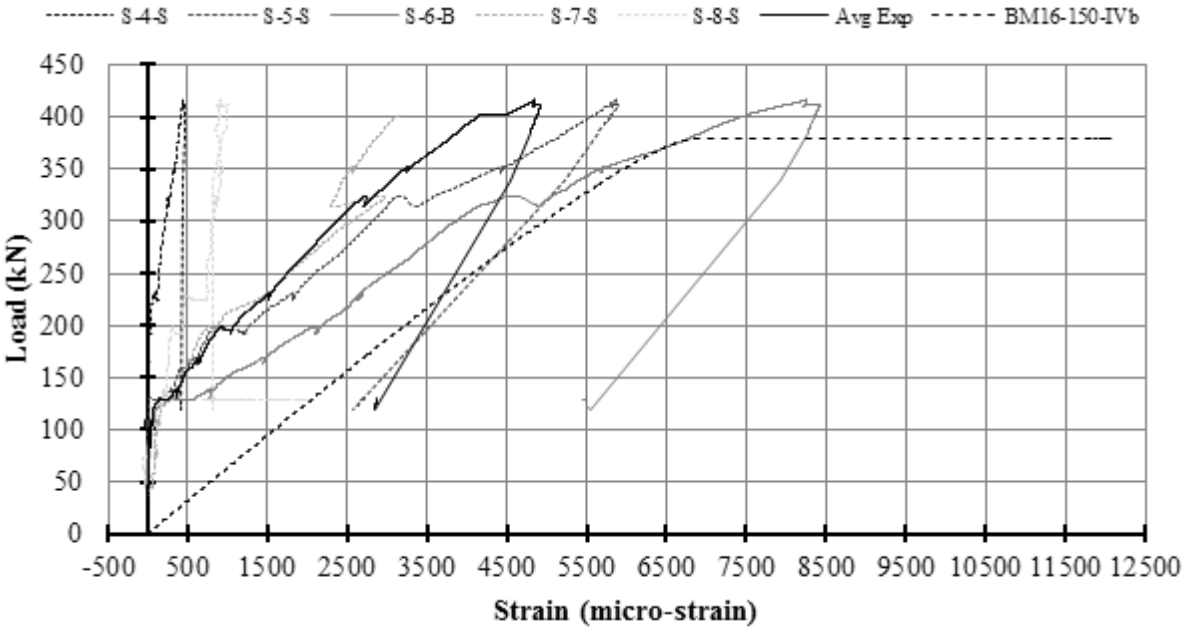

Figure E.155: BM16-150 Plot of Load vs Strain on Stirrups

A plot with all stirrup strain gauges may be found in the Results Chapter.

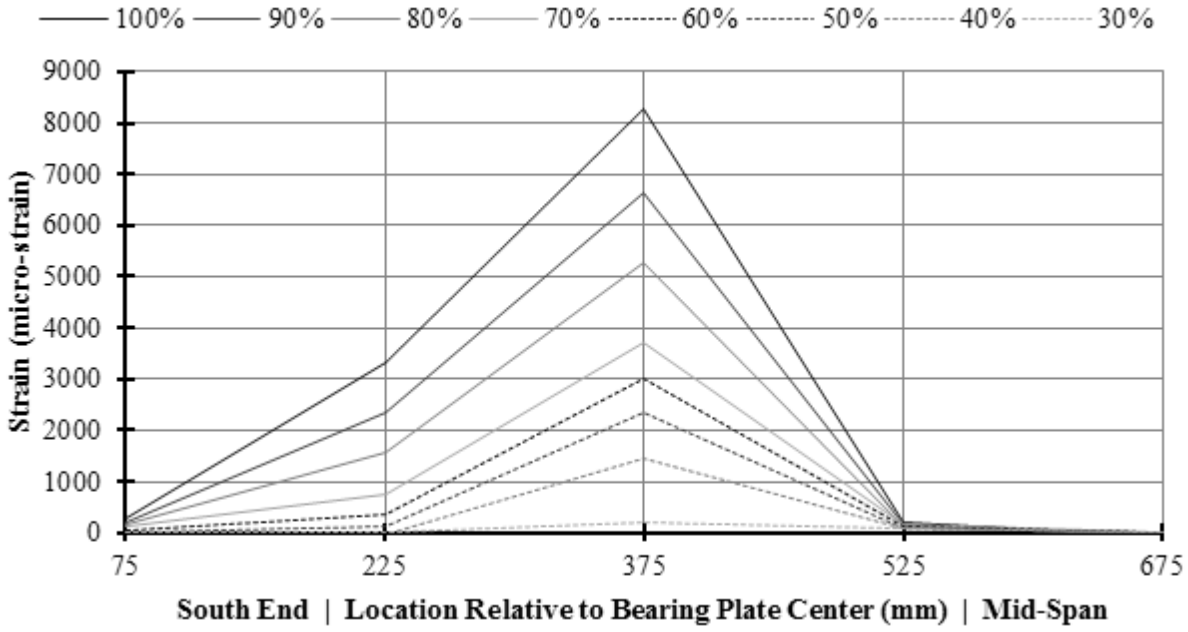

Figure E.156: BM16-150 Plot of Stirrup Strain vs Gauge Location with Increasing Load

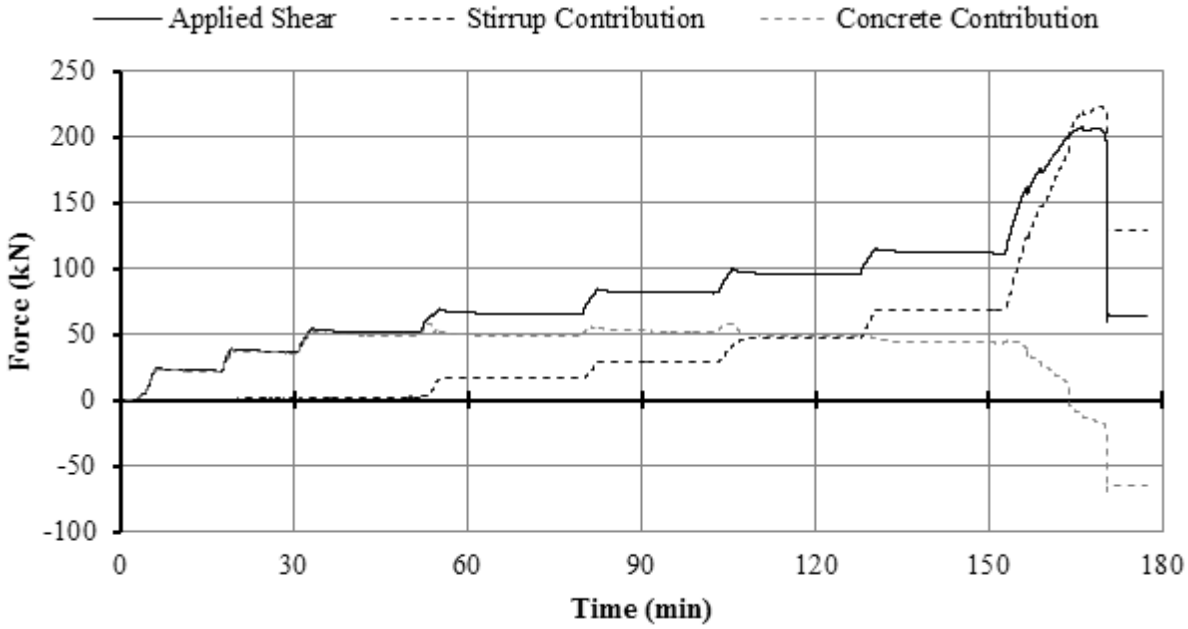

Figure E.157: BM16-150 Plot of Shear Contribution vs Time

E.11.1 BM16-150 Photographs

Figure E.158: BM16-150 Rebar Cage Elevation Photo

Figure E.159: BM16-150 Rebar Cage Cross-Section Photo

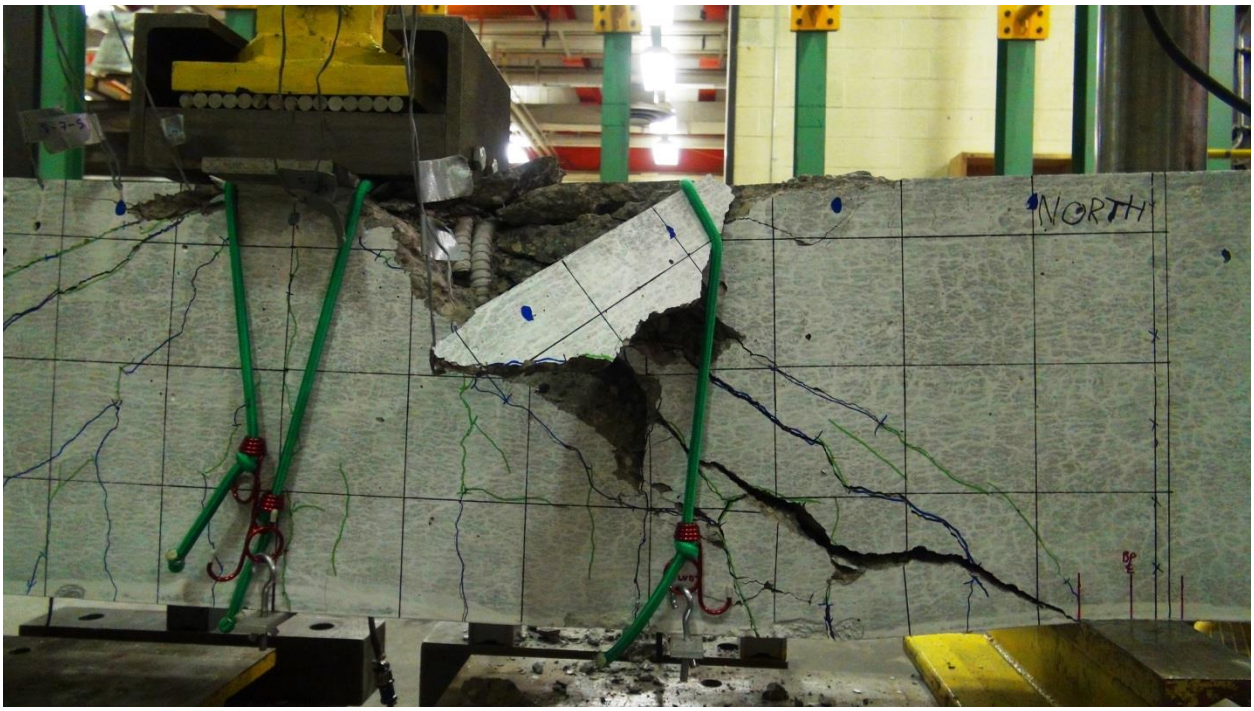

Figure E.160: BM16-150 Close-up Photo of Failure 1

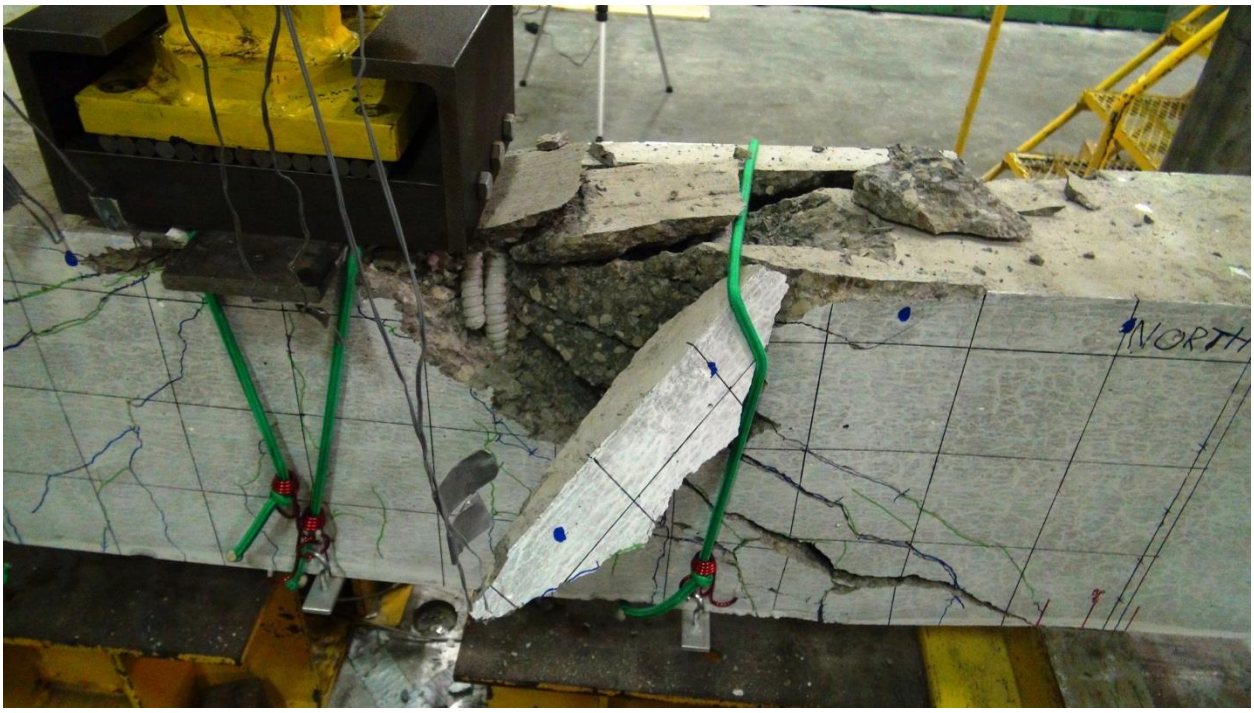

Figure E.161: BM16-150 Close-up Photo of Failure 2

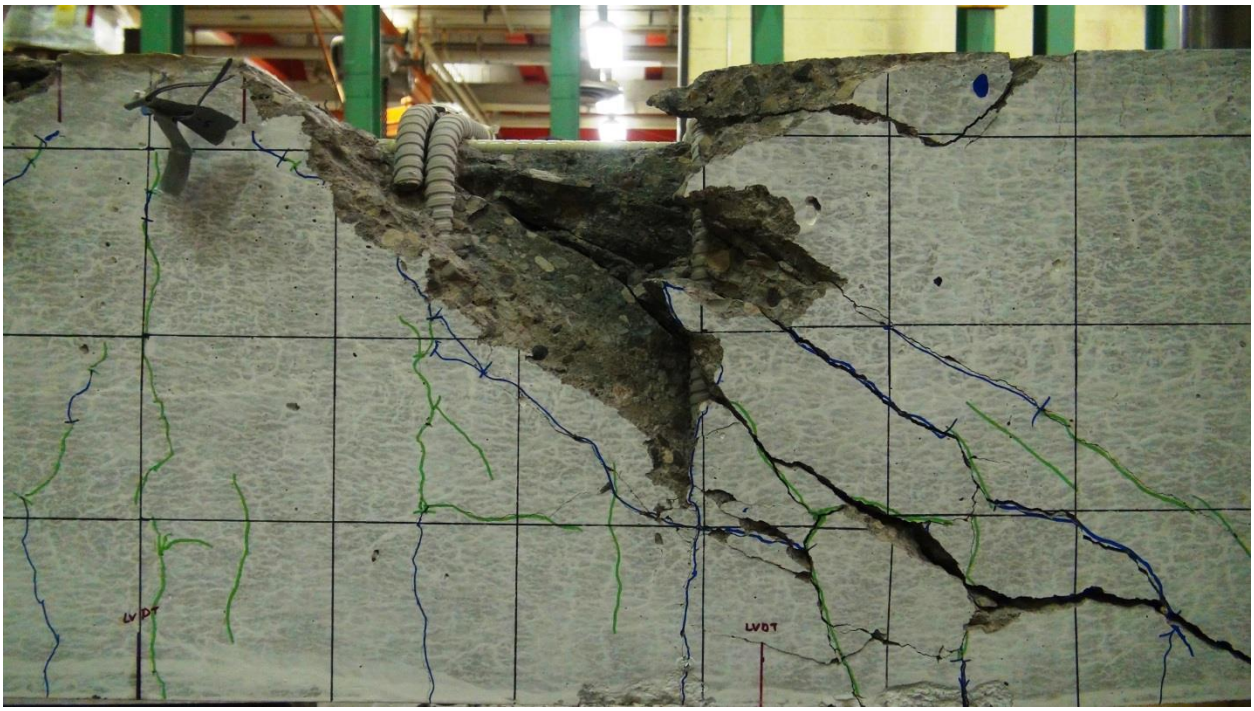

Figure E.162: BM16-150 Close-up Photo of Failure with Spalled Concrete Removed with Stirrups 9 and 10 Exposed

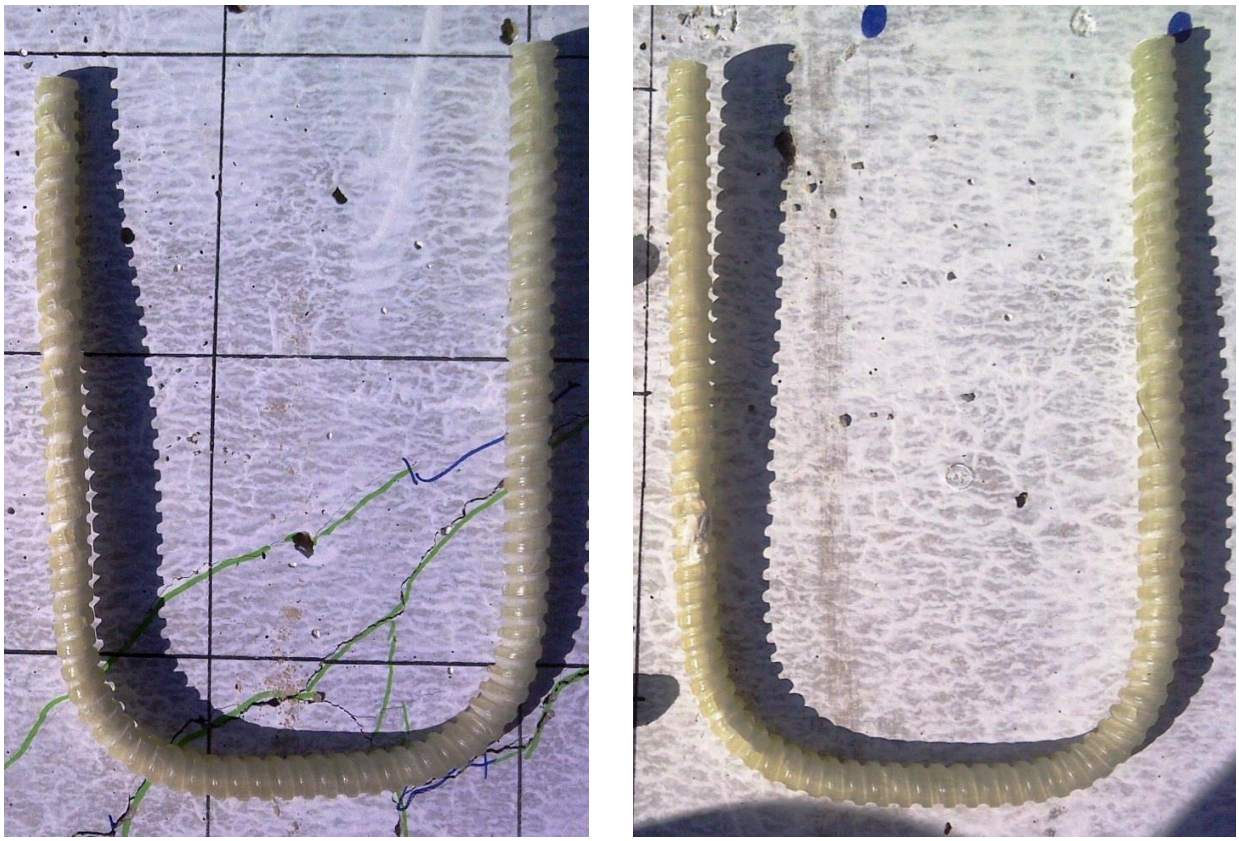

Figure E.163: BM16-150 Stirrup 10 & 11 Respectively

E.12 BM25-150

This was the seventh beam tested. The displacement controlled loading rate was 0.272 mm/min until the first crack measurement. The rate was then increased to 0.4 mm/min until after the final crack measurement at which point the rate was increased to 0.9 mm/min.

The beam failed in shear-compression / strut-crushing along a plane that ran diagonally from the load plate to the north bearing plate. A bottle shaped section of deformed concrete was located along the failure plane. The failure was unremarkable: peak load was not accompanied by loud noises, perceptible movements, or the ejection of concrete projectiles.

Peak load occurred at 415.8 kN and 22.07 mm of displacement, and failure took place in the un-instrumented north shear span 84 days after casting.

Strain gauges L-1B-C and S-8-B failed before peak load; strain gauge L-1A-B failed after peak load; all other strain gauges functioned adequately during the test.

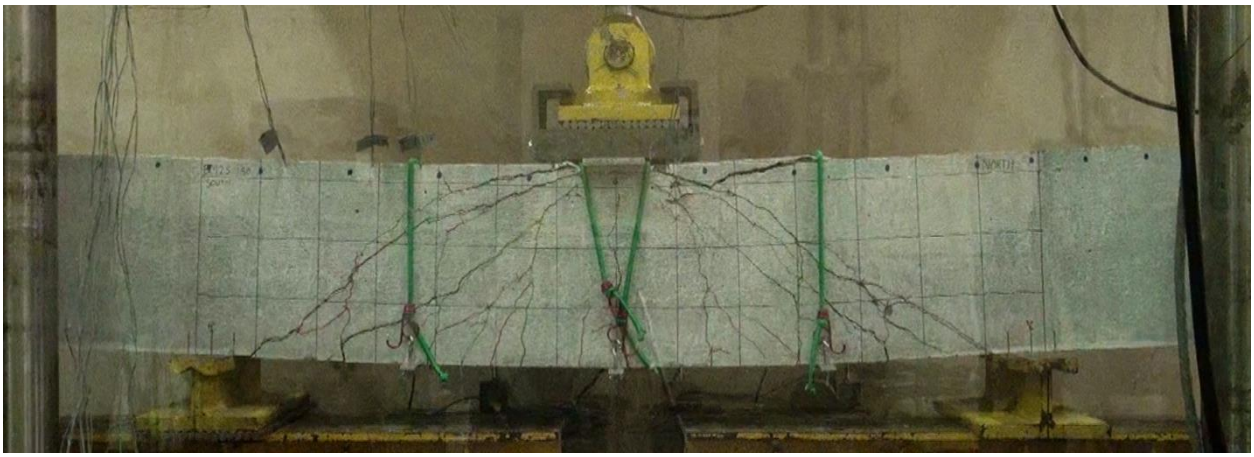

Figure E.164: BM25-150 At Peak Load

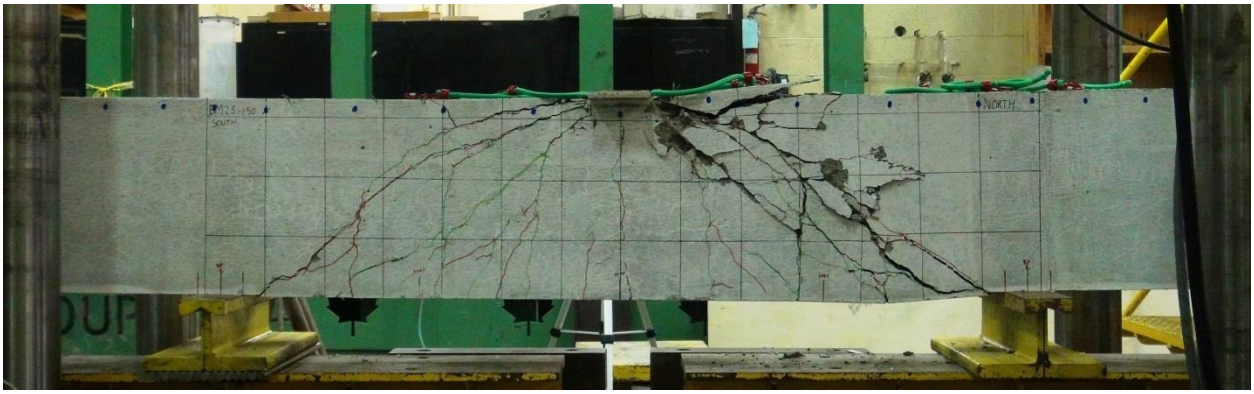

Figure E.165: BM25-150 After Testing

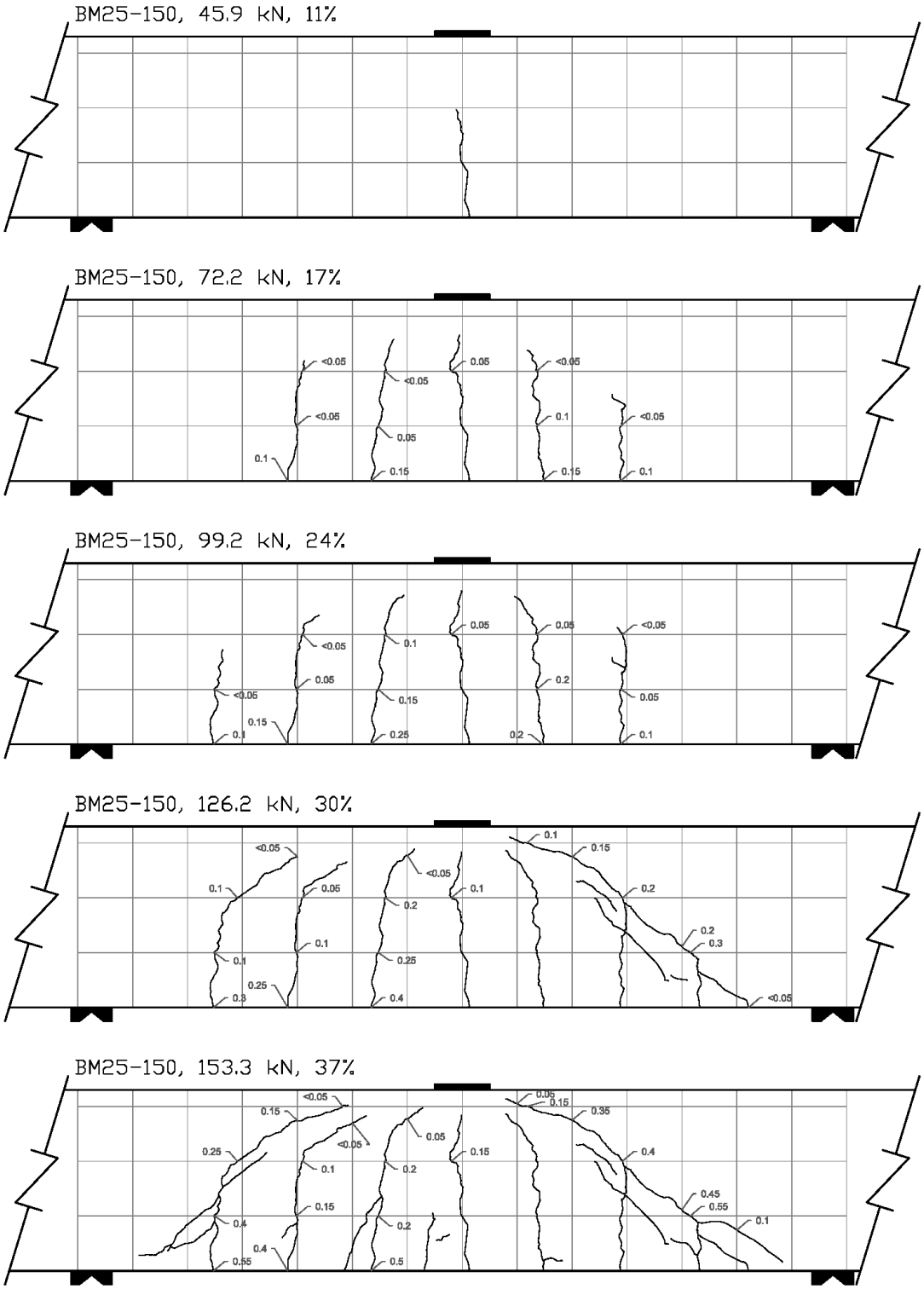

Figure E.166: BM25-150 Crack Diagram 1

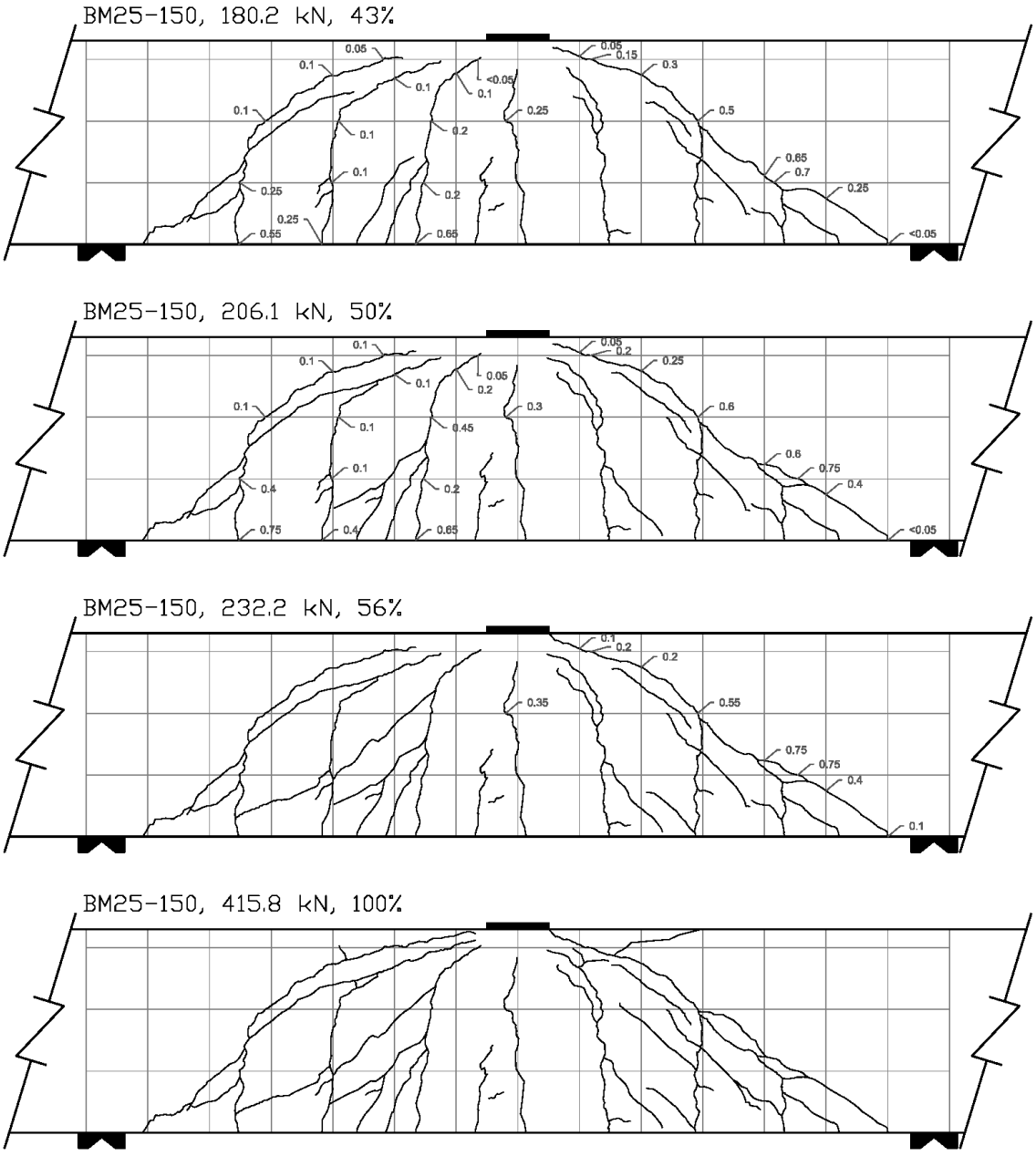

Figure E.167: BM25-150 Crack Diagram 2

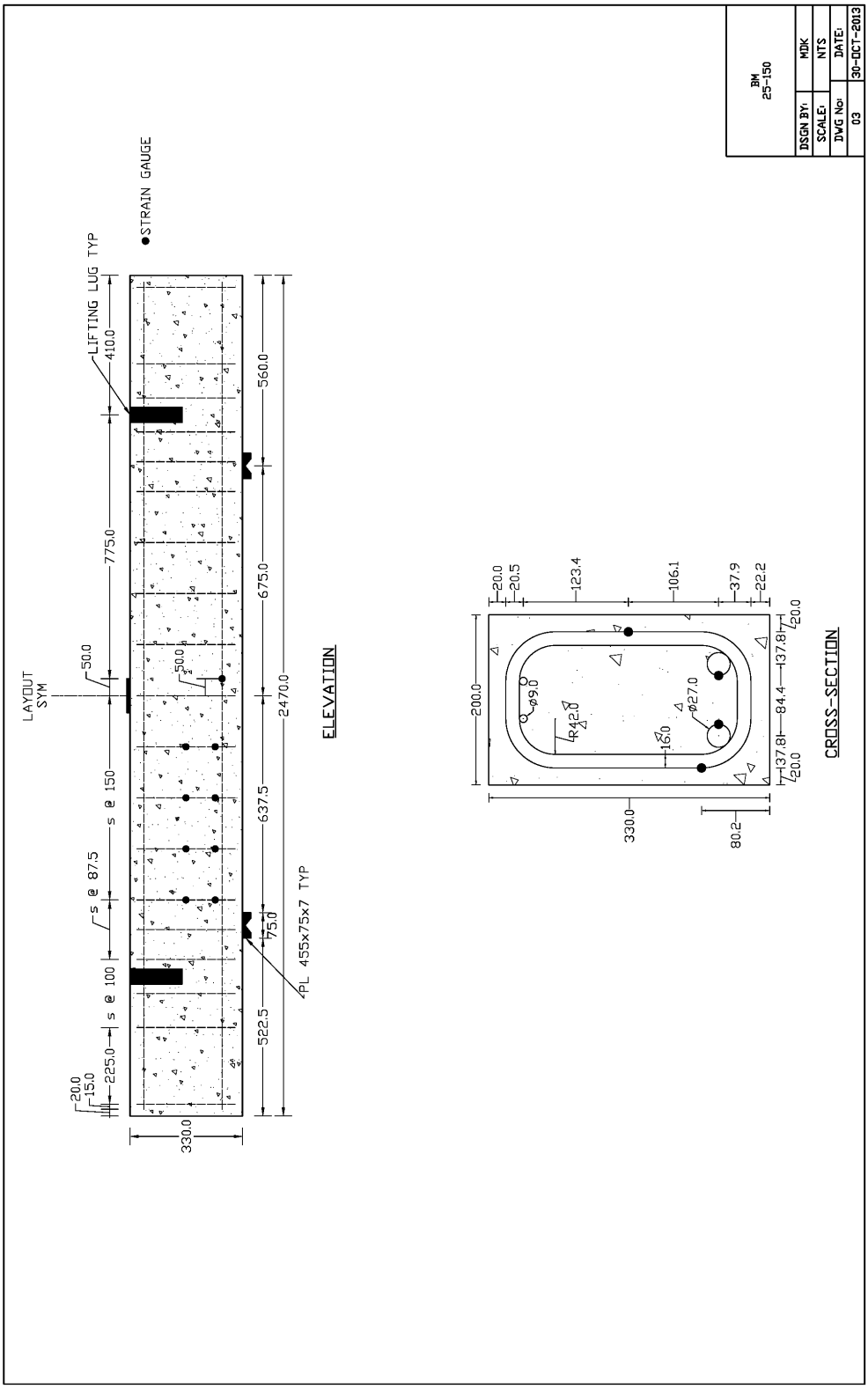

Figure E.168: BM25-150 Schematic Drawing

Table E.9: As-Designed and As-Constructed Parameter Chart for BM25-150

Parameter	As-Designed	As-Constructed
Beam Properties		
f'_c (MPa)	45	47.3 (28 day)
b (mm)	200	198.5**
h (mm)	330	333.0**
l (mm)	2470	-
d (mm)	270	273.5***
a/d	2.5	-
ρ_F (%)	1.82	-
ρ_v (%)	0.75	-
Longitudinal Bar Properties		
f_{Fu} (MPa)	1000	-
E_F (GPA)	60	-
A_F (mm^2)	491	-
n_{Bar} (amnt)	2	-
ε_{Fu} (%)	2.61*	-
Stirrup Properties		
$f_{Fu,straight}$ (MPa)	1000	-
$f_{Fu,bent}$ (MPa)	700	-
E_F (GPA)	50	-
A_F (mm^2)	113.1	-
r_{Bend} (mm)	42	-

** Rupture strain was only provided for dia. 16 bars; this value was assumed valid for all bars.*
*** Measured at midpoint of the failed shear span before testing, width is an average of top and bottom.*
**** Based on an average from measured bar depths before pour on north and south ends.*

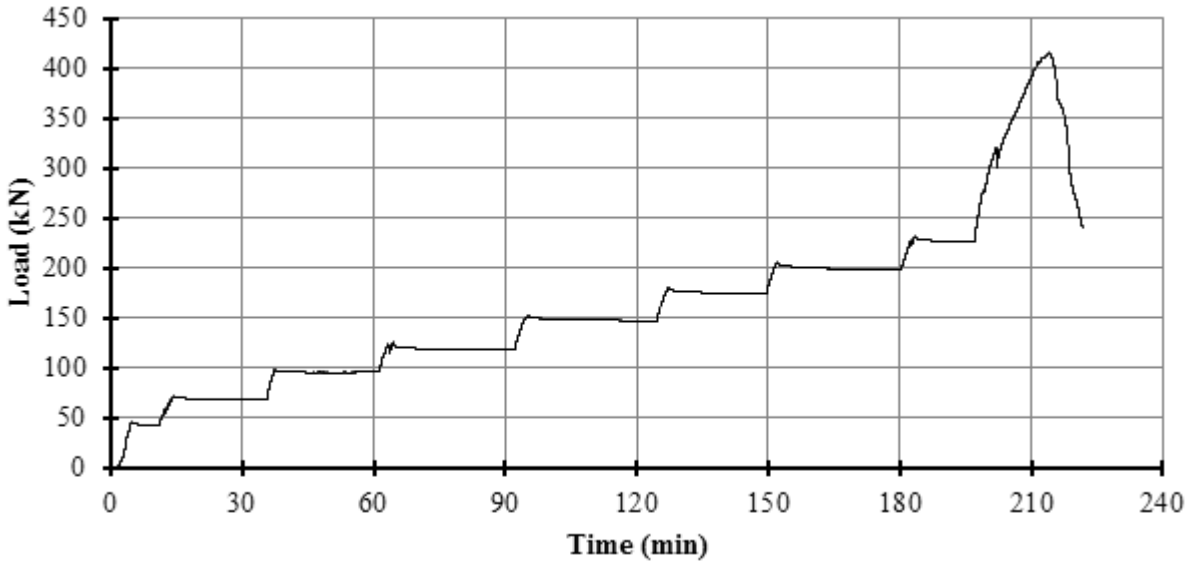

Figure E.169: BM25-150 Plot of Load vs Time

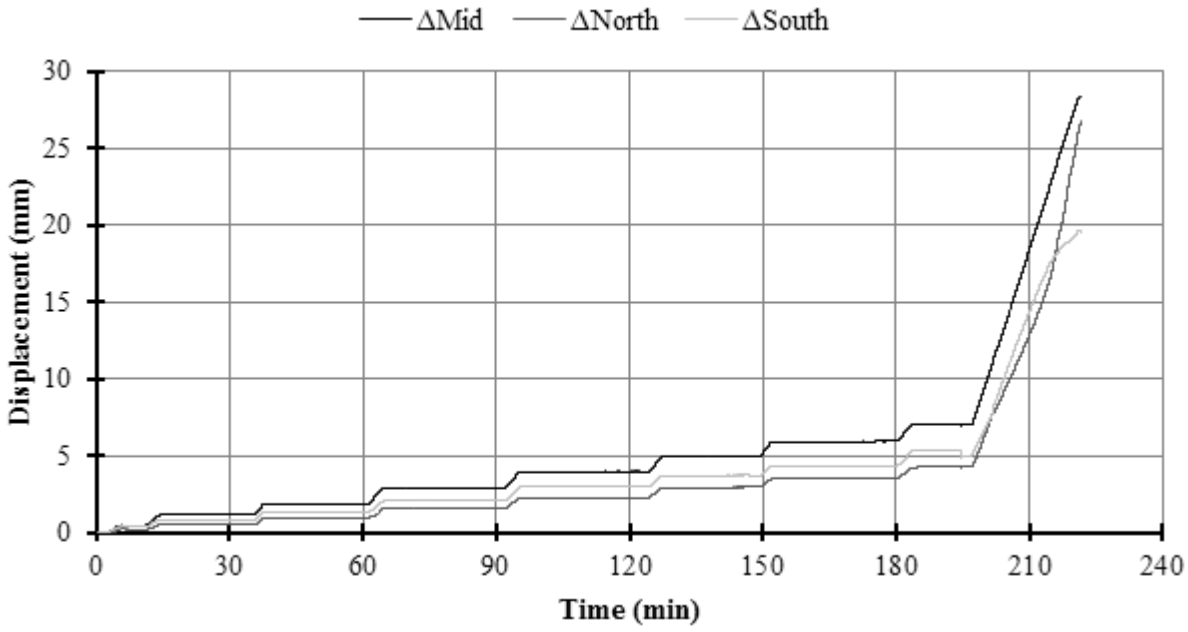

Figure E.170: BM25-150 Plot of Displacement vs Time

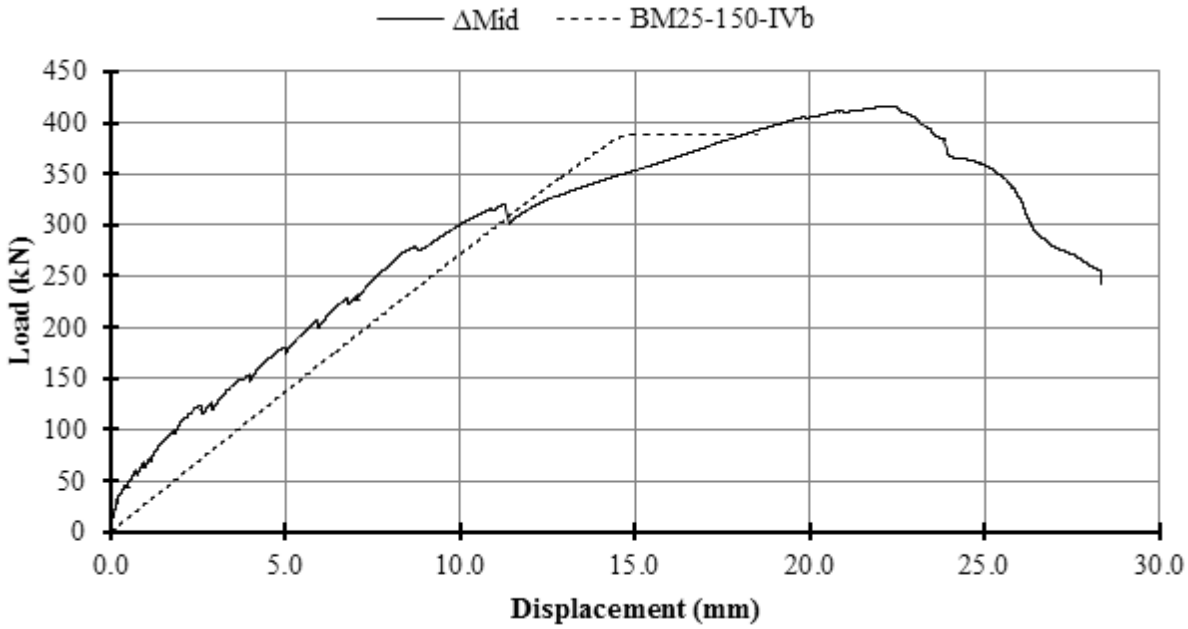

Figure E.171: BM25-150 Plot of Load vs Displacement

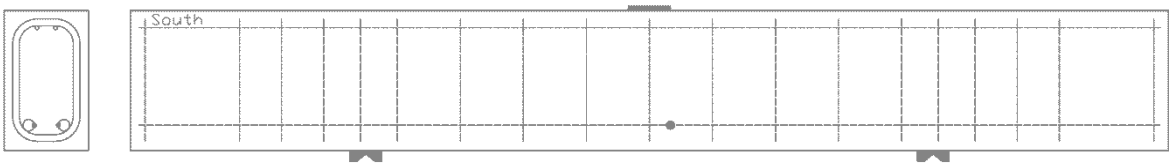

Figure E.172: BM25-150 Schematic of Mid-Span Strain Gauge Locations

A record of the specific longitudinal bar to which gauge A and B were attached was not kept.

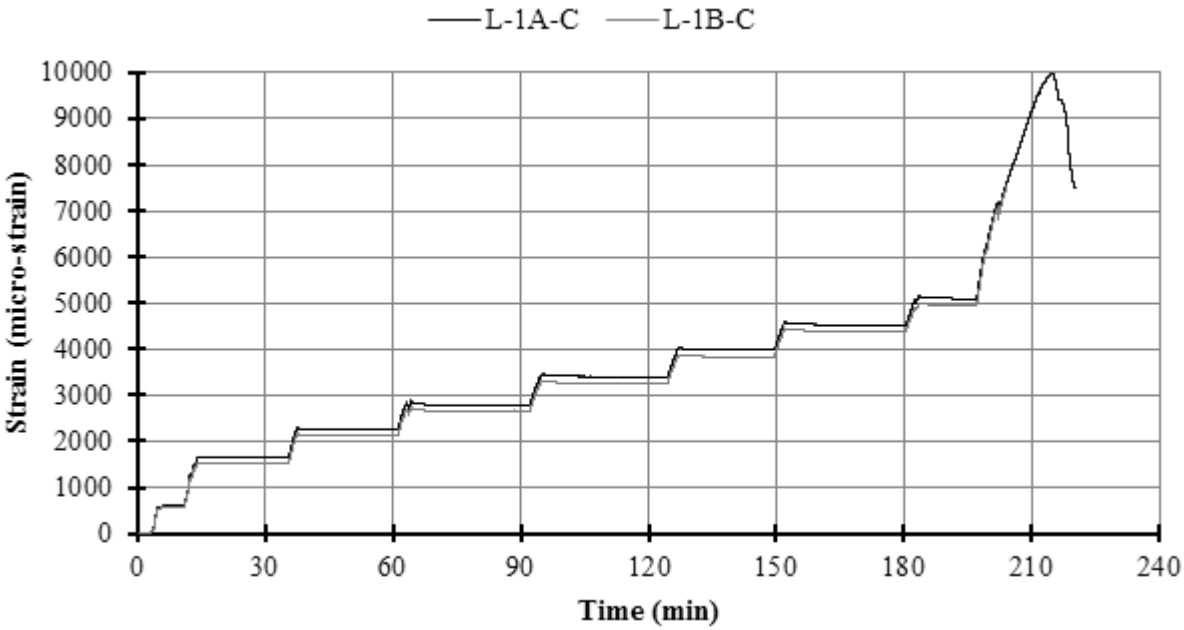

Figure E.173: BM25-150 Plot of Strain vs Time on Longitudinal Bars at Mid-Span

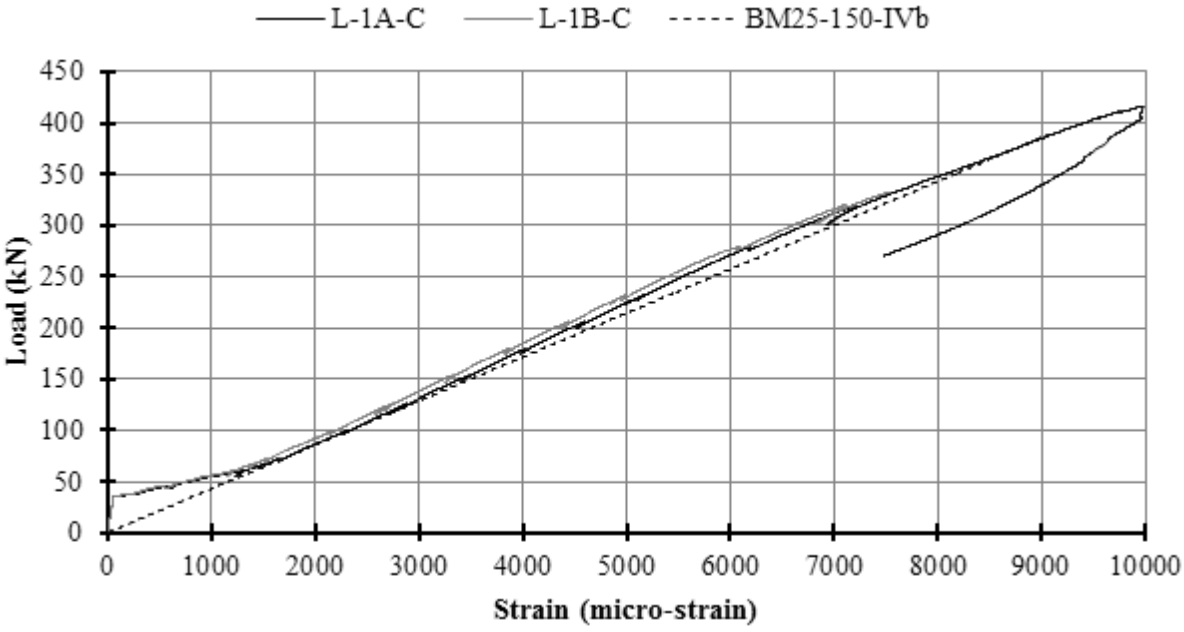

Figure E.174: BM25-150 Plot of Load vs Strain on Longitudinal Bars at Mid-Span

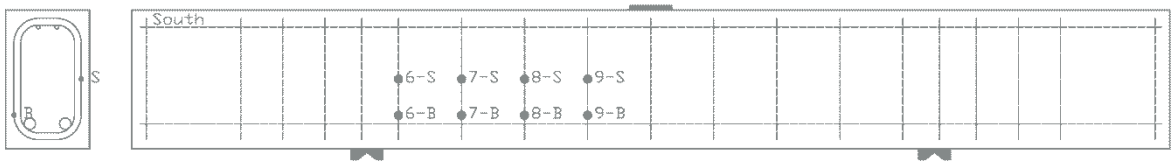

Figure E.175: BM25-150 Schematic of Stirrup Strain Gauge Locations

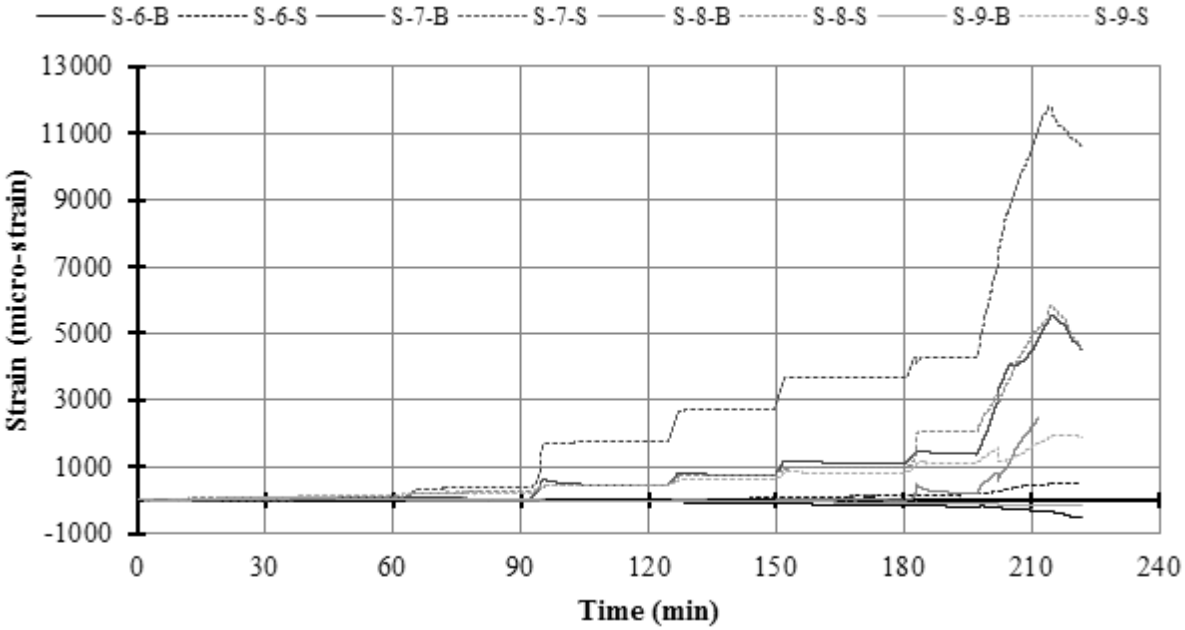

Figure E.176: BM25-150 Plot of Strain vs Time on Stirrups

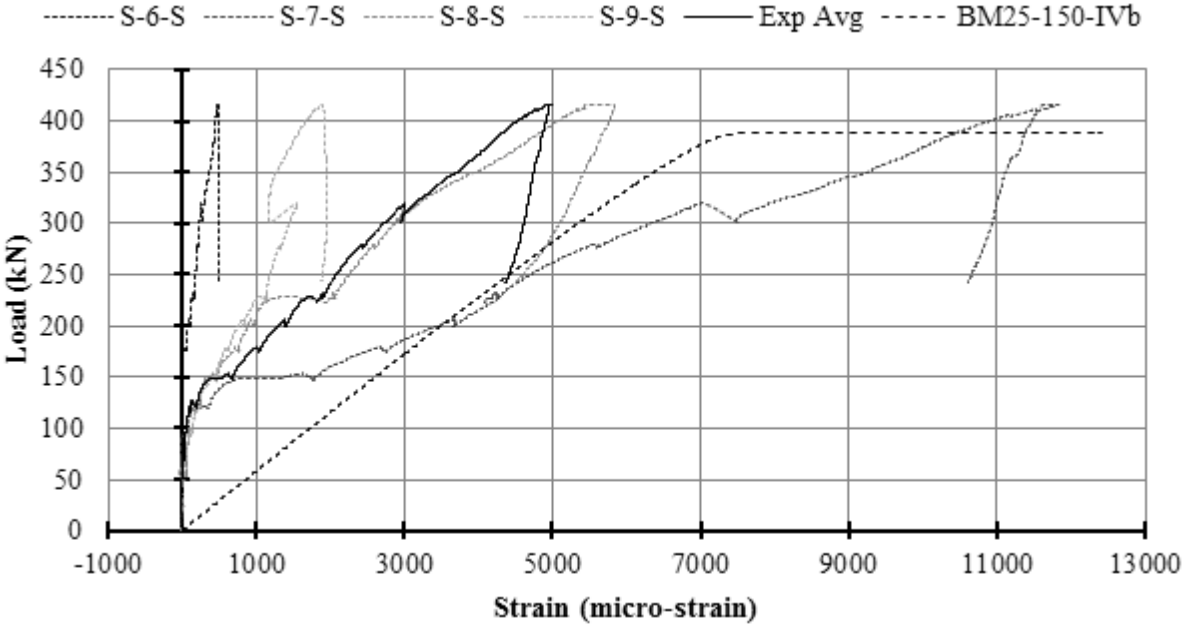

Figure E.177: BM25-150 Plot of Load vs Strain on Stirrups

A plot with all stirrup strain gauges may be found in the Results Chapter.

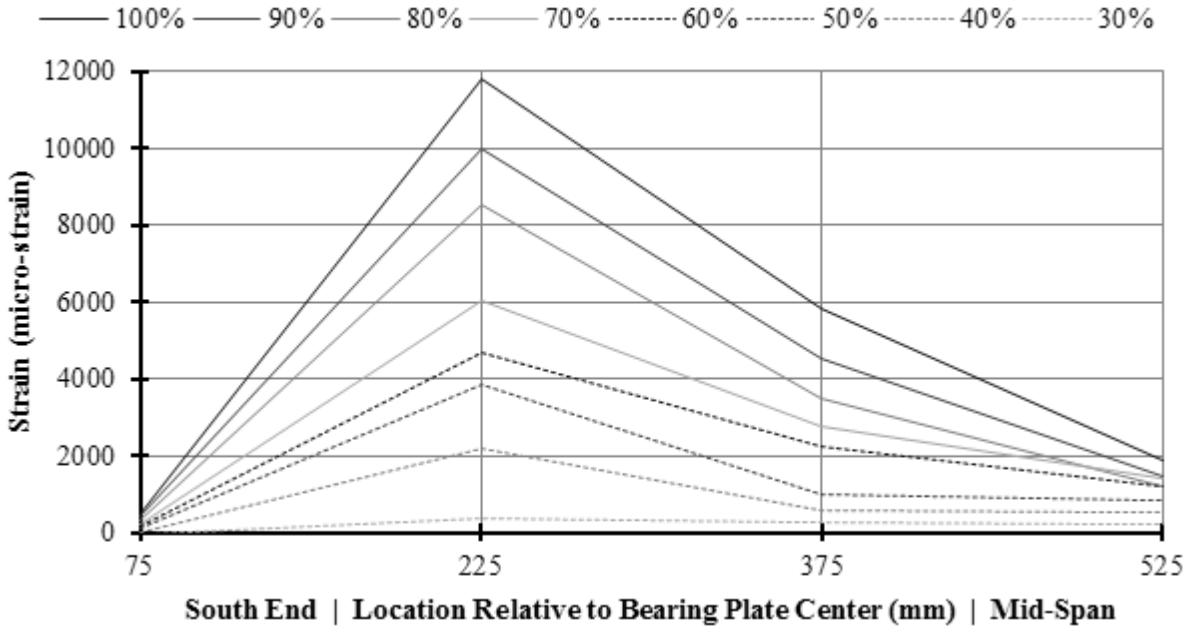

Figure E.178: BM25-150 Plot of Stirrup Strain vs Gauge Location with Increasing Load

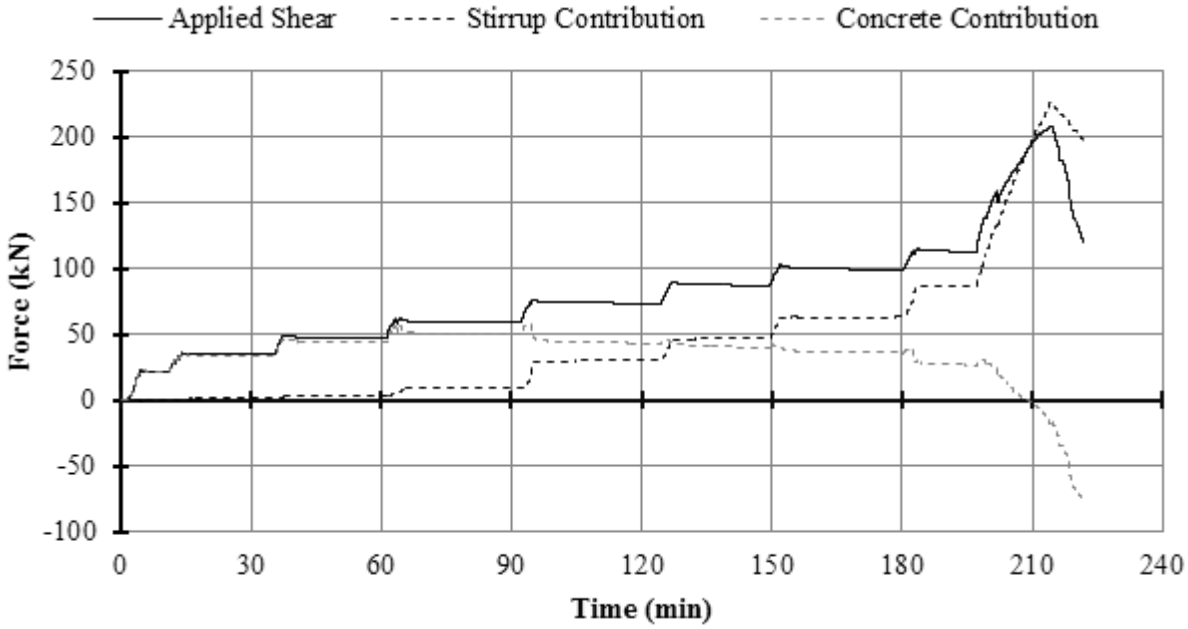

Figure E.179: BM25-150 Plot of Shear Contribution vs Time

E.12.1 BM25-150 Photographs

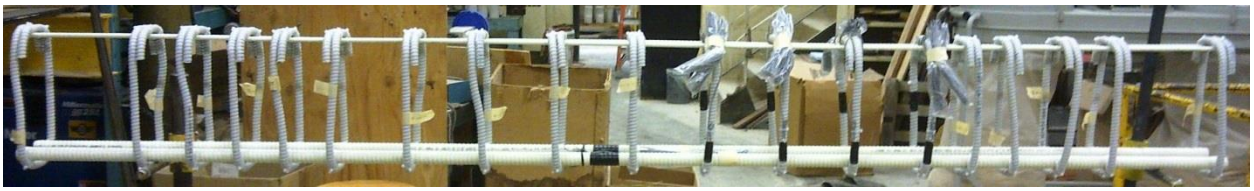

Figure E.180: BM25-150 Rebar Cage Elevation Photo

Figure E.181: BM25-150 Rebar Cage Cross-Section Photo

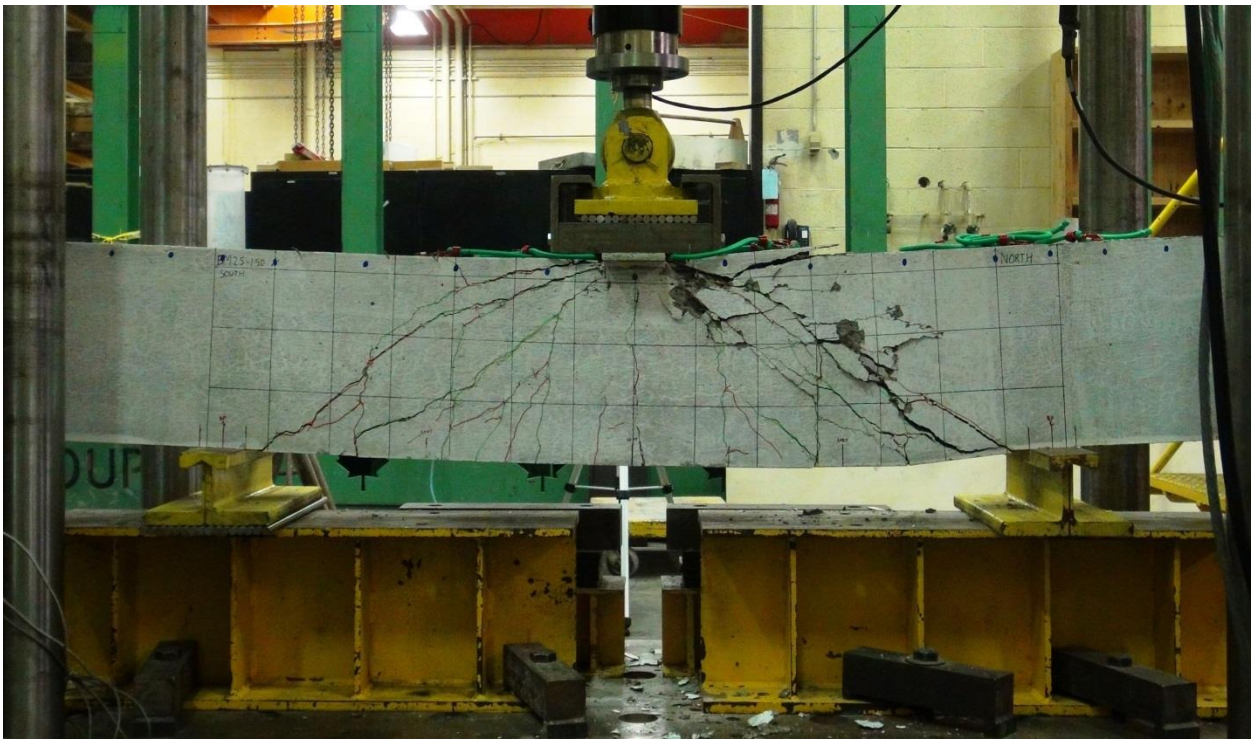

Figure E.182: BM25-150 Alternative Photo of Entire Beam Under Load After Testing

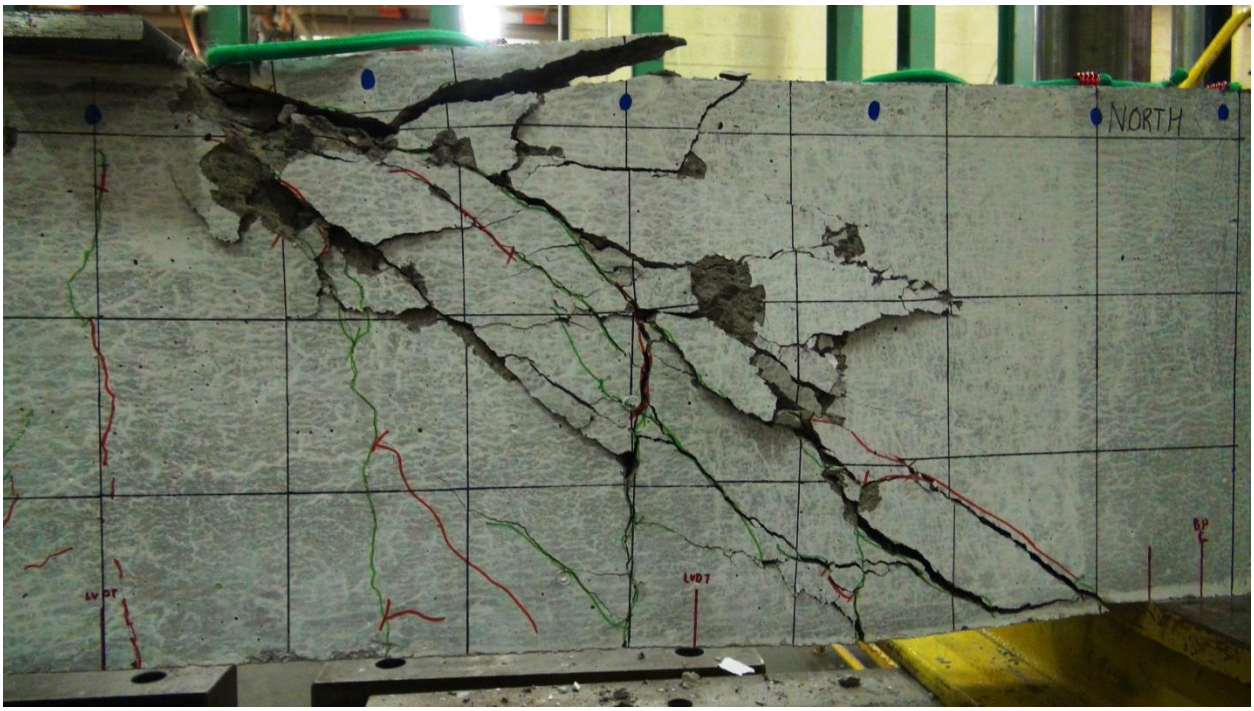

Figure E.183: BM25-150 Close-up Photo of Failure

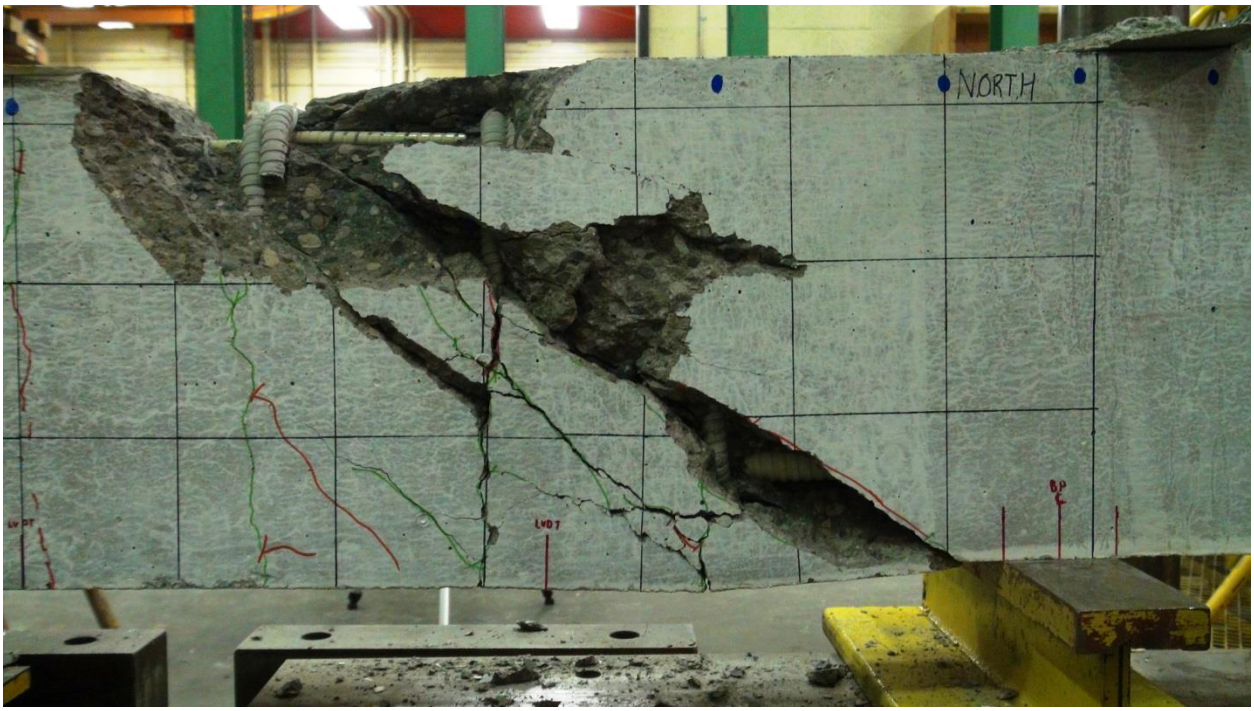

Figure E.184: BM25-150 Close-up Photo of Failure with Spalled Concrete Removed with Stirrups 11, 12, and 13 Exposed

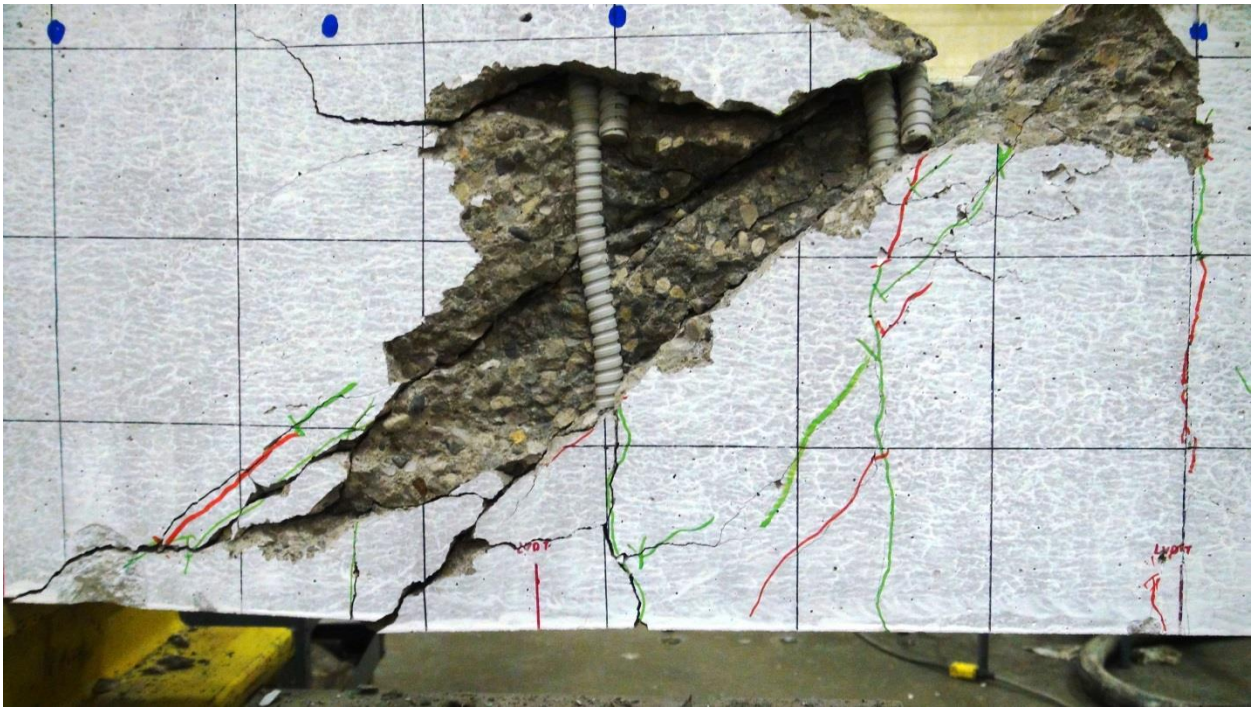

Figure E.185: BM25-150 Close-up Photo of Failure from Reverse with Spalled Concrete Removed with Stirrups 11 and 12

E.13 BM12-s230

This was the twelfth beam tested. The displacement controlled rate was 0.272 mm/min until the first crack measurement. The rate was then increased to 0.4 mm/min until after the final crack measurement after which the rate was increased to 1.0 mm/min.

The beam failed in shear-compression / strut-crushing along a plane that ran diagonally from the load plate to the north bearing plate. The failure was unremarkable: peak load was not accompanied by loud noises, perceptible movements, or the ejection of concrete projectiles. Peak load was followed a moment later by a large drop in load, which was accompanied by a popping noise characteristic of concrete fracture, widening of cracks, and the ejection of a few small concrete projectiles.

Peak load occurred at 466.9 kN and 12.52 mm of displacement, and failure took place in the un-instrumented north shear span 98 days after casting.

All strain gauges functioned adequately during testing.

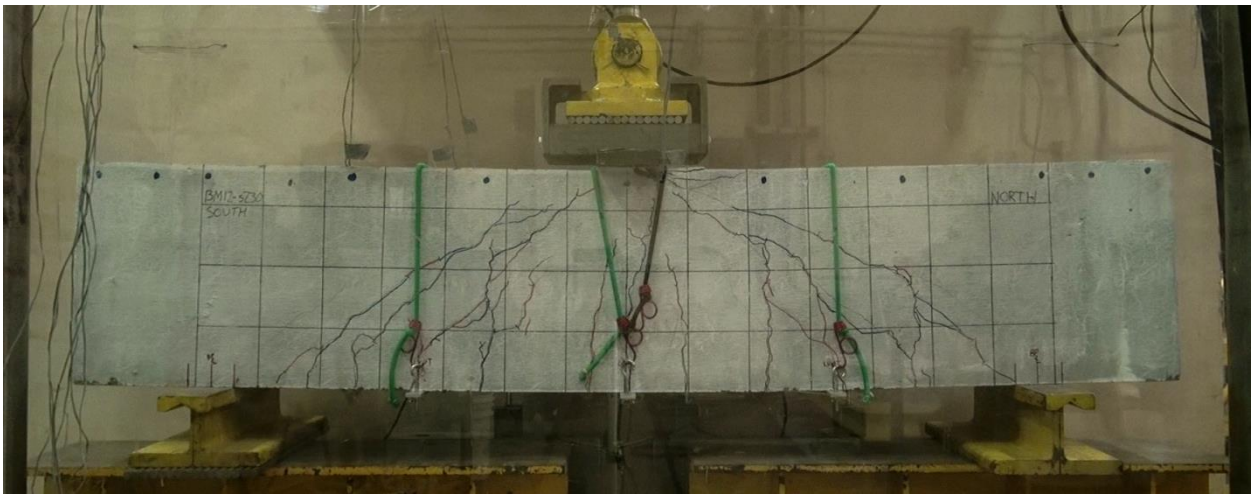

Figure E.186: BM12-s230 At Peak Load

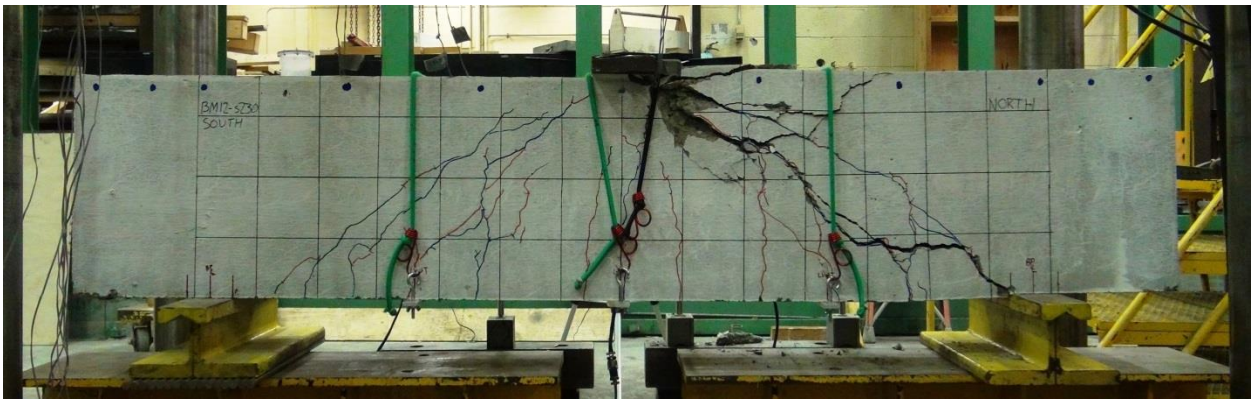

Figure E.187: BM12-s230 After Testing

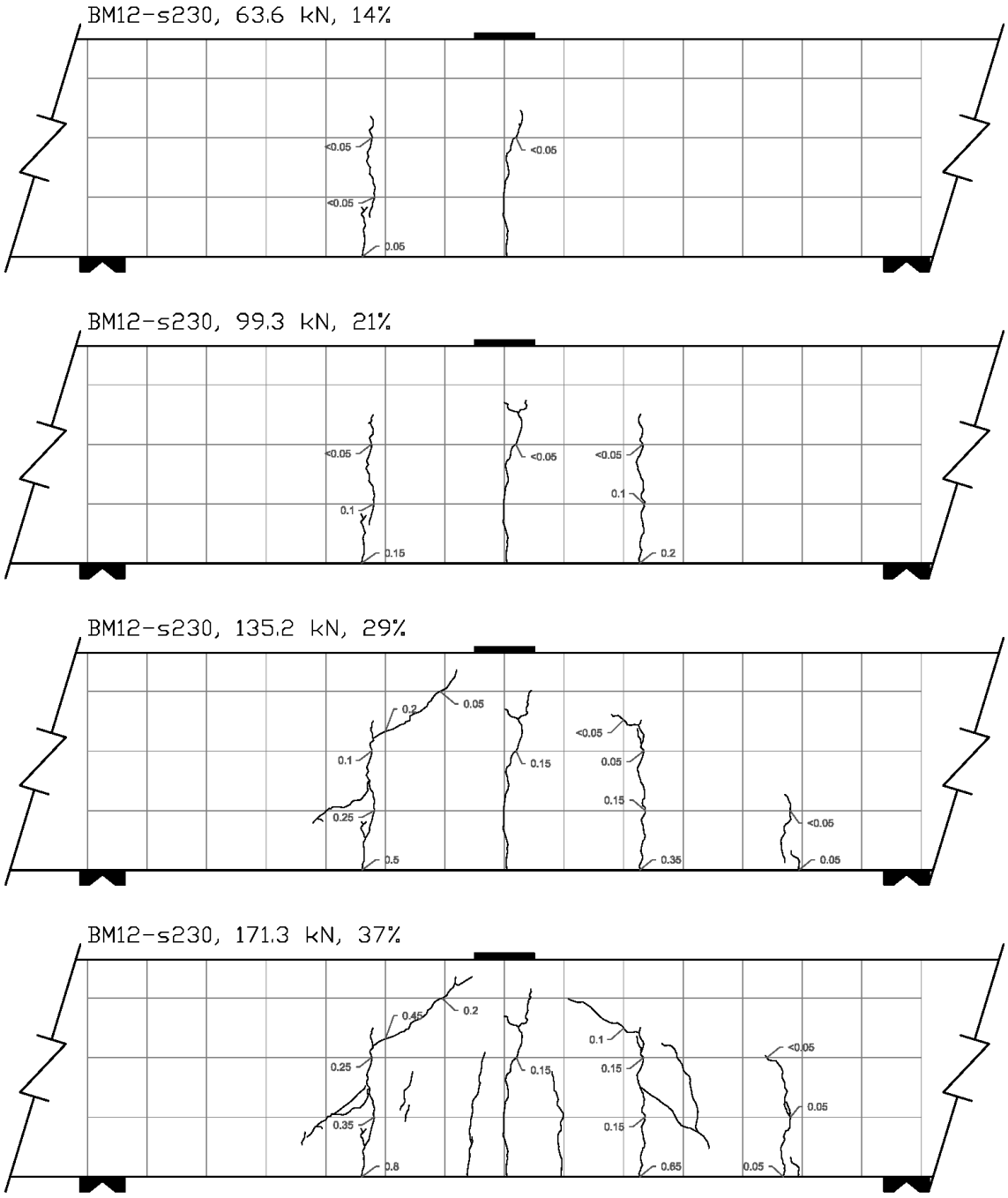

Figure E.188: BM12-s230 Crack Diagram 1

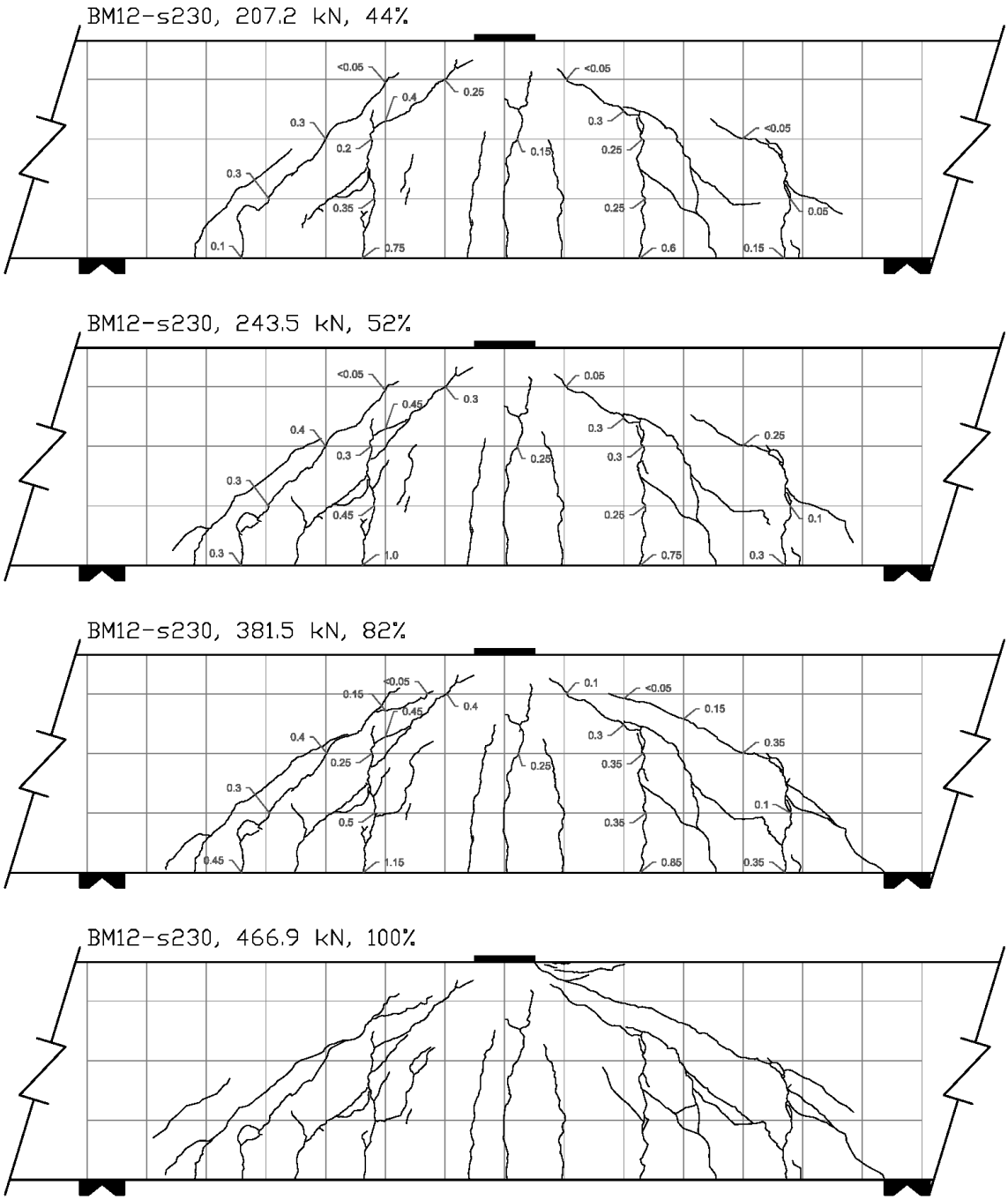

Figure E.189: BM12-s230 Crack Diagram 2

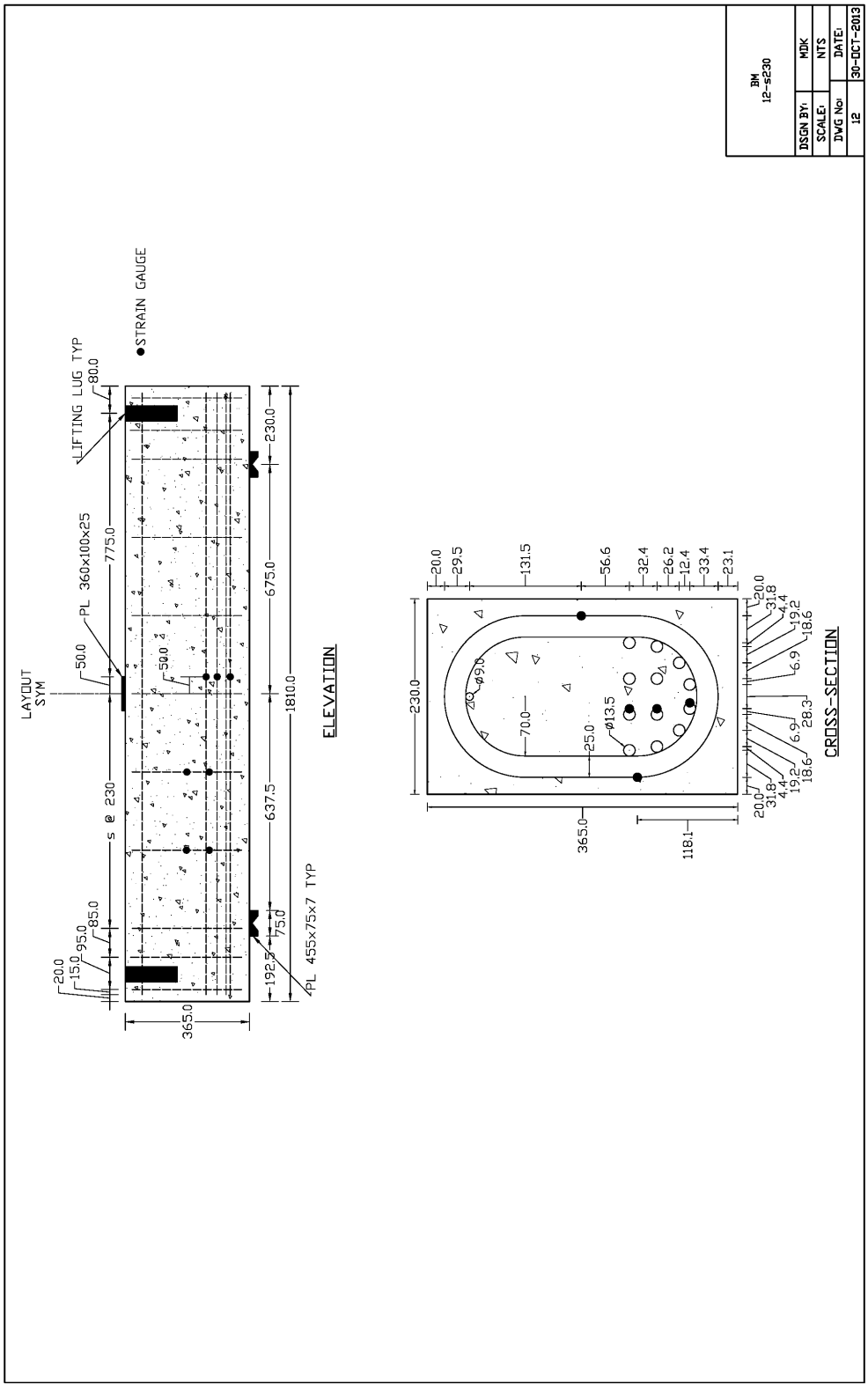

Figure E.190: BM12-s230 Schematic Drawing

Table E.10: As-Designed and As-Constructed Parameter Chart for BM12-s230

Parameter	As-Designed	As-Constructed
Beam Properties		
f'_c (MPa)	45	47.3 (28 day)
b (mm)	230	235.0**
h (mm)	365	360.0**
l (mm)	1810	-
d (mm)	270	274.6***
a/d	2.5	-
ρ_F (%)	2.18	-
ρ_v (%)	1.19	-
Longitudinal Bar Properties		
f_{Fu} (MPa)	1000	-
E_F (GPA)	60	-
A_F (mm^2)	113	-
n_{Bar} (amnt)	12	-
ε_{Fu} (%)	2.61*	-
Stirrup Properties		
$f_{Fu,straight}$ (MPa)	900	-
$f_{Fu,bent}$ (MPa)	550	-
E_F (GPA)	50	-
A_F (mm^2)	314.2	-
r_{Bend} (mm)	70	-

** Rupture strain was only provided for dia. 16 bars; this value was assumed valid for all bars.*
*** Measured at midpoint of the failed shear span before testing, width is an average of top and bottom.*
**** Based on an average from measured bar depths before pour on north and south ends.*

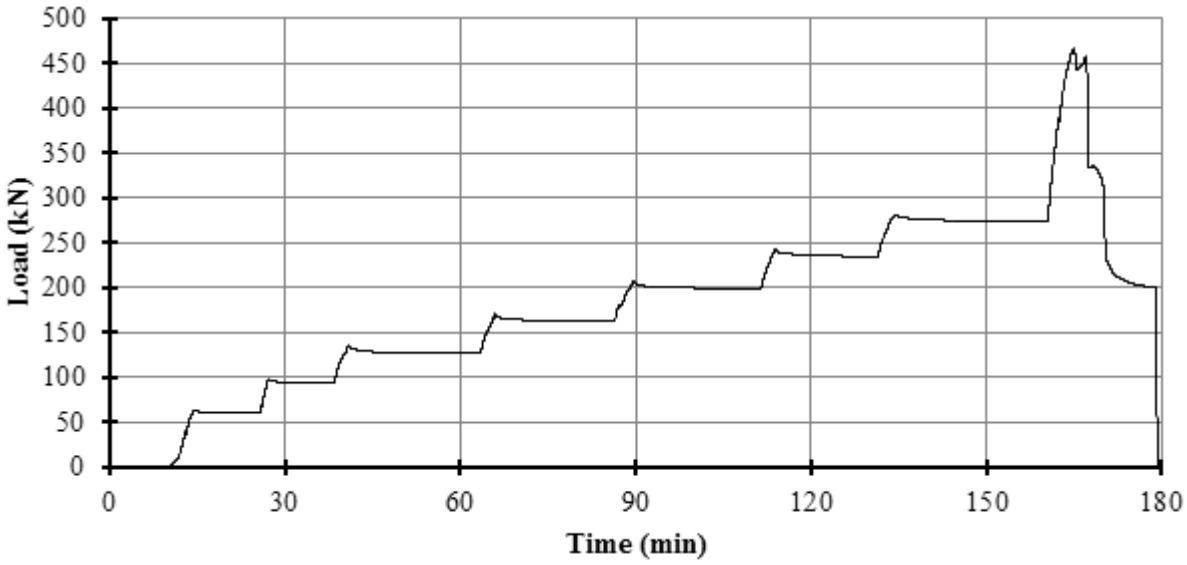

Figure E.191: BM12-s230 Plot of Load vs Time

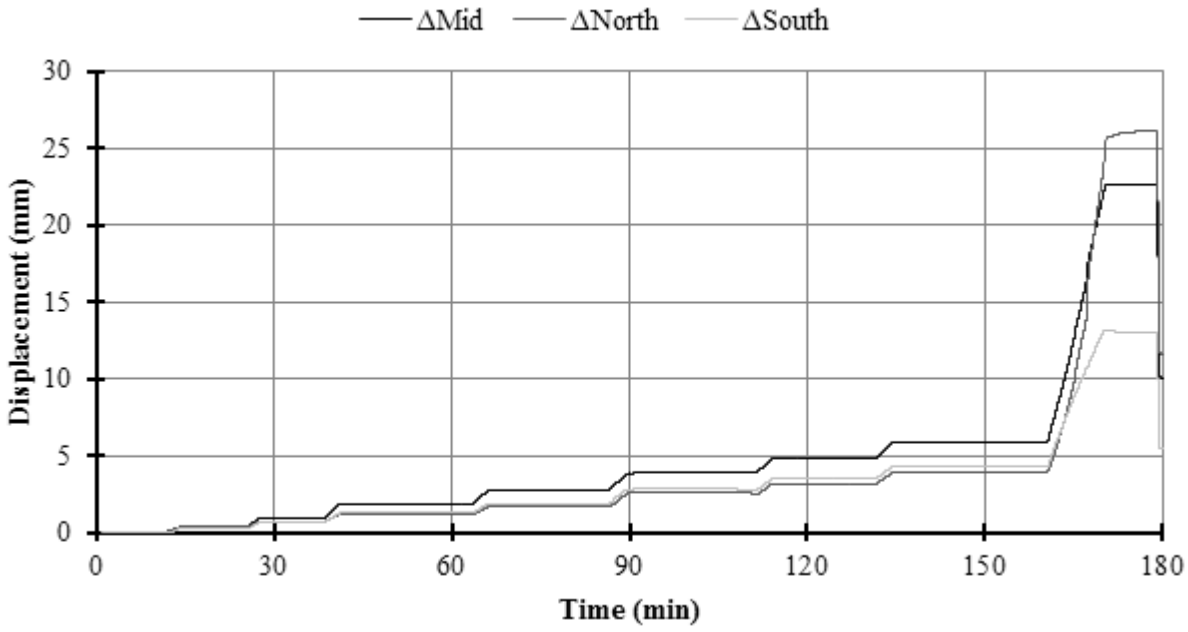

Figure E.192: BM12-s230 Plot of Displacement vs Time

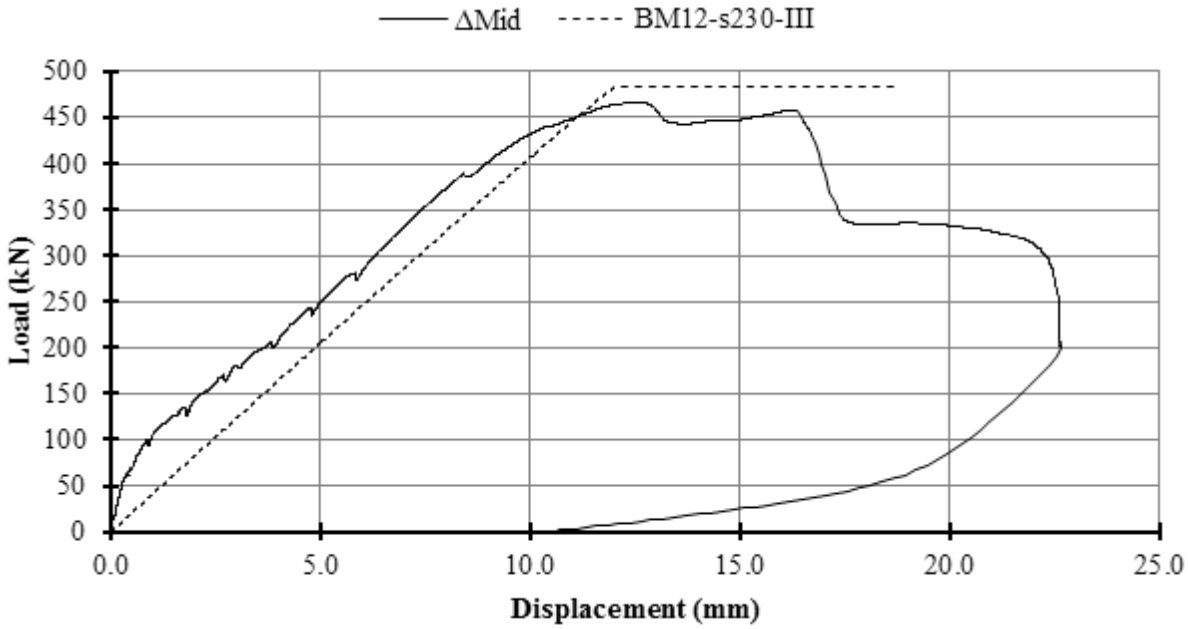

Figure E.193: BM12-s230 Plot of Load vs Displacement

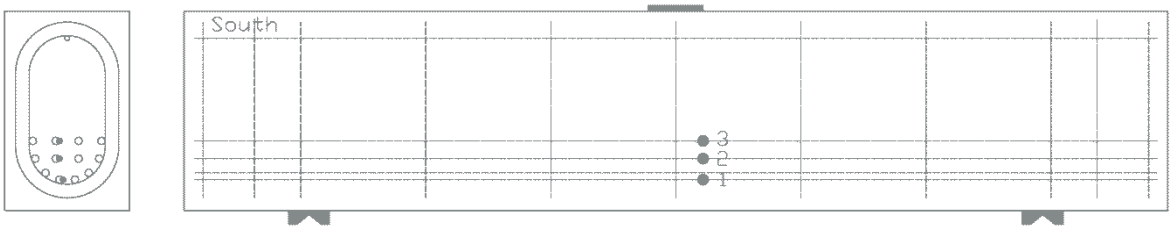

Figure E.194: BM12-s230 Schematic of Mid-Span Strain Gauge Locations

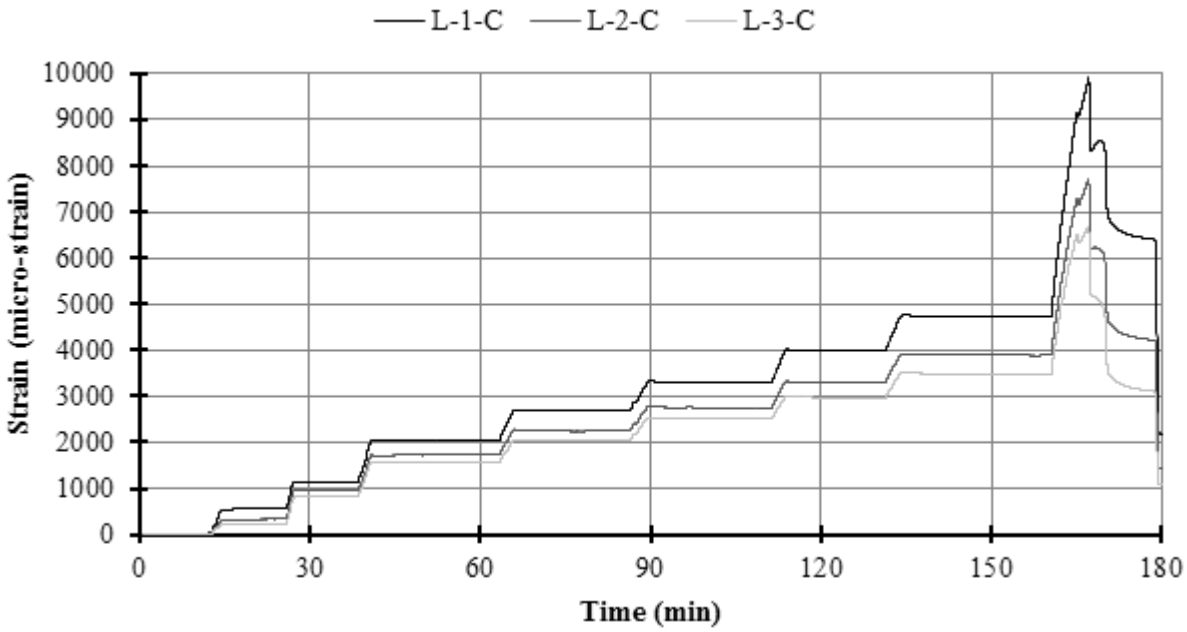

Figure E.195: BM12-s230 Plot of Strain vs Time on Longitudinal Bars at Mid-Span

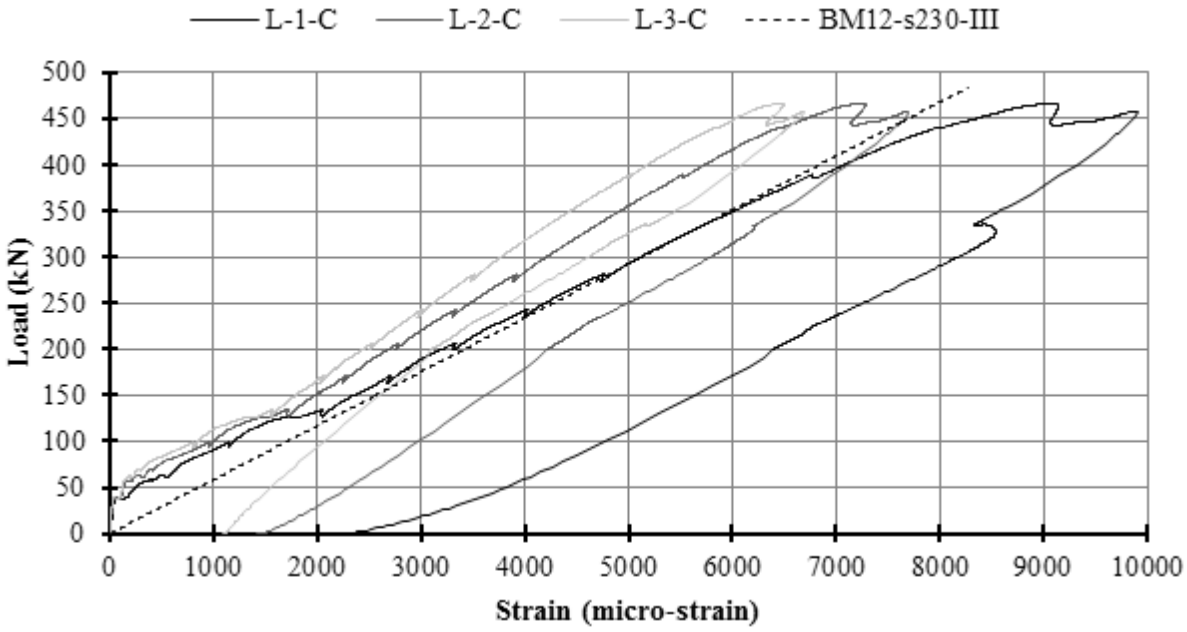

Figure E.196: BM12-s230 Plot of Load vs Strain on Longitudinal Bars at Mid-Span

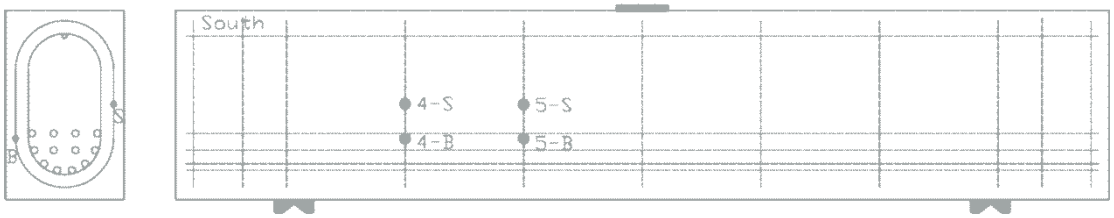

Figure E.197: BM12-s230 Schematic of Stirrup Strain Gauge Locations

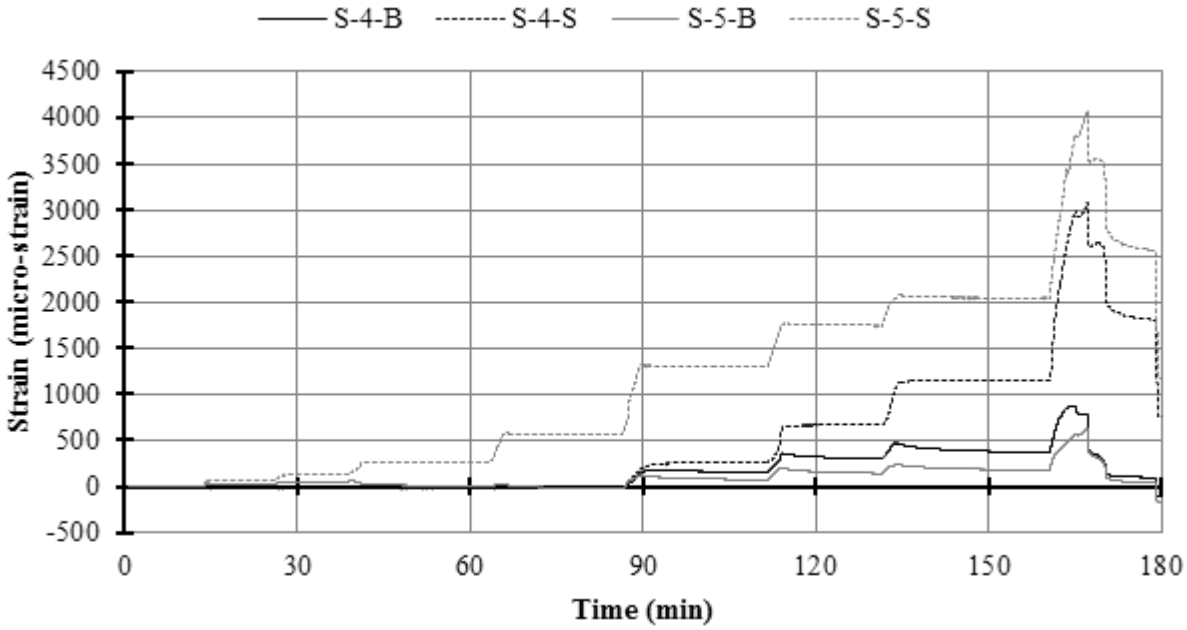

Figure E.198: BM12-s230 Plot of Strain vs Time on Stirrups

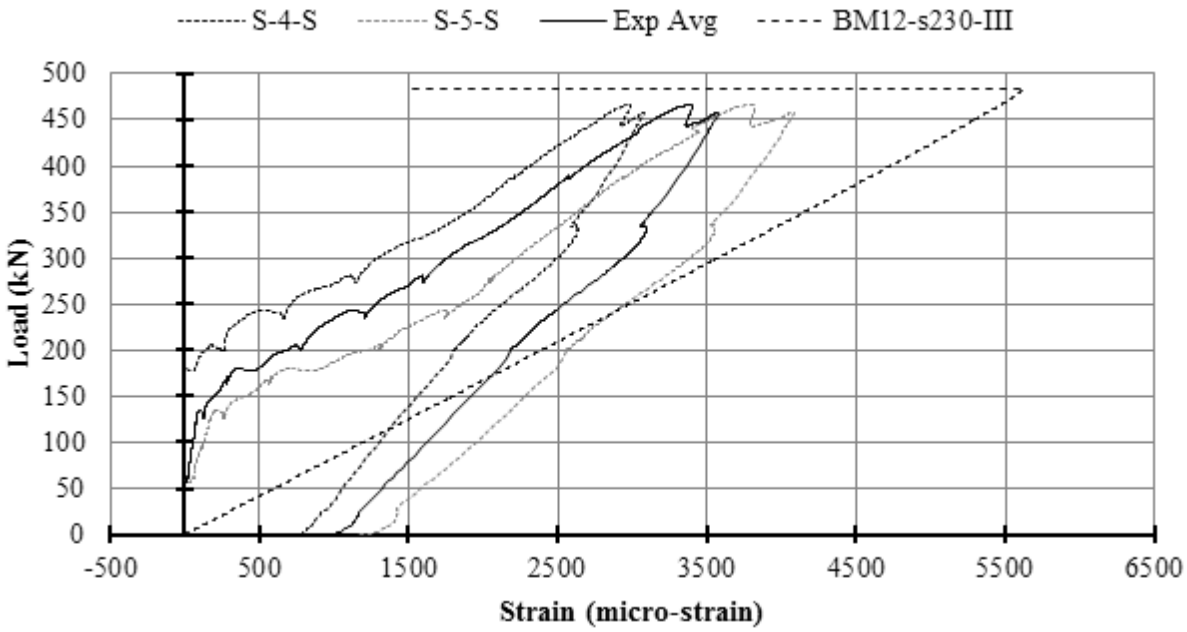

Figure E.199: BM12-s230 Plot of Load vs Strain on Stirrups

A plot with all stirrup strain gauges may be found in the Results Chapter.

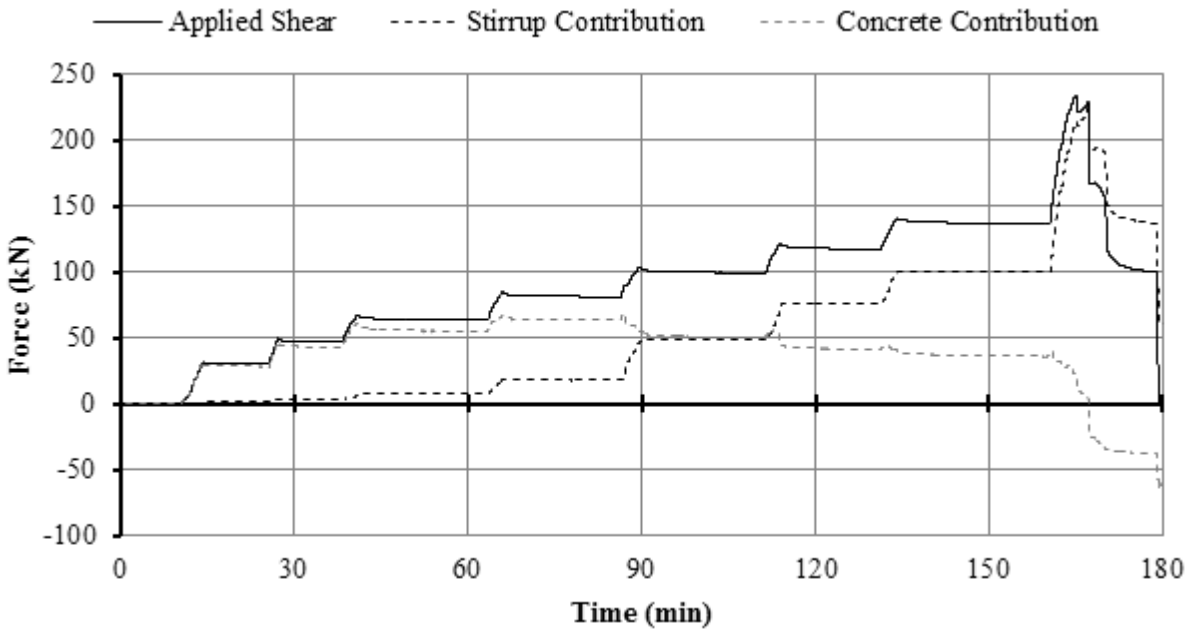

Figure E.200: BM12-s230 Plot of Shear Contribution vs Time

E.13.1 BM12-s230 Photographs

Figure E.201: BM12-s230 Rebar Cage Elevation Photo
Top framing bar not pictured.

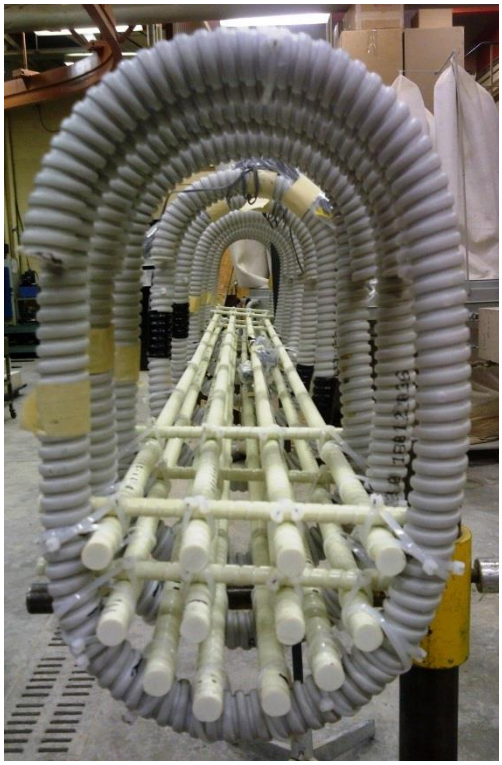

Figure E.202: BM12-s230 Rebar Cage Cross-Section Photo
Top framing bar not pictured.

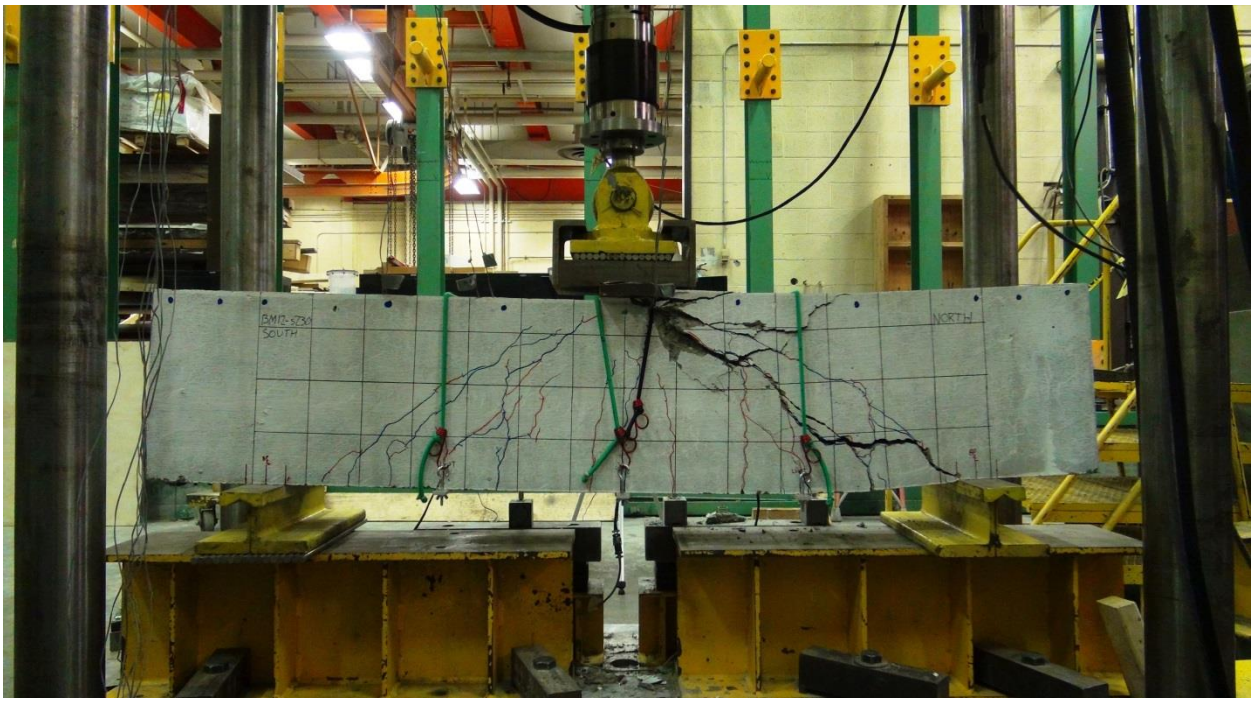

Figure E.203: BM12-s230 Alternative Photo of Entire Beam Under Load After Testing

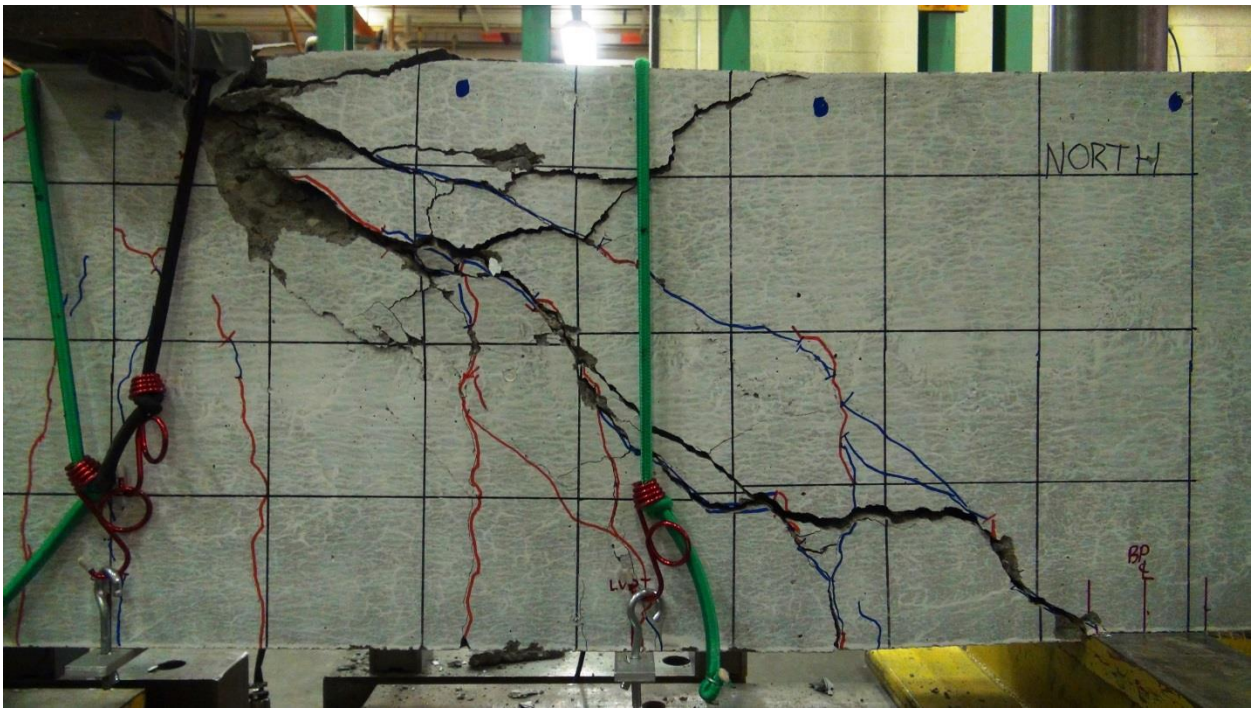

Figure E.204: BM12-s230 Close-up Photo of Failure

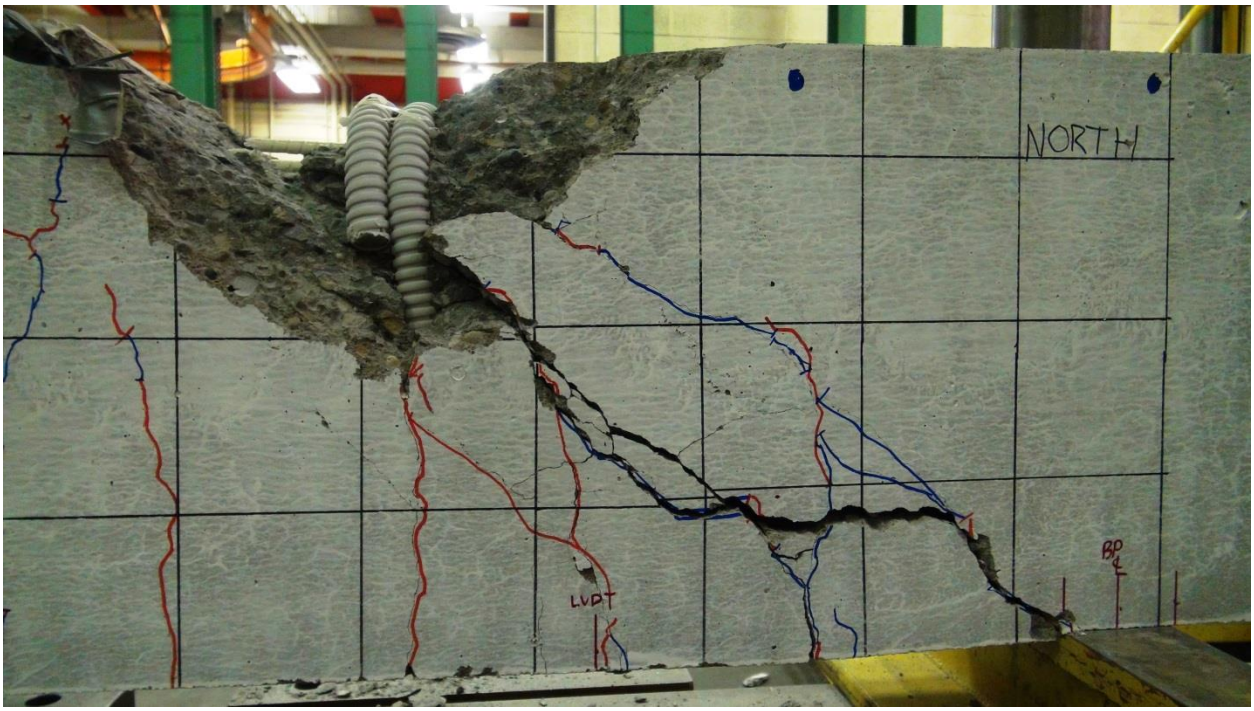

Figure E.205: BM12-s230 Close-up Photo of Failure with Spalled Concrete Removed with Stirrup 7 Exposed

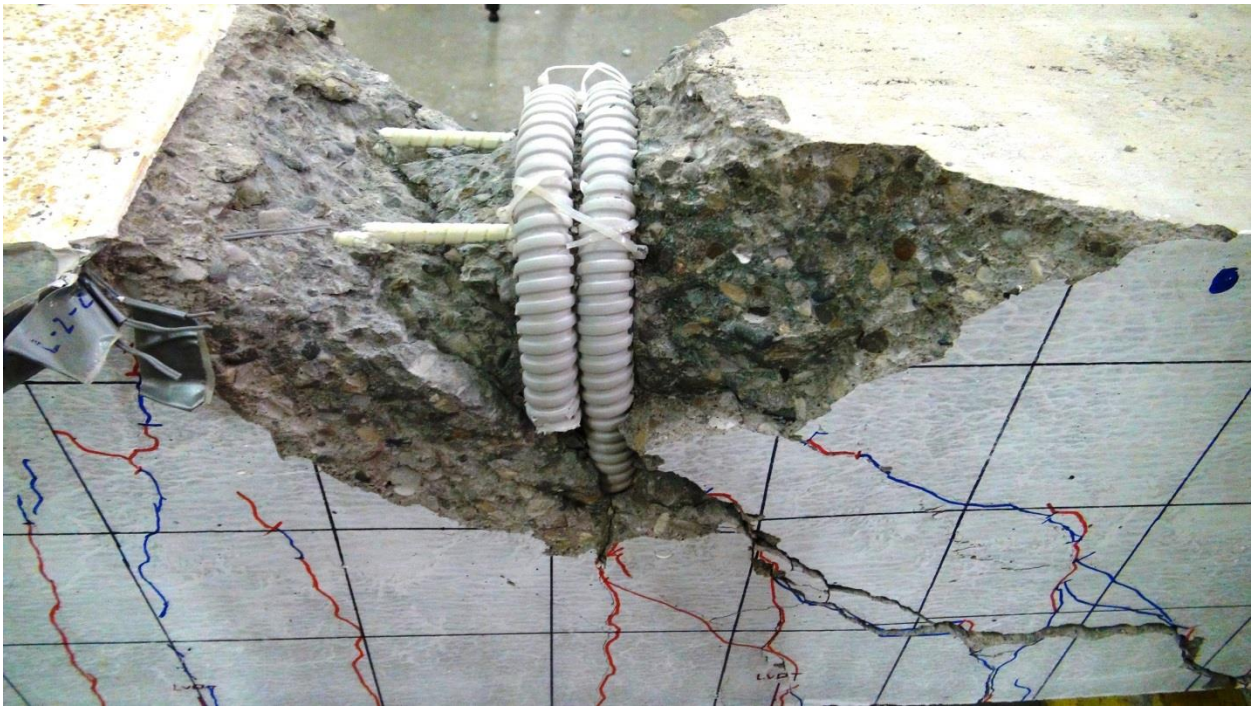

Figure E.206: BM12-s230 Close-up Photo of Exposed Stirrup 7

E.14 BM16-s230

This was the eleventh beam tested. The displacement controlled rate was 0.272 mm/min until the first crack measurement. The rate was then increased to 0.4 mm/min until after the final crack measurement after which the rate was increased to 1.0 mm/min.

The beam failed in shear-compression / strut-crushing along a plane that ran diagonally from the load plate to the north bearing plate. Peak load was unremarkable. A sudden large drop in load occurred a minute after peak load. The drop in load was preceded by flaking concrete and an occasional popping noise consistent with concrete fracture. The drop in load was accompanied by a loud banging noise, a jolting movement, and the ejection of large concrete projectiles. This was the most catastrophic failure witnessed in the testing program.

Peak load occurred at 450.8 kN and 21.95 mm of displacement, and failure took place in the un-instrumented north shear span 96 days after casting.

Strain gauges L-1-C and L-2-C failed before peak load; all other strain gauges functioned adequately during the test.

Two stirrups in the failed shear span were extracted to investigate if they had ruptured. The condition of the two stirrups was unremarkable. A portion of the straight part of stirrup 8 showed dramatic fibre waving, though it did not seem to have an effect on beam strength.

Issues

The north span LVDT gauge recorded a constant displacement until the jolt at peak load. No explanation for this is provided; the spring on the LVDT should have kept the core snug against the aluminum bar. This data was not included in the results.

The mid-span displacement gauge recorded two quick decreases in displacement which took place within the first ten minutes of testing. The reason for this is uncertain; however, it was thought that a grain of sand worked itself free from between the aluminum bar and the bottom of the beam. This would have caused the LVDT core to retract slightly. The data was corrected as indicated in the graphs, but a trace of the original data is still shown. This was thought to have a minimum effect on results.

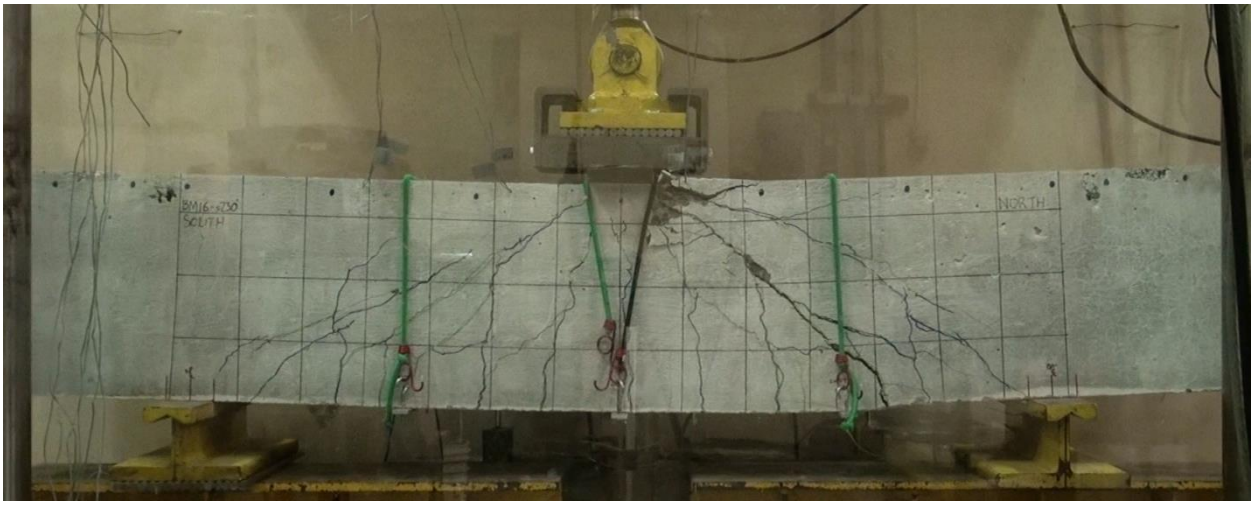

Figure E.207: BM16-s230 At Peak Load

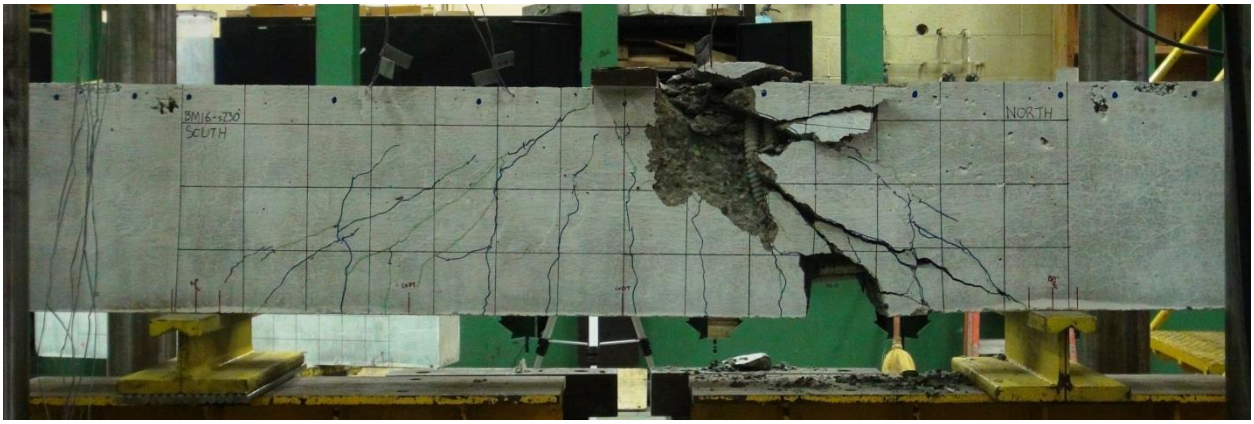

Figure E.208: BM16-s230 After Testing

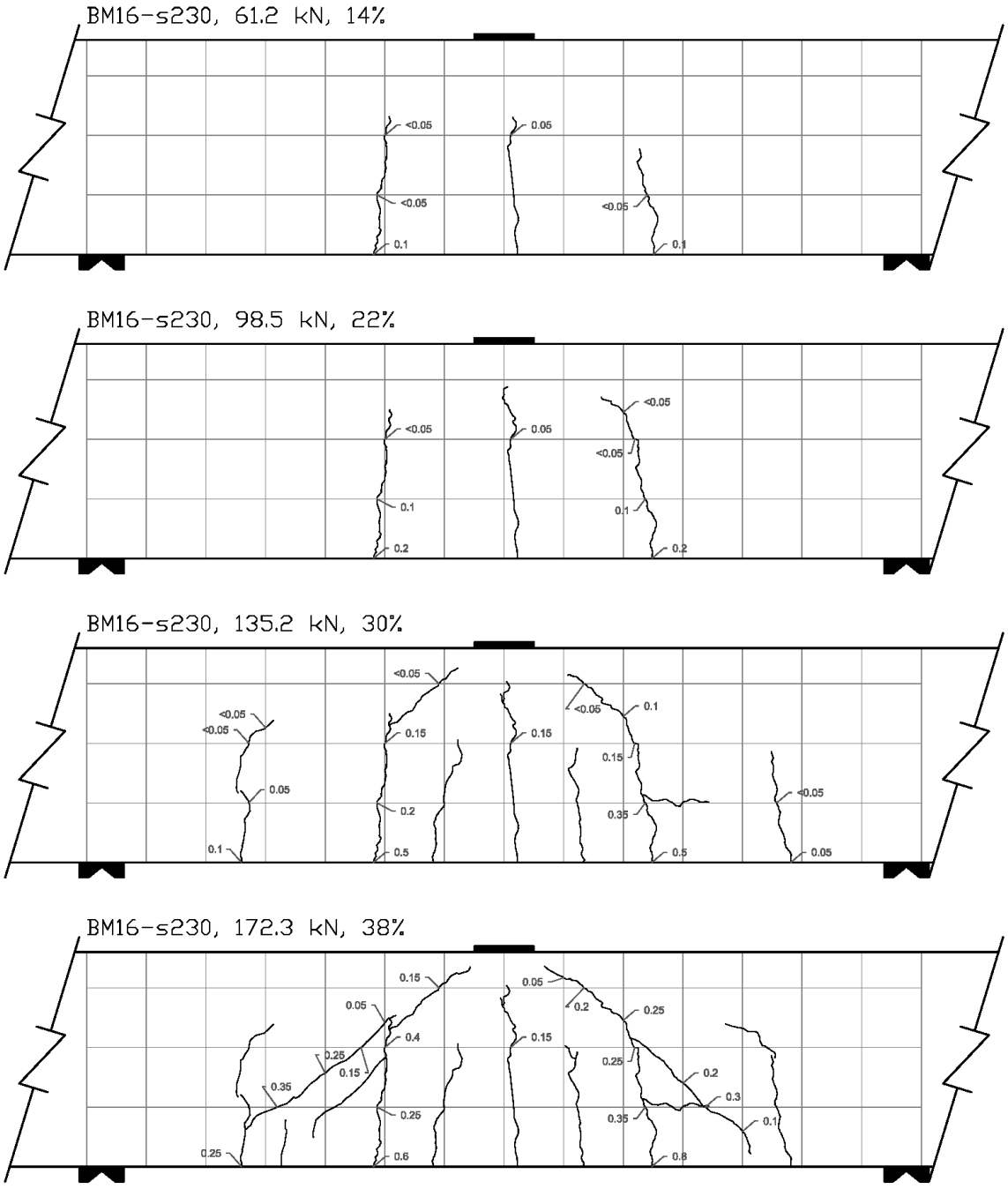

Figure E.209: BM16-s230 Crack Diagram 1

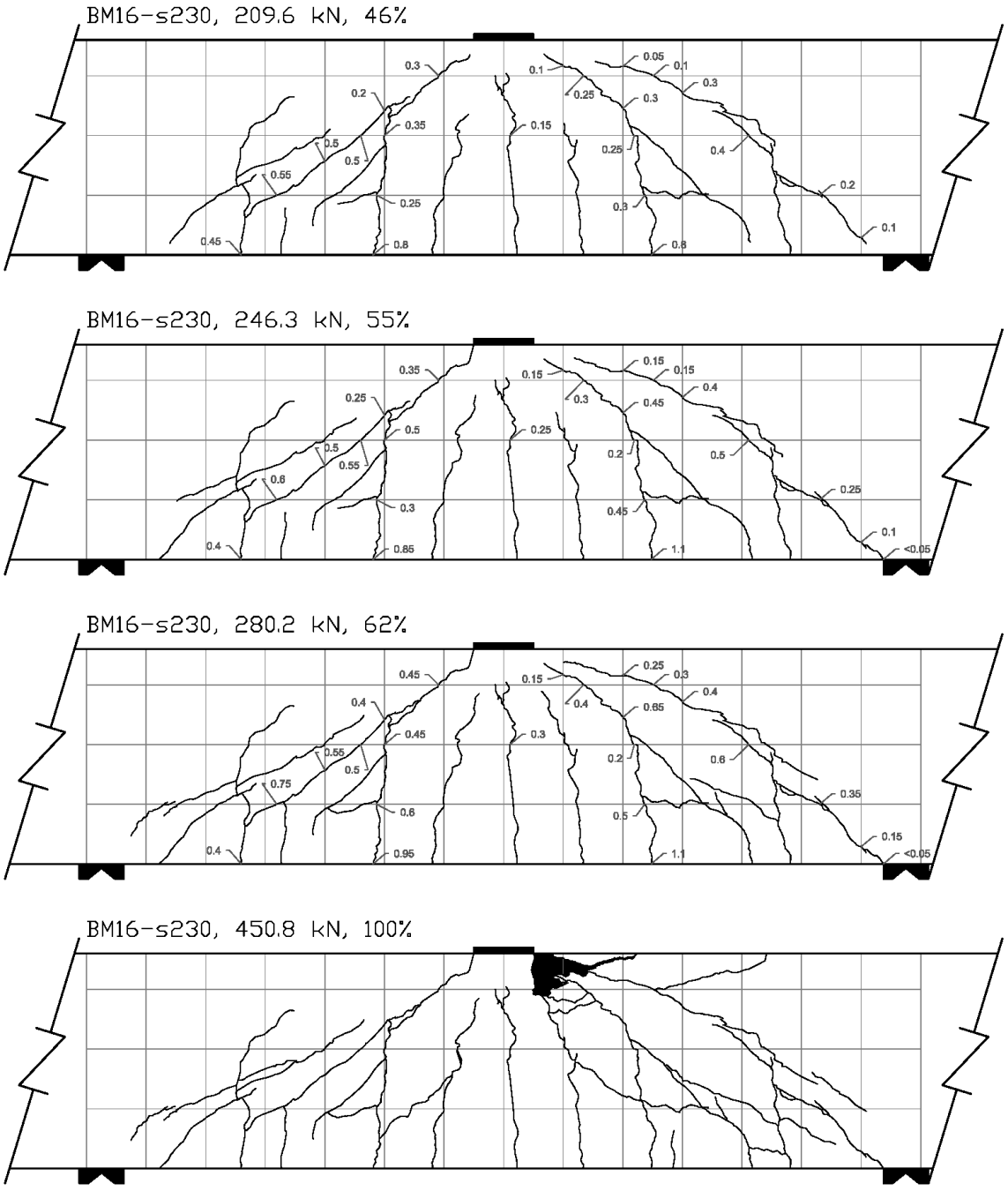

Figure E.210: BM16-s230 Crack Diagram 2

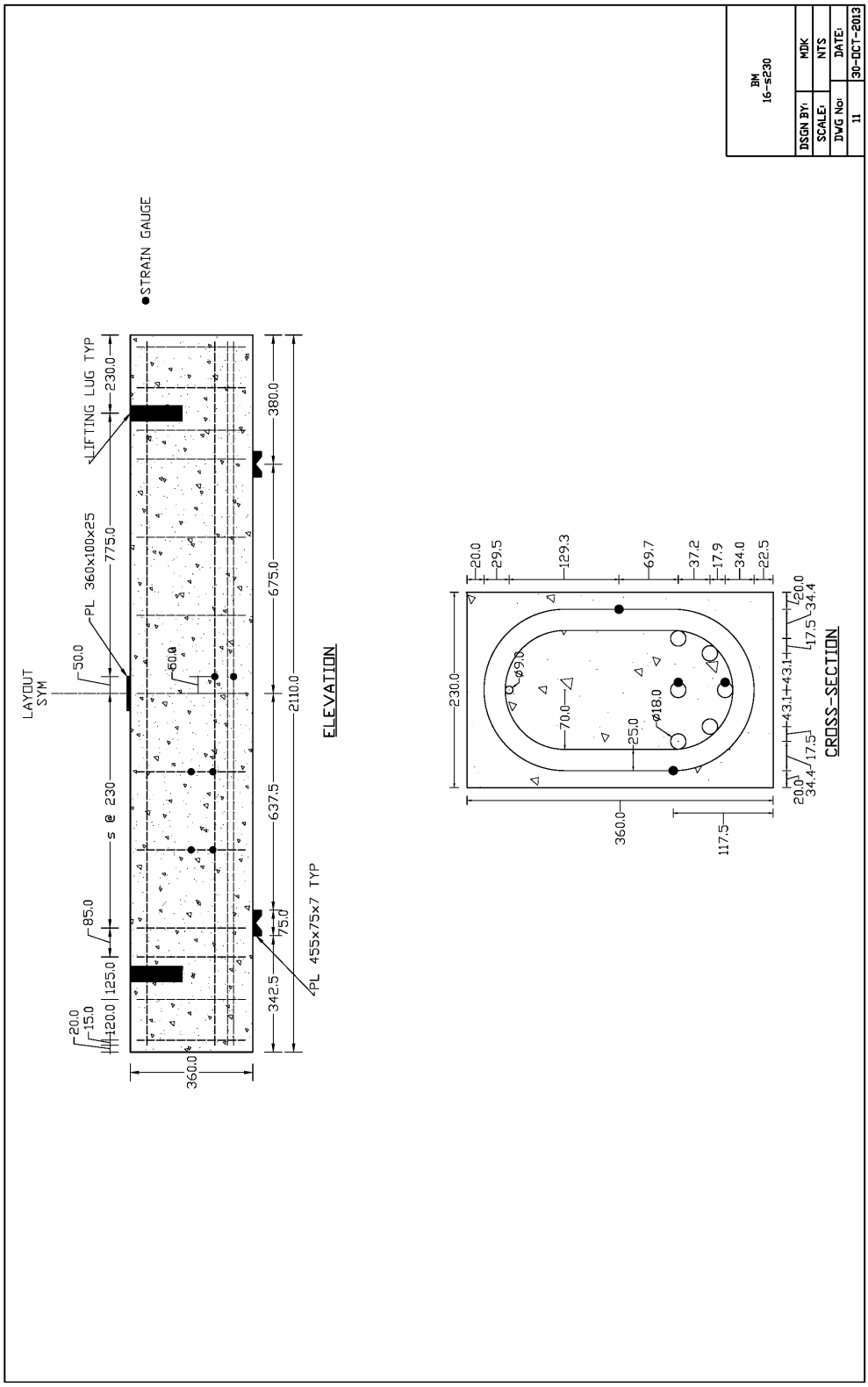

Figure E.211: BM16-s230 Schematic Drawing

Table E.11: As-Designed and As-Constructed Parameter Chart for BM16-s230

Parameter	As-Designed	As-Constructed
Beam Properties		
f'_c (MPa)	45	47.3 (28 day)
b (mm)	230	233.5**
h (mm)	360	360.0**
l (mm)	2110	-
d (mm)	270	271.6***
a/d	2.5	-
ρ_F (%)	1.94	-
ρ_v (%)	1.19	-
Longitudinal Bar Properties		
f_{Fu} (MPa)	1000	-
E_F (GPA)	64	-
A_F (mm^2)	201	-
n_{Bar} (amnt)	6	-
ε_{Fu} (%)	2.61*	-
Stirrup Properties		
$f_{Fu,straight}$ (MPa)	900	-
$f_{Fu,bent}$ (MPa)	550	-
E_F (GPA)	50	-
A_F (mm^2)	314.2	-
r_{Bend} (mm)	70	-

** Rupture strain was only provided for dia. 16 bars; this value was assumed valid for all bars.*
*** Measured at midpoint of the failed shear span before testing, width is an average of top and bottom.*
**** Based on an average from measured bar depths before pour on north and south ends.*

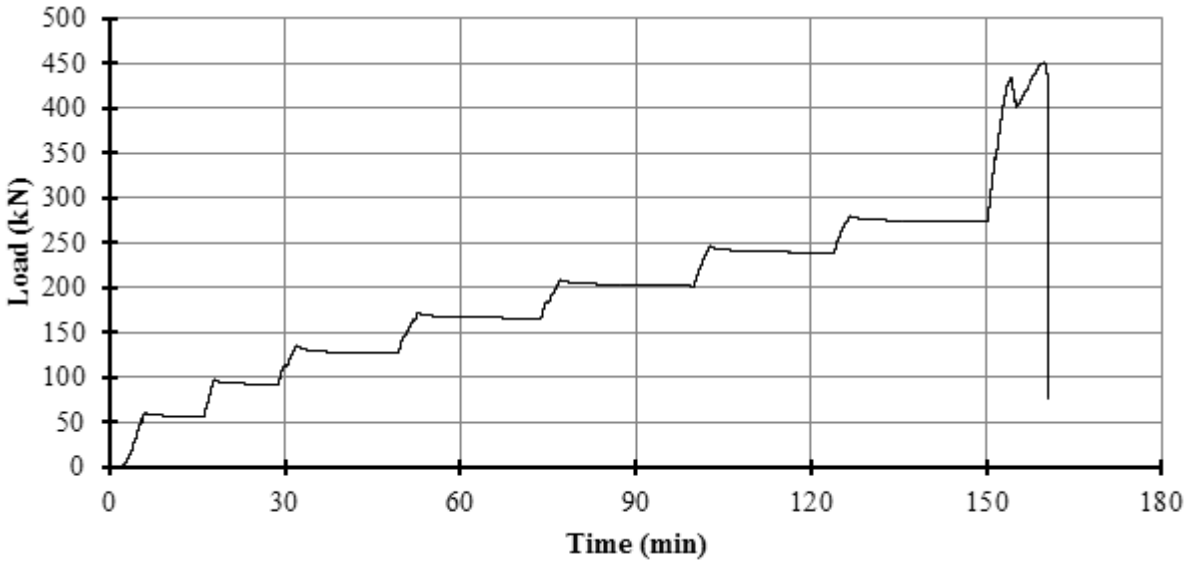

Figure E.212: BM16-s230 Plot of Load vs Time

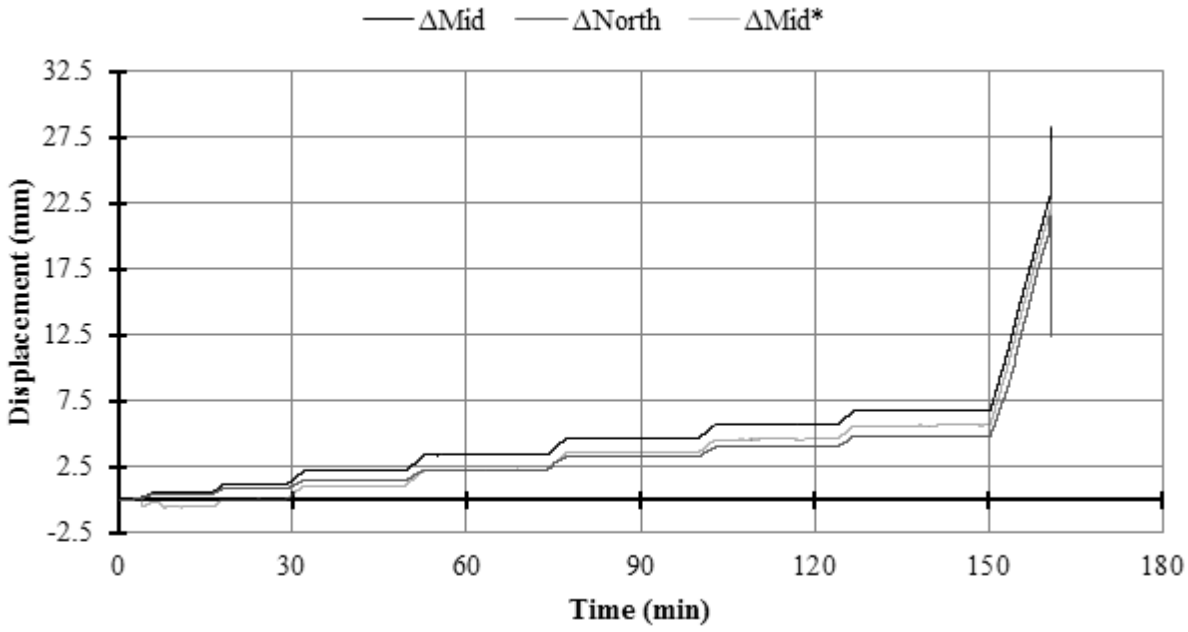

Figure E.213: BM16-s230 Plot of Displacement vs Time

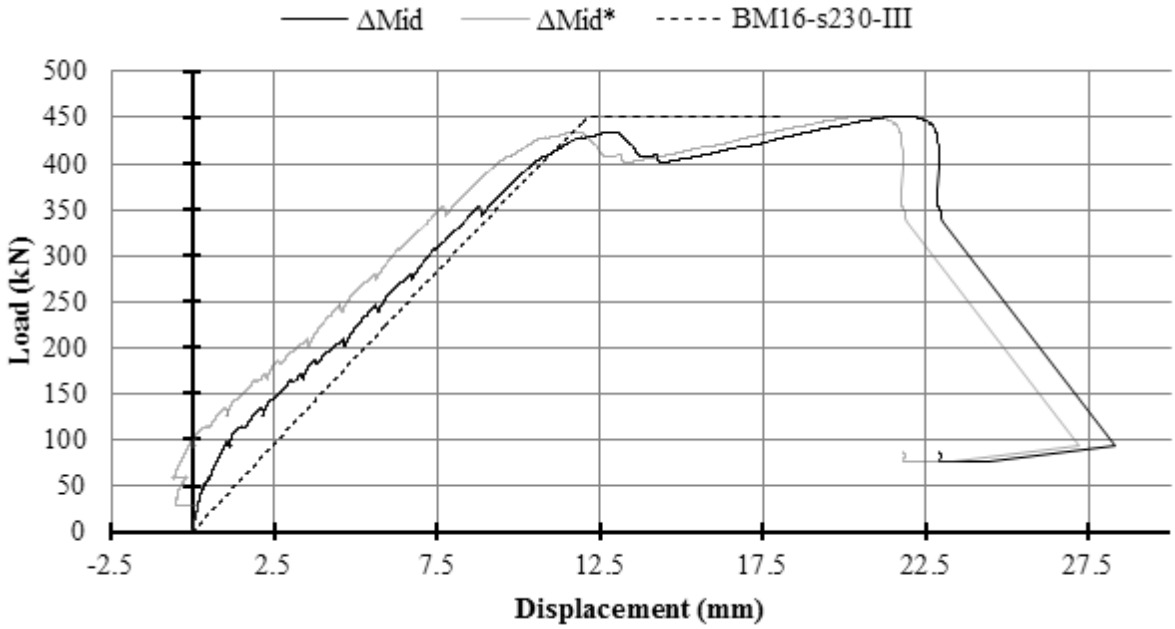

Figure E.214: BM16-s230 Plot of Load vs Displacement

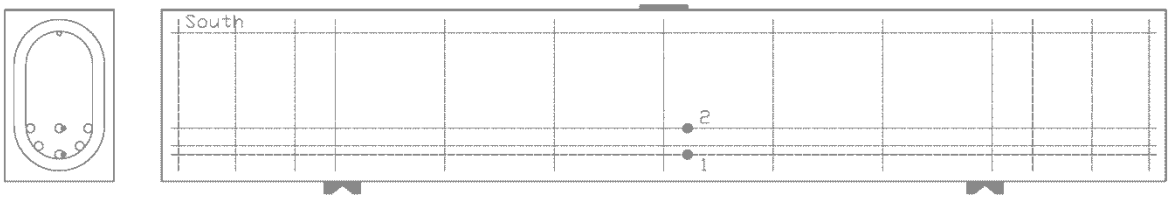

Figure E.215: BM16-s230 Schematic of Mid-Span Strain Gauge Locations

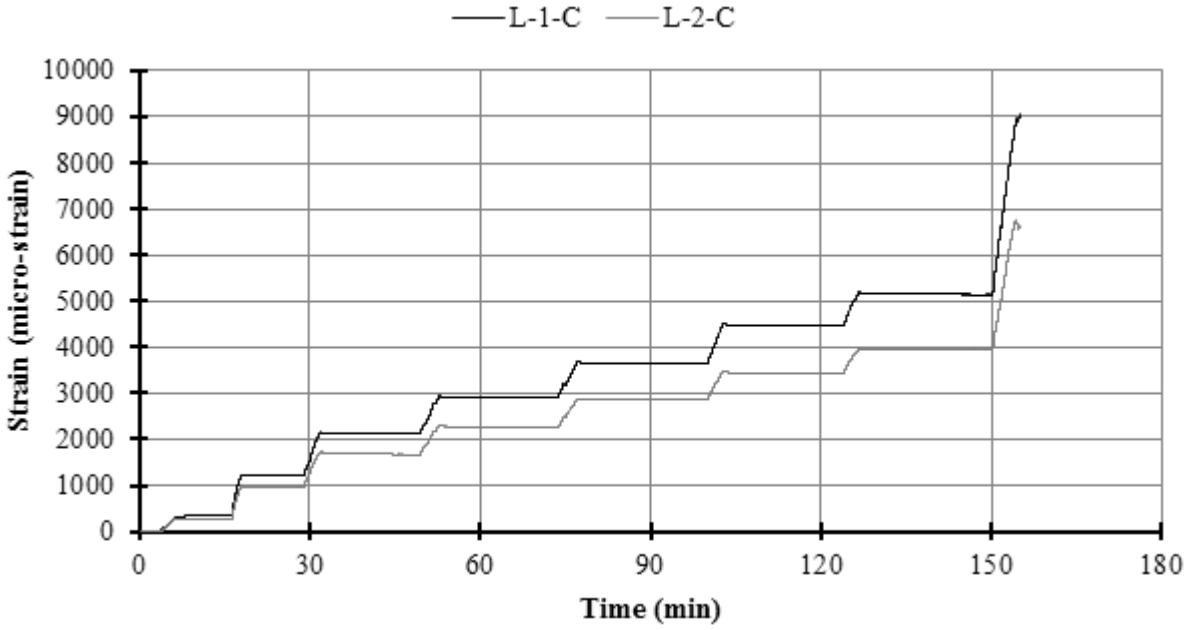

Figure E.216: BM16-s230 Plot of Strain vs Time on Longitudinal Bars at Mid-Span

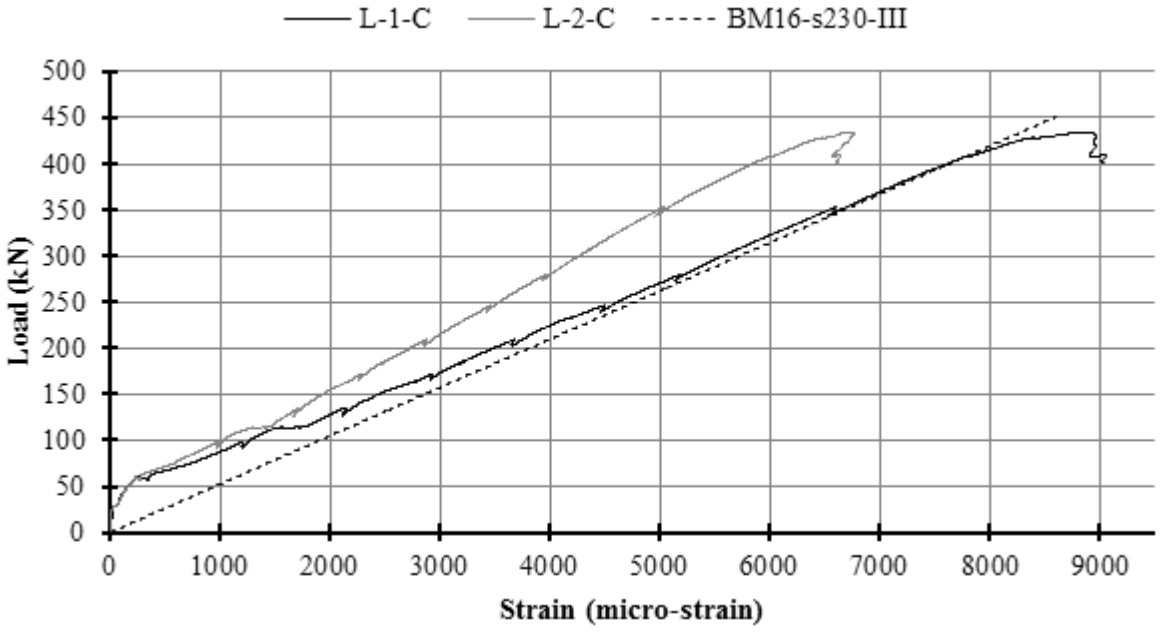

Figure E.217: BM16-s230 Plot of Load vs Strain on Longitudinal Bars at Mid-Span

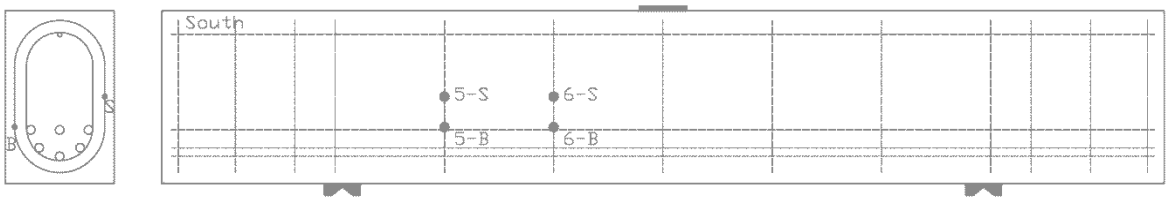

Figure E.218: BM16-s230 Schematic of Stirrup Strain Gauge Locations

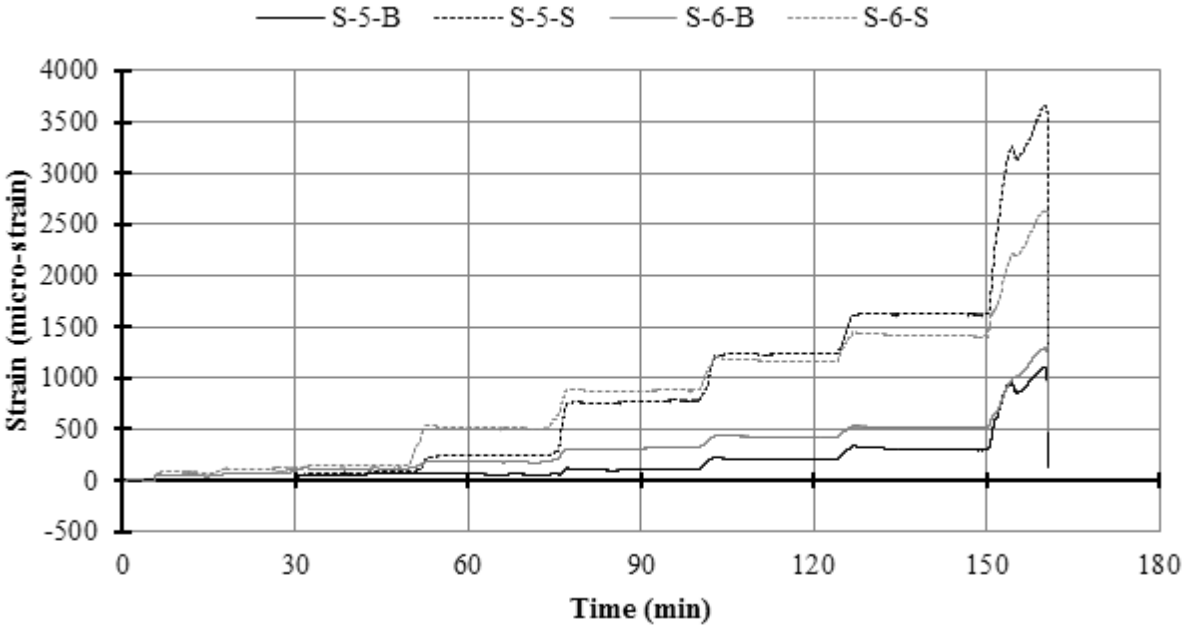

Figure E.219: BM16-s230 Plot of Strain vs Time on Stirrups

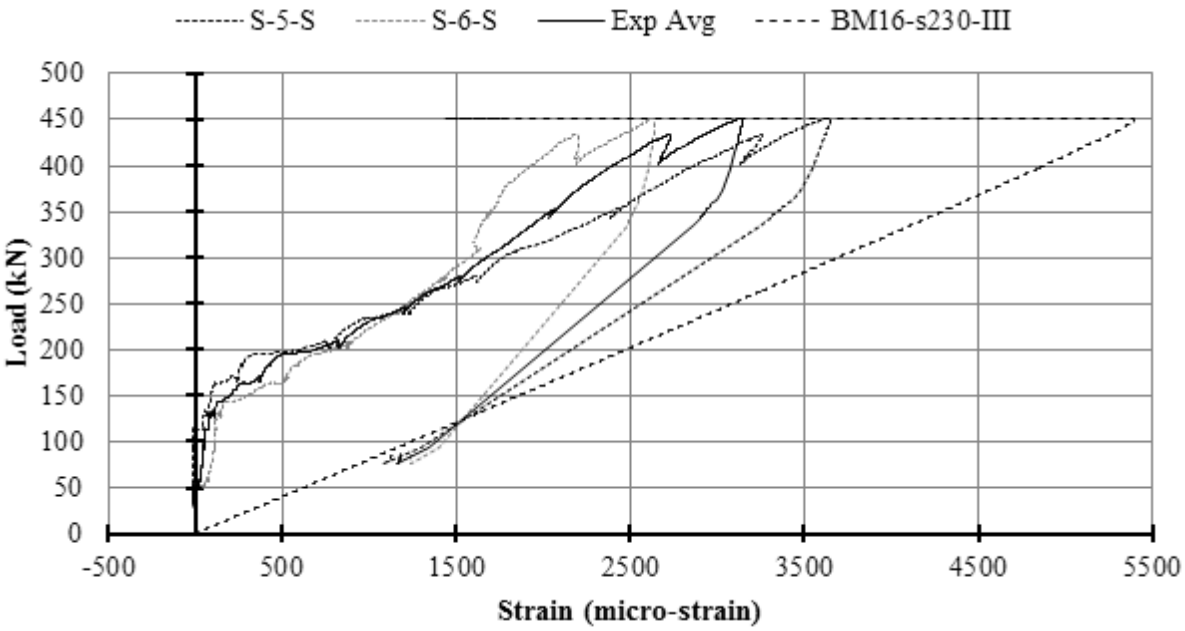

Figure E.220: BM16-s230 Plot of Load vs Strain on Stirrups

A plot with all stirrup strain gauges may be found in the Results Chapter.

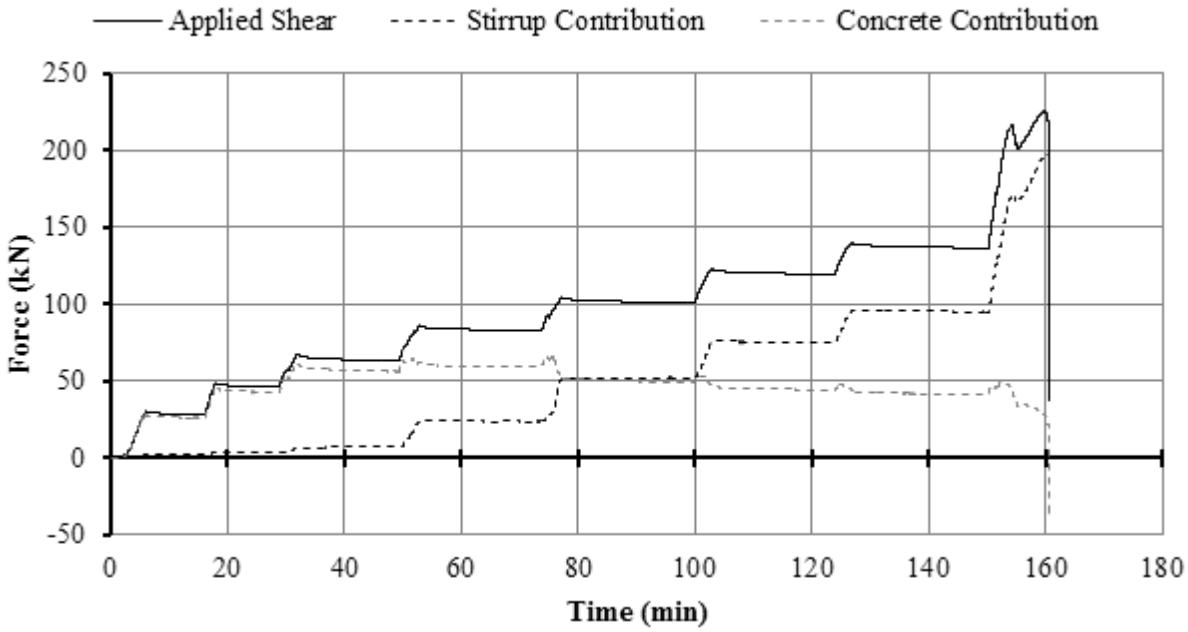

Figure E.221: BM16-s230 Plot of Shear Contribution vs Time

E.14.1 BM16-s230 Photographs

Figure E.222: BM16-s230 Rebar Cage Elevation Photo
Top framing bar not pictured.

Figure E.223: BM16-s230 Rebar Cage Cross-Section Photo
Top framing bar not pictured.

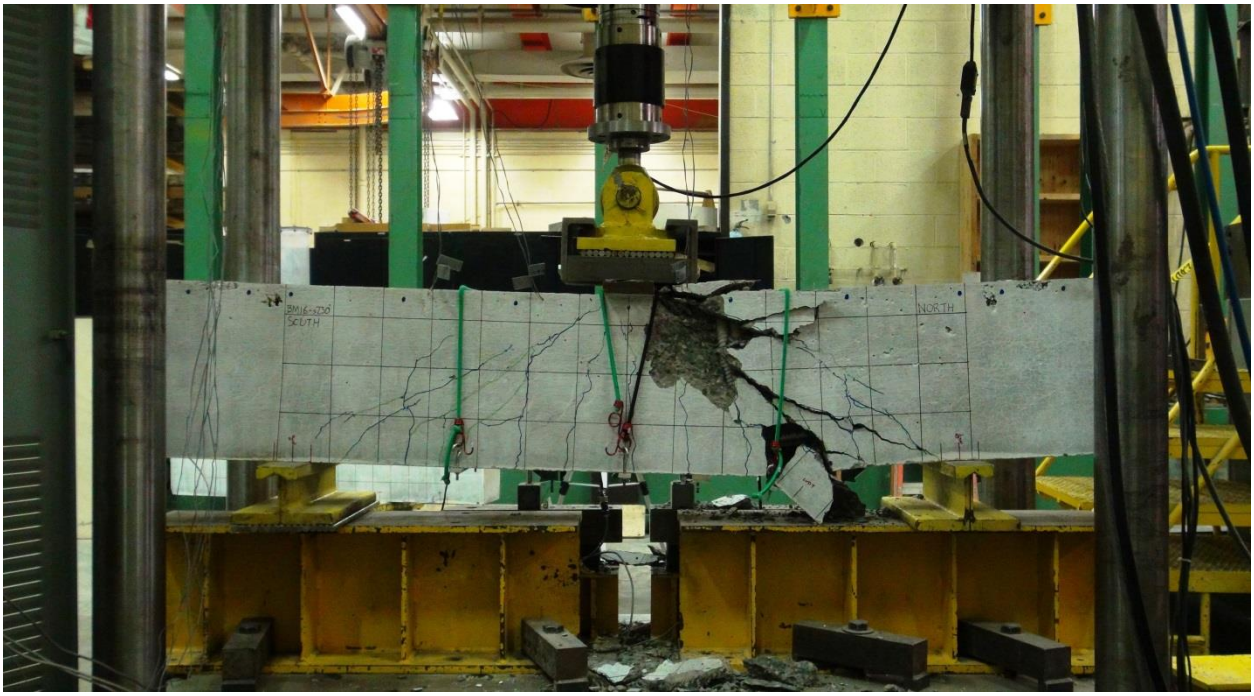

Figure E.224: BM16-s230 Alternative Photo of Entire Beam Under Load After Testing

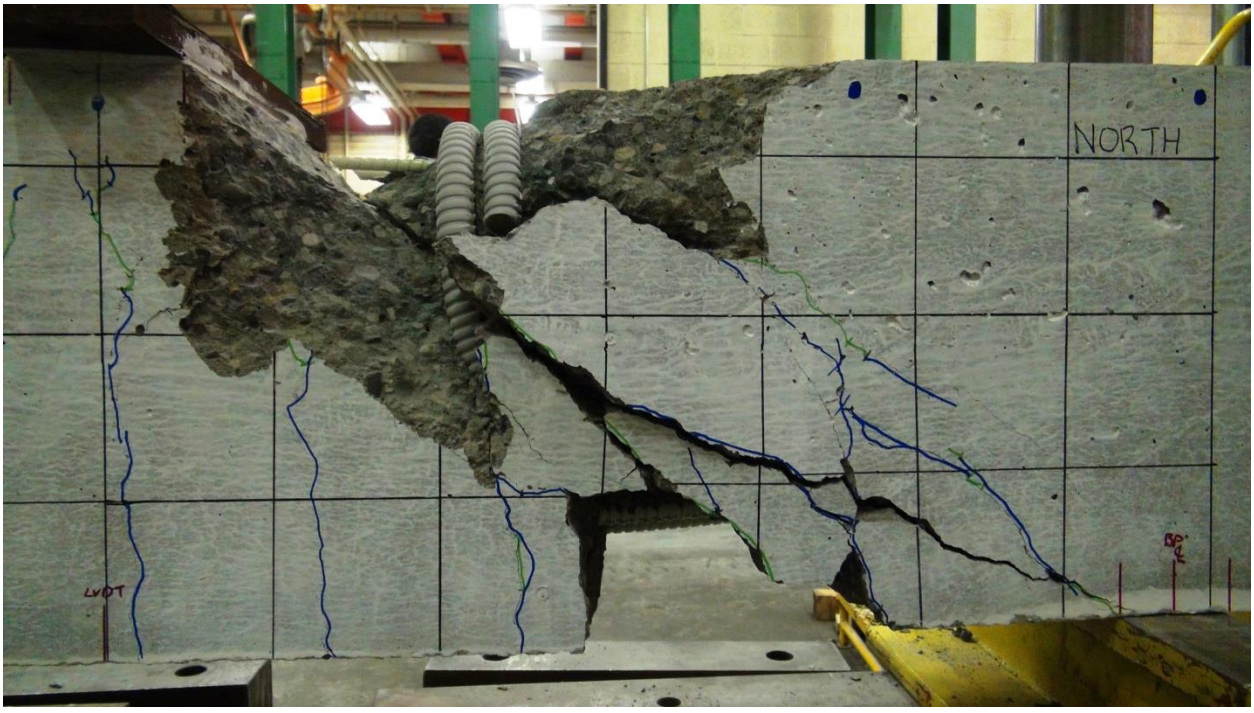

Figure E.225: BM16-s230 Close-up Photo Failure with Spalled Concrete Removed with Stirrup 8 Exposed

Figure E.226: BM16-s230 Photo of Exposed Stirrup 9 and Longitudinal Bars

Figure E.227: BM16-s230 Photo of Exposed Longitudinal Bars and Tensile Splitting Cracks

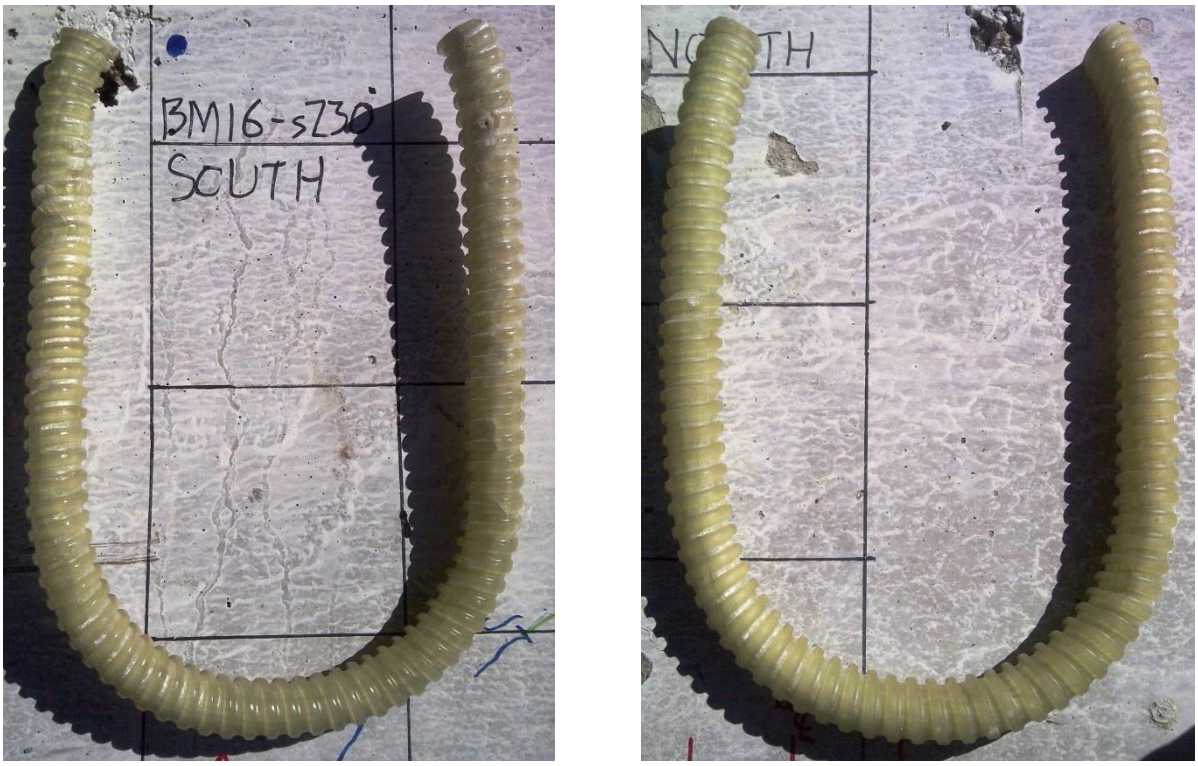

Figure E.228: BM16-s230 Stirrup 8 & 9 Respectively

Figure E.229: BM16-s230 Fibre Waving on Stirrup 8

E.15 BM25-s230

This was the tenth beam tested. The displacement controlled loading rate was 0.272 mm/min until the first crack measurement. The rate was then increased to 0.4 mm/min until after the final crack measurement at which point the rate was increased to 1.0 mm/min.

The beam failed in shear-compression / strut-crushing along a plane which ran diagonally from the load plate to the north bearing plate. Peak load was accompanied by some flaking of concrete, but was not accompanied by loud noises, perceptible movements, or the ejection of concrete projectiles.

Peak load occurred at 444.0 kN and 35.65 mm of displacement, and failure took place in the un-instrumented north shear span 92 days after casting.

Strain gauges L-1A-C, L-1B-C, and S-6-B failed before peak load; all other strain gauges functioned adequately during the test.

Issues

At different points during testing each of the three LVDTs stopped recording data properly. After peak load the core of the mid-span LVDT fell out, so the mid-span displacement data was augmented by appending the relative displacement of the test frame actuator to the mid-span LVDT data.

The north span LVDT also fell out; its displacement data was not augmented. The south span LVDT recorded a displacement spike and then recorded a constant displacement from that point on. The issues with the north and south span gauges are evident from the displacement-time graph.

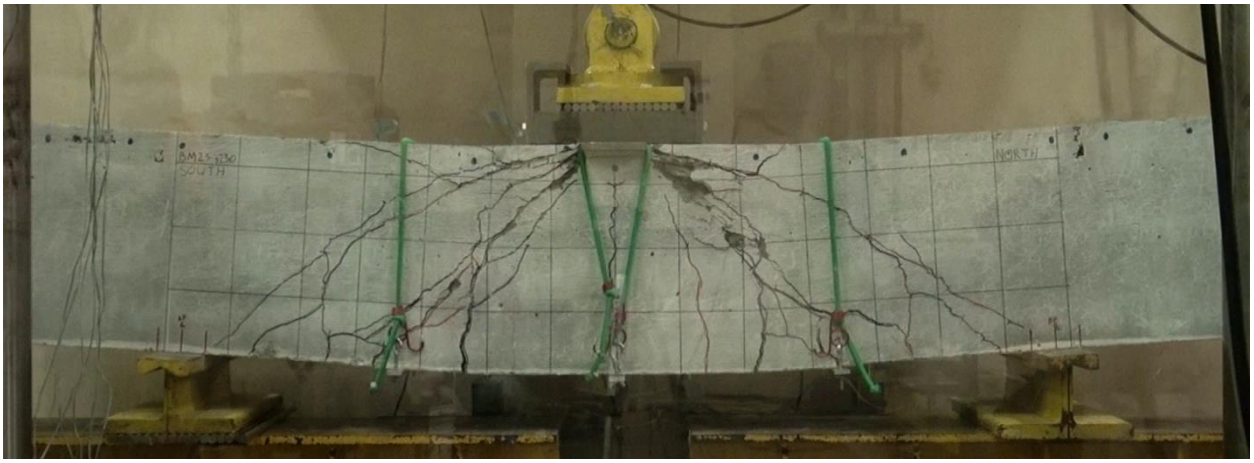

Figure E.230: BM25-s230 At Peak Load

Figure E.231: BM25-s230 After Testing

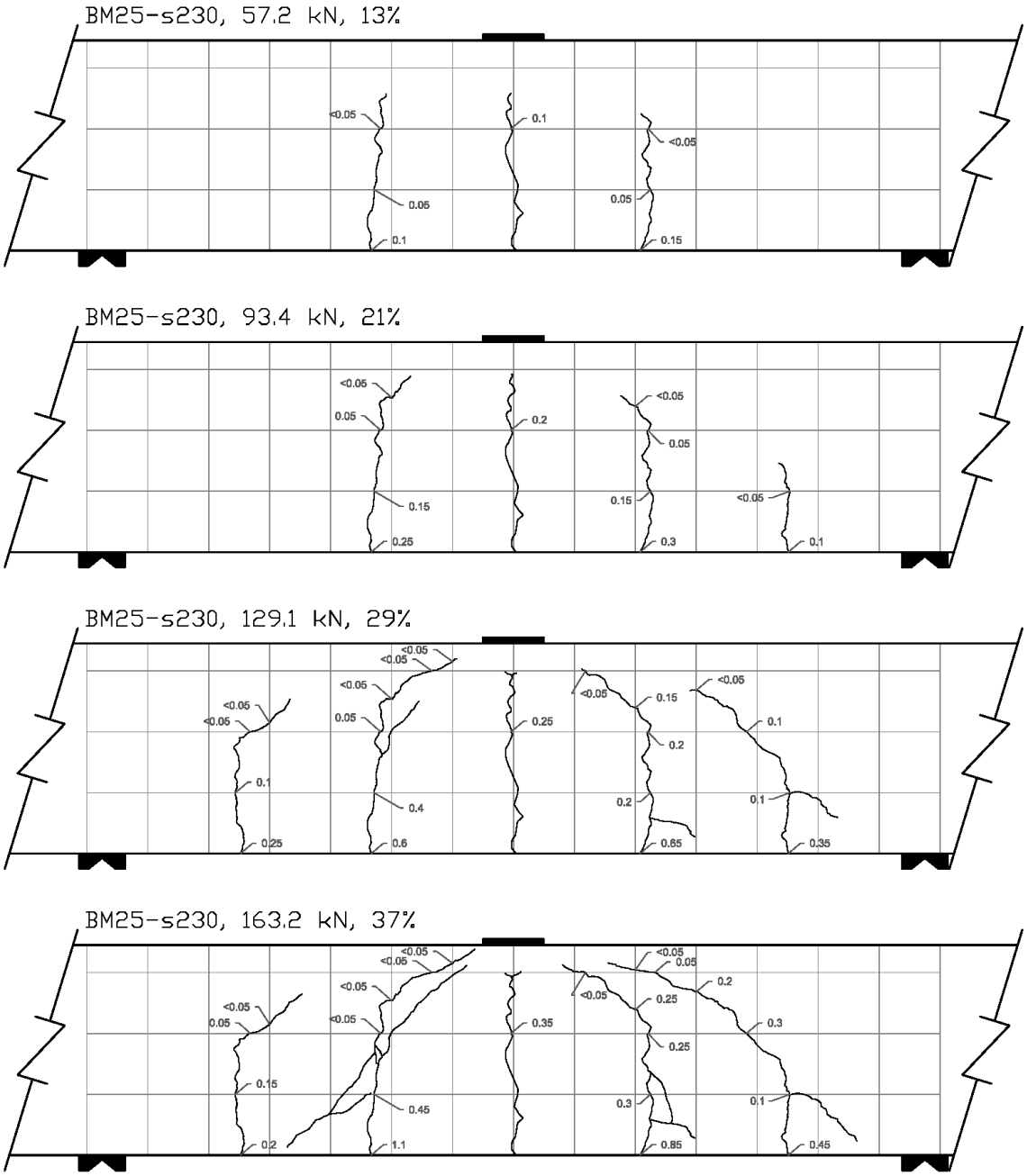

Figure E.232: BM25-s230 Crack Diagram 1

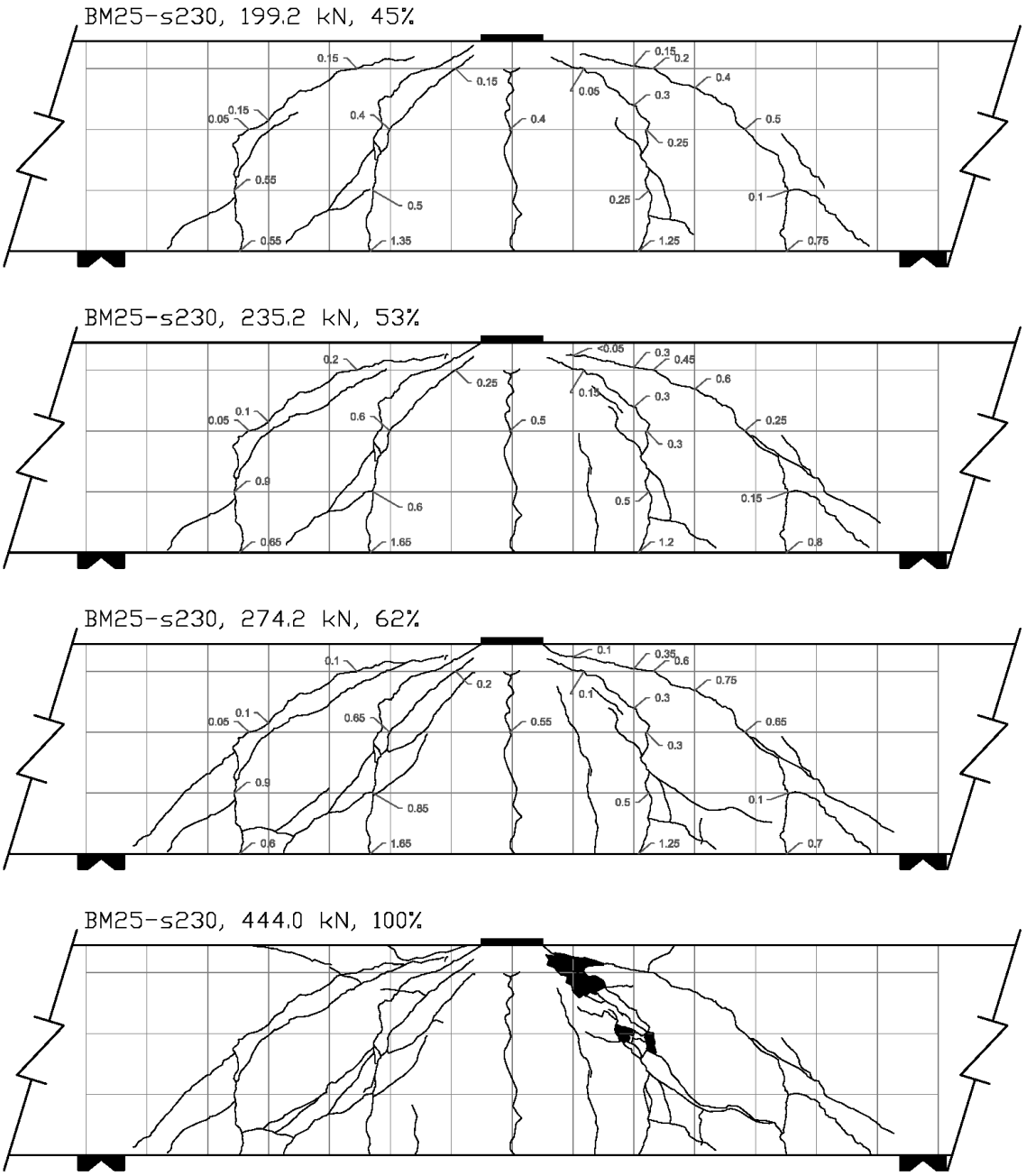

Figure E.233: BM25-s230 Crack Diagram 2

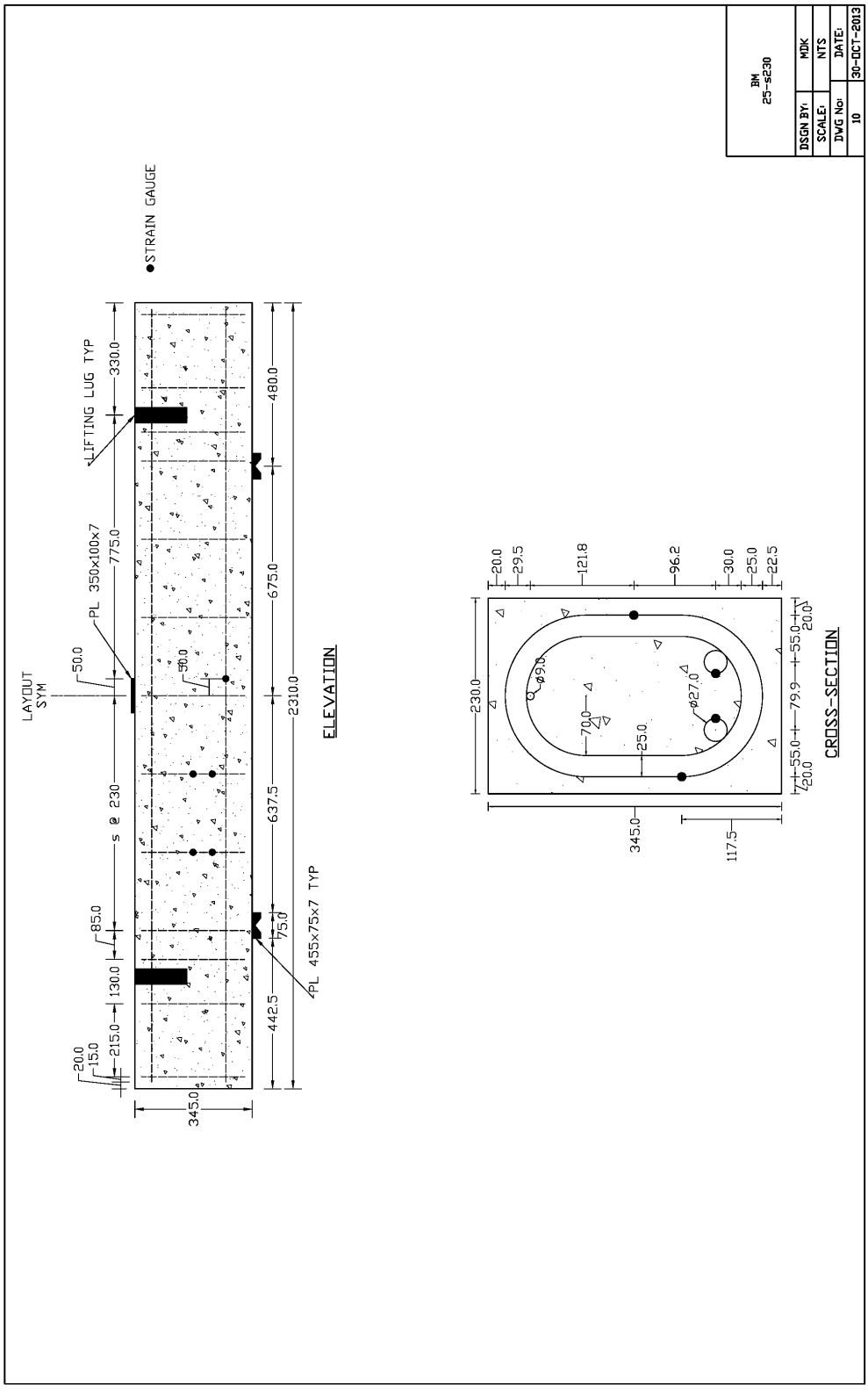

Figure E.234: BM25-s230 Schematic Drawing

Table E.12: As-Designed and As-Constructed Parameter Chart for BM25-s230

Parameter	As-Designed	As-Constructed
Beam Properties		
f'_c **(MPa)**	45	47.3 (28 day)
b **(mm)**	230	232.0**
h **(mm)**	345	348.0**
l **(mm)**	2310	-
d **(mm)**	270	273.0***
a/d	2.5	-
ρ_F **(%)**	1.58	-
ρ_v **(%)**	1.19	-
Longitudinal Bar Properties		
f_{Fu} **(MPa)**	1000	-
E_F **(GPA)**	60	-
A_F **(mm^2)**	491	-
n_{Bar} **(amnt)**	2	-
ε_{Fu} **(%)**	2.61*	-
Stirrup Properties		
$f_{Fu,straight}$ **(MPa)**	900	-
$f_{Fu,bent}$ **(MPa)**	550	-
E_F **(GPA)**	50	-
A_F **(mm^2)**	314.2	-
r_{Bend} **(mm)**	70	-

** Rupture strain was only provided for dia. 16 bars; this value was assumed valid for all bars.*
*** Measured at midpoint of the failed shear span before testing, width is an average of top and bottom.*
**** Based on an average from measured bar depths before pour on north and south ends.*

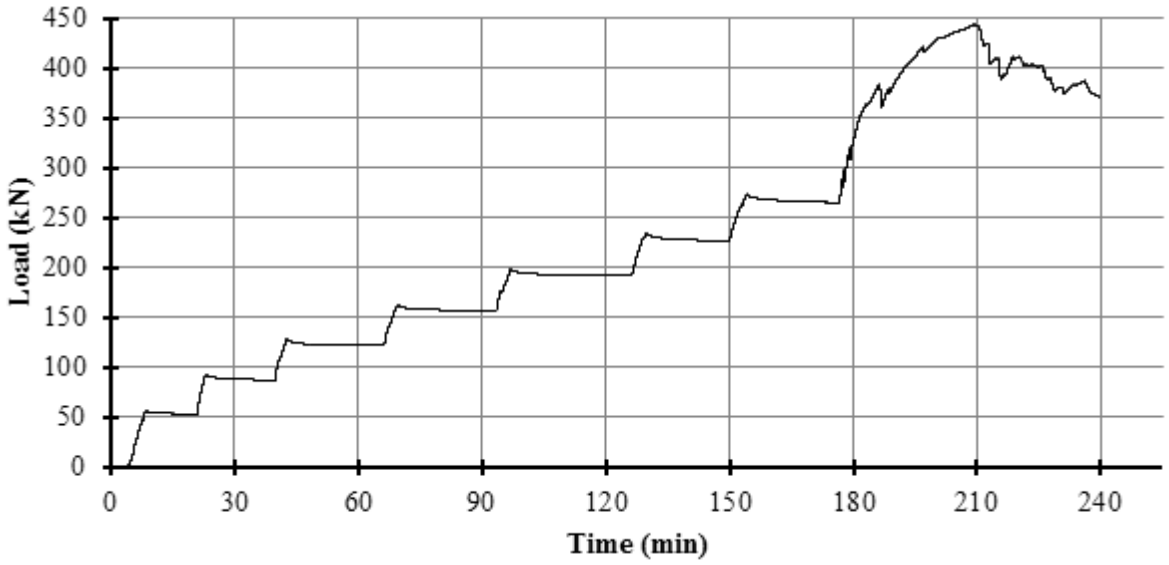

Figure E.235: BM25-s230 Plot of Load vs Time

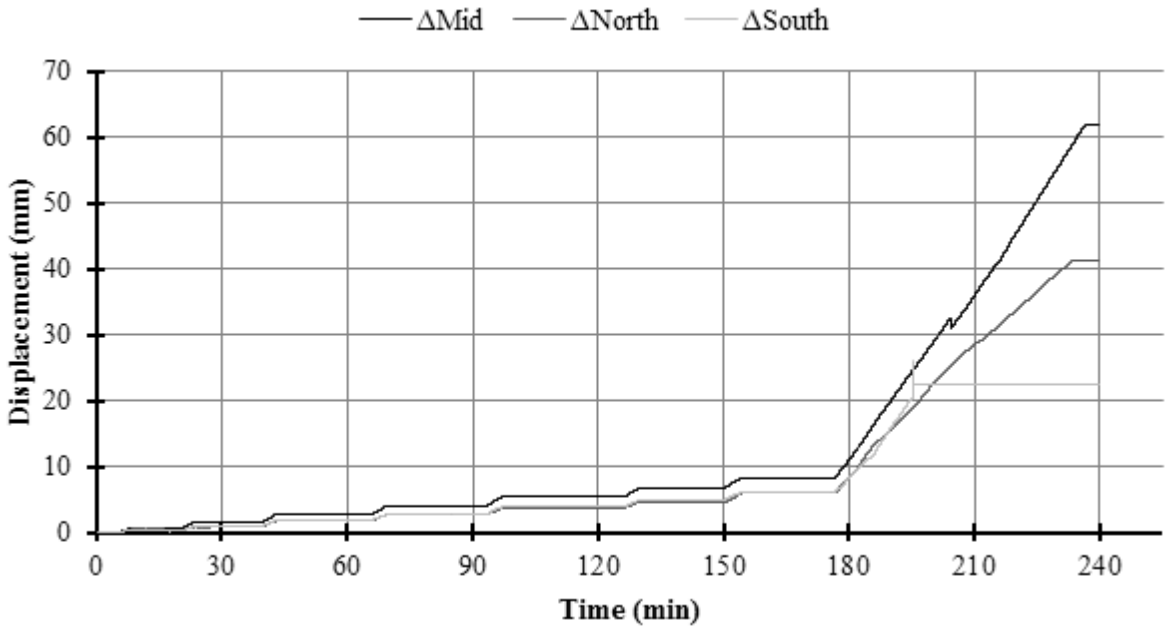

Figure E.236: BM25-s230 Plot of Displacement vs Time

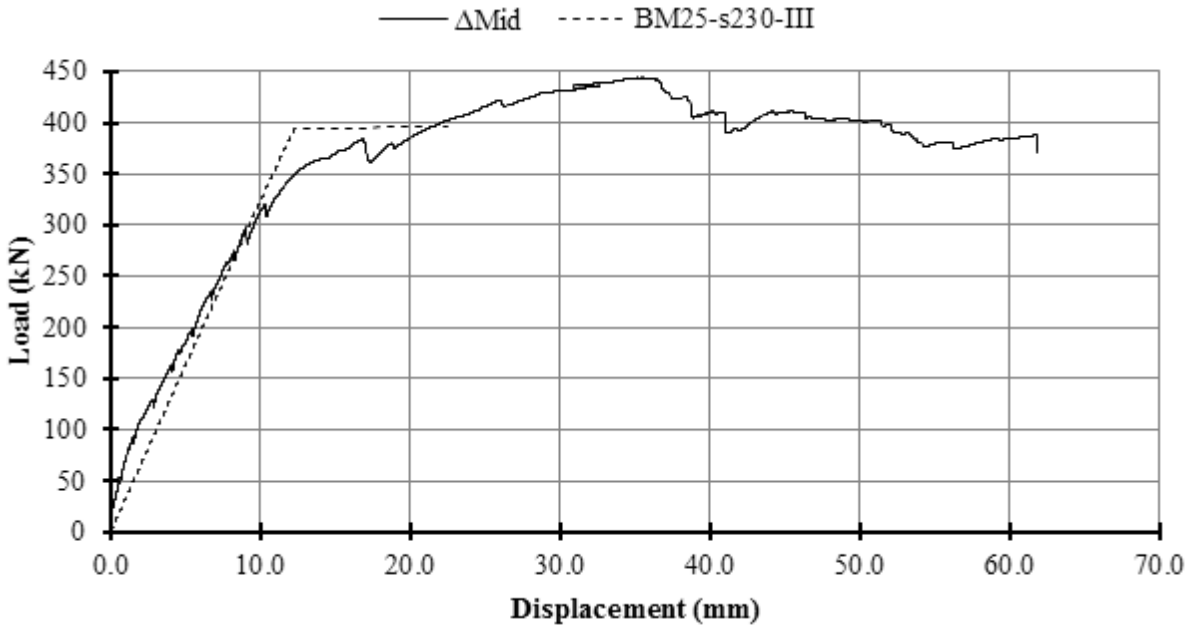

Figure E.237: BM25-s230 Plot of Load vs Displacement

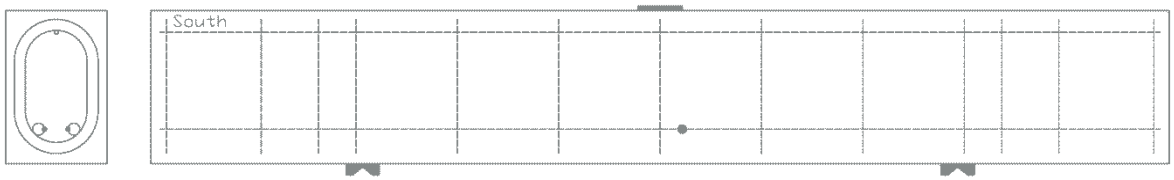

Figure E.238: BM25-s230 Schematic of Mid-Span Strain Gauge Locations

A record of the specific longitudinal bar to which gauge A and B were attached was not kept.

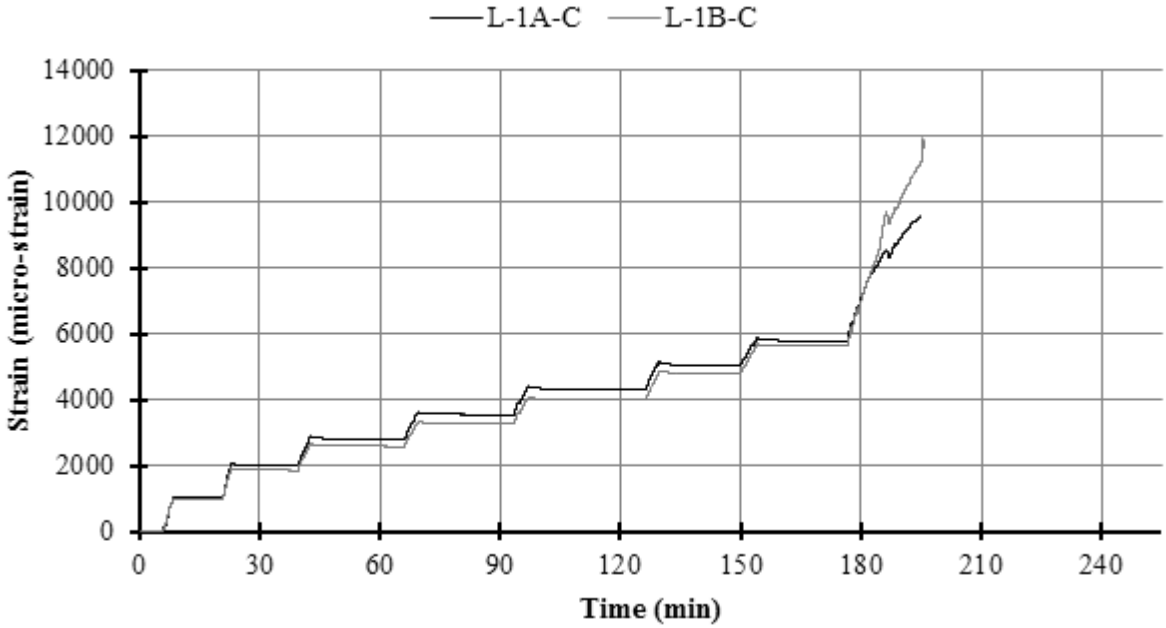

Figure E.239: BM25-s230 Plot of Strain vs Time on Longitudinal Bars at Mid-Span

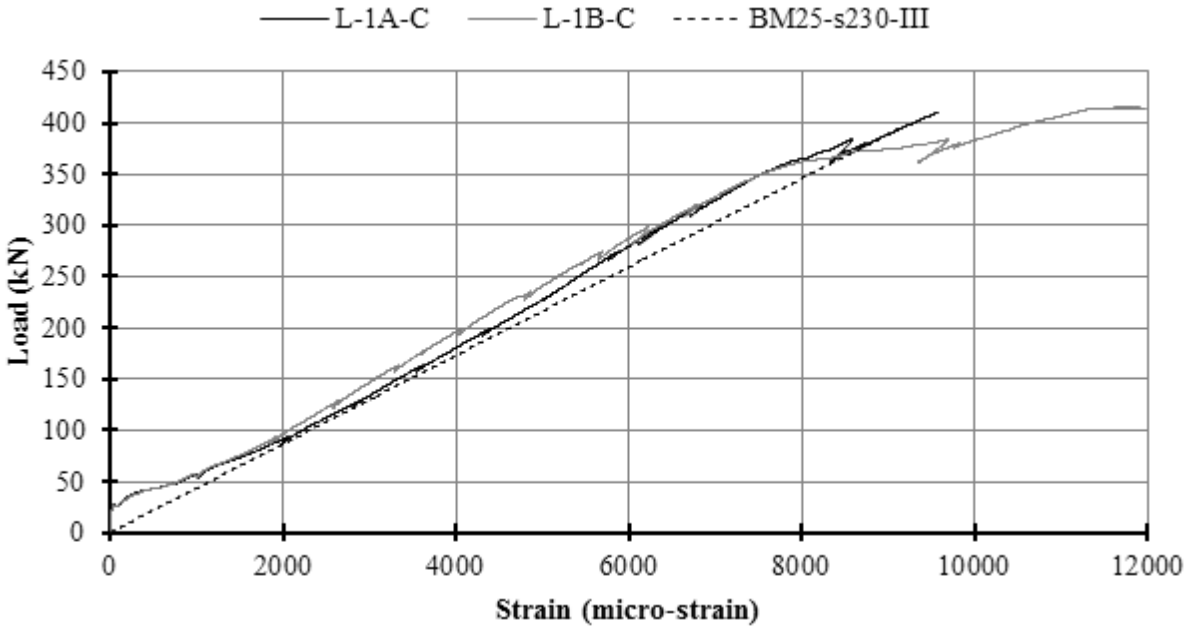

Figure E.240: BM25-s230 Plot of Load vs Strain on Longitudinal Bars at Mid-Span

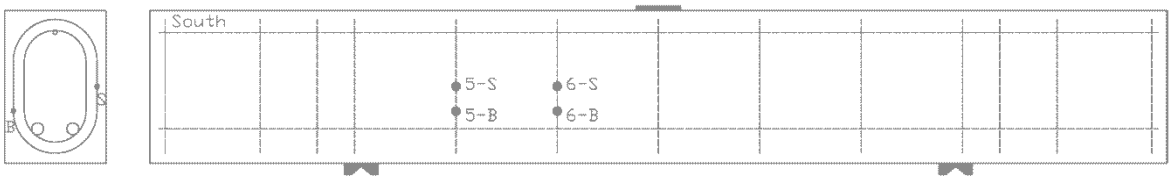

Figure E.241: BM25-s230 Schematic of Stirrup Strain Gauge Locations

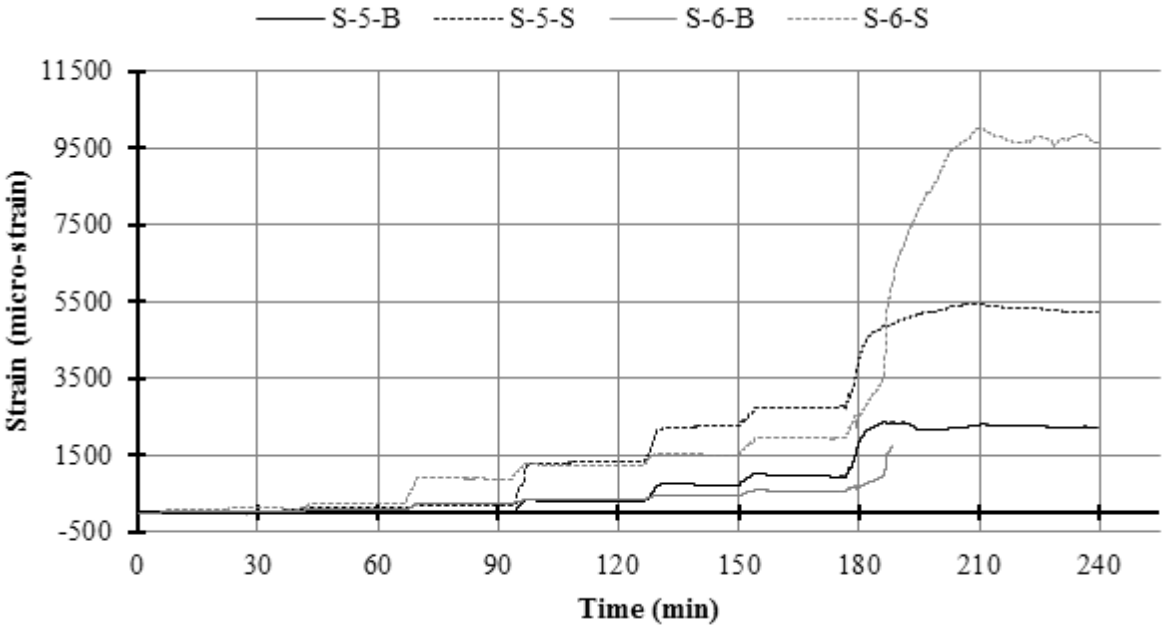

Figure E.242: BM25-s230 Plot of Strain vs Time on Stirrups

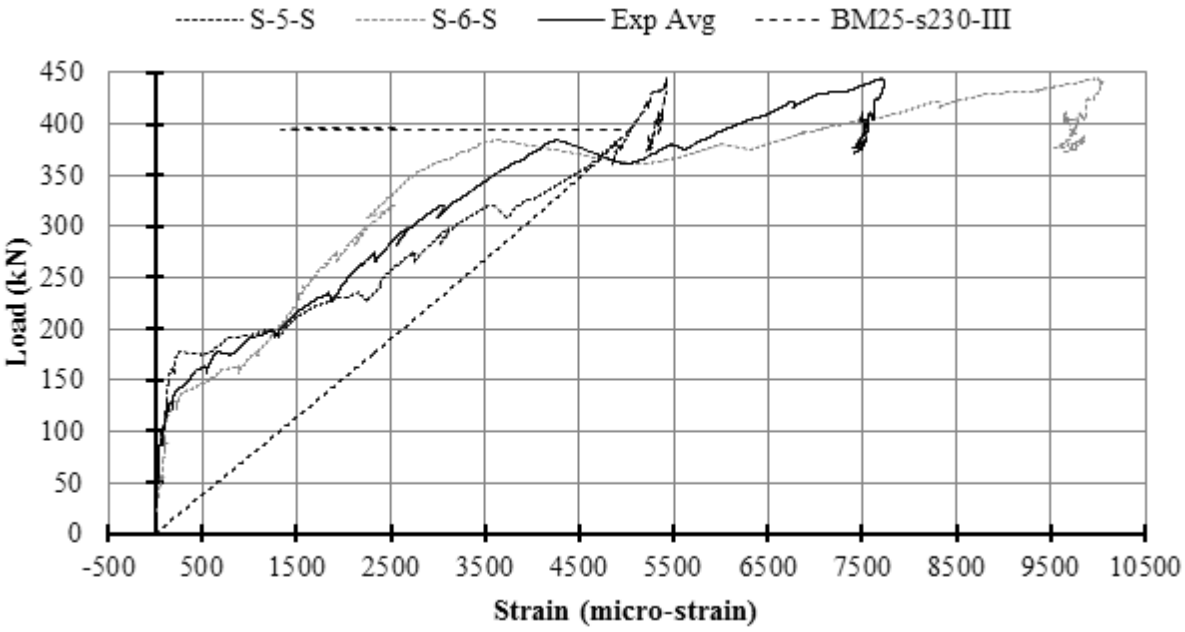

Figure E.243: BM25-s230 Plot of Load vs Strain on Stirrups

A plot with all stirrup strain gauges may be found in the Results Chapter.

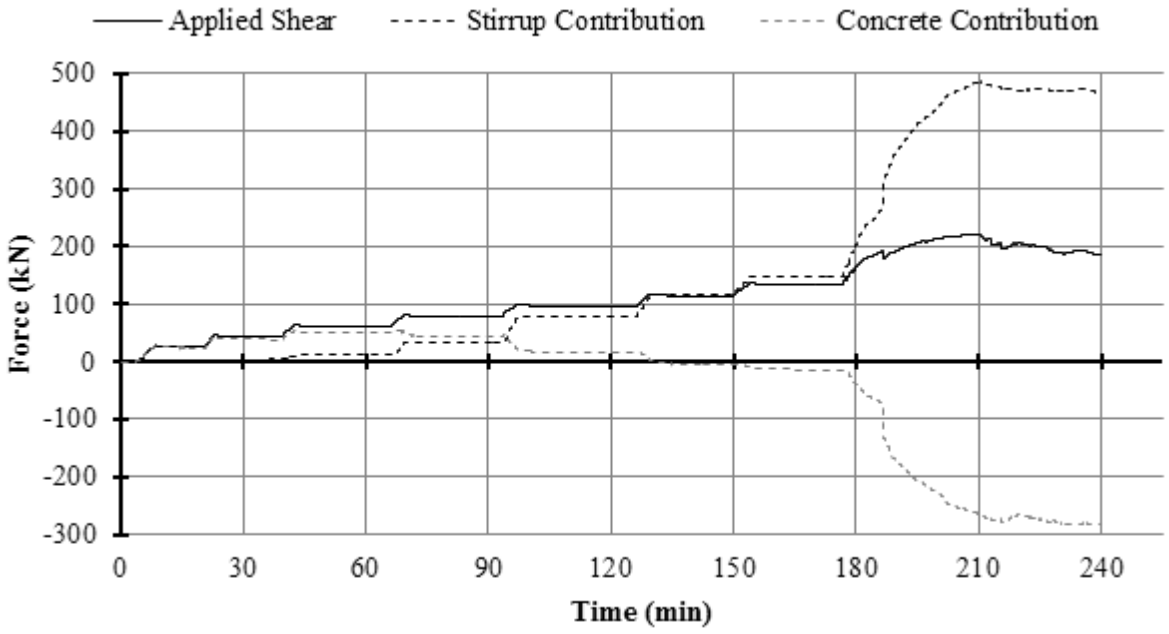

Figure E.244: BM25-s230 Plot of Shear Contribution vs Time

E.15.1 BM25-s230 Photographs

Figure E.245: BM25-s230 Rebar Cage Elevation Photo
Top framing bar not pictured.

Figure E.246: BM25-s230 Rebar Cage Cross-Section Photo
Top framing bar not pictured.

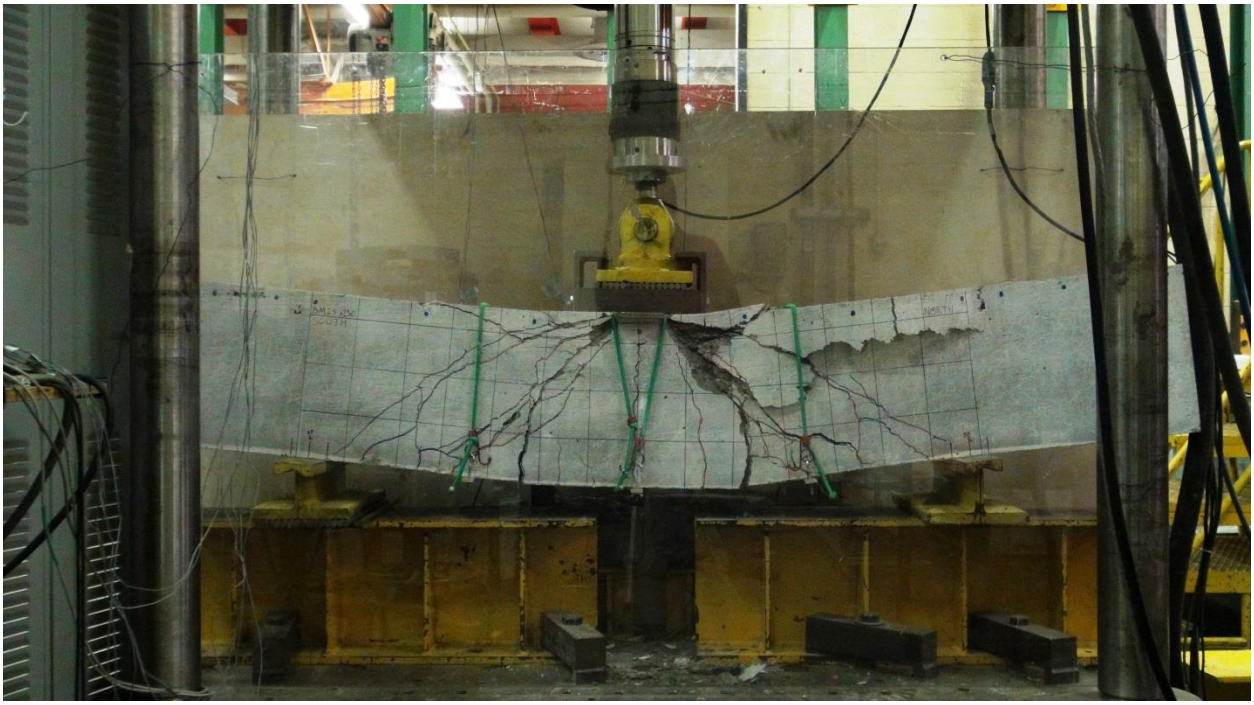

Figure E.247: BM25-s230 Alternative Photo of Entire Beam Under Load After Testing

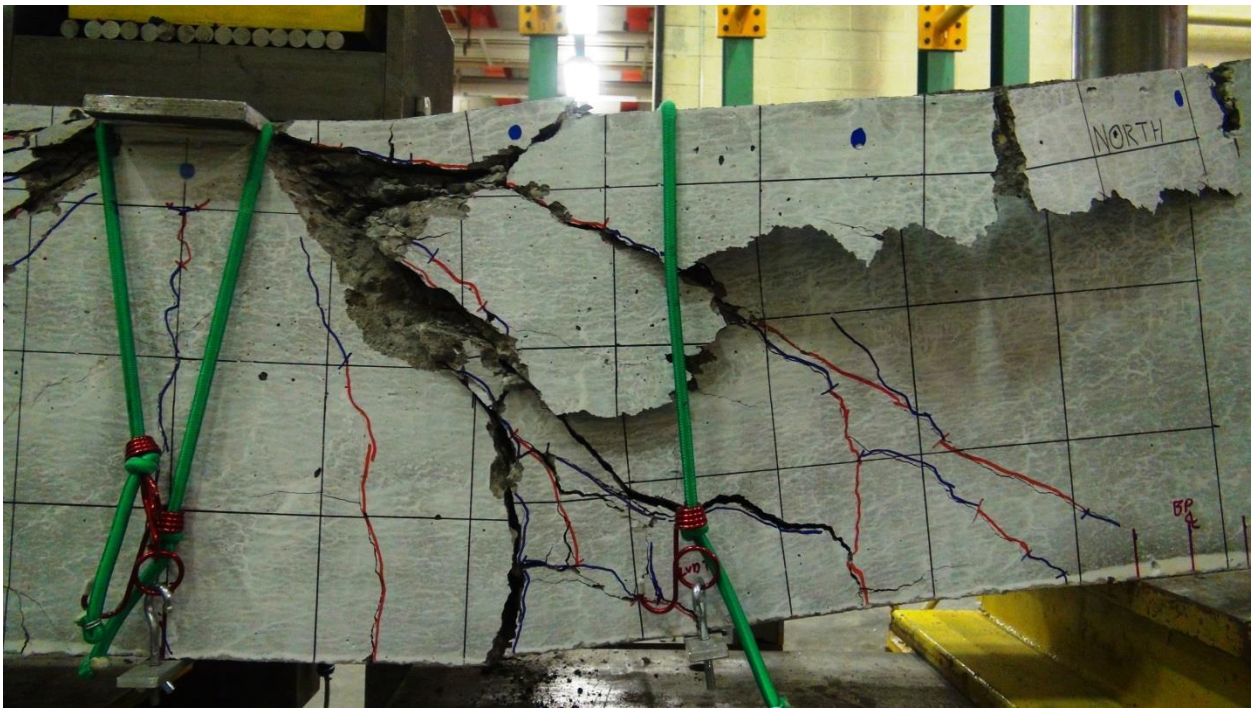

Figure E.248: BM25-s230 Close-up Photo of Failure

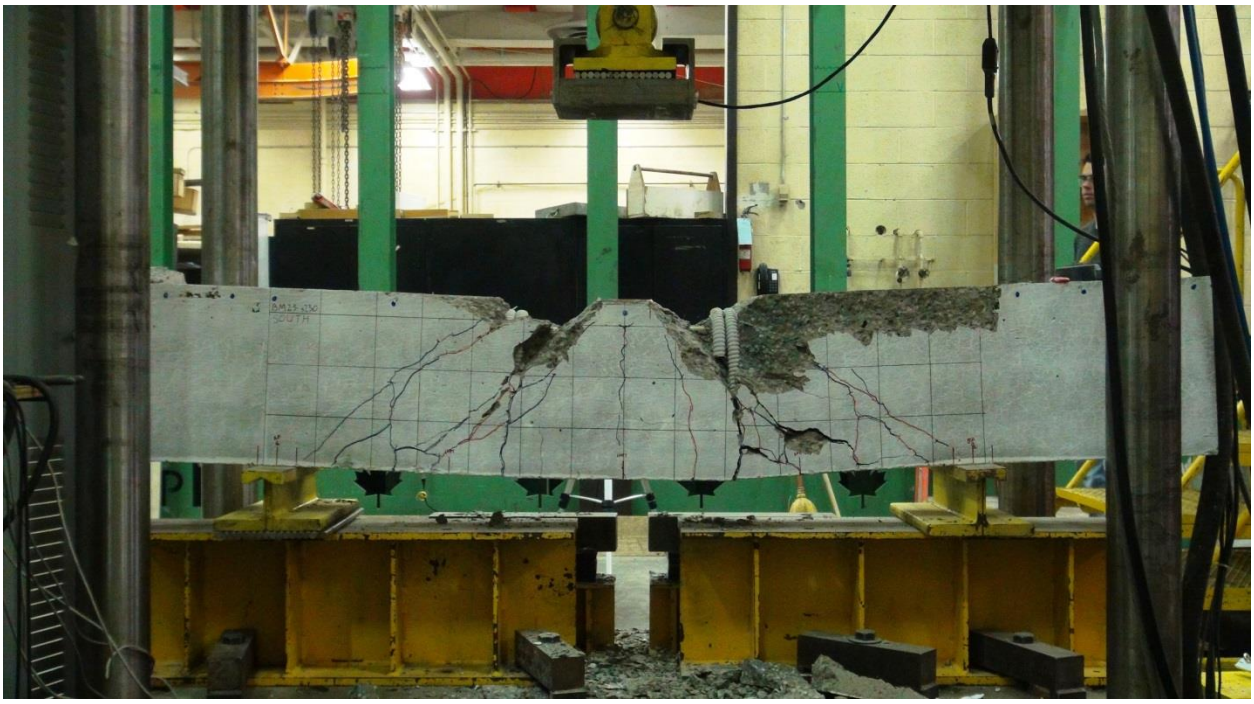

Figure E.249: BM25-s230 Photo of Failure with Spalled Concrete Removed with Stirrups 6 and 8 Exposed

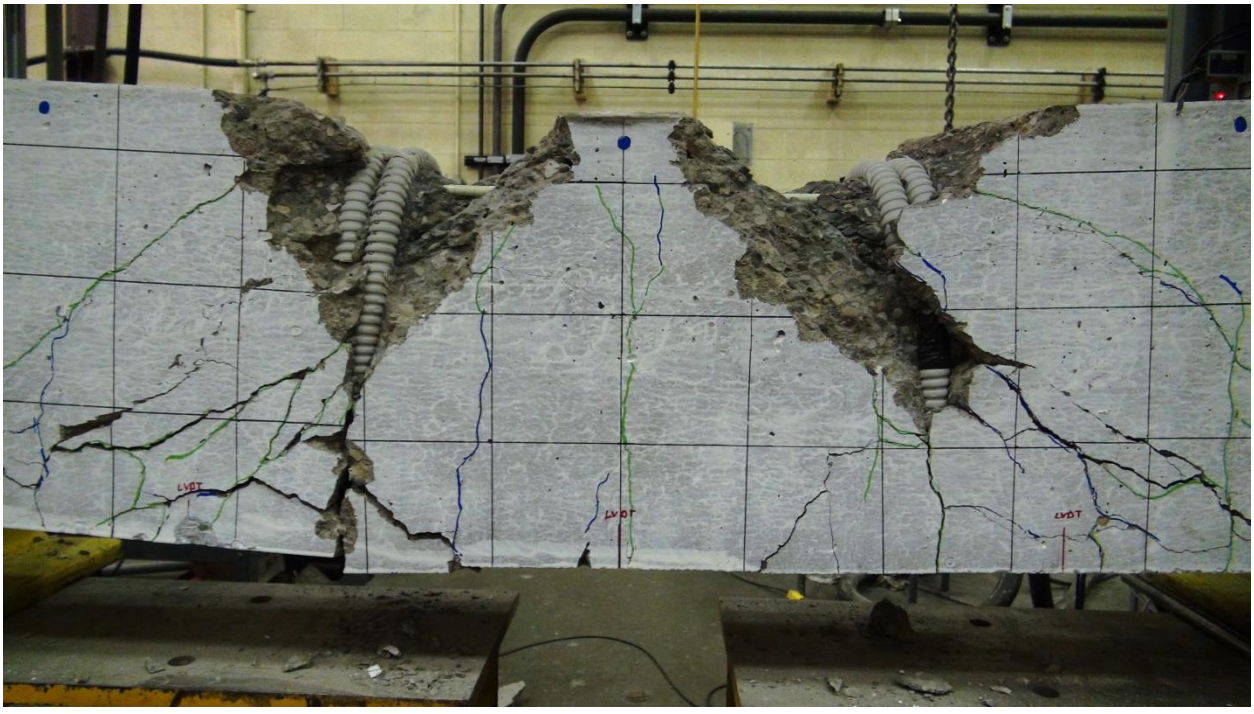

Figure E.250: BM25-s230 Photo of Failure from Reverse

F: MATLAB Code for the Indeterminate Strut-and-Tie Method

This appendix contains the MATLAB Code for the IST method. The main program is presented first, followed by the other user written functions which it calls. The functions are presented in the order of which they are called, and the filename of the function is bolded.

The initialInput and failureCheck functions are unique to each beam. Only one copy of those functions are included, and they are for BM25-220 using model III. It is very similar to, but not exactly the same as, the problem presented in Chapter 5. Though, using the details in Chapter 5, this code could be easily modified to reproduce the design example.

The procedure of the code is not explained here, but a knowledgeable reader should be able to follow along if they have read Chapter 5 and are familiar with coding in MATLAB. At all times descriptive variables names were used to ease understanding.

F.1 MATLAB Code

analysis.m

```
%Copyright: Martin D. Krall
%This is the MATLAB code for the indeterminate strut-and-tie analysis
%procedure of Martin D Krall's master's thesis, "Tests on Concrete Beams
%with GFRP Flexural and Shear Reinforcements & Analysis Method for
%Indeterminate Strut-and-Tie Models with Brittle Reinforcements",
% University of Waterloo, 2014.

%Reset working space
close all, clc, clear,
format long

%Import initial problem geometry, material properties, etc.
[x,y,indexOfElementNodes,area,lengths,phi,Etemp,fixedDOF,indexOfStruts,nodeDimensions,nodeStressL
imits,initialTangentModulus,strainAtPeakStress,concreteCylinderStrength,softening,beamWidth,model
,beamName,loadPoint] = initialInput;


%Define modeling constants
nsd = 2; % Number of space dimensions
ndof = 2; % Number of degrees-of-freedom per node
nnd = size(x,2); % Number of nodes
nel = size(indexOfElementNodes,2); % Number of elements
neq = nnd*ndof; % Number of equations (dofs)
nStruts = length(indexOfStruts); %Number of struts in the truss


%Define parameters for failure checks
stabilityFailureP = 0;
strutFailureP = zeros(1,nStruts);
nodeFailureP = zeros(1,nnd);
strutFailureCheck = zeros(1,nStruts);
nodeFailureCheck = zeros(1,nnd);
stabilityCheck1 = 0;
stabilityCheck2 = 0;
failure = 0;


%Define other model parameters
P = 0; %N, Applied load
PIncrement = 10; %N
PStop = 500000; %N, To prevent unintended infinite loops
tempA = floor(PStop / PIncrement); %To estimate maximum model run time
counter = 1; %To track of parameter values at different increments
f = zeros(neq,1); %N, Define the load vector
d = zeros(neq,1); %mm, Initialize displacement matrix
```

```
E(:,counter) = Etemp; %MPa, Elastic Modulus
tic;
time1 = tic; %Used to estimate model run time

%Identify the mid-span node for mid-span displacements
for i = 1:nnd
    if nodeDimensions(i,1) == 1
        midspanDisplacementNode = i;
    end
end

%Loop to iterate applied load
while (failure ~= 1)

    %Assign load to load vector
    P = P + PIncrement;  %N, Increment load
    load(counter) = P; %N, for plotting parameters against load
    f(loadPoint) = -P; %N, Vector used in truss solver

    %Calculation and assembly of element matrices
    K = zeros(neq); % Initialize stiffness matrix
    for e = 1:nel
        sctr = getsctr(e,indexOfElementNodes); %Correlates the local nodes with global nodes
        ke = trusselem(area(e),lengths(e),E(e,counter),phi(e)); %Individual element stiffness
matrix
        K(sctr,sctr) = K(sctr,sctr) + ke; %Assembled global stiffness matrix
    end

    if counter == 1
        K1 = K; %To track change in stiffness matrix from initial load to failrue load
    end

    %Solution to the truss system
    [d,R] = solvedr(K,f,fixedDOF); %Solves the force system. d = global displacements in mm, R =
reactions in N
    dMidSpan(counter) = d(midspanDisplacementNode*2); %mm, to later plot the mid-span
displacement against load

    %Solve for element internal strains, stresses, and forces
    for e = 1:nel
        %Assemble element local dipslacement matrix
        s = sin(phi(e));
        c = cos(phi(e));
        T = [c,s,0,0; %Transformation Matrix
            0,0,c,s];
        sctr = getsctr(e,indexOfElementNodes); %Correlates the local displacements with global
displacements
        elementGlobalDisplacements = [d(sctr(1)),d(sctr(2)),d(sctr(3)),d(sctr(4))]; %mm, local
element displacement matrix
        elementLocalDisplacements = T*elementGlobalDisplacements'; %mm, local element nodal
displacements in local element coordinate system
        %Calculation of strain, stress, and force values
        strain(e,counter) = [-1, 1]*elementLocalDisplacements/lengths(e);
        stress(e,counter) = strain(e,counter)*E(e,counter); %MPa
        force(e,counter) = area(e)*stress(e,counter); %N
    end

    %Compute new Strut Elasticity Values
    Etemp =
concreteStiffness(counter,E,strain,indexOfStruts,nStruts,strainAtPeakStress,concreteCylinderStren
gth,initialTangentModulus,softening,model);
    E(:,(counter + 1)) = Etemp'; %MPa, assign elasticity values for next iteration

    %Evaluate Failure Conditions
    %The following are used to pass values between functions
    TEMPstabilityFailureP = stabilityFailureP;
    TEMPstrutFailureP = strutFailureP;
    TEMPnodeFailureP = nodeFailureP;
    TEMPstabilityCheck1 = stabilityCheck1;
    TEMPstabilityCheck2 = stabilityCheck2;
    TEMPstrutFailureCheck = strutFailureCheck;
    TEMPnodeFailureCheck = nodeFailureCheck;

[failure,stabilityFailureP,strutFailureP,nodeFailureP,strutFailureCheck,nodeFailureCheck,stabilit
yCheck1,stabilityCheck2] =
failureCheck(TEMPstabilityFailureP,TEMPstrutFailureP,TEMPnodeFailureP,TEMPstrutFailureCheck,TEMPn
odeFailureCheck,TEMPstabilityCheck1,TEMPstabilityCheck2,E,indexOfStruts,counter,nodeStressLimits,
nodeDimensions,P,PIncrement,PStop,initialTangentModulus,nStruts,R,beamWidth,force,phi);

    %Other computations
    K2 = K; %To track change in stiffness matrix from initial load to failrue load.
```

```
    counter = counter + 1;
    %Block of code to check time to model completion
    time2 = toc;
    if round(counter/1000) == counter/1000
        estim = (time2 - time1) * tempA
    end
    time1 = time2;
end

%Outputs
stiffnessMatrixDifference = (K1-K2)./K1 % Shows the change in the stiffness matrix from the first
load increment to the last load increment. Use in code/error checking.
R %Output of final reactions
d %Output of final displacements

%Plots
plotCounter = 1; % Tracks figure number for output of plots

%The following block of code outputs the deformed shape of the truss for
%code/error checking.
maxDisplacement = abs(max(abs(d))); % To be used to find a scaling factor
xMax = max(x); % To be used to find a scaling factor
xMin = min(x);
yMax = max(y);
yMin = min(y);
if (xMax-xMin) >= (yMax-yMin) %This block is being used to find a scaling factor
    scaleFactor = abs((xMax-xMin)/20)/maxDisplacement; %Scaling factor is 1/20th of plot area for
largest displacement.
else
    scaleFactor = abs((yMax-yMin)/20)/maxDisplacement;
end
dScaled = d * scaleFactor %Scaling operation of displacements
%Block to allocate scaled displacements to the plot coordinates
for i = 1:length(x)
    displacedScaledCoordinatesX(i) = x(i) + dScaled(2*i-1);
    displacedScaledCoordinatesY(i) = y(i) + dScaled(2*i);
end
plot_truss = 'yes';  %Plot specs.
plot_nod = 'yes';
lineWidth = 1;
lineColour = 'b';
% plot truss deformed
plottruss(displacedScaledCoordinatesX,displacedScaledCoordinatesY,indexOfElementNodes,plot_truss,
plot_nod,lineWidth,lineColour);
figure(plotCounter)


%The following blocks of code output plots of potential interest in
%code/error checking, or for final results.

% for i = 1:nStruts
%     plotCounter = plotCounter + 1;
%     figure(plotCounter)
%     plot(load,strain(indexOfStruts(i),:)) % Load VS Strut Strain
%     temp = sprintf('strain for strut %d', indexOfStruts(i));
%     title(temp)
% end
% for i = 1:nStruts
%     plotCounter = plotCounter + 1;
%     figure(plotCounter)
%     plot(load,stress(indexOfStruts(i),:)) % Load VS Strut Stress
%     temp = sprintf('stress for strut %d', indexOfStruts(i));
%     title(temp)
% end
% for i = 1:nel
%     plotCounter = plotCounter + 1;
%     figure(plotCounter)
%     plot(load,force(i,:)) %Load VS Internal Force
%     temp = sprintf('force for element %d', i);
%     title(temp)
% end
% for i = 1:nStruts
%     plotCounter = plotCounter + 1;
%     figure(plotCounter)
%     plot(load,force(indexOfStruts(i),:)) % Load VS Internal Strut Force
%     temp = sprintf('force for strut %d', indexOfStruts(i));
%     title(temp)
% end
% Etemp = E;
% Etemp(:,counter) = []; %This makes sure that the sizes of the Etemp matrix and load vector
match for plotting
```

```
% for i = 1:nel
%     plotCounter = plotCounter + 1;
%     figure(plotCounter)
%     plot(load,Etemp(i,:)) % Load VS Elasticity
%     temp = sprintf('modulus for element %d', i);
%     title(temp)
% end
% for i = 1:nStruts
%     plotCounter = plotCounter + 1;
%     figure(plotCounter)
%     plot(load,Etemp(indexOfStruts(i),:)) % Load VS Strut Elasticity
%     temp = sprintf('modulus for strut %d', indexOfStruts(i));
%     title(temp)
% end


%Output a file of parameters of interest to text file
fileName = strcat(beamName,'.txt');
%Write to file
fileID = fopen(fileName,'w+');

%Beam Name
fprintf(fileID,'Beam: %s \r\n\r\n\r\n',beamName);

%Truss Solver Parameters
fprintf(fileID,'Truss Solver Parameters\r\n');
fprintf(fileID,'Node X Co-ordinates in mm\r\n');
fprintf(fileID,'%G, ',x');
fprintf(fileID,'\r\n\r\n');
fprintf(fileID,'Node Y Co-ordinates in mm\r\n');
fprintf(fileID,'%G, ',y');
fprintf(fileID,'\r\n\r\n');
fprintf(fileID,'Index of Element Nodes\r\nEnd 1: ');
fprintf(fileID,'%G, ',indexOfElementNodes(1,:));
fprintf(fileID,'\r\nEnd 2: ');
fprintf(fileID,'%G, ',indexOfElementNodes(2,:));
fprintf(fileID,'\r\n\r\n');
fprintf(fileID,'Index of Strut Elements\r\n');
fprintf(fileID,'%G, ',indexOfStruts');
fprintf(fileID,'\r\n\r\n');
fprintf(fileID,'Fixed Degrees of Freedom\r\n');
fprintf(fileID,'%G, ',fixedDOF');

%Truss Element Parameters
fprintf(fileID,'\r\n\r\n\r\n');
fprintf(fileID,'Truss Element Parameters\r\n');
fprintf(fileID,'Length of Elements in mm\r\n');
fprintf(fileID,'%G, ',lengths);
fprintf(fileID,'\r\n\r\n');
fprintf(fileID,'Angle of Elements in rad\r\n');
fprintf(fileID,'%G, ',phi);
fprintf(fileID,'\r\n\r\n');
fprintf(fileID,'Area of Elements in mm2\r\n');
fprintf(fileID,'%G, ',area);
fprintf(fileID,'\r\n\r\n');
fprintf(fileID,'Initial Elastic Modulus in MPa\r\n');
fprintf(fileID,'%G, ',E(:,1));

%Concrete Material Parameters
fprintf(fileID,'\r\n\r\n\r\n');
fprintf(fileID,'Concrete Material Model Paramters\r\n');
fprintf(fileID,'Concrete Cylinder Strength in MPa\r\n');
fprintf(fileID,'%G',concreteCylinderStrength);
fprintf(fileID,'\r\n\r\n');
fprintf(fileID,'Initial Tangent Modulus in MPa\r\n');
fprintf(fileID,'%G',initialTangentModulus);
fprintf(fileID,'\r\n\r\n');
fprintf(fileID,'Initial Strain at Peak Stress\r\n');
fprintf(fileID,'%G',strainAtPeakStress);
fprintf(fileID,'\r\n\r\n');
fprintf(fileID,'Softening Coefficients\r\n');
fprintf(fileID,'%G, ',softening');

%Misc
fprintf(fileID,'\r\n\r\n\r\n');
fprintf(fileID,'Miscellaneous Parameters\r\n');
fprintf(fileID,'Node Dimensions in mm\r\n');
fprintf(fileID,'Node X Dimension\r\n');
fprintf(fileID,'%G, ',nodeDimensions(:,1));
fprintf(fileID,'\r\n');
fprintf(fileID,'Node Y Dimension\r\n');
```

```
fprintf(fileID,'%G, ',nodeDimensions(:,2));
fprintf(fileID,'\r\n');
fprintf(fileID,'Node Hypotenuse Dimension\r\n');
fprintf(fileID,'%G, ',nodeDimensions(:,3));
fprintf(fileID,'\r\n\r\n');
fprintf(fileID,'Node Strength in MPa\r\n');
fprintf(fileID,'%G, ',nodeStressLimits);
fprintf(fileID,'\r\n\r\n');
fprintf(fileID,'Beam Width in mm\r\n');
fprintf(fileID,'%G',beamWidth);
fprintf(fileID,'\r\n\r\n');
fprintf(fileID,'Material Model\r\n');
fprintf(fileID,'%G',model);
fprintf(fileID,'\r\n\r\n');

%Results Output
fprintf(fileID,'\r\n\r\n\r\n');
fprintf(fileID,'Model Results\r\n');
fprintf(fileID,'Reactions Stability Failure in N\r\n');
fprintf(fileID,'%G, ',R);
fprintf(fileID,'\r\n\r\n');
fprintf(fileID,'Displacements at Stability Failure in mm\r\n');
fprintf(fileID,'%G, ',d);
fprintf(fileID,'\r\n\r\n');
fprintf(fileID,'P at Stability Failure in N\r\n');
fprintf(fileID,'%G',stabilityFailureP);
fprintf(fileID,'\r\n\r\n');
fprintf(fileID,'P at Strut Failures in N\r\n');
fprintf(fileID,'%G, ',strutFailureP);
fprintf(fileID,'\r\n\r\n');
fprintf(fileID,'P at Node Failures in N\r\n');
fprintf(fileID,'%G, ',nodeFailureP);
fprintf(fileID,'\r\n\r\n');
fprintf(fileID,'Strain at Stability Failure\r\n');
fprintf(fileID,'%G, ',strain(:,(counter-1)));
fprintf(fileID,'\r\n\r\n');
fprintf(fileID,'Maximum Strains \r\n');
for i = 1:nel
    maxStrain(i) = max(strain(i,:));
end
fprintf(fileID,'%G, ',maxStrain);
fprintf(fileID,'\r\n\r\n');
fprintf(fileID,'Maximum Stress \r\n');
for i = 1:nel
    maxStress(i) = max(stress(i,:));
end
fprintf(fileID,'%G, ',maxStress);
fprintf(fileID,'\r\n\r\n');
fclose(fileID);


%Output Results to MSExcel file
fileName = strcat(beamName,'Table.xlsx');
tableSize = 2 + 4 * nel;
T = zeros((counter-1),tableSize);
titleRow{1} = sprintf('Load');
titleRow{2} = sprintf('Mid-span Displacement');
temp = 2;
for i = 1:nel
    temp = temp + 1;
    titleRow{temp} = sprintf('Force %d', i);
end
for i = 1:nel
    temp = temp + 1;
    titleRow{temp} = sprintf('Stress %d', i);
end
for i = 1:nel
    temp = temp + 1;
    titleRow{temp} = sprintf('Strain %d', i);
end
for i = 1:nel
    temp = temp + 1;
    titleRow{temp} = sprintf('Elastic %d', i);
end

ETemp = E;
ETemp(:,counter) = []; %This makes sure that the size of E matched the rest of the table
T(:,1) = load';
T(:,2) = -1*dMidSpan'; %To output displacement as positive value.
temp = 2;
for i = 1:nel
```

```
    temp = temp + 1;
    T(:,temp) = force(i,:)';
end
for i = 1:nel
    temp = temp + 1;
    T(:,temp) = stress(i,:)';
end
for i = 1:nel
    temp = temp + 1;
    T(:,temp) = strain(i,:)';
end
for i = 1:nel
    temp = temp + 1;
    T(:,temp) = ETemp(i,:)';
end

xlswrite(fileName, titleRow, 'Sheet1') % Output the header row
xlswrite(fileName, T, 'Sheet1','A2') % Output data under the header row.

fprintf('done')
```

initialInput.m

```
function
[x,y,indexOfElementNodes,area,lengths,phi,E,fixedDOF,indexOfStruts,nodeDimensions,nodeStressLimit
s,initialTangentModulus,strainAtPeakStress,concreteCylinderStrength,softening,beamWidth,model,bea
mName,loadPoint] = initialInput;

%Beam Name
beamName = 'BM25-220-III';


%Define model variables
ndof = 2; %Number of degrees-of-freedom per node
nnp = 7; %Number of nodal points
nel = 12; %Number of elements
neq = ndof*nnp; %Number of equations


%Define physical parameters of the problem
%Geometric
beamWidth = 200; %mm
beamHeight = 330; %mm
effectiveDepth = 270; %mm
supportBearingLength = 75; %mm
loadingBearingLength = 100; %mm
areaFRPlongitudinal = 982; %mm2
areaFRPstirrups = 226; %mm2

%Material
concreteCylinderStrength = 47.3; %MPa 28d strength
concreteDensity = 2416.5; %kg/m3
crushingStrain = 0.0035; %For compressive stress block calculation
alpha1 = 0.85 - 0.0015*concreteCylinderStrength; %For compressive stress block calculation
beta1 = 0.97 - 0.0025*concreteCylinderStrength; %For compressive stress block calculation
EFRPLongitudinal = 60000; %MPa
EFRPStirrup = 50000; %MPa


%Concrete Material Model Parameters
%Define which elements are struts.
indexOfStruts = [4,5,9,10,11,12];
nStruts = length(indexOfStruts); %Number of struts in the truss
%Define initial element elastic moduli, concrete struts will have their moduli adjusted for
softening parameters.
%Elem = [1               ,2              ,3              ,4,5,6          ,7          ,8
,9,10,11,12]
E     =
[EFRPLongitudinal,EFRPLongitudinal,EFRPLongitudinal,1,1,EFRPStirrup,EFRPStirrup,EFRPStirrup,1,1
,1 ,1 ]; %MPa

%Elem   =   [1,2,3,4   ,5   ,6,7,8,9    ,10   ,11   ,12   ]
softening = [1,1,1,0.85,0.85,1,1,1,0.638,0.638,0.638,0.638];
%Softening coefficients come from the paper "An Indeterminate Strut-Tie
%Model and Load Distribution Ratio for RC Deep Beams - (I) Model & Load
%Distribution Ratio" by Kim, B., and Yun, Y. from Advances in Structural
%Engineering, Vol 14, No 6, 2011, pp 1031-1041.

model = 0; %0 for Modified Hognestad, 1 for Modified Thorenfeldt et al.

if model == 0
    %Model 0: Softening Coefficient Modified Hognestad Parabola Model as
    %presented in "An Indeterminate Strut-Tie
    %Model and Load Distribution Ratio for RC Deep Beams - (I) Model &
    %Load Distribution Ratio" by Kim, B., and Yun, Y. from Advances in
    %Structural Engineering, Vol 14, No 6, 2011, pp 1031-1041.

    Ec = 1.1*( (3300 * sqrt(concreteCylinderStrength) + 6900) * (concreteDensity / 2300)^1.5 );
%MPa
    %1.1 Increase for tangent modulus, see thesis
    strainAtPeakStress = 2 * concreteCylinderStrength/Ec;
    initialTangentModulus = Ec; %MPa

    for i = 1:nStruts %This block of codes from the concreteStiffness function of this MATLAB
program.
        ratio = 0; %strain = 0 on initial load step
        E(indexOfStruts(i)) = initialTangentModulus * (1 - ratio); %MPa
        if E(indexOfStruts(i)) < 0.01*initialTangentModulus
            E(indexOfStruts(i)) = 0.01*initialTangentModulus; %MPa
        end
    end
elseif model == 1
    %Model 1: Softening Coefficient Modified Thorenfeldt et al. Model as
```

```
    %presented in "Reinforced Concrete Mechanics and Design" by MacGregor
    %J., and Bartlett, F. First Canadian Edition. 2000 Pearson Education
    %Canada Inc., Toronto, Ontario, Canada. pp 62-63.

    nRatio = 0.8 + concreteCylinderStrength / 17;
    Ec = 1.1*( (3300 * sqrt(concreteCylinderStrength) + 6900) * (concreteDensity / 2300)^1.5 );
%MPa
    %1.1 Increase for tangent modulus, see thesis
    strainAtPeakStress = (concreteCylinderStrength / Ec) * (nRatio /(nRatio - 1));
    initialTangentModulus = Ec; %MPa

    for i = 1:nStruts %This block of code comes from the concreteStiffness function of this
MATLAB program.
        nRatio = 0.8 + softening(indexOfStruts(i))*concreteCylinderStrength / 17;
        A = (softening(indexOfStruts(i)) * concreteCylinderStrength * nRatio) /
(softening(indexOfStruts(i)) * strainAtPeakStress);
        ratio = 0; %strain = 0 on initial load step
        k = 1;
        B = nRatio - 1 + (ratio)^(k*nRatio);
        C = ratio * k * nRatio * ratio^(k*nRatio - 1);

        E(indexOfStruts(i)) = (A/B) * (1 - C/B);
        if E(indexOfStruts(i)) < 0.01*initialTangentModulus
            E(indexOfStruts(i)) = 0.01*initialTangentModulus;
        end
    end
end

%Compute compressive stress block for over reinforced failure
a1 = alpha1 * concreteCylinderStrength * beamWidth;
b1 = areaFRPlongitudinal * EFRPLongitudinal * crushingStrain;
c1 = -1 * areaFRPlongitudinal * EFRPLongitudinal * beta1 * effectiveDepth * crushingStrain;
depthCompressiveStressBlock = (-b1 + sqrt(b1^2 - 4*a1*c1)) / (2*a1); %mm
checkForce = alpha1 * concreteCylinderStrength * depthCompressiveStressBlock * beamWidth; %N
temp = effectiveDepth - depthCompressiveStressBlock / 2; %mm, to define the location of the nodes
below

%Define initial nodal co-ordinates in mm
%Node = [1  ,2  ,3  ,4  ,5   ,6   ,7   ]
x   =   [0  ,235,455,650,235 ,455 ,650 ]; % X coordinate
y   =   [0  ,0  ,0  ,0  ,temp,temp,temp]; % Y coordinate

%Define nodal connectivity
%indexOfElementNodes(i,e) returns the global node number associate with the i-th node of element
e
%Elem =               [1,2,3,4,5,6,7,8,9,10,11,12] %Element
indexOfElementNodes = [1,2,3,5,6,2,3,4,1,2 ,3 ,1; %Element End 1
                       2,3,4,6,7,5,6,7,5,6 ,7 ,7]; %Element End 2

%Define element length
lengths = zeros(nel,1); %mm
for i = 1:nel
    lx(i) = x(indexOfElementNodes(2,i)) - x(indexOfElementNodes(1,i)); %mm
    ly(i) = y(indexOfElementNodes(2,i)) - y(indexOfElementNodes(1,i)); %mm
    lengths(i) = sqrt(lx(i)^2+ly(i)^2); %mm
end

%Define element orientation
%In general, elements were input such that their southwest most end was
%node 1 and their northeast most end was node 2
phi = zeros(nel,1);
for i = 1:nel
    phi(i) = atan2(ly(i),lx(i)); %rad
end

%Define element areas. Tie areas are predefined, strut areas will be revised later
%Elem   = [1                  ,2                  ,3                  ,4,5,6              ,7
,8              ,9,10,11,12]
area    =
[areaFRPlongitudinal,areaFRPlongitudinal,areaFRPlongitudinal,1,1,areaFRPstirrups,areaFRPstirrups,
areaFRPstirrups,1,1 ,1 ,1 ]; %mm2


%Define Node Dimensions Manually in mm as described in the thesis
%All nodes are assumed to be right angle triangles
nodeDimensions = zeros(nnp,3);

%Node 1
nodeDimensions(1,1) = supportBearingLength; %x
nodeDimensions(1,2) = 2*(beamHeight - effectiveDepth); %y
nodeDimensions(1,3) = sqrt(nodeDimensions(1,1)^2 + nodeDimensions(1,2)^2); %hyp
```

```
%Node 2
nodeDimensions(2,2) = nodeDimensions(1,2); %y
nodeDimensions(2,1) = nodeDimensions(2,2) / tan(phi(10)); %x
nodeDimensions(2,3) = sqrt(nodeDimensions(2,1)^2 + nodeDimensions(2,2)^2); %hyp

%Node 3
nodeDimensions(3,2) = nodeDimensions(1,2); %y
nodeDimensions(3,1) = nodeDimensions(3,2) / tan(phi(11)); %x
nodeDimensions(3,3) = sqrt(nodeDimensions(3,1)^2 + nodeDimensions(3,2)^2); %hyp

%Node 4
nodeDimensions(4,2) = nodeDimensions(1,2); %y
nodeDimensions(4,1) = 1; %x This node has no real dimensions
nodeDimensions(4,3) = 1; %hyp This node has no real dimensions

%Node 7 <-
nodeDimensions(7,1) = loadingBearingLength / 2; %x
nodeDimensions(7,2) = depthCompressiveStressBlock; %y
nodeDimensions(7,3) = sqrt(nodeDimensions(7,1)^2 + nodeDimensions(7,2)^2); %hyp

%Node 6
nodeDimensions(6,2) = nodeDimensions(7,2); %y
nodeDimensions(6,1) = nodeDimensions(6,2) / tan(phi(10)); %x
nodeDimensions(6,3) = sqrt(nodeDimensions(6,1)^2 + nodeDimensions(6,2)^2); %hyp

%Node 5
nodeDimensions(5,2) = nodeDimensions(7,2); %y
nodeDimensions(5,1) = nodeDimensions(5,2) / tan(phi(9)); %x
nodeDimensions(5,3) = sqrt(nodeDimensions(5,1)^2 + nodeDimensions(5,2)^2); %hyp


%Define Strut Areas Manually in mm2 as described in the thesis
%Element 4 & 5 (Top Chord)
area(4) = depthCompressiveStressBlock * beamWidth;
area(5) = depthCompressiveStressBlock * beamWidth;

%Element 9
temp1 = nodeDimensions(1,1)*sin(phi(9)) + nodeDimensions(1,2)*cos(phi(9));
temp2 = nodeDimensions(5,1)*sin(phi(9)) + nodeDimensions(5,2)*cos(phi(9));
temp3 = [temp1,temp2];
area(9) = min(temp3) * beamWidth;

%Element 10
temp1 = nodeDimensions(2,1)*sin(phi(10)) + nodeDimensions(2,2)*cos(phi(10));
temp2 = nodeDimensions(6,1)*sin(phi(10)) + nodeDimensions(6,2)*cos(phi(10));
temp3 = [temp1,temp2];
area(10) = min(temp3) * beamWidth;

%Element 11
temp1 = nodeDimensions(3,1)*sin(phi(11)) + nodeDimensions(3,2)*cos(phi(11));
temp2 = nodeDimensions(7,1)*sin(phi(11)) + nodeDimensions(7,2)*cos(phi(11));
temp3 = [temp1,temp2];
area(11) = min(temp3) * beamWidth;

%Element 12
temp1 = nodeDimensions(1,1)*sin(phi(12)) + nodeDimensions(1,2)*cos(phi(12));
temp2 = nodeDimensions(7,1)*sin(phi(12)) + nodeDimensions(7,2)*cos(phi(12));
temp3 = [temp1,temp2];
area(12) = min(temp3) * beamWidth;


%Define Node Stress Limits
%Node =            [1   ,2   ,3   ,4   ,5   ,6   ,7   ]
nodeStressLimits = [0.75,0.65,0.65,0.65,0.75,0.75,0.85] * concreteCylinderStrength; %MPa


% Define boundary conditions
fixedDOF = zeros(neq,1); % array of flag indicating if a given dof is
                         % prescribed: fixed_dofs(i)==2 means that dof
                         % i is prescribed.
disp_bc = zeros(neq,1); % array of prescribed values

fixed = [2,7,13]';
fixedDOF(fixed)    = 2;

loadPoint = 14;

%output plots
plot_truss     = 'yes';
plot_nod       = 'yes';
```

```
% plot truss
 lineWidth = 2; %Width is selected here to differentiate the deformed shape from the original
shape
 lineColour = 'b';
 plottruss(x,y,indexOfElementNodes,plot_truss,plot_nod,lineWidth,lineColour);
```

getsctr.m

```
function   sctr = getsctr(e,IEN);

%Initialize
sctr = [];
ndof = 2;

%Scatter matrix for regular dof
sctr(1) = (IEN(1,e)-1)*ndof + 1;
sctr(2) = (IEN(1,e)-1)*ndof + 2;

sctr(3) = (IEN(2,e)-1)*ndof + 1;
sctr(4) = (IEN(2,e)-1)*ndof + 2;
```

trusselem.m

```
function ke = trusselem(Area,len,E,phi)
%Generate the element stiffness matrix for each element

const = Area*E/len; %Constant coefficient for each truss element

s = sin(phi);
c = cos(phi);
s2 = s^2;
c2 = c^2;

ke = const*[c2, c*s, -c2, -c*s; %Stiffness matrix for 2D
            c*s, s2, -c*s, -s2;
            -c2, -c*s, c2, c*s;
            -c*s, -s2, c*s, s2];
```

solvedr.m

```
function [d,R] = solvedr(K,f,fixedDOF)
%Partition and solve the system of equations
neq = size(K,1);
K0 = K;
%Satisfy boundary conditions
for n=1:neq
   if (fixedDOF(n) == 2)
         K(n,:) = zeros(1,neq);
         K(:,n) = zeros(neq,1);
         K(n,n) = 1.0;
   end
end
%Solve the FE system
d = K \ f;
%Reactions at nodes
R = K0*d-f;
```

concreteStiffness.m

```
function  Etemp =
concreteStiffness(counter,E,strain,indexOfStruts,nStruts,strainAtPeakStress,concreteCylinderStren
gth,initialTangentModulus,softening,model)
%Update the stiffness for each strut according to the material model

if model == 0
    %Model 0: Softening Coefficient Modified Hognestad Parabola Model as
    %presented in "An Indeterminate Strut-Tie Model and Load Distribution
    %Ratio for RC Deep Beams - (I) Model & Load Distribution Ratio" by Kim,
    %B., and Yun, Y. from Advances in Structural Engineering, Vol 14, No 6,
    %2011, pp 1031-1041.

    Etemp = E(:,counter);

    for i = 1:nStruts
        ratio = ( abs(strain(indexOfStruts(i),counter)) /
(softening(indexOfStruts(i))*strainAtPeakStress) );
        if ratio <= 1.0
            Etemp(indexOfStruts(i)) = initialTangentModulus * (1 - ratio);
        else
            Etemp(indexOfStruts(i)) = -initialTangentModulus * ( (ratio - 1) /
(2/softening(indexOfStruts(i)) - 1)^2 );
        end

        %To avoid problems associated with negative elastic moduli, moduli
        %computed to be below 1% of the initial value are set equal to 1%
        %of the initial value. At this point the elements will be very
        %flexible and transfer very little load.
        if Etemp(indexOfStruts(i)) > E(indexOfStruts(i),counter)
            Etemp(indexOfStruts(i)) = E(indexOfStruts(i),counter);
        end
        if Etemp(indexOfStruts(i)) < 0.01*E(indexOfStruts(i),1)
            Etemp(indexOfStruts(i)) = 0.01*E(indexOfStruts(i),1);
        end
    end

elseif model == 1
    %Model 1: Softening Coefficient Modified Thorenfeldt et al. Model as
    %presented in "Reinforced Concrete Mechanics and Design" by MacGregor
    %J., and Bartlett, F. First Canadian Edition. 2000 Pearson Education
    %Canada Inc., Toronto, Ontario, Canada. pp 62-63.

    Etemp = E(:,counter);

    for i = 1:nStruts
        nRatio = 0.8 + softening(indexOfStruts(i))*concreteCylinderStrength / 17;
        ratio =
abs(strain(indexOfStruts(i),counter))/(softening(indexOfStruts(i))*strainAtPeakStress);
        if ratio <+ 1
            k = 1;
        elseif ratio > 1
            k = 0.67 + softening(indexOfStruts(i))*concreteCylinderStrength / 62;
            if k < 1
                k = 1;
            end
        end
        A = (softening(indexOfStruts(i)) * concreteCylinderStrength * nRatio) /
(softening(indexOfStruts(i)) * strainAtPeakStress);
        B = nRatio - 1 + (ratio)^(k*nRatio);
        C = ratio * k * nRatio * ratio^(k*nRatio - 1);
        Etemp(indexOfStruts(i)) = (A/B) * (1 - C/B);

        %To avoid problems associated with negative elastic moduli, moduli
        %computed to be below 1% of the initial value are set equal to 1%
        %of the initial value. At this point the elements will be very
        %flexible and transfer very little load.
        if Etemp(indexOfStruts(i)) > E(indexOfStruts(i),counter)
            Etemp(indexOfStruts(i)) = E(indexOfStruts(i),counter);
        end
        if Etemp(indexOfStruts(i)) < 0.01*E(indexOfStruts(i),1)
            Etemp(indexOfStruts(i)) = 0.01*E(indexOfStruts(i),1);
        end
    end
end
```

failureCheck.m

```
function
[failure,stabilityFailureP,strutFailureP,nodeFailureP,strutFailureCheck,nodeFailureCheck,stabilit
yCheck1,stabilityCheck2] =
failureCheck(TEMPstabilityFailureP,TEMPstrutFailureP,TEMPnodeFailureP,TEMPstrutFailureCheck,TEMPn
odeFailureCheck,TEMPstabilityCheck1,TEMPstabilityCheck2,E,indexOfStruts,counter,nodeStressLimits,
nodeDimensions,P,PIncrement,PStop,initialTangentModulus,nStruts,R,beamWidth,force,phi)
%Check for stability failure and for nodal failures.
%FRP rupture not checked as FRP did not rupture during experimental tests

failureTemp = 0;

stabilityFailureP = TEMPstabilityFailureP;
strutFailureP = TEMPstrutFailureP ;
nodeFailureP = TEMPnodeFailureP;
stabilityCheck1 = TEMPstabilityCheck1;
stabilityCheck2 = TEMPstabilityCheck2;
strutFailureCheck = TEMPstrutFailureCheck;
nodeFailureCheck = TEMPnodeFailureCheck;

%Check for system failure (instability of the truss when both load paths fail)
%This check was hardcoded since there are only two well defined load paths
if E(indexOfStruts(6),(counter+1)) <= 0.01*E(indexOfStruts(6),1)
    stabilityCheck1 = 1
    'strut 12' %Print the failure check, and load it was activated.
    if strutFailureCheck(find(indexOfStruts == 12)) == 0
        strutFailureCheck(find(indexOfStruts == 12)) = 1;
        strutFailureP(find(indexOfStruts == 12)) = P
    end
end
for i = 1:(nStruts - 1)
    if E(indexOfStruts(i),(counter+1)) <= 0.01*E(indexOfStruts(i),1)
        stabilityCheck2 = 1
        temp = sprintf('strut %d', indexOfStruts(i))
        if strutFailureCheck(i) == 0
            strutFailureCheck(i) = 1;
            strutFailureP(i) = P
        end
    end
end
if (stabilityCheck1 == 1) & (stabilityCheck2 == 1)
    failureTemp = 1
    'stability' %Print the failure check, and load it was activated.
    stabilityFailureP = P;
end
stabilityCheck1 = 0;
stabilityCheck2 = 0;


%Node Strength
%Node1
strengthTemp = nodeStressLimits(1);
pressureX = abs(R(2) / (nodeDimensions(1,1) * beamWidth));
pressureY = abs(force(1,counter) / (nodeDimensions(1,2) * beamWidth));
resultant = sqrt( ( abs(force(12,counter))*sin(phi(12)) + abs(force(9,counter))*sin(phi(9)) )^2 +
( abs(force(12,counter))*cos(phi(12)) + abs(force(9,counter))*cos(phi(9)) )^2 );
pressureHyp = resultant / (nodeDimensions(1,3) * beamWidth);
temp = [pressureX,pressureY,pressureHyp];
pressureCheck = max(temp);
if pressureCheck > strengthTemp
    'node 1'
    if nodeFailureCheck(1) == 0
        nodeFailureCheck(1) = 1; %Print the failure check, and load it was activated.
        nodeFailureP(1) = P;
    end
end

%Node2
strengthTemp = nodeStressLimits(2);
pressureX = abs(force(6,counter) / (nodeDimensions(2,1) * beamWidth));
temp = abs([force(1,counter),force(2,counter)]);
pressureY = ( max(temp) ) / (nodeDimensions(2,2) * beamWidth);
pressureHyp = ( abs(force(10,counter)) ) / (nodeDimensions(2,3) * beamWidth);
temp = [pressureX,pressureY,pressureHyp];
pressureCheck = max(temp);
if pressureCheck > strengthTemp
    'node 2'
    if nodeFailureCheck(2) == 0
        nodeFailureCheck(2) = 1; %Print the failure check, and load it was activated.
        nodeFailureP(2) = P;
    end
```

```
end

%Node3
strengthTemp = nodeStressLimits(3);
pressureX = abs(force(7,counter) / (nodeDimensions(3,1) * beamWidth));
temp = abs([force(2,counter),force(3,counter)]);
pressureY = ( max(temp) ) / (nodeDimensions(3,2) * beamWidth);
pressureHyp = ( abs(force(11,counter)) ) / (nodeDimensions(3,3) * beamWidth);
temp = [pressureX,pressureY,pressureHyp];
pressureCheck = max(temp);
if pressureCheck > strengthTemp
    'node 3'
    if nodeFailureCheck(3) == 0
        nodeFailureCheck(3) = 1; %Print the failure check, and load it was activated.
        nodeFailureP(3) = P;
    end
end

%Node3
%node 4 has no actual dimensions in this model.

%Node5
strengthTemp = nodeStressLimits(5);
pressureX = abs(force(6,counter) / (nodeDimensions(5,1) * beamWidth));
pressureY = ( abs(force(4,counter)) ) / (nodeDimensions(5,2) * beamWidth);
pressureHyp = ( abs(force(9,counter)) ) / (nodeDimensions(5,3) * beamWidth);
temp = [pressureX,pressureY,pressureHyp];
pressureCheck = max(temp);
if pressureCheck > strengthTemp
    'node 5'
    if nodeFailureCheck(5) == 0
        nodeFailureCheck(5) = 1; %Print the failure check, and load it was activated.
        nodeFailureP(5) = P;
    end
end

%Node6
strengthTemp = nodeStressLimits(6);
pressureX = abs(force(7,counter) / (nodeDimensions(6,1) * beamWidth));
temp = abs([force(4,counter),force(5,counter)]);
pressureY = ( max(temp) ) / (nodeDimensions(6,2) * beamWidth);
pressureHyp = ( abs(force(10,counter)) ) / (nodeDimensions(6,3) * beamWidth);
temp = [pressureX,pressureY,pressureHyp];
pressureCheck = max(temp);
if pressureCheck > strengthTemp
    'node 6'
    if nodeFailureCheck(6) == 0
        nodeFailureCheck(6) = 1; %Print the failure check, and load it was activated.
        nodeFailureP(6) = P;
    end
end

%Node7
strengthTemp = nodeStressLimits(7);
pressureX = abs(P / (nodeDimensions(7,1) * beamWidth));
pressureY = abs(R(13) / (nodeDimensions(7,2) * beamWidth));
resultant = sqrt( ( abs(force(12,counter))*sin(phi(12)) + abs(force(11,counter))*sin(phi(11)) )^2
+ ( abs(force(12,counter))*cos(phi(12)) + abs(force(11,counter))*cos(phi(11)) +
abs(force(5,counter)) )^2 );
pressureHyp = resultant / (nodeDimensions(7,3) * beamWidth);
temp = [pressureX,pressureY,pressureHyp];
pressureCheck = max(temp);
if pressureCheck > strengthTemp
    'node 7'
    if nodeFailureCheck(7) == 0
        nodeFailureCheck(7) = 1; %Print the failure check, and load it was activated.
        nodeFailureP(7) = P;
    end
end


%Limiter for excessive iterations
if (P + PIncrement) > PStop
    failureTemp = 1 %Print that the program ended because it reached the iteration limit.
    'limiter'
end

%Check to end the main loop and output the results.
if failureTemp == 1
    failure = 1
elseif failureTemp == 0
```

```
    failure = 0;
end
```

Plottruss.m

```
function plottrus(x,y,IEN,plot_truss,plot_nod,lineWidth,lineColour)

nel = size(IEN,2); %Number of elements

%Check if truss plot is requested
if strcmpi(plot_truss,'yes')==1;
    for i = 1:nel
        XX = [x(IEN(1,i)) x(IEN(2,i)) x(IEN(1,i)) ];
        YY = [y(IEN(1,i)) y(IEN(2,i)) y(IEN(1,i)) ];

        line(XX,YY,'LineWidth',lineWidth,'Color',lineColour);hold on;

        %Check if node numbering is requested
        if strcmpi(plot_nod,'yes')==1;
            text(XX(1),YY(1),sprintf('%0.5g',IEN(1,i)));
            text(XX(2),YY(2),sprintf('%0.5g',IEN(2,i)));
        end
    end
    title('Truss Plot');
end
```